INFORMATION TO USERS

This manuscript has been reproduced from the microfilm master. UMI films the text directly from the original or copy submitted. Thus, some thesis and dissertation copies are in typewriter face, while others may be from any type of computer printer.

The quality of this reproduction is dependent upon the quality of the copy submitted. Broken or indistinct print, colored or poor quality illustrations and photographs, print bleedthrough, substandard margins, and improper alignment can adversely affect reproduction.

In the unlikely event that the author did not send UMI a complete manuscript and there are missing pages, these will be noted. Also, if unauthorized copyright material had to be removed, a note will indicate the deletion.

Oversize materials (e.g., maps, drawings, charts) are reproduced by sectioning the original, beginning at the upper left-hand corner and continuing from left to right in equal sections with small overlaps. Each original is also photographed in one exposure and is included in reduced form at the back of the book.

Photographs included in the original manuscript have been reproduced xerographically in this copy. Higher quality 6" x 9" black and white photographic prints are available for any photographs or illustrations appearing in this copy for an additional charge. Contact UMI directly to order.

UMI

A Bell & Howell Information Company
300 North Zeeb Road, Ann Arbor MI 48106-1346 USA
313/761-4700 800/521-0600

Reproduced with permission of the copyright owner. Further reproduction prohibited without permission.

Reproduced with permission of the copyright owner. Further reproduction prohibited without permission.

Reproduced with permission of the copyright owner. Further reproduction prohibited without permission.

ABSTRACT

Title of Dissertation: AEROELASTIC ANALYSIS OF
ADVANCED TILTROTOR AIRCRAFT

Venkataraman Srinivas, Doctor of Philosophy, 1995

Dissertation directed by: Dr. Inderjit Chopra, Professor
Department of Aerospace Engineering

The primary objective of this study is to provide a comprehensive validated analysis for advanced tiltrotor configurations. The first task is to identify the parameters and mechanisms causing tiltrotor instabilities; this is accomplished using a simple rigid-blade analysis. The main task is to develop an analysis, from first principles, capable of modeling complex tiltrotor configurations. Main modeling features are the following: rotor, wing and fuselage modeled as elastic beams with axial, flapwise, lagwise and torsional degrees-of-freedom, large pylon tilts, highly-twisted composite blades including modeling of nonclassical structural effects such as warping and transverse shear, advanced geometry rotor blades and wing with arbitrary sweep, anhedral, twist and planform taper variation along span, modeling of gimballed hubs, and fuselage, full wing-span and twin-rotor modeling. Analysis is performed using the finite-element method in space and time. Solution includes aircraft trim controls, rotor response, blade and hub loads, and system aeroelastic stability. Tiltrotor flight conditions handled include helicopter, conversion, and

Reproduced with permission of the copyright owner. Further reproduction prohibited without permission.

airplane modes. The accuracy of this analysis is established by validating the predictions for trim controls, rotor response, vibratory loads and aeroelastic stability with predictions from other established tiltrotor analyses as well as with test data. Parametric studies are performed to investigate the effects of blade tip sweep, anhedral and planform taper on aeroelastic stability in airplane mode. Studies show that blade tip sweepback of 30° and tip droop of 5°, given to outboard 15% span, result in predicted increases of 95 and 75 knots respectively in flutter speeds. However, large increases in power requirements in airplane mode are predicted for the 30° sweepback case. These results show that considerable gains can be achieved in tiltrotor aeroelastic performance by tailoring blade tip shapes, but the new configurations need to be designed for lower power requirements as well. Aeroelastic stability studies performed by modeling the complete configuration show that symmetric wing modes are more susceptible to instability than are antisymmetric wing modes. Inclusion of wing antisymmetric modes in the analysis does not change the flutter speed predictions for the configuration studied.

Reproduced with permission of the copyright owner. Further reproduction prohibited without permission.

Reproduced with permission of the copyright owner. Further reproduction prohibited without permission.

AEROELASTIC ANALYSIS OF ADVANCED TILTROTOR AIRCRAFT

by
Venkataraman Srinivas

Dissertation Submitted to the Faculty of the Graduate School
of The University of Maryland in partial fulfilment
of the requirements for the degree of
Doctor of Philosophy
1995

Advisory Committee:

Professor Inderjit Chopra, Chairman/Advisor
Associate Professor Roberto Celi
Associate Professor J. Gordon Leishman
Assistant Professor James D. Baeder
Assistant Professor Norman M. Wereley
Assistant Professor Balakumar Balachandran, Dean's Representative

Reproduced with permission of the copyright owner. Further reproduction prohibited without permission.

UMI Number: 9637730

UMI Microform 9637730
Copyright 1996, by UMI Company. All rights reserved.

This microform edition is protected against unauthorized copying under Title 17, United States Code.

UMI
300 North Zeeb Road
Ann Arbor, MI 48103

Reproduced with permission of the copyright owner. Further reproduction prohibited without permission.

Reproduced with permission of the copyright owner. Further reproduction prohibited without permission.

Reproduced with permission of the copyright owner. Further reproduction prohibited without permission.

Acknowledgments

I feel very fortunate to have had this opportunity to work with Dr.Chopra, my dissertation advisor. He has, through the years, given me and this work a definite sense of direction. I would like to thank him for all his support, encouragement and advise that made this work possible. I thank my committee members - Professors Celi, Leishman, Baeder, Wereley and Balachandran - for reviewing my dissertation and providing helpful suggestions. My special thanks to Dr.Mark Nixon for his role in getting me started on this problem and for being a great help during the entire duration of my research. I thank the Army Research Office for providing financial support for this research.

Many of my colleagues at the Rotorcraft Center provided valuable technical and moral support during my graduate school years. I thank Ashish and Ranjan for their invaluable support, in numerous instances, during the course of my study. I would also like to thank Judah, Vineet, Chris, Gil, Swami, Anita, Pierre, Farhan, Anne and others for their support and friendship. Many thanks are due to my friends, outside of school, who have provided much needed encouragement and support off-the-field.

Most importantly, I thank my family - my parents and my sister - for their unwavering support and encouragement that made me embark on this journey through graduate school. This one's for you!

Reproduced with permission of the copyright owner. Further reproduction prohibited without permission.

Table of Contents

Section			Page
Chapter 1: Introduction			**1**
1.1	Problem Statement		1
1.2	Background		4
	1.2.1	Advantages of the Tiltrotor	4
	1.2.2	Tiltrotor Development	7
	1.2.3	Tiltrotor Design Considerations	10
	1.2.4	Tiltrotor Whirl Flutter	13
1.3	Motivation		15
1.4	Literature Survey		16
	1.4.1	Tiltrotor Aeroelastic Research	16
	1.4.2	Research on Advanced Geometry Bladed Rotors	29
1.5	Current Work		33
	1.5.1	Objectives	33
	1.5.2	Scope of Present Research	34
1.6	Organization of the Dissertation		36
Chapter 2: Rigid Blade Tiltrotor Parametric Study			**41**
2.1	Frequency and Damping Characteristics of the Baseline System		42
2.2	Rotor Frequency		43

Reproduced with permission of the copyright owner. Further reproduction prohibited without permission.

2.3 Wing Sweep 47
2.4 Lock Number 48
2.5 Pitch-Flap Coupling 49
2.6 Pitch-Lag Coupling 50

Chapter 3: Elastic Blade Tiltrotor Model **66**

3.1 Tiltrotor Model 67
3.1.1 Reference Frames 67
3.1.2 Advanced Geometry Blade Transformation 71
3.1.3 Ordering Scheme 81
3.2 Equations of Motion 82
3.2.1 Derivation of Strain Energy 83
3.2.2 Derivation of Kinetic Energy 91
3.2.3 Structural Contributions to Mass, Damping and Stiffness Matrices 97
3.3 Aerodynamic Modeling 101
3.3.1 Local Blade Velocities 103
3.3.2 Blade Airloads 105
3.3.3 Work done by the Blade Airloads 109
3.3.4 Wing Aerodynamics 120

Chapter 4: Tiltrotor Analysis **124**

4.1 Free Vibration Analysis 124
4.2 Coupled Trim 126

Reproduced with permission of the copyright owner. Further reproduction prohibited without permission.

4.2.1 Vehicle Trim Analysis 126
4.2.2 Blade Response Analysis 131
4.2.3 Finite Element in Time 132
4.2.4 Inflow Modeling 135
4.2.5 Hub Loads 139
4.2.6 Trim Control Updates 141
4.2.7 Convergence of Coupled Trim 143
4.3 Stability Analysis 144
4.3.1 Rotor Equations 144
4.3.2 Wing Equations 146
4.3.3 Advanced Geometry Wing 147
4.3.4 Drive Train Dynamics 148
4.3.5 Analysis Procedure 150
4.3.6 Fixed Coordinate Transformation 150
4.3.7 Floquet Theory 152
4.3.8 Constant Coefficient Method 155

Chapter 5: Validation of Analysis **159**

5.1 Rigid Blade Analysis 159
5.1.1 Comparison with Elastic Blade Analysis 161
5.1.2 Comparison with Test Data 163
5.2 Elastic Blade Analysis 164
5.2.1 Trim Controls and Rotor Response 164

Reproduced with permission of the copyright owner. Further reproduction prohibited without permission.

5.2.2 Rotor Loads 166

5.2.3 Stability Results 167

Chapter 6: Parametric Studies **203**

6.1 Frequencies 204

6.2 Blade Response and Trim 206

6.2.1 Convergence Study 209

6.3 Stability at Cruise Speed 210

6.4 Flutter Speed Studies 214

6.5 Basic Performance Studies 217

6.5.1 Effect of Wake Modeling 221

6.6 Off-design Conditions 221

Chapter 7: Fuselage Modeling **263**

7.1 Wing Normal Mode Reduction 263

7.1.1 Wing Free Vibration 264

7.1.2 Implementation of Stability Analysis 264

7.2 Implementation of Fuselage Model 266

7.2.1 Free Vibration Analysis 268

7.2.2 Stability Analysis 269

7.2.3 Twin-Rotor Modeling 272

7.3 Results 275

7.3.1 Rigid Body Modes 275

7.3.2 Validation of Stability Predictions 278

Reproduced with permission of the copyright owner. Further reproduction prohibited without permission.

7.3.3 Parametric Studies 279

Chapter 8: Summary and Conclusions **307**

8.1 Rigid Blade Tiltrotor Analysis 308

8.2 Formulation of an Elastic Blade Tiltrotor Analysis 309

8.3 Validation Studies 310

8.4 Parametric Studies 313

8.5 Fuselage Modeling 316

8.6 Recommendations for Future Work 318

Appendix A: Rigid Blade Tiltrotor Model **322**

A.1 Analytical Model 322

A.1.1 Rotor and Hub Structural Model 323

A.1.2 Rotor Aerodynamics 327

A.1.3 Wing Structural Model 335

A.1.4 Wing Aerodynamics 337

A.1.5 Coupling of the Wing and Rotor Systems 340

A.2 Listing of Matrices 342

A.2.1 Listing of the Rotor/Wing Matrices 342

A.2.2 Listing of the Wing Element Matrices 352

Appendix B: Listing of the T_{FL} Matrix **365**

Appendix C: Rigid Blade Tiltrotor Trim **379**

C.1 Estimation of Fuselage Angle of Attack and Rotor Thrust 380

Reproduced with permission of the copyright owner. Further reproduction prohibited without permission.

C.2 Derivation of Blade and Hub Forces 382

C.3 Hub Force and Blade Moment Expressions 384

C.4 Estimation of Rotor Collective Pitch 391

C.5 Coupled Rotor/Airframe and Flapping Blade Analysis 391

Appendix D: Swept Tip Blade **394**

Bibliography **398**

Reproduced with permission of the copyright owner. Further reproduction prohibited without permission.

List of Tables

Table		Page
2.1	Frequencies of the baseline system	51
2.2	Baseline rotor system parameters	52
2.3	Baseline rotor blade inertia parameters	53
2.4	Baseline wing parameters	54
3.1	Nondimensionalization of physical quantities	123
5.1	XV-15 Aircraft Configuration - Loads Data	170
5.2	XV-15 Aircraft Configuration - Stability Data	171
6.1	Baseline system	223
7.1	XV-15 fuselage properties - 2 finite elements used	287

Reproduced with permission of the copyright owner. Further reproduction prohibited without permission.

List of Figures

Figure		Page
1.1	Tiltrotor in airplane mode	38
1.2	Hover efficiency as a function of disk loading for various VTOL configurations	39
1.3	Mechanism of tiltrotor whirl flutter	40
2.1	Rotor lag frequency variation with velocity	55
2.2	Baseline configuration frequencies	56
2.3	Baseline configuration damping	57
2.4	Frequencies (lag frequency $\nu_\zeta = 0.9$ x baseline ν_ζ)	58
2.5	Damping (lag frequency $\nu_\zeta = 0.9$ x baseline ν_ζ)	59
2.6	Flutter velocity variation with flap frequency (ν_β) factor	60
2.7	Flutter velocity variation with lag frequency (ν_ζ) factor	61
2.8	Flutter velocity variation with wing sweep angle	62
2.9	Flutter velocity variation with rotor Lock number (γ) factor	63
2.10	Flutter velocity variation with pitch-flap coupling	64
2.11	Flutter velocity variation with pitch-lag coupling	65
3.1	Coordinate systems for the advanced geometry blade	121
3.2	Wing reference frames	122
4.1	Forces acting on the tiltrotor in free flight	157
4.2	Azimuthal discretization into finite elements	158

Reproduced with permission of the copyright owner. Further reproduction prohibited without permission.

5.1 Rigid rotor model: Frequency variation with airspeed for zero precone case . . . 172
5.2 Rigid rotor model: Damping variation with airspeed for zero precone case . . . 173
5.3 Rigid rotor model: Root locus plot of eigenvalues with airspeed for zero precone case . . . 174
5.4 Rigid rotor model: Frequency variation with airspeed for 2.5^o precone case . . . 175
5.5 Rigid rotor model: Damping variation with airspeed for 2.5^o precone case . . . 176
5.6 Elastic rotor model: Frequency variation with airspeed for 2.5^o precone case . . . 177
5.7 Elastic rotor model: Damping variation with airspeed for 2.5^o precone case . . . 178
5.8 Rigid rotor model: Root locus plot of eigenvalues with airspeed for 2.5^o precone case . . . 179
5.9 Elastic rotor model: Root locus plot of eigenvalues with airspeed for 2.5^o precone case . . . 180
5.10 Effect of pitch-lag coupling on (wing beam mode) flutter speed . . . 181
5.11 Rigid rotor model: Predicted wing beam mode damping - effect of rotor precone . . . 182
5.12 Comparison of predicted flutter velocity variation with pitch-flap coupling (V-22 1/5th scale model) . . . 183

Reproduced with permission of the copyright owner. Further reproduction prohibited without permission.

5.13 Comparison of predicted wing beam mode damping variation with airspeed (V-22 1/5th scale model) 184
5.14 XV-15 aircraft pitch attitude variation with airspeed 185
5.15 XV-15 rotor collective variation with airspeed 186
5.16 XV-15 rotor longitudinal cyclic control variation with airspeed . . . 187
5.17 XV-15 rotor lateral cyclic control variation with airspeed 188
5.18 XV-15 rotor coning variation with airspeed 189
5.19 XV-15 rotor longitudinal flapping variation with airspeed 190
5.20 XV-15 rotor lateral flapping variation with airspeed 191
5.21 XV-15 rotor torque variation with airspeed 192
5.22 XV-15 oscillatory blade beam bending moment variation with airspeed, 35% radial location 193
5.23 XV-15 oscillatory blade chord bending moment variation with airspeed, 35% radial location 194
5.24 XV-15 oscillatory blade torsion moment variation with airspeed, 35% radial location 195
5.25 Validation of wing symmetric beam mode frequencies for the XV-15 196
5.26 Validation of wing symmetric beam mode damping for the XV-15 . 197
5.27 Validation of wing symmetric chord mode frequencies for the XV-15 198
5.28 Validation of wing symmetric chord mode damping for the XV-15 . 199
5.29 Validation of wing symmetric torsion mode frequencies for the XV-15 200
5.30 Validation of wing symmetric torsion mode damping for the XV-15 201

Reproduced with permission of the copyright owner. Further reproduction prohibited without permission.

5.31 Comparison of XV-15 wing beam mode damping with full scale test data 202
6.1 Blade pretwist distribution 224
6.2 Advanced tip configurations (shaded area denotes typical section) . 225
6.3 Swept tip and shear tip configurations (c = blade chord, shaded area denotes typical section) 226
6.4 First coupled blade mode shape of baseline configuration (V = 240 knots) 227
6.5 Second coupled blade mode shape of baseline configuration (V = 240 knots) 228
6.6 Third coupled blade mode shape of baseline configuration (V = 240 knots) 229
6.7 Fourth coupled blade mode shape of baseline configuration (V = 240 knots) 230
6.8 Fifth coupled blade mode shape of baseline configuration (V = 240 knots) 231
6.9 Effect of blade tip sweep (outboard 15% span) on rotating natural frequencies ($\theta_0 = 0$) 232
6.10 Effect of blade tip anhedral (outboard 15% span) on rotating natural frequencies ($\theta_0 = 0$) 233
6.11 Effect of blade tip planform taper (outboard 15% span) on rotating natural frequencies ($\theta_0 = 0$, constant thrust-weighted solidity) . . . 234

Reproduced with permission of the copyright owner. Further reproduction prohibited without permission.

6.12 Tip response $(v/R, w/R, \phi)$ variation with blade tip sweep (outboard 15% span, $V = 240$ knots, $C_T/\sigma = 0.01$) 235

6.13 Torsion response along blade span ($V = 240$ knots, $C_T/\sigma = 0.01$) . 236

6.14 Tip response $(v/R, w/R, \phi)$ variation with blade tip anhedral (outboard 15% span, $V = 240$ knots, $C_T/\sigma = 0.01$) 237

6.15 Torsion response along blade span ($V = 240$ knots, $C_T/\sigma = 0.01$) . 238

6.16 Tip response $(v/R, w/R, \phi)$ variation with blade tip planform taper (outboard 15% span, $V = 240$ knots, $C_T/\sigma = 0.01$, constant thrust-weighted solidity) 239

6.17 Torsion response along blade span ($V = 240$ knots, $C_T/\sigma = 0.01$) . 240

6.18 Collective pitch variation ($V = 240$ knots, $C_T/\sigma = 0.01$) 241

6.19 Convergence of blade torsional response for 30° forward sweep for blade tip (outboard 15% span, $C_T/\sigma = 0.01$, $V = 240$ knots) with increased number of spanwise finite elements and increased number of blade modes 242

6.20 Effect of blade tip sweep (outboard 15% span) on blade damping ($V = 240$ knots, $C_T/\sigma = 0.01$) 243

6.21 Effect of blade tip sweep (outboard 15% span) on wing damping ($V = 240$ knots, $C_T/\sigma = 0.01$) 244

6.22 Effect of blade tip anhedral (outboard 15% span) on blade damping ($V = 240$ knots, $C_T/\sigma = 0.01$) 245

6.23 Effect of blade tip anhedral (outboard 15% span) on wing damping ($V = 240$ knots, $C_T/\sigma = 0.01$) 246

Reproduced with permission of the copyright owner. Further reproduction prohibited without permission.

6.24 Effect of blade tip planform taper (outboard 15% span) on blade damping (V = 240 knots, C_T/σ = 0.01, constant thrust-weighted solidity) 247

6.25 Effect of blade tip planform taper (outboard 15% span) on wing damping (V = 240 knots, C_T/σ = 0.01, constant thrust-weighted solidity) 248

6.26 Effect of velocity on stability for straight blade (C_T/σ = 0.01) . . . 249

6.27 Effect of velocity on stability for 30° backward sweep for blade tip (outboard 15% span, C_T/σ = 0.01) 250

6.28 Effect of velocity on stability for 30° forward sweep for blade tip (outboard 15% span, C_T/σ = 0.01) 251

6.29 Effect of velocity on stability for 5° droop for blade tip (outboard 15% span, C_T/σ = 0.01) 252

6.30 Effect of velocity on stability for 5° anhedral for blade tip (outboard 15% span, C_T/σ = 0.01) 253

6.31 Effect of velocity on stability for 3:1 planform taper for blade tip (outboard 15% span, C_T/σ = 0.01, constant thrust-weighted solidity) 254

6.32 Rotor power requirements for outboard 15% tip sweep (C_T/σ = 0.01, V = 240 knots) 255

6.33 Variation of angle-of-attack along blade span for a straight blade configuration (C_T/σ = 0.01, V = 240 knots) 256

Reproduced with permission of the copyright owner. Further reproduction prohibited without permission.

6.34 Contribution of a unit lift force to thrust, drag and power for a straight blade configuration ($C_T/\sigma = 0.01$, $V = 240$ knots) 257

6.35 Variation of angle-of-attack along blade span for unswept blade, 30 deg. sweep forward for blade tip and 30 deg. sweep backward for blade tip ($C_T/\sigma = 0.01$, $V = 240$ knots) 258

6.36 Propeller efficiency plot for outboard 15% tip sweep ($C_T/\sigma = 0.01$, $V = 240$ knots) 259

6.37 Rotor power requirements for outboard 15% tip anhedral ($C_T/\sigma = 0.01$, $V = 240$ knots) 260

6.38 Propeller efficiency plot for outboard 15% tip anhedral ($C_T/\sigma = 0.01$, $V = 240$ knots) 261

6.39 Comparison of predicted rotor torque using different inflow models ($C_T/\sigma = 0.01$) 262

7.1 Schematic of finite element model of fuselage and wing showing number of elements used for each component 284

7.2 Assembly of wing and fuselage 15 dof elements showing global displacement numbering (example with 2 elements for wing semi-span and 2 elements for fuselage, 1 fore and 1 aft) - schematic, not drawn to scale 285

7.3 Right-handed and left-handed reference frames used for the right and left rotor systems respectively 286

7.4 First fuselage/wing rigid body mode 288

7.5 Second fuselage/wing rigid body mode 289

Reproduced with permission of the copyright owner. Further reproduction prohibited without permission.

7.6 Third fuselage/wing rigid body mode 290
7.7 Fourth fuselage/wing rigid body mode 291
7.8 Fifth fuselage/wing rigid body mode 292
7.9 Sixth fuselage/wing rigid body mode 293
7.10 Validation of wing antisymmetric beam mode frequencies for the XV-15 294
7.11 Validation of wing antisymmetric beam mode damping for the XV-15 295
7.12 Validation of wing antisymmetric chord mode frequencies for the XV-15 296
7.13 Validation of wing antisymmetric chord mode damping for the XV-15 297
7.14 Validation of wing antisymmetric torsion mode frequencies for the XV-15 298
7.15 Validation of wing antisymmetric torsion mode damping for the XV-15 299
7.16 Effect of velocity on antisymmetric wing mode stability for straight blade (C_T/σ=0.01) 300
7.17 Effect of velocity on antisymmetric wing mode stability for 30° backward sweep for blade tip (outboard 15% span, C_T/σ=0.01) 301
7.18 Effect of velocity on antisymmetric wing mode stability for 30° forward sweep for blade tip (outboard 15% span, C_T/σ=0.01) 302

Reproduced with permission of the copyright owner. Further reproduction prohibited without permission.

7.19 Effect of velocity on antisymmetric wing mode stability for 5° droop for blade tip (outboard 15% span, C_T/σ=0.01) 303

7.20 Effect of velocity on antisymmetric wing mode stability for 5° anhedral for blade tip (outboard 15% span, C_T/σ=0.01) 304

7.21 Effect of velocity on antisymmetric wing mode stability for 3:1 planform taper for blade tip (outboard 15% span, C_T/σ=0.01) 305

7.22 Effect of velocity on antisymmetric wing mode stability for straight blade neglecting all six fuselage/wing rigid body modes (C_T/σ=0.01) 306

A.1 Coordinate systems for rotor and wing 361

A.2 Velocity and force components on a typical blade section 362

A.3 Wing element degrees-of-freedom (v, w and ϕ are lagwise, flapwise and torsional displacements respectively) 363

A.4 Schematic of the swept wing configuration 364

Reproduced with permission of the copyright owner. Further reproduction prohibited without permission.

Nomenclature

(quantitites nondimensional unless otherwise specified)

A	blade cross-sectional area, sq.ft.
$\hat{A}$	stability matrix
a	reference lift-curve slope, /rad
$a.c.$	aerodynamic center
C	damping matrix
c_d	section drag coefficient
C_H	inplane force coefficient
c_l	section lift coefficient
c_{l_α}	lift-curve slope, /rad
c_m	airfoil section pitching moment coefficient
C_{M_x}	rotor rolling moment coefficient
C_{M_y}	rotor pitching moment coefficient
C_Q	torque coefficient, power coefficient
C_T	thrust coefficient
C_Y	side-force coefficient
c	blade chord
$c.g.$	center of gravity
D	drag force per unit length
E	Young's modulus, lb/sq.ft.
EA	extensional stiffness
EI_b	wing section beamwise stiffness

Reproduced with permission of the copyright owner. Further reproduction prohibited without permission.

EI_c	local lag bending stiffness, wing section chordwise stiffness
EI_f	local flap bending stiffness
EET	extension-twist coupling stiffness
ETC	twist chordwise-bending coupling stiffness
ETF	twist flapwise-bending coupling stiffness
EES_c	extension chordwise-shear coupling stiffness
EES_f	extension flapwise-shear coupling stiffness
EFS_c	flapwise-bending chordwise-shear coupling stiffness
ECS_f	chordwise-bending flapwise-shear coupling stiffness
$e.a.$	elastic axis
e_A	chordwise offset of tension axis ahead of elastic axis
e_d	chordwise offset of aerodynamic center behind elastic axis
e_g	chordwise offset of center of gravity ahead of elastic axis
F	forcing term
F_r	radial shear force
F_x	tangential shear force
F_z	normal shear force
$\frac{f}{A}$	fuselage flat plate area
G	shear modulus, lb/sq.ft.
GA_c	chordwise shear stiffness
GA_f	flapwise shear stiffness
GJ	wing section torsional stiffness
H	rotor inplane shear force, shape function matrix

Reproduced with permission of the copyright owner. Further reproduction prohibited without permission.

h	pylon height
I_b	blade flap inertia about axis of rotation, slug sq.ft.
I_β	blade flap inertia about flap hinge
$I^\star_{\beta}$	blade cyclic mode flap inertia
$I^\star_{\beta_0}$	blade collective mode flap inertia
I_ζ	blade lag inertia about lag hinge
$I^\star_{\zeta}$	blade cyclic mode lag inertia
$I^\star_{\zeta_0}$	blade collective mode lag inertia
$I^\star_{\beta\alpha}$	blade pylon-coupled flap inertia
$I^\star_{\zeta\alpha}$	blade pylon-coupled lag inertia
$I^\star_{0}$	rotor speed perturbation inertia
$I^\star_{\zeta_0\alpha}$	rotor pylon-coupled collective lag inertia
$[J]$	Jacobian matrix
K	stiffness matrix
k	stress-strain stiffness matrix term
k_m	torsional mass radius of gyration
k_{m_1}	flapwise mass radius of gyration
k_{m_2}	chordwise mass radius of gyration
k_β	kinematic pitch-flap coupling
k_ζ	kinematic pitch-lag coupling
L	aerodynamic force, lift force
L_1	projected length along blade spanwise direction
L_2	projected length along blade chordwise direction

Reproduced with permission of the copyright owner. Further reproduction prohibited without permission.

L_3	projected length along normal direction to blade
M	aerodynamic moment, mass matrix, Mach number
M_x	rotor hub rolling moment
M_y	rotor hub pitching moment
m	mass per unit length, blade number
N_b	number of blades
n	number of harmonics
n_1	number of finite elements used to model wing semi-span
n_2	number of finite elements used to model part of fuselage ahead of the wing attachment point
n_3	number of finite elements used to model part of fuselage aft of the wing attachment point
$\hat{p}$	vector of modal degrees-of-freedom
Q	rotor torque, lb ft.
Q'	material stiffness, lb/sq.ft.
$\hat{Q}$	vector of global displacements for complete aircraft
q	dynamic pressure, lb/sq.ft.
$\hat{q}$	vector of discretized blade displacements
R	rotor radius (ft.), blade radial force
r	dimensional radial location, ft.
S	strain-stress compliance matrix, planform area (sq.ft.)
$S^{\star}_{\beta}$	blade cyclic mode first flap moment
$S^{\star}_{\beta_0}$	blade collective mode first flap moment

Reproduced with permission of the copyright owner. Further reproduction prohibited without permission.

$S^{\star}_{\zeta}$	blade first lag mass moment
$\vec{R}$	position vector
s	local coordinate
T	kinetic energy, rotor thrust (lb), transformation matrix
T_{FL}	transformation matrix for blade loads from undeformed reference frame into nonrotating frame
t	time
$t.a.$	tension axis
U	elastic strain energy, total velocity
u	axial geometric displacement, velocity
u_e	axial elastic displacement
u_P	velocity normal to rotor disk
u_R	radial velocity (across span)
u_T	tangential velocity
$\hat{u}$	vector of blade displacements
V	airspeed, strain energy
V^*	forward flight speed (nondimensionalized by cruise tip speed)
V_f^*	flutter speed (nondimensional)
$\vec{V}$	velocity
v	chordwise (lead-lag) displacement
v_s	shear-related lag displacement
W	work done, weight of aircraft (lb)
w	beamwise (flap) displacement

Reproduced with permission of the copyright owner. Further reproduction prohibited without permission.

w_s	shear-related flap displacement
x	longitudinal coordinate (nondimensional)
$\hat{x}_h$	vector of hub displacements
x_h	longitudinal translation of wing-tip, positive aft
x_t	longitudinal offset of horizontal tail e.a. from aircraft c.g.
x_w	longitudinal offset of wing e.a. from aircraft c.g.
$\hat{Y}$	system state vector for stability analysis
Y_w	wing semi-span
y_h	lateral translation of wing-tip, positive towards right
z_h	vertical translation of wing-tip, positive up
z_t	vertical offset of horizontal tail e.a. from aircraft c.g.
z_w	vertical offset of wing e.a. from aircraft c.g.

Greek Symbols

(all angles are in radians)

α	angle-of-attack
α_h	pitch rotation, positive nose-down
α_p	rotor pylon angle, 0° for helicopter mode and 90° for airplane mode
α_x	pylon yaw rotation
α_y	pylon pitch rotation
α_z	pylon roll rotation
β	blade flap angle
β_0	rotor collective flap angle

Reproduced with permission of the copyright owner. Further reproduction prohibited without permission.

β_{1c}	rotor longitudinal flapping
β_{1s}	rotor lateral flapping
β_G	gimbal angle in rotating frame
β_{GC}	gimbal angle (cosine) in fixed frame
β_{GS}	gimbal angle (sine) in fixed frame
β_p	blade precone angle
γ	Lock number
δ	variation
ϵ	strain, small quantity
ζ	damping ratio (% of critical), blade lag angle
ζ_0	rotor collective lag angle
ζ_{1c}	rotor fixed-frame longitudinal lag angle
ζ_{1s}	rotor fixed-frame lateral lag angle
ζ_h	yaw rotation, positive counter-clockwise (seen from above)
η, ζ	blade cross-sectional coordinates
η_r	distance from elastic axis to 3/4 chord
θ	blade section pitch angle
θ_0	blade time-varying pitch control
θ_{tw}	blade twist
θ_{1c}	rotor lateral cyclic input
θ_{1s}	rotor longitudinal cyclic input
θ_{75}	rotor collective pitch input at 75% blade span
Λ	wing sweep angle, transformation matrix

Reproduced with permission of the copyright owner. Further reproduction prohibited without permission.

Λ_1	sweep, positive forward
Λ_2	anhedral, positive up
Λ_3	pretwist, positive nose-up
λ_T	warping function
λ_i	induced inflow at the rotor disk
μ	advance ratio ($V/\Omega R$)
ν_β	rotating flap frequency (per rev)
ν_ζ	rotating lag frequency (per rev)
$\hat{\xi}$	vector of temporal discrete displacements
π	ratio of circumference of a circle to its diameter
ρ	air density, material density (slug/cubic ft.)
σ	stress (lb/sq.ft.), rotor solidity (thrust-weighted)
σ_x	rotor solidity (based on local chord)
Φ	modal matrix, Floquet state transition matrix
ϕ	torsional displacement
$\hat{\phi}$	elastic torsion
ϕ_h	roll rotation, positive for top of pylon (in hover) moving towards right
ψ	blade azimuth angle
Ω	rotational speed of rotor, rad/sec
ω	blade rotating frequency

Reproduced with permission of the copyright owner. Further reproduction prohibited without permission.

Superscripts and Subscripts

$(\hat{..})$	unit vector
$(..)'$	derivative with respect to longitudinal coordinate
$(..)''$	second derivative with respect to longitudinal coordinate
$(\dot{..})$	time derivative of quantity
$(\overset{*}{..})$	derivative w.r. to azimuth angle
$(\overset{**}{..})$	second derivative w.r. to azimuth angle
$(..)^A$	aerodynamic term
$(..)^G$	global matrix or vector
$(..)^H$	fixed-frame hub load
$(..)^S$	structural term
$(..)^T$	transpose of a vector or matrix
$(..)_0$	trim value, initial value
$(..)_1$	corresponding to the right half of the aircraft configuration
$(..)_2$	corresponding to the left half of the aircraft configuration
$(..)_b$	blade term
$(..)_{bb}$	blade-blade coupling term
$(..)_{bh}$	blade-hub coupling term
$(..)_f$	fuselage term, final value
$(..)_{ff}$	fuselage matrix
$(..)_h$	hub term
$(..)_{hb}$	hub-blade coupling term
$(..)_{hh}$	hub-hub coupling term

Reproduced with permission of the copyright owner. Further reproduction prohibited without permission.

$(..)_{hr}$	hub-rotor coupling matrix
$(..)_i$	intermediate set of displacements including gimbal displacements and rotor free-rotation (for windmilling condition)
$(..)_{NL}$	nonlinear term
$(..)_r$	rotor term
$(..)_{r_1}$, $(..)_{r_2}$	right and left rotors respectively
$(..)_{rh}$	rotor-hub coupling matrix
$(..)_{rr}$	rotor matrix
$(..)_{rw}$	rotor-wing coupling matrix
$(..)_t$	horizontal tail term
$(..)_w$	wing term
$(..)_{wr}$	wing-rotor coupling matrix
$(..)_{ww}$	wing matrix
$(..)_{w_1}$, $(..)_{w_2}$	right and left wing semi-spans respectively
$(..)^{\star}_{\beta}$	flap velocity term
$(..)^{\star}_{\zeta}$	lag velocity term
$(..)_\theta$	pitch control term
$(..)_\lambda$	inflow velocity term
$(..)_\mu$	hub inplane velocity term

Reproduced with permission of the copyright owner. Further reproduction prohibited without permission.

Chapter 1

Introduction

1.1 Problem Statement

Fixed-wing aircraft are capable of efficient long-range high-speed flight. Helicopters, although not capable of high-speed flight comparable to that of fixed-wing aircraft, have VTOL (Vertical Take-Off and Landing) capability. The demand for machines that possessed the combined capabilities of fixed-wing airplanes and helicopters translated into the tiltrotor concept. For reasons explained in a following section, tiltrotor aircraft have a unique ability to combine efficient VTOL capability with efficient long-range cruise performance. In operation, the tiltrotor takes off vertically like a helicopter. Then the wing-tip mounted rotor systems are pivoted forward to achieve high speed axial flight capability. Figure 1.1 shows a tiltrotor in the airplane mode of operation.

Along with the considerations of increased VTOL and efficient long-range cruise performance, new considerations such as tiltrotor aeroelastic instabilities, rotor-wing aerodynamic interference particularly in vertical flight, gust response characteristics and control characteristics in transition flight have to be addressed. There also arises a higher level of complexity in predicting these aeroelastic instability

Reproduced with permission of the copyright owner. Further reproduction prohibited without permission.

mechanisms. Present tiltrotor configurations incorporate the use of a gimballed rotor system. Such a rotor behaves like an articulated rotor in flap mode and like a hingeless rotor in lag mode. The gimbal mechanism plays an important role in transferring the rotor forces to the pylon and, therefore, has a considerable influence on the stability of the system.

Tiltrotor aircraft, like all other types of aircraft, are susceptible to certain types of aeroelastic instabilities. These instabilities are caused by complex interactions between aerodynamic, inertial, and elastic forces from the rotor blades and the fuselage/wing [1]-[3]. The instability mechanisms are directly influenced by various rotor and wing design parameters. Conventional rotary-wing aeroelasticity problems such as pitch-flap, flap-lag, ground resonance and air resonance instabilities, and fixed-wing instabilities such as wing flutter and divergence should be avoided in the design phase. In addition, there exist unique instability problems in tiltrotors that arise from aeroelastic coupling between the rotor forces and wing displacements. One such instability occurs in high speed axial flight and is referred to as tiltrotor whirl flutter. This is caused by the large in-plane rotor forces acting to destabilize the wing, and has been the subject of great interest over the years [4]-[39]. In this context, the stability characteristics of advanced tiltrotors with features such as advanced geometry blades, composite coupled blades, kinematic blade couplings, and modern rotor hub designs should be examined.

The rotor blades, gimbal, pylon and wing have to be modeled in sufficient detail to predict the occurrence of aeroelastic instabilities accurately. The presence of the gimbal and wing degrees-of-freedom increases the complexity of the problem.

Reproduced with permission of the copyright owner. Further reproduction prohibited without permission.

The governing equations are nonlinear coupled differential equations in the spatial and temporal coordinates. Many researchers have contributed to the development of the coupled set of rotor equations [40]-[46]. The blade, gimbal, and wing equations have been derived under various simplifying assumptions for the tiltrotor configuration [5], [35]-[39]. Solution of these equations provides the rotor and wing response for any given flight condition. Trim is the estimation of rotor controls and vehicle orientation for steady flight in any flight condition. The tiltrotor aircraft equilibrium equations, which are used in the trim procedure, are very complex as they cover both helicopter and airplane modes, and encompass hover, transition, and forward flight conditions. Therefore, the trim procedure covering all flight conditions becomes quite involved.

Modification of the above analyses for advanced configurations with composites, advanced geometry blades, kinematic couplings and bearingless rotors adds a further level of complexity to an already complex problem. Blade kinematic couplings, such as pitch-flap and pitch-lag couplings, modify the rotor response and also alter the aeroelastic stability of the rotor system. These couplings can be treated analytically with otherwise uncoupled rigid blade models or by using elastic beam models for the blade. Composite materials have higher strength-to-weight and stiffness-to-weight ratios and better fatigue characteristics than conventional metals and are, therefore, now widely used in blade construction [1]. They also provide the opportunity for tailoring the blade structural properties by introducing distributed couplings such as pitch-flap, pitch-lag, and extension-torsion coupling. These structural couplings have a substantial influence on rotor dynamics similar

Reproduced with permission of the copyright owner. Further reproduction prohibited without permission.

to those of kinematic couplings. Advanced geometry rotor blades utilizing blade distributed twist, sweep, anhedral and planform taper along the blade span can help modify the vibratory forces on the rotor, delay drag divergence and minimize induced power losses.

The afore mentioned tiltrotor configurations are being investigated by designers today; it is therefore imperative that a good robust design and analysis tool be developed for handling complex tiltrotor configurations and predicting tiltrotor aeroelastic phenomena accurately. Although adequate analyses exist for modeling tiltrotor aeroelastic behavior, these analyses are not equipped to model advanced geometry composite-coupled tiltrotors with bearingless and elastomeric hubs.

1.2 Background

1.2.1 Advantages of the Tiltrotor

The tiltrotor is an efficient hovering aircraft because of its relatively low disk loading compared to most other VTOL configurations (except for the helicopter). In Figure 1.2, the hover efficiency is shown versus the disk loading for several V/STOL configurations [47]. Low disk loading usually results in low tip-speeds (due to large disk area generating the same thrust) and low downwash velocities producing low noise levels and power requirements and high fuel efficiency. The figure provides a comparison of the hovering efficiencies of different VTOL configurations.

The conventional helicopter is most efficient for vertical flight, but it is limited in range and forward flight velocity. Compound helicopters and stopped-rotor configurations such as the X-wing are expected to achieve higher forward speeds, but

Reproduced with permission of the copyright owner. Further reproduction prohibited without permission.

suffer from performance deficiencies, particularly in hover and low speed flight. Thus, the compound helicopter development has not had great success so far primarily because it is, at best, a marginal improvement over the conventional helicopter configuration. For the compound configuration, auxiliary propulsion devices and stub-wing surfaces are usually added, thus achieving a higher-speed capability but with significant performance trade-offs, particularly in hover. The X-wing configuration has an additional weight penalty and complexity associated with the circulation control airfoil system. The vectored-thrust fixed-wing airplane (such as the Harrier) and the fan-in-wing (Lift Fan) are VTOL vehicles that have found limited appeal, primarily for military applications. These concepts are not suited for civilian applications due to economic viability. Also, these high speed aircraft do not compete for the same missions as tiltrotors.

The Tiltwing Concept

In the recent past, the tiltwing was considered a viable alternative to the tiltrotor. The tiltwing configuration involves a fixed-wing that can pivot about its elastic axis. There are two rotors mounted rigidly on the wing tips, one at each tip. For vertical take-off and landing, the wing along with the rotors is tilted so that the rotor axes point along the vertical direction. After take-off, the wing/rotor combination is tilted forward, thus converting to airplane mode of flight.

The tiltwing configuration has certain distinct advantages over the tiltrotor. The wing chord remains aligned with the rotor axis and consequently with the rotor flow field for the tiltwing case; the rotor/wing aerodynamic interference effects are

Reproduced with permission of the copyright owner. Further reproduction prohibited without permission.

therefore reduced for the tiltwing configuration. Also, on liftoff, the wing has its chordwise direction (which is stronger than the flapwise direction) in the direction of vertical take-off; hence less wing structure is required for the tiltwing to support the fuselage than that required for the tiltrotor [47]. Hence, the tiltwing has thinner and more aerodynamically-efficient wings than the tiltrotor. Also, the tiltwing, as it has been defined in the industry, does not have the cyclic control mechanisms that are present in a tiltrotor; this reduces the complexity of controls in the tiltwing.

The absence of cyclic controls in a tiltwing necessitates an auxiliary tail rotor for directional control in hover and low speed flight [47]; this results in a considerable weight penalty in the design and significant power requirements in operating the tail rotor. The tail rotor is unnecessary in high speed flight and hence has to be stopped, thus adding further complexity to the tiltwing system. The tiltwing concept also avoids the complexity of typical rotor-type flapping hinges by using rigid propellers as rotors; the drawback is that propellers have a much higher disk loading than rotors in generating the same thrust with the same number of blades (since propellers usually have smaller radii than rotors). Tiltwings are hence noisier. The tiltwing cannot hover for long durations because its higher disk loading corresponds to higher power requirements for vertical flight performance. The tiltwing also cannot fly forward in conversion flight for any significant duration, since the wing (in conversion flight) would not be aligned with the forward velocity of the aircraft and would hence create an enormous drag on the aircraft. This drawback of the tiltwing also limits its conversion corridor as compared to that of

Reproduced with permission of the copyright owner. Further reproduction prohibited without permission.

the tiltrotor. The tiltwing also requires high-lift devices on the wing in conversion mode; this adds to complexity and to pilot workload in operating these devices. In case of power failure, the tiltwing has to remain in airplane mode and land only in a normal airstrip. On the contrary, the tiltrotor can convert to helicopter mode and autorotate to land in a small and restricted area. The tiltwing is also limited in sideward and rearward flight as compared to the tiltrotor. The tiltwing, although a viable concept for tiltrotor-type missions, does not measure up to the tiltrotor in performance and capabilities [47].

1.2.2 Tiltrotor Development

The tiltrotor concept was demonstrated by Transcendental Aircraft Corporation and Bell Helicopter Company in the early 1950's. The first aircraft that was successfully test flown in 1954, the Transcendental Model 1-G, had two 3-bladed 17-foot diameter fully-articulated tiltrotors. The U.S. Air Force then got involved in the project and data were obtained by Transcendental on the stresses of the rotor blades, shaft and control linkages and on rotor response. Studies done under this project indicated that a mechanical instability could occur in the conversion mode. This project did not proceed much further due to lack of funding [39].

Bell Helicopter was involved in the development of the XV-3, which had a 3-bladed 23-foot diameter fully-articulated tiltrotor system. The first XV-3 was badly damaged in an accident in 1956 that was attributed to a blade oscillation problem. The second XV-3 was designed to have a two-bladed teetering rotor system to eliminate the blade oscillation problem. This aircraft was successfully test

Reproduced with permission of the copyright owner. Further reproduction prohibited without permission.

flown and achieved full conversion to airplane mode in late 1958. Problem areas were, however, identified in high speed airplane mode of flight. Two critical problems were low stability margins in high speed flight and transient blade flapping during maneuvers [4]. The low aeroelastic stability margins were found to arise from a combination of blade flapping and aircraft pitching motion. Subsequent full-scale investigations conducted in the NASA 40 x 80-foot wind tunnel resulted in the discovery of the whirl flutter phenomenon in tiltrotors [39].

The Composite Aircraft Program, begun by the U.S. Army in 1965, led to the construction of a 0.133-scale semi-span aeroelastic model of the 38.5-foot diameter Bell Model 266 tiltrotor. This model, subsequently transferred to NASA Langley, was the subject of a joint NASA/Bell study on tiltrotor stability, dynamics and loads at the Langley Transonic Dynamics Tunnel (TDT) [5]. These tests were crucial in establishing an understanding of the stability and load characteristics of tiltrotors. Bell Helicopter then worked on developing a 25-foot diameter, 3-bladed gimballed hub tiltrotor, designated as the Model 300. The success of this project led to the NASA contract to Bell in 1973 to design and manufacture two tiltrotor research aircraft (originally designated as the Model 301) designated as the XV-15 [47].

A great amount of expertise was gained in tiltrotor aeroelasticity from the 25-foot diameter XV-15 tiltrotor flight, and wind tunnel tests and through aeroelastic analyses formulated specifically to predict tiltrotor behavior. The XV-15 provided a good platform for tests as well as validation of the aeroelastic analyses with test data. NASA and Bell Helicopter Company have conducted a number of tests with

Reproduced with permission of the copyright owner. Further reproduction prohibited without permission.

the XV-15 configuration since 1978. On the analysis side, the aeroelastic analysis CAMRAD [48] developed by Johnson [49] was among the earliest comprehensive analyses for tiltrotor configurations. Predictions were validated with measured wing frequencies and damping obtained from wind tunnel and flight tests. The good correlations obtained from the analysis provided the designers with confidence on aeroelastic stability margins of tiltrotors in high speed flight.

The V-22 tiltrotor program, begun in 1983 for the U.S. Navy, is the first production tiltrotor program. The full-scale development program is being carried out jointly by Bell Helicopter Textron Inc. and Boeing Helicopter Company. Tests conducted with a 1/5-scale semi-span aeroelastic model of the 38-foot diameter V-22 in the NASA Langley TDT [50] in 1984 provided data to aid in full-scale development and to establish a data base for analytical validation. The influence of critical design parameters such as wing stiffnesses, rotor coning, and pitch-flap coupling were determined experimentally. Comprehensive tiltrotor aeroelastic analyses such as CAMRAD, DYN4 [5] (Bell's tiltrotor aeroelastic analysis) and PASTA [35] were used to predict aeroelastic stability and correlate with wind tunnel data [50]. Specific areas of deficiency, such as modeling of kinematic couplings and compressibility aerodynamics, in these aeroelastic analyses were identified during this study. Details of the 1/5th-scale V-22 aeroelastic model test program were summarized by Settle and Kidd [51]. The V-22 is now in the production stage.

A Short Haul Civil Tiltrotor (SHCT) program is currently under way to develop a civilian tiltrotor for the next century. This project is being carried out by NASA in collaboration with the helicopter industry.

Reproduced with permission of the copyright owner. Further reproduction prohibited without permission.

1.2.3 Tiltrotor Design Considerations

It has been mentioned earlier that tiltrotors combine the VTOL performance capabilities of helicopters with efficient long range cruise capabilities of fixed-wing turbo-prop airplanes. The design considerations for such an aircraft, which are very complex, include those of helicopters as well as propeller aircraft. Important design considerations for tiltrotors are aeroelastic stability, vibratory loads, aerodynamic performance, control system loads, rotor/wing aerodynamic interference, gust response, external and internal noise, and yaw stability in hover. Aeroelastic stability, which is a major concern in tiltrotor development, is the subject of this study. It is therefore described in great detail in the subsequent sections.

Vibratory loads in an aircraft cause considerable discomfort to passengers and damage to the structure through fatigue. Minimization of vibratory loads is also an important consideration for tiltrotors. The effect of rotor vibratory loads is mitigated at the fuselage by the presence of the wing; the tiltrotor wing absorbs a significant portion of the vibration caused by the rotors [52]. Flight testing of the 3-bladed XV-15 tiltrotor revealed large 2/rev pylon loads [53]; the source of these loads was the 1/rev and 3/rev rotor loads acting through the gimbal mechanism. This problem was reduced by applying cyclic control correction to obtain zero flapping and hence obtain zero 1/rev flapping moment. Another important source of vibratory loads is the wing aerodynamic interference effect in high speed airplane mode flight. This wing interference produced large N/rev shear forces at the hub for an N-bladed rotor. Testing of the Bell Model 266 showed large N/rev pylon forces that increased with increase in forward speed [5].

Reproduced with permission of the copyright owner. Further reproduction prohibited without permission.

Aerodynamic design of the rotor blades for a tiltrotor poses great design problems arising primarily from the differences in the thrust requirements and rotor inflow between helicopter and airplane modes of operation [54],[55]. In hover, the total rotor inflow is smaller than that in the airplane mode; the induced inflow comprises all of the total inflow at the rotor disk. The blade loading is very high in hover as the rotor thrust supports the complete weight of the tiltrotor. Also, the tiltrotor wing in hover is placed perpendicular to the direction of the rotor and pylon; the rotor inflow, hence, produces a large download on the wing that can be as large as 10-15 percent of the total rotor thrust [56]. Thus, there is an additional penalty on blade loading due to this wing download. In airplane mode of operation, the rotor inflow is very high due to the high forward flight velocity though the induced inflow component is very small (much smaller than in hover). This is because the rotor, in axial mode, has to produce less thrust, just enough to overcome the aircraft drag. The lift force comes primarily from the tiltrotor wing. These conflicting aerodynamic environments of operation result in a design compromise in the amount of blade pretwist, rotor planform, and airfoil section selection.

Important aerodynamic parameters considered for the V-22 blades were rotor diameter, twist, chord, taper ratio, number of blades, tip speed, and airfoil section [55]. Rotor blade pretwist distribution for tiltrotors is a compromise between efficient hover performance and efficient airplane cruise performance. Ideal twist (which results in minimum power requirements) is simulated in tiltrotors using a bilinear twist variation with blade span; the magnitude of twist is determined as a

Reproduced with permission of the copyright owner. Further reproduction prohibited without permission.

compromise between helicopter and airplane conditions. The rotor diameter was fixed for the V-22 primarily from storage considerations for shipboard operations. A 3-bladed rotor was chosen due to considerable expertise obtained for such a configuration from previous tiltrotor projects such as the XV-15. The hover tip speed was selected on the basis of maximizing thrust for a given power level. In airplane mode, the forward flight velocity combines with the tip speed to produce very high velocities at the rotor tip, and therefore high compressibility effects. To reduce these effects, the rotor tip speed is decreased for airplane mode of operation. The forward flight tip speed was selected based on maximum airspeed, maximum range and service ceiling considerations. The tip speed in airplane mode is 16 % lower than the hover tip speed (the corresponding figure for the XV-15 is 20 %). Airfoil section selection for tiltrotors is similar to that for helicopter blades; thicker sections near the blade root to accommodate blade structure, moderate thickness (12 to 15 %) in the middle section for maximum lift, and thin sections (9 %) for the outboard part of the blade to minimize drag divergence effects. The airfoil sections selected should also have small pitching moment coefficients to minimize blade cyclic torsional response and control system loads. Blade twist, chord and taper ratio are chosen based on a compromise between figure of merit in hover and propeller efficiency in airplane mode.

Gust response characteristics are important to dynamic stability of the vehicle and affect passenger comfort (particularly for civilian operations). Research on this topic has been focused on alleviation of blade bending loads and drive-train loads resulting from different types of gust loading [5],[57]. The use of active controls

Reproduced with permission of the copyright owner. Further reproduction prohibited without permission.

has been suggested [58] to alleviate this problem.

External noise levels are very important for both military and civilian applications [59]. The external noise levels associated with a tiltrotor in airplane mode are similar to that of turbo-prop aircraft, and are significantly lesser than that of helicopters in forward flight [59]. The absence of a tail rotor in tiltrotors decreases the noise levels in hover as compared to that of a helicopter. Conversion mode in tiltrotors, however, poses a considerable noise problem [60]; the noise in transition is created by blade-vortex interaction and interactions of the vortices with the rotor pylon and wing. The acoustic performance of a tiltrotor defines its viability as a civilian transport vehicle, both for its passengers as well as for bystanders. The transition flight noise level is a serious cause of concern that is being addressed in the development of the Short Haul Civil Tiltrotor (SHCT).

1.2.4 Tiltrotor Whirl Flutter

The phenomenon of whirl flutter occurs due to aeroelastic interaction between the rotor/propeller and the wing. A lot of attention was focused on this phenomenon due to two disasters that occurred on Lockheed Electra turboprop aircraft in 1959 and 1960. The phenomenon that resulted in these crashes was fixed-wing whirl flutter, which, as the name implies, is associated with conventional fixed-wing aircraft. A NASA Langley wind-tunnel investigation into the accidents [61] revealed that this phenomenon could occur in the Electra if the engine nacelle stiffness was reduced, for example, by structural failure.

In tiltrotors, the phenomenon of whirl flutter was observed, in the late 1950's,

Reproduced with permission of the copyright owner. Further reproduction prohibited without permission.

as a reduction of stability margins in high speed axial flight of the Bell XV-3 aircraft. The low stability margins were found to be a result of the large inplane forces generated by a combination of blade flapping and aircraft pitching motions [4].

The tiltrotor stability problem differs from the conventional propeller whirl flutter due to additional flapping, feathering, and bending degrees of freedom, control system flexibility, and blade kinematic and elastic couplings which are present in tiltrotor configurations [50]. Both instabilities are a result of precession-generated aerodynamic forces; but the presence of flapping in the rotor causes a major difference in the tiltrotor instability. The propeller whirl flutter can be described as an increasing amplitude whirl resulting from precession-generated aerodynamic hub moment and gyroscopic coupling between the propeller shaft pitch and yaw motions. The tiltrotor usually has a gimballed hub; this flapping degree-of-freedom can cause the instability in the pitch or yaw directions alone. The instability in a tiltrotor is of aerodynamic origin since the gyroscopic coupling between pitch and yaw motions is absent in a gimballed rotor.

Mechanism of Tiltrotor Whirl Flutter

Figure 1.3 shows a schematic of the mechanism of tiltrotor whirl flutter. Consider a nose-up pylon pitch rate perturbation of a tiltrotor in high speed axial flight; the rotor is spinning in the counter-clockwise direction as seen from the pylon mast. The rotor has a gimballed hub and the swashplate can be assumed to be fixed relative to the pylon mast. The spinning rotor, reacting to the pitch-rate

Reproduced with permission of the copyright owner. Further reproduction prohibited without permission.

perturbation $\dot{\phi}$, generates a flapping reaction such that the rotor has a nose-down flapping β with respect to the pylon mast. Such a reaction causes an angle-of-attack decrease on the far side of the rotor and an angle-of-attack increase on the near side of the rotor. Since the blades are at high collective pitch setting, the perturbation forces on the blades, due to the change in angle-of-attack, have components in the thrust (axial, T) and drag (inplane, H) directions. The resultant thrust (in the axial direction) creates a couple that tends to restore the rotor to its position perpendicular to the pylon mast. The resultant inplane force, however, is in the vertical direction from the far and near sides of the rotor; the inplane force, in this case, is directed vertically upward. Large unbalanced inplane shear forces are created in this manner. These forces act to destabilize the wing; this is the mechanism of tiltrotor whirl flutter. The symptom of whirl flutter is that the tiltrotor wing gets into instability. This aeroelastic instability results primarily from the feedback effects between the wing motion and the inplane rotor forces.

1.3 Motivation

Advanced geometry rotor blades utilizing blade distributed twist, sweep, anhedral and planform taper along the blade span have been utilized in many helicopter configurations to improve performance. It appears natural that such concepts can be exploited in tiltrotor configurations as well. Large blade pretwist is already employed in tiltrotor designs to provide for a more uniform inflow distribution and reduced induced power losses in high speed axial flight. The use of advanced geometry blade design concepts in tiltrotor configurations could have a considerable

Reproduced with permission of the copyright owner. Further reproduction prohibited without permission.

impact on rotor performance, vibratory hub loads and noise levels.

Advanced geometry modifications may also affect the aeroelastic stability characteristics of the rotor. The load redistribution due to advanced geometry modifications could alter the destabilizing forces thereby accelerating or delaying the occurrence of instabilities. Therefore, these configurations need to be aeroelastically investigated; their effect on the rotor loads and aeroelastic stability need to be modeled and studied. Important effects of blade sweep are the structural flap bending-torsion and lag-axial kinematic couplings. Similarly, blade tip droop causes lag bending-torsion and flap-axial couplings. The dynamic effects of these couplings could have significant effects on loads and stability.

1.4 Literature Survey

The present study is focused on improving the aeroelastic performance of tiltrotors and on developing a comprehensive analysis tool to investigate advanced configurations. Tailoring blade tip geometry to improve aeroelastic performance is another focus of this work. The survey of literature comprises of two parts: (1) the first section deals with previous work in the area of tiltrotor aeroelastic research, both experimental and analytical work, and (2) the second section describes the work done in the area of advanced geometry blades for rotor systems and their effects on the aeroelastic behavior of rotorcraft.

1.4.1 Tiltrotor Aeroelastic Research

The first mention of the possibility of whirl flutter phenomenon occurring in propeller aircraft was made in an investigation by Taylor and Browne [62] in 1938.

Reproduced with permission of the copyright owner. Further reproduction prohibited without permission.

This phenomenon, however, was not encountered until much later due to the high margins of safety used in the aircraft design process at that time. Some early investigations into this phenomenon were performed by Richardson and others [6], [7] who studied the problem of whirl flutter associated with hinged or flexible propeller systems. These theoretical investigations had difficulties in predicting whirl flutter occurrence under the flight conditions where it was found to occur in experiments. These and other studies were reviewed in detail by Reed [9], [10].

Hall [11] examined the role of the negative in-plane (H-force) damping on the high inflow tiltrotor behavior and its role in the phenomenon of whirl flutter. He investigated the 2-bladed XV-3 tiltrotor configuration with the help of the full-scale test results and model tests. This investigation focused on the influence of various parameters on the stability of the rotor and pylon, in particular forward speed, pylon pitch and yaw spring rate, and pitch/flap coupling. For this study, he derived the equations of motion for a two-bladed rotor on a pylon; the degrees-of-freedom were the teetering flap angle, pylon pitch and pylon yaw. A rotating flap frequency equal to the rotational speed was assumed; hence no hub restraint was modeled and no hub moment due to flapping is transmitted to the pylon motion. The aerodynamic forces were expressed in terms of integrals of blade section forces, but they were not expanded out explicitly in coefficient form. Hall solved for the dynamic behavior of the system through numerical time-integration and obtained the transient response rather than calculate the stability eigenvalues of the system from linearized equations. The advantage in this method was that the exact, nonlinear aerodynamic forces could be included in the analysis. This

Reproduced with permission of the copyright owner. Further reproduction prohibited without permission.

study was probably the earliest attempt in systematic theoretical modeling of the tiltrotor aeroelastic behavior.

Gaffey et al. [5] performed a tiltrotor aeroelastic study focusing on wing stability, gust response and ride quality. Design considerations with respect to these factors were discussed. The influence of the blade frequencies and pitch/flap coupling on the rotor and rotor/wing stability were discussed. The study showed that a hingeless rotor (with $\nu_\beta > 1$/rev) increased stability and reduced flapping significantly, but also increased blade loads compared to a rotor with $\nu_\beta = 1$/rev. Theoretical predictions were compared with test results for proprotor/wing stability, flapping angles, loads, vibration and gust response. This work led to the development of Bell's two comprehensive tiltrotor aeroelastic codes, DYN4 (rigid blade code) and DYN5 (includes elastic blade modes).

Tiller and Nicholson [12] discussed the stability and control considerations in tiltrotor aircraft with respect to various design parameters. They showed that tiltrotors with positive pitch/flap coupling and clockwise rotation of the right rotor produce, through negative H-force (Figure 1.3), an increasing negative damping with forward speed. This negative damping required a larger horizontal tail to stabilize the short-period mode (the rotor contribution to negative damping was about 30 to 40 percent of the stabilizer damping). The rotor influence on all aircraft stability derivatives was systematically analyzed in this study.

Young and Lytwyn [13] developed a four degree-of-freedom theoretical model for studying tiltrotor dynamics. This model consisted of two fixed-frame flapping angles, and pylon pitch and yaw motions. A study was carried out to tune the

Reproduced with permission of the copyright owner. Further reproduction prohibited without permission.

rotor flap frequency to maximize whirl flutter stability. They found an optimum value at about $\nu_\beta = 1.1$/rev. This was accomplished by minimizing the coupling term between the rotor and pylon resulting in increased system stability. They found that the power-on case was less stable than the windmilling case, but this conclusion was specific to high rotor blade mean angle-of-attack (which is not the case in high speed cruise flight). Their theoretical model was for an N-bladed rotor ($N_b > 2$) on an elastically-restrained pylon. The optimum value for ν_β of 1.1/rev requires an increase in flapping restraint for an articulated or gimballed rotor system. Wernicke and Gaffey [15] concluded that since an increase in flapping restraint increases the blade loads, the applicability of blade flap frequency tuning is limited.

An analytical investigation by Edenborough [17] on the XV-3 configuration used an analytical model that included a wing beamwise translation degree-of-freedom in addition to the conventional pylon pitch and yaw motions. This investigation reported the effects of several major parameters on stability: blade pitch-flap coupling is destabilizing, increased blade flapping restraint is stabilizing and increase in pylon pitch and yaw stiffnesses is stabilizing. A similar mathematical model developed by DeLarm [25] substantiated these trends obtained by Edenborough. Kaza [32] conducted a theoretical study on the effect of steady-state coning angle and flapping restraint and showed that these parameters have a significant effect on system stability.

In the late 1960's and early 1970's, Bell Helicopter Company and Boeing Vertol Company worked independently on two proprotor designs. The Bell design had a

Reproduced with permission of the copyright owner. Further reproduction prohibited without permission.

gimballed hub and a stiff inplane cantilever blade attachment to the hub. Hence ν_β = 1/rev (slightly above 1/rev, due to the presence of a weak hub spring) and $\nu_\zeta >$ 1/rev. The Bell rotor also incorporated positive pitch-flap coupling to increase the blade flap-lag stability. The design study performed by Bell for this project is described in Ref. [33]. The Boeing design had a cantilever or a hingeless hub with soft inplane blade attachment; hence $\nu_\beta > 1$/rev and $\nu_\zeta < 1$/rev. The Boeing design study is reported in detail in Ref. [34]. The different placement of the blade flap and lag frequencies resulted in very different dynamic characteristics for the two configurations.

Kvaternik [35], [36], [37] conducted extensive parametric studies on tiltrotor aeroelastic instabilities using a rigid blade axial flight analytical model; rigid flapping and lead-lag degrees-of-freedom were included for the rotor blades. This model included all six degrees of freedom at the pylon pivot point. These studies confirmed previously observed trends in aeroelastic predictions. Some new observations from this work were: wing aerodynamics was stabilizing, windmilling configuration was more conservative than the power-on case, high rotor precone was destabilizing, both positive and negative pitch-flap coupling was destabilizing and blade lag dynamics was necessary for accurate modeling of tiltrotor aeroelastic behavior. The mathematical model was later extended to include a modal representation of the airframe structure and developed into a code called Proprotor Aeroelastic STability Analysis (PASTA).

Johnson [38] developed a detailed theoretical model for a tiltrotor on a cantilevered wing, operating in high inflow axial flight (cruise condition). The equa-

Reproduced with permission of the copyright owner. Further reproduction prohibited without permission.

tions of motion and hub forces of the rotor were determined including the shaft motion for a 3-bladed tiltrotor. Each blade consisted of two degrees-of-freedom: rigid flap and lag. The general behavior of the high inflow rotor was investigated and, in particular, the stability of the tiltrotor and cantilevered wing configuration. The effects of various elements of the theoretical model were examined, and the predictions were compared with experimental data from wind tunnel tests of two full-scale proprotors. Effects of several parameters on system stability were examined, including blade aerodynamics (in particular, the sensitivity of the lift coefficient to changes in angle-of-attack), forward speed, rotor flap and lag frequencies, wing aerodynamics, power-on and windmilling flight, compressibility, wing stiffnesses, gust loading, and rotor control inputs. The theoretical model consisted of nine degrees-of-freedom - 3 flap modes for a 3-bladed rotor, 3 lag modes and 3 wing modes (2 elastic bending and 1 torsional mode). Gimbal degrees-of-freedom were not modeled; instead, the behavior of the gimbal in collective and cyclic flap modes was modeled using different input frequencies for these modes. For the rotor, it was assumed that the blade flap and lag motions were not coupled; only pure out-of-plane and pure in-plane motions were considered. The model neglected the higher bending modes of the blades, and the blade elastic torsion modes. For the support, the model used only simplified structural modes of the wing. The model, however, incorporated most of the important features of the tiltrotor aeroelastic system. From a comparison of the behavior of a gimballed stiff-inplane rotor and a hingeless soft-inplane rotor, it was concluded that the placement of the rotor blade natural frequencies of first mode bending - the flap frequency ν_β and the

Reproduced with permission of the copyright owner. Further reproduction prohibited without permission.

lag frequency ν_ζ - significantly influences the dynamics of the proprotor and wing. Furthermore, the rotor lag degrees of freedom were found to have a very important effect on the tiltrotor dynamics for both the soft-inplane ($\nu_\zeta < 1$/rev) and the stiff in-plane ($\nu_\zeta > 1$/rev) configurations. This study proved to be a valuable guideline for researchers on the phenomenon of predicting tiltrotor whirl flutter. Johnson extended this mathematical model to include elastic blade deflections, including coupled bending modes and elastic torsional modes and helicopter and conversion modes of operation [63], [64]. These models formed the basis for the tiltrotor modeling in CAMRAD [48] which is probably the most comprehensive code to-date in modeling aeroelastic behavior of tiltrotor aircraft.

The predictive capability of rigid-blade linear analyses for tiltrotor stability is discussed in Ref. [52]. Rigid-blade analyses can predict tiltrotor stability even for hingeless and bearingless designs so long as the effective blade couplings are accurately included. This prediction capability can be attributed to the presence of high inflow aerodynamics; due to high collective pitch in high speed flight, both flap and lag bending motions produce large changes in the blade lift which has significant components in both inplane and out-of-plane directions. This results in the perturbation terms (primarily due to lift coefficient sensitivity to angle-of-attack even in the lag direction) to dominate over terms related to the deflected trim position. Rigid-blade analyses often give inaccurate predictions of deflected trim position; but the presence of high inflow aerodynamics results in good stability predictions in high speed axial flight. This is, however, not the case with the helicopter mode where the inflow is much smaller and the perturbation motion

Reproduced with permission of the copyright owner. Further reproduction prohibited without permission.

does not have a large effect on lag motion. Therefore, lag dynamics due to the deflected trim position dominate. Rigid-blade analyses for tiltrotors are, therefore, limited to high speed axial flight conditions. Also, the analysis of advanced rotor configurations cannot be accurately performed using rigid-blade analysis since coupling terms cannot be captured properly with rigid analyses. Thus, a nonlinear elastic-blade tiltrotor formulation becomes necessary for such configurations.

Some of the recent developments in tiltrotor dynamics were assessed by Johnson [52] in 1985. The report expressed concern regarding the treatment of new rotor designs such as bearingless rotors and modeling of high speed aerodynamics. Past experience has shown that fuselage vibration in tiltrotors is not a significant problem as the wing dynamics absorbs a significant portion of the vibratory loads thus preventing large vibration from being transmitted to the fuselage. Furthermore, the large conversion flight corridor of tiltrotors provides the ability for tilting the rotors such that wake-induced vibration can be minimized at low speeds. The study also emphasized the role of pitch-lag coupling in destabilizing the system in high speed flight. Precone is given to the rotor to minimize the blade root bending moments in the helicopter mode, but a large precone in low thrusting conditions (such as tiltrotor cruise) produces a significant negative pitch-lag coupling that can be destabilizing to the system. The study also discusses the possibility of air resonance in soft-inplane rotors in low speed flight when the aerodynamic damping is low.

Refs. [38], [52] and [65] discuss the large influence of the collective lag mode dynamics on whirl flutter stability. The dynamics of the collective lag mode of

Reproduced with permission of the copyright owner. Further reproduction prohibited without permission.

the rotor amounts to a rotational speed perturbation. It has been shown that a windmilling rotor with rotor speed perturbation is a better representation of the powered tiltrotor case than is the constant rotor speed case [65]. For the case of a cantilevered wing (considering only symmetric wing modes), the inclusion of engine and drive shaft dynamics does not change the overall dynamics significantly. This assumption does not necessarily hold true when antisymmetric modes of a tiltrotor in free-flight are considered. Antisymmetric wing modes cause opposing reactions from the two wing-tip rotors, thus adding stiffness to the drive system and altering the dynamics of the problem.

The earliest comprehensive elastic-blade analysis for tiltrotors was developed by Johnson [63] and implemented in CAMRAD [48]. CAMRAD is capable of analyzing articulated, teetering, gimballed and hingeless rotors for helicopters and tiltrotors. Its formulation is based on rotor modes: coupled flap-lag bending modes and uncoupled torsion modes; axial modes are not included. Its capability in analyzing bearingless rotors is not adequate due to the presence of multiple load paths for such configurations. Since torsional modes are uncoupled and axial modes are absent, CAMRAD is limited in its capability to analyze composite-coupled rotor configurations since bending-torsion and axial-related composite-couplings cannot be accurately modeled. The code, however, has detailed modeling of the airframe (six rigid body motions and up to ten elastic modes), airframe aerodynamics, and rotor-body and body-tail aerodynamic interference. The predictive capabilities of CAMRAD have been the subject of a number of investigations [49], [50], [66], [67].

The aeroelastic stability analyses that were used in the design of the V-22

Reproduced with permission of the copyright owner. Further reproduction prohibited without permission.

aircraft were validated with model test results in a study by Popelka et al. [50]. Extensive correlation efforts using both DYN4 and CAMRAD resulted in improvements to the analyses and increased analytical capabilities. DYN4 was modified to include the pitch-lag coupling terms accurately. Both codes agreed well with the test data. A lot of physical understanding was obtained from the correlation effort. The validated codes were then used in further prediction efforts to aid in the continuing design process of the V-22.

The available literature on the aeroelastic analysis of tiltrotors with composite blades is limited. Nixon [68] conducted a study to passively control the deformation of the rotor blade to obtain an optimum twist in both helicopter and airplane flight modes. The study showed that significant performance improvements could be achieved with realistic extension-twist coupled blade designs based on structural strength constraints. Bauchau et al. [69] conducted an investigation with ATB (Advanced Technology Blades) to improve the performance of the configuration by using extension-twist coupled blades. This study tried to maintain the ATB characteristics, while trying to achieve a twist-change of two degrees between hover and forward flight (utilizing the rotor speed difference between the two operating conditions). However, only a half-degree twist-change due to extension-twist coupling could be achieved under the ATB constraints.

Kottapalli and Meza [67] investigated the differences between the XV-15 stability with metal blades and with composite ATB (improved for tiltrotor performance). This study discussed the pitch-flap flutter possibilities of the XV-15 ATB blades due to adverse chordwise mass distribution. Composite couplings were,

Reproduced with permission of the copyright owner. Further reproduction prohibited without permission.

however, not investigated in this study.

Nixon [39] developed an elastic-blade tiltrotor analysis to examine, in specific, composite-coupled rotor blades for tiltrotors. Important aspects of the model were the inclusion of a large pylon angle, accurate modeling of pitch-lag coupling related to rotor precone, hub-related gimbal degrees of freedom and additional elastic coupling terms for accurate modeling of the anisotropic blades and the wing. The accuracy of the analysis was demonstrated by a comparison with experimental results and other analyses. A significant conclusion was that elastic bending-twist coupling of the rotor blade is a very effective means of increasing the whirl flutter speed, and the magnitude of coupling, required for increased stability, does not have an adverse effect on performance or blade loads. Another important conclusion was that passive blade twist control using elastic extension-twist coupling of the rotor blade can significantly improve tiltrotor aerodynamic performance; this, however, is at a cost of reduction of stability margins. The analysis was merged by Nixon into the University of Maryland Advanced Rotorcraft Code (UMARC) [70]. UMARC is a finite-element based code that can model elastic-blades with completely coupled axial, flap, lag and torsional motions; hence bearingless rotors, composite-coupled rotors and advanced geometry rotors can be modeled. The code can also model articulated, hingeless and gimballed rotors.

Alleviation of whirl flutter in tiltrotors has also been investigated by means of active control. Nasu [71] developed control laws based on harmonic balance algorithms and feedback of wing-tip velocity and acceleration measurements. The stability of the system was improved by cyclic pitch inputs determined from the

Reproduced with permission of the copyright owner. Further reproduction prohibited without permission.

closed-loop system. Vorwald and Chopra [72] developed a multiple-input/multiple-output controller to solve the same problem. The controller was based on feedback of wing motion and utilizing rotor cyclic corrective input. Results showed that the whirl flutter speed could be increased by using this method.

Tiltrotor Aeroelastic Testing

Relatively few efforts have been made in the area of model-scale and full-scale testing of tiltrotors. Results from an experimental investigation conducted on a scaled model of the XV-3 tiltrotor were reported by Edenborough [17]. The effect of pylon pitch and yaw stiffnesses, pitch-flap coupling and flapping restraint were studied; the test results helped validate an analytical model for the prediction of tiltrotor stability.

Experimental results from a model test in the tiltrotor development program were reported by Gaffey et al. [5]. Data were presented for proprotor/wing stability, blade flapping angles, hub loads and gust response characteristics and were used to validate in-house aeroelastic codes at Bell Helicopter Company.

Bell Helicopter Company and Boeing Vertol Company conducted two full-scale tests with their tiltrotor designs in the NASA Ames 40 x 80-foot Wind Tunnel. The results of these investigations is reported in Refs. [33] and [34] respectively. The two configurations differed primarily in their dynamic characteristics (rotor blade flap and lag frequencies). Valuable data obtained from these tests, such as the effects of wing stiffnesses, blade frequencies and control inputs on rotor/wing stability and gust response characteristics, were used to validate a variety of tiltrotor

Reproduced with permission of the copyright owner. Further reproduction prohibited without permission.

codes and helped greatly in the design of the XV-15 and V-22 configurations.

In the mid-1980's, Popelka et al. [50] conducted tests on a 1/5th-scale aeroelastic model of the V-22 in the NASA Langley Transonic Dynamics Tunnel (TDT). Design changes which were determined to be beneficial as a result of the tests (and analysis) were incorporated into the full-scale V-22 design. Minimum wing spar stiffness requirements for adequate stability were defined as a result of the experimental study. The hub design was modified based on tests done with a coning hinge hub. A large data base of parameter sensitivities, including effects of blade stiffness, control system stiffness, pitch-flap coupling and hub flapping restraint was established that provided guidelines for future design changes. These tests also served to validate aeroelastic stability analyses such as DYN4 and CAMRAD. The TDT tests of the scaled model have proven to be very valuable in the V-22 full-scale design process.

As part of the V-22 development program, a joint study was undertaken by Bell and Boeing [73] to correlate their predictions with XV-15 full-scale flight test data. The report also discussed some cases with the Model 300 tiltrotor. The areas of focus were performance and handling qualities, rotor shake-test natural frequencies, rotating system and control loads, and wing-pylon-rotor aeroelastic stability. This report compared predictions of comprehensive aeroelastic codes such as DYN4, DYN5, and PASTA with the stability test data. The results from this report were used extensively in the present study to validate the new and improved analysis developed as part of this work.

Reproduced with permission of the copyright owner. Further reproduction prohibited without permission.

1.4.2 Research on Advanced Geometry Bladed Rotors

Considerable research efforts were made in the application of swept-tip blades to improve rotor aerodynamic performance [74], [75]; specific studies were conducted to examine the potential of swept-tip blades in achieving reductions in power required. These studies also discussed the importance of adequate modeling of the aerodynamics of a swept-tip rotor to capture the phenomena accurately. Desopper's study [74] involved using a simple rigid-blade dynamic model with detailed CFD calculations for the rotor aerodynamics. He concluded that more accurate structural and dynamic modeling was required than the simple rigid-blade model that was used in the study. It was shown that tip sweep and droop can reduce the rotor power requirements.

Tarzanin and Vlaminck [76] studied blade sweep effects on the hub loads of an articulated rotor. Sweep effects were modeled using an equivalent model with chordwise offsets of the center of gravity (c.g.) and aerodynamic center (a.c.) from the shear center for the swept part of the blade. They concluded from this study that there was no single optimum sweep angle for all airspeeds and configurations. It was also observed that the effects of sweep, particularly through structural flap-torsion coupling in the blade, were very sensitive to the torsional stiffness of the blade. The report cited the need for a better structural model of the swept rotor.

Celi and Friedmann [77] developed a special finite element for modeling a swept tip. Comparison of the earlier approximate models (which assume offsets of c.g. and aerodynamic center from the elastic axis to model sweep) to this refined model showed that the predictions from the approximate model were in error, particu-

Reproduced with permission of the copyright owner. Further reproduction prohibited without permission.

larly for a hingeless rotor. Benquet and Chopra [78] developed an elastic-blade formulation based on Hamilton's principle for a advanced tip blade. Blade sweep, droop, planform taper and pretwist were modeled in this analysis.

The studies in Refs. [77] and [78], however, used linear transformation relations between the displacements of the tip element and its inboard element. Panda [79] derived nonlinear transformation relations between adjacent elements by imposing proper constraints and compatibility conditions. The study by Kim and Chopra [80] investigated the effects of tip sweep, droop and planform taper on the rotor response and loads. A finite element method was used for structural analysis and a three-dimensional finite difference analysis was used for the aerodynamics in this study. It was observed that the effect of using the nonlinear transformation (over the linear transformation) is significant, particularly to the torsional response of advanced tip blades. The effect of three-dimensional aerodynamics on the blade loads is quite significant for advanced tip blades.

An analytical study of the aeroelastic behavior of composite rotor blades with straight and swept tips was conducted by Yuan and Friedmann [81], [82]; only the hover case was examined. The rotor blade is modeled with beam-type finite elements and swept tip was modeled by a single element. The blade section properties were calculated with a composite cross-section analysis for arbitrary cross-sections developed by Kosmatka and Friedmann [83]. The effects of pretwist, anisotropic behavior, transverse shear and out-of-plane warping were modeled. The study concluded that ply orientation in the composite-laminates has a significant influence on blade stability. Any undesirable flap-torsion and lag-torsion couplings

Reproduced with permission of the copyright owner. Further reproduction prohibited without permission.

caused by tip sweep and anhedral respectively can be negated using appropriate ply orientation.

The previously described formulations all had one significant modeling limitation - they were formulated for advanced tip shapes only. The work of Bir and Chopra [84] included variation of sweep, droop, planform taper and pretwist along the entire span of the blade. Also, the time-varying control pitch angle was included independently through transformation matrices. Nonlinear transformations for deformations between elements were derived for moderate deflections. The effect of fuselage motion on stability was also included. The results from this study showed that both sweep and droop have a strong influence on aeroelastic, as well as aeromechanical stability. Tip droop is significantly stabilizing.

An alternate approach to model the advanced geometry rotor was suggested by Bauchau and Kang [85]; the idea was to use a multibody formulation to describe the complete system. In classical methods, elastic motion is represented only in the local reference frame. The multibody approach, based on the work in Ref. [86], refers all motion, rigid and elastic, to a single inertial frame. This method is very powerful in dealing with arbitrary configurations in a relatively simple manner. The disadvantage of this method is the enormous computational effort required to obtain a solution.

Considerable effort has gone into aeroelastic optimization of composite and advanced geometry rotors. Celi and Friedmann [87] conducted an optimization study for rotors with swept tips; the objective function was the peak-to-peak oscillatory vertical hub shear and constraints were imposed on blade aeroelastic

Reproduced with permission of the copyright owner. Further reproduction prohibited without permission.

stability, natural frequencies and autorotation properties. Friedmann et al. [88] conducted a similar optimization study for composite rotor blades with swept tips. An optimization study conducted by Ganguli and Chopra [89], [90] used a variable geometry rotor to minimize the hub loads and dynamic stresses of composite and advanced geometry rotors subject to frequency placement, autorotational and aeroelastic stability constraints.

All the research described in this section on advanced geometry rotors is specific to helicopter configurations. Since the tiltrotor has a pylon/wing combination between the rotor system and the fuselage, and since the tiltrotor operating conditions are wider and more diverse (compared to a helicopter), the above formulations and results cannot be applied directly to tiltrotor configurations. The tiltrotor is mounted on the tip of the wing; the rotor forces are transmitted onto the wing undergoing beamwise, chordwise and torsional displacements. The tiltrotor problem is, therefore, very different from the helicopter aeroelastic problem. The rotor forces, in tiltrotors, are oriented in different directions in airplane conditions (compared to the rotor forces in helicopter condition). The present study focuses on the formulation and analysis of an advanced geometry tiltrotor aircraft and investigates the effects of advanced blade geometry on predicted tiltrotor aeroelastic stability.

Reproduced with permission of the copyright owner. Further reproduction prohibited without permission.

1.5 Current Work

1.5.1 Objectives

A primary objective of this research is to provide a comprehensive analysis tool to help in the design and development of an advanced tiltrotor aircraft. A first step in this direction is to model the tiltrotor using a simple linear rigid blade formulation that can help provide a basic physical understanding of the phenomena causing the unique tiltrotor instabilities. An advanced nonlinear tiltrotor model is then formulated to design and analyze specific tiltrotor configurations in detail; an elastic model of the rotor as well as of the wing and fuselage is formulated as part of this study. This formulation is an improvement over that by Johnson [48] in its modeling of composite-coupled advanced geometry rotors and that by Nixon [39] in its modeling of advanced geometry rotors, fuselage, full wing-span and twin-rotors.

The next objective of this research is to perform a parametric study of tiltrotor high speed whirl flutter instability in axial flight. Such a study helps identify the parameters and the mechanisms that cause the occurrence of the instabilities.

The predicted results from the present comprehensive analysis have to be validated with other state-of-the-art analyses and available test data to explore the strengths and weaknesses of the predictions.

Based on the preliminary parametric study of tiltrotor instability in high speed axial flight, modified tiltrotor designs are then considered to alleviate the problem of whirl flutter.

Reproduced with permission of the copyright owner. Further reproduction prohibited without permission.

The final objective of this research is to study the effect of modeling the full tiltrotor configuration versus modeling only the rotor/wing coupled system on aeroelastic stability. The tiltrotor fuselage, full wing-span and twin-rotors are modeled. The predicted stability of the complete configuration is investigated. Importance of including wing antisymmetric modes and fuselage/wing rigid modes on the predicted stability is examined.

1.5.2 Scope of Present Research

The primary focus of the present research is the development of a robust and detailed tiltrotor formulation capable of modeling various aspects of present-day tiltrotor designs. The rotor, wing and fuselage are modeled using an elastic beam model that undergoes axial, flapwise, lagwise and torsional deflections. Finite element discretization based on Hamilton's principle is used to model the rotor blades, wing and fuselage. Advanced geometry rotors with blade sweep, anhedral, pretwist and planform taper variation with span are considered; the wing geometry can also be modeled likewise. Highly-twisted composite-coupled rotor blades and wing are modeled including nonclassical structural effects such as transverse shear and section warping. Rotor blade pitch-flap and pitch-lag kinematic couplings, and gimballed hubs, typical of present-day tiltrotor designs, are modeled in this study. The rotor drive-shaft is modeled in either the windmilling or in the powered configuration. The model developed in this study is also compatible with conventional rotor designs such as articulated, hingeless and bearingless rotors. The present study deals with the development of such a formulation from first principles. A

Reproduced with permission of the copyright owner. Further reproduction prohibited without permission.

fallout of this formulation is that the coupled rotor/wing equations derived can be modified to study similar coupled rotor/body stability problems as well. The analysis covers helicopter mode (hover as well as forward flight), conversion mode and airplane mode of flight. It is based on finite-element theory in space and time. The free vibration characteristics of the system are obtained by solving the finite-element model in space, and the rotor steady periodic response is obtained from a solution of the finite-element model in time. The analysis provides solutions for the vehicle trim controls, rotor periodic response, blade and hub loads, and rotor-wing-airframe aeroelastic stability.

The present research also focuses on a parametric study of tiltrotor whirl flutter using a simple rigid-bladed rotor formulation. The effects of rotor flap and lag frequencies, wing frequencies, wing sweep, rotor Lock number, rotor pitch-flap and pitch-lag couplings on tiltrotor whirl flutter are investigated as part of this study.

The results obtained from the comprehensive elastic model are validated with other analyses and available test data. The rotor response, trim controls, hub loads and aeroelastic stability are examined for typical tiltrotor configurations.

A parametric study is performed with advanced geometry tiltrotor configurations to examine the effect of rotor tip sweep, anhedral and planform taper on the whirl flutter speed and also on indicative performance parameters. This study provides insight into possible design modifications to expand the tiltrotor flight envelope.

Finally, the effect of modeling of the complete tiltrotor configuration is examined. The fuselage is modeled as an elastic beam using finite elements; it has all

Reproduced with permission of the copyright owner. Further reproduction prohibited without permission.

six rigid body degrees-of-freedom as well as elastic deflections. The tiltrotor wing is modeled as a full-span wing. Both the left and right tiltrotors are modeled as contrarotating rotors. This model helps to study the effects of wing symmetric and antisymmetric modes as well as those of fuselage motion.

1.6 Organization of the Dissertation

The first section of this chapter discussed the problems associated with tiltrotors, specifically, the aeroelastic stability of tiltrotors that are addressed as part of this study. The subsequent sections addressed the background behind tiltrotor development, design considerations and the mechanism of tiltrotor whirl flutter. The motivation behind the present study has been discussed in the subsequent section. A survey of literature on tiltrotor aeroelastic research, including experimental research, and research on advanced geometry rotors was discussed in the next section. The objectives and scope of the present study were presented subsequently.

The remainder of this dissertation is organized into six parts; first is the study based on a simple rigid-blade tiltrotor model for axial flight. Chapter 2 presents the results from a parametric study of tiltrotor whirl flutter stability obtained using a rigid-blade tiltrotor formulation.

Chapter 3 deals with the formulation of an elastic rotor model including advanced geometry composite-coupled blades for tiltrotors. Chapter 4 presents the analysis used in obtaining the results from the elastic-blade tiltrotor formulation.

A validation study is reported in Chapter 5. This study discusses the comparison of rotor response, trim controls, loads and aeroelastic stability with available

Reproduced with permission of the copyright owner. Further reproduction prohibited without permission.

test data and other comparable analyses.

The results obtained from a detailed parametric study of advanced geometry bladed tiltrotor whirl flutter stability is presented in Chapter 6; the effects of blade tip sweep, anhedral and planform taper on aeroelastic stability of the wing modes and on performance are investigated.

Chapter 7 deals with the fuselage model incorporated into the elastic-blade tiltrotor formulation; correlation of wing stability predictions, obtained using this model, with flight test data is presented.

The final part of this dissertation reports the significant conclusions obtained from all parts of the present study, which is presented in Chapter 8. Some suggestions for future work are also included.

Reproduced with permission of the copyright owner. Further reproduction prohibited without permission.

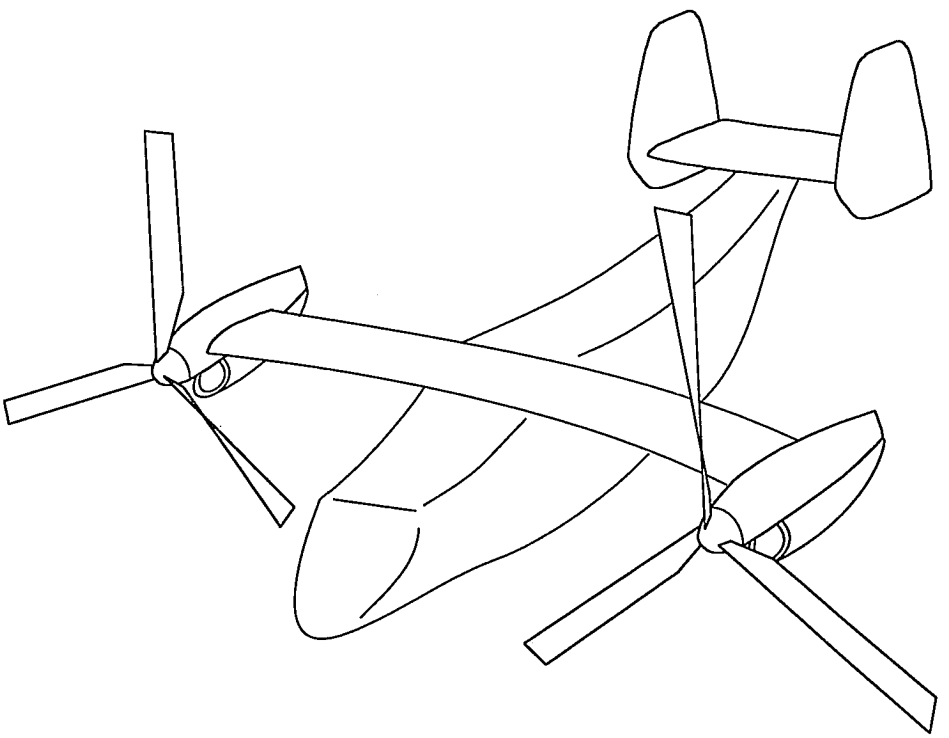

Figure 1.1: Tiltrotor in airplane mode

Reproduced with permission of the copyright owner. Further reproduction prohibited without permission.

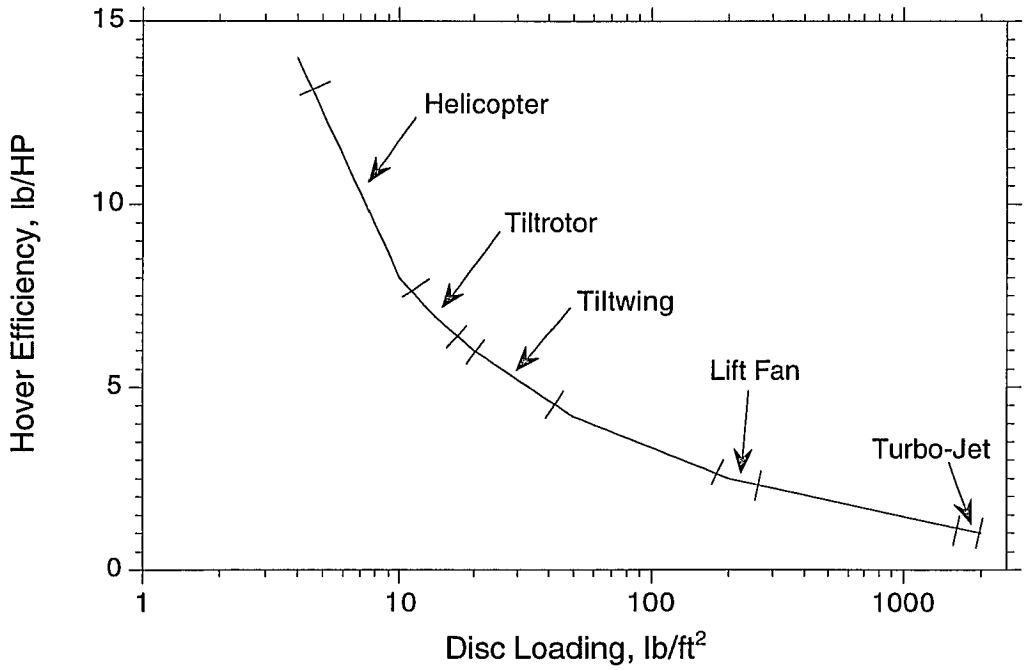

Figure 1.2: Hover efficiency as a function of disk loading for various VTOL configurations

Reproduced with permission of the copyright owner. Further reproduction prohibited without permission.

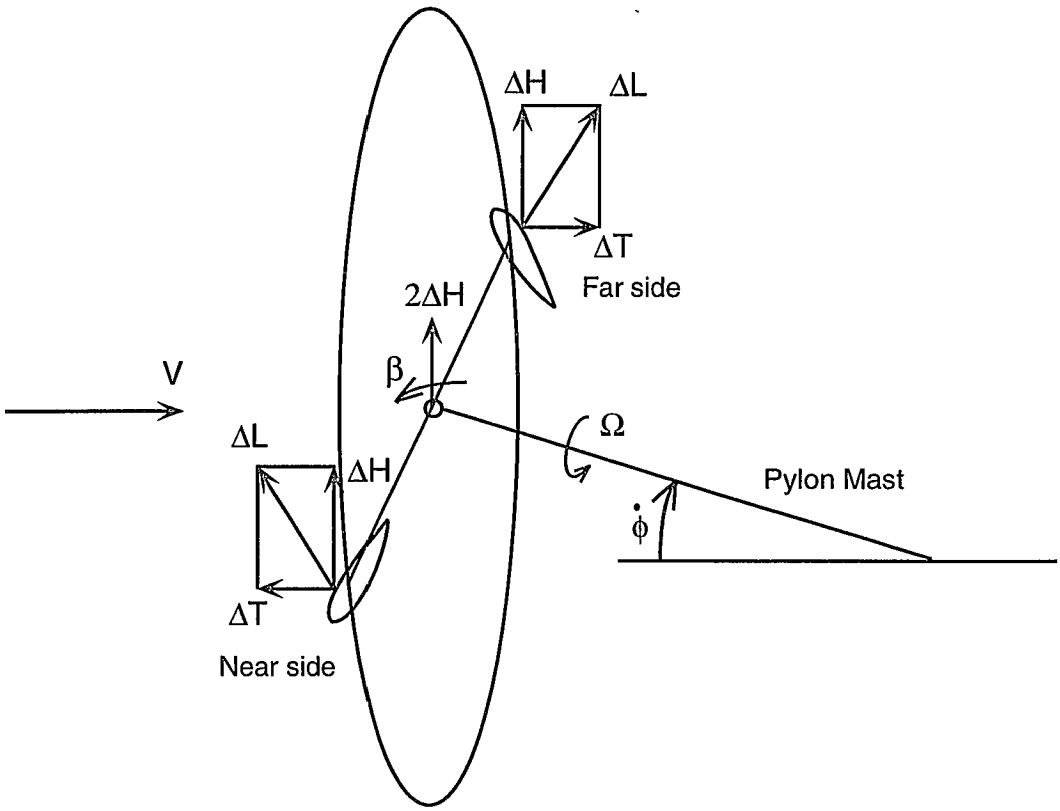

Figure 1.3: Mechanism of tiltrotor whirl flutter

Reproduced with permission of the copyright owner. Further reproduction prohibited without permission.

Chapter 2

Rigid Blade Tiltrotor Parametric Study

The objective of this parametric study is to gain a physical insight into the phenomenon of whirl flutter and to examine the influence of system design parameters on flutter characteristics. The study is based on the tiltrotor model described in Appendix A. The discussion focuses on the characteristics of a baseline configuration (the Bell 25-ft diameter proprotor described in Ref. [38]) and the effects of key system design parameters on stability of this system. These parameters include blade frequencies, wing sweep, Lock number, and blade pitch-flap and pitch-lag couplings. All the results presented in this study are for a windmilling configuration. This assumption implies that the rotor torque is not transferred to the wing-tip and that the wing vertical bending slope does not contribute to pylon roll and hence to inplane motion of the rotor system. This assumption of a windmilling rotor was shown to provide a conservative estimate of system stability (compared to the powered case) by Johnson [38].

Reproduced with permission of the copyright owner. Further reproduction prohibited without permission.

2.1 Frequency and Damping Characteristics of the Baseline System

The in-vacuo frequencies of the baseline wing and rotor system are given in Table 2.1. The rotor design parameters are listed in Table 2.2 and the rotor blade inertial parameters are given in Table 2.3. Table 2.4 shows the properties of the wing and pylon.

The rotating lag frequency changes with collective pitch (and therefore with forward flight velocity) so its value for the baseline configuration is presented in Figure 2.1. The in-vacuo cyclic flap frequency is related to the gimbal dynamics and hence does not change significantly with collective pitch. The collective flap frequency ν_{β_0} is dominated by the rotational stiffness contribution and hence changes very little with the collective pitch. Changes in collective flap frequency with rotor collective pitch are therefore ignored.

The frequency and damping of the wing and rotor modes for the baseline system are shown as a function of forward flight velocity in Figures 2.2 and 2.3 respectively. Since the rotating flap frequency ν_β becomes less than 1/rev with the inclusion of aerodynamics, the low frequency fixed-frame $\beta - 1$ flap mode is progressive. The $\beta - 1$ and $\zeta - 1$ mode frequencies cross the fundamental wing mode frequencies and hence affect the damping of the wing modes at the cross-over frequencies. Damping spikes occur in the beam and chord modes of the wing where the rotor $\zeta - 1$ frequency crosses over those wing frequencies. The beam and chord mode damping decrease rapidly as the $\beta - 1$ frequency approaches those wing frequencies. The wing chord mode has a damping peak at the frequency cross-over point because

Reproduced with permission of the copyright owner. Further reproduction prohibited without permission.

the $\zeta - 1$ mode damping is higher than the chord mode damping at the velocity corresponding to frequency cross-over. Also the beam mode has a damping peak because the $\zeta - 1$ mode damping is greater than the beam mode damping at the velocity where those frequencies cross-over. To study this phenomenon further, the baseline lag frequency curve is decreased throughout the speed range by a factor of 0.9. Figures 2.4 and 2.5 show the frequency and damping plots for the rotor and wing modes as a function of forward flight velocity. As shown, the decrease in lag frequency shifts the cross-over point with the chord frequency to a lower velocity where the corresponding chord mode damping is higher than the $\zeta - 1$ mode damping. The result is a damping valley in the chord mode and a damping peak in the $\zeta - 1$ mode at the forward flight velocity where the two modes coalesce.

The flutter velocity V_f^* is 1.095 times the nominal tiltrotor cruise tip speed. The damping of the wing beam, chord and torsion modes become negative (unstable) for forward flight velocities of 1.095, 1.1 and 1.365 respectively (Figure 2.3). These baseline cases shows the same trends as those in Refs.[38] and [39].

2.2 Rotor Frequency

The influence of rotor in-vacuo flap and lag frequencies on stability is examined in this section. The flap and lag frequencies are parametrically varied from 0.9 to 2.5 of their baseline values independently. The purpose of this study is to provide an insight into the optimal selection of rotor and wing properties to delay instabilities. The results of the ν_β and ν_ζ frequency sweeps are shown in Figures 2.6 and 2.7 respectively. The following observations are drawn from this study:

Reproduced with permission of the copyright owner. Further reproduction prohibited without permission.

(1) The beam and chord mode V_f^* increase sharply with increasing ν_β for factors between 0.9 and 1.3. One significant factor in this phenomenon is the decrease in the $\beta - 1$ frequency with increasing ν_β. The damped rotating flap frequency is less than unity, which results in a progressive $\beta - 1$ mode. As the ν_β factor is increased, the flap frequency increases approaching closer to unity thereby reducing the frequency of the progressive $\beta - 1$ mode. This decrease in the $\beta - 1$ frequency increases the velocity at which it crosses over the $\zeta - 1$ and the wing beam and chord frequencies. This delays the occurrence of flutter upto a higher velocity.

(2) The wing beam mode does not become unstable above about $1.4\nu_\beta$. At high ν_β factors, the $\beta + 1$ high frequency mode gets farther away from the wing beam mode. Hence the blade flap mode has only a slightly destabilizing influence on the wing beam mode contrary to the effect it has at lower ν_β factors. Also, as ν_β increases, the torsion frequency increases due to mechanical coupling between the rotor flap and wing torsion modes. This effect too has a stabilizing influence on the wing beam mode.

(3) A $\zeta + 1$ instability occurs at ν_β factors higher than 1.35. As a result, the flutter speed V_f^* drops drastically over the range $1.35\nu_\beta$ to $1.55\nu_\beta$, then increasing over the range $1.6\nu_\beta$ to $2.0\nu_\beta$. At these ν_β factors, the high frequency $\beta + 1$ mode shifts to a higher frequency and gets closer to the $\zeta + 1$ high frequency mode. As these modes interact, the damping of the $\zeta + 1$ mode decreases drastically, driving this mode unstable over this range of ν_β. The mechanism of this instability is flap-lag flutter.

(4) The wing chord mode becomes unstable at higher velocities for high ν_β. Its

Reproduced with permission of the copyright owner. Further reproduction prohibited without permission.

flutter speed increases due to decreased interaction with the high frequency $\beta + 1$ mode.

(5) The torsion mode stays relatively stable compared to the wing beam and chord modes and the rotor $\zeta + 1$ mode. The flutter speed of the torsion mode increases with increasing ν_β factors.

(6) The chord mode V_f^* increases with ν_ζ factors until about $1.9\nu_\zeta$ beyond which it remains almost constant. As the ν_ζ factor increases, the $\zeta - 1$ mode shifts to a higher frequency. This shift decreases the interaction of the wing chord mode with this lag mode (which is its closest neighbor), thus increasing the flutter velocity of the chord mode. At very high ν_ζ, this interaction is minimal; hence the flutter velocity of the chord mode asymptotes to a constant value.

(7) The beam mode V_f^* increases with ν_ζ factor, reaching a maximum around $1.3\nu_\zeta$ and then decreases to roughly its value at the baseline ν_ζ. As the lag frequency increases, the $\zeta - 1$ mode crosses the beam mode at higher velocities, where more damping is available in the $\zeta - 1$ mode to be transferred to the beam mode. This effect is hence stabilizing to the beam mode until about $1.3\nu_\zeta$. Beyond this ν_ζ factor, the beam mode coalesces with the $\beta - 1$ mode as the $\zeta - 1$ mode shifts farther away. This interaction with the flap mode decreases the damping of the beam mode driving it unstable at lower velocities for ν_ζ factors greater than 1.3.

(8) The chord V_f^* is lower than the beam V_f^* for factors between $1.0\nu_\zeta$ and $1.3\nu_\zeta$. Increasing ν_ζ in this range contributes to increased damping in the beam mode because of its interaction with the lag mode. During this process, very little effect of the lag mode is experienced in the chord mode because of the low velocity

Reproduced with permission of the copyright owner. Further reproduction prohibited without permission.

at which these two modes cross-over.

It can be concluded from this section that optimum flap and lag frequencies exist which can significantly increase the system flutter velocity. The flutter velocity has been shown to increase from $1.095V^*$ to roughly $1.34V^*$ by increasing the flap frequency by a factor of 1.35 from the baseline and from $1.095V^*$ to $1.23V^*$ for a lag frequency factor of 1.3. The tuning of the flap frequency could be more restrictive than tuning the lag frequency because of the flap frequency having a direct impact on handling qualities, etc., The lag frequency, however, can be increased slightly since the rotor is already stiff in-plane and making it a slightly stiffer in-plane might not have a severe impact on the loads. Similar conclusions were obtained in the studies reported in Refs. [38] and [39] although the specific gains in flutter velocity were different from those obtained in this study.

Also, the low frequency rotor modes, $\beta - 1$ and $\zeta - 1$, are found to be important system parameters, and their placement on the frequency plot has a direct impact on system stability. The low frequency flap mode has an adverse effect on the damping of the wing beam and chord modes at cross-over. The low frequency lag mode however has a beneficial effect on these wing modes since it transfers additional damping to the wing beam and chord modes at cross-over. Hence the low frequency $\zeta - 1$ mode should be made to cross the wing beam and chord mode frequencies before the low frequency $\beta - 1$ mode interacts with the wing modes. Some instability mechanisms observed in this study are:

a) The low frequency $\zeta - 1$ mode interacts with the low frequency $\beta - 1$ mode weakening the flap mode interaction with the wing modes. This phenomenon is

Reproduced with permission of the copyright owner. Further reproduction prohibited without permission.

lag-dominated and was observed in the pitch-flap coupling parametric study as well. The low frequency lag mode normally acts as a barrier between the low frequency flap mode and the wing beam or chord modes.

b) The low frequency $\beta - 1$ mode interacts with either the wing beam and chord modes causing flutter. This is flap-dominated and hence is not affected by the lag mode.

c) Coalescence of the high frequency $\beta + 1$ and $\zeta + 1$ rotor modes to produce a rotor flap-lag instability.

Increased separation between the wing torsion and wing beam frequencies (as effected by increasing ν_β) has a beneficial effect on the wing beam mode flutter velocity. Also, the chord mode flutter velocity is unaffected by the upward shift in the wing torsion frequency.

2.3 Wing Sweep

The effects of wing sweep, especially forward sweep, on stability are examined in this section. Forward wing sweep is typically considered for tiltrotor configurations to give a greater flap clearance for the rotor blades from the wing. The sweep angle is varied while maintaining the wing length, measured along the wing elastic axis, and the streamwise chord length constant. The pylon and rotor system, however, remains oriented in the free stream direction as in the baseline configuration.

The influence of sweeping the wing forward is shown in Figure 2.8. This plot shows that the wing beam and chord mode flutter velocities decrease with forward sweep. This can be attributed to the reorientation of destabilizing rotor forces

Reproduced with permission of the copyright owner. Further reproduction prohibited without permission.

with respect to the wing. The torsion mode flutter velocity, however, increases with forward wing sweep. This is due to the change in the pylon properties with respect to the wing elastic axis.

2.4 Lock Number

Lock number simultaneously shows the influence of changes in altitude, lift curve slope and blade inertia on aeroelastic stability. The results from parametric changes in Lock number from 0.50 to 1.70 of its baseline value of 3.83 are shown in Figure 2.9. The figure shows that at Lock numbers above 1.4 times the baseline value, the chord mode becomes unstable before the beam mode while at lower factors the beam mode becomes unstable first. As the Lock number factor increases, the effectiveness of the pitch-flap coupling increases. This, in turn, reduces the rotor rotating-frame flap frequency to much lower than 1.0 (it was lower than 1.0 for the baseline case too), which raises the $\beta - 1$ progressive flap frequency. The $\beta - 1$ frequency continues to increase with velocity, crossing the beam frequency at progressively lower velocities for higher Lock number factors. At high Lock numbers, the $\zeta - 1$ frequency crosses the $\beta - 1$ frequency very close to the beam frequency, thereby weakening the beam mode coalescence with the flap mode. This stabilizing influence of the lag mode raises the beam mode flutter velocity above where it would have been, had the lag mode interference not been present. The chord mode does not benefit from this phenomenon (because its frequency is higher than that of the beam mode) which results in the chord mode becoming unstable first.

The trend of decreasing flutter velocity with increasing Lock number is also

Reproduced with permission of the copyright owner. Further reproduction prohibited without permission.

evident in Figure 2.9. At higher Lock numbers, the rotor aerodynamic forces are higher compared to the rotor inertial forces. The higher aerodynamic forces cause the system to get into flutter at lower forward flight speeds than for lower Lock numbers, when the rotor aerodynamic forces are lower. This proves, yet again, that aerodynamic forces cause flutter. Also, the flutter manifests itself usually by the wing bending mode(s) going unstable as a result of excitation by rotor forces.

2.5 Pitch-Flap Coupling

Pitch-flap coupling is an important design for tiltrotor designs due to flap clearance considerations. Employing this coupling can significantly reduce blade flapping with negligible effect on blade loads. Negative δ_3 (flap up producing pitch up) decreases the flap frequency while positive δ_3 increases the flap frequency.

Figure 2.10 shows the variation in flutter velocity of different modes with pitch-flap coupling (baseline $\delta_3 = -15^o$). The mode of instability changes from the chord mode at zero and low negative δ_3 to the beam mode for higher negative δ_3. Starting from large negative δ_3, both the wing beam and chord modes are stabilized due to increase (less negative) in δ_3. But the beam mode is stabilized more due to the increase in the flap frequency (due to less negative δ_3) which in turn raises the wing torsion frequency increasing its separation from the beam frequency. This has a beneficial effect in increasing the beam mode flutter velocity.

At positive δ_3, a strong lag mode instability is observed. The $\zeta - 1$ mode frequency decreases with velocity, as always. The flap frequency increases with increase in δ_3. For increasing positive δ_3, the low frequency flap mode turns regres-

Reproduced with permission of the copyright owner. Further reproduction prohibited without permission.

sive since its frequency increases beyond unity. The two low frequency flap and lag modes coalesce driving the low frequency lag mode unstable (as explained in the observations in the rotor frequency section). This instability occurs earlier at higher positive δ_3 since the flap frequency is higher and coalesces earlier with the $\zeta - 1$ mode.

2.6 Pitch-Lag Coupling

The presence of rotor precone (given to alleviate flap bending moments at the blade root in hover) usually results in effective pitch-lag coupling for the rotor blade [38]. Figure 2.11 shows the variation in flutter velocity of different modes with pitch-lag coupling (baseline $\delta_4 = 0^o$). Negative δ_4 (refers to lag back causing pitch up) decreases the lag frequency whereas positive δ_4 increases the lag frequency.

Negative δ_4 causes a downward shift in the $\zeta - 1$ frequency curve which then crosses-over the wing beam mode at a lower velocity. At this lower velocity, the low frequency lag mode has lower damping to transfer to the beam mode. The beam mode, thus, goes unstable at lower velocities than for the baseline case.

Increasing positive δ_4 results in the chord mode going unstable at lower velocities compared to the baseline. This is due to the mechanical coupling between the rotor lag and the wing chord modes.

Reproduced with permission of the copyright owner. Further reproduction prohibited without permission.

Rotating Blade Frequencies (per rev, in-vacuo)	
ν_β	1.02
ν_{β_0}	1.85
ν_ζ	see Figure 2.1
ν_{ζ_0}	0
Wing Frequencies (per rev)	
beam mode	0.42
chord mode	0.70
torsion mode	1.30

Table 2.1: Frequencies of the baseline system

Reproduced with permission of the copyright owner. Further reproduction prohibited without permission.

Number of blades	3
Radius	12.5 ft.
Lock number	3.83
Rotor Solidity	0.089
Lift curve slope	5.73/rad.
Pitch-flap coupling	-0.268
Tip speed	600 ft/sec.
Rotational speed	48 rad/sec.

Table 2.2: Baseline rotor system parameters

Reproduced with permission of the copyright owner. Further reproduction prohibited without permission.

I_b	105 $slug\ ft^2$
$I^{\star}_{\beta}$	1.0
$I^{\star}_{\beta_0}$	0.779
$I^{\star}_{\zeta}$	0.67
$I^{\star}_{\zeta_0}$	0.67
$I^{\star}_{0}$	1.0
$I^{\star}_{\beta\alpha}$	1.0
$I^{\star}_{\zeta_0\alpha}$	0.787
$S^{\star}_{\zeta}$	1.035
$S^{\star}_{\beta_0}$	1.212
$M^{\star}_{b}$	6.16
(windmilling case)	
$I^{\star}_{\zeta_0}$	1.0
$I^{\star}_{\zeta_0\alpha}$	1.0
ν_{ζ_0}	0

Table 2.3: Baseline rotor blade inertia parameters

Reproduced with permission of the copyright owner. Further reproduction prohibited without permission.

Span, y_w/R	1.333
Chord, c_w/R	0.413
Mast height, h/R	0.342
Number of finite elements used	4

Property	Root element	2nd element	3rd element	Pylon element
Length, l/R	4.55	4.55	4.55	3.0
Inertia, I_{cg}	1.0	1.0	1.0	$63.3\cos^2\Lambda$
S_α	0.05	0.05	0.05	$9.09\cos\Lambda$
Mass	1.0	1.0	1.0	14.54
Beamwise Stiffness	3.13e7	3.13e7	3.13e7	3.13e7
Chordwise Stiffness	8.48e7	8.48e7	8.48e7	8.48e7
Torsional Stiffness	1.62e7	1.62e7	1.62e7	1.62e7
Aerodynamic Center, e/c	0.051	0.051	0.051	0

Table 2.4: Baseline wing parameters

Reproduced with permission of the copyright owner. Further reproduction prohibited without permission.

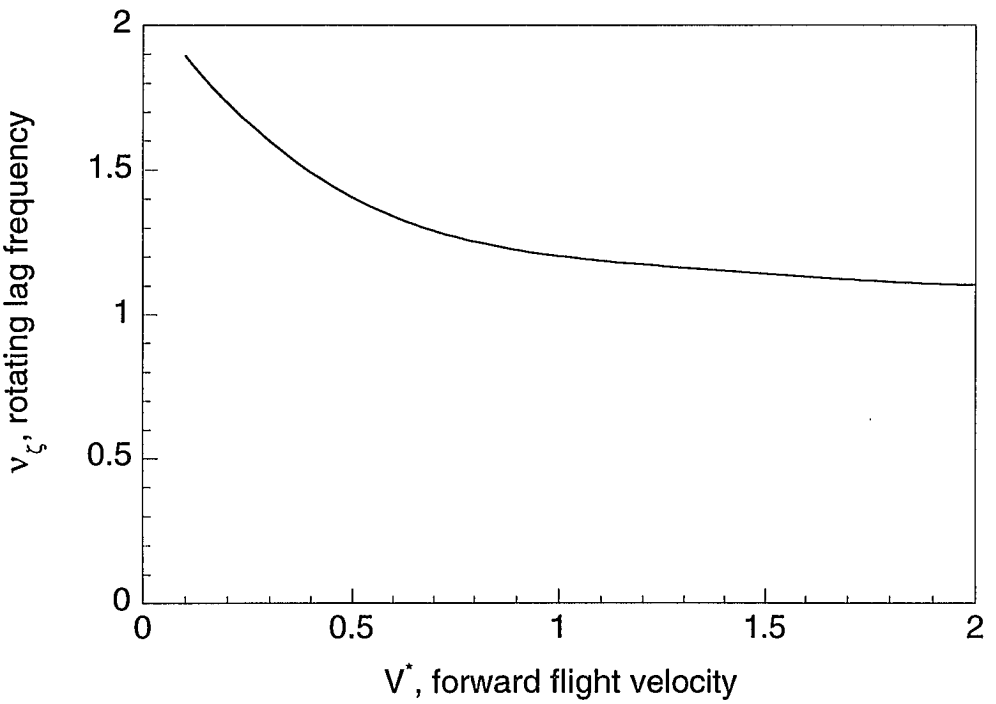

Figure 2.1: Rotor lag frequency variation with velocity

Reproduced with permission of the copyright owner. Further reproduction prohibited without permission.

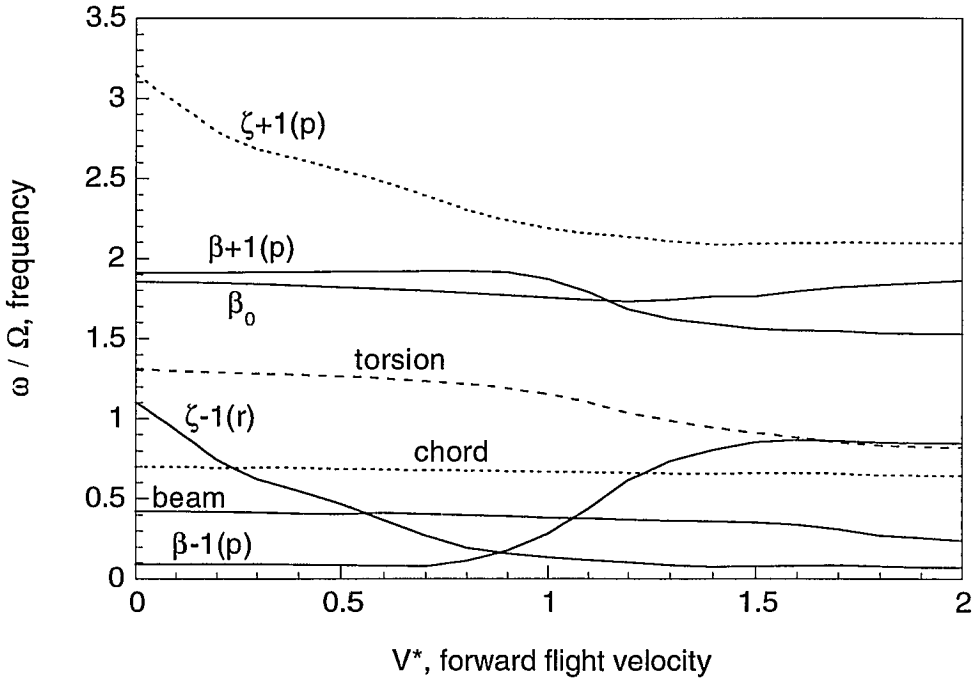

Figure 2.2: Baseline configuration frequencies

Reproduced with permission of the copyright owner. Further reproduction prohibited without permission.

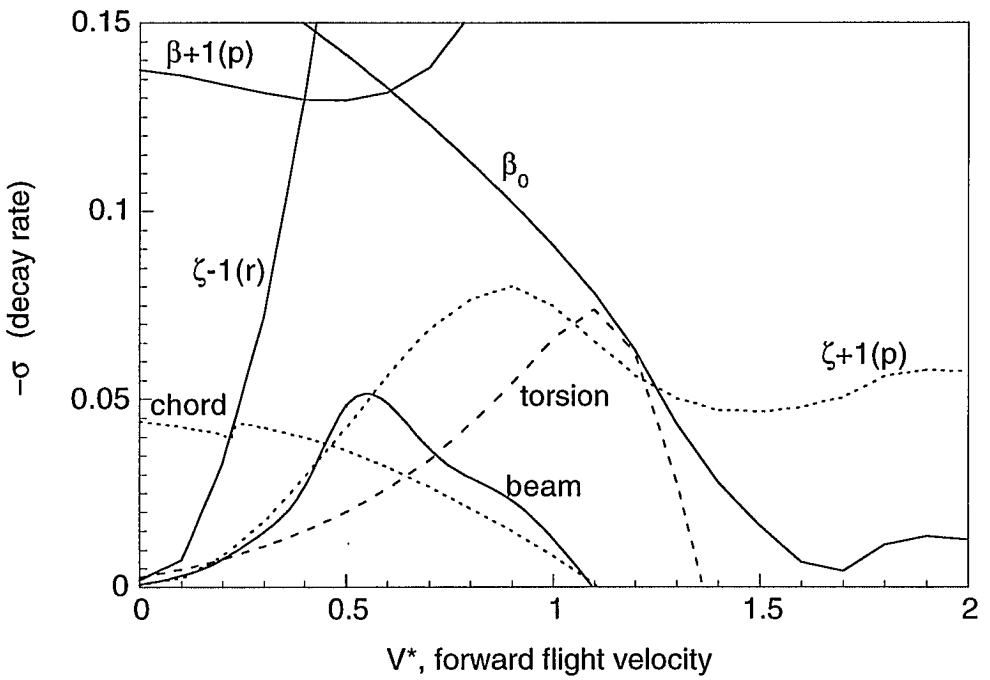

Figure 2.3: Baseline configuration damping

Reproduced with permission of the copyright owner. Further reproduction prohibited without permission.

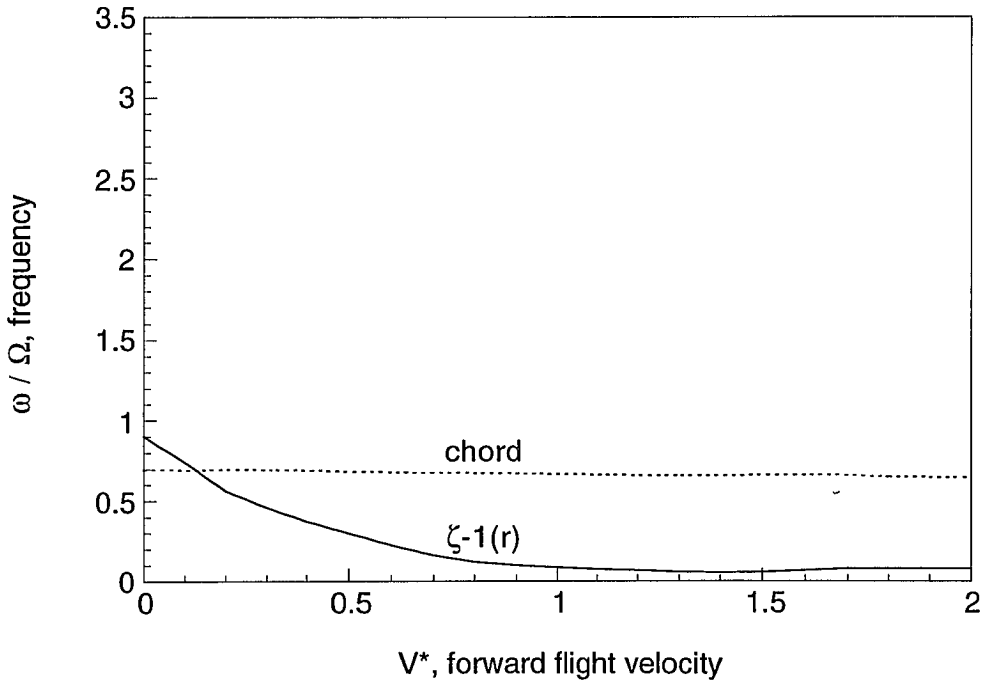

Figure 2.4: Frequencies (lag frequency $\nu_\zeta = 0.9$ x baseline ν_ζ)

Reproduced with permission of the copyright owner. Further reproduction prohibited without permission.

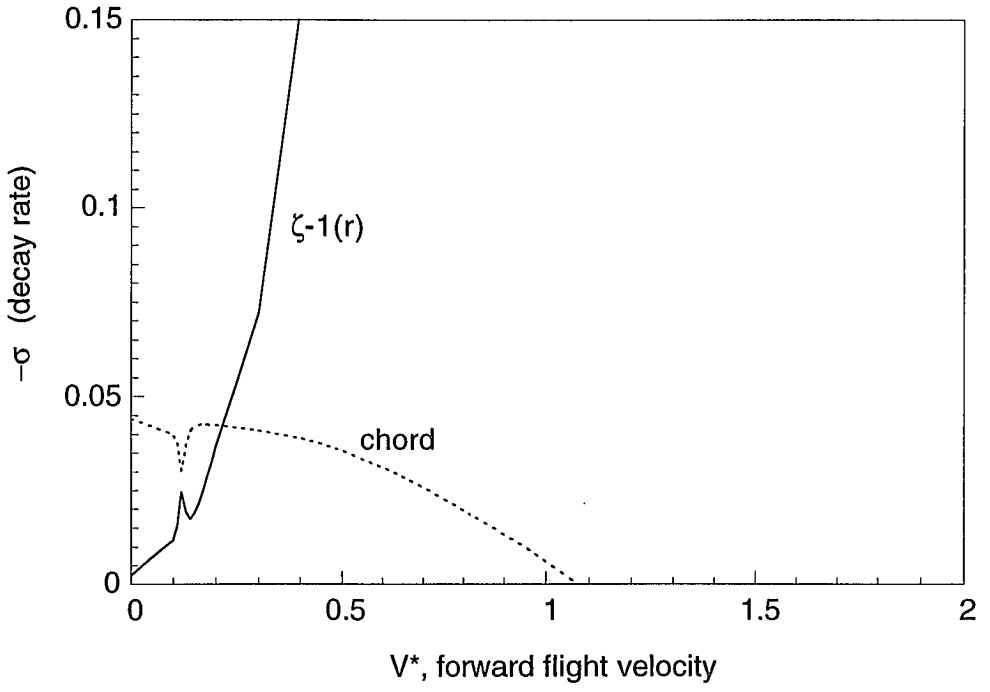

Figure 2.5: Damping (lag frequency $\nu_\zeta = 0.9$ x baseline ν_ζ)

Reproduced with permission of the copyright owner. Further reproduction prohibited without permission.

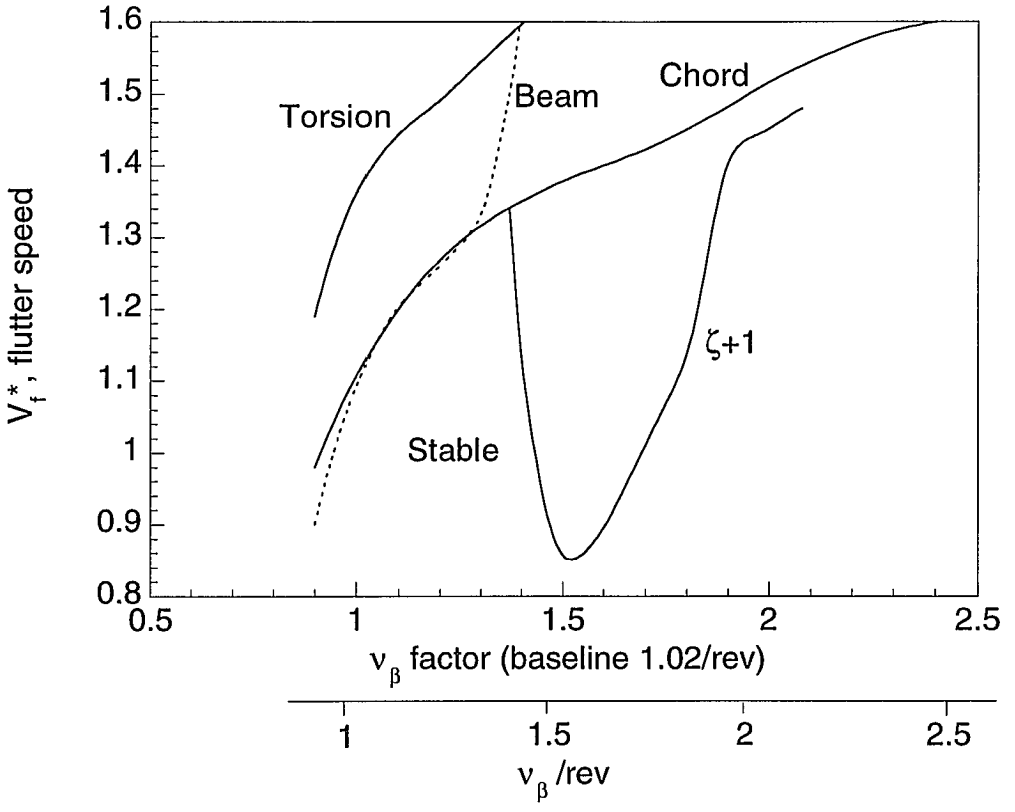

Figure 2.6: Flutter velocity variation with flap frequency (ν_β) factor

Reproduced with permission of the copyright owner. Further reproduction prohibited without permission.

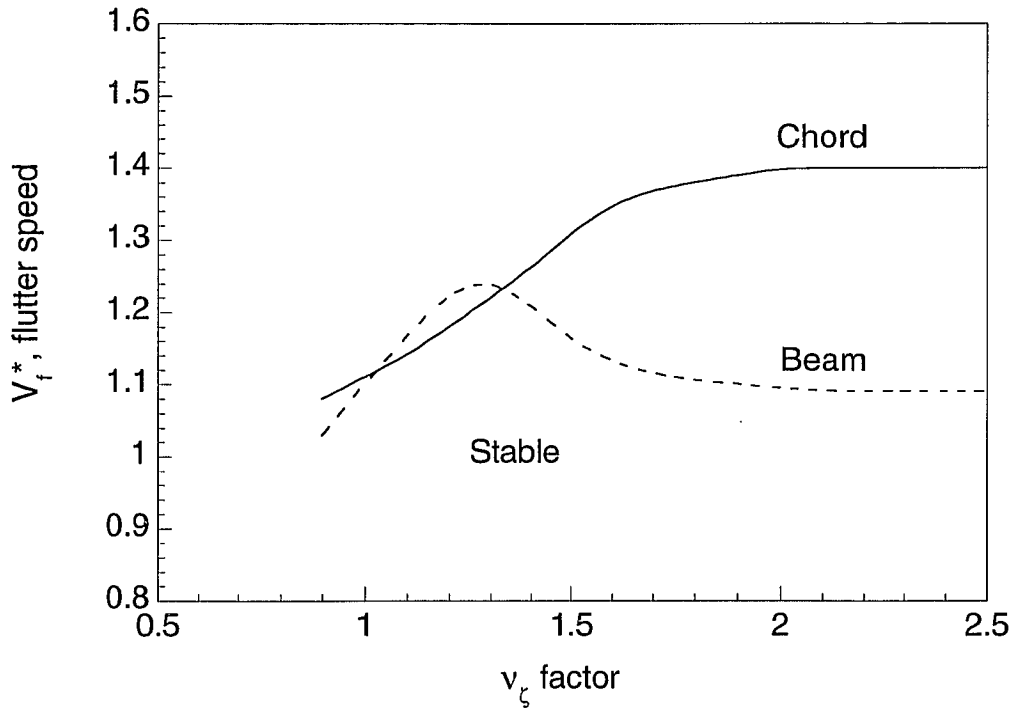

Figure 2.7: Flutter velocity variation with lag frequency (ν_ζ) factor

Reproduced with permission of the copyright owner. Further reproduction prohibited without permission.

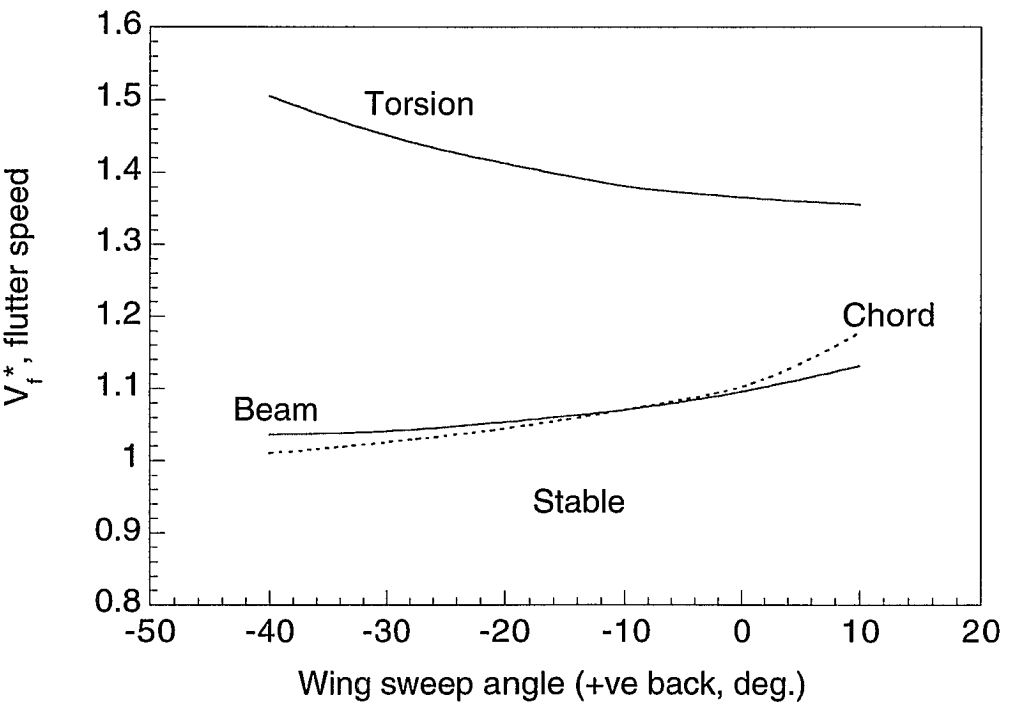

Figure 2.8: Flutter velocity variation with wing sweep angle

Reproduced with permission of the copyright owner. Further reproduction prohibited without permission.

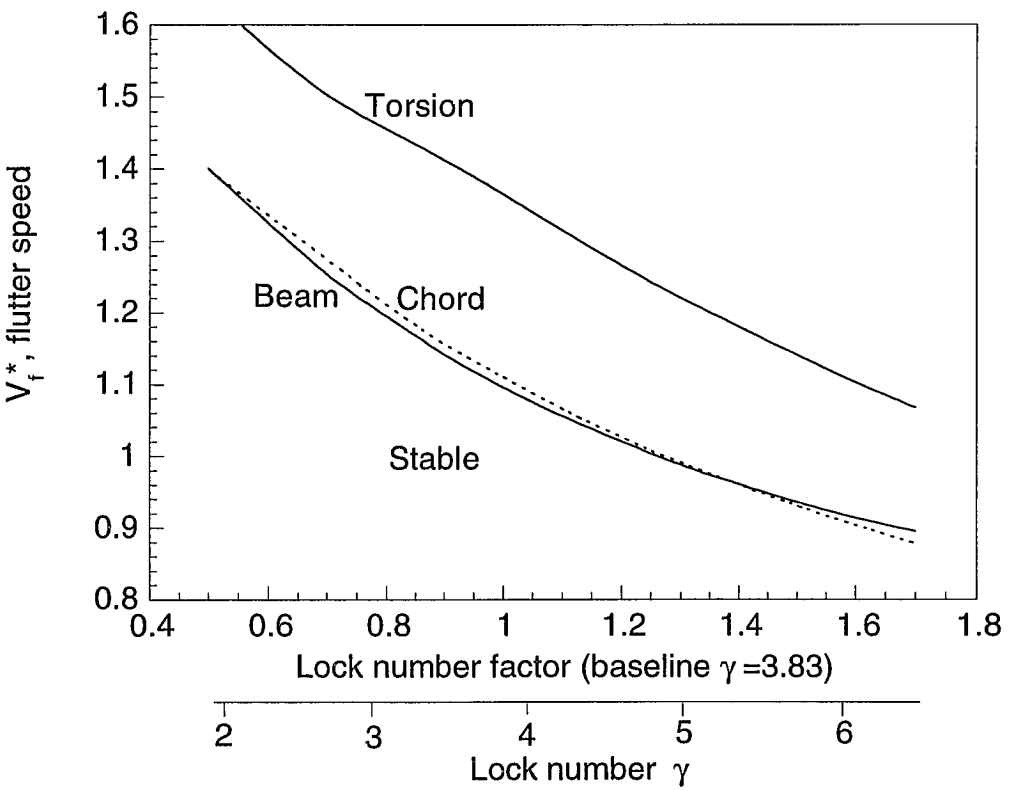

Figure 2.9: Flutter velocity variation with rotor Lock number (γ) factor

Reproduced with permission of the copyright owner. Further reproduction prohibited without permission.

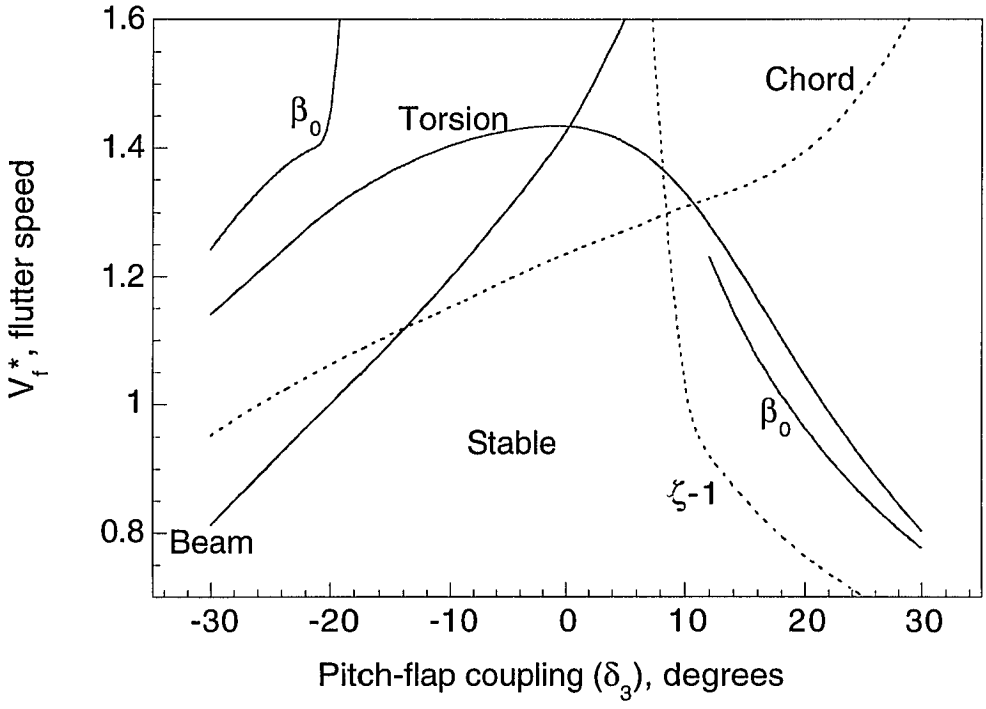

Figure 2.10: Flutter velocity variation with pitch-flap coupling

Reproduced with permission of the copyright owner. Further reproduction prohibited without permission.

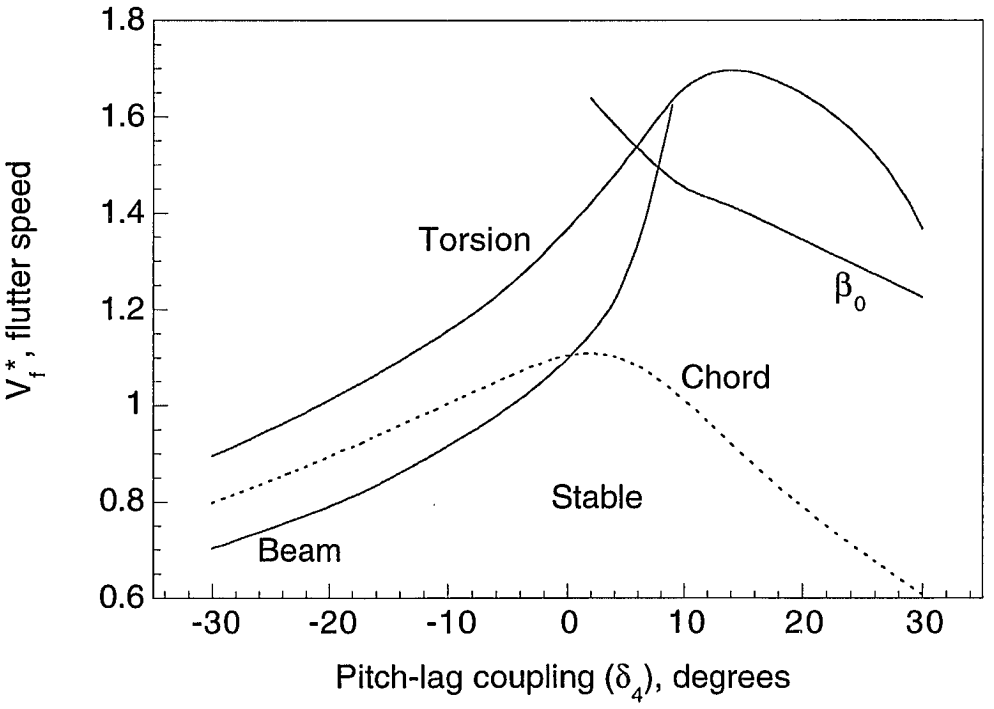

Figure 2.11: Flutter velocity variation with pitch-lag coupling

Reproduced with permission of the copyright owner. Further reproduction prohibited without permission.

Chapter 3

Elastic Blade Tiltrotor Model

An aeroelastic formulation for tiltrotors with highly-twisted, composite-coupled, advanced geometry blades with sweep, anhedral, pretwist and planform taper variation along blade span is presented in this chapter. The blade is composed of an arbitrary number of Euler-Bernoulli type straight beam segments each with different sweep, anhedral, pretwist and planform taper [90]. The only constraint imposed on the formulation is that the elastic axes of different beam segments used in the model are connected as piecewise continuous straight lines (Figure 3.1). Coupled-composite rotor blades including extension-torsion and bending-torsion coupled blades are modeled in this formulation. The formulation also handles offsets of blade section center of mass, aerodynamic center and tension center from the elastic axis. Blade kinematic pitch-flap and pitch-lag couplings are also modeled. Each blade segment is modeled using one or more finite elements and inter-segment compatibility relations are satisfied using nonlinear transformations. The tiltrotor wing is also modeled using beam finite elements; wing sweep, anhedral and planform taper are also included in the formulation. The blade and wing equations are derived in nonlinear form using Hamilton's principle.

Reproduced with permission of the copyright owner. Further reproduction prohibited without permission.

3.1 Tiltrotor Model

3.1.1 Reference Frames

The coordinate systems and transformations associated with the frames of reference used in the formulation of the tiltrotor structural model are defined in this section. For the present formulation, an inertial frame of reference is placed at a given point on the wing elastic axis (usually the wing-tip) before deformation as illustrated in Figure 3.2. The origin of this frame of reference is at the pivot point of the pylon which is assumed to be on the wing elastic axis. Since the wing itself is flexible, a deformed wing reference frame is required to describe the motion of the wing. This motion is similar to the hub motion in a helicopter.

There are six degrees of freedom at the point that the rotor pylon connects to the wing, three associated with translation and three with rotation. These six degrees of freedom are similar to hub degrees of freedom of a helicopter and will henceforth be referred to likewise. The original UMARC formulation had five fuselage degrees of freedom for a helicopter configuration which are x_f (longitudinal translation, positive aft), y_f (lateral translation, positive towards right), z_f (vertical translation, positive up), α_s (pitch rotation, positive nose-down) and ϕ_s (roll rotation, positive retreating side up in helicopter mode). The new tiltrotor hub degrees of freedom include all the above as well as ζ_h (yaw rotation, positive in the direction of rotor rotation in helicopter mode). The definition of these degrees of freedom is based on a starboard tiltrotor wing and rotor system. The inertial and deformed wing reference frames are shown in Figure 3.2.

Reproduced with permission of the copyright owner. Further reproduction prohibited without permission.

The hub reference frame is offset from the wing deformed frame by the pylon height and is fixed in space and orientation to the tip of the pylon. The pylon angle α_p is assumed to be a large steady input angle (no small-angle assumptions are made). The pylon angle is zero when the pylon is vertical (helicopter mode) and 90 degrees when the pylon points straight forward (airplane mode). A rotating system for the blade is defined by going from the hub frame through an inplane rotation equal to the azimuth angle.

The gimballed frame is defined as a transformation oriented at angles β_{GC} and β_{GS} with respect to the hub fixed-frame. The same transformation can be considered in the rotating frame as a single degree of freedom β_G that can be written as

$$\beta_G = \beta_{GC} \cos\psi + \beta_{GS} \sin\psi \tag{3.1}$$

where β_G is a function of time and

$$\overset{\star}{\beta}_G = \overset{\star}{\beta}_{GC} \cos\psi + \overset{\star}{\beta}_{GS} \sin\psi + \beta_{GS} \cos\psi - \beta_{GC} \sin\psi \tag{3.2}$$

For convenience, the fixed system gimbal degrees of freedom β_{GC} and β_{GS} are considered part of the hub degrees of freedom thus making it a total of eight hub degrees-of-freedom. The gimbal can be locked out of the model when conventional articulated, hingeless or bearingless rotor configurations are modeled.

The undeformed frame is obtained by starting from the rotating frame and going through the precone angle β_p and the gimbal angle β_G. The next transformation is from the undeformed frame to the control pitch frame through the time varying

Reproduced with permission of the copyright owner. Further reproduction prohibited without permission.

control pitch angle. The blade control pitch angle is a large angle for tiltrotors in high speed axial flight since the rotors operate in high inflow conditions.

This is followed by the most important transformation for the advanced geometry blade formulation involving the sweep, anhedral and pretwist variation along the blade span. The last transformation is from the cross-section frame to the deformed frame of the blade. There are thus a total of eight different coordinate systems from the inertial to the deformed system. They are as follows: inertial (i), deformed wing (w), hub (h), rotating (r), undeformed blade (u), control pitch (p), cross-section (c) and deformed blade (d). Each set of unit vector triads are related to another set through the following transformation relations:

$$\begin{Bmatrix} \hat{I}_d \\ \hat{J}_d \\ \hat{K}_d \end{Bmatrix} = [T_{dc}] \begin{Bmatrix} \hat{I}_c \\ \hat{J}_c \\ \hat{K}_c \end{Bmatrix} \tag{3.3}$$

$$\begin{Bmatrix} \hat{I}_c \\ \hat{J}_c \\ \hat{K}_c \end{Bmatrix} = [T_{cp}] \begin{Bmatrix} \hat{I}_p \\ \hat{J}_p \\ \hat{K}_p \end{Bmatrix} \tag{3.4}$$

$$\begin{Bmatrix} \hat{I}_p \\ \hat{J}_p \\ \hat{K}_p \end{Bmatrix} = [T_{pu}] \begin{Bmatrix} \hat{I}_u \\ \hat{J}_u \\ \hat{K}_u \end{Bmatrix} \tag{3.5}$$

$$\begin{Bmatrix} \hat{I}_u \\ \hat{J}_u \\ \hat{K}_u \end{Bmatrix} = [T_{ur}] \begin{Bmatrix} \hat{I}_r \\ \hat{J}_r \\ \hat{K}_r \end{Bmatrix} \tag{3.6}$$

$$\begin{Bmatrix} \hat{I}_r \\ \hat{J}_r \\ \hat{K}_r \end{Bmatrix} = [T_{rh}] \begin{Bmatrix} \hat{I}_h \\ \hat{J}_h \\ \hat{K}_h \end{Bmatrix} \tag{3.7}$$

$$\begin{Bmatrix} \hat{I}_h \\ \hat{J}_h \\ \hat{K}_h \end{Bmatrix} = [T_{hw}] \begin{Bmatrix} \hat{I}_w \\ \hat{J}_w \\ \hat{K}_w \end{Bmatrix} \tag{3.8}$$

$$\begin{Bmatrix} \hat{I}_w \\ \hat{J}_w \\ \hat{K}_w \end{Bmatrix} = [T_{wi}] \begin{Bmatrix} \hat{I}_i \\ \hat{J}_i \\ \hat{K}_i \end{Bmatrix} \tag{3.9}$$

Reproduced with permission of the copyright owner. Further reproduction prohibited without permission.

where T_{dc}, for example, is the transformation matrix between the deformed (d) frame and the cross-section (c) frame. The transformation matrices are listed below:

$$[T_{dc}] = \begin{bmatrix} 1 - v'^2/2 - w'^2/2 & v' & w' \\ -v'\cos\theta_1 & -v'w'\sin\theta_1 & (1 - w'^2/2)\sin\theta_1 \\ -w'\sin\theta_1 & +(1 - v'^2/2)\cos\theta_1 & \\ -w'\cos\theta_1 & -v'w'\cos\theta_1 & (1 - w'^2/2)\cos\theta_1 \\ +v'\sin\theta_1 & -(1 - v'^2/2)\sin\theta_1 & \end{bmatrix} \tag{3.10}$$

where $\theta_1 = \theta_0 + \hat{\phi}$ in the straight blade formulation.

$$[T_{pu}] = \begin{bmatrix} 1 & 0 & 0 \\ 0 & \cos\theta_0 & \sin\theta_0 \\ 0 & -\sin\theta_0 & \cos\theta_0 \end{bmatrix} \tag{3.11}$$

$$[T_{ur}] = \begin{bmatrix} \cos\beta_{pg} & 0 & -sin\beta_{pg} \\ 0 & 1 & 0 \\ \sin\beta_{pg} & 0 & \cos\beta_{pg} \end{bmatrix} \tag{3.12}$$

where $\beta_{pg} = \beta_p + \beta_G$.

$$[T_{rh}] = \begin{bmatrix} \cos\psi & \sin\psi & 0 \\ -\sin\psi & \cos\psi & 0 \\ 0 & 0 & 1 \end{bmatrix} \tag{3.13}$$

$$[T_{hw}] = \begin{bmatrix} \cos\alpha_p & 0 & sin\alpha_p \\ 0 & 1 & 0 \\ -\sin\alpha_p & 0 & \cos\alpha_p \end{bmatrix} \tag{3.14}$$

$$\begin{aligned} [T_{wi}] = & \begin{bmatrix} \cos\zeta_h & \sin\zeta_h & 0 \\ -\sin\zeta_h & \cos\zeta_h & 0 \\ 0 & 0 & 1 \end{bmatrix} \\ & \times \begin{bmatrix} \cos\alpha_h & 0 & sin\alpha_h \\ 0 & 1 & 0 \\ -\sin\alpha_h & 0 & \cos\alpha_h \end{bmatrix} \\ & \times \begin{bmatrix} 1 & 0 & 0 \\ 0 & \cos\phi_h & -\sin\phi_h \\ 0 & \sin\phi_h & \cos\phi_h \end{bmatrix} \end{aligned} \tag{3.15}$$

Reproduced with permission of the copyright owner. Further reproduction prohibited without permission.

The transformation T_{dc} listed here is the same transformation used in the UMARC formulation [70]. The transformation T_{pu} accounts for the time varying pitch angle of the blade with respect to the hub frame. The time varying pitch angle θ_0 includes the blade collective and cyclic pitch but does not include the blade pretwist. This part of the formulation is different from the conventional formulation presented in Ref. [70]. Transformation T_{hw} is a function of the pylon angle setting α_p which is an input quantity. Both the pylon angle and the blade pitch angle are large angles (no small-angle assumptions are made).

3.1.2 Advanced Geometry Blade Transformation

The coordinate systems defining the blade geometry are shown in Figure 3.1. Each segment is assigned a coordinate system to describe its orientation with respect to the main blade undeformed coordinate system. At the kth inter-segment junction, the inboard segment is called segment 1 and the outboard segment is called segment 2. The undeformed segment 1 triad is denoted by $(\hat{i}_1, \hat{j}_1, \hat{k}_1)$ and the undeformed segment 2 triad is denoted by $(\hat{i}_2, \hat{j}_2, \hat{k}_2)$. These triads are related to one another through a sequence of transformations involving the sweep, anhedral, pretwist and pitch control angles. This part of the formulation is described in detail in Ref. [84].

Sweep Transformation

Let the undeformed segments 1 and 2 have a sweep forward of Λ_1^1 and Λ_1^2 respectively with reference to the undeformed frame. The coordinate transformation from the undeformed frame to the undeformed segment 2 frame for a sweep alone

Reproduced with permission of the copyright owner. Further reproduction prohibited without permission.

is given by:

$$\begin{Bmatrix} \hat{i}_2 \\ \hat{j}_2 \\ \hat{k}_2 \end{Bmatrix} = \left[T^2_{\Lambda_1}\right] \begin{Bmatrix} \hat{i}_u \\ \hat{j}_u \\ \hat{k}_u \end{Bmatrix} \tag{3.16}$$

where

$$\left[T^2_{\Lambda_1}\right] = \begin{bmatrix} \cos\Lambda^2_1 & 0 & -\sin\Lambda^2_1 \\ 0 & 1 & 0 \\ \sin\Lambda^2_1 & 0 & \cos\Lambda^2_1 \end{bmatrix} \tag{3.17}$$

Similarly, for undeformed segment 1, the transformation is given as

$$\begin{Bmatrix} \hat{i}_1 \\ \hat{j}_1 \\ \hat{k}_1 \end{Bmatrix} = \left[T^1_{\Lambda_1}\right] \begin{Bmatrix} \hat{i}_u \\ \hat{j}_u \\ \hat{k}_u \end{Bmatrix} \tag{3.18}$$

where

$$\left[T^1_{\Lambda_1}\right] = \begin{bmatrix} \cos\Lambda^1_1 & 0 & -\sin\Lambda^1_1 \\ 0 & 1 & 0 \\ \sin\Lambda^1_1 & 0 & \cos\Lambda^1_1 \end{bmatrix} \tag{3.19}$$

where Λ_1 is the sweep forward between the undeformed frame and the segment undeformed system.

Anhedral Transformation

Let the undeformed segments 1 and 2 have an anhedral upward of Λ^1_2 and Λ^2_2 respectively with reference to the undeformed frame. The coordinate transformation from the undeformed frame to the undeformed segment 2 frame for a sweep alone is given by:

$$\begin{Bmatrix} \hat{i}_2 \\ \hat{j}_2 \\ \hat{k}_2 \end{Bmatrix} = \left[T^2_{\Lambda_2}\right] \begin{Bmatrix} \hat{i}_u \\ \hat{j}_u \\ \hat{k}_u \end{Bmatrix} \tag{3.20}$$

Reproduced with permission of the copyright owner. Further reproduction prohibited without permission.

where

$$\left[T^2_{\Lambda_2}\right] = \begin{bmatrix} \cos\Lambda^2_2 & 0 & -\sin\Lambda^2_2 \\ 0 & 1 & 0 \\ \sin\Lambda^2_2 & 0 & \cos\Lambda^2_2 \end{bmatrix} \tag{3.21}$$

Similarly, for undeformed segment 1, the transformation is given as

$$\begin{Bmatrix} \hat{i}_1 \\ \hat{j}_1 \\ \hat{k}_1 \end{Bmatrix} = \left[T^1_{\Lambda_2}\right] \begin{Bmatrix} \hat{i}_u \\ \hat{j}_u \\ \hat{k}_u \end{Bmatrix} \tag{3.22}$$

where

$$\left[T^1_{\Lambda_2}\right] = \begin{bmatrix} \cos\Lambda^1_2 & 0 & -\sin\Lambda^1_2 \\ 0 & 1 & 0 \\ \sin\Lambda^1_2 & 0 & \cos\Lambda^1_2 \end{bmatrix} \tag{3.23}$$

Pretwist Transformation

Let the undeformed segments 1 and 2 have a pretwist nose-up of Λ^1_3 and Λ^2_3 respectively with reference to the undeformed frame. The coordinate transformation from the undeformed frame to the undeformed segment 2 frame for a pretwist alone is given by:

$$\begin{Bmatrix} \hat{i}_2 \\ \hat{j}_2 \\ \hat{k}_2 \end{Bmatrix} = \left[T^2_{\Lambda_3}\right] \begin{Bmatrix} \hat{i}_u \\ \hat{j}_u \\ \hat{k}_u \end{Bmatrix} \tag{3.24}$$

where

$$\left[T^2_{\Lambda_3}\right] = \begin{bmatrix} \cos\Lambda^2_3 & 0 & -\sin\Lambda^2_3 \\ 0 & 1 & 0 \\ \sin\Lambda^2_3 & 0 & \cos\Lambda^2_3 \end{bmatrix} \tag{3.25}$$

Similarly, for undeformed segment 1, the transformation is given as

$$\begin{Bmatrix} \hat{i}_1 \\ \hat{j}_1 \\ \hat{k}_1 \end{Bmatrix} = \left[T^1_{\Lambda_3}\right] \begin{Bmatrix} \hat{i}_u \\ \hat{j}_u \\ \hat{k}_u \end{Bmatrix} \tag{3.26}$$

Reproduced with permission of the copyright owner. Further reproduction prohibited without permission.

where

$$\left[T^1_{\Lambda_3}\right] = \begin{bmatrix} \cos\Lambda^1_3 & 0 & -\sin\Lambda^1_3 \\ 0 & 1 & 0 \\ \sin\Lambda^1_3 & 0 & \cos\Lambda^1_3 \end{bmatrix} \tag{3.27}$$

where Λ_3 is the pretwist nose-up between the undeformed frame and the segment undeformed system.

Transformation due to Sweep, Anhedral and Pretwist

The transformation between the undeformed frame and the undeformed segment 2 system with arbitrary sweep Λ_1 (positive for sweep forward), followed by anhedral Λ_2 (positive for anhedral up, negative anhedral is referred to as droop) and then followed by pretwist rotation Λ_3 (positive for rotation nose-up) is given by:

$$\begin{Bmatrix} \hat{i}_2 \\ \hat{j}_2 \\ \hat{k}_2 \end{Bmatrix} = \left[T^2_\Lambda\right] \begin{Bmatrix} \hat{i}_u \\ \hat{j}_u \\ \hat{k}_u \end{Bmatrix} \tag{3.28}$$

where

$$\left[T^2_\Lambda\right] = \begin{bmatrix} C_1C_2 & S_1C_2 & S_2 \\ -S_1C_3 - C_1S_2S_3 & C_1C_3 - S_1S_2S_3 & C_2S_3 \\ S_1S_3 - C_1S_2C_3 & -C_1S_3 - S_1S_2C_3 & C_2C_3 \end{bmatrix} \tag{3.29}$$

where C_i and S_i represent $\cos\Lambda_i$ and $\sin\Lambda_i$ respectively for $i = 1$ to 3 for segment 2 of the blade.

Similar relations for undeformed segment 1 is given by:

$$\begin{Bmatrix} \hat{i}_1 \\ \hat{j}_1 \\ \hat{k}_1 \end{Bmatrix} = \left[T^1_\Lambda\right] \begin{Bmatrix} \hat{i}_u \\ \hat{j}_u \\ \hat{k}_u \end{Bmatrix} \tag{3.30}$$

Reproduced with permission of the copyright owner. Further reproduction prohibited without permission.

where

$$\left[T_\Lambda^1\right] = \begin{bmatrix} C_1C_2 & S_1C_2 & S_2 \\ -S_1C_3 - C_1S_2S_3 & C_1C_3 - S_1S_2S_3 & C_2S_3 \\ S_1S_3 - C_1S_2C_3 & -C_1S_3 - S_1S_2C_3 & C_2C_3 \end{bmatrix} \tag{3.31}$$

Deformed Blade Geometry

It is necessary to define the position vector of an arbitrary point on the deformed blade in order to derive the blade equations of motion. The transformation T_{dc} is used to describe the transformation from the cross-section reference frame to the blade deformed frame. This transformation, however, needs to be defined differently for the advanced geometry blade formulation.

$$[T_{dc}] = \begin{bmatrix} 1-\frac{v'^2}{2}-\frac{w'^2}{2} & v' & w' \\ -v'C^1 & -v'w'S^1 & \left(1-\frac{w'^2}{2}\right)S^1 \\ -w'S^1 & +\left(1-\frac{v'^2}{2}\right)C^1 & \\ -w'C^1 & -v'w'C^1 & \left(1-\frac{w'^2}{2}\right)C^1 \\ +v'S^1 & -\left(1-\frac{v'^2}{2}\right)S^1 & \end{bmatrix} \tag{3.32}$$

where $C^1 = \cos\theta_1$, $S^1 = \sin\theta_1$, v and w are the blade lag and flap deformations and

$$\theta_1(s) = \theta_{tw}(s) + \phi(s) - \int_0^s w'v''\, ds - \theta_{tw}(0) - \phi(0) + \theta_1(0) \tag{3.33}$$

or, simply stated,

$$\theta_1(s) = \theta_{tw}(s) + \hat{\phi}(s) \tag{3.34}$$

Reproduced with permission of the copyright owner. Further reproduction prohibited without permission.

s is the local coordinate along the segment and θ_{tw} is the blade twist. The effects of the time varying pitch control angle θ_0 have been separated out of this transformation and included separately.

Between elements, there is a continuity of displacement for the elastic twist, axial, lag and flap deflections and continuity of slope for the flap and lag bending motions. The relationship between the translational degrees-of-freedom at the intersegment junction between two segments is linear and can be written as

$$\begin{Bmatrix} u_{e_2} \\ v_2 \\ w_2 \end{Bmatrix} = [T_s] \begin{Bmatrix} u_{e_1} \\ v_1 \\ w_1 \end{Bmatrix} \tag{3.35}$$

where T_s is the transformation matrix between the two segments and is defined as $T_s = T_{\Lambda^2}.T_{\Lambda^1}^T$.

The relationship of the bending slopes and twist between any two segments at the intersegment junction, however, is nonlinear and is derived below. This is similar to the derivation in Ref. [84]. Let U and D be the deformations of any given segment of the blade in the undeformed and deformed frames respectively.

$$U_2 = T_s U_1 \tag{3.36}$$

$$D_2 = T_s D_1 \tag{3.37}$$

At the intersegment junction, the following relations hold:

$$\begin{aligned} D_2 &= T_{dc_2}\left(v_2', w_2', \theta_{1_2}\right) U_2 \\ D_1 &= T_{dc_1}\left(v_1', w_1', \theta_{1_1}\right) U_1 \end{aligned} \tag{3.38}$$

From the above equations, the following relationship between the deformations of segment 1 and 2 is obtained:

$$D_2 = T_s D_1 = T_s T_{dc_1} U_1 = T_s T_{dc_1} T_s^T U_2$$

Reproduced with permission of the copyright owner. Further reproduction prohibited without permission.

$$= T_s T_{dc_1} T_s^T T_{dc_2}^T D_2 \tag{3.39}$$

or

$$T_{dc_2} = T_s T_{dc_1} T_s^T \tag{3.40}$$

The above nonlinear equation gives the transformation between the variables v_2', w_2', θ_{1_2} and v_1', w_1', θ_{1_1} at the inter-segment junction. In terms of the deformations, the above equation can be written as

$$\begin{Bmatrix} \theta_{1_2} \\ w_2' \\ v_2' \end{Bmatrix} = \left(T_\Lambda^* + \bar{T}^K\right) \cdot \begin{Bmatrix} \theta_{1_1} \\ w_1' \\ v_1' \end{Bmatrix} = T_{\Lambda R} \cdot \begin{Bmatrix} \theta_{1_1} \\ w_1' \\ v_1' \end{Bmatrix} \tag{3.41}$$

where

$$T_\Lambda^* = \begin{bmatrix} T_{11} & -T_{12} & T_{13} \\ -T_{21} & T_{22} & -T_{23} \\ T_{31} & -T_{32} & T_{33} \end{bmatrix}_s \tag{3.42}$$

The subscript s in the above transformation matrix implies that the elements are obtained from the intersegment transformation matrix, T_s. T_Λ^* is the constant part of the transformation which is independent of the segment transformation variables. The $\bar{T}^K$ matrix gives rise to a nonlinear transformation since it depends on the segment deformations themselves and is given as

$$\begin{aligned} \bar{T}_{i1}^K &= a_{i1}\theta_{1_1} + b_{i1}v_1' \\ \bar{T}_{i2}^K &= a_{i2}w_1' + b_{i2}\theta_{1_1} \\ \bar{T}_{i3}^K &= a_{i3}v_1' + b_{i3}w_1' \end{aligned} \tag{3.43}$$

where $i = 1, 3$ and

$$\begin{aligned} a_{11} &= -\left(T_{s_{22}}T_{s_{32}} + T_{s_{23}}T_{s_{33}}\right)/2 \quad b_{11} = T_{s_{23}}T_{s_{31}} \\ a_{12} &= -(T_{s_{21}}T_{s_{31}} + T_{s_{23}}T_{s_{33}})/2 \quad b_{12} = -T_{s_{22}}T_{s_{31}} \end{aligned}$$

Reproduced with permission of the copyright owner. Further reproduction prohibited without permission.

$$
\begin{aligned}
a_{13} &= -(T_{s_{21}}T_{s_{31}} + T_{s_{22}}T_{s_{32}})/2 \quad b_{13} = T_{s_{23}}T_{s_{32}} \\
a_{21} &= -(T_{s_{12}}T_{s_{32}} + T_{s_{13}}T_{s_{33}})/2 \quad b_{21} = T_{s_{13}}T_{s_{31}} \\
a_{22} &= -(T_{s_{11}}T_{s_{31}} + T_{s_{13}}T_{s_{33}})/2 \quad b_{22} = -T_{s_{12}}T_{s_{31}} \\
a_{23} &= -(T_{s_{11}}T_{s_{31}} + T_{s_{12}}T_{s_{32}})/2 \quad b_{23} = -T_{s_{13}}T_{s_{32}} \\
a_{31} &= -(T_{s_{12}}T_{s_{22}} + T_{s_{13}}T_{s_{32}})/2 \quad b_{31} = T_{s_{13}}T_{s_{21}} \\
a_{32} &= -(T_{s_{12}}T_{s_{22}} + T_{s_{13}}T_{s_{32}})/2 \quad b_{32} = -T_{s_{12}}T_{s_{21}} \\
a_{33} &= -(T_{s_{11}}T_{s_{21}} + T_{s_{12}}T_{s_{22}})/2 \quad b_{33} = -T_{s_{13}}T_{s_{22}}
\end{aligned} \tag{3.44}
$$

The relations given in Eq. 3.35 and Eq. 3.41 represent the intersegment compatibility relations.

Position Vector of an Arbitrary Point on the Deformed Blade

Consider a segment k undergoing deformation. Let point P be a generic point on the elastic axis of the undeformed segment (see Figure 3.1), and Q be an arbitrary point in the section normal to elastic axis at point P. Let P_1 and Q_1 be the corresponding positions of these points in the deformed frame. The position vector of point Q_1 in the deformed segment cross-section is given by

$$
\begin{aligned}
\vec{r} &= O\vec{Q}_1 = O\vec{A}_1 + A_1\vec{A}_2 + \ldots + \\
&\quad A_{k-1}\vec{A}_k + A_k\vec{P} + P\vec{P}_1 + P_1\vec{Q}_1
\end{aligned} \tag{3.45}
$$

Let $OA_1 = l_0$, $A_1A_2 = l_1$,..., $A_{k-1}A_k = l_{k-1}$. Then,

$$
\vec{r} = \sum_{p=0}^{k-1} l_p\hat{i}_p + s\hat{i}_k + \bar{x}\hat{i}_k + \bar{y}\hat{j}_k + \bar{z}\hat{k}_k \tag{3.46}
$$

Reproduced with permission of the copyright owner. Further reproduction prohibited without permission.

where subscript p refers to the pth segment inboard of the kth segment, and s is the distance of point P from the junction A_k and

$$\begin{aligned} \bar{x} &= u - \lambda_T \hat{\phi}' - v'(\bar{y} - v) - w'(\bar{z} - w) \\ \bar{y} &= v + \eta \cos\theta_1 - \zeta \sin\theta_1 \\ \bar{z} &= w + \eta \sin\theta_1 + \zeta \cos\theta_1 \end{aligned} \tag{3.47}$$

where

$$u = u_e + \bar{u} \tag{3.48}$$

and u_e, v and w are elastic deformations for the kth blade segment. u_e is the axial elastic displacement. Radial shortening $\bar{u}$ is experienced at the point $(s, 0, 0)$ on the elastic axis of the kth blade segment. The net radial shortening at location s of the kth segment is obtained by summing the contributions from the inboard segments and the current segment.

$$\bar{u}(s) = \bar{u}\big|_0^s + \sum_{p=0}^{k-1} T_{kp_{11}} \bar{u}^p \tag{3.49}$$

where $T_{kp_{11}}$ is the transformation relating the axial displacement in the kth segment coordinate system to the axial displacement in the pth segment coordinate system.

$$T_{kp} = T_s = T_\Lambda^k \cdot T_\Lambda^{pT} \tag{3.50}$$

It is necessary to express the position vector in terms of one set of coordinates only, therefore, we need to find expressions for $\hat{i}_p$ in terms of $\hat{i}_k$, $\hat{j}_k$ and $\hat{k}_k$. Relative to the main blade reference triad $\hat{i}_u, \hat{j}_u, \hat{k}_u$ we can write the triads for the pth and kth segments as

$$\begin{Bmatrix} \hat{i}_p \\ \hat{j}_p \\ \hat{k}_p \end{Bmatrix} = \Lambda'_p \begin{Bmatrix} \hat{i}_u \\ \hat{j}_u \\ \hat{k}_u \end{Bmatrix} \tag{3.51}$$

Reproduced with permission of the copyright owner. Further reproduction prohibited without permission.

$$\left\{ \begin{array}{c} \hat{i}_k \\ \hat{j}_k \\ \hat{k}_k \end{array} \right\} = \mathbf{\Lambda'}_k \left\{ \begin{array}{c} \hat{i}_u \\ \hat{j}_u \\ \hat{k}_u \end{array} \right\} \tag{3.52}$$

where $\mathbf{\Lambda'}_p = T_{dc}.T_{cp}$.

Substituting $\hat{i}_u, \hat{j}_u, \hat{k}_u$ from Eq. 3.52 into Eq. 3.51 yields

$$\left\{ \begin{array}{c} \hat{i}_p \\ \hat{j}_p \\ \hat{k}_p \end{array} \right\} = \mathbf{\Lambda'}_p \mathbf{\Lambda'}_k{}^T \left\{ \begin{array}{c} \hat{i}_k \\ \hat{j}_k \\ \hat{k}_k \end{array} \right\} \tag{3.53}$$

from where we get

$$\hat{i}_p = T_{pk_1}\hat{i}_k + T_{pk_2}\hat{j}_k + T_{pk_3}\hat{k}_k \tag{3.54}$$

where the elements of the transformation T_{pk} are defined as

$$T_{pk_i} = \sum_{n=1}^{3} \Lambda'_{p_{1n}} \Lambda'_{k_{in}}, \qquad i = 1, 3 \tag{3.55}$$

Substituting Eq. 3.54 in Eq. 3.46, we obtain the position vector for the kth segment as

$$\vec{r} = x_k\hat{i}_k + y_k\hat{j}_k + z_k\hat{k}_k \tag{3.56}$$

where

$$\begin{aligned} x_k &= s + \bar{x} + L_1 \\ y_k &= \bar{y} + L_2 \\ z_k &= \bar{z} + L_3 \end{aligned} \tag{3.57}$$

and

$$\begin{aligned} L_1 &= \sum_{p=0}^{k-1} T_{pk_1} l_p \\ L_2 &= \sum_{p=0}^{k-1} T_{pk_2} l_p \\ L_3 &= \sum_{p=0}^{k-1} T_{pk_3} l_p \end{aligned} \tag{3.58}$$

Reproduced with permission of the copyright owner. Further reproduction prohibited without permission.

are the projected lengths of the inboard segments on the kth segments.

The expression for the position vector derived in this section is used to formulate the governing equations of motion for an advanced geometry blade.

3.1.3 Ordering Scheme

The present formulation is developed in nondimensional form consistent with that used in UMARC. The physical quantities are nondimensionalized by reference parameters such as mass, length and time associated with the rotor system as given in Table 3.1. The reference mass parameter m_0 is defined as the distributed mass of a uniform blade which has the same flap inertia as the blade under consideration (which may be nonuniform). This parameter is given by

$$m_0 = \frac{3I_\beta}{R^3} = \frac{3\int_0^R mr^2 dr}{R^3} \tag{3.59}$$

This formulation is developed in an explicit nonlinear form; hence the need for an ordering scheme exists to prevent the higher order terms from proliferating. Terms of order ϵ^{n+2} and higher are ignored when terms of order ϵ^n exist in the same energy expression, where ϵ is a quantity equivalent to the maximum bending rotation expected in the beam model. The ordering scheme used in this formulation is similar to that used in Ref. [39] but slightly different from that used in previous formulations associated with UMARC. As elastic coupling in rotor blades can result in large elastic twist, the present ordering scheme considers elastic twist to be of order 1 rather than of order ϵ as it has been in past formulations. The order of important nondimensional quantities associated with this formulation are listed as

Reproduced with permission of the copyright owner. Further reproduction prohibited without permission.

follows:

$$
\begin{aligned}
O(1) &= \mu, \frac{x}{R}, \frac{h}{R}, \frac{m}{m_0}, \frac{\partial}{\partial\psi}, \frac{\partial}{\partial x}, \\
&\quad \cos\psi, \sin\psi, \cos\theta_1, \sin\theta_1, \cos\alpha_p, \sin\alpha_p, \\
&\quad \theta_0, \theta_1, \theta_t, \hat{\phi} \qquad (3.60) \\
O(\epsilon) &= \frac{v}{R}, \frac{w}{R}, \beta_p, \beta_{GC}, \beta_{GS}, \\
&\quad \frac{x_h}{R}, \frac{y_h}{R}, \frac{z_h}{R}, \frac{\overset{\star}{x}_h}{R}, \frac{\overset{\star}{y}_h}{R}, \frac{\overset{\star}{z}_h}{R}, \\
&\quad \alpha_h, \phi_h, \zeta_h, \overset{\star}{\alpha}_h, \overset{\star}{\phi}_h, \overset{\star}{\zeta}_h, \\
&\quad \frac{\eta_r}{R}, \frac{e_d}{R}, \frac{e_A}{R}, \frac{e_g}{R} \qquad (3.61) \\
O(\epsilon^2) &= \frac{u_e}{R} \qquad (3.62)
\end{aligned}
$$

3.2 Equations of Motion

The derivation of the system equations of motion is based on Hamilton's variational principle generalized for a nonconservative system which can be expressed as

$$\delta\Pi = \int_{t_1}^{t_2} (\delta U - \delta T - \delta W)\, dt = 0 \qquad (3.63)$$

δU is the variation of the elastic strain energy, δT is the variation of kinetic energy, and δW is the work done by nonconservative forces which are of aerodynamic origin. The contributions to these energy expressions from the rotor blades, hub, and wing may be summed as

$$
\begin{aligned}
\delta U &= \left(\sum_{m=1}^{N_b} \delta U_b \right) + \delta U_h + \delta U_w \qquad (3.64) \\
\delta T &= \left(\sum_{m=1}^{N_b} \delta T_b \right) + \delta T_h + \delta T_w \qquad (3.65)
\end{aligned}
$$

Reproduced with permission of the copyright owner. Further reproduction prohibited without permission.

$$\delta W = \left(\sum_{m=1}^{N_b} \delta W_b \right) + \delta W_h + \delta W_w \tag{3.66}$$

where the subscripts b, h and w refer to the blade, hub and wing respectively. Derivation of the system elastic strain energy follows closely the formulation in Ref. [84] but some modifications are needed to include the gimbal motion and pitch-lag coupling due to rotor precone. The rotor blade kinetic energy is derived including the effects of hub motion and gimbal degrees-of-freedom. It is similar to the derivation in Ref. [39] in handling hub and gimbal motions but is different from that derivation since the present model is capable of modeling arbitrary blade and wing geometry.

For the formulation of the strain and kinetic energies, the rotor blade is assumed to be a long and slender beam constructed from anisotropic materials undergoing elastically coupled deformation. The blade may deform in extension u_e, lag bending v, flap bending w, and torsion $\hat{\phi}$, and both built-in pretwist and elastic twist deformation may be large.

3.2.1 Derivation of Strain Energy

Modeling of highly-twisted composite-coupled rotor blades is included in the derivation of strain energy. In this formulation, classical effects such as bending and torsional deformations as well as nonclassical effects such as transverse shear and section warping contributions are included. In the analysis, complex warping and transverse shear effects are captured using a detailed local cross-section analysis and the effective properties are then used to characterize the global beam analysis.

The variation of the elastic strain energy is given by

Reproduced with permission of the copyright owner. Further reproduction prohibited without permission.

$$\delta U = \int_0^R \iint_A \{\sigma_{xx}\delta\epsilon_{xx} + \sigma_{x\eta}\delta\epsilon_{x\eta} + \sigma_{x\zeta}\delta\epsilon_{x\zeta}\}\, d\eta d\zeta dx \tag{3.67}$$

The general form of the variation of strain energy involves six stress terms instead of only the above three terms. The plane stress assumption, which is valid for slender beams, is applied in a general form to simplify the analysis. The uniaxial stress assumption states that $\sigma_{\eta\eta} = \sigma_{\eta\zeta} = \sigma_{\zeta\zeta} = 0$.

The elastic stress-strain relationships employed in this formulation are given by

$$\begin{Bmatrix} \sigma_{xx} \\ \sigma_{x\zeta} \\ \sigma_{x\eta} \end{Bmatrix} = \begin{bmatrix} Q'_{11} & Q'_{15} & Q'_{16} \\ Q'_{15} & Q'_{55} & Q'_{56} \\ Q'_{16} & Q'_{56} & Q'_{66} \end{bmatrix} \begin{Bmatrix} \epsilon_{xx} \\ \epsilon_{x\zeta} \\ \epsilon_{x\eta} \end{Bmatrix} \tag{3.68}$$

where the Q'_{ij} represent the material stiffness at a location in the cross section.

The strain-displacement relations are defined as

$$\begin{aligned} \epsilon_{xx} &= u' + \frac{1}{2}v'^2 + \frac{1}{2}w'^2 + \frac{1}{2}\left(\eta^2 + \zeta^2\right)\hat{\phi}'^2 \\ &\quad + \left(\eta^2 + \zeta^2\right)\theta'_0\hat{\phi}' - v''[\eta\cos\theta_1 - \zeta\sin\theta_1] \\ &\quad - w''[\eta\sin\theta_1 + \zeta\cos\theta_1] + \left(\hat{\phi}'\lambda_T\right)' \end{aligned} \tag{3.69}$$

$$\epsilon_{x\eta} = v'_s\cos\theta_1 + w'_s\sin\theta_1 + (d\lambda_T/d\eta - \zeta)\,\hat{\phi}' \tag{3.70}$$

$$\epsilon_{x\zeta} = w'_s\cos\theta_1 - v'_s\sin\theta_1 + (d\lambda_T/d\zeta + \eta)\,\hat{\phi}' \tag{3.71}$$

where λ_T in the above expression refers to the torsion-related out-of-plane warping terms and the subscript s refers to the shear deformation components of the lag and flap degrees of freedom.

A substitution of variables is made to eliminate the kinematic contribution of foreshortening from the axial displacement variable u. This substitution provides a convenient way of developing the centrifugal stiffening terms associated with

Reproduced with permission of the copyright owner. Further reproduction prohibited without permission.

foreshortening in the kinetic energy expressions rather than in the strain energy expressions [46].

$$u'_e = u' + \frac{1}{2}v'^2 + \frac{1}{2}w'^2 \tag{3.72}$$

The same substitution is made in the kinetic energy derivation.

The new strain-displacement relations can be written as

$$\begin{aligned}\epsilon_{xx} &= u'_e + \frac{1}{2}\left(\eta^2+\zeta^2\right)\hat{\phi}'^2 + \left(\hat{\phi}'\lambda_T\right)' - v''[\eta\cos\theta_1 - \zeta\sin\theta_1] \\ &\quad -w''[\eta\sin\theta_1 + \zeta\cos\theta_1] + \left(\eta^2+\zeta^2\right)\theta'_0\hat{\phi}' \qquad (3.73)\\ \epsilon_{x\eta} &= v'_s\cos\theta_1 + w'_s\sin\theta_1 + \left(d\lambda_T/d\eta - \zeta\right)\hat{\phi}' \qquad (3.74)\\ \epsilon_{x\zeta} &= w'_s\cos\theta_1 - v'_s\sin\theta_1 + \left(d\lambda_T/d\zeta + \eta\right)\hat{\phi}' \qquad (3.75)\end{aligned}$$

The stress-strain relations are substituted into the strain energy variational which is then expressed in strain terms. The strain-displacement relationship is used to obtain the strain energy variational in terms of the displacement vector. The strain energy expression is then integrated over the cross-sectional area of the blade.

$$\delta U = \int_0^R \delta\hat{u}_i \mathrm{k}_{ij}\hat{u}_j\,dx + \int_0^R \delta\hat{u}_i D_i\,dx \tag{3.76}$$

where $(i,j = 1,9)$, and the strain vector is defined as:

$$\delta\hat{u}_i = \left\{\delta u'_e\;\delta v'\;\delta v''\;\delta w'\;\delta w''\;\delta\hat{\phi}\;\delta\hat{\phi}'\;\delta v'_s\;\delta w'_s\right\} \tag{3.77}$$

The first integral of Eqn. 3.76 represents the linear part of the strain energy and the second term represents the nonlinear contribution to the strain energy. The diagonal and nonzero off-diagonal terms of the symmetric linear cross section stiffness

Reproduced with permission of the copyright owner. Further reproduction prohibited without permission.

matrix are listed as follows:

$$
\begin{aligned}
k_{11} &= EA \\
k_{13} &= -EA_c \cos\theta_1 \\
k_{15} &= -EA_c \sin\theta_1 \\
k_{17} &= EET + EA_{r^2}\theta_0' \\
k_{18} &= EES_f \cos\theta_1 - EES_c \sin\theta_1 \\
k_{19} &= EES_f \sin\theta_1 + EES_c \cos\theta_1 \\
k_{22} &= 0 \\
k_{33} &= EI_c \cos^2\theta_1 + EI_f \sin^2\theta_1 \\
k_{35} &= EI_c \cos\theta_1 \sin\theta_1 - EI_f \cos\theta_1 \sin\theta_1 \\
k_{37} &= -EIC \cos\theta_1 + ETF \sin\theta_1 \\
k_{38} &= (EFS_c + ECS_f)\cos\theta_1 \sin\theta_1 \\
k_{39} &= EFS_c \sin^2\theta_1 - ECS_f \cos^2\theta_1 \\
k_{44} &= 0 \\
k_{55} &= EI_f \cos^2\theta_1 + EI_c \sin^2\theta_1 \\
k_{57} &= -ETF \cos\theta_1 - EIC \sin\theta_1 \\
k_{58} &= ECS_f \sin^2\theta_1 - EFS_c \cos^2\theta_1 \\
k_{59} &= -(EFS_c + ECS_f)\cos\theta_1 \sin\theta_1 \\
k_{66} &= 0 \\
k_{77} &= GJ \\
k_{88} &= GA_c \cos^2\theta_1 + GA_f \sin^2\theta_1
\end{aligned}
$$

Reproduced with permission of the copyright owner. Further reproduction prohibited without permission.

$$
\begin{aligned}
k_{89} &= (GA_c - GA_f)\cos\theta_1 \sin\theta_1 \\
k_{99} &= GA_f \cos^2\theta_1 + GA_c \sin^2\theta_1
\end{aligned} \tag{3.78}
$$

with $\theta_1 = \theta_t + \hat{\phi}$ and the cross section integrals given as follows: the classical cross section properties,

$$EA = \iint_A Q'_{11} d\eta d\zeta \tag{3.79}$$

$$EA_c = \iint_A Q'_{11} \eta d\eta d\zeta \tag{3.80}$$

$$EA_{r^2} = \iint_A Q'_{11} \left(\eta^2 + \zeta^2\right) d\eta d\zeta \tag{3.81}$$

$$EI_c = \iint_A Q'_{11} \eta^2 d\eta d\zeta \tag{3.82}$$

$$EI_f = \iint_A Q'_{11} \zeta^2 d\eta d\zeta \tag{3.83}$$

$$
\begin{aligned}
GJ = \iint_A \big[& Q'_{55}(\psi_{uT,\zeta} + \eta)^2 + Q'_{66}(\psi_{uT,\eta} - \zeta)^2 \\
& + 2Q'_{56}(\psi_{uT,\zeta} + \eta)(\psi_{uT,\eta} - \zeta)\big] d\eta d\zeta
\end{aligned} \tag{3.84}
$$

the shear-related stiffnesses,

$$GA_f = \iint_A Q'_{55} d\eta d\zeta \tag{3.85}$$

$$GA_c = \iint_A Q'_{66} d\eta d\zeta \tag{3.86}$$

the anisotropic material coupling stiffnesses,

$$EET = \iint_A [Q'_{15}(\psi_{uT,\zeta} + \eta) + Q'_{16}(\psi_{uT,\eta} - \zeta)] d\eta d\zeta \tag{3.87}$$

$$ETC = \iint_A [Q'_{15}(\psi_{uT,\zeta} + \eta) + Q'_{16}(\psi_{uT,\eta} - \zeta)] \eta d\eta d\zeta \tag{3.88}$$

$$ETF = \iint_A [Q'_{15}(\psi_{uT,\zeta} + \eta) + Q'_{16}(\psi_{uT,\eta} - \zeta)] \zeta d\eta d\zeta \tag{3.89}$$

the shear-related anisotropic material coupling stiffnesses,

$$EES_c = \iint_A Q'_{15} d\eta d\zeta \tag{3.90}$$

Reproduced with permission of the copyright owner. Further reproduction prohibited without permission.

$$EES_f = \iint_A Q'_{16} d\eta d\zeta \tag{3.91}$$

$$ECS_f = \iint_A Q'_{16}\, \eta d\eta d\zeta \tag{3.92}$$

$$EFS_c = \iint_A Q'_{15}\, \zeta d\eta d\zeta \tag{3.93}$$

and because symmetry in geometry and Q'_{11} is assumed about the chord line, the following section properties become zero,

$$\iint_A Q'_{11}\, \zeta d\eta d\zeta = 0 \tag{3.94}$$

$$\iint_A Q'_{11}\, \eta\zeta d\eta d\zeta = 0 \tag{3.95}$$

It is necessary to include the shear effects into an anisotropic, rotating beam dynamic analysis. The shear degrees of freedom could be condensed into the bending degrees of freedom for lag and flap. Such a static condensation of the shear deformation effects has been implemented into a UMARC analysis by Nixon [39]. Consider a 9x9 stiffness matrix k_{ij}. The second, fourth and sixth rows and columns of this matrix can be eliminated assuming that the strain energy terms associated with the corresponding deformations $\delta v'$, $\delta w'$, and $\delta\hat{\phi}$ are small. Now consider the new 6x6 stiffness matrix k_{ij} where F are the forces in the three orthogonal directions and M are the moments.

$$\begin{bmatrix} F_x \\ F_y \\ F_z \\ M_x \\ -M_y \\ M_z \end{bmatrix} = [\mathrm{k}_{ij}] \begin{bmatrix} u'_e \\ v'_s \\ w'_s \\ \hat{\phi}' \\ w'' \\ v'' \end{bmatrix} \tag{3.96}$$

It has been shown by Hodges *et al.* [91] that the shear forces associated with shear deformation can be assumed to be negligible. The same, however, cannot be assumed for the shear deformations themselves. This implies that $F_y = F_z = 0$.

Reproduced with permission of the copyright owner. Further reproduction prohibited without permission.

To implement this, the compliance matrix S_{ij} is obtained by inverting the stiffness matrix. The second and third rows and columns corresponding to F_y and F_z are eliminated and a 4x4 compliance matrix S'_{ij} is obtained. The new compliance matrix satisfies

$$\begin{bmatrix} u'_e \\ \hat{\phi}' \\ w'' \\ v'' \end{bmatrix} = \left[S'_{ij}\right] \begin{bmatrix} F_x \\ M_x \\ -M_y \\ M_z \end{bmatrix} \tag{3.97}$$

The bending related compliance terms implicitly include the effects of shear deformation due to the matrix inversion performed earlier. The new stiffness matrix k'_{ij} is obtained by inverting the 4x4 compliance matrix. The vector of displacement variations is

$$\delta\hat{u}_i = \left\{ \begin{array}{cccc} \delta u'_e & \delta v'' & \delta w'' & \delta\hat{\phi}' \end{array} \right\} \tag{3.98}$$

The new stiffness matrix can be written as:

$$\begin{aligned}
\mathrm{k}'_{11} &= EA \\
\mathrm{k}'_{12} &= -EA_c \cos\theta_1 \\
\mathrm{k}'_{13} &= -EA_c \sin\theta_1 \\
\mathrm{k}'_{14} &= EET + EA_{r^2}\theta'_0 \\
\mathrm{k}'_{22} &= EI_c \cos^2\theta_1 + EI_f \cos^2\theta_1 \\
\mathrm{k}'_{23} &= (EI_c - EI_f)\cos\theta_1 \sin\theta_1 \\
\mathrm{k}'_{24} &= -ETC \cos\theta_1 + ETF \sin\theta_1 \\
\mathrm{k}'_{33} &= EI_f \cos^2\theta_1 + EI_c \sin^2\theta_1 \\
\mathrm{k}'_{34} &= -ETF \cos\theta_1 + ETC \sin\theta_1 \\
\mathrm{k}'_{44} &= GJ
\end{aligned} \tag{3.99}$$

Reproduced with permission of the copyright owner. Further reproduction prohibited without permission.

where the material constants listed above are the effective material properties after static condensation derived for $\theta_1 = 0$. It should be noted that the coupling stiffnesses related to anisotropic material properties such as EET, ETC and ETF are not affected by the static condensation. The nonlinear stiffness terms written in terms of the effective material properties are given below:

$$
\begin{aligned}
D_1 &= EETv''w' \\
D_2 &= 0 \\
D_3 &= GJ\hat{\phi}'w' + EETu_e'w' + GJv''w'^2 + 2ETCv''w'\cos\theta_1 + \\
&\quad ETFw'w''\cos\theta_1 - 2ETFv''w'\sin\theta_1 + ETCw'w''\sin\theta_1 \\
D_4 &= GJ\hat{\phi}'v'' + EETu_e'v'' + GJv''^2w' + ETCv''^2\cos\theta_1 + \\
&\quad ETFv''w''\cos\theta_1 - ETFv''^2\sin\theta_1 + ETCv''w''\sin\theta_1 \\
D_5 &= ETFv''w'\cos\theta_1 + ETCv''w'\sin\theta_1 \\
D_6 &= -ETF\hat{\phi}'v''\cos\theta_1 - ETFv''^2w'\cos\theta_1 + ETC\hat{\phi}'w''\cos\theta_1 + \\
&\quad ETCv''w'w''\cos\theta_1 - EI_fv''w''\cos^2\theta_1 + EI_cv''w''\cos^2\theta_1 - \\
&\quad ETC\hat{\phi}'v''\sin\theta_1 + EA_cu_e'v''\sin\theta_1 - ETCv''^2w'\sin\theta_1 - \\
&\quad ETF\hat{\phi}'w''\sin\theta_1 - ETFv''w''w'\sin\theta_1 + EI_fv''^2\cos\theta_1\sin\theta_1 - \\
&\quad EI_cv''^2\cos\theta_1\sin\theta_1 - EI_fw''^2\cos\theta_1\sin\theta_1 + EI_cw''^2\cos\theta_1\sin\theta_1 + \\
&\quad EI_fv''w''\sin^2\theta_1 - EI_cv''w''\sin^2\theta_1 \\
D_7 &= GJv''w'
\end{aligned}
\tag{3.100}
$$

where D_i corresponds to the variational displacement vector without the shear degrees-of-freedom:

Reproduced with permission of the copyright owner. Further reproduction prohibited without permission.

$$\delta\hat{u}_i = \left\{ \begin{array}{cccccc} \delta u_e' & \delta v' & \delta v'' & \delta w' & \delta w'' & \delta\hat{\phi} \quad \delta\hat{\phi}' \end{array} \right\} \tag{3.101}$$

The stiffness matrix obtained from a static condensation of the cross-section properties is then applied to solve the dynamic problem. It has been shown in Ref. [39] that the dynamic effects associated with the shear deformations are negligible. This method of developing the cross-section stiffness matrix from the effective material properties facilitates the application of other sophisticated cross-section analyses to obtain the blade properties. The properties obtained in this procedure can be used in the dynamic analysis.

Hub Elastic Strain Energy

The strain energy contribution of the hub is given entirely by the gimbal system when hub springs are included in the model. This is given by

$$U_h = \frac{1}{2}K_{\beta_{GC}}\beta_{GC}^2 + \frac{1}{2}K_{\beta_{GS}}\beta_{GS}^2 \tag{3.102}$$

and the variation of the strain energy is

$$\delta U_h = K_{\beta_{GC}}\beta_{GC}\delta\beta_{GC} + K_{\beta_{GS}}\beta_{GS}\delta\beta_{GS} \tag{3.103}$$

The other hub degrees of freedom do not have any direct elastic strain contribution.

3.2.2 Derivation of Kinetic Energy

In this section, the velocity components in the three principal directions are derived. There are two contributions to these velocities: the blade motion and the hub motion. Hub motion is a resultant of wing motion and fuselage motion (which is considered in Chapter 7). The expression of the velocity vector for the motion of the blade and hub together can be written relative to any frame of reference as

Reproduced with permission of the copyright owner. Further reproduction prohibited without permission.

$$\vec{V} = \vec{V}_b + \vec{V}_h \tag{3.104}$$

where $\vec{V}_b$ represents the blade contribution and $\vec{V}_h$ represents the hub contribution to the total velocity.

The inertial (i) reference system is located on the right wing, oriented along with the wing before deformation. The wing deformed system (w) is located on the wing undergoing translational and rotational displacements.

$$\vec{R}_{\text{deformed wing}} = \vec{R}_1 = \{x_h, y_h, z_h\} \begin{Bmatrix} \hat{I}_i \\ \hat{J}_i \\ \hat{K}_i \end{Bmatrix} \tag{3.105}$$

$$\vec{R}_{\text{hub}} = \vec{R}_2 = \{0, 0, h\} [T_{hw}] \begin{Bmatrix} \hat{I}_w \\ \hat{J}_w \\ \hat{K}_w \end{Bmatrix} \tag{3.106}$$

Any point on the elastic axis of the undeformed rotor blade is written in terms of the azimuth angle (ψ), precone angle (β_p) and gimbal angle (β_G), control pitch angle (θ_1) and advanced blade geometry angles (Λ_1, Λ_2 and Λ_3).

$$\vec{R}_{\text{undeformed blade}} = \vec{R}_3 = \{x, 0, 0\} [T_{cp}][T_{pu}][T_{ur}][T_{rh}] \begin{Bmatrix} \hat{I}_h \\ \hat{J}_h \\ \hat{K}_h \end{Bmatrix} \tag{3.107}$$

where $[T_{cp}]$ is the transformation matrix for advanced blade geometry, $[T_{pu}]$ is the transformation through the control pitch angle, $[T_{ur}]$ is the transformation for rotor precone and blade gimbal angles, and $[T_{rh}]$ is the transformation for the azimuth angle. The position vector of the deformed blade elastic axis in the undeformed blade reference frame is given by

$$\vec{R}_{\text{deformed blade}} = \vec{R}_4 = \{u, v, w\} \begin{Bmatrix} \hat{I}_c \\ \hat{J}_c \\ \hat{K}_c \end{Bmatrix} \tag{3.108}$$

Reproduced with permission of the copyright owner. Further reproduction prohibited without permission.

and the position vector of any arbitrary point on the blade cross-section with respect to the undeformed blade reference frame is expressed as

$$\vec{R}_{\text{arbitrary point}} = \vec{R}_5 = \{0, \eta, \zeta\}\,[T_{dc}] \begin{Bmatrix} \hat{I}_c \\ \hat{J}_c \\ \hat{K}_c \end{Bmatrix} \tag{3.109}$$

where $[T_{dc}]$ is the transformation from the deformed blade reference frame to the undeformed blade frame.

The position vector of an arbitrary point on the cross section of the deformed blade is written in the inertial reference frame as

$$\begin{aligned} \vec{R} &= (\{x_h, y_h, z_h\} + \{0, 0, h\}\,[T_{hi}] + \{(x+u), v, w\}\,[T_{ci}] \\ &\quad + \{0, \eta, \zeta\}\,[T_{di}]) \begin{Bmatrix} \hat{I}_i \\ \hat{J}_i \\ \hat{K}_i \end{Bmatrix} \end{aligned} \tag{3.110}$$

The contribution of the blade and hub velocities is determined by taking the time derivative of the position vector in the inertial frame. The blade and hub degrees of freedom are functions of time as is the azimuth angle ψ which can be written as Ωt. After carrying out the transformations and applying the ordering scheme, the velocity due to blade and hub motions is

$$\vec{V} = \vec{V}_b + \vec{V}_h = \frac{d\vec{R}}{dt} = V_x \hat{I}_i + V_y \hat{J}_i + V_z \hat{K}_i \tag{3.111}$$

$$\begin{aligned} \vec{V} &= \frac{d\vec{R}}{dt} = \frac{\partial \vec{R}}{\partial t} + \vec{\omega} \times \vec{R} \\ &= \frac{\partial \vec{R}_1}{\partial t} + \vec{\omega}_{hi} \times \vec{R}_2 + \frac{\partial \vec{R}_3}{\partial t} + \vec{\omega}_{ci} \times \vec{R}_3 \\ &\quad + \frac{\partial \vec{R}_4}{\partial t} + \vec{\omega}_{ci} \times \vec{R}_4 + \frac{\partial \vec{R}_5}{\partial t} + \vec{\omega}_{di} \times \vec{R}_5 \end{aligned} \tag{3.112}$$

where $\vec{w}$ are the time-rates of change of the transformation matrices. $\vec{w}_{hi}$ is the angular velocity of the hub reference frame with respect to the inertial frame, $\vec{w}_{ci}$

Reproduced with permission of the copyright owner. Further reproduction prohibited without permission.

is the angular velocity of the undeformed blade reference frame with respect to the inertial frame, and $\vec{w}_{di}$ is the angular velocity of the deformed blade frame with respect to the inertial frame. These angular velocities are obtained by differentiating the corresponding transformation matrices (listed in a previous section) with respect to the azimuth angle ψ.

The variation of velocity is expressed as

$$\delta\vec{V} = \delta\vec{V}_b + \delta\vec{V}_h = \delta V_x \hat{I}_i + \delta V_y \hat{J}_i + \delta V_z \hat{K}_i \tag{3.113}$$

The kinetic energy for the blade and hub system is given by

$$T = \frac{1}{2}\int_0^R \iint_A \rho_s \vec{V} \cdot \vec{V}\, d\eta\, d\zeta\, dx \tag{3.114}$$

where $\vec{V}$ is the velocity as defined by Eqn. 3.111 and ρ_s is the mass density of any arbitrary point in the system. In the present formulation, the mass density of the hub is zero because the mass of the pylon and rotor hub is considered part of the wing. The variation of the kinetic energy is given by

$$\delta T = \int_0^R \iint_A \rho_s \vec{V} \cdot \delta\vec{V}\, d\eta\, d\zeta\, dx \tag{3.115}$$

Integration over the cross section area results in the following definitions for the mass constants of the blade:

$$m = \iint_A \rho_s\, d\eta\, d\zeta \tag{3.116}$$

$$me_g = \iint_A \rho_s \eta\, d\eta\, d\zeta \tag{3.117}$$

$$mk_{m1}^2 = \iint_A \rho_s \zeta^2\, d\eta\, d\zeta \tag{3.118}$$

$$mk_m^2 = \iint_A \rho_s \left(\zeta^2 + \eta^2\right)\, d\eta\, d\zeta \tag{3.119}$$

Reproduced with permission of the copyright owner. Further reproduction prohibited without permission.

where m represents the blade mass per unit length, e_g is the mass center of gravity offset from the elastic axis which is positive forward, k_{m1} and k_{m2} are the flapwise and chordwise mass radii of gyration, respectively, and k_m is the torsional mass radius of gyration so that mk_m^2 represents the torsional mass moment of inertia about the elastic axis. Because a symmetrical airfoil is assumed about the chordline, the following integrations are zero:

$$\iint_A \rho_s \zeta \, d\eta d\zeta = 0 \tag{3.120}$$

$$\iint_A \rho_s \zeta \eta \, d\eta d\zeta = 0 \tag{3.121}$$

The variation in nondimensional kinetic energy, after integrating over the blade cross-section, is written as

$$\begin{aligned}
\delta T \;=\; & \int_0^1 m \Big[T_u \delta u + T_{\overset{\star}{u}} \delta \overset{\star}{u} + T_v \delta v + T_{\overset{\star}{v}} \delta \overset{\star}{v} + T_w \delta w + T_{\overset{\star}{w}} \delta \overset{\star}{w} \\
& + T_{\hat{\phi}} \delta \hat{\phi} + T_{\overset{\star}{\hat{\phi}}} \delta \overset{\star}{\hat{\phi}} + T_{v'} \delta v' + T_{\overset{\star}{v'}} \delta \overset{\star}{v'} + T_{w'} \delta w' + T_{\overset{\star}{w'}} \delta \overset{\star}{w'} \\
& + T_{\overset{\star}{x_h}} \delta \overset{\star}{x_h} + T_{\overset{\star}{y_h}} \delta \overset{\star}{y_h} + T_{\overset{\star}{z_h}} \delta \overset{\star}{z_h} + T_{\alpha_h} \delta \alpha_h + T_{\overset{\star}{\alpha_h}} \delta \overset{\star}{\alpha_h} \\
& + T_{\phi_h} \delta \phi_h + T_{\overset{\star}{\phi_h}} \delta \overset{\star}{\phi_h} + T_{\zeta_h} \delta \zeta_h + T_{\overset{\star}{\zeta_h}} \delta \overset{\star}{\zeta_h} \\
& + T_{\beta_{GC}} \delta \beta_{GC} + T_{\overset{\star}{\beta_{GC}}} \delta \overset{\star}{\beta}_{GC} + T_{\beta_{GS}} \delta \beta_{GS} + T_{\overset{\star}{\beta_{GS}}} \delta \overset{\star}{\beta}_{GS} \Big] \, dx
\end{aligned} \tag{3.122}$$

where T_u, $T_{\overset{\star}{u}}$, etc., are the coefficients of δu, $\delta \overset{\star}{u}$, etc., respectively in the δT expression. These coefficients contain terms dependent on blade displacements, hub displacements and their velocities. Consider the term T_u. This term contributes to the blade axial displacement (u) equation. The equations of motion are written in terms of the displacements, velocities and accelerations. T_u is a function of constants (rotor parameters and operating condition), displacements (u, v, x_h, y_h, etc.,), and velocities ($\overset{\star}{u}$, $\overset{\star}{v}$, $\overset{\star}{x_h}$, $\overset{\star}{y_h}$, etc.,). For example, consider

Reproduced with permission of the copyright owner. Further reproduction prohibited without permission.

$$T_u = a_1 u + a_2 x_h + b_1 \overset{\star}{u} + b_2 \overset{\star}{y_h} + c_1 \tag{3.123}$$

where a_1, a_2, b_1, b_2 and c_1 are constants. Terms in T_u that are functions of constants only (such as c_1) contribute to the constant forcing term of the u equation. Terms in T_u that are functions of blade and hub displacements only (such as a_1 and a_2) contribute to the stiffness terms (K matrix) of the u equation. And, terms in the T_u expression that are functions of blade and hub velocities only (such as b_1 and b_2) contribute to the damping terms (C matrix) of the u equation.

Consider another term, $T_{\overset{\star}{u}}$. This term contributes to the $\overset{\star}{u}$ equation. But, in the present formulation, the $\overset{\star}{u}$ equation is not expressed explicitly; it is a part of the u equation. $T_{\overset{\star}{u}}$ can be integrated by parts as follows:

$$\begin{aligned} \int_0^1 T_{\overset{\star}{u}} \delta\overset{\star}{u} &= T_{\overset{\star}{u}} \delta u|_0^1 - \int_0^1 \frac{d}{dt}\left(T_{\overset{\star}{u}}\right) \delta u \\ &= 0 - \int_0^1 \frac{d}{dt}\left(T_{\overset{\star}{u}}\right) \delta u \end{aligned} \tag{3.124}$$

The first term on the right hand side of the equation is zero when integrated over the azimuth due to enforcement of periodic response over one rotor revolution. $T_{\overset{\star}{u}}$ already contains expressions dependent on constants, blade and hub displacements and velocities. When this term is differentiated with respect to time (or azimuth angle), its derivative consists of terms that are dependent on blade and hub displacements and their velocities, as well as blade and hub accelerations. For example, consider

$$T_{\overset{\star}{u}} = d_1 u + d_2 y_h + e_1 \overset{\star}{u} + e_2 \overset{\star}{v} + e_3 \overset{\star}{z_h} + f_1 \tag{3.125}$$

where d_1, d_2, e_1, e_2, e_3 and f_1 are constants.

Reproduced with permission of the copyright owner. Further reproduction prohibited without permission.

$$\frac{d}{dt}\left(T_{\overset{\star}{u}}\right) = d_1 \overset{\star}{u} + d_2 \overset{\star}{y_h} + e_1 \overset{\star\star}{u} + e_2 \overset{\star\star}{v} + e_3 \overset{\star\star}{z_h} \tag{3.126}$$

The kinetic energy contribution to the u equation is the coefficient of the δu term in the δT expression. $\frac{d}{dt}\left(T_{\overset{\star}{u}}\right)$ contains expressions dependent on blade and hub velocities (such as d_1 and d_2) which contribute to the damping terms (C matrix) and acceleration expressions (such as e_1, e_2 and e_3) which contribute to the inertial terms (M matrix) of the u equation. The kinetic energy contribution to the u equation, for the given example, is written as

$$\begin{aligned} &\underbrace{\int_0^1 m[e_1 \overset{\star\star}{u} + e_2 \overset{\star\star}{v} + e_3 \overset{\star\star}{z_h}]dx}_{\text{inertial terms}} \\ &+ \underbrace{\int_0^1 m[(d_1 - b_1)\overset{\star}{u} + (d_2 - b_2)\overset{\star}{y_h}]dx}_{\text{damping terms}} \\ &+ \underbrace{\int_0^1 m[-a_1 u - a_2 x_h]dx}_{\text{stiffness terms}} = \underbrace{\int_0^1 m c_1 dx}_{\text{forcing term}} \end{aligned} \tag{3.127}$$

This procedure, shown for the u equation, is repeated for the other blade displacements (v, w, ϕ, v' and w') as well as for the hub displacements (x_h, y_h, z_h, α_h, ϕ_h, ζ_h, β_{GC} and β_{GS}) to obtain the kinetic energy contributions to their respective equations.

3.2.3 Structural Contributions to Mass, Damping and Stiffness Matrices

The contributions of the structural model to the element mass, damping, and stiffness matrices are derived based on the strain and kinetic energies formulated in the present analysis.

A fifteen degree-of-freedom finite element [70] is used in the discretization of the

Reproduced with permission of the copyright owner. Further reproduction prohibited without permission.

blade. The continuous degrees-of-freedom for the blade are related to the discrete degrees-of-freedom for this element as follows:

$$\hat{u} = [H_s]\ \hat{q} \tag{3.128}$$

$$\hat{u}' = [H_s']\ \hat{q} \tag{3.129}$$

$$\hat{u}'' = [H_s'']\ \hat{q} \tag{3.130}$$

$$\overset{\star}{\hat{u}} = [H_s]\ \overset{\star}{\hat{q}} \tag{3.131}$$

$$\overset{\star\star}{\hat{u}} = [H_s]\ \overset{\star\star}{\hat{q}} \tag{3.132}$$

where the shape function matrix is defined as

$$[H_s] = \begin{bmatrix} H_u & 0 & 0 & 0 \\ 0 & H_b & 0 & 0 \\ 0 & 0 & H_b & 0 \\ 0 & 0 & 0 & H_{\hat{\phi}} \end{bmatrix} \tag{3.133}$$

The discrete (nodal) degrees of freedom are defined as

$$\hat{q} = \left[u_1\ u_2\ u_3\ u_4\ v_1\ v_1'\ v_2\ v_2'\ w_1\ w_1'\ w_2\ w_2'\ \hat{\phi}_1\ \hat{\phi}_2\ \hat{\phi}_3\right] \tag{3.134}$$

The hub degrees of freedom are already discrete, and may be written in matrix form as

$$\hat{x}_h = [x_h\ y_h\ z_h\ \alpha_h\ \phi_h\ \zeta_h\ \beta_{GC}\ \beta_{GS}] \tag{3.135}$$

The total energy variation contains variational terms of both the blade and the hub. The terms which are coefficients of the blade variational degrees of freedom $\delta\hat{q}$ constitute the blade equations, and the terms which are coefficients of the hub variational degrees of freedom $\delta\hat{x}_h$ constitute the hub equations. The blade equations may be written in matrix form as:

$$\delta U_i - \delta T_i = \delta\hat{q}^T \Big([M_{bb}]\overset{\star\star}{\hat{q}} + [C_{bb}]\overset{\star}{\hat{q}} + [K_{bb}]\hat{q} + [M_{bh}]\overset{\star\star}{\hat{x}}_h$$

Reproduced with permission of the copyright owner. Further reproduction prohibited without permission.

$$+[C_{bh}]\overset{\star}{\hat{x}}_h+[K_{bh}]\hat{x}_h-F_b\Big)_i \tag{3.136}$$

where i indicates the ith element of N_b elements into which the blade has been discretized. In the energy expressions, each of these matrices may be partitioned by the blade and hub degrees of freedom; (u, v, w, or $\hat{\phi}$) of the blade, and (x_h, y_h, z_h, α_h, ϕ_h, ζ_h, β_{GC}, or β_{GS}) of the hub.

$$[M_{bb}] = \begin{bmatrix} M_{uu} & M_{uv} & M_{uw} & M_{u\hat{\phi}} \\ M_{vu} & M_{vv} & M_{vw} & M_{v\hat{\phi}} \\ M_{wu} & M_{wv} & M_{ww} & M_{w\hat{\phi}} \\ M_{\hat{\phi}u} & M_{\hat{\phi}v} & M_{\hat{\phi}w} & M_{\hat{\phi}\hat{\phi}} \end{bmatrix} \tag{3.137}$$

The blade-hub matrices are partitioned as follows:

$$[M_{bh}] = \begin{bmatrix} M_{ux_h} & M_{uy_h} & M_{uz_h} & M_{u\alpha_h} & M_{u\phi_h} & M_{u\zeta_h} & M_{u\beta_{GC}} & M_{u\beta_{GS}} \\ M_{vx_h} & M_{vy_h} & M_{vz_h} & M_{v\alpha_h} & M_{v\phi_h} & M_{v\zeta_h} & M_{v\beta_{GC}} & M_{v\beta_{GS}} \\ M_{wx_h} & M_{wy_h} & M_{wz_h} & M_{w\alpha_h} & M_{w\phi_h} & M_{w\zeta_h} & M_{w\beta_{GC}} & M_{w\beta_{GS}} \\ M_{\hat{\phi}x_h} & M_{\hat{\phi}y_h} & M_{\hat{\phi}z_h} & M_{\hat{\phi}\alpha_h} & M_{\hat{\phi}\phi_h} & M_{\hat{\phi}\zeta_h} & M_{\hat{\phi}\beta_{GC}} & M_{\hat{\phi}\beta_{GS}} \end{bmatrix} \tag{3.138}$$

Hub Matrices

The hub equations can be written in matrix form as

$$\Delta = \delta\hat{x}_h^T\Big([M_{hb}]\overset{\star\star}{\hat{q}}+[C_{hb}]\overset{\star}{\hat{q}}+[K_{hb}]\hat{q}+[M_{hh}]\overset{\star\star}{\hat{x}}_h+ [C_{hh}]\overset{\star}{\hat{x}}_h+[K_{hh}]\hat{x}_h-F_h\Big) \tag{3.139}$$

These matrices are partitioned by the associated degrees of freedom in the hub and blade similar to the blade matrices.

Wing Matrices

The wing is discretized as an elastic beam using the same 15 degree-of-freedom beam element as that used for the rotor blade. The rotor blade formulation can

Reproduced with permission of the copyright owner. Further reproduction prohibited without permission.

hence be used to obtain the wing matrices with a few modifications. Since the wing is fixed, the rotational speed is set to zero ($\Omega = 0$). Also, there are no precone-associated terms in the wing formulation. There is no twist or pitch angle for the wing; this implies that θ_1 is equal to zero. Applying the above mentioned modifications and neglecting all hub motion related terms from the rotor formulation, the wing mass, damping and stiffness matrices can be obtained.

$$[M_{ww}] = [M_{bb}], (\beta_p = \Omega = \theta_1 = 0) \tag{3.140}$$

$$[K_{ww}] = [K_{bb}], (\beta_p = \Omega = \theta_1 = 0) \tag{3.141}$$

$$[C_{ww}] = 0 \tag{3.142}$$

The motion of the wing is coupled to the hub (for stability calculations) by the six wing nodal displacements which correspond to six of the hub degrees-of-freedom (for a straight wing) as follows:

Wing dof		Hub dof
u	=	y_h
v	=	$-x_h$
v'	=	ζ_h
w	=	z_h
w'	=	$-\phi_h$
$\hat{\phi}$	=	$-\alpha_h$

(3.143)

where u, v, v', w, w', and $\hat{\phi}$ represent the discrete degrees of freedom at the point where the rotor pylon connects with the wing.

Reproduced with permission of the copyright owner. Further reproduction prohibited without permission.

For an advanced geometry wing with sweep, anhedral, pretwist and planform taper with span, the rotor/wing assembly equations have to be modified accordingly. Sweep is denoted by Λ_1 (positive for sweep forward), anhedral is denoted by Λ_2 (positive for anhedral up, negative anhedral is referred to as droop) and pretwist with respect to the wing root is Λ_3 (positive for rotation nose-up). The order of transformation is the same as for the blade: first sweep, followed by anhedral and then by wing pretwist. The transformation matrix is similar to that used for the blade:

$$[T_\Lambda^{ag}] = \begin{bmatrix} C_1C_2 & S_1C_2 & S_2 \\ -S_1C_3 - C_1S_2S_3 & C_1C_3 - S_1S_2S_3 & C_2S_3 \\ S_1S_3 - C_1S_2C_3 & -C_1S_3 - S_1S_2C_3 & C_2C_3 \end{bmatrix} \tag{3.144}$$

where C_i and S_i represent $\cos\Lambda_i$ and $\sin\Lambda_i$ respectively for $i = 1$ to 3 for the wing and the subscript ag refers to the advanced geometry axis of the wing. The wing translational displacements (at the pylon location) can be written as

$$\begin{Bmatrix} u_{ag} \\ v_{ag} \\ w_{ag} \end{Bmatrix} = [T_\Lambda^{ag}] \begin{Bmatrix} y_h \\ -x_h \\ z_h \end{Bmatrix} \tag{3.145}$$

and the wing rotational displacements (at the pylon location) are given by

$$\begin{Bmatrix} v'_{ag} \\ w'_{ag} \\ \hat{\phi}_{ag} \end{Bmatrix} = [T_\Lambda^{ag}] \begin{Bmatrix} \zeta_h \\ -\phi_h \\ -\alpha_h \end{Bmatrix} \tag{3.146}$$

For trim and performance analysis, the wing is assumed to be rigid, and the hub degrees of freedom are fixed.

3.3 Aerodynamic Modeling

The tiltrotor configuration requires several major modifications to the helicopter aerodynamic modeling as available in UMARC. The modifications are required

Reproduced with permission of the copyright owner. Further reproduction prohibited without permission.

due to the large angle-of-attack of the pylon and the additional hub degrees of freedom. Since the required changes are extensive, it is necessary to rederive the new aerodynamic expressions for the tiltrotor from first principles. Furthermore, since advanced geometry blades are modeled in this tiltrotor formulation, the aerodynamic modeling becomes more involved than that given in Ref. [39].

The aerodynamic formulation discussed in this section is based on quasi-steady linear aerodynamic modeling. This assumes that the blade loads are a function of instantaneous blade section angle-of-attack at each spanwise location. Also, the section airfoil characteristics are based on static data. The local velocities on the blade are functions of the free stream velocity, blade motion relative to an inertial frame and hub motion relative to an inertial frame. Fuselage motion is not considered in this chapter. The blade loads are motion dependent, and hence contribute to the system mass, damping and stiffness matrices as well as to the load vector. The local velocities on the blade are calculated in the deformed reference frame. The aerodynamic forces too are calculated in the deformed frame. This is advantageous since the high inflow aerodynamics as seen in the hub frame can be treated in exactly the same manner in the deformed frame as would low inflow aerodynamics in the undeformed frame. Specifically, the inflow velocity and resultant angle-of-attack in the deformed frame can be assumed to be small, which simplifies the equations to a large extent. The significant differences between this formulation and previous formulations is in the transformation matrices that relate the blade loads and velocities from the deformed frame to the inertial frame.

Linear compressibility effects are included in the formulation through a Prandtl-

Reproduced with permission of the copyright owner. Further reproduction prohibited without permission.

Glauert compressibility correction. Nonlinear compressibility effects such as shock-induced stall are, however, not included in the formulation. These effects could be important particularly in the airplane mode when tip Mach numbers of 0.8 and above are encountered. Such high tip Mach numbers exist in airplane mode operation at advance ratios of 0.8 and higher. The assumption of linear compressible aerodynamics breaks down at these high speeds and a more detailed analysis has to be performed including the nonlinear compressibility effects as well.

3.3.1 Local Blade Velocities

The reference frames defined in the structural model section are used in deriving the velocity components in the deformed reference frame. The three components of the blade velocities arise from the blade motion, hub motion and the aircraft forward flight velocity. The velocity vector can be written as

$$\vec{V} = \vec{V}_b + \vec{V}_h - \vec{V}_a \tag{3.147}$$

where $\vec{V}_b, \vec{V}_h,$ and $\vec{V}_a$ represent the blade, hub and relative wind contributions, respectively, to the total velocity. $\mu = V/\Omega R$ is defined as the advance ratio and λ_i is the induced flow produced by the thrusting rotor. The advance ratio in the tiltrotor formulation is defined in a slightly different form than that used in pure helicopter notation where $\mu = V\cos\alpha_s/\Omega R$. The induced inflow is defined in the hub reference frame and the advance ratio is defined in the inertial frame. The relative wind velocity is written as

$$\vec{V}_a = (\{\mu, 0, 0\} + \{0, 0, -\lambda_i\}[T_{hi}]) \begin{Bmatrix} \hat{I}_i \\ \hat{J}_i \\ \hat{K}_i \end{Bmatrix} \tag{3.148}$$

Reproduced with permission of the copyright owner. Further reproduction prohibited without permission.

The blade and hub velocities are determined by taking the time derivative of the position vector of an arbitrary point with respect to an inertial frame. The position vector can be expressed in the inertial frame as

$$\begin{aligned}\vec{R} &= (\{x_h, y_h, z_h\}+\{0,0,h\}\,[T_{hi}]+\{(x+u), v, w\}\,[T_{ci}] \\ &\quad +\{0,\eta_r,0\}\,[T_{di}])\left\{\begin{array}{c}\hat{I}_i\\ \hat{J}_i\\ \hat{K}_i\end{array}\right\}\end{aligned} \tag{3.149}$$

The blade and hub degrees of freedom are functions of time as is the azimuth angle ψ which is written as Ωt.

$$\vec{V}_b + \vec{V}_h = \frac{d\vec{R}}{dt} = V_{b_x}\hat{I}_i + V_{b_y}\hat{J}_i + V_{b_z}\hat{K}_i \tag{3.150}$$

The total nondimensional velocity is transformed into the deformed frame as

$$\begin{aligned}\vec{V}_b+\vec{V}_h-\vec{V}_a &= \left(\left\{V_{b_x}, V_{b_y}, V_{b_z}\right\}+\{-\mu,0,0\}+\right. \\ &\quad \left.\{0,0,\lambda_i\}\,[T_{hi}]\right)\,[T_{id}]\left\{\begin{array}{c}\hat{I}_d\\ \hat{J}_d\\ \hat{K}_d\end{array}\right\}\end{aligned} \tag{3.151}$$

which can be written as

$$\vec{V} = U_r\hat{I}_d + U_t\hat{J}_d + U_p\hat{K}_d \tag{3.152}$$

where U_r, U_t, and U_p are the radial, tangential and the inflow components of the velocity in the blade deformed frame. The following substitution is made to account for kinematic pitch-lag and pitch-flap coupling in the rotor system controls geometry

$$\theta_1 = \theta_1 + k_\beta\beta_G + k_\zeta\zeta \tag{3.153}$$

where k_β and k_ζ are the pitch-flap and pitch-lag coupling parameters respectively.

Reproduced with permission of the copyright owner. Further reproduction prohibited without permission.

3.3.2 Blade Airloads

The circulatory forces per unit length are calculated in non-dimensional form using quasi-steady strip theory and are expressed in the deformed reference frame as:

$$\left(\bar{L}_w\right)_C = \frac{\gamma \bar{V}^2}{6a}\left(C_l \cos\alpha + C_d \sin\alpha\right) \tag{3.154}$$

$$\left(\bar{L}_v\right)_C = \frac{\gamma \bar{V}^2}{6a}\left(C_l \sin\alpha - C_d \cos\alpha\right) \tag{3.155}$$

$$\left(\bar{L}_u\right)_C = \frac{\gamma \bar{V}^2}{6a}\left(-C_d \sin\Lambda\right) \tag{3.156}$$

$$\left(\bar{M}_{\hat{\phi}}\right)_C = \frac{\gamma \bar{V}^2}{6a}\left(\frac{c}{R}C_m\right) - e_d\left(\bar{L}_w\right)_C \tag{3.157}$$

where

$$c_l = c_0 + c_1\alpha \tag{3.158}$$

$$c_d = d_0 + d_1|\alpha| + d_2\alpha^2 \tag{3.159}$$

$$c_m = f_0 + f_1\alpha \tag{3.160}$$

and

$$\sin\alpha \simeq \alpha \simeq -\frac{U_P}{U_T} \tag{3.161}$$

$$\cos\alpha \simeq 1 \tag{3.162}$$

$$\bar{V} \simeq U_T \tag{3.163}$$

$$\sin\Lambda \simeq \frac{U_R}{U_T} \tag{3.164}$$

c_0, c_1, d_0, d_1, d_2, f_0 and f_1 are airfoil section coefficients obtained from data tables. The coefficient f_1 is the same as $-e_d$ using in Eqn. 3.157. The coefficient c_1 is the same as c_{l_α}. Mach number effects are included as correction factors to the incompressible section lift, drag and moment characteristics.

Reproduced with permission of the copyright owner. Further reproduction prohibited without permission.

The approximations of Eqns. 3.161-3.164 and the expressions for the aerodynamic coefficients in Eqns. 3.158-3.160 are substituted into the expressions for rotor forces from Eqns. 3.154-3.157:

$$\left(\bar{L}_w\right)_C = \frac{\gamma}{6a}\left(c_0 {U_T}^2 - (c_1 + d_0)\, U_T U_P + d_1 |U_P| U_P\right) \tag{3.165}$$

$$\left(\bar{L}_v\right)_C = \frac{\gamma}{6a}\left(-d_0 {U_T}^2 - (c_0 U_P - d_1 |U_P|)\, U_T + (c_1 - d_2)\, {U_P}^2\right) \tag{3.166}$$

$$\left(\bar{L}_u\right)_C = \frac{\gamma}{6a}\left(-d_0 U_R U_T\right) \tag{3.167}$$

$$\left(\bar{M}_{\hat{\phi}}\right)_C = \frac{\gamma}{6a}\frac{c}{R}\left(f_0\left({U_T}^2 + {U_P}^2\right) + e_d U_T U_P\right) - e_d\left(\bar{L}_w\right)_C \tag{3.168}$$

The aerodynamic forces of the deformed frame are transformed into the undeformed frame through the transformation

$$\begin{Bmatrix} \left(L_u^A\right)_C \\ \left(L_v^A\right)_C \\ \left(L_w^A\right)_C \end{Bmatrix} = [T_{ud}] \begin{Bmatrix} \left(\bar{L}_u\right)_C \\ \left(\bar{L}_v\right)_C \\ \left(\bar{L}_w\right)_C \end{Bmatrix} \tag{3.169}$$

$$\left(M_{\hat{\phi}}^A\right)_C = \left(\bar{M}_{\hat{\phi}}\right)_C \tag{3.170}$$

Static and dynamic stall effects can be included as described in Ref. [70]. Nonlinear compressible aerodynamics such as drag divergence and Mach tuck can be included in the present formulation using data tables although such tables are not used in the present analysis.

Mach Number Perturbations

Perturbations in the local Mach number contribute significantly to the airloads on the blade. The perturbation of lift coefficient is

$$\delta c_l = \frac{\partial c_l}{\partial \alpha}\delta\alpha + \frac{\partial c_l}{\partial M}\delta M \tag{3.171}$$

Reproduced with permission of the copyright owner. Further reproduction prohibited without permission.

where

$$\alpha = -\frac{U_P}{U_T} \tag{3.172}$$

$$\delta\alpha = -\frac{U_P \delta U_T - U_T \delta U_P}{{U_T}^2} \tag{3.173}$$

$$M = \frac{M_{tip}}{V_{tip}} V = M_{tip} \frac{U_T}{\Omega R} \tag{3.174}$$

$$\delta M = M_{tip} \frac{\delta U_T}{\Omega R} \tag{3.175}$$

The Prandtl-Glauert compressibility correction factor (from linear subsonic theory) is applied to the lift-curve slope. The partial derivatives of the lift-curve slope are given by (Ref. [70])

$$\frac{\partial c_l}{\partial \alpha} = \frac{c_1}{\sqrt{1 - M^2}} \tag{3.176}$$

$$\frac{\partial c_l}{\partial M} = \frac{c_1 \alpha M}{\left(1 - M^2\right)^{3/2}} \tag{3.177}$$

These equations contribute additional terms to the airloads as derived in the previous subsection.

$$\left(\bar{L}_w\right)_C = \frac{\gamma}{6a} \left(c_0 {U_T}^2 - \left(c_1 + d_0\right) U_T U_P + d_1 |U_P| U_P + c_2 M_{tip} U_T \left({U_T}^2 + {U_P}^2 \right) \right) \tag{3.178}$$

$$\left(\bar{L}_v\right)_C = \frac{\gamma}{6a} \left(-d_0 {U_T}^2 - \left(c_0 U_P - d_1 |U_P|\right) U_T + \left(c_1 - d_2\right) {U_P}^2 - c_2 M_{tip} U_P \left({U_T}^2 + {U_P}^2 \right) \right) \tag{3.179}$$

$$\left(\bar{L}_u\right)_C = \frac{\gamma}{6a} \left(-d_0 U_R U_T \right) \tag{3.180}$$

$$\left(\bar{M}_{\hat{\phi}}\right)_C = \frac{\gamma}{6a} \frac{c}{R} \left(f_0 \left({U_T}^2 + {U_P}^2 \right) - f_1 U_T U_P \right) - e_d \left(\bar{L}_w\right)_C \tag{3.181}$$

where

$$c_2 = -\frac{1}{2} \alpha \sqrt{1 - M^2}\, c_1 \tag{3.182}$$

Reproduced with permission of the copyright owner. Further reproduction prohibited without permission.

Reverse Flow

When the tiltrotor is in high speed helicopter mode or in transition mode, reverse flow could occur over the inboard sections of the retreating blade. This occurs when the forward flight velocity exceeds the local rotational velocity of the blade section. The aerodynamic center of the airfoil section shifts from around the quarter chord to the three-quarter chord position when reverse flow exists over that section. The velocity terms derived have to be modified for the reverse flow case when $U_T < 0$.

$$e_d{}^{rev} = e_d + \frac{c}{2R} \tag{3.183}$$

$$\eta_r{}^{rev} = x_{ac} - \frac{c}{4R} - e_d \tag{3.184}$$

In some portions of the reverse flow region, a condition exists where the tangential velocity is of the same order of magnitude as the normal velocity. This condition leads to unrealistically high angles-of-attack. If no static stall model is used, the computed section lift coefficient, under these conditions, could be unrealistically high. In such cases, the section lift coefficient should be bounded (by a maximum of about 1.5) in the analysis.

Noncirculatory Airloads

Noncirculatory contributions to the rotor blade aerodynamics arise from pitching and plunging motions of the airfoil section and act in the undeformed reference frame. These effects are included in the analysis as

$$\left(L_w^A\right)_{NC} = \frac{\gamma\pi\frac{c}{R}}{12a}\left[-\frac{\overset{\star\star}{w}}{R} + \left(\frac{c}{4R} + \frac{e_d}{R}\right)\overset{\star\star}{\theta}_1 + (x + \mu\sin\psi\cos\alpha_p)\,\overset{\star}{\theta}_1\right] \tag{3.185}$$

Reproduced with permission of the copyright owner. Further reproduction prohibited without permission.

$$\left(M_{\hat{\phi}}^{A}\right)_{NC} = \frac{\gamma\pi\frac{c}{R}}{12a}\left[\frac{c}{4R}+\frac{e_d}{R}\left(\frac{\overset{\star\star}{w}}{R}-\overset{\star\star}{\theta}_1\right)-\frac{c}{2R}+\right.$$
$$\left.\frac{e_d}{R}\left(x+\mu\sin\psi\cos\alpha_p\right)\overset{\star}{\theta}_1-\frac{c^2\overset{\star\star}{\theta}_1}{32R^2}\right] \tag{3.186}$$

The above expressions match those derived in Ref. [39].

The total airloads in the undeformed frame are given by

$$L_u^A = \left(L_u^A\right)_C \tag{3.187}$$

$$L_v^A = \left(L_v^A\right)_C \tag{3.188}$$

$$L_w^A = \left(L_w^A\right)_C + \left(L_w^A\right)_{NC} \tag{3.189}$$

$$M_{\hat{\phi}}^A = \left(M_{\hat{\phi}}^A\right)_C + \left(M_{\hat{\phi}}^A\right)_{NC} \tag{3.190}$$

3.3.3 Work done by the Blade Airloads

The work done on the system is a result of the aerodynamic forces from the rotor system and the wing. The blade airloads associated with blade, gimbal and hub motion contribute to the mass, damping and stiffness matrices. The variation of work done by the hub, rotor and wing system is written as

$$\delta W = \left[\sum_{m=1}^{N_b}\delta W_b\right] + \delta W_h + \delta W_w \tag{3.191}$$

where δW_b, δW_h and δW_w represent the work performed by perturbations of the blade, hub and wing degrees of freedom respectively.

$$\delta W_b = \int_0^R \left(L_u^A\delta u + L_v^A\delta v + L_w^A\delta w + M_{\hat{\phi}}^A\delta\hat{\phi}\right)dx \tag{3.192}$$

where L_u^A, L_v^A, L_w^A, and $M_{\hat{\phi}}^A$ are the distributed aerodynamic forces acting in the rotating blade reference frame.

$$\delta W_h = F_{x_h}\delta x_h + F_{y_h}\delta y_h + F_{z_h}\delta z_h + M_{\alpha_h}\delta\alpha_h + M_{\phi_h}\delta\phi_h$$

Reproduced with permission of the copyright owner. Further reproduction prohibited without permission.

$$+M_{\zeta_h}\delta\zeta_h + M_{\beta_{GC}}\delta\beta_{GC} + M_{\beta_{GS}}\delta\beta_{GS} \tag{3.193}$$

where each generalized force is the net load acting on the associated hub degree of freedom. The wing aerodynamic model is similar to the rotor aerodynamic model described in this section but with the rotational speed and precone angle set to zero.

The net forces and moments are written as a sum of distributed forces and moments that act along the blade span on all N_b blades.

$$F_{x_h} = \sum_{m=1}^{N_b}\int_0^R F_{x_h}^A dx \tag{3.194}$$

$$F_{y_h} = \sum_{m=1}^{N_b}\int_0^R F_{y_h}^A dx \tag{3.195}$$

$$F_{z_h} = \sum_{m=1}^{N_b}\int_0^R F_{z_h}^A dx \tag{3.196}$$

$$M_{\alpha_h} = \sum_{m=1}^{N_b}\int_0^R M_{\alpha_h}^A dx \tag{3.197}$$

$$M_{\phi_h} = \sum_{m=1}^{N_b}\int_0^R M_{\phi_h}^A dx \tag{3.198}$$

$$M_{\zeta_h} = \sum_{m=1}^{N_b}\int_0^R M_{\zeta_h}^A dx \tag{3.199}$$

$$M_{\beta_{GC}} = \sum_{m=1}^{N_b}\int_0^R M_{\beta_{GC}}^A dx \tag{3.200}$$

$$M_{\beta_{GS}} = \sum_{m=1}^{N_b}\int_0^R M_{\beta_{GS}}^A dx \tag{3.201}$$

The distributed section aerodynamic blade loads are transformed into the hub reference frame using the T_{FL} matrix as follows:

Reproduced with permission of the copyright owner. Further reproduction prohibited without permission.

$$\left\{ \begin{array}{c} F^A_{x_h} \\ F^A_{y_h} \\ F^A_{z_h} \\ M^A_{\alpha_h} \\ M^A_{\phi_h} \\ M^A_{\zeta_h} \\ M^A_{\beta_{GC}} \\ M^A_{\beta_{GS}} \end{array} \right\} = T_{FL} \left\{ \begin{array}{c} L^A_u \\ L^A_v \\ L^A_w \\ M^A_{\hat{\phi}} \end{array} \right\} \tag{3.202}$$

The transformation T_{FL} is different from that derived for earlier helicopter and straight-bladed tiltrotor formulations and has been rederived in this study. The present T_{FL} matrix is different from that associated with the original UMARC formulation because of the three additional hub forces: $M^A_{\zeta_h}, M^A_{\beta_{GC}}$, and $M^A_{\beta_{GS}}$ and is essentially different from the derivation in Ref. [39] due to the modeling of advanced geometry blades as well as composite-coupled blades and blade kinematic couplings in the present analysis.

The T_{FL} Matrix

The T_{FL} matrix transforms the blade airloads from the undeformed reference frame into the non-rotating frame. $M^A_{\beta_{GC}}$ and $M^A_{\beta_{GS}}$, are defined in the hub system while the rest of the generalized forces are defined in the inertial frame. The transformation for the forces is

$$\left\{ \begin{array}{c} F^A_{x_h} \\ F^A_{y_h} \\ F^A_{z_h} \end{array} \right\} = T_{ic} \left\{ \begin{array}{c} L^A_u \\ L^A_v \\ L^A_w \end{array} \right\} \tag{3.203}$$

The transformation for the hub moments involves contributions from blade forces as well as blade moments.

$$\left\{ \begin{array}{c} -M^A_{\phi_h} \\ -M^A_{\alpha_h} \\ M^A_{\zeta_h} \end{array} \right\} = T_{id} \left\{ \begin{array}{c} \bar{M}^A_{\hat{\phi}} \\ 0 \\ 0 \end{array} \right\} + r_{ic} \times \left\{ L^A_u \hat{I}_u + L^A_v \hat{J}_u + L^A_w \hat{K}_u \right\} \tag{3.204}$$

Reproduced with permission of the copyright owner. Further reproduction prohibited without permission.

where r_{ic} is the position vector (in the inertial frame) of an arbitrary point on the elastic axis of the blade.

The gimbal moments are similarly given by

$$\left\{ \begin{array}{c} M^A_{\beta_{GS}} \\ -M^A_{\beta_{GC}} \\ M^A_{\zeta_h} \end{array} \right\} = T_{hd} \left\{ \begin{array}{c} \bar{M}^A_{\hat{\phi}} \\ 0 \\ 0 \end{array} \right\} + r_{hc} \times \left\{ L^A_u \hat{I}_u + L^A_v \hat{J}_u + L^A_w \hat{K}_u \right\} \tag{3.205}$$

The T_{FL} matrix is separated into component matrices depending on whether these matrices contain blade displacements, hub displacements, both or neither and also into linear and nonlinear components.

$$T_{FL} = (T_{FL})_c + (T_{FL})_q + (T_{FL})_{x_h} + (T_{FL})_{q^2} + (T_{FL})_{qx_h} + (T_{FL})_{x_h^2} \tag{3.206}$$

where the subscript c indicates the constant terms, subscripts q and x_h indicate linear terms associated with the blade and hub degrees of freedom, respectively, and q^2, qx_h, and x_h^2 indicate terms nonlinear in the blade and hub degrees of freedom. The derivation of this matrix is described in great detail in Ref. [39]; the same procedure is used in this formulation to rederive the matrix. The constant and linear contributions to the T_{FL} matrix are listed in Appendix B.

Discretization of Blade Equations

The work done on the blade results in the blade equations which also have hub motion contributions, and the work done on the hub results in the hub equations which also have blade motion contributions. The work done by the blade can be written in nondimensional form as

$$\delta W_b = \frac{\gamma}{6} \int_0^R \delta \hat{u}^T \hat{L}^A dr \tag{3.207}$$

Reproduced with permission of the copyright owner. Further reproduction prohibited without permission.

where

$$\delta\hat{u}^T = \left[u\ v\ w\ \hat{\phi}\right]^T \tag{3.208}$$

$$\hat{L}^A = \left[L_u^A\ L_v^A\ L_w^A\ M_{\hat{\phi}}^A\right]^T \tag{3.209}$$

$\hat{L}^A$, the aerodynamic force vector, can be expressed as a sum of constant, linear and nonlinear contributions of blade and hub motion.

$$\hat{L}^A = \left[\hat{L}^A\right]_c + \left[\hat{L}^A\right]_q + \left[\hat{L}^A\right]_{x_h} + \left[\hat{L}^A\right]_{q^2} + \left[\hat{L}^A\right]_{qx_h} + \left[\hat{L}^A\right]_{x_h^2} \tag{3.210}$$

The displacement vector, $\hat{u}$, may be discretized in terms of the spatial shape functions matrix, $[H_s]$, and the blade discrete degrees of freedom vector, $\hat{q}$ as

$$\hat{u} = [H_s]\,\hat{q} \tag{3.211}$$

$$\hat{u}' = [H_s']\,\hat{q} \tag{3.212}$$

$$\overset{\star}{\hat{u}} = [H_s]\ \overset{\star}{\hat{q}} \tag{3.213}$$

The shape function matrix is defined as

$$[H] = \begin{bmatrix} H_u & 0 & 0 & 0 \\ 0 & H_b & 0 & 0 \\ 0 & 0 & H_b & 0 \\ 0 & 0 & 0 & H_{\hat{\phi}} \end{bmatrix} \tag{3.214}$$

The discrete degrees of freedom are

$$\hat{q} = \left[u_1\ u_2\ u_3\ u_4\ v_1\ v_1'\ v_2\ v_2'\ w_1\ w_1'\ w_2\ w_2'\ \hat{\phi}_1\ \hat{\phi}_2\ \hat{\phi}_3\right] \tag{3.215}$$

and

$$\hat{x}_h = [x_h\ y_h\ z_h\ \alpha_h\ \phi_h\ \zeta_h\ \beta_{GC}\ \beta_{GS}] \tag{3.216}$$

Reproduced with permission of the copyright owner. Further reproduction prohibited without permission.

The linear terms, $\left(\hat{L}^A\right)_q$ and $\left(\hat{L}^A\right)_{x_h}$, of the aerodynamic force vector can be written in coefficient form as

$$\begin{aligned}\left(\hat{L}^A\right)_q + \left(\hat{L}^A\right)_{x_h} &= [A_u]\hat{u} + [A_{u'}]\hat{u}' + [A_{\overset{\star}{u}}]\overset{\star}{\hat{u}} \\ &\quad + [A_{\overset{\star\star}{u}}]\overset{\star\star}{\hat{u}} + [A_{x_h}]\hat{x}_h + [A_{\overset{\star}{x}_h}]\overset{\star}{\hat{x}}_h \end{aligned} \tag{3.217}$$

Substituting Eqns. 3.211-3.217 into the expression for virtual work Eqn. 3.207 gives

$$\begin{aligned}\delta W_b &= \delta\hat{q}^T\left(\left[M^A_{bb}\right]\overset{\star\star}{\hat{q}} + \left[C^A_{bb}\right]\overset{\star}{\hat{q}} + \left[K^A_{bb}\right]\hat{q} + \left[C^A_{bh}\right]\overset{\star}{\hat{x}}_h + \left[K^A_{bh}\right]\hat{x}_h \right. \\ &\quad \left. + \left[F^A_b\right]_c + \left[F^A_b\right]_{q^2} + \left[F^A_b\right]_{qx_h} + \left[F^A_b\right]_{x_h^2}\right) \end{aligned} \tag{3.218}$$

where

$$\left[M^A_{bb}\right] = \frac{\gamma}{6} l \int_0^1 [H_s]^T [A_{\overset{\star\star}{u}}][H_s]\, ds \tag{3.219}$$

$$\left[C^A_{bb}\right] = \frac{\gamma}{6} l \int_0^1 [H_s]^T [A_{\overset{\star}{u}}][H_s]\, ds \tag{3.220}$$

$$\left[K^A_{bb}\right] = \frac{\gamma}{6} l \int_0^1 \left([H_s]^T [A_u][H_s] + [H'_s]^T [A_{u'}][H'_s]\right)\, ds \tag{3.221}$$

$$\left[C^A_{bh}\right] = \frac{\gamma}{6} l \int_0^1 [H_s]^T [A_{\overset{\star}{x}_h}]\, ds \tag{3.222}$$

$$\left[K^A_{bh}\right] = \frac{\gamma}{6} l \int_0^1 [H_s]^T [A_{x_h}]\, ds \tag{3.223}$$

$$\left[F^A_b\right]_0 = \frac{\gamma}{6} l \int_0^1 [H_s]^T \left[L^A\right]_0\, ds \tag{3.224}$$

$$\left[F^A_b\right]_{q^2} = \frac{\gamma}{6} l \int_0^1 [H_s]^T \left[L^A\right]_{q^2}\, ds \tag{3.225}$$

$$\left[F^A_b\right]_{qx_h} = \frac{\gamma}{6} l \int_0^1 [H_s]^T \left[L^A\right]_{qx_h}\, ds \tag{3.226}$$

$$\left[F^A_b\right]_{x_h^2} = \frac{\gamma}{6} l \int_0^1 [H_s]^T \left[L^A\right]_{x_h^2}\, ds \tag{3.227}$$

The nonlinear load vectors F are linearized about the deflected trim position and can hence contribute to the system stiffness and damping matrices.

Reproduced with permission of the copyright owner. Further reproduction prohibited without permission.

Discretization of Hub Equations

The hub-blade and hub-hub equations resulting from the variation of work done by the blade forces on the hub are presented here. The work done on the hub can be expressed as

$$\begin{aligned}\delta W_h &= \sum_{m=1}^{N_b}\int_0^R \Big(F^A_{x_h}\delta x_h + F^A_{y_h}\delta y_h + F^A_{z_h}\delta z_h + M^A_{\alpha_h}\delta\alpha_h + M^A_{\phi_h}\delta\phi_h + M^A_{\zeta_h}\delta\zeta_h \\ &\qquad + M^A_{\beta_{GC}}\delta\beta_{GC} + M^A_{\beta_{GS}}\delta\beta_{GS}\Big)\,dx \qquad (3.228)\\ &= \sum_{m=1}^{N_b}\int_0^R \delta\hat{x}_h^T\hat{F}_h^A\,dr \qquad (3.229)\end{aligned}$$

where

$$\delta\hat{x}_h = [\delta x_h\ \delta y_h\ \delta z_h\ \delta\alpha_h\ \delta\phi_h\ \delta\zeta_h\ \delta\beta_{GC}\ \delta\beta_{GS}]^T \qquad (3.230)$$

$$\hat{F}_h^A = \left[F^A_{x_h}\ F^A_{y_h}\ F^A_{z_h}\ M^A_{\alpha_h}\ M^A_{\phi_h}\ M^A_{\zeta_h}\ M^A_{\beta_{GC}}\ M^A_{\beta_{GS}}\right]^T \qquad (3.231)$$

The transformation of the aerodynamic loads from the blade to the hub is given by

$$\hat{F}_h^A = [T_{FL}]\hat{L}^A \qquad (3.232)$$

The hub aerodynamic force vector is divided into components as

$$\hat{F}_h^A = \left(\hat{F}_h^A\right)_c + \left(\hat{F}_h^A\right)_q + \left(\hat{F}_h^A\right)_{x_h} + \left(\hat{F}_h^A\right)_{q^2} + \left(\hat{F}_h^A\right)_{qx_h} + \left(\hat{F}_h^A\right)_{x_h^2} \qquad (3.233)$$

and by using the T_{FL} transformation matrix,

$$\left(\hat{F}_h^A\right)_c = \left(\hat{L}^A\right)_c (T_{FL})_c \qquad (3.234)$$

$$\left(\hat{F}_h^A\right)_q = \left(\hat{L}^A\right)_c (T_{FL})_q + \left(\hat{L}^A\right)_q (T_{FL})_c \qquad (3.235)$$

$$\left(\hat{F}_h^A\right)_{x_h} = \left(\hat{L}^A\right)_c (T_{FL})_{x_h} + \left(\hat{L}^A\right)_{x_h} (T_{FL})_c \qquad (3.236)$$

Reproduced with permission of the copyright owner. Further reproduction prohibited without permission.

$$\left(\hat{F}_h^A\right)_{q^2} = \left(\hat{L}^A\right)_c (T_{FL})_{q^2} + \left(\hat{L}^A\right)_q (T_{FL})_q + \left(\hat{L}^A\right)_{q^2} (T_{FL})_c \tag{3.237}$$

$$\left(\hat{F}_h^A\right)_{qx_h} = \left(\hat{L}^A\right)_q (T_{FL})_{x_h} + \left(\hat{L}^A\right)_{x_h} (T_{FL})_q \tag{3.238}$$

$$\left(\hat{F}_h^A\right)_{x_h^2} = \left(\hat{L}^A\right)_c (T_{FL})_{x_h^2} + \left(\hat{L}^A\right)_{x_h} (T_{FL})_{x_h} + \left(\hat{L}^A\right)_{x_h^2} (T_{FL})_c \tag{3.239}$$

The linear contribution to the force vector is given by

$$\left(\hat{F}_h^A\right)_L = \left(\hat{L}^A\right)_c (T_{FL})_q + \left(\hat{L}^A\right)_q (T_{FL})_c + \left(\hat{L}^A\right)_c (T_{FL})_{x_h} + \left(\hat{L}^A\right)_{x_h} (T_{FL})_c \tag{3.240}$$

The linear contribution to the damping and stiffness matrices can be derived as follows:

$$\left(\hat{L}^A\right)_c (T_{FL})_q = (T_{FL})_c^u \hat{u} + (T_{FL})_c^{u'} \hat{u}' \tag{3.241}$$

$$\left(\hat{L}^A\right)_c (T_{FL})_{x_h} = (T_{FL})_c^{x_h} \hat{x}_h \tag{3.242}$$

The linear force vector can be rewritten as

$$\begin{aligned}\left(\hat{F}_h^A\right)_L = {} & (T_{FL})_c^u \hat{u} + (T_{FL})_c^{u'} \hat{u}' \\ & + (T_{FL})_c \left([A_u]\hat{u} + [A_{u'}]\hat{u}' + [A_{u}^{\star}] \overset{\star}{\hat{u}} + [A_{u}^{\star\star}] \overset{\star\star}{\hat{u}} \right) \\ & + (T_{FL})_c^{x_h} \hat{x}_h + (T_{FL})_c \left([A_{x_h}]\hat{x}_h + [A_{x_h}^{\star}] \overset{\star}{\hat{x}}_h \right)\end{aligned} \tag{3.243}$$

Substitution of Eqns. 3.211-3.217 into the expression for the hub virtual work (Eqn. 3.229) yields the element hub-blade and hub-hub damping and stiffness matrices and load vectors.

$$\begin{aligned}\delta W_h = \sum_{m=1}^{N_b} \delta \hat{x}_h^T \Big(& \left[C_{hb}^A\right] \overset{\star}{\hat{q}} + \left[K_{hb}^A\right] \hat{q} + \left[C_{hh}^A\right] \overset{\star}{\hat{x}}_h + \left[K_{hh}^A\right] \overset{\star}{\hat{x}}_h \\ & + \left[F_h^A\right]_c + \left[F_h^A\right]_{q^2} + \left[F_h^A\right]_{qx_h} + \left[F_h^A\right]_{x_h^2} \Big)\end{aligned} \tag{3.244}$$

where the system matrices are defined as

$$\left[M_{hb}^A\right] = \frac{\gamma}{6} l \int_0^1 (T_{FL})_c [A_{u}^{\star\star}][H_s]\, ds \tag{3.245}$$

Reproduced with permission of the copyright owner. Further reproduction prohibited without permission.

$$\left[C^A_{hb}\right] = \frac{\gamma}{6} l \int_0^1 (T_{FL})_c [A^{\star}_u][H_s]\, ds \tag{3.246}$$

$$\left[K^A_{hb}\right] = \frac{\gamma}{6} l \int_0^1 (T_{FL})^u_c [H_s] + (T_{FL})^{u'}_c [H'_s] + ((T_{FL})_c [A_u][H_s] + (T_{FL})_c [A_{u'}][H'_s])\, ds \tag{3.247}$$

$$\left[C^A_{hh}\right] = \frac{\gamma}{6} l \int_0^1 (T_{FL})_c [A^{\star}_{x_h}]\, ds \tag{3.248}$$

$$\left[K^A_{hh}\right] = \frac{\gamma}{6} l \int_0^1 (T_{FL})^{x_h}_c + (T_{FL})_c [A_{x_h}]\, ds \tag{3.249}$$

$$\left[F^A_h\right]_c = \frac{\gamma}{6} l \int_0^1 (F^A_h)_c\, ds \tag{3.250}$$

$$\left[F^A_h\right]_{q^2} = \frac{\gamma}{6} l \int_0^1 (F^A_h)_{q^2}\, ds \tag{3.251}$$

$$\left[F^A_h\right]_{qx_h} = \frac{\gamma}{6} l \int_0^1 (F^A_h)_{qx_h}\, ds \tag{3.252}$$

$$\left[F^A_h\right]_{x^2_h} = \frac{\gamma}{6} l \int_0^1 (F^A_h)_{x^2_h}\, ds \tag{3.253}$$

Nonlinear Forces

The nonlinear forces contribute to the mass, damping and stiffness matrices when linearized about the trim position. The procedure used in this formulation is similar to other UMARC formulations and also to that in Ref. [39] in that the nonlinear components of the T_{FL} matrix are also included. The force vector F is written for the ith blade element as a sum of constant and nonlinear parts as

$$[F]_i = [F_c]_i + [F_{NL}]_i \tag{3.254}$$

The nonlinear forces are linearized about the trim position using a first order Taylor approximation.

$$[F_{NL}]_i = \left([F_{NL}] \mid_c + \frac{\partial [F_{NL}]}{\partial \hat{q}} \hat{q} + \frac{\partial [F_{NL}]}{\partial \overset{\star}{\hat{q}}} \overset{\star}{\hat{q}} + \frac{\partial [F_{NL}]}{\partial \hat{x}_h} \hat{x}_h + \frac{\partial [F_{NL}]}{\partial \overset{\star}{\hat{x}}_h} \overset{\star}{\hat{x}}_h \right)_i \tag{3.255}$$

Reproduced with permission of the copyright owner. Further reproduction prohibited without permission.

The nonlinear blade aerodynamic forces are written in coefficient form as

$$\begin{aligned}\left[L^A\right]_{nl} &= \left[L^A\right]_{q^2} + \left[L^A\right]_{qx_h} + \left[L^A\right]_{x_h^2} \\ &= [A_u]_{nl}\hat{u} + [A_{u'}]_{nl}\hat{u}' + [A_{\overset{\star}{u}}]_{nl}\,\overset{\star}{\hat{u}} + \\ &\quad [A_{x_h}]_{nl}\hat{x}_h + [A_{\overset{\star}{x}_h}]_{nl}\,\overset{\star}{\hat{x}}_h \end{aligned} \tag{3.256}$$

where after linearization about the deflected trim position, the nonlinear A matrices are defined as:

$$[A_u]_{nl} = \left[\frac{\partial}{\partial u}\left[L^A\right]_{nl}\ \frac{\partial}{\partial v}\left[L^A\right]_{nl}\ \frac{\partial}{\partial w}\left[L^A\right]_{nl}\ \frac{\partial}{\partial \hat{\phi}}\left[L^A\right]_{nl}\right] \tag{3.257}$$

$$[A_{u'}]_{nl} = \left[\frac{\partial}{\partial u'}\left[L^A\right]_{nl}\ \frac{\partial}{\partial v'}\left[L^A\right]_{nl}\ \frac{\partial}{\partial w'}\left[L^A\right]_{nl}\ \frac{\partial}{\partial \hat{\phi}'}\left[L^A\right]_{nl}\right] \tag{3.258}$$

$$\left[A_{\overset{\star}{u}}\right]_{nl} = \left[\frac{\partial}{\partial\,\overset{\star}{u}}\left[L^A\right]_{nl}\ \frac{\partial}{\partial\,\overset{\star}{v}}\left[L^A\right]_{nl}\ \frac{\partial}{\partial\,\overset{\star}{w}}\left[L^A\right]_{nl}\ \frac{\partial}{\partial\,\overset{\star}{\hat{\phi}}}\left[L^A\right]_{nl}\right] \tag{3.259}$$

$$[A_{x_h}]_{nl} = \frac{\partial}{\partial \hat{x}_h}\left[L^A\right]_{nl} \tag{3.260}$$

$$\left[A_{\overset{\star}{x}_h}\right]_{nl} = \frac{\partial}{\partial\,\overset{\star}{\hat{x}}_h}\left[L^A\right]_{nl} \tag{3.261}$$

The damping and stiffness matrix contributions to the blade equations from the nonlinear aerodynamic forces can be obtained by substituting into the virtual work expression.

$$\left[C^A_{bb}\right]_{nl} = -\frac{\gamma}{6} l \int_0^1 [H_s]^T [A_{\overset{\star}{u}}]_{nl} [H_s]\, ds \tag{3.262}$$

$$\left[K^A_{bb}\right]_{nl} = -\frac{\gamma}{6} l \int_0^1 \left([H_s]^T [A_u]_{nl} [H_s] + [H'_s]^T [A_{u'}]_{nl} [H'_s]\right)\, ds \tag{3.263}$$

$$\left[C^A_{bh}\right]_{nl} = -\frac{\gamma}{6} l \int_0^1 [H_s]^T [A_{\overset{\star}{x}_h}]_{nl}\, ds \tag{3.264}$$

$$\left[K^A_{bh}\right]_{nl} = -\frac{\gamma}{6} l \int_0^1 [H_s]^T [A_{x_h}]_{nl}\, ds \tag{3.265}$$

These contributions from the nonlinear force vector can be added to the already obtained matrices from the linear forces and can be used in the stability analysis

Reproduced with permission of the copyright owner. Further reproduction prohibited without permission.

of the system.

The nonlinear forces on the hub are given by

$$\begin{aligned}\left(\hat{F}_h^A\right)_{nl} &= [T_{FL}]\,[L^A]_{nl} \\ &= \left(\hat{F}_h^A\right)_{q^2} + \left(\hat{F}_h^A\right)_{qx_h} + \left(\hat{F}_h^A\right)_{x_h^2} \end{aligned} \tag{3.266}$$

Repeating the same process for the hub forces, the nonlinear forces can be written in coefficient form as follows:

$$\begin{aligned}\left(\hat{F}_h^A\right)_{nl} &= [T_{FL}]_c\left([A_u]_{nl}\hat{u} + [A_{u'}]_{nl}\hat{u}'\right) + \left[A_u^h\right]_{nl}\hat{u} + \left[A_{u'}^h\right]_{nl}\hat{u}' \\ &\quad + [T_{FL}]_c[A_{\overset{\star}{u}}]_{nl}\overset{\star}{\hat{u}} + \left[A_{\overset{\star}{u}}^h\right]_{nl}\overset{\star}{\hat{u}} \\ &\quad + [T_{FL}]_c[A_{x_h}]_{nl}\hat{x}_h + \left[A_{x_h}^h\right]_{nl}\hat{x}_h \\ &\quad + [T_{FL}]_c\left[A_{\overset{\star}{x}_h}\right]_{nl}\overset{\star}{\hat{x}}_h + \left[A_{\overset{\star}{x}_h}^h\right]_{nl}\overset{\star}{\hat{x}}_h \end{aligned} \tag{3.267}$$

where

$$\left[A_u^h\right]_{nl} = \left[\hat{L}^A\right]_c \frac{\partial}{\partial\hat{u}}(T_{FL})_{q^2} + \left[\hat{L}^A\right]_q \frac{\partial}{\partial\hat{u}}(T_{FL})_q + \frac{\partial}{\partial\hat{u}}\left[\hat{L}^A\right]_q (T_{FL})_q \tag{3.268}$$

$$\left[A_{u'}^h\right]_{nl} = \left[\hat{L}^A\right]_c \frac{\partial}{\partial\hat{u}'}(T_{FL})_{q^2} + \left[\hat{L}^A\right]_q \frac{\partial}{\partial\hat{u}'}(T_{FL})_q + \frac{\partial}{\partial\hat{u}'}\left[\hat{L}^A\right]_q (T_{FL})_q \tag{3.269}$$

$$\left[A_{\overset{\star}{u}}^h\right]_{nl} = \left[\hat{L}^A\right]_c \frac{\partial}{\partial\overset{\star}{\hat{u}}}(T_{FL})_{q^2} + \left[\hat{L}^A\right]_q \frac{\partial}{\partial\overset{\star}{\hat{u}}}(T_{FL})_q + \frac{\partial}{\partial\overset{\star}{\hat{u}}}\left[\hat{L}^A\right]_q (T_{FL})_q \tag{3.270}$$

$$\left[A_{x_h}^h\right]_{nl} = \left[\hat{L}^A\right]_c \frac{\partial}{\partial\hat{x}_h}(T_{FL})_{q^2} + \left[\hat{L}^A\right]_q \frac{\partial}{\partial\hat{x}_h}(T_{FL})_q + \frac{\partial}{\partial\hat{x}_h}\left[\hat{L}^A\right]_q (T_{FL})_q \tag{3.271}$$

$$\begin{aligned}\left[A_{\overset{\star}{x}_h}^h\right]_{nl} &= \left[\hat{L}^A\right]_c \frac{\partial}{\partial\overset{\star}{\hat{x}}_h}(T_{FL})_{q^2} + \left[\hat{L}^A\right]_q \frac{\partial}{\partial\overset{\star}{\hat{x}}_h}(T_{FL})_q \\ &\quad + \frac{\partial}{\partial\overset{\star}{\hat{x}}_h}\left[\hat{L}^A\right]_q (T_{FL})_q \end{aligned} \tag{3.272}$$

The contributions to the damping and stiffness matrices of the hub equations from the nonlinear forces are obtained by substituting these equations into the

Reproduced with permission of the copyright owner. Further reproduction prohibited without permission.

expression for the virtual work.

$$\left[C^A_{hb}\right]_{nl} = -\frac{\gamma}{6} l \int_0^1 \left[(T_{FL})_c [A^{\star}_{u}]_{nl} [H_s] + \left[A^h_{\star u}\right]_{nl} [H_s]\right] ds \tag{3.273}$$

$$\left[K^A_{hb}\right]_{nl} = -\frac{\gamma}{6} l \int_0^1 \left[(T_{FL})_c [A_u]_{nl} [H_s] + (T_{FL})_c [A_{u'}]_{nl} [H'_s] + \left[A^h_u\right]_{nl} [H_s] + \left[A^h_{u'}\right]_{nl} [H'_s]\right] ds \tag{3.274}$$

$$\left[C^A_{hh}\right]_{nl} = -\frac{\gamma}{6} l \int_0^1 \left[(T_{FL})_c [A^{\star}_{x_h}]_{nl} + \left[A^h_{\star x_h}\right]_{nl}\right] ds \tag{3.275}$$

$$\left[K^A_{hh}\right]_{nl} = -\frac{\gamma}{6} l \int_0^1 \left[(T_{FL})_c [A_{x_h}]_{nl} + \left[A^h_{x_h}\right]_{nl}\right] ds \tag{3.276}$$

3.3.4 Wing Aerodynamics

The wing aerodynamic model is similar to that used for the blade modeling. Linear wing aerodynamics is considered for both trim and stability predictions. For stability purposes, the constant load vector is not considered. The wing aerodynamics hence contribute only to the linear mass, damping and stiffness wing matrices. The wing matrices are obtained from the blade expressions by setting the azimuth angle ψ to 90° and the pylon angle α_p to 0°. Also the rotational speed Ω and the precone angle β_p are set to zero to obtain the wing matrices. θ_1 in the blade expressions is now equivalent to the sum of the wing and fuselage incidence angles.

The aerodynamic velocity components are written, as for the blade, as tangential, normal and radial components. These terms contribute to the wing mass, damping and stiffness element matrices similar to the blade equations. Compressibility corrections and noncirculatory airloads are modeled for the wing similar to those of the blade.

Reproduced with permission of the copyright owner. Further reproduction prohibited without permission.

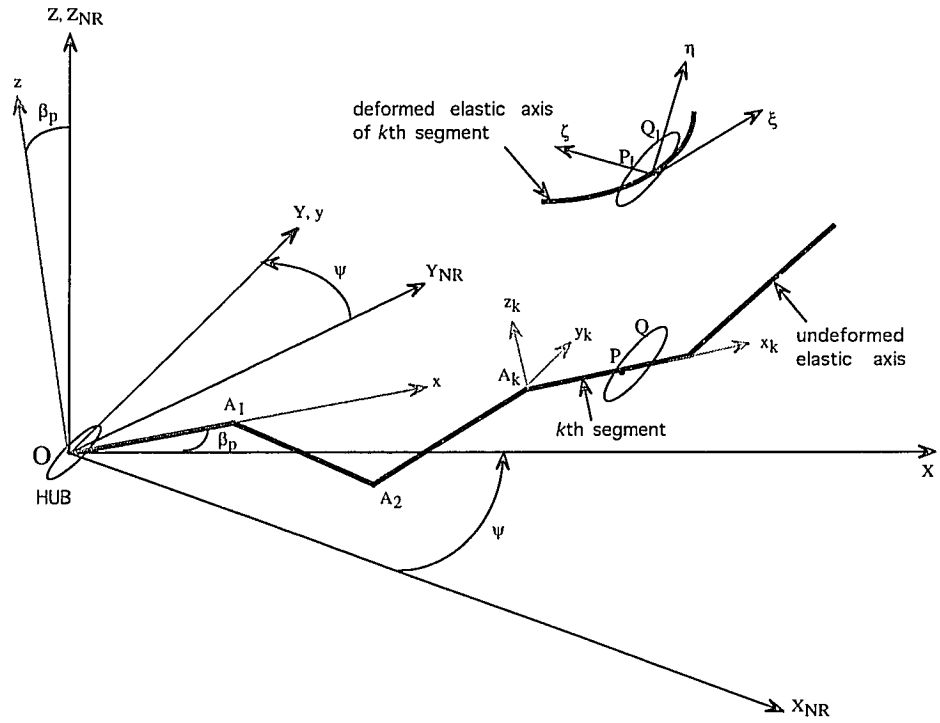

Figure 3.1: Coordinate systems for the advanced geometry blade

Reproduced with permission of the copyright owner. Further reproduction prohibited without permission.

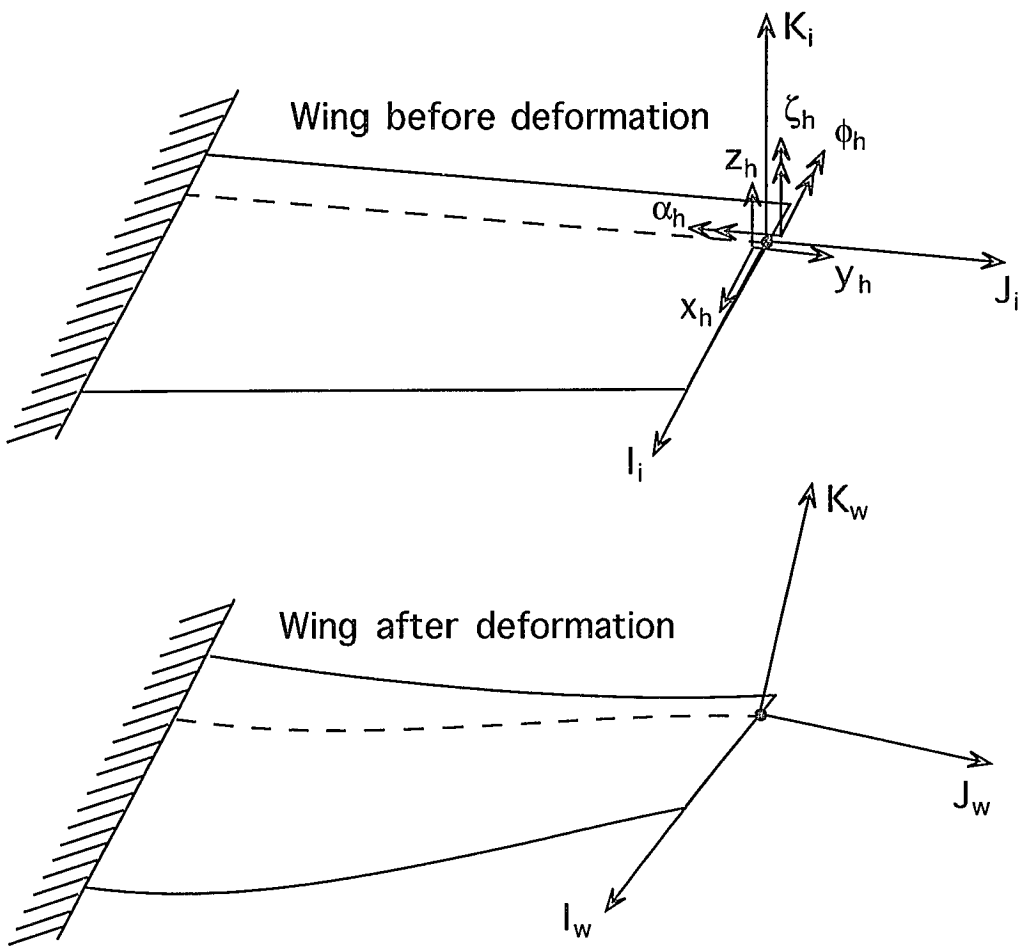

Figure 3.2: Wing reference frames

Reproduced with permission of the copyright owner. Further reproduction prohibited without permission.

Physical Quantity	Reference Parameter
Length	R
Time	Ω^{-1}
Mass/Length	m_0
Velocity	ΩR
Acceleration	$\Omega^2 R$
Force	$m_0 \Omega^2 R^2$
Moment	$m_0 \Omega^2 R^3$
Energy/Work	$m_0 \Omega^2 R^3$

Table 3.1: Nondimensionalization of physical quantities

Reproduced with permission of the copyright owner. Further reproduction prohibited without permission.

Chapter 4

Tiltrotor Analysis

The analysis consists of three parts: a free vibration analysis of the system, a coupled-trim procedure and a rotor-wing stability analysis.

4.1 Free Vibration Analysis

A finite element analysis is performed on the system to obtain the natural vibration characteristics. To begin with, the rotor blade and wing are discretized and modeled with as many finite elements as required by their geometric and structural complexities. Typically, 5 to 10 finite elements are needed to accurately model the blade/wing. The 15 degree-of-freedom element, mentioned in previous sections, is used to model the blades and the wing. The finite elements are assembled using standard assembly procedure. At this point, the natural vibration analysis of wing and rotor blade is performed separately.

The system stiffness and mass matrices are assembled individually for the rotor blade and for the wing. The damping matrix is set to be zero; no structural damping is included at this stage of the analysis. The appropriate boundary conditions for the blade and wing are applied. The wing is assumed to be cantilevered at the

Reproduced with permission of the copyright owner. Further reproduction prohibited without permission.

root; hence all six degrees-of-freedom associated with the root node of the wing are constrained. The rotor blade can be articulated, hingeless or bearingless. A hingeless blade is cantilevered at its root; this is similar to the wing case. For an articulated rotor system, the blade flap rotation degree-of-freedom at its root is unconstrained; the other five degrees-of-freedom at the root node are constrained. Bearingless rotor blades usually have kinematic constraints that are functions of two or more degrees-of-freedom at the root node of the torque-tube. The application of the blade constraint equations for different rotor systems as modeled in the UMARC formulation is discussed in considerable detail in Ref. [70].

The homogeneous system of equations is then solved to obtain the natural frequencies and eigenmodes of the blade and wing separately. The blade equations are written as

$$[M_{bb}]^S \overset{\star\star}{\hat{q}}_b + [K_{bb}]^S \hat{q}_b = 0 \tag{4.1}$$

and the wing equations are expressed similarly as

$$[M_{ww}]^S \overset{\star\star}{\hat{q}}_w + [K_{ww}]^S \hat{q}_w = 0 \tag{4.2}$$

where the superscript S indicates that only structural contributions are included for the calculation of the system natural vibration characteristics. These two systems are solved, independently of one another, using standard eigenvalue solution techniques. All the eigenvalues obtained from this analysis are positive and real, and all the eigenvectors are real and orthogonal.

Reproduced with permission of the copyright owner. Further reproduction prohibited without permission.

4.2 Coupled Trim

The coupled trim analysis involves simultaneous solution of the vehicle equilibrium equations and the blade steady periodic response equations. The vehicle trim controls depend directly on the steady aerodynamic loads from the rotor which are dependent on the blade response. The blade response, in turn, is dependent on the trim control settings. This interdependence between the blade response and trim control angles requires the simultaneous solution of both sets of equations. The initial controls estimate is an extremely important step of the trim analysis since convergence and robustness of the process depend on it. A rigid-blade analysis to predict the trim controls in hover, high speed axial flight and conversion flight conditions was developed by Nixon [39] and is included in Appendix C. Based on these initial controls, the elastic blade response equations are solved using a Newton approach along with the force residual equations.

4.2.1 Vehicle Trim Analysis

The vehicle trim equations are nonlinear, and to solve these, initial estimates of the control angles are necessary (since iterative schemes have to be used). The trim equations define the trim state; they consist of the vehicle force residuals $\hat{F}$ and the trim controls $\hat{\theta}$. The force vector defines the equilibrium of the rotor and airframe forces and moments which are functions of the trim controls and blade response. The trim control vector has to be then solved for in the trim analysis. The control vector used in the analysis depends on the type of trim procedure being carried out. There are three types of trim analyses available in this formulation:

Reproduced with permission of the copyright owner. Further reproduction prohibited without permission.

axisymmetric trim, wind tunnel trim and free flight trim. Axisymmetric trim is a very simple scheme applicable to hover (helicopter mode) and airplane modes of operation; the rotor thrust alone is trimmed for in this case. Wind tunnel trim assumes a cantilevered wing and a rotor model (excluding the fuselage). The rotor thrust and rotor cyclic flapping are trimmed in this method. The most general trim option is the free flight trim; this method includes a balance of forces from the rotor, wing, fuselage and empennage.

Axisymmetric Trim

The axisymmetric trim model is valid for hover as well as for high speed axial flight. This assumes that the vehicle center of gravity acts though the rotor thrust axis such that no cyclic control is required to balance the aircraft moments. The pylon angle for this analysis is set to 90° (even for analyzing the hover condition). The force vector consists of only one residual:

$$F_1 = T - T_i \tag{4.3}$$

where T is the calculated thrust based on the current value of rotor collective and T_i is the desired thrust level. $T_i = \frac{W}{2}$ for the hover case and is equal to one-half the total airplane drag for the high speed axial flight case. The corresponding trim control vector is defined as

$$\hat{\theta}^T = [\theta_{75}] \tag{4.4}$$

where θ_{75} is the collective pitch setting at 75% blade span.

Reproduced with permission of the copyright owner. Further reproduction prohibited without permission.

Wind Tunnel Trim

Wind tunnel trim refers to trimming the rotor to a given rotor thrust and zero cyclic flapping. Wing, fuselage and empennage aerodynamic forces are not considered when trimming to a wind tunnel condition. The fuselage angle-of-attack is assumed to be zero, and the pylon is set at an angle α_p with respect to the wing (not necessarily at 90° as for the airplane mode). The force vector for this case is

$$F_1 = T - T_i \tag{4.5}$$

$$F_2 = M_y \tag{4.6}$$

$$F_3 = M_x \tag{4.7}$$

where F_1 is the thrust residual; F_2 and F_3 are the pitch and roll moment residuals at the rotor hub. These determine the collective and cyclic pitch controls required in any flight condition. The trim control vector is expressed as

$$\hat{\theta}^T = [\theta_{75}\ \theta_{1c}\ \theta_{1s}] \tag{4.8}$$

where θ_{1c} and θ_{1s} are the rotor lateral and longitudinal cyclic pitch angles. The control input to a rotor blade section is given by

$$\theta(x, \psi) = \theta_{75} + \theta_{tw}\left(\frac{r}{R} - 0.75\right) + \theta_{1c}\cos\psi + \theta_{1s}\sin\psi \tag{4.9}$$

where θ_{tw} is the linear twist between the blade tip and the blade root.

Free Flight Trim

Lateral symmetry (zero aircraft yaw angle) is assumed in free level flight. This implies that only one half of the system needs to be considered; the right tiltrotor

Reproduced with permission of the copyright owner. Further reproduction prohibited without permission.

system is considered for this analysis. The symmetric flight assumption implies that the aircraft roll and yaw moments and side force are in balance between the two rotors. The free flight trim option can be used in hover, helicopter forward flight, conversion mode or in high speed airplane mode.

Figure 4.1 shows a tiltrotor in conversion mode of flight and the forces acting on the system. Steady rotor thrust, drag and pitching moment contribute to the trim equations. Aerodynamic forces from the wing, fuselage and empennage are included in the equilibrium equations. The wing, fuselage and tail incidence angles are hence included in this trim procedure. The horizontal component of the rotor thrust balances the aircraft drag; the wing lift and vertical component of the rotor thrust balance the weight of the aircraft. The thrust and drag in the equations are the sum total from both rotors. The force residual vector can be written as

$$\begin{aligned}
\text{Drag: } F_1 &= (D_f + D_w + D_t)\cos\alpha - (L_f + L_w + L_t)\sin\alpha \\
&\quad -(T\sin\alpha_p - H\cos\alpha_p) \qquad (4.10) \\
\text{Thrust: } F_2 &= (L_f + L_w + L_t)\cos\alpha + (D_f + D_w + D_t)\sin\alpha \\
&\quad +(T\cos\alpha_p + H\sin\alpha_p) - W \qquad (4.11) \\
\text{Pitch: } F_3 &= M_y + M_{y_f} - W(z_w\sin\alpha + x_w\cos\alpha) - D_f z_w \\
&\quad +M_w + M_t - D_t(z_w - z_t) - L_t(x_t - x_w) \\
&\quad +H\left[h + Y_w(\tan\Lambda_{2_w}\cos\alpha_p - \tan\Lambda_{1_w}\sin\alpha_p)\right] \\
&\quad -e_{d_w}\left(D_w\sin\alpha + L_w\cos\alpha\right) \qquad (4.12) \\
\text{Roll: } F_4 &= M_x \qquad (4.13)
\end{aligned}$$

α_p is the rotor pylon angle with respect to the vertical (0° represents helicopter

Reproduced with permission of the copyright owner. Further reproduction prohibited without permission.

hover mode and 90° represents airplane mode) and α is the angle-of-attack of the fuselage. e_{d_w} is the distance of the wing aerodynamic center behind the wing elastic axis. F_1 and F_2 are the vertical and horizontal force residuals respectively; F_3 represents the longitudinal pitching moment about the wing elastic axis (at the pylon attachment point to the wing) and F_4 is the lateral (rolling) moment residual about the rotor hub. T, H, M_x, and M_y are the rotor thrust, drag, rolling and pitching moments respectively from both the rotors. L, D, M are the lift, drag and pitching moment contributions from the fuselage, wing and horizontal tail (with subscripts f, w, and t respectively). W is the total weight of the aircraft. x_t and x_w are the longitudinal moment arms about the aircraft c.g. for the tail and wing respectively. Similarly, z_t and z_w are the vertical moment arms about the aircraft c.g. This trim analysis was originally developed by Nixon [39] and has been improved upon in this study with the inclusion of more terms in the trim equations. The fuselage forces appearing in the residual equations are defined as follows:

$$D_f = \frac{\mu^2}{2}\frac{\gamma N_b}{3\sigma a}\frac{f}{A} \tag{4.14}$$

$$D_w = \frac{\mu^2}{2}\frac{\gamma N_b}{3\sigma a}S_w c_{d_w} \tag{4.15}$$

$$D_t = \frac{\mu^2}{2}\frac{\gamma N_b}{3\sigma a}S_t c_{d_t} \tag{4.16}$$

$$L_f = \frac{\mu^2}{2}\frac{\gamma N_b}{3\sigma a}S_t c_{l_f} \tag{4.17}$$

$$L_w = \frac{\mu^2}{2}\frac{\gamma N_b}{3\sigma a}S_w c_{l_{\alpha_w}}(\alpha + \alpha_{0_w}) \tag{4.18}$$

$$L_t = \frac{\mu^2}{2}\frac{\gamma N_b}{3\sigma a}S_t c_{l_{\alpha_t}}(\alpha + \alpha_{0_t}) \tag{4.19}$$

$$M_{y_f} = \frac{\mu^2}{2}\frac{\gamma N_b}{3\sigma a}c_{M_f} \tag{4.20}$$

Reproduced with permission of the copyright owner. Further reproduction prohibited without permission.

$$M_w = \frac{\mu^2}{2}\frac{\gamma N_b}{3\sigma a} S_w c_{m_w} c_w \tag{4.21}$$

$$M_t = \frac{\mu^2}{2}\frac{\gamma N_b}{3\sigma a} S_t c_{m_t} c_t \tag{4.22}$$

f/A is the fuselage flat plate area for calculating the drag, α is the angle-of-attack of the fuselage and α_0 is the incidence angle with respect to the fuselage. c_{M_f} is the fuselage pitching moment coefficient excluding the wing and tail.

The trim control vector for the free flight trim case is

$$\hat{\theta}^T = [\alpha,\ \theta_{75},\ \theta_{1c},\ \theta_{1s}] \tag{4.23}$$

4.2.2 Blade Response Analysis

The steady rotor blade response is calculated for a hub-fixed condition. The hub motion terms are hence neglected from the blade response equations.

$$\hat{x}_h = 0 \tag{4.24}$$

$$\overset{\star}{\hat{x}}_h = 0 \tag{4.25}$$

$$\overset{\star\star}{\hat{x}}_h = 0 \tag{4.26}$$

The response equations are written in matrix form as

$$\int_0^{2\pi} (\delta\hat{q}_b)^T \left([M_{bb}] \overset{\star\star}{\hat{q}}_b + [C_{bb}] \overset{\star}{\hat{q}}_b + [K_{bb}]\, \hat{q}_b - \hat{F}_b \right) d\psi = 0 \tag{4.27}$$

To reduce computational time, the blade response equations are solved using a normal mode approach. The natural modes calculated in the free vibration analysis are used in the solution procedure. Typically, 5 to 10 normal modes are used in the calculation of results. The global displacements are related to the modal displacements by

Reproduced with permission of the copyright owner. Further reproduction prohibited without permission.

$$\hat{q}_b = [\Phi]\hat{p}_b \tag{4.28}$$

where $[\Phi]$ is the N^G x m modal matrix, and N^G is the number of blade global degrees-of-freedom and m is the number of modes used in the analysis. Substituting this into Eqn. 4.27, the modal response equations are written as

$$\int_0^{2\pi} (\delta\hat{p}_b)^T \left([M^p_{bb}] \overset{**}{\hat{p}}_b + [C^p_{bb}] \overset{*}{\hat{p}}_b + [K^p_{bb}]\hat{p}_b - \hat{F}^p_b \right) d\psi = 0 \tag{4.29}$$

where the mass, damping and stiffness matrices and the load vector are defined as

$$[M^p_{bb}] = [\Phi]^T [M_{bb}] [\Phi] \tag{4.30}$$

$$[C^p_{bb}] = [\Phi]^T [C_{bb}] [\Phi] \tag{4.31}$$

$$[K^p_{bb}] = [\Phi]^T [K_{bb}] [\Phi] \tag{4.32}$$

$$[F^p_b] = [\Phi]^T [F_b] \tag{4.33}$$

and the superscript p denotes the modal matrices.

4.2.3 Finite Element in Time

The solution of the blade response equations given by Eqn. 4.29 is obtained in this analysis using a finite element in time procedure. This is the same procedure used in earlier UMARC formulations and is briefly described in this section for the sake of completeness. The blade response is solved for separately in the spanwise and azimuthal coordinates. The spanwise response is obtained as a global vector of discrete displacements (or in terms of normal modes) from the finite element discretization of the blade based on Hamilton's principle. The azimuthal response is obtained from a temporal finite element discretization using the finite element in time procedure.

Reproduced with permission of the copyright owner. Further reproduction prohibited without permission.

The damping and stiffness matrices of the response equations have periodic coefficients, while the mass matrix is independent of such terms. The equations are written in first order form and then integrated. Eqn. 4.29 can be expressed as

$$\int_0^{2\pi} \begin{Bmatrix} \delta\hat{p}_b \\ \delta \overset{\star}{\hat{p}}_b \end{Bmatrix}^T \begin{Bmatrix} \hat{F}_b^p - [C]_b^p \overset{\star}{\hat{p}}_b - [K]_b^p \hat{p}_b \\ [M]_b^p \overset{\star}{\hat{p}}_b \end{Bmatrix} d\psi = \begin{Bmatrix} \delta\hat{p}_b \\ \delta \overset{\star}{\hat{p}}_b \end{Bmatrix}^T \begin{Bmatrix} [M]_b^p \overset{\star}{\hat{p}}_b \\ 0 \end{Bmatrix} \Bigg|_0^{2\pi} \tag{4.34}$$

where the right hand side of the equation is zero due to the enforced periodicity of the system response.

$$\overset{\star}{\hat{p}}(2\pi) = \overset{\star}{\hat{p}}(0) \tag{4.35}$$

Since the right hand side is equal to zero, the equations can be written in notational form as

$$\int_0^{2\pi} \delta\hat{y}^T [Q]\, d\psi = 0 \tag{4.36}$$

where

$$\hat{y} = \begin{Bmatrix} \delta\hat{p}_b \\ \delta \overset{\star}{\hat{p}}_b \end{Bmatrix} \tag{4.37}$$

and

$$[Q] = \begin{Bmatrix} \hat{F}_b^p - [C]_b^p \overset{\star}{\hat{p}}_b - [K]_b^p \hat{p}_b \\ [M]_b^p \overset{\star}{\hat{p}}_b \end{Bmatrix} \tag{4.38}$$

The $[Q]$ matrix is nonlinear since it contains nonlinear terms from $\hat{F}_b^p$. One rotor revolution 2π is discretized into a finite number of time elements, similar to spatial discretization, as shown in Figure 4.2. Typically 5 to 10 elements are used in the azimuthal discretization; for hover, however, one time element is sufficient since periodicity in the response is zero. The response equations are then written as the summation of the response over each time element as

Reproduced with permission of the copyright owner. Further reproduction prohibited without permission.

$$\sum_{i=1}^{N_t} \int_{\psi_i}^{\psi_i+1} \delta\hat{y}_i^T [Q]_i \, d\psi = 0 \tag{4.39}$$

where N_t is the number of time elements used. The equations are linearized using a first order Taylor expansion about the current blade response estimate $\hat{y}_0$.

$$\sum_{i=1}^{N_t} \int_{\psi_i}^{\psi_i+1} \delta\hat{y}_i^T \left([Q(y_0)]_i + [K_t(\hat{y}_0)]_i \Delta\hat{y}_i \right) \, d\psi = 0 \tag{4.40}$$

where

$$[K_t]_i = \begin{bmatrix} \frac{\partial F_b}{\partial \hat{p}_b} - [K]_b & \frac{\partial F_b}{\partial \dot{\hat{p}}_b} - [C]_b \\ 0 & [M]_b \end{bmatrix} \tag{4.41}$$

The finite element in time procedure results in converting the differential equations for the blade response into algebraic equations. This is accomplished by expressing the time variation of the modal displacement vector in terms of the temporal shape functions H and temporal discrete displacement vector $\hat{\xi}$.

$$\hat{p}_b(\psi) = [H_t(s)]\hat{\xi} \tag{4.42}$$

where s is the local time coordinate defined as:

$$s = \frac{\psi - \psi_i}{\psi_{i+1} - \psi_i} \tag{4.43}$$

and $\psi_{i+1} - \psi_i$ is the time span of the ith element. The matrix H depends on the level of approximation in describing the response variation within each time element; the default used in the current analysis is 6 nodes per time element which results in a set of six 5th-order polynomials for H. The response equations can then be expressed in first-order form as

$$\sum_{i=1}^{N_t} \int_{\psi_i}^{\psi_i+1} \delta\hat{\xi}_i^T [N]^t \left([Q]_i + [K_t]_i [N] \Delta\hat{\xi}_i \right) \, d\psi = 0 \tag{4.44}$$

Reproduced with permission of the copyright owner. Further reproduction prohibited without permission.

where

$$N = \left\{ \begin{array}{c} [H_t(\psi)] \\ \left[\overset{\star}{H}_t\ (\psi)\right] \end{array} \right\} \tag{4.45}$$

Standard finite element integration and assembly procedures are applied to the finite elements in time and the global azimuthal equations are written as

$$[Q]^G + [K]_t^G \Delta\hat{\xi}^G = 0 \tag{4.46}$$

subject to

$$\hat{\xi}(0) = \hat{\xi}(2\pi) \tag{4.47}$$

$$\overset{\star}{\hat{\xi}}\,(0) = \overset{\star}{\hat{\xi}}\,(2\pi) \tag{4.48}$$

4.2.4 Inflow Modeling

Momentum Analysis

The rotor wake determines the induced inflow distribution over the rotor disk and plays a very important role in the prediction of blade response, vibratory loads, acoustic signature and rotor performance. The inflow induced at the rotor disk by the wake, λ_i, depends on the rotor thrust and is updated in each iteration of the coupled trim analysis. The simplest inflow models are the uniform inflow model and the radially nonuniform inflow model, which are based on momentum theory. The uniform inflow model is adequate for tiltrotor stability analysis in high speed flight when thrust level is low and the total inflow in very high due to forward speed, and the induced inflow is a very small component. This value of induced inflow depends on the rotor thrust as well as on the total airflow through the rotor

Reproduced with permission of the copyright owner. Further reproduction prohibited without permission.

disk. The simplest uniform inflow model that is applicable to high speed airplane mode is given by

$$\lambda_i = \frac{C_T}{2\frac{V_v}{\Omega R}} \tag{4.49}$$

But when thrust levels are high, as in hover and conversion mode, a simple radially varying inflow model is incorporated to account the inflow variation due to large spanwise pretwist in the rotor blades. Such a model was developed by Gessow and Myers [92] and is implemented in the present analysis.

$$\lambda_i = \left(\frac{V_v}{2\Omega R} + \frac{\sigma_x a}{16}\right)\left[-1 + \sqrt{1 + \frac{2\left(\theta\frac{r}{R} - \frac{V_v}{\Omega R}\right)}{\frac{4V_v^2}{\sigma_x a(\Omega R)^2} + \frac{V_v}{\Omega R} + \frac{\sigma_x a}{16}}}\right] \tag{4.50}$$

where V_v is the dimensional velocity normal to the rotor disk (such as the forward flight velocity in airplane mode) and

$$\sigma_x = \sigma\frac{c_{local}}{c_{ref}} \tag{4.51}$$

and

$$\sigma = \frac{N_b c_{ref}}{\pi R} \tag{4.52}$$

and c is the blade chord. In hover, the expression for the radially varying inflow velocity reduces to

$$\lambda_i = \frac{\sigma_x a}{16}\left[-1 + \sqrt{1 + \frac{32\theta\frac{r}{R}}{\sigma_x a}}\right] \tag{4.53}$$

This model is important for tiltrotors in high thrust level condition since the blades are highly twisted and, therefore, the induced inflow varies considerably along the blade span. No blade tip loss correction factor is included in the above equations. The blade pretwist distribution is, as mentioned earlier, very large and almost

Reproduced with permission of the copyright owner. Further reproduction prohibited without permission.

bilinear (to simulate almost ideal twist) for most tiltrotors. The magnitude of pretwist is a compromise between requirements for helicopter and airplane modes of flight.

Vortex Models (Prescribed and Free Wake)

The uniform and linear wake models as well as the radially varying inflow model capture the global effects of the rotor wake and are usually satisfactory for high speed airplane mode or in axisymmetric hover condition, particularly for rotor performance and stability predictions. But such momentum-theory based models are usually not sufficient for the prediction of rotor vibratory loads particularly in tiltrotor conversion modes.

To predict the local inflow variations across the rotor disk, more complex models such as the prescribed wake and free wake models are required. These complex models predict the induced inflow distribution by modeling the gradients of circulation, spanwise and azimuthally. Conservation of vorticity (Helmholtz theorem) dictates that trailed or shed vorticity is created in the wake with a magnitude proportional to the spanwise or temporal gradients of the blade bound circulation. Furthermore, conservation of vorticity for a three-dimensional blade requires that the bound circulation itself be trailed into the wake at both the blade root and significantly at the blade tip. The prescribed and free wake models take into account the convection of the trailed and shed vorticity in the rotor wake and predict the resultant induced inflow distribution on the rotor disk.

Prescribed wake models usually assume that the blade tip vortices, which are

Reproduced with permission of the copyright owner. Further reproduction prohibited without permission.

the most dominant features of the wake, are convected at the free stream velocity. More sophisticated prescribed wake models incorporate empirical or semi-empirical factors to model the rotor tip vortex structure. But all the prescribed wake models assume that the rotor tip vortex geometry be *prescribed, a priori,* as a function of the rotor parameters and flight condition.

Free wake models, on the other hand, attempt to calculate the geometry of the rotor wake, primarily those of the blade tip vortices. The wake geometry is calculated taking into account the mutual interference effects of the tip vortices on one another. Once a calculated wake geometry is obtained, this wake geometry is used to calculate the local induced inflow distribution across the rotor disk.

Prescribed and free wake models have been incorporated in this tiltrotor analysis similar to those in earlier UMARC formulations. These wake models are adapted from the implementation in Ref. [48]. A new wake analysis developed by Bagai and Leishman [93] has also been implemented in this analysis; this free-wake analysis is based on a pseudo-implicit two-step predictor-corrector scheme which has better numerical convergence characteristics than the original analysis in Ref. [48]. Details of the implementation of this new analysis are discussed in Ref. [94]. Some of the improvements of this analysis over that in Ref. [48] are: (1) superior convergence characteristics of the free-wake geometry in low speed flight (including hover), (2) a capability of fine discretization of the rotor disk in both the spanwise and azimuthal directions, and (3) elimination of many tuning factors, such as artificially large vortex core radii and damping factors between successive wake geometry iterations. The formulation in Ref. [93] was modified in

Reproduced with permission of the copyright owner. Further reproduction prohibited without permission.

the implementation described in Ref. [94] to account for blade oscillatory flap, lag and torsional deformations as well as for advanced blade geometry such as sweep and anhedral.

The rotor inflow prediction for tiltrotors in hover and conversion modes, in particular, should also include some interference effects from the wing and fuselage for accurate modeling. Existing wing/fuselage/rotor aerodynamic interference models in the literature are constantly being revised to accurately predict this phenomenon. Such an interference model is not included in the present formulation.

4.2.5 Hub Loads

Solution of the force residual equations requires the hub loads arising from the rotating blade loads. The rotating blade aerodynamic and inertial loads are calculated and summed in the present analysis using a force summation approach in the rotating frame. Aerodynamic blade loads have been derived in the previous chapter. The inertial contributions of the blade loads are derived for a helicopter configuration in Ref. [89]; the inertial loads are derived for an advanced geometry rotor and remain the same for helicopter and tiltrotor formulations. The inertial blade loads are nonlinear functions of the blade displacement, velocities and accelerations. The blade displacements and velocities are obtained from solution of the finite element in time equations. The blade accelerations are then calculated from a rearrangement of the equations of motion.

$$\overset{\star\star}{\hat{q}}_b = [M_{bb}]^{-1}\left(\hat{F}_b - [C_{bb}]\,\overset{\star}{\hat{q}}_b - [K_{bb}]\hat{q}_b\right) \tag{4.54}$$

Reproduced with permission of the copyright owner. Further reproduction prohibited without permission.

The accelerations could have been calculated from the velocity information by differentiation. But this procedure results in a decrease in numerical accuracy which is circumvented by obtaining the accelerations directly from the equations of motion. The inertial and aerodynamic forces are then summed at each blade section.

$$L_u = L_u^A + L_u^I \tag{4.55}$$

$$L_v = L_v^A + L_v^I \tag{4.56}$$

$$L_w = L_w^A + L_w^I \tag{4.57}$$

$$M_u = M_{\hat{\phi}}^A + M_{\hat{\phi}}^I \tag{4.58}$$

$$M_v = M_{\hat{\phi}}^A v' + M_v^I \tag{4.59}$$

$$M_w = M_{\hat{\phi}}^A w' + M_w^I \tag{4.60}$$

where these forces and moments are defined in the undeformed blade system. The integrated forces and moments at the blade root are then obtained by numerical integration along the blade span.

$$F_x = \int_0^R L_u \, dr \tag{4.61}$$

$$F_y = \int_0^R L_v \, dr \tag{4.62}$$

$$F_z = \int_0^R L_w \, dr \tag{4.63}$$

$$M_x = \int_0^R [M_u + L_w v - L_v w] \, dr \tag{4.64}$$

$$M_y = \int_0^R [M_v - L_w(r+u) + L_u w] \, dr \tag{4.65}$$

$$M_z = \int_0^R [M_w + L_v(r+u) - L_u v] \, dr \tag{4.66}$$

Reproduced with permission of the copyright owner. Further reproduction prohibited without permission.

The integrated loads are then transformed to the fixed frame using a Fourier coordinate transformation (FCT).

$$F_x^H = \sum_{m=1}^{N_b} \left(F_x^m \cos\psi_m - F_y^m \sin\psi_m - \beta_p F_z^m \cos\psi_m \right) \tag{4.67}$$

$$F_y^H = \sum_{m=1}^{N_b} \left(F_x^m \sin\psi_m + F_y^m \cos\psi_m - \beta_p F_z^m \sin\psi_m \right) \tag{4.68}$$

$$F_z^H = \sum_{m=1}^{N_b} \left(F_z^m + \beta_p F_x^m \right) \tag{4.69}$$

$$M_x^H = \sum_{m=1}^{N_b} \left(M_x^m \cos\psi_m - M_y^m \sin\psi_m - \beta_p M_z^m \cos\psi_m \right) \tag{4.70}$$

$$M_y^H = \sum_{m=1}^{N_b} \left(M_x^m \sin\psi_m + M_y^m \cos\psi_m - \beta_p M_z^m \sin\psi_m \right) \tag{4.71}$$

$$M_z^H = \sum_{m=1}^{N_b} \left(M_z^m + \beta_p M_x^m \right) \tag{4.72}$$

where m is the blade number (from 1 to N_b blades). The hub forces are then expressed in terms of their harmonics by expanding in terms of Fourier series.

$$f(\psi) = f_0 + \sum_{n=1}^{\infty} \left(f_{nc} \cos n\psi + f_{ns} \sin n\psi \right) \tag{4.73}$$

where f_0 is the steady component of the hub force and n represents the number of the harmonic of the force. The steady components of the hub loads are used in the trim equations. The harmonic components of the hub loads are the vibratory loads for the airframe.

4.2.6 Trim Control Updates

The vehicle trim force residual equations are nonlinear algebraic equations and are solved using a Newton approach. These equations are linearized about the control vector obtained from the initial controls estimate. A Jacobian matrix consisting of the sensitivity of each force residual to each control variable is calculated at

Reproduced with permission of the copyright owner. Further reproduction prohibited without permission.

the start of the coupled trim procedure. This matrix is then used to calculate the change in control vector to minimize the residuals in each iteration.

$$\hat{F}\left(\hat{\theta}_i + \Delta\hat{\theta}_i\right) = \hat{F}\left(\hat{\theta}_i\right) + [J]\Delta\hat{\theta}_i = 0 \tag{4.74}$$

where $[J]$ is the vehicle Jacobian matrix.

$$[J] = \frac{\partial\hat{F}}{\partial\hat{\theta}}|_{\hat{\theta}=\hat{\theta}_0} \tag{4.75}$$

The Jacobian matrix is calculated numerically by perturbing the control vector elements, one at a time.

$$[J] = \frac{\hat{F}\left(\hat{\theta} + \Delta\hat{\theta}\right) - \hat{F}\left(\hat{\theta}\right)}{\Delta\hat{\theta}} \tag{4.76}$$

The Jacobian matrix is calculated at the initial controls obtained from the rigid blade trim procedure; it is hence imperative that good estimates for the initial controls are obtained from the rigid blade trim analysis. The Jacobian can be recalculated if the rigid blade trim values are unsatisfactory for a particular case.

The nonlinearity of the analysis requires judicious selection of the control vector updates to retain numerical stability of the solution. The trim control updates at each trim iteration are obtained from the Jacobian matrix and the force residual vector.

$$\Delta\hat{\theta}_i = -[J]^{-1}\hat{F}\left(\hat{\theta}_i\right) \tag{4.77}$$

To maintain numerical stability of trim updates, a damping factor R is used.

$$\hat{\theta}_{i+1} = \hat{\theta}_i + (1 - R)\Delta\hat{\theta}_i \tag{4.78}$$

where $0 < R < 1$ and R is typically set to decay exponentially with trim iteration number.

Reproduced with permission of the copyright owner. Further reproduction prohibited without permission.

4.2.7 Convergence of Coupled Trim

Convergence of the coupled trim solution is achieved when both the force residual and blade response equations are numerically satisfied to within a specified tolerance. The blade differential equations in time are transformed to nonlinear algebraic equations using the finite element in time procedure. The solution to the blade equations is written similar to the vehicle trim equations as

$$\hat{\xi} = \hat{\xi}_0 + \Delta\hat{\xi} \tag{4.79}$$

The updates for the steady global solution are given by

$$\hat{\xi}^G_{i+1} = \hat{\xi}^G_i + \Delta\hat{\xi}^G_i \tag{4.80}$$

where convergence is obtained when $\Delta\xi^G_i \approx 0$. Specifically, blade response convergence is obtained when

$$\frac{\sqrt{\sum_{j=1}^{N_\psi}(q_{i+1} - q_i)^2}}{\sqrt{\sum_{j=1}^{N_\psi} q^2_{i+1}}} < \epsilon_1 \tag{4.81}$$

where N_ψ is the total number of azimuthal gaussian integration points. Similarly, vehicle trim convergence is obtained when

$$\sqrt{\sum_{i=1}^{n} F_i^2} < \epsilon_2 \tag{4.82}$$

where n is the total length of the force residual vector (which varies with the trim method used in the analysis).

Typical convergence tolerances for ϵ_1, the blade response convergence criterion, and ϵ_2, the vehicle trim convergence criterion, are 0.005 and 0.0001 respectively.

Reproduced with permission of the copyright owner. Further reproduction prohibited without permission.

4.3 Stability Analysis

Stability is calculated using a linearized eigenanalysis of the system. The linearized perturbed differential equations of motion of the system are derived about the trim condition. The system matrices derived for the blade response analysis are utilized in the stability analysis assuming that the state variables are small perturbations about the known state vector which is calculated from the coupled trim procedure. An eigenanalysis is performed on the homogeneous system of equations to determine system stability. The wing is represented by a finite element model with beamwise, chordwise, torsion and axial degrees-of-freedom. The normal mode approximation is, at present, not being made for the wing representation; it is described in Chapter 7 and is included in the results presented in that chapter. The coupled rotor/wing equations are transformed to the fixed frame using a multiblade coordinate transformation. Floquet theory or constant coefficient approximation is used to solve for the roots of the equations. Constant coefficient matrices are used to obtain the results presented in this analysis. This assumption is valid since whirl flutter occurs in high speed forward flight when the flow about the rotor is axisymmetric and the system equations are independent of the rotor blade azimuth angle. Floquet theory, however, has been implemented for the tiltrotor analysis and can be used when necessary.

4.3.1 Rotor Equations

The blade equations are written for each blade in terms of the discrete displacements along the blade span. The blade finite elements are assembled using stan-

Reproduced with permission of the copyright owner. Further reproduction prohibited without permission.

dard finite element assembly procedure. Following assembly, the appropriate blade boundary conditions are applied. The equations are then summed over N_b blades. The nonlinear contributions to the force vectors are linearized by using a first-order Taylor expansion for each of the blades. The hub displacement vector $\hat{x}_h$ is as defined in the previous chapter. The rotor and hub system equations can be written as

$$\begin{bmatrix} M_{rr} & M_{rh} \\ M_{hr} & M_{hh} \end{bmatrix} \begin{Bmatrix} \overset{\star\star}{\hat{q}}_r \\ \overset{\star\star}{\hat{x}}_h \end{Bmatrix} + \begin{bmatrix} C_{rr} & C_{rh} \\ C_{hr} & C_{hh} \end{bmatrix} \begin{Bmatrix} \overset{\star}{\hat{q}}_r \\ \overset{\star}{\hat{x}}_h \end{Bmatrix} + \begin{bmatrix} K_{rr} & K_{rh} \\ K_{hr} & K_{hh} \end{bmatrix} \begin{Bmatrix} \hat{q}_r \\ \hat{x}_h \end{Bmatrix} = 0 \tag{4.83}$$

where

$$\hat{q}_r = \{(\hat{q}_b)_1^T \ (\hat{q}_b)_2^T \ \cdots \ (\hat{q}_b)_{N_b}^T\} \tag{4.84}$$

The wing equations are not part of the system equations yet and are added in the following section.

Normal Mode Reduction

The size of the rotor problem as solved using a complete finite element method is extremely large. The computational effort can be significantly reduced by transforming the blade equations into modal space. For this purpose, the normal modes of the blade are calculated about the deformed trim position. These normal modes hence include nonlinear structural blade couplings. Typically, 5 to 10 normal modes are required to model the blade response; this compares very favorably with around 50 to 100 discrete displacements required for the same purpose.

Reproduced with permission of the copyright owner. Further reproduction prohibited without permission.

$$\hat{q}_r = \left\{ \begin{array}{c} (\delta\hat{q}_b)_1 \\ (\delta\hat{q}_b)_2 \\ \vdots \\ (\delta\hat{q}_b)_{N_b} \end{array} \right\} = \left[\begin{array}{cccc} \Phi & & & \\ & \Phi & & \\ & & \ddots & \\ & & & \Phi \end{array} \right] \hat{q}_r = \left\{ \begin{array}{c} (\delta\hat{p}_b)_1 \\ (\delta\hat{p}_b)_2 \\ \vdots \\ (\delta\hat{p}_b)_{N_b} \end{array} \right\} = [\Phi]\,\hat{p}_r \tag{4.85}$$

where Φ is the blade modal matrix. The blade-related matrices are then transformed into modal space as:

$$\left[\begin{array}{cc} \bar{M}_{rr} & \bar{M}_{rh} \\ \bar{M}_{hr} & M_{hh} \end{array} \right] \left\{ \begin{array}{c} \overset{\star\star}{\hat{p}}_r \\ \overset{\star\star}{\hat{x}}_h \end{array} \right\} + \left[\begin{array}{cc} \bar{C}_{rr} & \bar{C}_{rh} \\ \bar{C}_{hr} & C_{hh} \end{array} \right] \left\{ \begin{array}{c} \overset{\star}{\hat{p}}_r \\ \overset{\star}{\hat{x}}_h \end{array} \right\} + \left[\begin{array}{cc} \bar{K}_{rr} & \bar{K}_{rh} \\ \bar{K}_{hr} & K_{hh} \end{array} \right] \left\{ \begin{array}{c} \hat{p}_r \\ \hat{x}_h \end{array} \right\} = 0 \tag{4.86}$$

where the transformations are given by:

$$\begin{aligned} \bar{M}_{rr} &= [\Phi]^T M_{rr} [\Phi] \\ \bar{M}_{rh} &= [\Phi]^T M_{rh} \\ \bar{M}_{hr} &= M_{hr} [\Phi] \\ \bar{C}_{rr} &= [\Phi]^T C_{rr} [\Phi] \\ \bar{C}_{rh} &= [\Phi]^T C_{rh} \\ \bar{C}_{hr} &= C_{hr} [\Phi] \\ \bar{K}_{rr} &= [\Phi]^T K_{rr} [\Phi] \\ \bar{K}_{rh} &= [\Phi]^T K_{rh} \\ \bar{K}_{hr} &= K_{hr} [\Phi] \end{aligned} \tag{4.87}$$

4.3.2 Wing Equations

The six discrete wing degrees-of-freedom correspond to six of the eight hub degrees-of-freedom. These displacements for a straight wing correspond as follows:

Wing dof Hub dof

Reproduced with permission of the copyright owner. Further reproduction prohibited without permission.

$$
\begin{aligned}
u_1 &= y_h \\
v_1 &= -x_h \\
v_1' &= \zeta_h \\
w_1 &= z_h \\
w_1' &= -\phi_h \\
\hat{\phi}_1 &= -\alpha_h
\end{aligned} \tag{4.88}
$$

Since the two gimbal fixed-frame degrees-of-freedom are considered part of the hub in this formulation, the size of the 'wing' matrices increases by two due to assembly. Assembly of the matrices is done according to standard finite element assembly procedure; coefficients of hub displacements from the hub matrices are added to the coefficients of the corresponding wing displacements from the wing matrices.

$$
\hat{x}_w = \left\{ \begin{array}{c} \beta_{GC} \\ \beta_{GS} \\ \hat{q}_w \end{array} \right\} \tag{4.89}
$$

The new ww matrices hence contain the two gimbal terms as well as the wing matrices. The system equations can then be written in matrix form as

$$
\begin{aligned}
\left[\begin{array}{cc} \bar{M}_{rr} & \bar{M}_{rw} \\ \bar{M}_{wr} & \bar{M}_{ww} \end{array} \right] \left\{ \begin{array}{c} \overset{\star\star}{\hat{p}}_r \\ \overset{\star\star}{\hat{x}}_w \end{array} \right\} + \left[\begin{array}{cc} \bar{C}_{rr} & \bar{C}_{rw} \\ \bar{C}_{wr} & \bar{C}_{ww} \end{array} \right] \left\{ \begin{array}{c} \overset{\star}{\hat{p}}_r \\ \overset{\star}{\hat{x}}_w \end{array} \right\} \\
+ \left[\begin{array}{cc} \bar{K}_{rr} & \bar{K}_{rw} \\ \bar{K}_{wr} & \bar{K}_{ww} \end{array} \right] \left\{ \begin{array}{c} \hat{p}_r \\ \hat{x}_w \end{array} \right\} = 0
\end{aligned} \tag{4.90}
$$

4.3.3 Advanced Geometry Wing

The previous section dealt with the wing equations for a straight wing. The rotor/wing coupling equations are evidently different for a wing with sweep, droop

Reproduced with permission of the copyright owner. Further reproduction prohibited without permission.

and pretwist along its semi-span. Sweep is denoted by Λ_1 (positive for sweep forward), anhedral is denoted by Λ_2 (positive for anhedral up, negative anhedral is referred to as droop) and pretwist with respect to the wing root is Λ_3 (positive for rotation nose-up). The order of transformation is the same as for the blade: first sweep, followed by anhedral and then by wing pretwist. The transformation between the inertial frame and the advanced geometry frame was derived for the blade in the previous chapter.

$$\begin{Bmatrix} \hat{i}_{ag} \\ \hat{j}_{ag} \\ \hat{k}_{ag} \end{Bmatrix} = [T_\Lambda^{ag}] \begin{Bmatrix} \hat{i}_i \\ \hat{j}_i \\ \hat{k}_i \end{Bmatrix} \tag{4.91}$$

where the subscript ag refers to the advanced geometry axis of the wing and

$$[T_\Lambda^{ag}] = \begin{bmatrix} C_1C_2 & S_1C_2 & S_2 \\ -S_1C_3 - C_1S_2S_3 & C_1C_3 - S_1S_2S_3 & C_2S_3 \\ S_1S_3 - C_1S_2C_3 & -C_1S_3 - S_1S_2C_3 & C_2C_3 \end{bmatrix} \tag{4.92}$$

where C_i and S_i represent $\cos\Lambda_i$ and $\sin\Lambda_i$ respectively for $i = 1$ to 3 for the wing.

The matrices associated with the hub displacements and rotations are then transformed through this matrix $[T_\Lambda^{ag}]$ and then assembled with the wing equations for the advanced geometry wing. Efficient implementation of this procedure is far more difficult than can be inferred from a description of the procedure.

4.3.4 Drive Train Dynamics

The engine drive train dynamics is very important to tiltrotor high speed stability [65]. The conclusion in this reference is that modeling a windmilling rotor system without modeling of detailed engine and transmission effects is similar to modeling the behavior of a typical powered tiltrotor system. Hence, a simple engine drive train dynamics model is included in this study. The drive shaft is considered to

Reproduced with permission of the copyright owner. Further reproduction prohibited without permission.

be rigid. The rotor can be either in the powered condition or in the windmilling condition. Modes of the drive system interconnect shaft are not considered in the analysis. For the windmilling assumption, the rotor rotational degree-of-freedom about its own shaft is independent of wing bending slope degree-of-freedom. In axial flight, the hub degree-of-freedom ϕ_h corresponds to a rotation about the shaft, and is thus used to model the windmilling rotor system. The assembly process described in the above section is modified so that ϕ_h is not constrained to the corresponding wing motion. This amounts to performing the wing-assembly with 5 hub degrees-of- freedom instead of 6, where the hub degree-of-freedom ϕ_h no longer corresponds to the wing degree-of-freedom w_1'. This results in one additional global degree-of-freedom in the wing displacement vector:

$$\hat{x}_w = \left\{ \begin{array}{c} \beta_{GC} \\ \beta_{GS} \\ \phi_h \\ \hat{q}_w \end{array} \right\} \tag{4.93}$$

There is also one additional row and column in each of the ww system matrices, one additional column in the rw matrices, and one additional row in the wr system matrices of Eqn. 4.90.

For the powered condition, the hub rotation ϕ_h corresponds to w_1' of the wing. The wing displacement vector hence looks like before.

$$\hat{x}_w = \left\{ \begin{array}{c} \beta_{GC} \\ \beta_{GS} \\ \hat{q}_w \end{array} \right\} \tag{4.94}$$

An advanced engine drive train model can, however, be included by modeling the inertia, damping and stiffness properties of the drive shaft. The drive shaft and pylon can be modeled with finite elements and their modal representation can be

Reproduced with permission of the copyright owner. Further reproduction prohibited without permission.

obtained. A similar representation of the aircraft fuselage can also be included in this formulation.

4.3.5 Analysis Procedure

The stability analysis procedure used in this formulation is similar to that available in UMARC [70]. The system equations are transformed into first-order form for eigenanalysis. A system state vector is defined as

$$\hat{Y} = \begin{Bmatrix} \overset{\star}{\hat{p}}_r \\ \overset{\star}{\hat{x}}_w \\ \hat{p}_r \\ \hat{x}_w \end{Bmatrix} \tag{4.95}$$

The system equations are then written in first order form as:

$$\begin{bmatrix} \bar{M}_{rr} & \bar{M}_{rw} & 0 & 0 \\ \bar{M}_{wr} & \bar{M}_{ww} & 0 & 0 \\ 0 & 0 & I & 0 \\ 0 & 0 & 0 & I \end{bmatrix} \overset{\star}{\hat{Y}} + \begin{bmatrix} \bar{C}_{rr} & \bar{C}_{rw} & \bar{K}_{rr} & \bar{K}_{rw} \\ \bar{C}_{wr} & \bar{C}_{ww} & \bar{K}_{wr} & \bar{K}_{ww} \\ I & 0 & 0 & 0 \\ 0 & I & 0 & 0 \end{bmatrix} \hat{Y} = 0 \tag{4.96}$$

Eqn. 4.96 can be rearranged notationally as

$$\overset{\star}{\hat{Y}} = [A(\psi, \hat{Y}_0)]\hat{Y} \tag{4.97}$$

The stability matrix $\hat{A}$ is a function of the trim solution vector $\hat{Y}_0$.

4.3.6 Fixed Coordinate Transformation

The blade equations, at this point, are still in the rotating frame. The wing equations, however, are formulated in the fixed frame. It is then advantageous to transform the blade equations into the fixed frame too. This is done using a Fixed Coordinate Transformation. This procedure involves transforming the blade rotating frame coordinates into fixed frame coordinates and then transforming the

Reproduced with permission of the copyright owner. Further reproduction prohibited without permission.

blade equations into fixed frame equations. The fixed-frame coordinates $\hat{\xi}$ are related to the blade rotating frame coordinates $\hat{p}$ by

$$\hat{p}_r = [A_b]\hat{\xi} \tag{4.98}$$

where A_b is a transformation matrix of size mN_b x mN_b (m is the number of modes used to represent the blade response and N_b is the number of blade) given by

$$[A_b] = \begin{bmatrix} a_b & 0 & \dots & 0 \\ 0 & a_b & \dots & 0 \\ 0 & 0 & \ddots & 0 \\ 0 & 0 & \dots & a_b \end{bmatrix} \tag{4.99}$$

and

$$a_b = \begin{cases} \{1, \cos\psi_b, \dots, \cos(n\psi_b), \sin\psi_b, \dots, \sin(n\psi_b), (-1)^b\} \\ \quad \text{if } N_b \text{ even} \\ \{1, \cos\psi_b, \dots, \cos(n\psi_b), \sin\psi_b, \dots, \sin(n\psi_b)\} \\ \quad \text{if } N_b \text{ odd} \end{cases} \tag{4.100}$$

$$n = \begin{cases} \frac{N_b-2}{2} & \text{if } N_b \text{ even} \\ \frac{N_b-1}{2} & \text{if } N_b \text{ odd} \end{cases} \tag{4.101}$$

$$\hat{\xi} = \begin{Bmatrix} \xi^{(1)} \\ \xi^{(2)} \\ \vdots \\ \xi^{(m)} \end{Bmatrix} \tag{4.102}$$

Each element in the above column vector represents a row vector of length equal to N_b.

$$\xi^{(k)^T} = \begin{Bmatrix} \xi_0 \\ \xi_{1c} \\ \xi_{2c} \\ \vdots \\ \xi_{ns} \\ \xi_{n/2} \end{Bmatrix} \tag{4.103}$$

The blade equations are then transformed into the fixed frame by the following procedure:

$$\frac{1}{N_b}\sum_{m=1}^{N_b}(equation)$$

Reproduced with permission of the copyright owner. Further reproduction prohibited without permission.

$$\frac{2}{N_b}\sum_{m=1}^{N_b}(equation)\cos(k\psi_m)$$
$$\frac{2}{N_b}\sum_{m=1}^{N_b}(equation)\sin(k\psi_m)$$
$$\frac{1}{N_b}\sum_{m=1}^{N_b}(equation)(-1)^m \tag{4.104}$$

The system equations can be expressed in the fixed-frame as

$$\begin{bmatrix} \bar{M}_{r_f r_f} & \bar{M}_{r_f w} \\ \bar{M}_{w r_f} & \bar{M}_{ww} \end{bmatrix} \begin{Bmatrix} \overset{\star\star}{\hat{\xi}} \\ \overset{\star\star}{\hat{x}}_w \end{Bmatrix} + \begin{bmatrix} \bar{C}_{r_f r_f} & \bar{C}_{r_f w} \\ \bar{C}_{w r_f} & \bar{C}_{ww} \end{bmatrix} \begin{Bmatrix} \overset{\star}{\hat{\xi}} \\ \overset{\star}{\hat{x}}_w \end{Bmatrix} + \begin{bmatrix} \bar{K}_{r_f r_f} & \bar{K}_{r_f w} \\ \bar{K}_{w r_f} & \bar{K}_{ww} \end{bmatrix} \begin{Bmatrix} \hat{\xi} \\ \hat{x}_w \end{Bmatrix} = 0 \tag{4.105}$$

The fixed-frame system of equations are then transformed into first-order form as described in the previous section.

$$\overset{\star}{\hat{Y}}_f = [A_f(\psi)]\hat{Y}_f \tag{4.106}$$

where $[A_f(\psi)]$ is the fixed-frame stability matrix and $\hat{Y}_f$ is the fixed-frame vector of state variables:

$$\hat{Y}_f = \begin{Bmatrix} \overset{\star}{\hat{\xi}} \\ \overset{\star}{\hat{x}}_w \\ \hat{\xi} \\ \hat{x}_w \end{Bmatrix} \tag{4.107}$$

The solution of this system provides the stability eigenvalues.

4.3.7 Floquet Theory

The linearized first-order equations for the system could contain periodic coefficients due to azimuthal dependence of the blade forces. The stability of such a linear periodic system can be determined using Floquet theory. The details of the application of Floquet Theory is discussed in detail in Refs. [70] and [95]. The system equations are written as

Reproduced with permission of the copyright owner. Further reproduction prohibited without permission.

$$\overset{\star}{\hat{Y}} = [A]\hat{Y} \tag{4.108}$$

The solution of this system can be expressed as a linear combination of the state variables at time ψ_0.

$$\hat{Y}(\psi) = [\Phi(\psi, \psi_0)]\hat{Y}(\psi_0) \tag{4.109}$$

where Φ is known as the state transition matrix and

$$[\Phi(\psi_0, \psi_0)] = [I] \tag{4.110}$$

Substitution of Eqn. 4.108 into Eqn. 4.109 gives

$$[\overset{\star}{\Phi}] = [A][\Phi] \tag{4.111}$$

For a rotor operating in steady flight,

$$[A(\psi + 2\pi)] = [A(\psi)] \tag{4.112}$$

and the transition matrix can be written as

$$[\Phi(\psi, \psi_0)] = [P(\psi)]e^{[B(\psi - \psi_0)]} \tag{4.113}$$

where $[P]$ is a periodic matrix of period 2π and $[P(\psi_0)] = [I]$. The exponential growth/decay of the solution then depends only on $[B]$. The Floquet transition matrix is defined by

$$[Q] = [\Phi(\psi_0 + 2\pi, \psi_0)] \tag{4.114}$$

which may be written as

$$[Q] = e^{2\pi[B]} \tag{4.115}$$

Reproduced with permission of the copyright owner. Further reproduction prohibited without permission.

If $[\Lambda]$ is the eigenvalue matrix of $[B]$, and $[S]$ its corresponding modal matrix, then $[B] = [S][\Lambda][S]^{-1}$ and

$$[Q] = e^{2\pi[B]} = [S]e^{2\pi[\Lambda]}[S]^{-1} \tag{4.116}$$

$[S]$ is also the modal matrix of $[Q]$, and the eigenvalue matrix associated with the Floquet transition matrix is

$$[\Theta] = e^{2\pi[\Lambda]} \tag{4.117}$$

Hence,

$$[\Lambda] = \frac{1}{2\pi}\ln[\Theta] \tag{4.118}$$

The system is unstable if the real part of any eigenvalue is positive, $Re(\Lambda_i) > 0$. The Floquet transition matrix Q is computed by integrating Eqn. 4.111 over one rotor revolution starting with the initial conditions given by Eqn. 4.110. The eigenvalues of $[B]$ determine the system stability, but these eigenvalues are shown to be the same as the eigenvalues of the Floquet transition matrix $[Q]$:

$$\theta_k = Re(\theta_k) + iIm(\theta_k) = e^{2\pi(\alpha_k + i\omega_k)} \tag{4.119}$$

The Floquet stability eigenvalues are thus given by the kth eigenvalue of $[Q]$ as

$$\alpha_k = \frac{1}{2\pi}\ln\sqrt{Re^2(\theta_k) + Im^2(\theta_k)} \tag{4.120}$$

$$\omega_k = \frac{1}{2\pi}\tan^{-1}\left[\frac{Im(\theta_k)}{Re(\theta_k)}\right] \pm n\Omega;\ n = 0, 1, 2, \ldots \tag{4.121}$$

where α_k and ω_k are the decay rate and frequency of the kth mode, respectively. The frequency is multivalued since it is obtained by using a tangent-inverse; it is the sum of a principal part and an integer multiple of the rotor rotational speed

Reproduced with permission of the copyright owner. Further reproduction prohibited without permission.

(as shown in Eqn.4.121). Determination of the actual frequency value through this approach is made by identifying the corresponding mode associated with the frequency.

4.3.8 Constant Coefficient Method

In an axisymmetric flight such as hover (helicopter mode) or in airplane forward flight mode, the matrix A_f is independent of the azimuth angle ψ. In such cases, the system equations involve constant coefficients. There are other instances such as in low speed helicopter forward flight or tiltrotor conversion mode when the system periodicity is weak. It is under such circumstances that the constant coefficient method of solution for stability eigenvalues can be used. The inherent attributes of the periodic system can be captured by averaging the system stability matrix over one complete rotor revolution. The resulting system is thus independent of any periodic terms. The constant coefficient approximation is made as

$$[A_{fc}] = \frac{1}{2\pi} \int_0^{2\pi} [A_f]\, d\psi \tag{4.122}$$

and the system can be written as

$$\overset{\star}{\hat{Y}} = [A_{fc}]\, \hat{Y} \tag{4.123}$$

This system can then be solved using standard eigenanalysis procedure.

This method is very efficient computationally over the Floquet analysis. Identification of the system modes obtained from Floquet analysis is difficult because the frequencies obtained could differ from the actual system frequencies by integer multiples of the rotor fundamental frequency; the constant coefficient method pro-

Reproduced with permission of the copyright owner. Further reproduction prohibited without permission.

vides the actual frequencies and the identification of system modes is hence made a lot easier.

The constant coefficient method can be used extensively for tiltrotors since periodicity is important in a relatively small portion of the flight envelope (in conversion mode).

Reproduced with permission of the copyright owner. Further reproduction prohibited without permission.

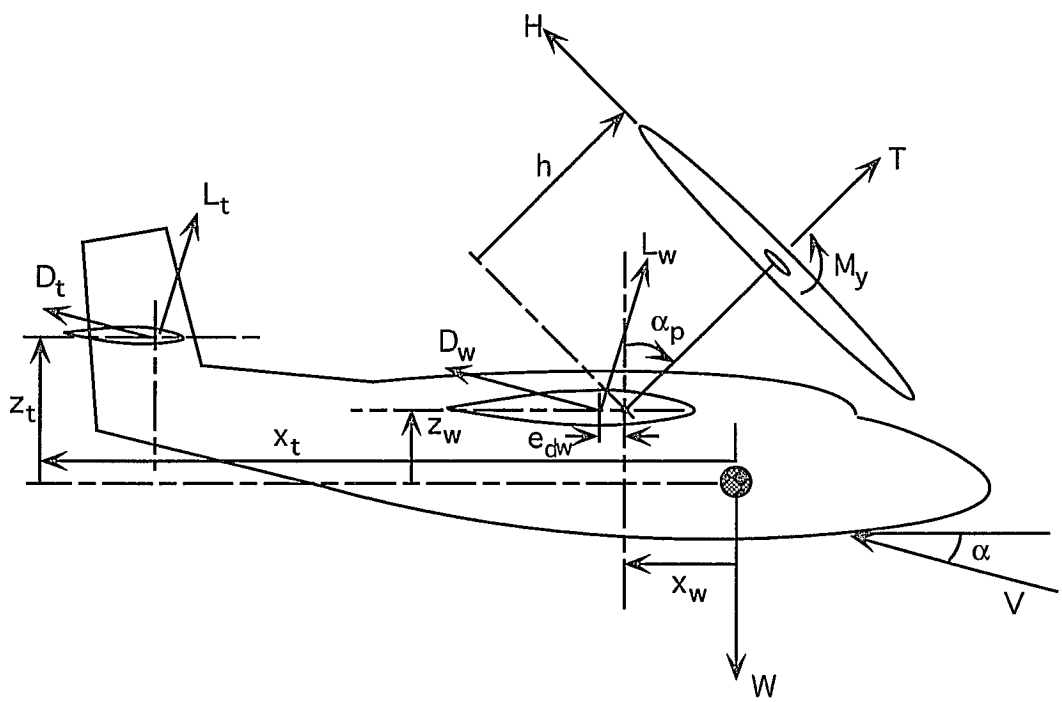

Figure 4.1: Forces acting on the tiltrotor in free flight

Reproduced with permission of the copyright owner. Further reproduction prohibited without permission.

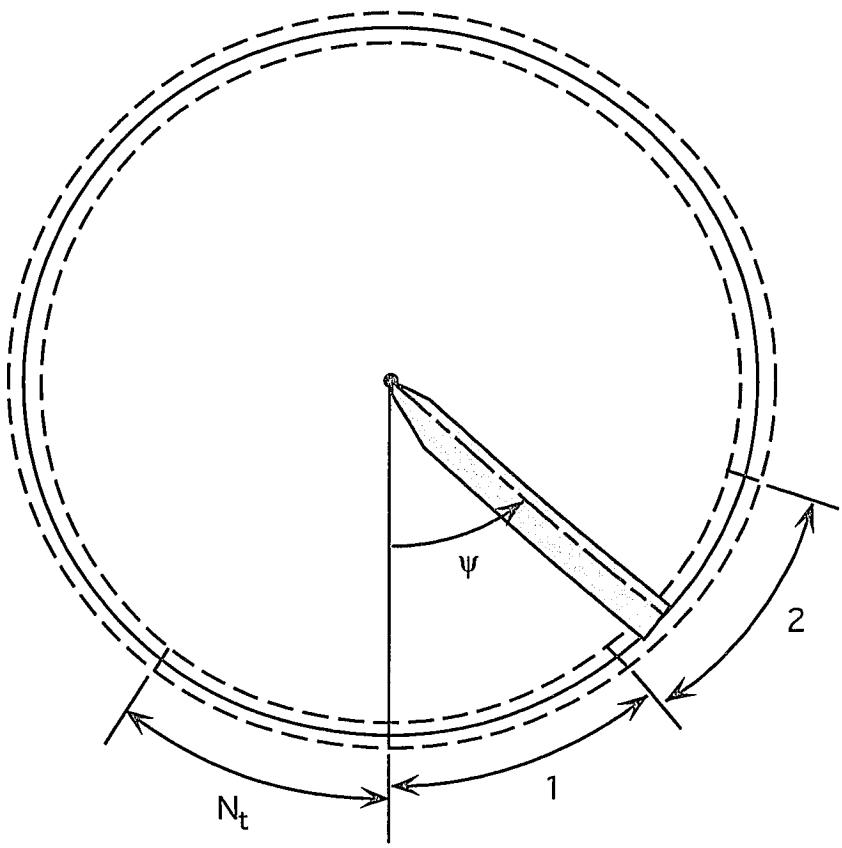

Figure 4.2: Azimuthal discretization into finite elements

Reproduced with permission of the copyright owner. Further reproduction prohibited without permission.

Chapter 5

Validation of Analysis

In this chapter, the analyses developed thus far in this study are validated with other analyses and available test data. Results computed with the rigid blade analysis presented in Chapter 2 are compared to the results from the elastic blade analysis developed in Chapters 3 and 4 to examine some of the strengths and limitations of the simple rigid blade analysis. Then, the elastic blade analysis is validated with other established comprehensive tiltrotor aeroelastic analyses, and with test data.

5.1 Rigid Blade Analysis

The first case studied was the baseline configuration used in Chapter 2, that of the XV-15 tiltrotor without any rotor precone. The tiltrotor is in the airplane mode of flight and the simple rigid blade analysis is used to predict the stability of the configuration. Figures 5.1 and 5.2 show the predicted frequency and damping plots of the stability eigenvalues, as a function of axial flight velocity. The quantities shown are non-dimensionalized; the frequency by the rotor cruise rotating frequency and the velocity by the rotor cruise tip speed. The damping

Reproduced with permission of the copyright owner. Further reproduction prohibited without permission.

plot shows the negative of the real part of the stability eigenvalue (and not the damping ratio). This is done to show all the modes on the same plot in a compact form. Any mode whose damping goes below zero (on the plot) becomes unstable. The reference rotational frequency is 8.62 Hz and the rotor cruise tip speed (ΩR) is 340 knots. The study was conducted upto a forward flight velocity of 680 knots ($V^*=V/\Omega R=2$), even though it is recognized that such velocities are unattainable with present-day configurations. The damping for the regressing flap ($\beta - 1$) and the regressing lag ($\zeta - 1$) modes are generally very high for most of the speed range studied. These modes transfer additional (positive or negative) damping to other modes whenever their frequencies coalesce with those of the wing modes. Figure 5.2 shows that the wing beam and chord modes become unstable around a forward flight velocity of 375 knots; the occurrence of whirl flutter at this speed makes the configuration unstable.

The results shown in Figures 5.1 and 5.2 are condensed and plotted in a root locus plot in Figure 5.3. This plot shows the imaginary part of the stability root (damped frequency) against the real part (damping). The eigenvalues are plotted for forward flight speeds from 0 to 500 knots, the arrow indicating the direction of increasing forward speed. A negative real part indicates positive damping in the mode and a positive real part indicates negative damping. Any mode becomes unstable when its real part becomes positive. The figures shows that all the wing modes become unstable with increasing forward flight speed (although at different speeds).

Reproduced with permission of the copyright owner. Further reproduction prohibited without permission.

5.1.1 Comparison with Elastic Blade Analysis

Figures 5.4 and 5.5 show the predicted frequency and damping plots for the XV-15 configuration (with a 2.5^o rotor precone), obtained from the rigid blade analysis. The frequency plot shows that the frequency cross-over points are at lower forward speeds than for the case with no rotor precone. This affects the wing modes adversely by transferring negative damping to these modes, thereby causing them to become unstable at a lower forward speed. In this case, the wing beam mode is predicted to become unstable around 275 knots. The decrease in the predicted flutter speed is about 95 knots due to the inclusion of 2.5^o rotor precone. The wing chord mode then becomes unstable followed by the wing torsion mode.

These predictions are compared to the results in Figures 5.6 and 5.7 which show the frequency and damping plots from the elastic blade analysis. Comparing Figures 5.4 and 5.6, the cross-over points for the frequencies of different modes are quite identical for the rigid blade and elastic blade analyses. The magnitudes of the damped frequencies from the rigid blade analysis, across the velocity range studied, are very close to those predicted by the elastic blade model. For the comparison of damping plots (Figures 5.5 and 5.7), both analyses predict the wing beam mode to become unstable around 275 knots ($V/\Omega R = 0.81$).

Another similarity is that the wing chord and torsion modes become unstable at speeds somewhat higher than that for the wing beam mode. The rigid blade analysis predicts the wing chord and torsion modes to become unstable at around 310 and 355 knots respectively and the elastic blade analysis predicts both these modes becoming unstable around 330 knots. This shows that the rigid blade anal-

Reproduced with permission of the copyright owner. Further reproduction prohibited without permission.

ysis captures the main features of tiltrotor instability mechanisms (although the flutter speeds are somewhat different) while retaining simplicity in the model. The damping values for the blade modes, however, are not predicted as well with the rigid blade model. The reason is that uncoupled blade flap and lag modes were assumed in the rigid blade model; and at high forward speeds, and subsequently at high collective settings, the blade flap and lag modes become more and more coupled. This is reflected in the poor comparison between the blade mode (aerodynamic) damping values predicted by the two analyses.

Root locus plots from the rigid blade and elastic blade analyses are shown in Figures 5.8 and 5.9 respectively. The velocity range for these results in from 0 to 500 knots. Again, these figures clearly show that the behavior of the wing modes is very similar for the two cases; the stability of the wing modes is dependent mainly on the accurate evaluation of steady rotor forcing. The similarity between the two plots show that the stability of the wing modes, and consequently the whirl flutter speed, can be predicted well by rigid blade analyses, particularly for simple straight rectangular blades. The behavior of the blade modes, however, shows some differences. Blade modes predicted with the rigid blade analysis behave differently from the coupled blade modes predicted with elastic blade analysis.

Figure 5.10 shows the comparison of predicted flutter velocity with variation in pitch-lag coupling, from both analyses. Blade kinematic pitch-lag coupling is quite similar to a rotor precone effect [38]. In fact, this plot can be interpreted as a variation of flutter speed with rotor precone. The present rigid rotor model, however, does not include rotor precone; this was done to keep the rigid rotor model

Reproduced with permission of the copyright owner. Further reproduction prohibited without permission.

very simple. The precone is hence converted to an equivalent pitch-lag coupling and its effect on flutter speed is studied. Rotor precone and pitch-lag coupling are both modeled in the present elastic blade analysis; hence blade precone angles (corresponding to pitch-lag couplings) were directly input into the elastic blade analysis. The figure shows very good agreement between flutter speeds predicted using an equivalency approach between the two tiltrotor models. The plot also shows that the effects of rotor precone and pitch-lag coupling on whirl flutter stability are identical.

The effect of rotor precone with forward flight speed on the damping of the wing beam mode, predicted with the rigid blade analysis, is shown in Figure 5.11. With no rotor precone, the predicted flutter speed is as high as 370 knots, compared to the 275 knots flutter speed for the 2.5^o precone case. Similar predictions were reported in Ref. [38].

5.1.2 Comparison with Test Data

Figure 5.12 shows the predicted flutter velocity variation with pitch-flap coupling for a 1/5th scale V-22 aeroelastic model that was tested in the NASA Langley TDT wind tunnel [50]. Predictions from the present rigid rotor and elastic rotor analyses as well as those from CAMRAD and DYN4 are shown in the plot. The rigid blade analysis correlates very well with test data as well as with other analyses. Although only two data points were taken during the test, the data show the expected trend in variation of flutter speed with pitch-flap coupling. Small differences among analyses predictions may be attributed to differences in modeling

Reproduced with permission of the copyright owner. Further reproduction prohibited without permission.

of rotor compressibility effects and in the inclusion of wing aerodynamic damping [50].

Predicted wing beam mode damping ratio variation with wind tunnel speed along with test data and predictions from other analyses are shown in Figure 5.13. CAMRAD, DYN4, the present elastic blade analysis and the present rigid blade analysis are quite close. All the analyses, however, tend to underpredict the damping peak that occurs at lower speeds.

5.2 Elastic Blade Analysis

The elastic blade analysis, in contrast to the rigid blade analysis, involves a free flight trim scheme, detailed blade load calculations and an involved stability analysis procedure. This analysis is validated with analytical predictions and flight test data for the XV-15 configuration in the airplane mode from Ref. [73]. A radially varying inflow model based on momentum theory is used in the current analysis for all the predictions given in this section.

5.2.1 Trim Controls and Rotor Response

XV-15 flight test data for trim controls, rotor response and loads in the airplane mode were taken from Flight 167 for aircraft S/N 702 at a density altitude of 7,769 feet and true airspeed ranging from 154 to 314 knots [73]. Error bands for the measured flight test data were not given in Ref. [73]. Relevant input data for this flight test are shown in Table 5.1. The current predictions are from the elastic blade analysis developed in Chapters 3 and 4. Bell Helicopter Company's comprehensive rotorcraft analysis code C81 [96], [97] was used to predict the trim

Reproduced with permission of the copyright owner. Further reproduction prohibited without permission.

controls and rotor response for this test condition. This code analytically models many of the configuration issues such as detailed fuselage, wing and interactional aerodynamics that are not modeled in the present elastic blade analysis.

Aircraft pitch attitude variation with airspeed is shown in Figure 5.14. Wing flaps were used in trimmed flight below speeds of 190 knots; the C81 analysis included the effect of wing flaps in predicting the trimmed condition. The current elastic blade analysis, however, does not include modeling of wing flaps. Good correlation is obtained between the current analysis and flight test data, considering that the current model does not incorporate wing flaps and detailed interactional aerodynamics effects. The current elastic rotor analysis predictions agree well with those from the C81 analysis.

Rotor collective pitch variation with airspeed is shown in Figure 5.15. Good correlation is obtained from the current analysis with C81 predictions as well as test data. It may be possible to improve the correlation if more detailed fuselage and interactional aerodynamics modeling are included in the current analysis. The longitudinal and lateral cyclic controls variation with airspeed are shown in Figures 5.16 and 5.17 respectively. The C81 analysis held the longitudinal and lateral cyclic controls fixed throughout the speed range at 1.5^o and -2.0^o respectively and therefore, the C81 results are not shown in these plots. The predictions from the current analysis compare well with test data.

Rotor flap response is plotted in Figures 5.18, 5.19 and 5.20. Rotor coning (collective flap) is shown in Figure 5.18; neither test data nor C81 predictions were available for this case. The coning angle increases with forward flight speed; this

Reproduced with permission of the copyright owner. Further reproduction prohibited without permission.

can be attributed to the increased thrust produced from a rotor to overcome drag at higher forward speeds. The longitudinal and lateral flapping angles are shown in Figures 5.19 and 5.20. These flapping angles are hub rotations of the gimbal system and not the tip flapping angles. The current analysis accurately predicts the longitudinal gimbal flapping. The predictions from these two analyses for the lateral flapping angle capture the trends accurately, but are not very accurate in predicting the magnitudes. Overall, the current analysis predicts the rotor flapping response satisfactorily.

5.2.2 Rotor Loads

Flight test data on rotor loads for tiltrotor configurations are limited. The Bell-Boeing XV-15 report [73] contains some data on loads in the airplane mode of operation as well as predictions from the comprehensive rotorcraft code C81. Figure 5.21 shows the variation of main rotor torque with airspeed for the XV-15 configuration. The current elastic rotor analysis compares well with the test data and with the C81 code predictions; a radially varying inflow model based on momentum theory was used in the predictions from the current analysis. The figure also shows predictions from the present analysis assuming a tip loss factor of 3%. This means that the outboard 3% span of the rotor blade is not producing any lift force due to pressure equalization and, consequently, loss of lift at the blade tip. Predicted rotor torque, including the tip loss factor, is higher by about 6% compared to the predictions with no tip loss factor.

Figures 5.22 to 5.24 show the variation of blade oscillatory peak-to-peak mo-

Reproduced with permission of the copyright owner. Further reproduction prohibited without permission.

ments with airspeed at the 35% radial location of the blade. Blade beamwise and chordwise bending moments are plotted in Figures 5.22 and 5.23 respectively. Test data and C81 code predictions are also plotted. The current analysis predicts the magnitude of the beamwise moment satisfactorily, although the variation with airspeed is not captured well. On the other hand, the chordwise bending moment is predicted more accurately by the current analysis than by the C81 analysis. Overall, the current analysis predicts the blade loads satisfactorily given the lack of modeling of interactional effects between the rotor and wing/fuselage in this analysis. The variation of blade torsion moment is shown in Figure 5.24. No flight data were available for this case. The torsion moment is one order of magnitude lower than the blade beamwise and chordwise moments at the same location.

5.2.3 Stability Results

Ref. [73] contains flight test data and predictions from comprehensive analyses on stability of the wing modes in high speed axial flight. The aeroelastic stability test data were taken at an altitude of 10,000 feet and at a rotor speed of 517 rpm. The rotor hub had a precone angle of 2.5^o and data were taken in a windmilling condition. Table 5.2 contains relevant aircraft configuration characteristics for this flight test.

Three comprehensive rotorcraft analyses - DYN4, DYN5 and PASTA - were used in predicting the stability characteristics reported in Ref. [73]. DYN4 is a linear aeroelastic eigenvalue analysis for wing-pylon-rotor stability of tiltrotor aircraft in airplane mode. In DYN4, airframe dynamics is represented by a series

Reproduced with permission of the copyright owner. Further reproduction prohibited without permission.

of lumped masses, springs and hinges. Appropriate fuselage rigid body degrees of freedom are included. Only windmilling flight can be modeled by this analysis. DYN5 is a nonlinear, aeroelastic analysis in which more flexibility is available to model the rotor blades including precone, pitch-flap coupling and hub restraint. The wing-pylon-fuselage dynamics is represented by upto nine normal modes obtained from a NASTRAN analysis. These modes are fully coupled with the rotor modes through a component modes approach. The output from DYN5 consists of a time-domain response of the system to any input disturbance; system stability is then determined from this time-history response. This analysis can model both windmilling and powered configurations. PASTA is an aeroelastic eigenvalue analysis similar to DYN4; only windmilling flight is considered in the modeling.

Figures 5.25 to 5.30 show the damped frequencies and damping ratios of the wing symmetric beam, chord and torsion modes. Predictions from DYN4, DYN5, PASTA and the current analysis are correlated with XV-15 flight test data. Test data exist only for a small range of forward speeds from about 200 to 225 knots. The damped frequency variation with airspeed for the symmetric wing beam mode is shown in Figure 5.25. The plot shows that all analyses predict the frequencies well. Figure 5.26 shows the variation of damping ratio (as a percentage of the critical damping ratio) with airspeed for the same mode. The DYN4 analysis overpredicts the damping of the mode considerably. Predictions of the other analyses correlate well with the limited test data.

The damped frequency and damping ratio variations with airspeed for the wing symmetric chord mode are given in Figures 5.27 and 5.28. Frequency predictions

Reproduced with permission of the copyright owner. Further reproduction prohibited without permission.

from all the analyses correlate well with test data. The damping, however, is underpredicted by DYN4, DYN5 and PASTA. The current analysis predicts the magnitude of the damping ratio better than the other analyses, although none of the analyses captures the trend in the test data. Wing symmetric torsion mode frequency and damping variation with airspeed is shown in Figures 5.29 and 5.30 respectively. The frequencies are predicted satisfactorily by all the analyses. All of the analyses, however, underpredict the damping variation. The current analysis does atleast as well as the other analyses in this respect.

Figure 5.31 shows the predicted damping values for the XV-15 wing beam mode with forward speed. The plot also shows full-scale wind tunnel test data from Ref. [63]. Test data, in this case, are available for a wider speed range than those from Ref. [73]; the data were taken in the NASA Ames 40 x 80 foot wind tunnel and are hence distinctly different from the flight test data for the wing beam mode damping taken at 10,000 ft altitude. Predicted damping results from Ref. [63] are also shown. The early CAMRAD analysis in Ref. [63] is a rigid blade analysis based on coupled flap and lag blade modes and blade torsion modes. The current analysis compares favorably with test data and with the other analysis.

Reproduced with permission of the copyright owner. Further reproduction prohibited without permission.

Density altitude	7,769 feet
Nacelle angle	0°
Rotor hub precone	1.5^o
Rotor speed	517 rpm
Downstop stiffness	50,000 lb/in
Gross weight	13,934 lbs
C.G. station line	299.4 in.
Wing flap setting	0°
Longitudinal swashplate rigging	1.5^o
Lateral swashplate rigging	-2.0^o
Condition	Powered

Table 5.1: XV-15 Aircraft Configuration - Loads Data

Reproduced with permission of the copyright owner. Further reproduction prohibited without permission.

Density altitude	10,000 feet
Nacelle angle	0°
Rotor hub precone	2.5^o
Rotor speed	517 rpm
Downstop stiffness	50,000 lb/in
Gross weight	13,934 lbs
C.G. station line	299.4 in.
Wing flap setting	0°
Condition	Windmilling

Table 5.2: XV-15 Aircraft Configuration - Stability Data

Reproduced with permission of the copyright owner. Further reproduction prohibited without permission.

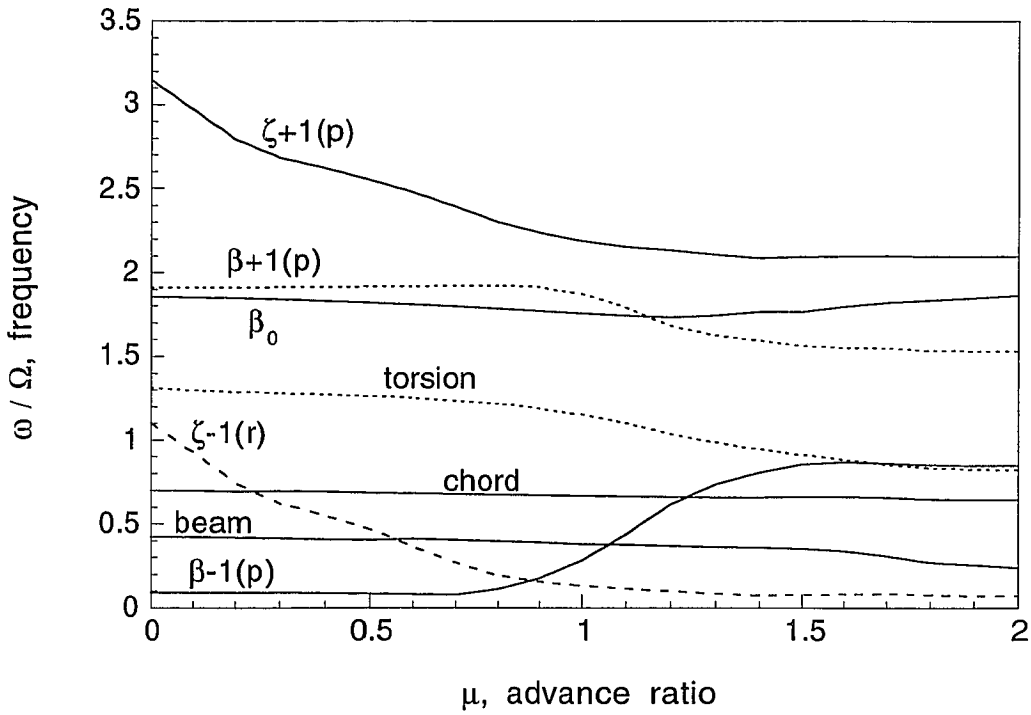

Figure 5.1: Rigid rotor model: Frequency variation with airspeed for zero precone case

Reproduced with permission of the copyright owner. Further reproduction prohibited without permission.

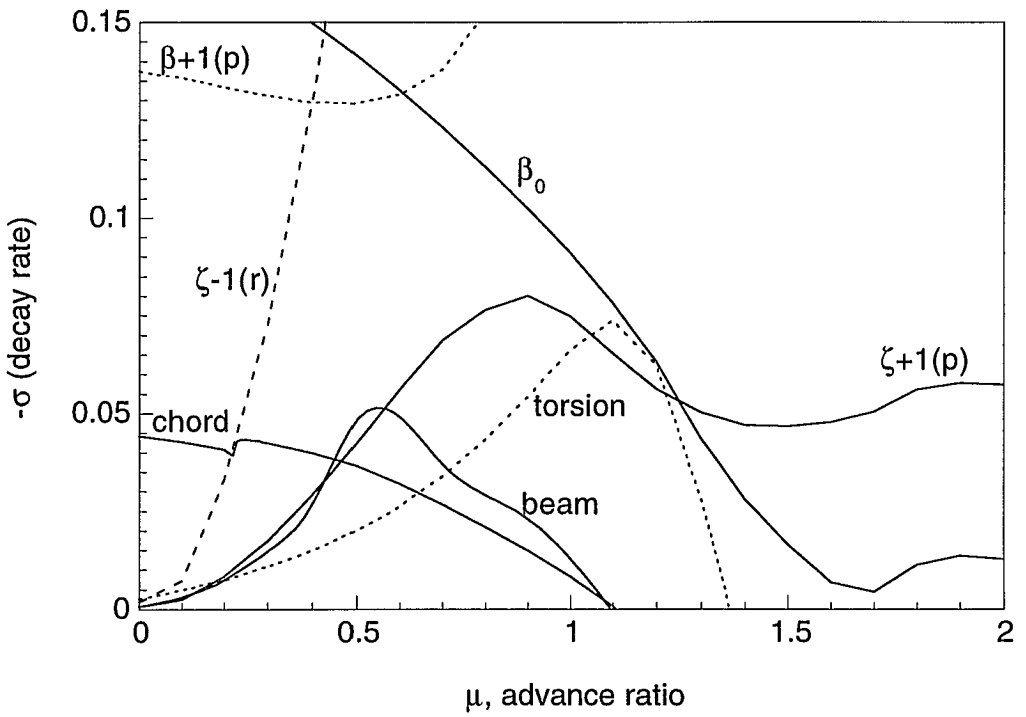

Figure 5.2: Rigid rotor model: Damping variation with airspeed for zero precone case

Reproduced with permission of the copyright owner. Further reproduction prohibited without permission.

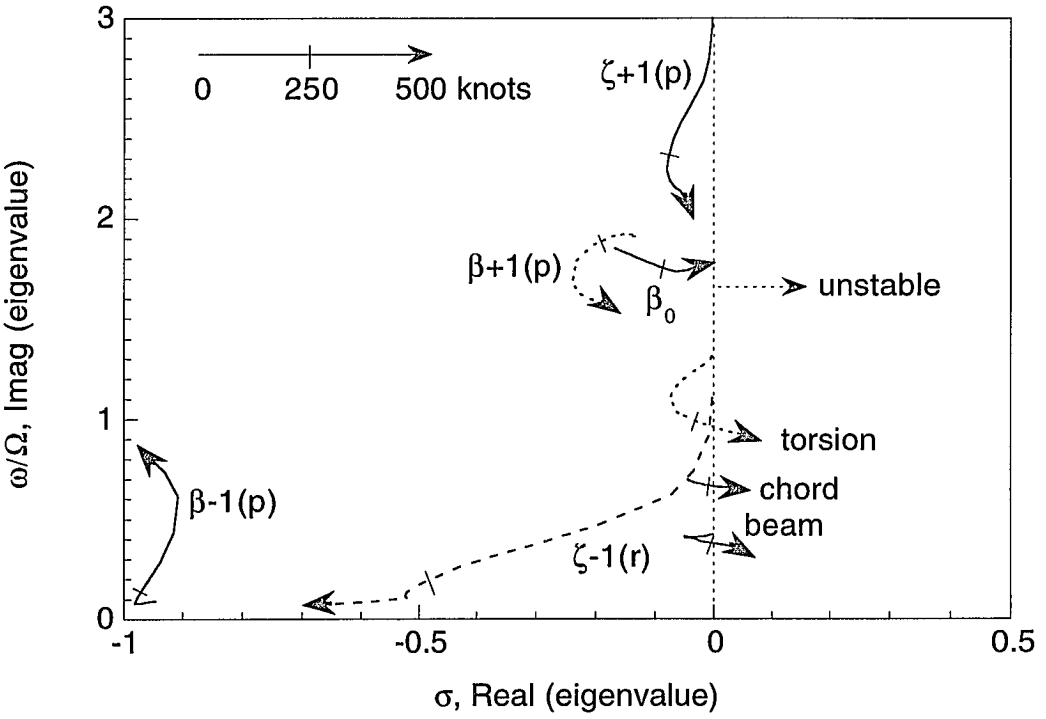

Figure 5.3: Rigid rotor model: Root locus plot of eigenvalues with airspeed for zero precone case

Reproduced with permission of the copyright owner. Further reproduction prohibited without permission.

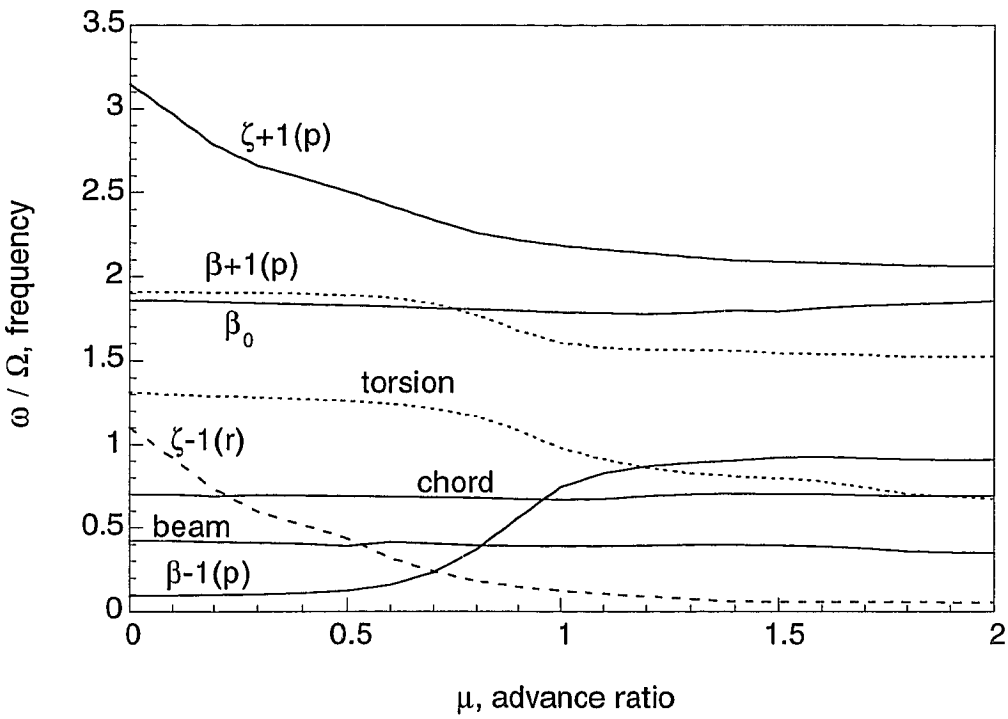

Figure 5.4: Rigid rotor model: Frequency variation with airspeed for 2.5^o precone case

Reproduced with permission of the copyright owner. Further reproduction prohibited without permission.

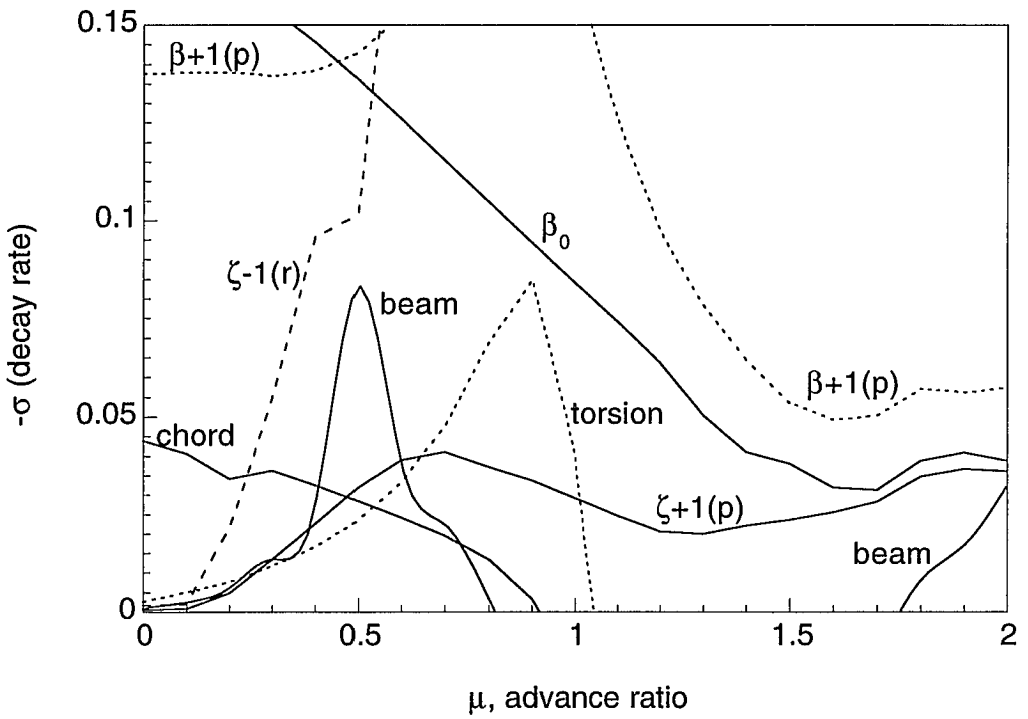

Figure 5.5: Rigid rotor model: Damping variation with airspeed for 2.5^o precone case

Reproduced with permission of the copyright owner. Further reproduction prohibited without permission.

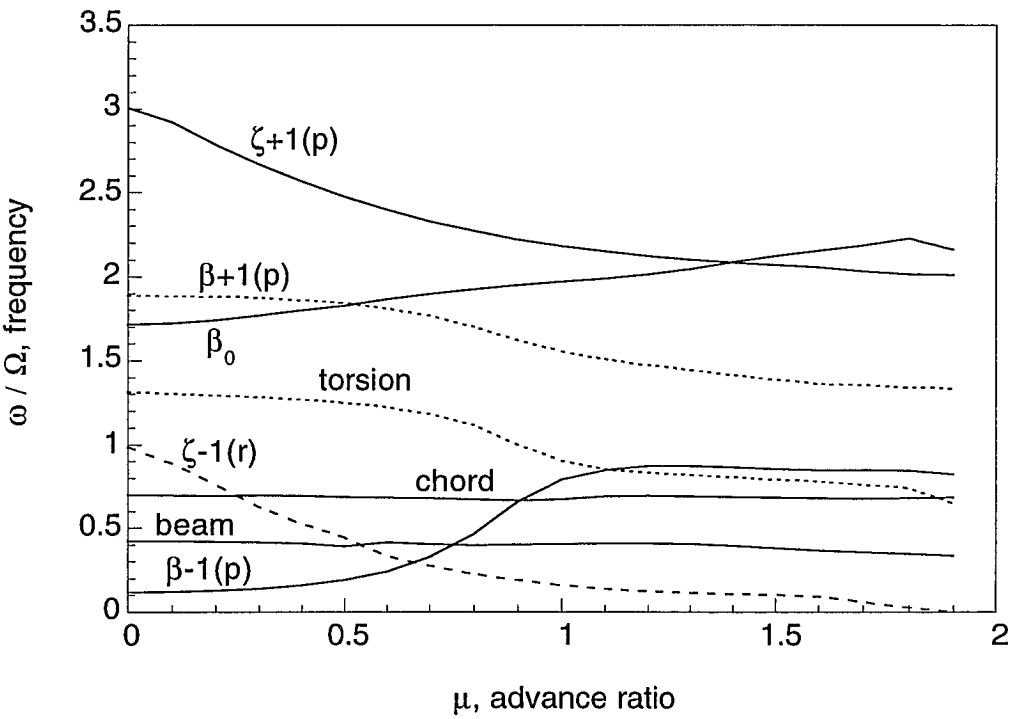

Figure 5.6: Elastic rotor model: Frequency variation with airspeed for 2.5^o precone case

Reproduced with permission of the copyright owner. Further reproduction prohibited without permission.

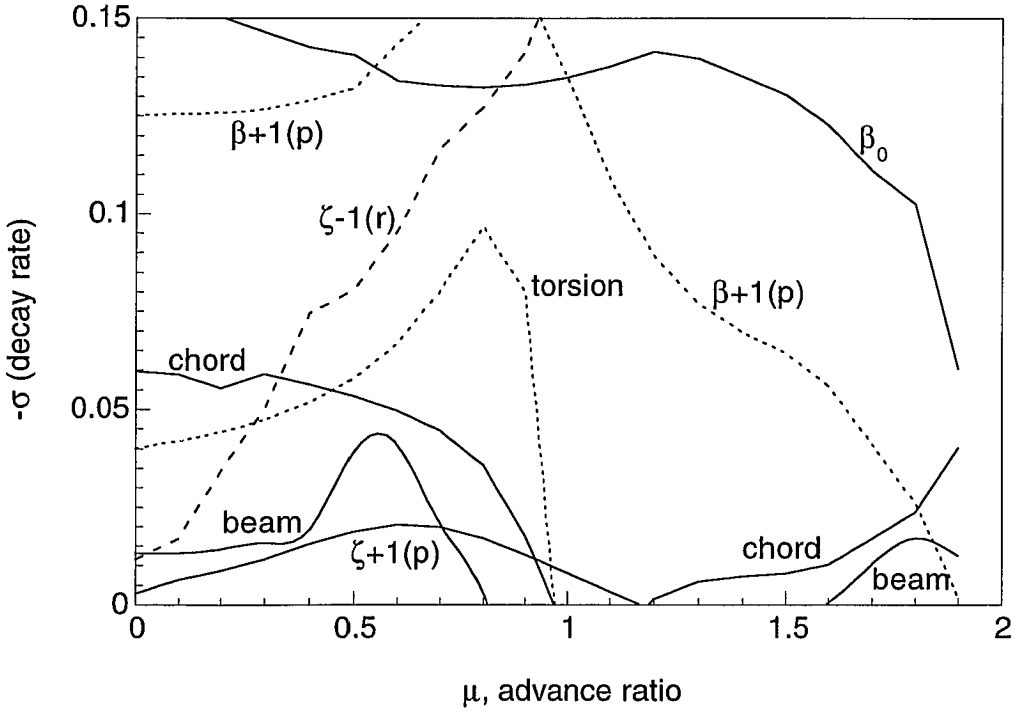

Figure 5.7: Elastic rotor model: Damping variation with airspeed for 2.5^o precone case

Reproduced with permission of the copyright owner. Further reproduction prohibited without permission.

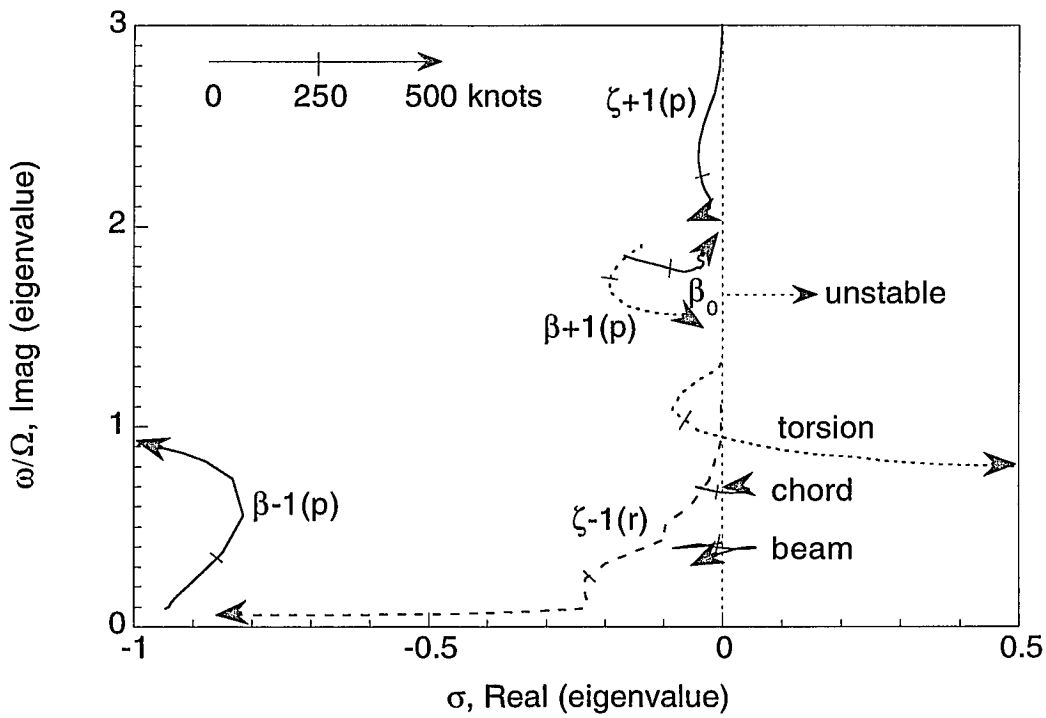

Figure 5.8: Rigid rotor model: Root locus plot of eigenvalues with airspeed for 2.5^o precone case

Reproduced with permission of the copyright owner. Further reproduction prohibited without permission.

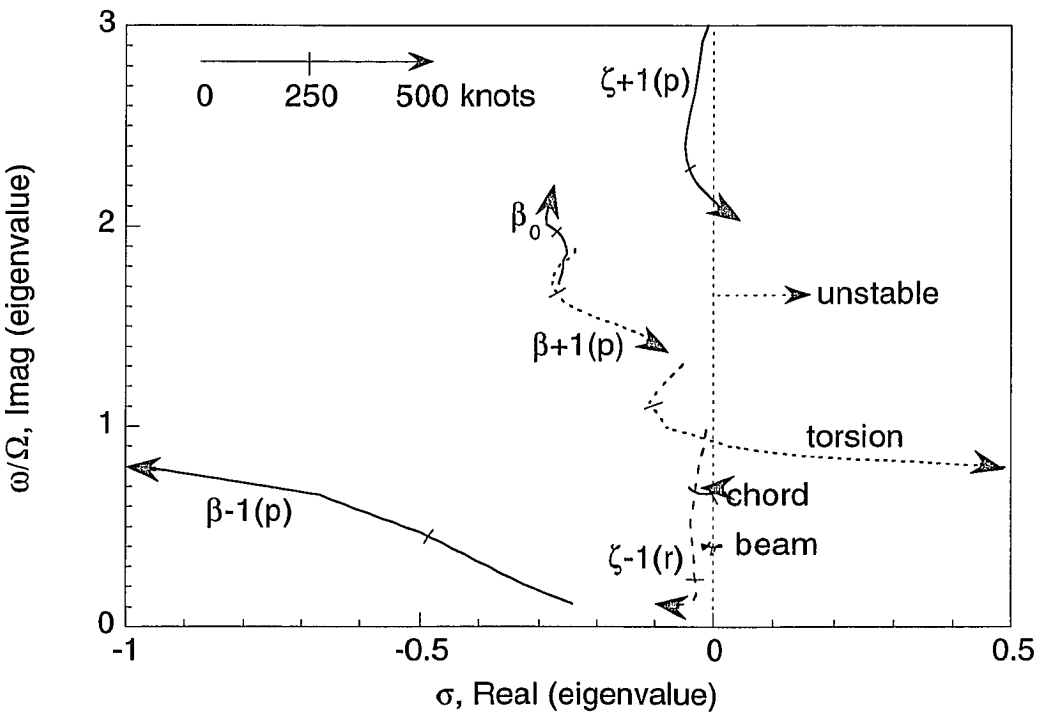

Figure 5.9: Elastic rotor model: Root locus plot of eigenvalues with airspeed for 2.5^o precone case

Reproduced with permission of the copyright owner. Further reproduction prohibited without permission.

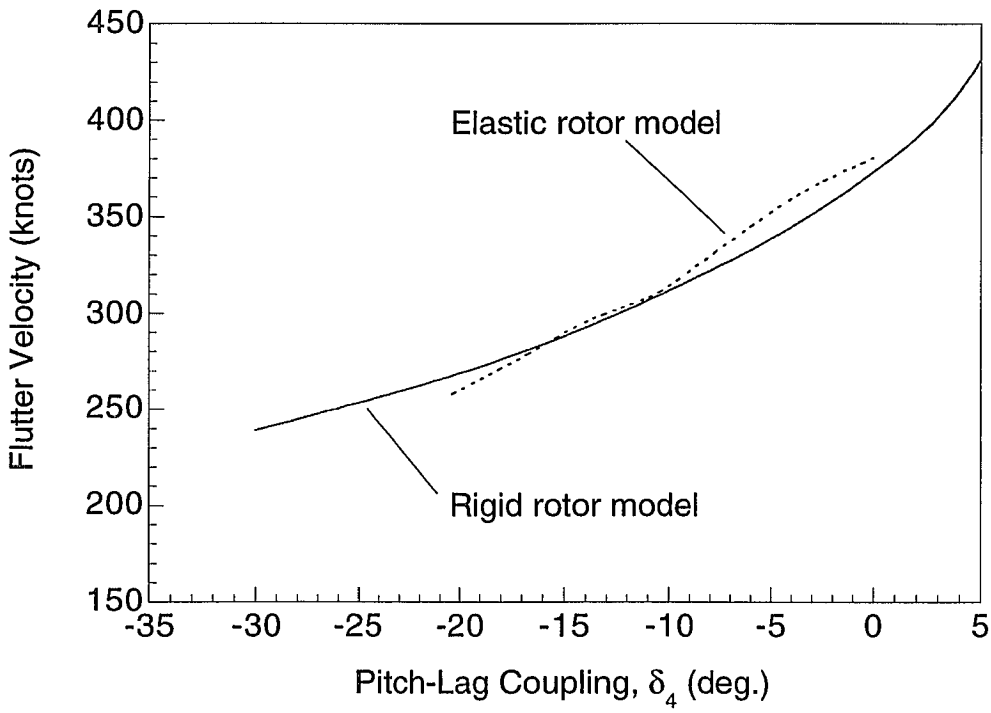

Figure 5.10: Effect of pitch-lag coupling on (wing beam mode) flutter speed

Reproduced with permission of the copyright owner. Further reproduction prohibited without permission.

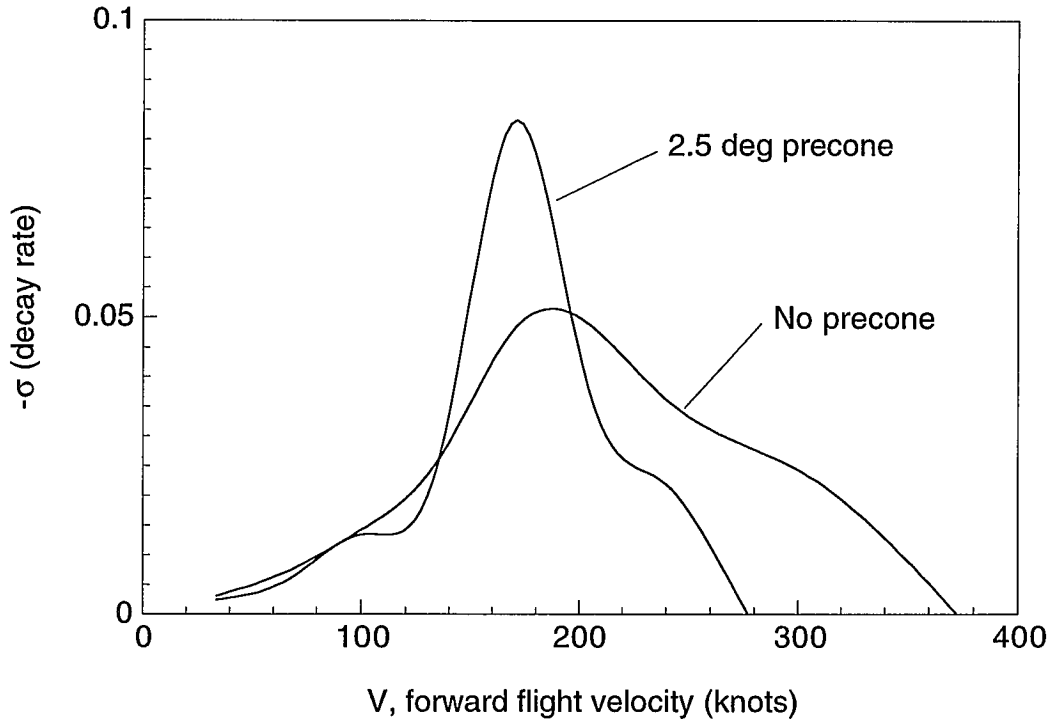

Figure 5.11: Rigid rotor model: Predicted wing beam mode damping - effect of rotor precone

Reproduced with permission of the copyright owner. Further reproduction prohibited without permission.

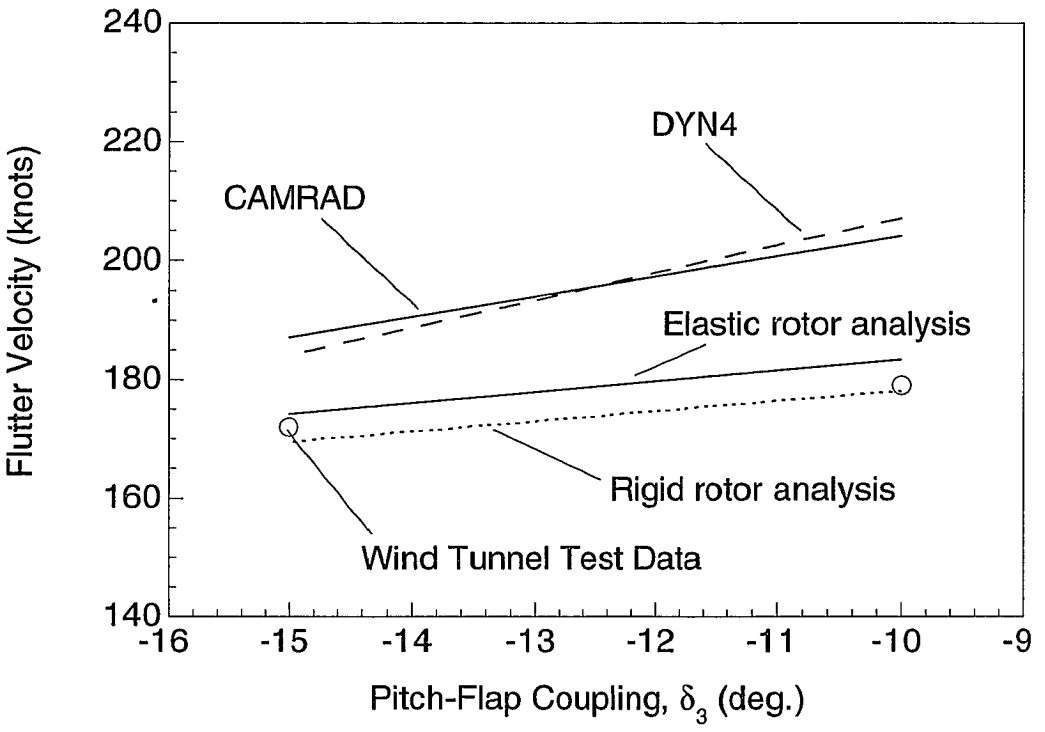

Figure 5.12: Comparison of predicted flutter velocity variation with pitch-flap coupling (V-22 1/5th scale model)

Reproduced with permission of the copyright owner. Further reproduction prohibited without permission.

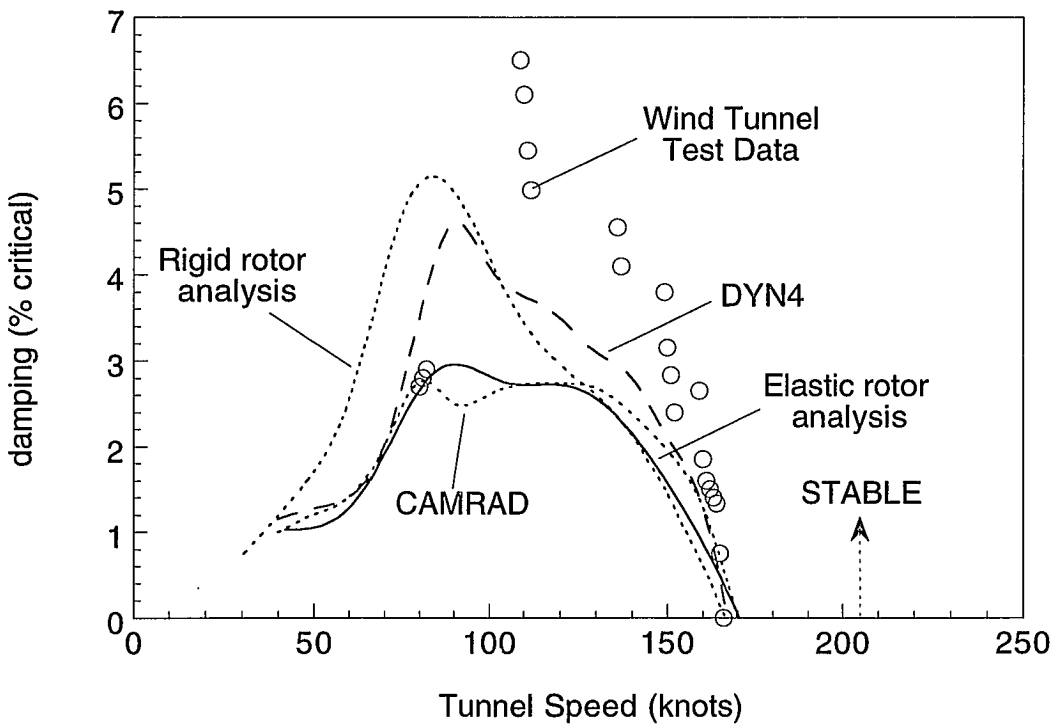

Figure 5.13: Comparison of predicted wing beam mode damping variation with airspeed (V-22 1/5th scale model)

Reproduced with permission of the copyright owner. Further reproduction prohibited without permission.

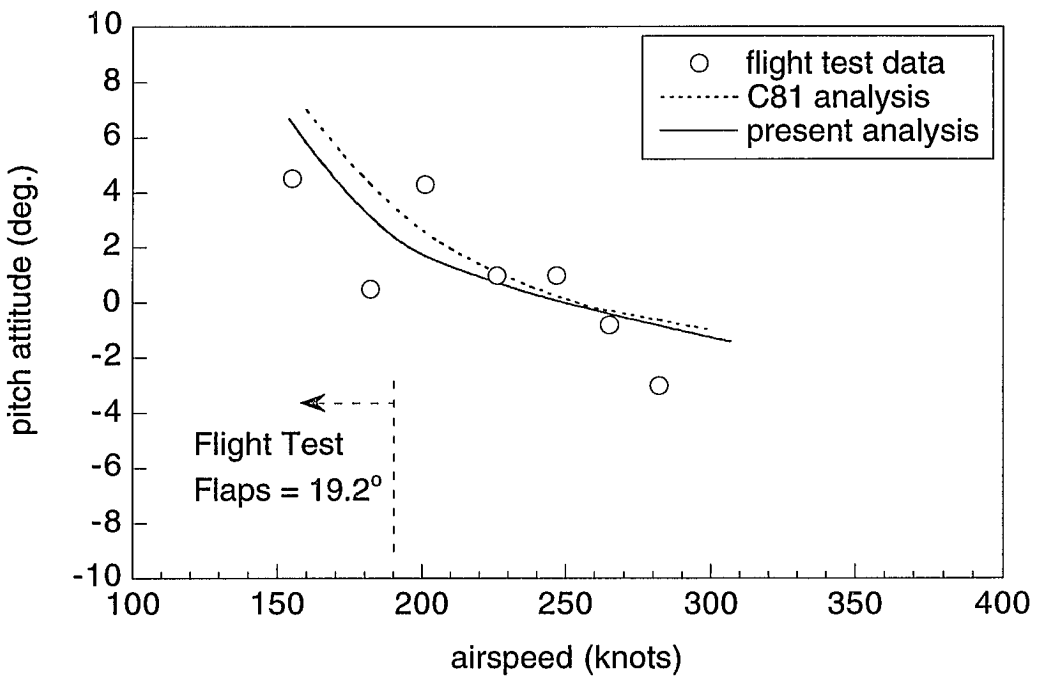

Figure 5.14: XV-15 aircraft pitch attitude variation with airspeed

Reproduced with permission of the copyright owner. Further reproduction prohibited without permission.

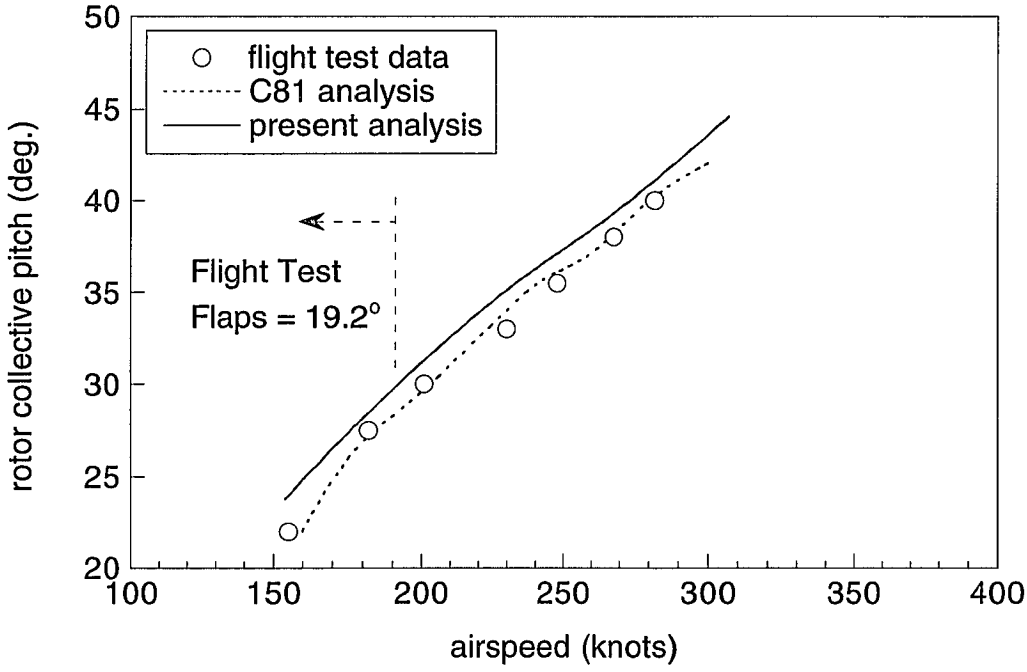

Figure 5.15: XV-15 rotor collective variation with airspeed

Reproduced with permission of the copyright owner. Further reproduction prohibited without permission.

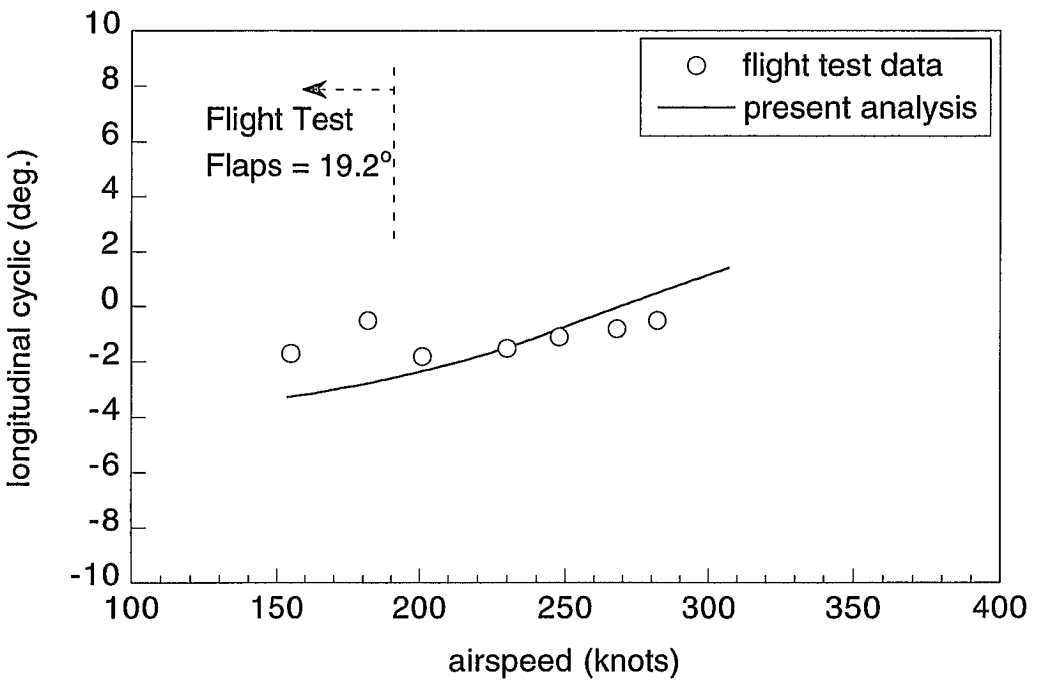

Figure 5.16: XV-15 rotor longitudinal cyclic control variation with airspeed

Reproduced with permission of the copyright owner. Further reproduction prohibited without permission.

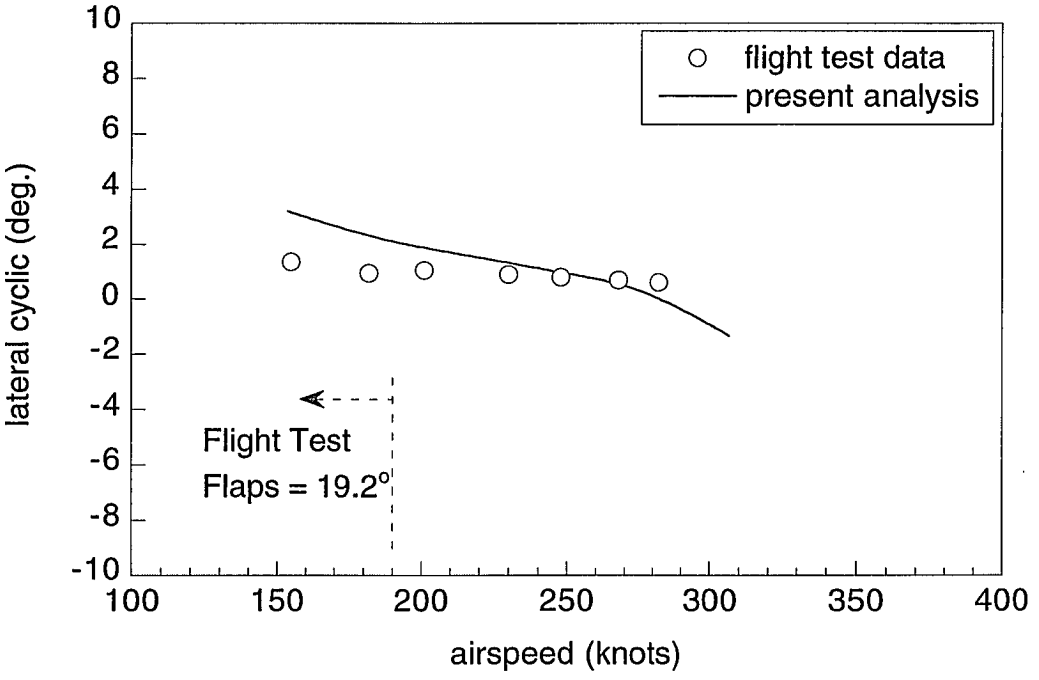

Figure 5.17: XV-15 rotor lateral cyclic control variation with airspeed

Reproduced with permission of the copyright owner. Further reproduction prohibited without permission.

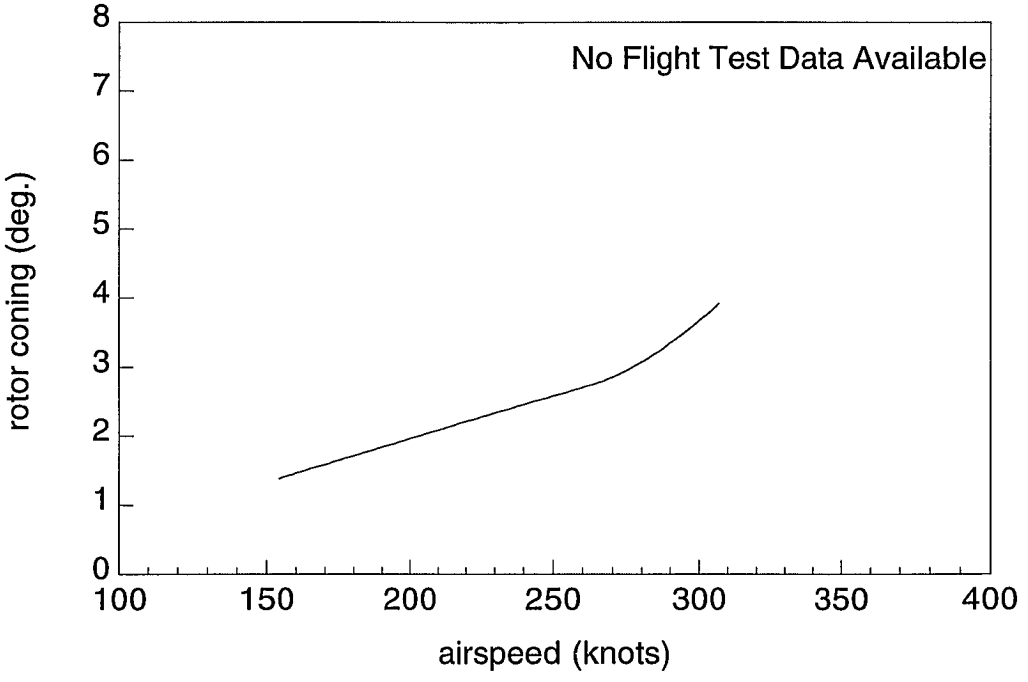

Figure 5.18: XV-15 rotor coning variation with airspeed

Reproduced with permission of the copyright owner. Further reproduction prohibited without permission.

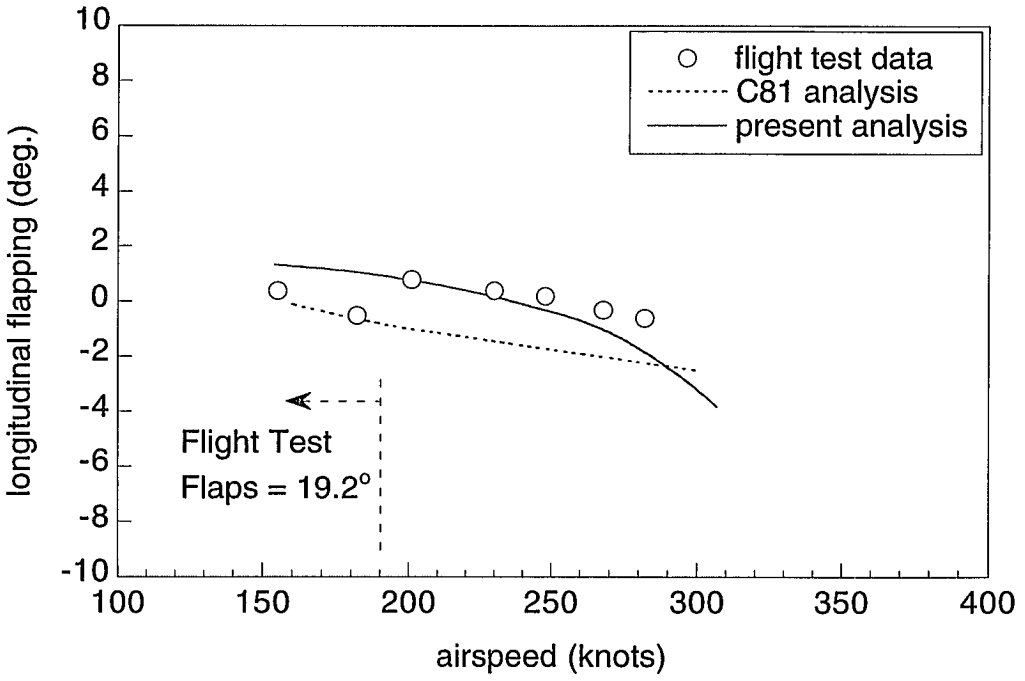

Figure 5.19: XV-15 rotor longitudinal flapping variation with airspeed

Reproduced with permission of the copyright owner. Further reproduction prohibited without permission.

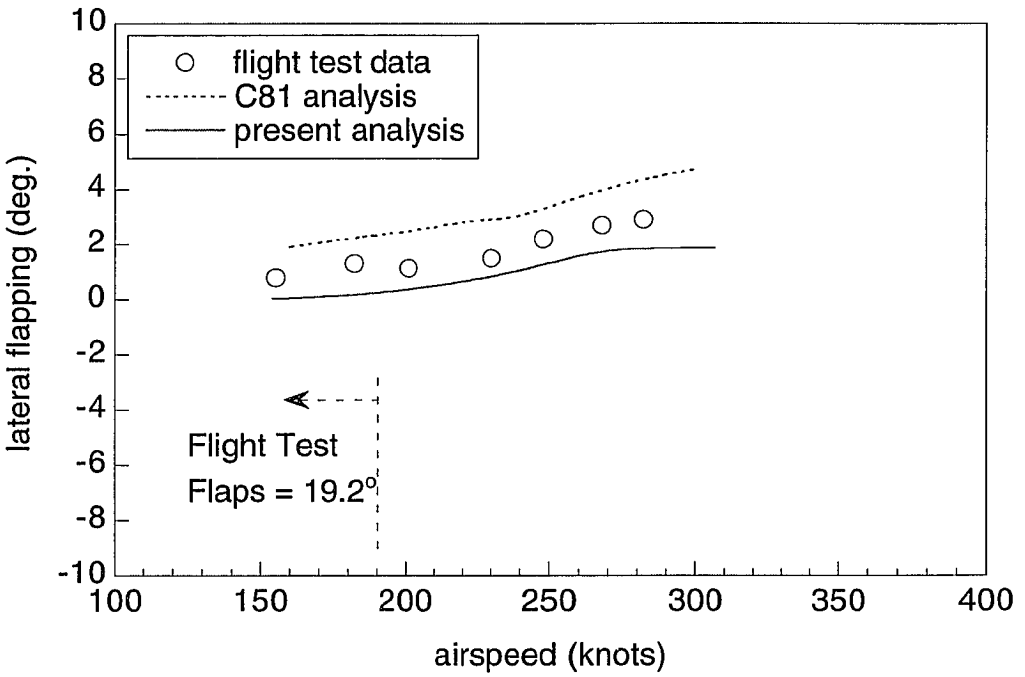

Figure 5.20: XV-15 rotor lateral flapping variation with airspeed

Reproduced with permission of the copyright owner. Further reproduction prohibited without permission.

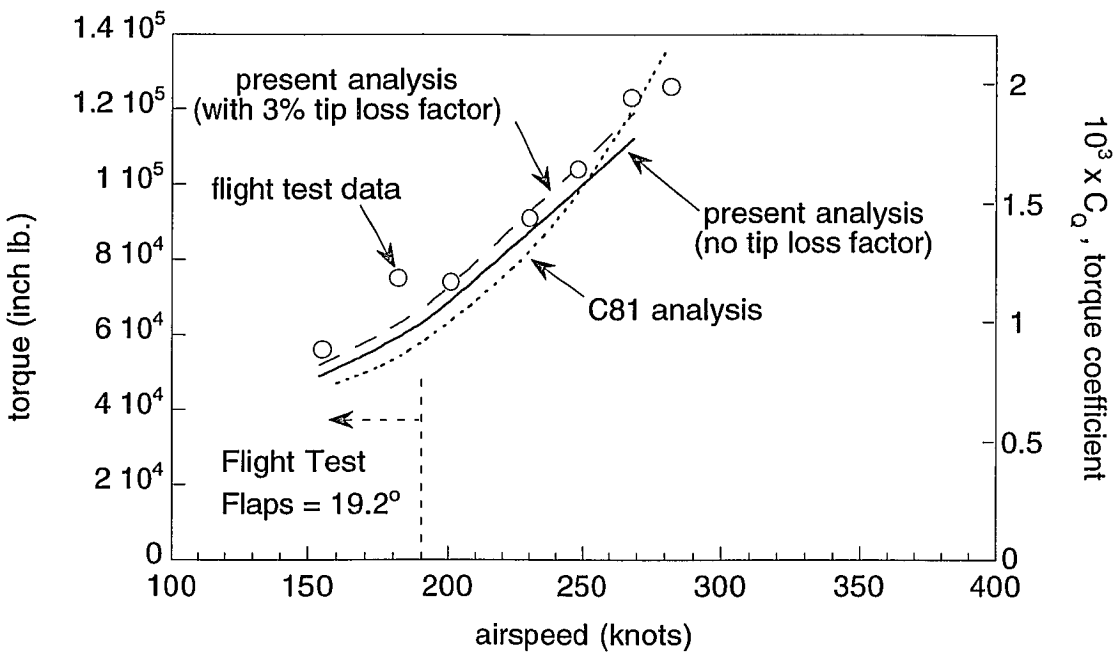

Figure 5.21: XV-15 rotor torque variation with airspeed

Reproduced with permission of the copyright owner. Further reproduction prohibited without permission.

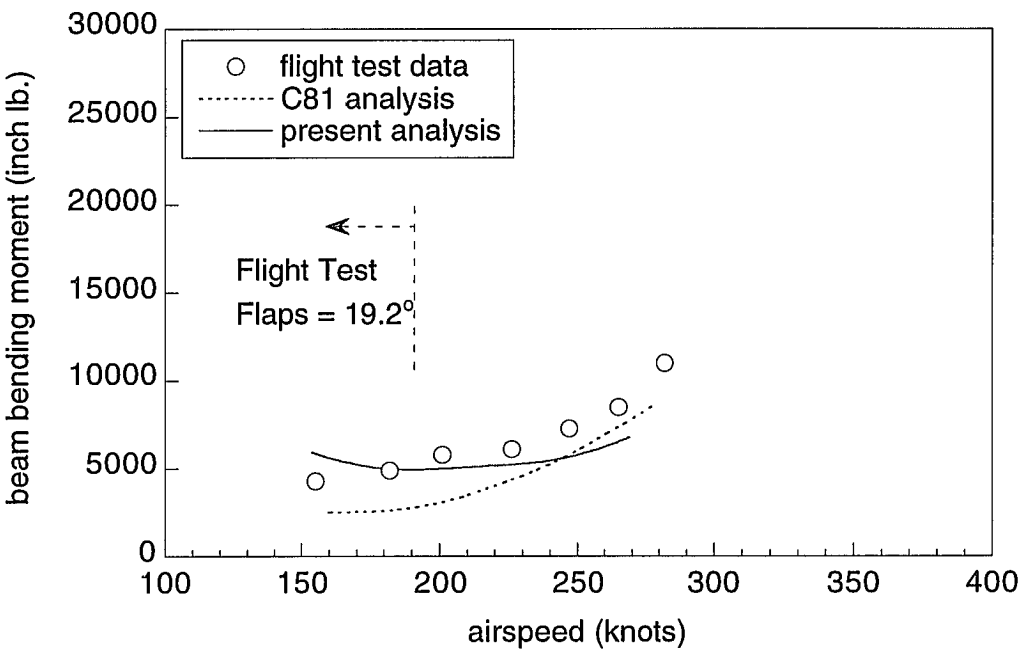

Figure 5.22: XV-15 oscillatory blade beam bending moment variation with airspeed, 35% radial location

Reproduced with permission of the copyright owner. Further reproduction prohibited without permission.

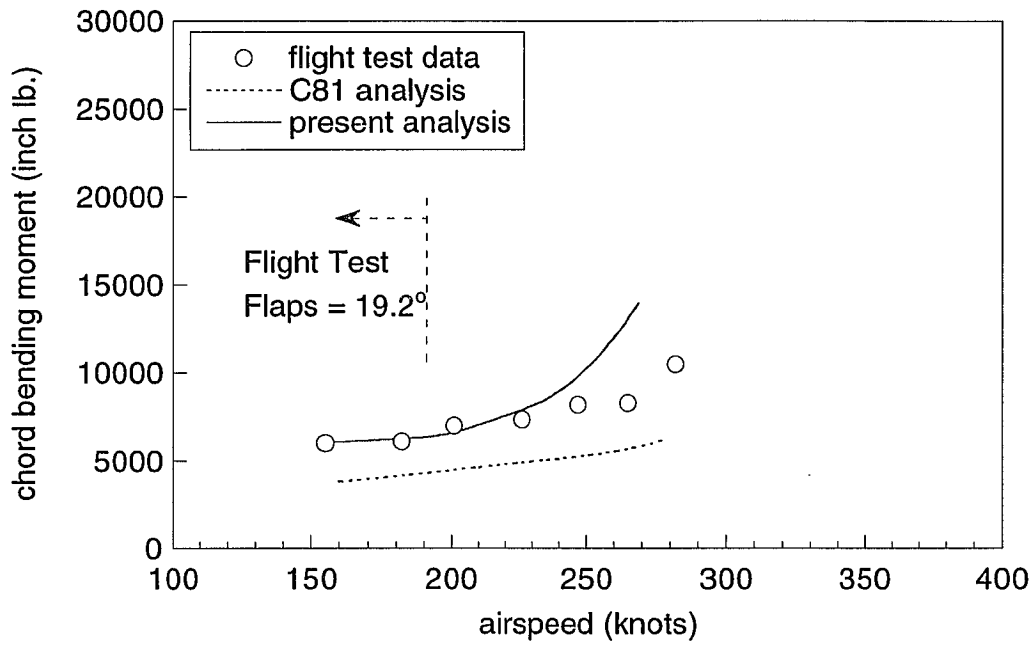

Figure 5.23: XV-15 oscillatory blade chord bending moment variation with airspeed, 35% radial location

Reproduced with permission of the copyright owner. Further reproduction prohibited without permission.

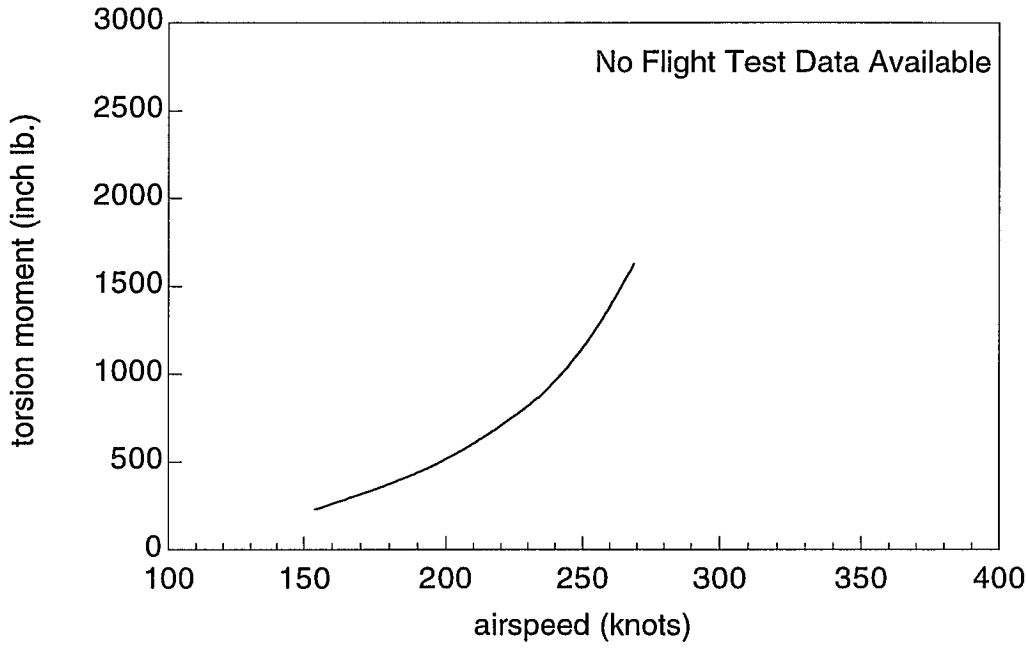

Figure 5.24: XV-15 oscillatory blade torsion moment variation with airspeed, 35% radial location

Reproduced with permission of the copyright owner. Further reproduction prohibited without permission.

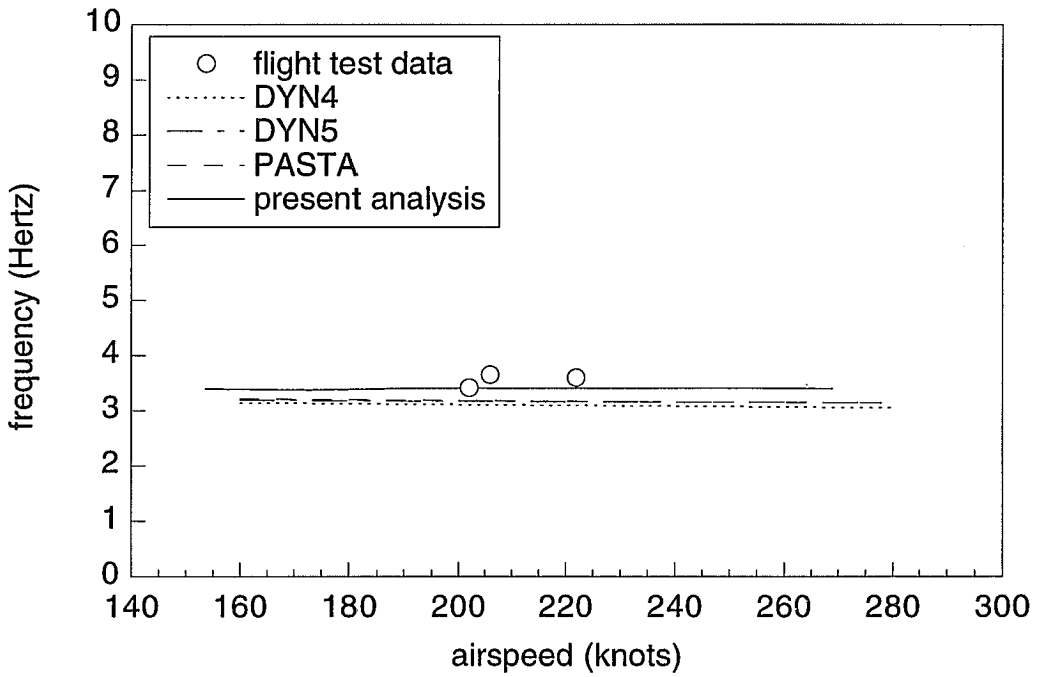

Figure 5.25: Validation of wing symmetric beam mode frequencies for the XV-15

Reproduced with permission of the copyright owner. Further reproduction prohibited without permission.

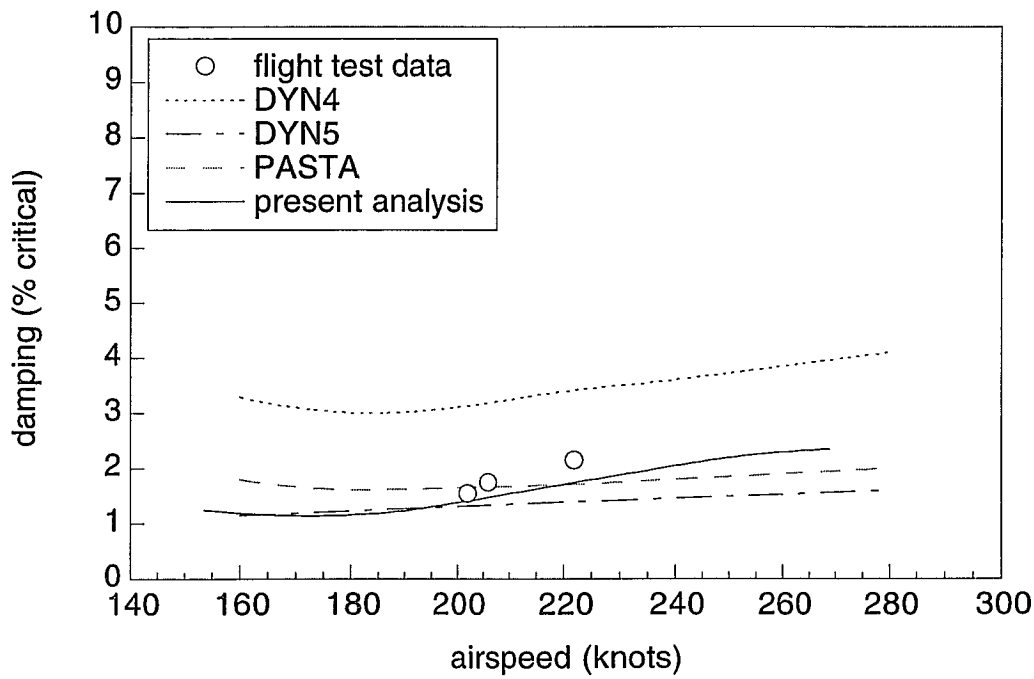

Figure 5.26: Validation of wing symmetric beam mode damping for the XV-15

Reproduced with permission of the copyright owner. Further reproduction prohibited without permission.

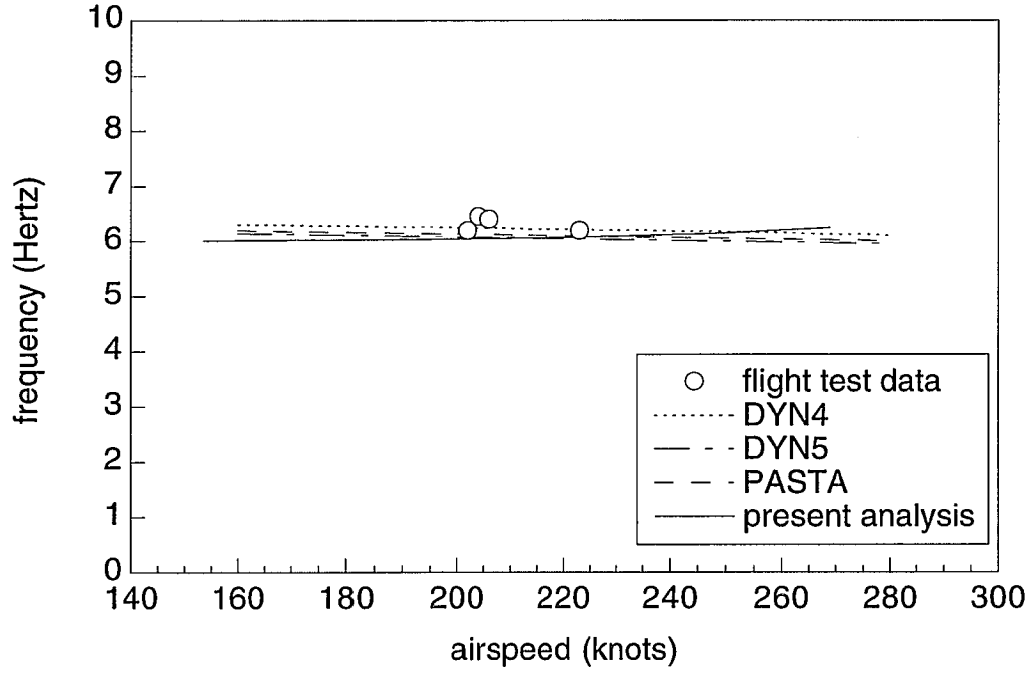

Figure 5.27: Validation of wing symmetric chord mode frequencies for the XV-15

Reproduced with permission of the copyright owner. Further reproduction prohibited without permission.

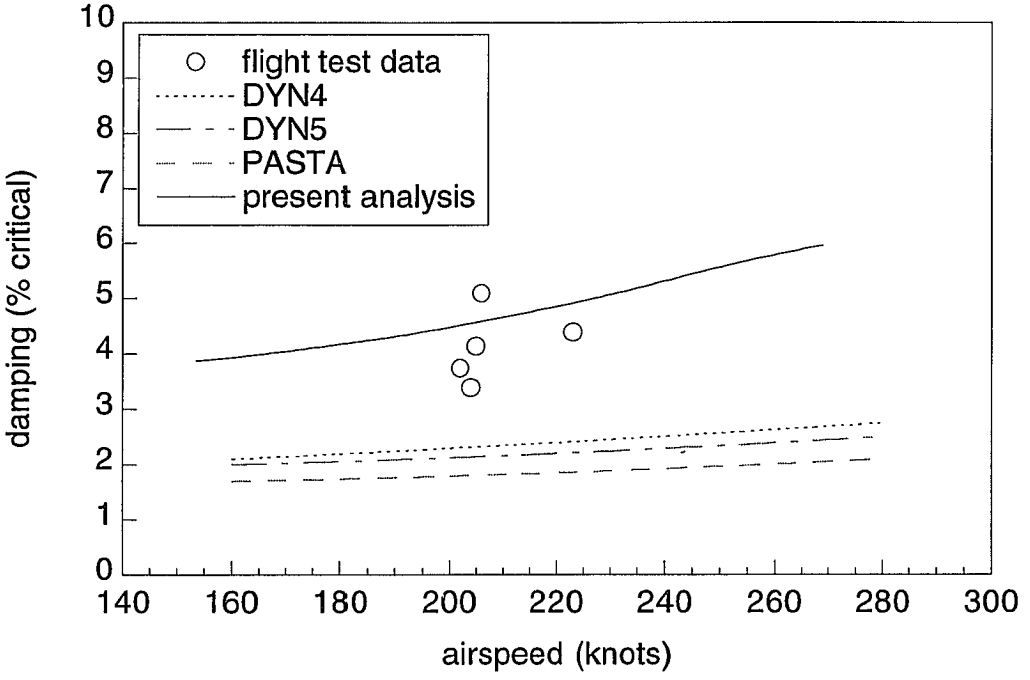

Figure 5.28: Validation of wing symmetric chord mode damping for the XV-15

Reproduced with permission of the copyright owner. Further reproduction prohibited without permission.

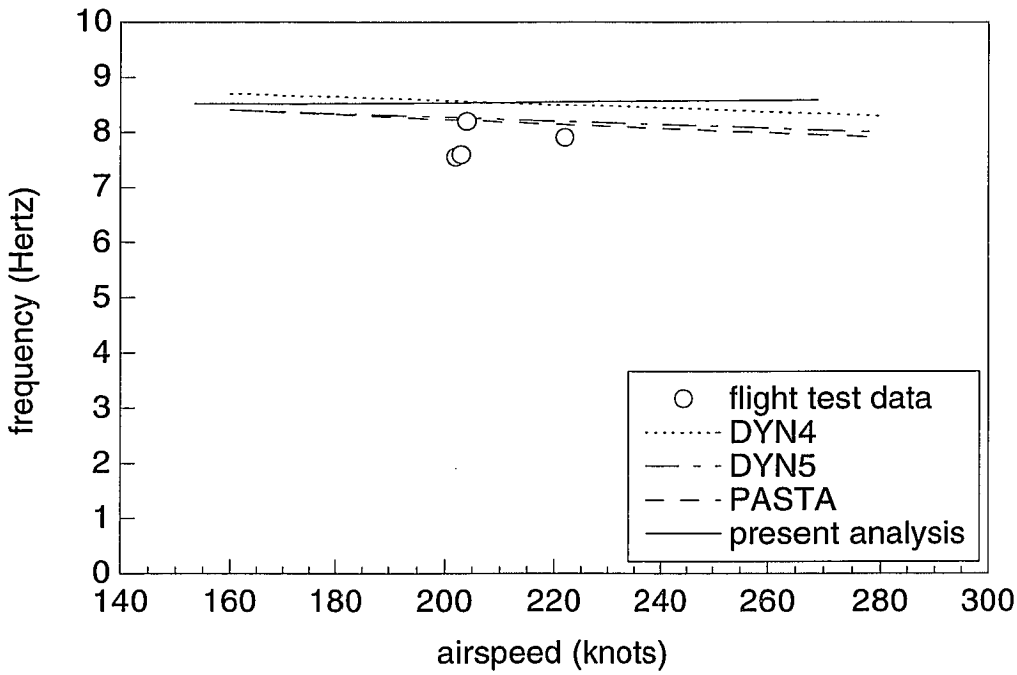

Figure 5.29: Validation of wing symmetric torsion mode frequencies for the XV-15

Reproduced with permission of the copyright owner. Further reproduction prohibited without permission.

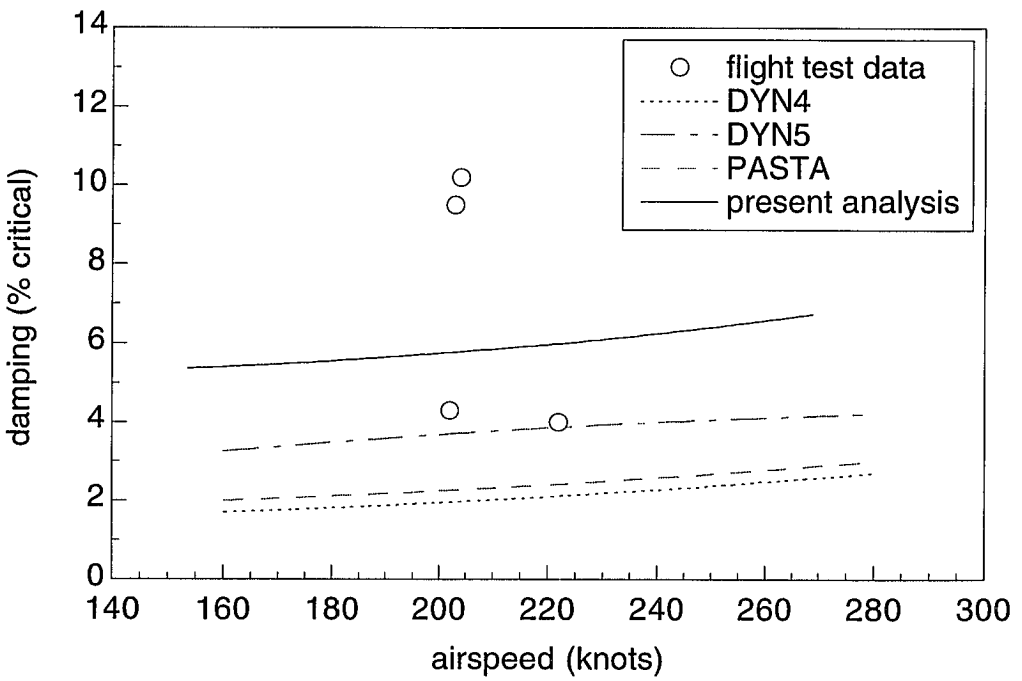

Figure 5.30: Validation of wing symmetric torsion mode damping for the XV-15

Reproduced with permission of the copyright owner. Further reproduction prohibited without permission.

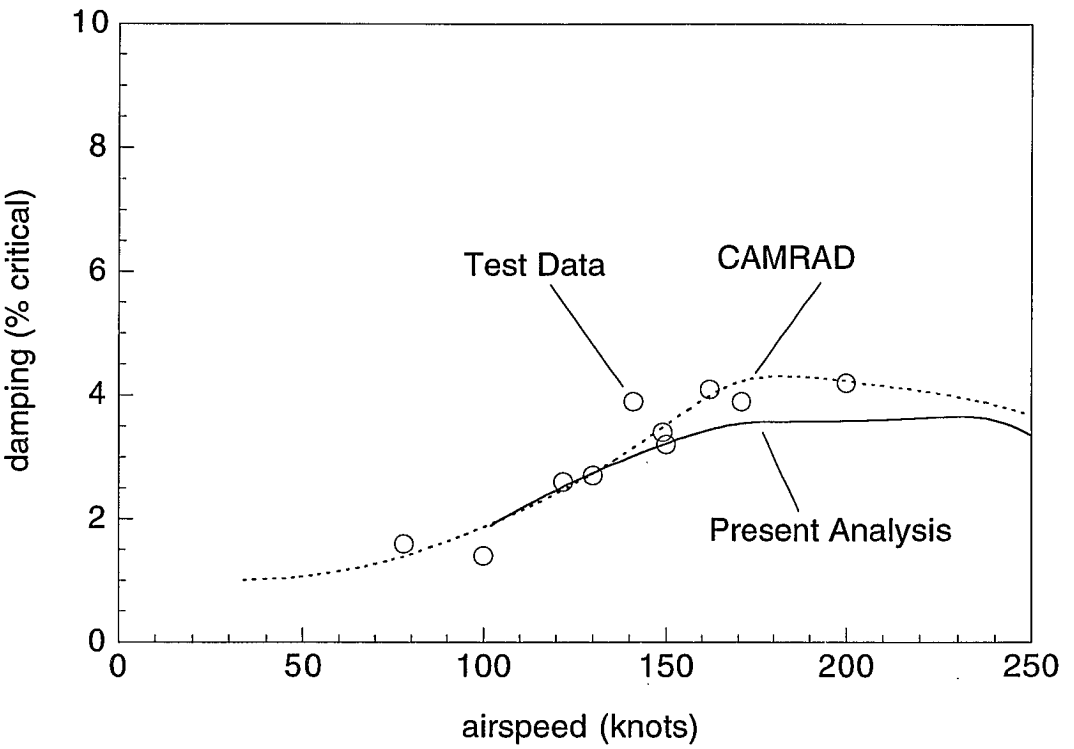

Figure 5.31: Comparison of XV-15 wing beam mode damping with full scale test data

Reproduced with permission of the copyright owner. Further reproduction prohibited without permission.

Chapter 6

Parametric Studies

The baseline configuration chosen for this analysis is the Bell-designed, full scale, gimballed, stiff in-plane XV-15 model tested in the NASA Ames 40x80 ft Wind Tunnel [38]. The description of the baseline configuration is given in Table 6.1. The baseline rotor system has positive pitch-flap coupling (flap-up nose-up) with δ_3 of -22.5^o and a rotor precone β_p of 2.5^o. The rotor blade has a high nonlinear pretwist distribution (40° at the blade root to -8° at the tip) as shown in Figure 6.1. A forward flight velocity of 240 knots has been chosen for the cases in this study since this represents the cruise velocity for this configuration. For advanced geometry rotor configurations, tip sweep, anhedral and planform taper are given to the outer 15% of the blade. Figure 6.2 shows a schematic of various blade configurations studied. The figure also shows typical sections assumed for the aerodynamic analysis. Note that tapering the blade tip, decreases the solidity of the rotor. The blade chord is, therefore, modified to maintain the thrust-weighted solidity constant. The taper ratio is expressed as the ratio of root chord to tip chord (and not the root chord if the taper is extended all the way to the blade root).

Reproduced with permission of the copyright owner. Further reproduction prohibited without permission.

Tip sweep is modeled in this study with the typical section aligned perpendicular to the swept elastic axis. A frequently-used method of blade construction (with tip sweep) is to align the typical section, even in the swept portion of the blade, perpendicular to the unswept axis of the blade (shear tip). These two cases are illustrated in Figure 6.3. The blade shown on the top part of the figure represents the manner in which the blade is modeled in this study. Typical errors associated with this modeling approximation are discussed in Appendix D. The errors arising from this assumption are shown in the appendix to be small.

6.1 Frequencies

The bending frequencies and mode shapes of the baseline elastic rotor trimmed at a forward flight velocity of 240 knots ($V/\Omega R = 0.7$) are shown in Figures 6.4 to 6.8. Five blade modes have been used in this study; their flap, lag and torsion components are shown in these figures. The first fundamental lag and flap modes from Ref. [63] are also shown in Figures 6.4 and 6.5 respectively. The analysis in Ref. [63] assumed uncoupled torsional motion; torsion displacements are, therefore, not shown in the corresponding calculations. The frequencies and mode shapes calculated with the present analysis compare favorably with those from Ref. [63]. Most of the modes are coupled because of the large blade pretwist, c.g. offsets and high collective pitch settings. The first mode is predominantly the fundamental lag mode with a large participation of the flap mode. It represents a stiff-inplane rotor. The second mode is the fundamental flap mode with a small coupling of the lag mode. The third mode is a coupled flap-lag-torsion mode; the first torsion

Reproduced with permission of the copyright owner. Further reproduction prohibited without permission.

mode shape is coupled with the second flap and lag mode shapes in this mode. The fourth mode is the fundamental torsion mode with negligible participation from the flap and lag modes. The fifth mode is predominantly the second torsion mode. Due to the couplings, it becomes quite difficult to identify some of the modes as is the case with the third and fourth modes.

The effect of tip sweep on the fundamental rotating blade frequencies is shown in Figure 6.9. The first lag and flap modes are not significantly affected by sweeping the blade tip and, therefore, are not presented. Tip sweep has a considerable influence on the third coupled flap-lag-torsion mode and fourth predominantly torsion mode. Frequencies of the third and fourth modes are quite close and tip sweep increases the torsional frequency due to coupling. Since sweep causes an effective c.g. offset, the torsional inertia of the blade about its straight elastic axis increases. The torsional stiffness of the blade, too, is increased with increase in sweep due to a propeller moment effect. Net effect is that the torsional frequencies increase with both forward and backward sweep; the frequency increases by about 25% from its baseline value for a 40° sweep case. The increase in the inertia about the straight elastic axis (not about the elastic axis of the swept segment) manifests itself in a decrease in the frequency of the coupled flap-lag-torsion mode; the frequency decreases by about 20% from the baseline value for 40° sweep. This mode becomes more bending-torsion coupled with increasing sweep, both for forward and backward sweep. It is important to note that the baseline configuration has rotor blades with c.g. behind the elastic axis, for most part of the blade [39]. The effects of sweeping the tip forward and backward are therefore, in this case, not exactly

Reproduced with permission of the copyright owner. Further reproduction prohibited without permission.

identical.

The effect of tip anhedral on the fundamental rotating blade frequencies is shown in Figure 6.10. Tip anhedral affects all the modes to varying degrees. There is a considerable decrease in the coupled flap-lag-torsion mode frequency with both positive and negative anhedral angles; the frequency decreases by about 20% from its baseline value for 40° anhedral. This is similar to the sweep case. With an increase in anhedral angle, there is a larger coupling of lag amplitude in the coupled modes. The first lag mode frequency, by itself, is only slightly reduced with anhedral angle; the change is less than 5% from its baseline value for 40° anhedral. The torsion mode frequency, in this case, decreases slightly with anhedral angle. This is probably due to the increase in torsional inertia being greater than the increase in the torsional stiffness due to propeller moment. These effects, however, need not necessarily be the same for other rotor configurations. The effect of blade tip planform taper on the rotating natural frequencies is negligible and is shown in Figure 6.11.

6.2 Blade Response and Trim

The results presented in this section are for a tiltrotor in the airplane mode. Each configuration analyzed has been trimmed to a C_T/σ of 0.01 for a cruise velocity of 240 knots (equivalent to $\mu = V/\Omega R = 0.7$); the rotor collective pitch is adjusted to achieve the desired thrust. The control pitch is given about the straight elastic axis of the blade. Uniform inflow over the rotor disk is used in the predictions. The blade span is modeled using six finite elements and the finite element in time

Reproduced with permission of the copyright owner. Further reproduction prohibited without permission.

is performed using six time elements around the rotor azimuth. Five coupled blade modes are used in the trim and stability analyses.

The variation of the blade tip response with sweep angle is shown in Figure 6.12. The flap, lag and torsion response at the blade tip decrease in magnitude for sweep back and increase in magnitude for the sweep forward case. The reason for this behavior can be found in the spanwise torsion response, which is shown in Figure 6.13. The torsion response for the no-sweep baseline case is also shown on the same plot. For a tip sweep back, the tip element produces a large nose down pitching moment on the rest of the blade which can be seen in the figure. The tip element, when swept forward, produces a large nose-up pitching moment on the rest of the blade. The tip itself twists in a direction opposite to the rest of the blade, relieving the elastic twist built-up from the root. For the sweep forward case, the elastic torsion helps to increase the angle of attack over most part of the blade (except at the tip). The rotor thrust is therefore greater for forward sweep compared to the sweep back case, at the same collective. This also means that the blade loading is shifted inboard for the sweep back case and shifted outboard for sweep forward. Increased loading outboard increases the flap, lag and torsion response of the tip. The tip response is higher in magnitude for the sweep forward case than for sweep back.

The variation of the tip response with anhedral is shown in Figure 6.14. The plot shows that, with tip droop, the flap and lag response increase and the torsion response decreases in magnitude. The response, though, does not change as much with anhedral as it does with sweep. For example, for a 30° tip droop, the flapping

Reproduced with permission of the copyright owner. Further reproduction prohibited without permission.

angle increases from about 1.8^o (baseline value) to 2.3^o and the lagging angle increases from around 3° to 4°. This could be attributed to the presence of 2.5^o blade precone in the baseline configuration, which is similar to the presence of anhedral. Addition of tip anhedral to the already preconed configuration does not change the tip response by much whereas inclusion of tip droop causes the blade precone effect to be mitigated, thereby changing the response considerably. Figure 6.15 shows the spanwise torsion response variation with anhedral. The spanwise torsion response for 30° tip droop is almost zero while the baseline and 30° anhedral cases exhibit considerable nose-down torsional response (about 2° at the tip).

The variation of tip response with blade tip planform taper is shown in Figure 6.16. Flap and lag responses increase in magnitude with increasing tip taper while the torsion response decreases in magnitude with increasing taper. The spanwise nose-down torsional response (Figure 6.17) decreases in magnitude with increasing taper; this causes the blade loading to shift slightly outboard with increasing taper. All configurations analyzed have c.g. ahead of a.c. for the outboard part of the blade and c.g. behind a.c. for the inboard part of the blade. The nose-down torsional moment caused by a.c. behind c.g. therefore decreases with increasing taper as more chord is moved inboard. Also, the loading shifts inboard with increasing taper since more of the blade has been removed from the tip and added inboard; but this, combined with the outboard shifting of loading due to lower nose-down torsional response, results in a slight outboard shift of the blade loading. The flap and lag tip response are larger for the tapered case, due to the outboard shift in loading, than for the untapered blade.

Reproduced with permission of the copyright owner. Further reproduction prohibited without permission.

Figure 6.18 shows the collective pitch variation to trim various configurations to a thrust level of $C_T/\sigma = 0.01$ at a velocity of 240 knots. More collective pitch is required to trim for sweep back and less collective is required for sweep forward than the baseline configuration. Sweep forward causes a nose-up torsional response over the unswept part of the blade which increases the rotor thrust for a given collective. Therefore, lower collective pitch is required for the sweep forward case to trim to a desired thrust level. For the anhedral case, more collective is required to trim for tip droop as well as for large tip anhedral. This is due to reduction in the lifting capability (at a given rotor collective) of the tip element with anhedral or droop, which is now partially out of the plane of rotation. A larger collective pitch is therefore required to achieve the same rotor thrust as the baseline configuration. The tapered tip case shows a very small increase in collective required with increasing taper, maintaining solidity of the rotor constant. Taper results in lower blade area at the tip and higher blade area inboard, which decreases the net lifting capability of the rotor. A slightly higher collective pitch is therefore required for the tapered case compared to the baseline configuration.

6.2.1 Convergence Study

The results presented in this chapter were based on a spanwise discretization into six finite elements for the blade; five blade modes were used in the coupled trim and stability analyses. Figure 6.19 shows the convergence of blade torsional response variation with blade span for 30° forward sweep given to the blade tip (outboard 15% span) at a forward flight velocity of 240 knots and a C_T/σ of 0.01. Three

Reproduced with permission of the copyright owner. Further reproduction prohibited without permission.

cases are presented on the plot: the first is the baseline case with six elements and five blade modes (solid line), the second is the case with six elements and ten blade modes (dotted line), and the third case is with 12 elements and five blade modes (dashed line). Inclusion of more blade modes in the response calculations alters the blade torsional response by less than 4% from the baseline; the rotor flap and lag responses do not change significantly. Furthermore, trim controls and system stability are not affected significantly by the inclusion of more blade modes in the analysis. The baseline case includes five blade modes, three modes of which are predominantly torsion modes; the rotor response is therefore captured well by including just the first five blade modes.

The same figure shows the torsional response variation with blade span for 12 spanwise finite elements. The response differs from the baseline response by less than 2%; flap and lag responses do not change significantly. This shows that blade tip sweep is adequately modeled using six finite elements. Similar trends were observed for backward sweep given to blade tip and blade tip anhedral.

6.3 Stability at Cruise Speed

The effect of the advanced geometry blades on the rotor and wing stability has been studied. The rotor was assumed to be in the windmilling configuration to obtain these results, since this assumption has been shown [49], [63] to give conservative results for damping estimates. The inherent structural damping of all blade and wing modes are assumed to be zero. The effect of the tip shapes on the rotor fixed-system stability was studied. These results were obtained including wing motion;

Reproduced with permission of the copyright owner. Further reproduction prohibited without permission.

they are therefore similar to the 'shaft-free' stability results. Five blade modes have been used. Results are presented for the damping ratio ζ (as a percentage of the critical damping ratio) of the first two coupled blade modes; the first being predominantly lag and second mode being predominantly flap. The gimbal flap modes are highly damped and their damping is not significantly affected by tip sweep, anhedral and planform taper; they are therefore not shown in the plots. The other blade modes, too, are not significantly affected and are not shown in the plots. The effect of blade tip configurations on the wing mode stability is also studied.

The effect of tip sweep variation on the blade damping ratio is shown in Figure 6.20. The first collective mode is the rotor collective lag windmilling mode which is not shown because it is highly damped. The second collective mode is a very highly damped collective flap mode and is not significantly affected by the tip modifications. The high and low frequency rotor cyclic modes (in the fixed frame) are often referred to as progressing and regressing modes. The high and low frequency cyclic modes of the lag and flap modes are affected considerably by changes in tip sweep, and are shown in Figure 6.20. It is seen that the lag mode damping for both high and low frequency modes are very large. Regressing lag mode damping increases with tip sweep back. Small sweep forward upto 10° does not change its damping by much; but a further sweep forward causes an increase in the damping of the mode. Similar behavior is shown by the low frequency flap mode too. Progressing lag mode damping decreases with tip sweep back, increases for small values of tip sweep forward, and then decreases for further sweep for-

Reproduced with permission of the copyright owner. Further reproduction prohibited without permission.

ward. Decreases in damping are not very crucial since this mode is highly damped anyway. Note that the high frequency flap mode exhibits interesting behavior. It is stabilized for tip sweep back and destabilized for sweep forward. Baseline configuration has a positive pitch-flap coupling that is destabilizing to the system. Sweep forward introduces more positive pitch-flap coupling, which destabilizes the blade even further. Sweep backward, on the other hand, decreases the positive pitch-flap coupling thereby stabilizing the blade. This mode, which was found to be marginally stable for the baseline case, becomes unstable for even small values of tip sweep forward.

The wing beam, chord and torsion modes were found to be less damped for a small forward sweep, as shown in Figure 6.21. The wing chord and beam mode damping values increased with 10° to 20° tip sweep back. This plot shows that the whirl flutter stability margin at cruise increases with marginal blade tip sweep back. Sweep forward, on the other hand, generally decreases the stability margin at the cruise speed.

The effect of blade tip anhedral was examined next. The variation of the blade mode damping ratios are shown in Figure 6.22. Blade tip droop decreases the high frequency lag mode damping but the mode still stays stable. Inclusion of tip droop up to 15° increases the low frequency lag mode damping due to the decrease in the destabilizing pitch-lag coupling. Tip anhedral was found to increase the lag mode damping to very high values. This phenomenon is due to the increase in the destabilizing negative pitch-lag coupling with increasing anhedral (up). Inclusion of even small tip anhedral is destabilizing to the blade flap modes. Regressing flap

Reproduced with permission of the copyright owner. Further reproduction prohibited without permission.

mode becomes unstable for even a 5° tip anhedral. The high frequency flap mode undergoes a similar change with anhedral (up); damping in this mode becomes negative for blade tip anhedral (up) above 5°.

Figure 6.23 shows the variation of wing damping ratios with blade tip anhedral. The addition of a small blade tip anhedral decreases the damping for the wing beam, chord and torsion modes. This is due to an increase in the destabilizing precone effect brought about by tip anhedral. Anhedral of about 5° makes the wing chord mode unstable. A small blade tip droop, on the other hand, could be beneficial to stability. The figure shows that low values of blade tip droop (about 5°) stabilizes the wing beam and chord modes. This is due to the alleviation of the blade negative pitch-lag coupling brought about by the 2.5^o blade precone. Increasing the tip droop beyond 10° decreases the damping of all the wing modes. These results show that tip anhedral has a very strong effect on system stability. The inclusion of 5° of tip anhedral/droop causes a drastic change in stability; this is due to the centrifugal forces from the tip element causing a bending-torsion coupling. Tip sweep does not have such a powerful effect as tip anhedral/droop on the stability at cruise speed.

Variation in blade mode damping ratios with tip planform taper is shown in Figure 6.24. Blade modes remain stable for the tip taper configurations considered. Progressing lag mode and regressing flap mode are affected by taper; these modes however remain highly damped for all cases considered. Effect of taper on wing damping is plotted in Figure 6.25. Tip taper has some destabilizing effect on all the wing modes. Taper affects the blade loading directly by shifting it outboard thus

Reproduced with permission of the copyright owner. Further reproduction prohibited without permission.

increasing the loading of the tapered tip. This is due to the dynamic torsional response variation of the blade with increasing taper. The blade loading, when shifted outboard, adversely affects the damping that the rotor system provides to wing modes, particularly the wing chord mode.

6.4 Flutter Speed Studies

The results described in previous sections were obtained at cruise of 240 knots corresponding to an advance ratio of 0.7. At higher speeds, the destabilizing forces from the rotor may cause one or more of the wing modes to become unstable. This is referred to as whirl flutter. A velocity sweep from an advance ratio of 0.4 (about 140 knots) to an advance ratio of 1.0 (roughly 340 knots) was performed and the damped frequencies and damping values were calculated for the baseline configuration. Figure 6.26 shows the variation of damping of different rotor and wing modes with advance ratio. The damping shown in Figures 6.26 to 6.31 are the negative real parts of the stability eigenvalues (and not the damping ratios); plotting the figures in this manner allows more information to be shown on the same plot. A mode becomes unstable when the negative of the real part of its stability eigenvalue becomes negative. Modes with a damping (negative decay rate) greater than 0.2 are very stable and are not shown in the plot. The wing beam mode is close to the instability boundary but is predicted to remain stable upto 340 knots. The wing chord mode, however, becomes unstable around an advance ratio of 0.81 which corresponds to about 275 knots. This flutter speed agrees with other analyses, Johnson [63] and Nixon [39]. These analyses, however,

Reproduced with permission of the copyright owner. Further reproduction prohibited without permission.

predict the wing beam mode becoming unstable before the chord mode which is not the case with the current analysis. The analysis in Ref. [63] considers coupled bending modes and uncoupled torsion modes while the current analysis considers fully-coupled bending-torsion modes.

The next case examined was a rotor with the outboard 15% of the blade given a 30° sweep back. The damping plot for this case is shown in Figure 6.27. The damping plot shows a remarkable increase in the damping values of many modes over the baseline case. The wing beam mode is stabilized by the addition of blade tip sweep. And most significantly, the wing chord mode is also dramatically stabilized; the chord mode does not become unstable in the range of velocities studied. The wing beam mode shows a decrease in the damping beyond speeds of 300 knots; this mode becomes unstable only around a speed of 370 knots (though this instability is not shown in this plot), which is an increase of flutter speed of 95 knots over the baseline. Figure 6.27 shows that blade tip sweep (backwards) has a large beneficial effect on the stability of the wing modes and on the occurrence of whirl flutter. A backward sweep causes a negative pitch-flap coupling (flap-up pitch-down) over most part of the blade. This effect offsets some or all of the destabilizing effects of the positive pitch-flap coupling in the baseline configuration. The effect of tip sweep is to alter the torsional response along the blade span; it couples more with the blade flap mode than with the rigid gimbal flap mode.

The effect of a 30° tip sweep forward was studied next, and is shown in Figure 6.28. The high frequency flap mode stays unstable for all forward speeds investigated. The low frequency flap mode becomes unstable around 285 knots, and the

Reproduced with permission of the copyright owner. Further reproduction prohibited without permission.

wing chord mode becomes unstable around 300 knots. The plot shows that this configuration is unstable for all forward speeds studied; this is due to the destabilizing pitch-flap coupling caused by tip sweep forward. The high frequency flap mode is destabilized for all speeds examined.

The next case studied had a 5° droop given to the blade tip. The 5° tip droop was chosen to try and offset the destabilizing pitch-lag coupling caused by the 2.5^o precone. The damping plot for this case is shown in Figure 6.29. The results shows that no instabilities are predicted to occur up to an advance ratio of 1.0 (roughly 340 knots); the wing chord mode becomes unstable around a speed of 350 knots. This is a definite improvement over the baseline configuration, where the predicted instability occurred around 275 knots. The wing beam, chord, and torsion modes are all stabilized by the inclusion of small values of tip droop. The rotor modes are not destabilized by this tip droop.

A 5° tip anhedral case was examined next, and this is shown in Figure 6.30. The above case showed that a 5° tip droop has a very beneficial effect on flutter speed compared to the baseline configuration. This case shows just the opposite. Tip anhedral destabilizes the blade and wing modes. Progressing flap mode remains unstable from forward speeds of around 140 knots. Regressing flap mode becomes unstable around 225 knots and of the wing modes, the chord mode becomes unstable around 220 knots. Overall destabilizing effect of tip anhedral is due to the increase in the destabilizing pitch-lag coupling.

Effect of tip planform taper is shown in Figure 6.31. Root chord to tip chord ratio of 3:1 was chosen for the outboard 15% blade span for this case. Inclusion

Reproduced with permission of the copyright owner. Further reproduction prohibited without permission.

of planform taper decreases the stability margin of the rotor high frequency flap mode, but the mode remains marginally stable. The chord mode is destabilized by planform taper and becomes unstable around a speed of 260 knots (compared to the baseline case chord mode becoming unstable at 275 knots). Planform taper (for this configuration) therefore destabilizes the system and accelerates the occurrence of whirl flutter.

6.5 Basic Performance Studies

Rotor performance parameters such as main rotor power required and rotor propeller efficiency in cruise flight were studied for different tip configurations. Figure 6.32 shows the rotor power required for different rotor tip sweep angles. Study was done for $C_T/\sigma = 0.01$ and at a forward flight velocity of 240 knots. Figure shows that the horsepower required increases for tip sweep backward and decreases for tip sweep forward. Tip sweep (forward and backward) decreases the effective rotational speed of the tip element; the beneficial effect of sweep is that the tip mach number, for the swept tip, decreases considerably and adverse compressibility effects are decreased. In this case, however, the dynamic effects (rotor response variation with span) are more important to the power required than are the aerodynamic effects. Figure 6.13 shows the torsion response variation along the blade span for different tip sweep angles; the figure shows that tip sweep forward increases the loading at the blade tip, whereas tip sweep backward decreases the loading at the blade tip. This is due to the dynamic pitch-flap coupling resulting from tip sweep and is equivalent to changing the blade pretwist distribution along

Reproduced with permission of the copyright owner. Further reproduction prohibited without permission.

the span.

This large change in power requirements requires closer examination: the variation of blade section angle-of-attack with span for the straight blade configuration in airplane mode cruise ($V = 240$ knots, $\mu = 0.7$), trimmed to a $C_T/\sigma = 0.01$ at 52° rotor collective pitch, is shown in Figure 6.33. The variation in pretwist distribution along the blade span along with the variation in the inflow angle (due to the forward flight velocity) results in a positive angle-of-attack over the entire blade span for this flight condition. Figure 6.34 shows the components of lift force per unit length of blade span for a straight blade configuration that contribute to rotor thrust, drag and power. Blade section lift and drag act perpendicular and parallel to the relative wind at any blade section; the relative wind at the blade root is perpendicular to the rotor disk and the relative wind at the blade tip is at an angle of about 35° with respect to the rotor disk (at an advance ratio of 0.7). The lift forces generated by any blade section, inboard or outboard, hence, have large components contributing to the induced drag. For the inboard sections, almost all the lift generated acts in the rotor drag direction and very little contributes to rotor thrust. The lift on the outboard sections of the rotor blade contributes significantly to rotor thrust as well as rotor drag. Since the contribution from section lift to rotor drag is significant over the entire blade span, the contribution of the entire blade span to rotor power is significant as shown in the plot.

Figure 6.35 shows the angle-of-attack variation with blade span for three different configurations: straight blade, 30° sweep forward for blade tip and 30° sweep back for blade tip. These results are for trimmed configurations. Different tor-

Reproduced with permission of the copyright owner. Further reproduction prohibited without permission.

sional responses over the blade span for these configurations necessitate different collective pitch angles to trim these cases to the same thrust. Baseline configuration has a non-zero angle-of-attack over the inboard section of the blade; as explained earlier, the lift from the inboard sections contributes to rotor power. Angle-of-attack at the blade tip is quite high; this too contributes to rotor power.

The next case, the 30° forward sweep given to the blade tip, has lower angles-of-attack over the inboard sections of the blade; this results in lower lift from these sections and lower rotor power. Also, the blade tip is not as heavily loaded as for the baseline case; the peak loading shift to about 0.8R from the tip which results in lower power compared to the baseline configuration. The third case, the 30° backward sweep given to the blade tip, has higher angles-of-attack over inboard blade sections compared to the baseline case; this results in higher rotor power for this case. Blade tip is also more heavily loaded in this case compared to the other two cases; this too results in an increase in rotor power. Sweep forward case is hence a more efficient configuration than the sweep backward case and the baseline case for the given rotor parameters (the sweep back case can be made more efficient by redesigning the blade pretwist distribution in accordance with the torsional response variation with blade span). This observation highlights the trade-offs inherent in making design changes; the sweep forward case has very poor stability characteristics but better performance characteristics than the sweep backward case.

Another measure of performance is the rotor propeller efficiency in axial flight. Propeller efficiency is defined as a ratio of the useful power (thrust times the

Reproduced with permission of the copyright owner. Further reproduction prohibited without permission.

forward velocity) to the total power required by the rotor. Figure 6.36 shows the propeller efficiency variation with blade tip sweep angle. The figure shows that the propeller efficiency increases for a tip sweep forward and decreases for a tip sweep backward (due to the corresponding decrease and increase in the total power required as seen from the previous plot). Propeller efficiency variation with tip sweep angle is the opposite trend as rotor power variation with tip sweep. As the power requirements for generating a given thrust increase, the propeller efficiency of the configuration decreases. The baseline propeller efficiency is very low for this configuration since the operating thrust level is low ($C_T/\sigma = 0.01$).

The rotor power required for tip anhedral is shown in figure 6.37. Figure 6.15 shows that the tip loading is higher for the droop case than it is for the anhedral (up) case; the tip element is hence producing more lift in the tip drooped configuration, due to the presence of dynamic effects. The rotor power requirement for the tip droop case is therefore lower than for the tip anhedral (up) case, although the change is insignificant between the tip droop and the baseline cases.

Figure 6.38 shows the propeller efficiency variation with blade tip anhedral angle. The plot shows a decrease in the propeller efficiency with tip anhedral (up), which is consistent with the increase in power required for the same case. It should be noted that the tip anhedral/droop angles of more than 10° are not likely to be used, because of its powerful effect on system stability.

Reproduced with permission of the copyright owner. Further reproduction prohibited without permission.

6.5.1 Effect of Wake Modeling

In the coupled trim and stability studies reported earlier in this chapter, a uniform inflow model was used for the calculation of the rotor loads and stability. The influence of this simplifying assumption on the prediction of rotor thrust and stability was observed to be negligible (as compared to using more sophisticated wake models). Figure 6.39 shows the influence of different aerodynamic models on the predicted rotor torque values in an axial flight condition. The three models considered for this study were the uniform inflow (based on momentum theory), radially varying inflow (based on blade-element momentum theory) and free wake models. All three aerodynamic models predicted the increase in rotor torque with airspeed; this effect can be attributed to the larger inflow (hence larger collective for same thrust, and larger compressibility effects) at higher forward flight speeds. The uniform inflow model, however, underpredicted the increase in torque with airspeed, as compared to the other two models. The radially varying inflow model predictions were almost equal to the free wake predictions of rotor torque; the radial variation model is therefore a good approximation to the free wake model for performance predictions for the case of a tiltrotor in high speed axial flight when the rotors are lightly loaded.

6.6 Off-design Conditions

The parametric studies on system stability reported earlier in this chapter were done for an axial flight condition for a speed range of 140 to 340 knots. It was observed that tip sweep backward and tip droop were significantly stabilizing. The

Reproduced with permission of the copyright owner. Further reproduction prohibited without permission.

stability characteristics of these configurations were then studied in hover and in conversion mode; tip droop and tip sweep back were found to have no adverse effects on stability at these off-design operating conditions.

Reproduced with permission of the copyright owner. Further reproduction prohibited without permission.

Rotor Properties	
Number of blades	3
Radius	12.5 ft
Lock number	3.83
Solidity	0.089
Lift curve slope	5.7/rad
Pitch-flap coupling	-0.268 ($\delta_3 = -22.5^o$)
Hub Precone	2.5^o
Root Cut-out	10%
Tip speed	600 ft/s
Rotational speed	48.0 rad/s
Blade flap inertia I_b	105 slug-ft^2
Wing Properties	
Semi-span/R	1.333
Chord/R	0.413
Pylon height/R	0.342

Table 6.1: Baseline system

Reproduced with permission of the copyright owner. Further reproduction prohibited without permission.

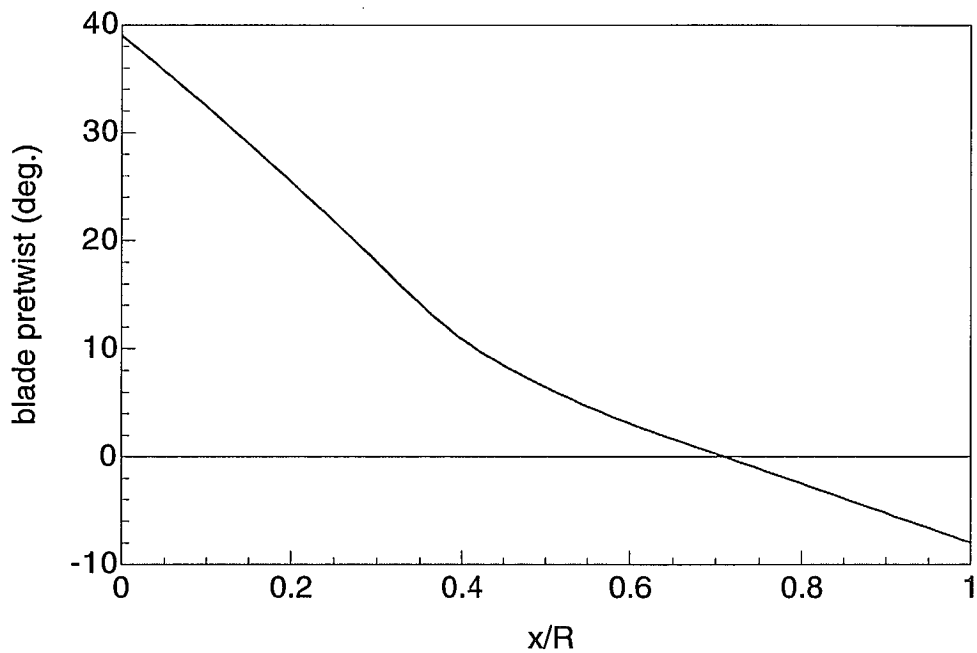

Figure 6.1: Blade pretwist distribution

Reproduced with permission of the copyright owner. Further reproduction prohibited without permission.

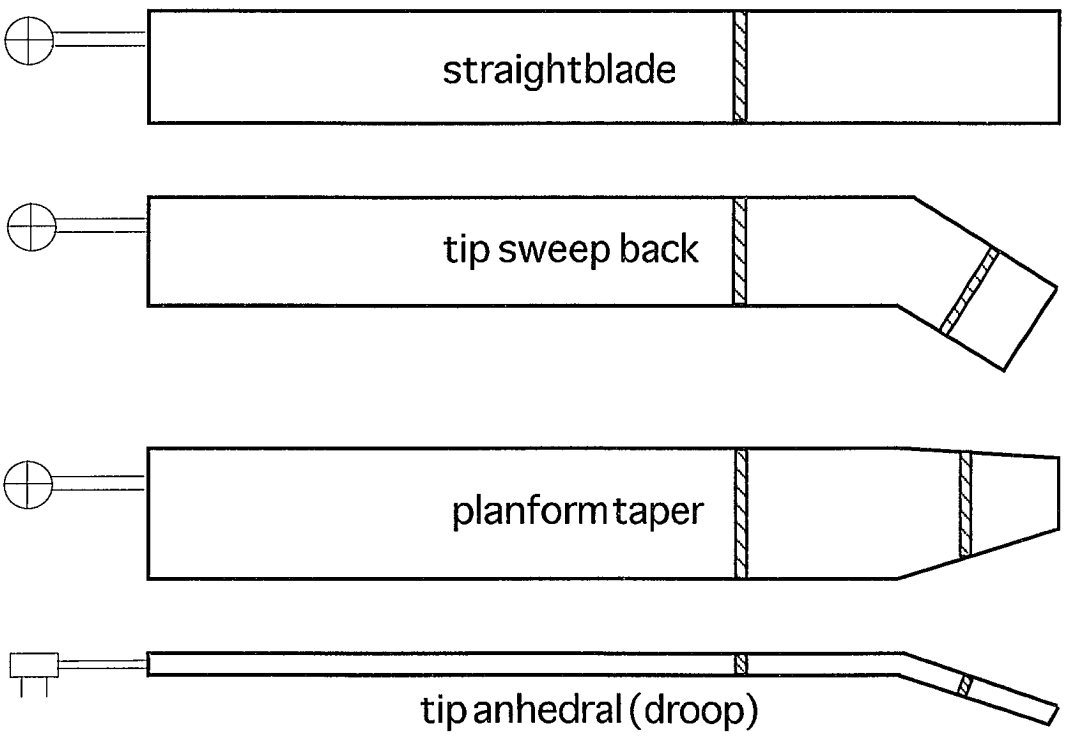

Figure 6.2: Advanced tip configurations (shaded area denotes typical section)

Reproduced with permission of the copyright owner. Further reproduction prohibited without permission.

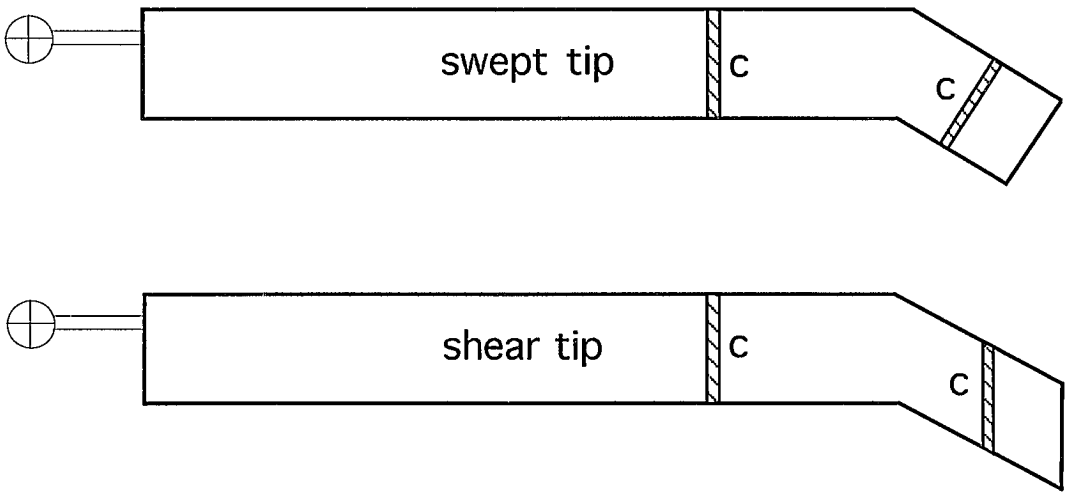

Figure 6.3: Swept tip and shear tip configurations (c = blade chord, shaded area denotes typical section)

Reproduced with permission of the copyright owner. Further reproduction prohibited without permission.

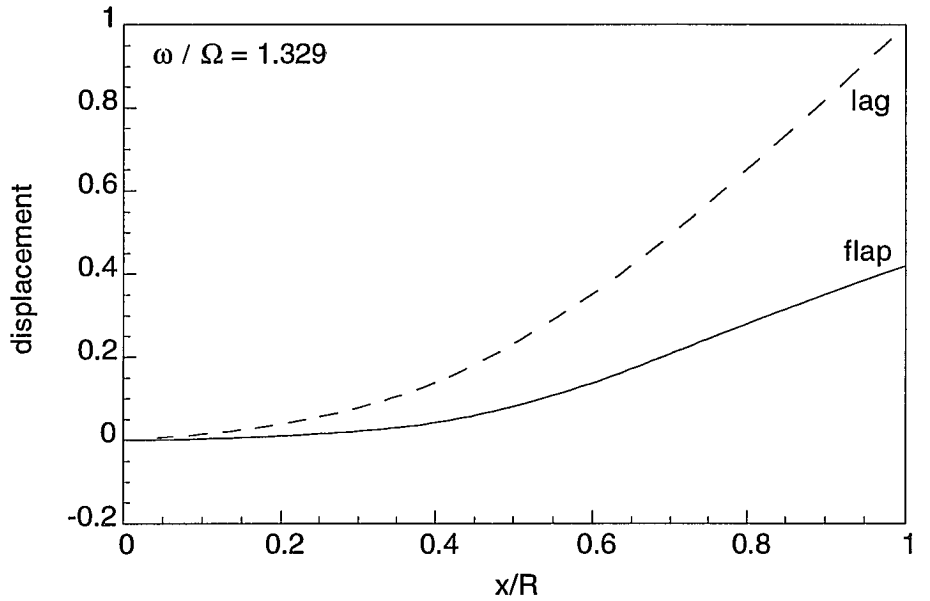

(a) calculations from Ref. [63]

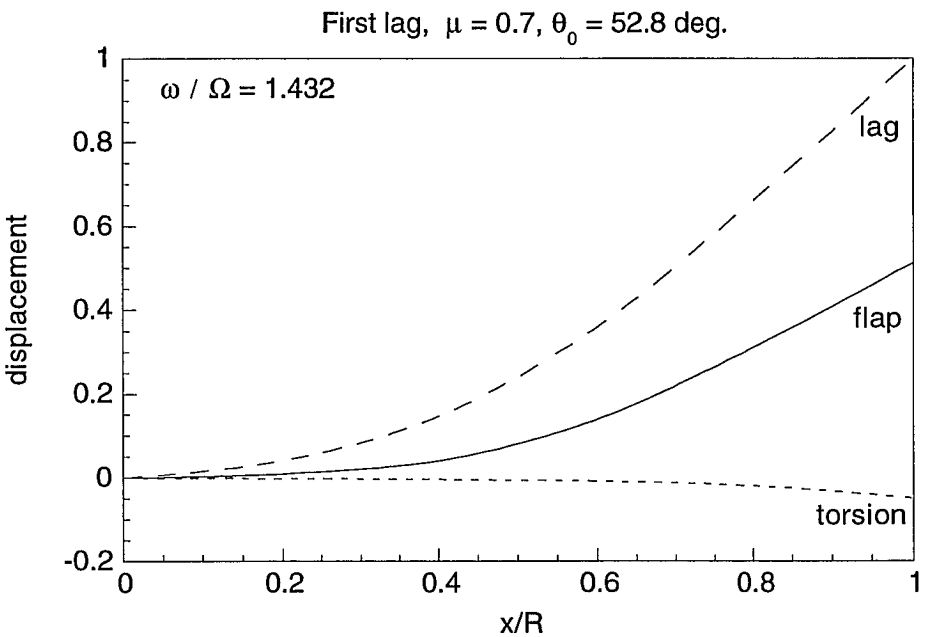

(b) calculated from present analysis

Figure 6.4: First coupled blade mode shape of baseline configuration ($V = 240$ knots)

Reproduced with permission of the copyright owner. Further reproduction prohibited without permission.

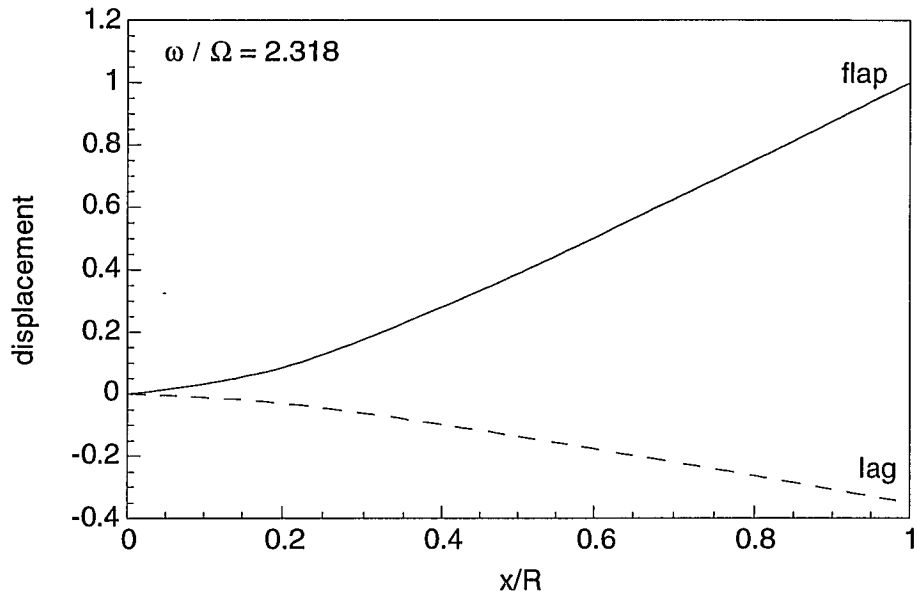

(a) calculations from Ref. [63]

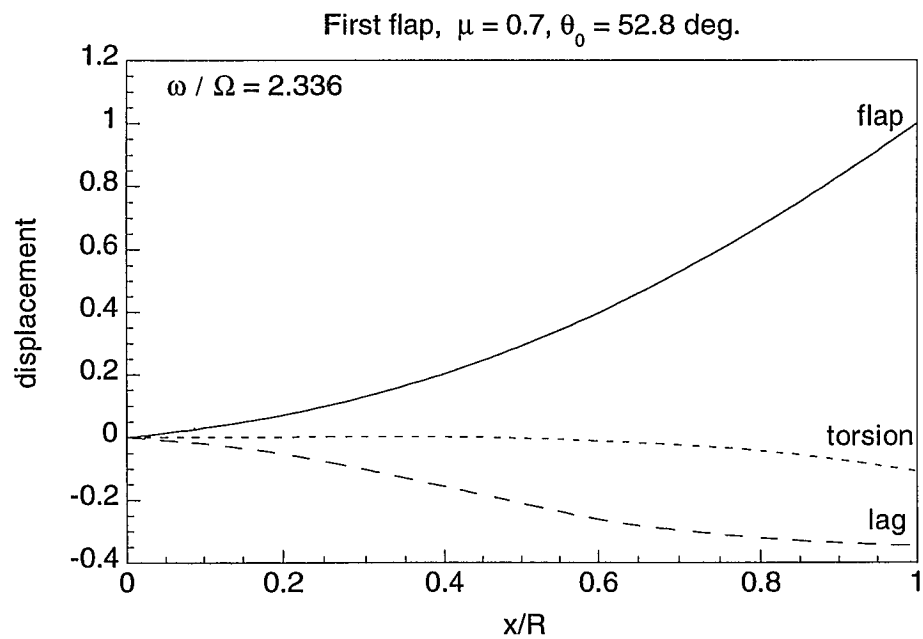

(b) calculated from present analysis

Figure 6.5: Second coupled blade mode shape of baseline configuration ($V = 240$ knots)

Reproduced with permission of the copyright owner. Further reproduction prohibited without permission.

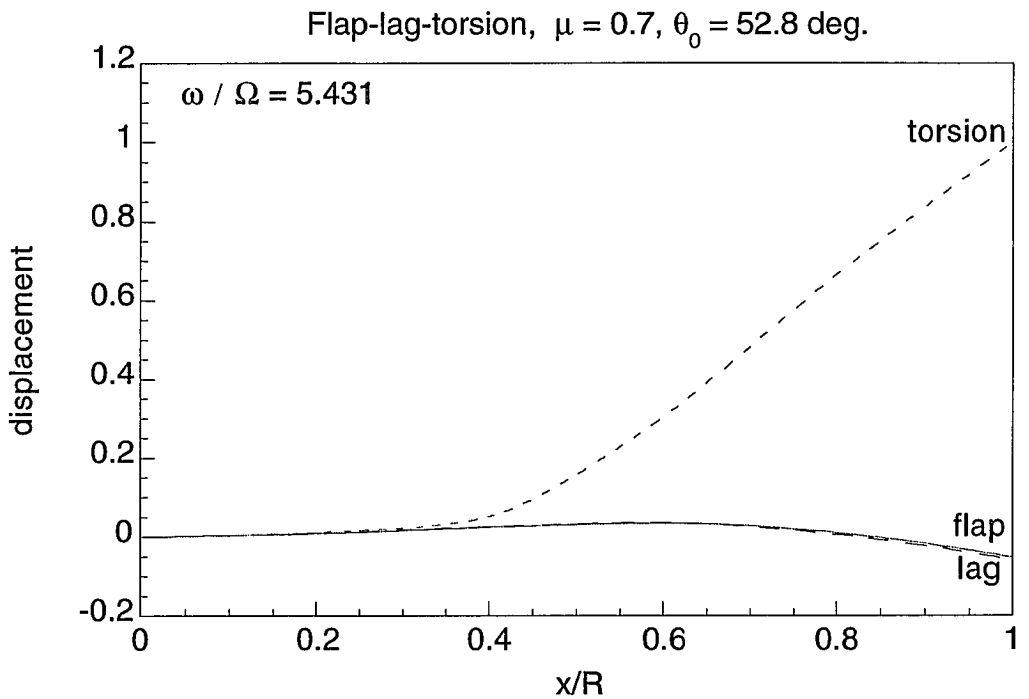

Figure 6.6: Third coupled blade mode shape of baseline configuration ($V = 240$ knots)

Reproduced with permission of the copyright owner. Further reproduction prohibited without permission.

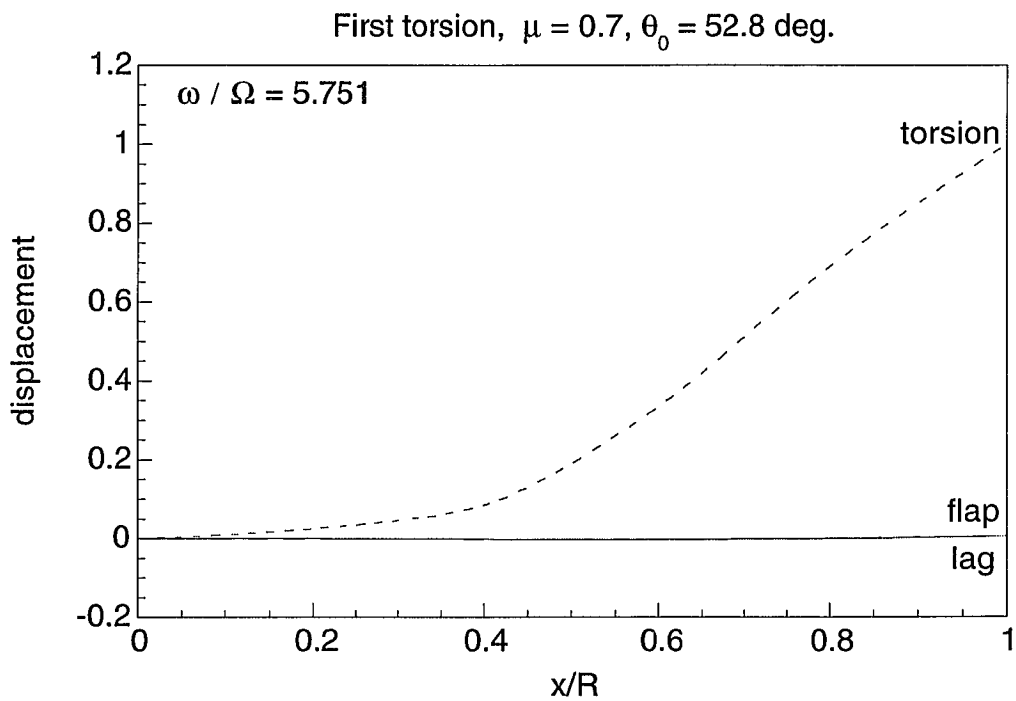

Figure 6.7: Fourth coupled blade mode shape of baseline configuration ($V = 240$ knots)

Reproduced with permission of the copyright owner. Further reproduction prohibited without permission.

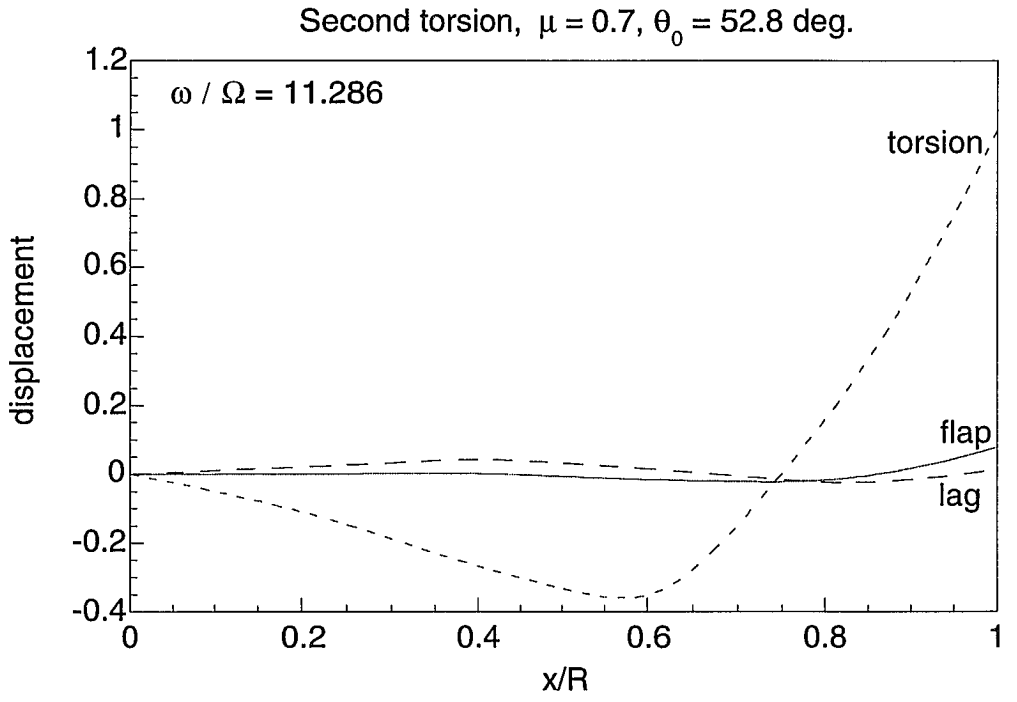

Figure 6.8: Fifth coupled blade mode shape of baseline configuration ($V = 240$ knots)

Reproduced with permission of the copyright owner. Further reproduction prohibited without permission.

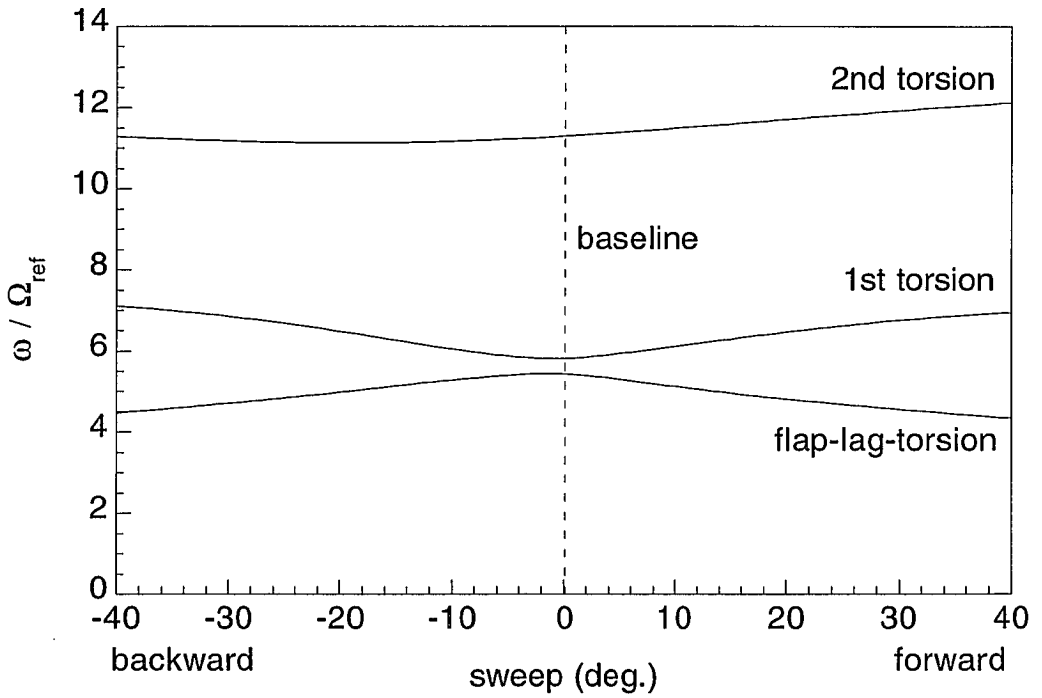

Figure 6.9: Effect of blade tip sweep (outboard 15% span) on rotating natural frequencies ($\theta_0 = 0$)

Reproduced with permission of the copyright owner. Further reproduction prohibited without permission.

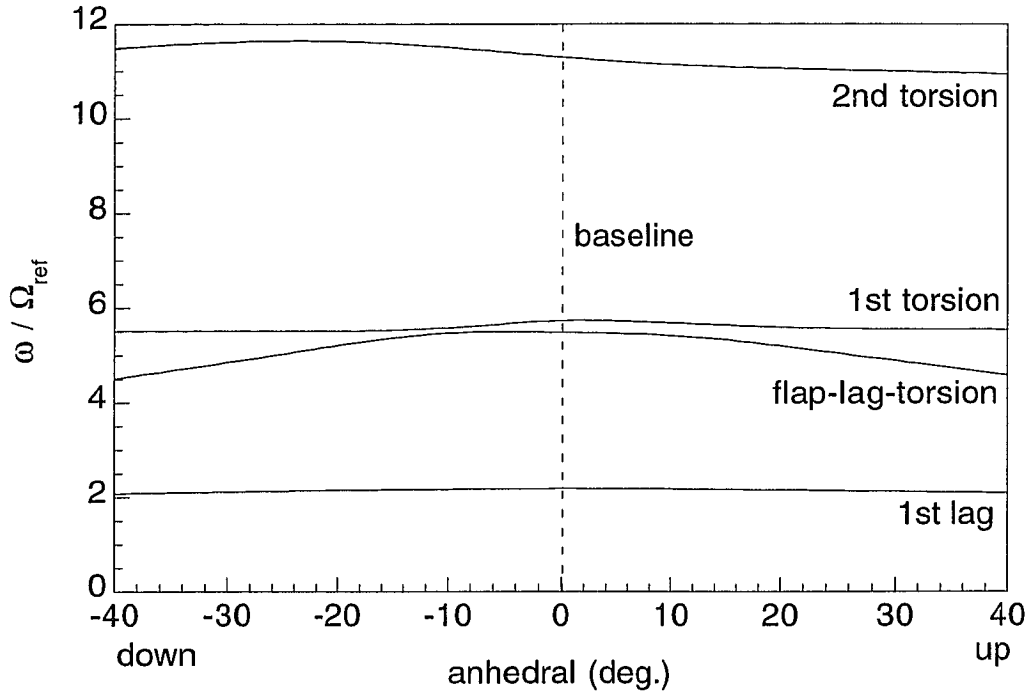

Figure 6.10: Effect of blade tip anhedral (outboard 15% span) on rotating natural frequencies ($\theta_0 = 0$)

Reproduced with permission of the copyright owner. Further reproduction prohibited without permission.

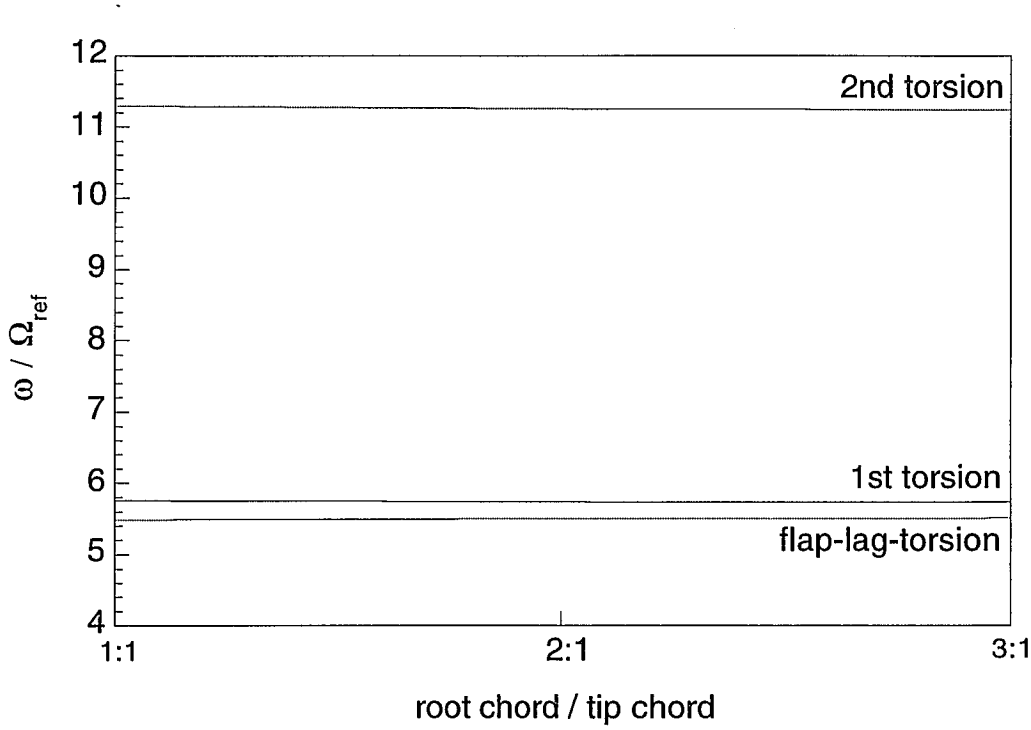

Figure 6.11: Effect of blade tip planform taper (outboard 15% span) on rotating natural frequencies ($\theta_0 = 0$, constant thrust-weighted solidity)

Reproduced with permission of the copyright owner. Further reproduction prohibited without permission.

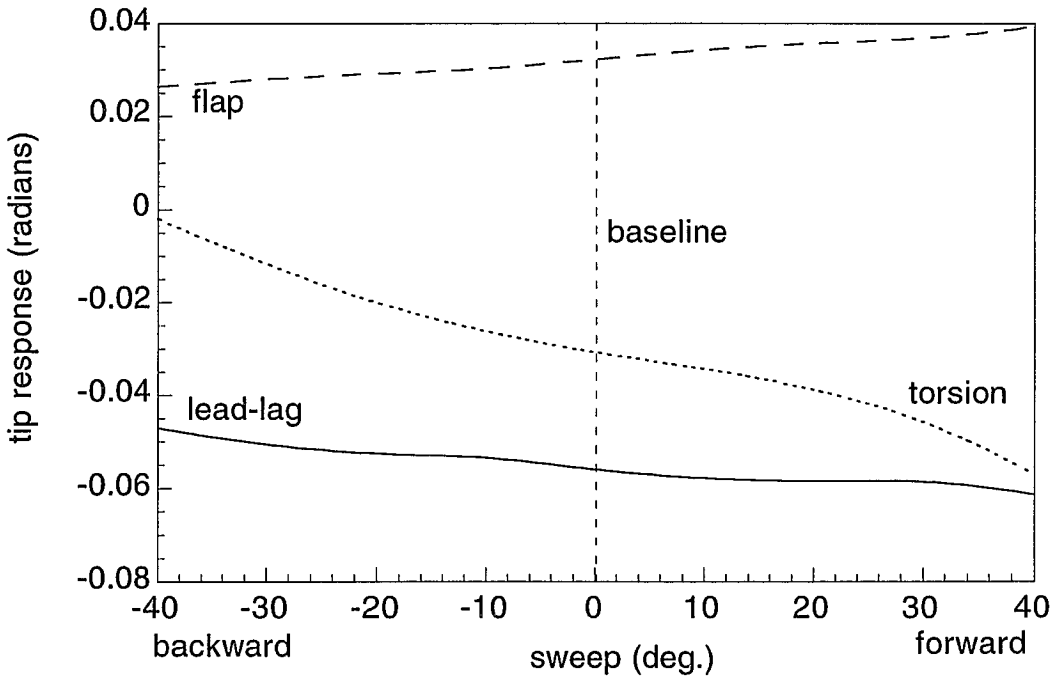

Figure 6.12: Tip response $(v/R, w/R, \phi)$ variation with blade tip sweep (outboard 15% span, $V = 240$ knots, $C_T/\sigma = 0.01$)

Reproduced with permission of the copyright owner. Further reproduction prohibited without permission.

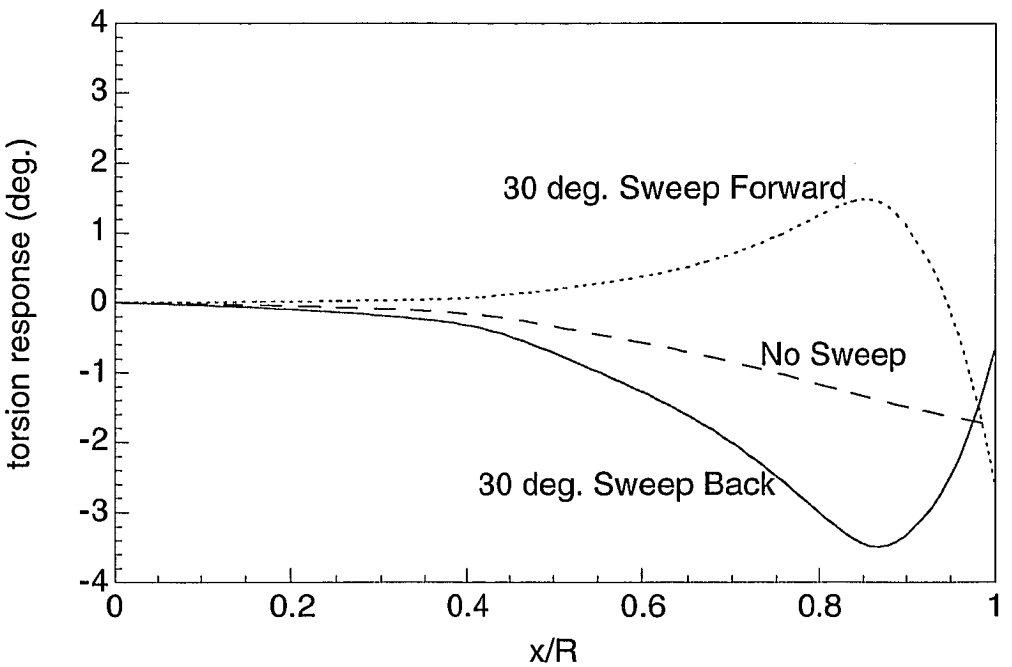

Figure 6.13: Torsion response along blade span ($V = 240$ knots, $C_T/\sigma = 0.01$)

Reproduced with permission of the copyright owner. Further reproduction prohibited without permission.

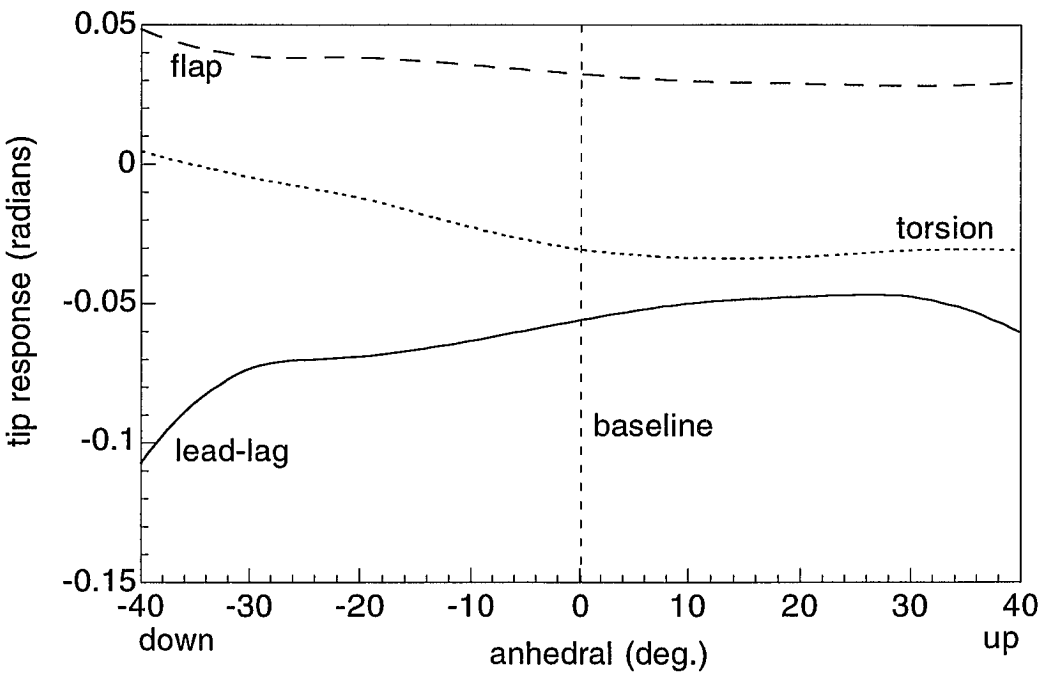

Figure 6.14: Tip response $(v/R, w/R, \phi)$ variation with blade tip anhedral (outboard 15% span, $V = 240$ knots, $C_T/\sigma = 0.01$)

Reproduced with permission of the copyright owner. Further reproduction prohibited without permission.

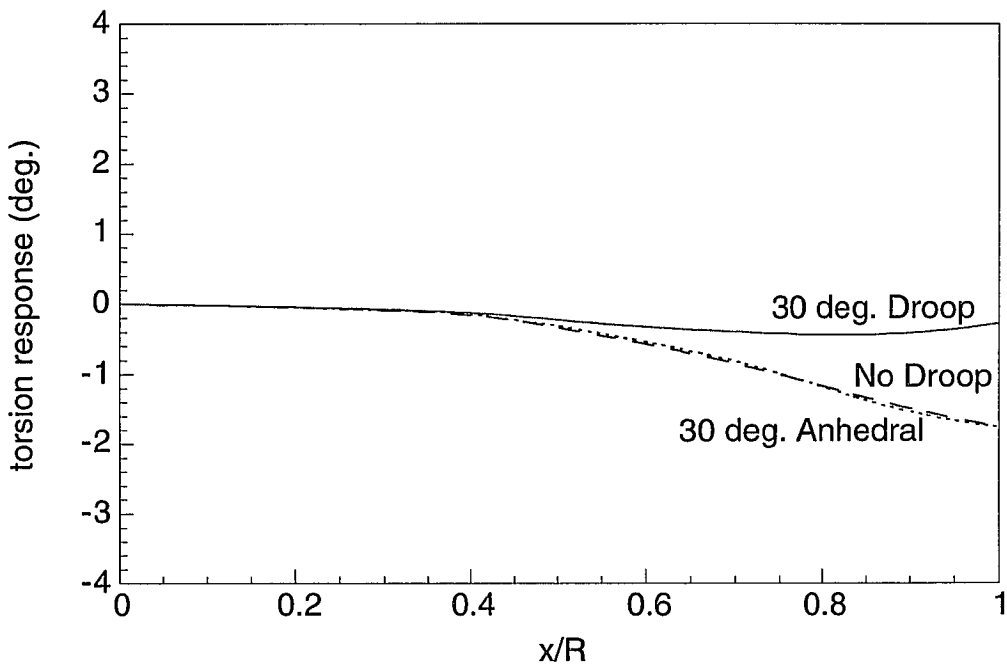

Figure 6.15: Torsion response along blade span ($V = 240$ knots, $C_T/\sigma = 0.01$)

Reproduced with permission of the copyright owner. Further reproduction prohibited without permission.

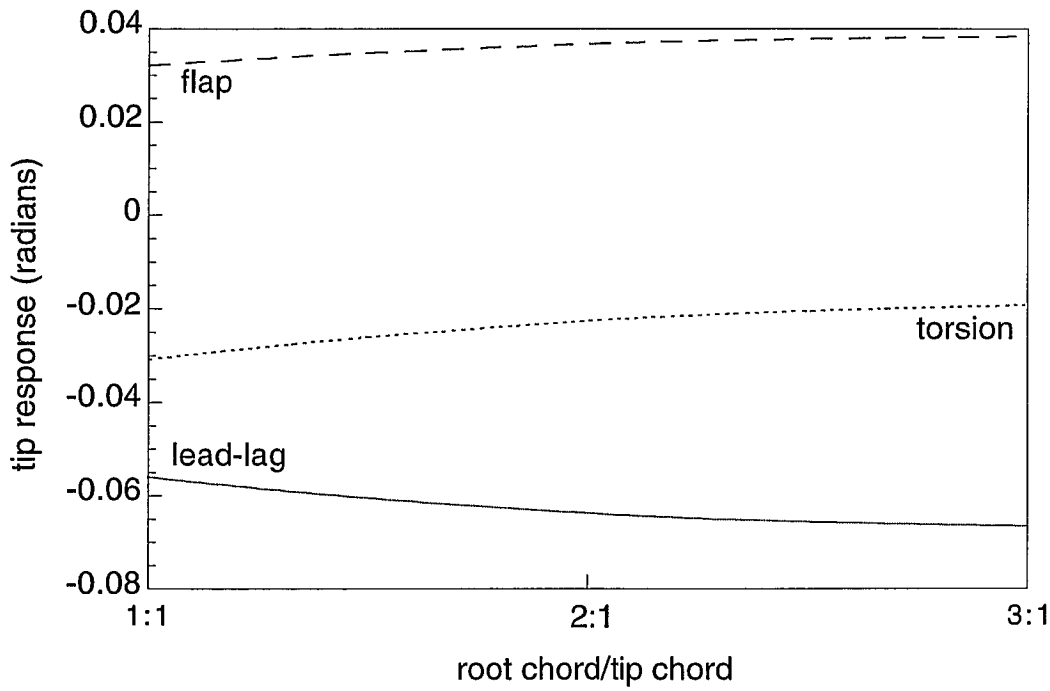

Figure 6.16: Tip response $(v/R, w/R, \phi)$ variation with blade tip planform taper (outboard 15% span, $V = 240$ knots, $C_T/\sigma = 0.01$, constant thrust-weighted solidity)

Reproduced with permission of the copyright owner. Further reproduction prohibited without permission.

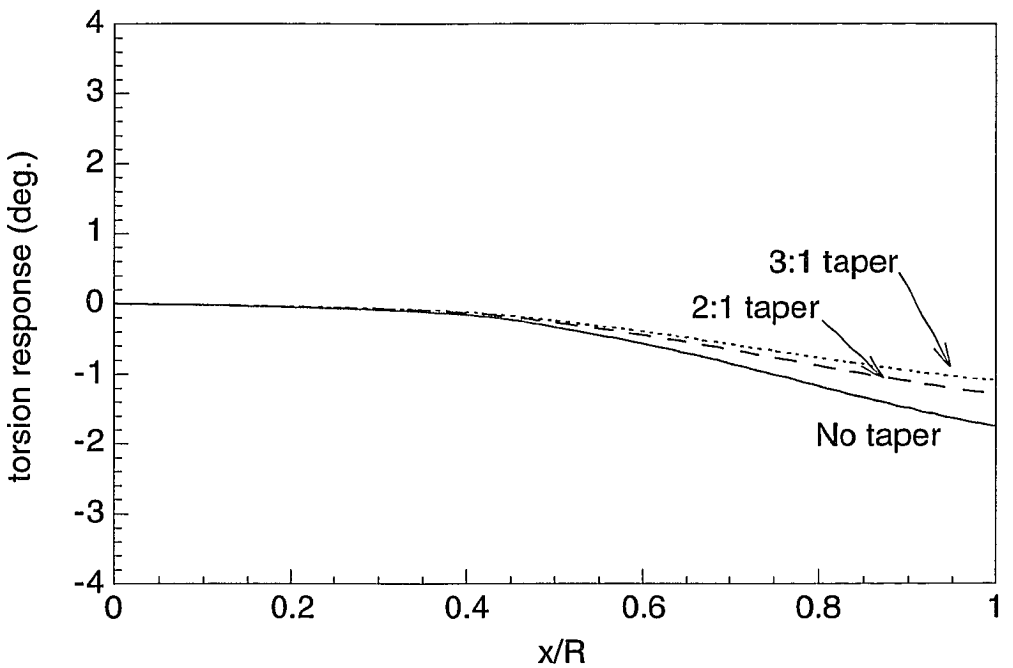

Figure 6.17: Torsion response along blade span ($V = 240$ knots, $C_T/\sigma = 0.01$)

Reproduced with permission of the copyright owner. Further reproduction prohibited without permission.

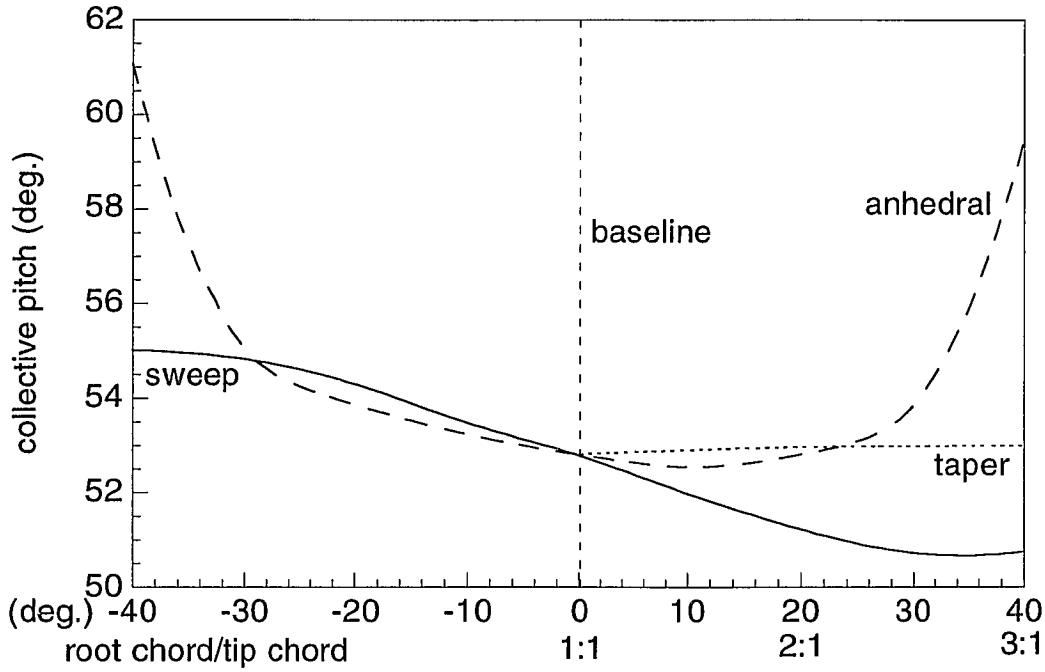

Figure 6.18: Collective pitch variation ($V = 240$ knots, $C_T/\sigma = 0.01$)

Reproduced with permission of the copyright owner. Further reproduction prohibited without permission.

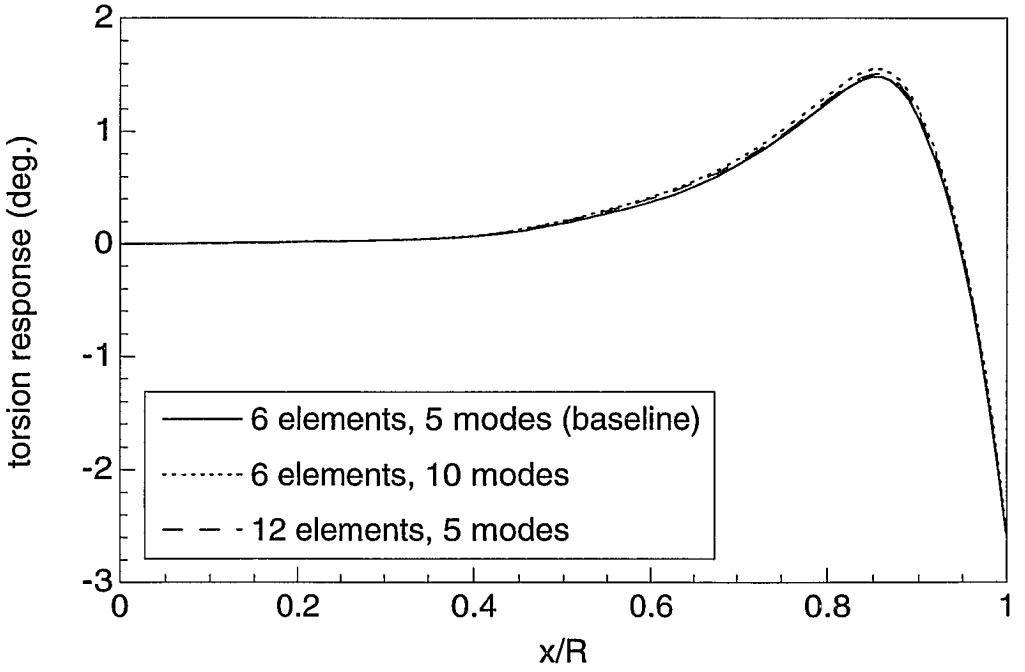

Figure 6.19: Convergence of blade torsional response for 30° forward sweep for blade tip (outboard 15% span, $C_T/\sigma = 0.01$, $V = 240$ knots) with increased number of spanwise finite elements and increased number of blade modes

Reproduced with permission of the copyright owner. Further reproduction prohibited without permission.

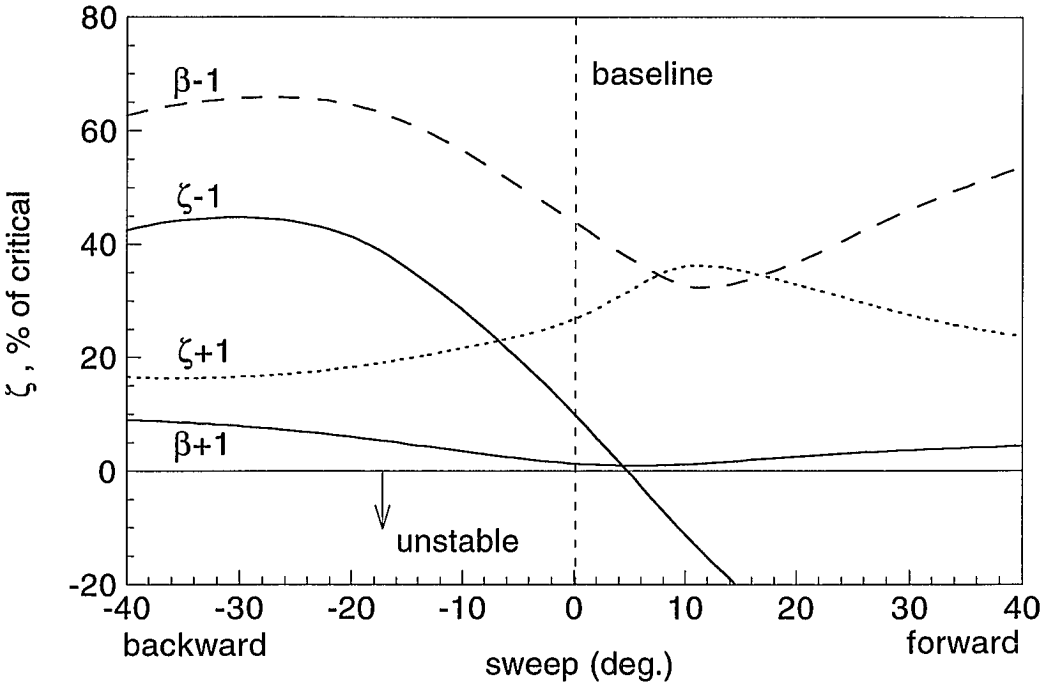

Figure 6.20: Effect of blade tip sweep (outboard 15% span) on blade damping (V = 240 knots, $C_T/\sigma = 0.01$)

Reproduced with permission of the copyright owner. Further reproduction prohibited without permission.

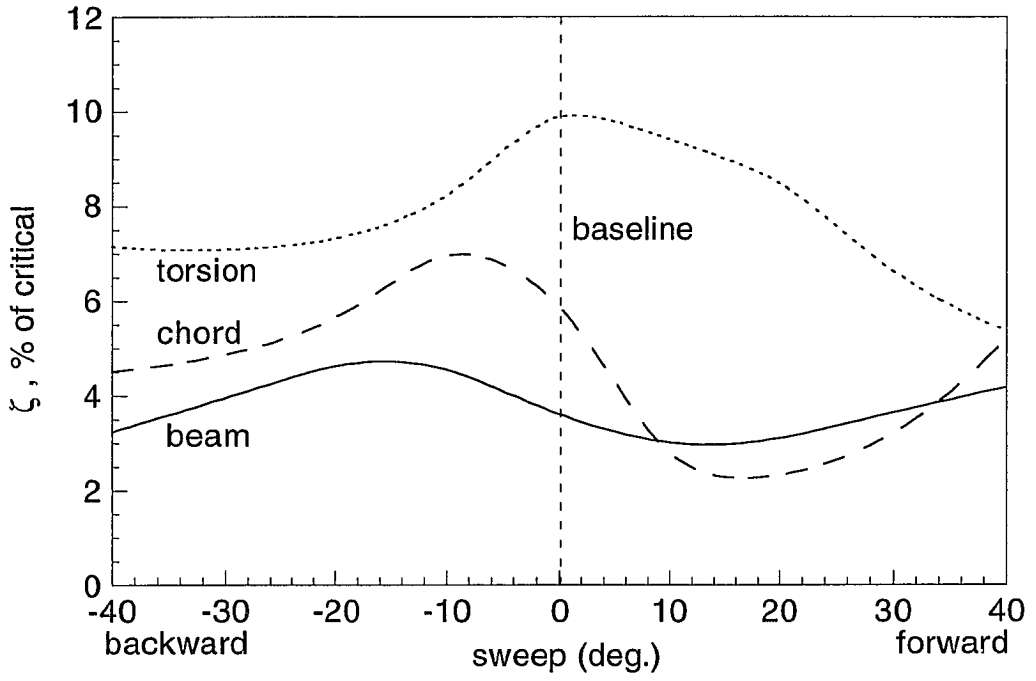

Figure 6.21: Effect of blade tip sweep (outboard 15% span) on wing damping (V = 240 knots, $C_T/\sigma = 0.01$)

Reproduced with permission of the copyright owner. Further reproduction prohibited without permission.

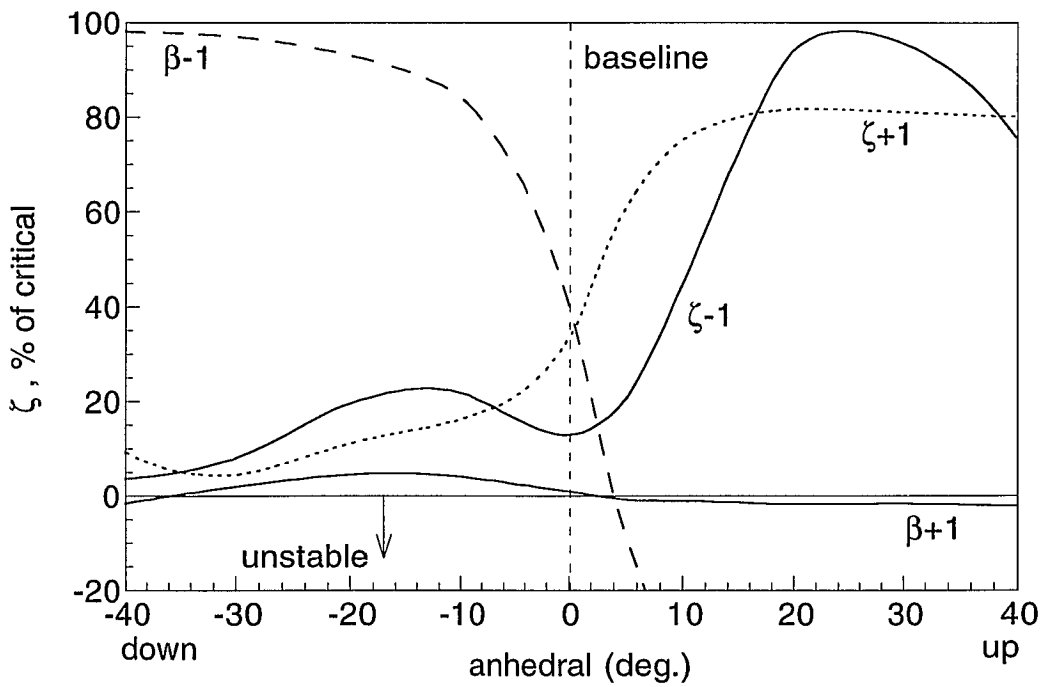

Figure 6.22: Effect of blade tip anhedral (outboard 15% span) on blade damping ($V = 240$ knots, $C_T/\sigma = 0.01$)

Reproduced with permission of the copyright owner. Further reproduction prohibited without permission.

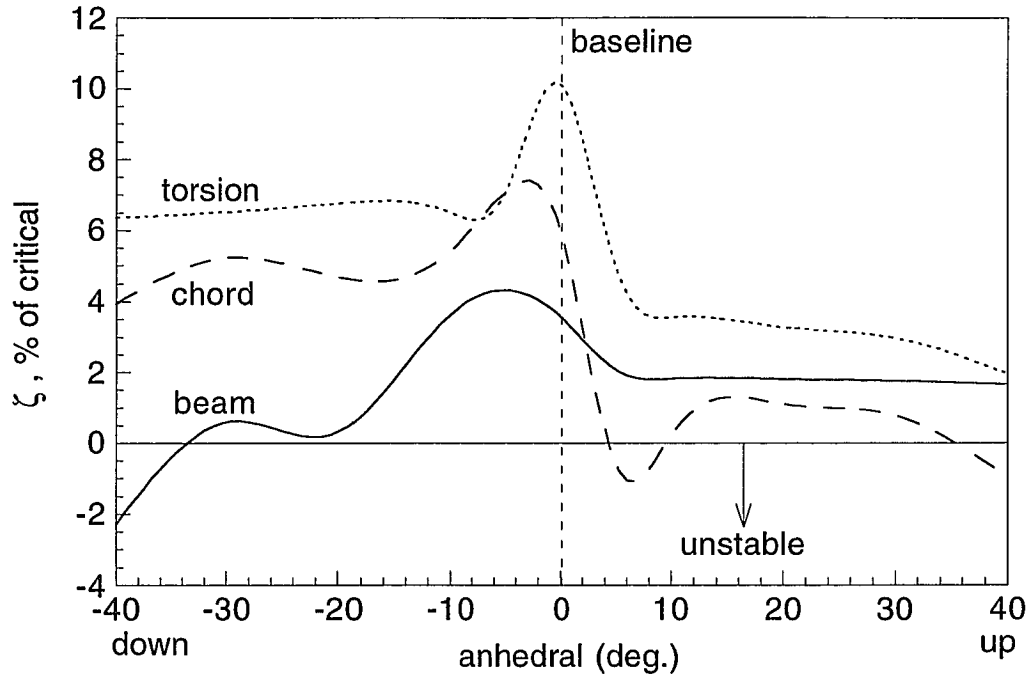

Figure 6.23: Effect of blade tip anhedral (outboard 15% span) on wing damping ($V = 240$ knots, $C_T/\sigma = 0.01$)

Reproduced with permission of the copyright owner. Further reproduction prohibited without permission.

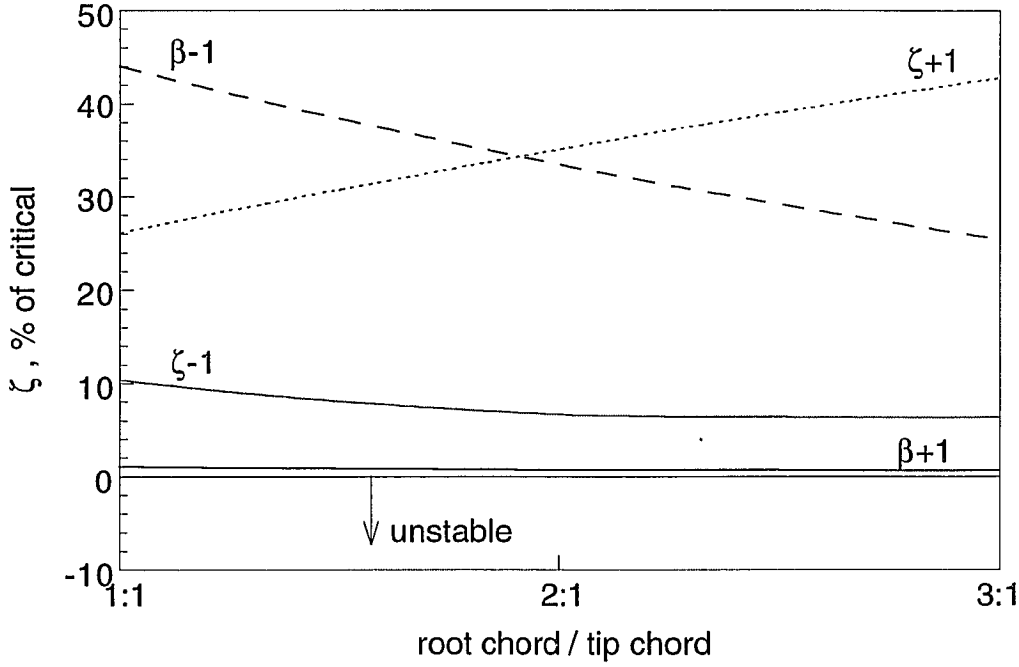

Figure 6.24: Effect of blade tip planform taper (outboard 15% span) on blade damping ($V = 240$ knots, $C_T/\sigma = 0.01$, constant thrust-weighted solidity)

Reproduced with permission of the copyright owner. Further reproduction prohibited without permission.

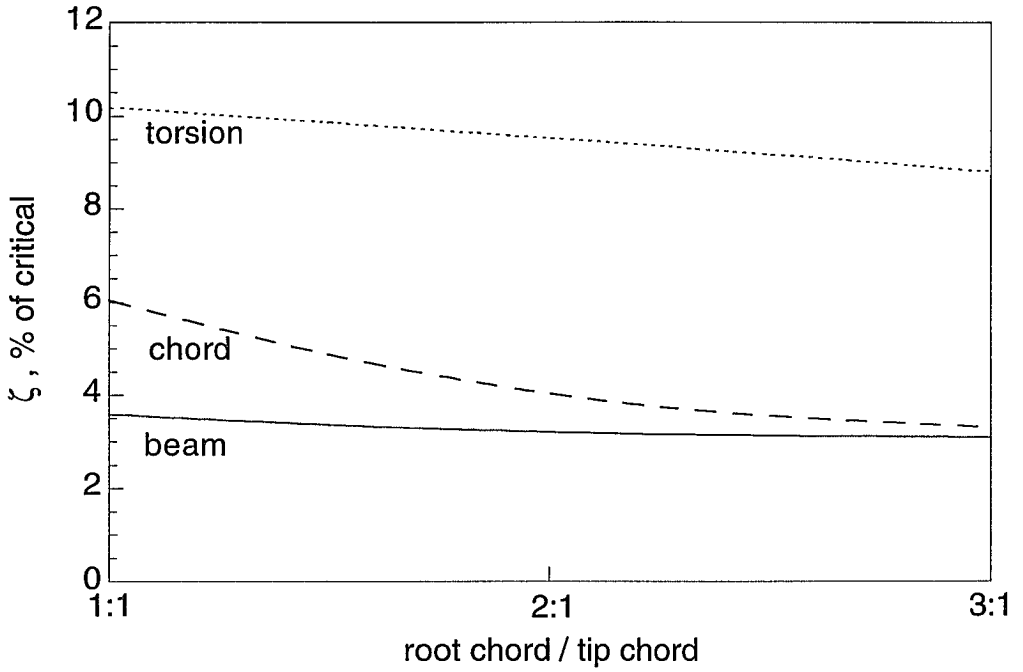

Figure 6.25: Effect of blade tip planform taper (outboard 15% span) on wing damping ($V = 240$ knots, $C_T/\sigma = 0.01$, constant thrust-weighted solidity)

Reproduced with permission of the copyright owner. Further reproduction prohibited without permission.

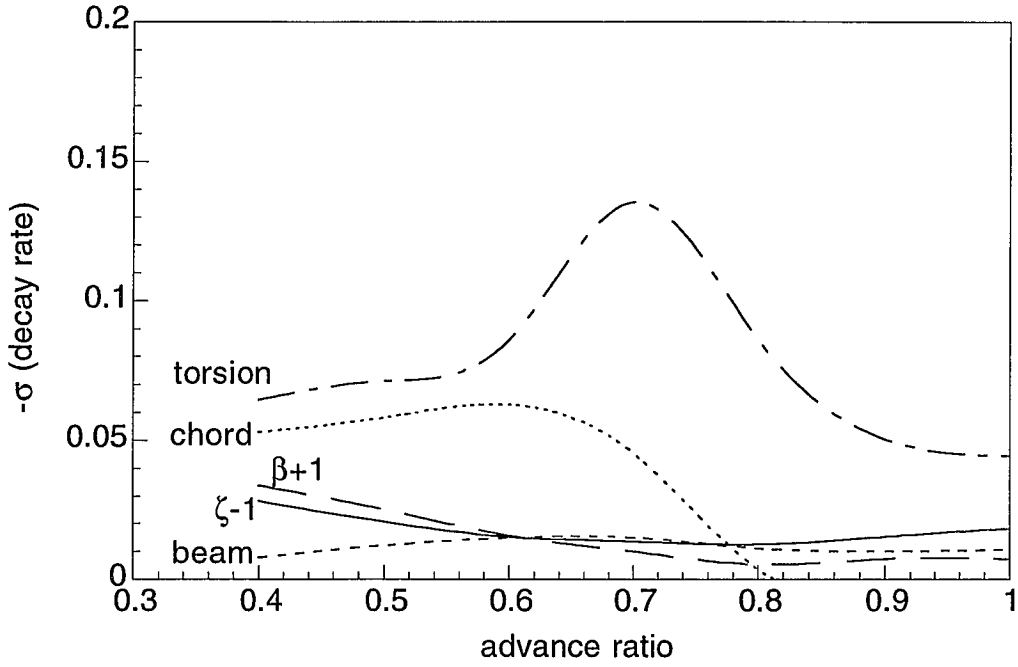

Figure 6.26: Effect of velocity on stability for straight blade ($C_T/\sigma = 0.01$)

Reproduced with permission of the copyright owner. Further reproduction prohibited without permission.

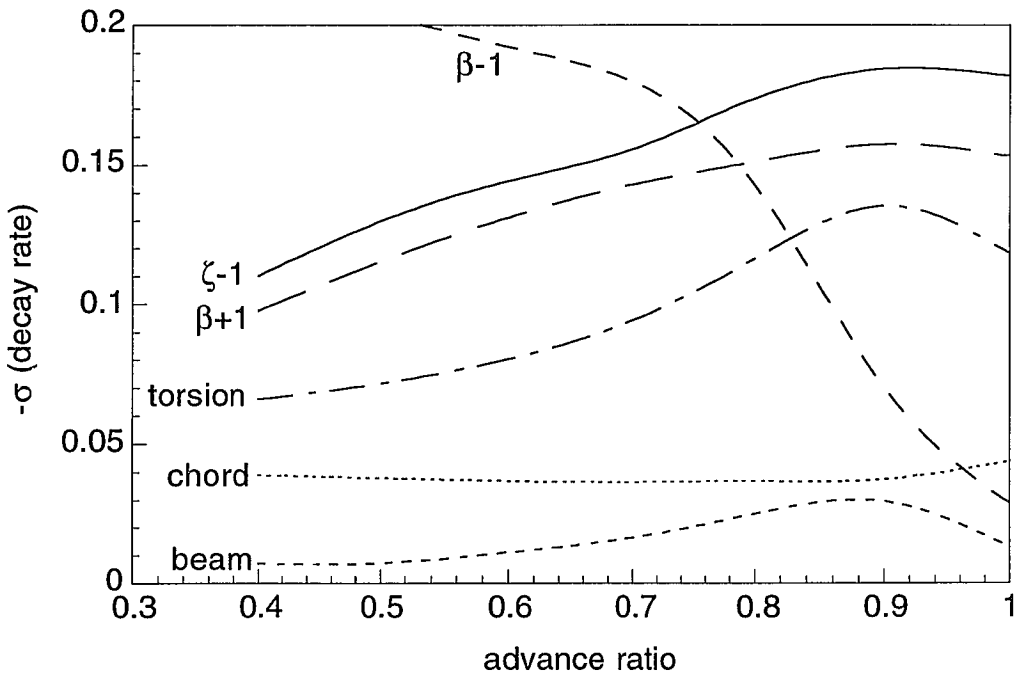

Figure 6.27: Effect of velocity on stability for 30° backward sweep for blade tip (outboard 15% span, $C_T/\sigma = 0.01$)

Reproduced with permission of the copyright owner. Further reproduction prohibited without permission.

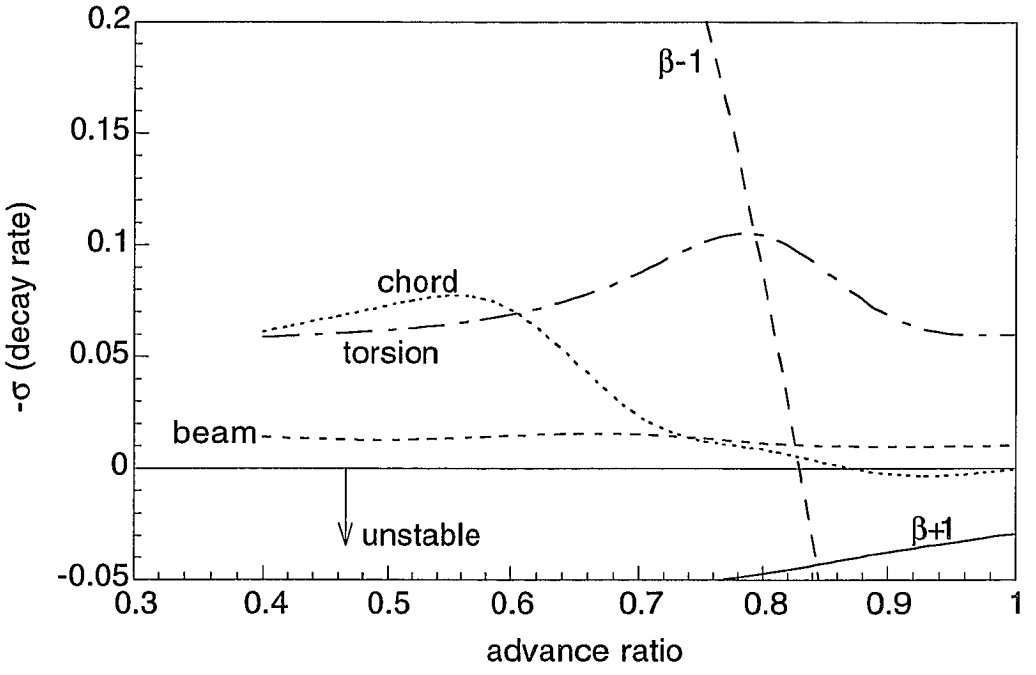

Figure 6.28: Effect of velocity on stability for 30° forward sweep for blade tip (outboard 15% span, $C_T/\sigma = 0.01$)

Reproduced with permission of the copyright owner. Further reproduction prohibited without permission.

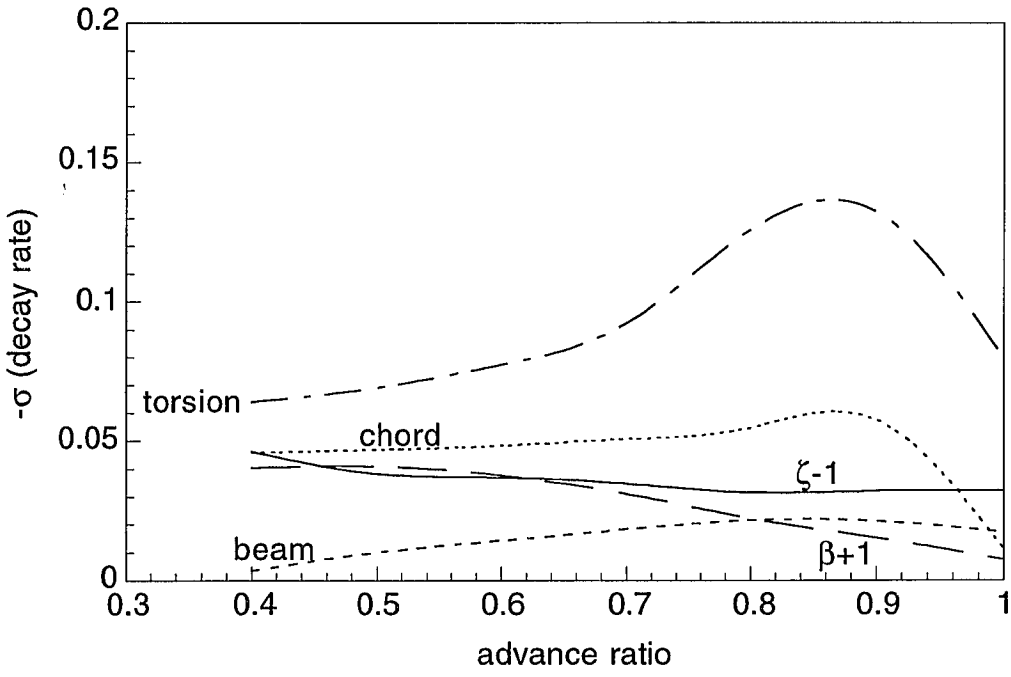

Figure 6.29: Effect of velocity on stability for 5° droop for blade tip (outboard 15% span, $C_T/\sigma = 0.01$)

Reproduced with permission of the copyright owner. Further reproduction prohibited without permission.

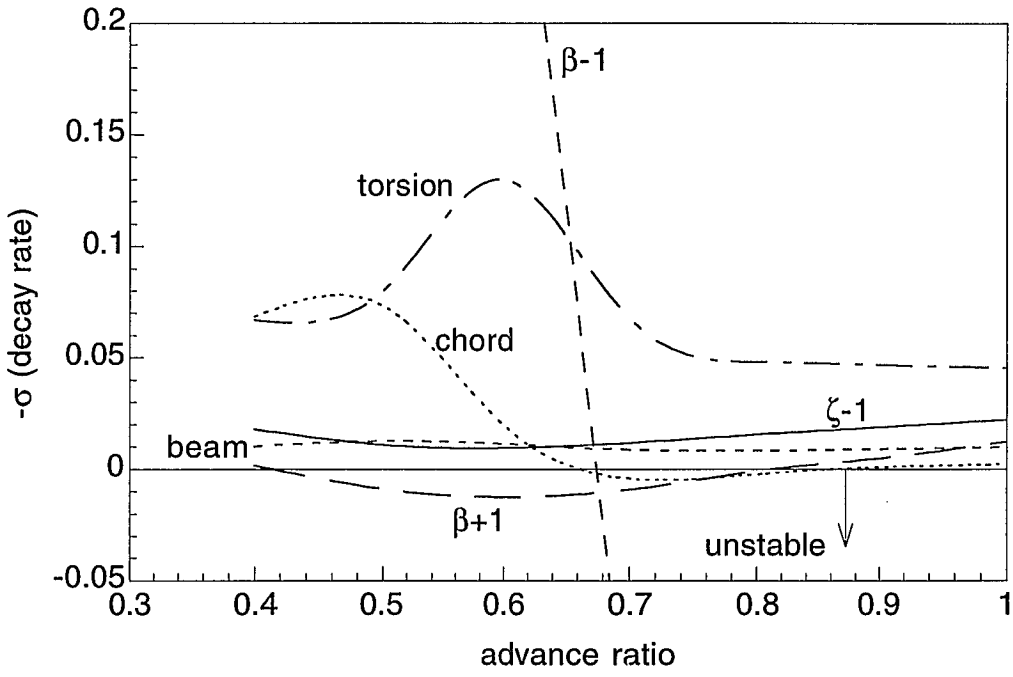

Figure 6.30: Effect of velocity on stability for 5° anhedral for blade tip (outboard 15% span, $C_T/\sigma = 0.01$)

Reproduced with permission of the copyright owner. Further reproduction prohibited without permission.

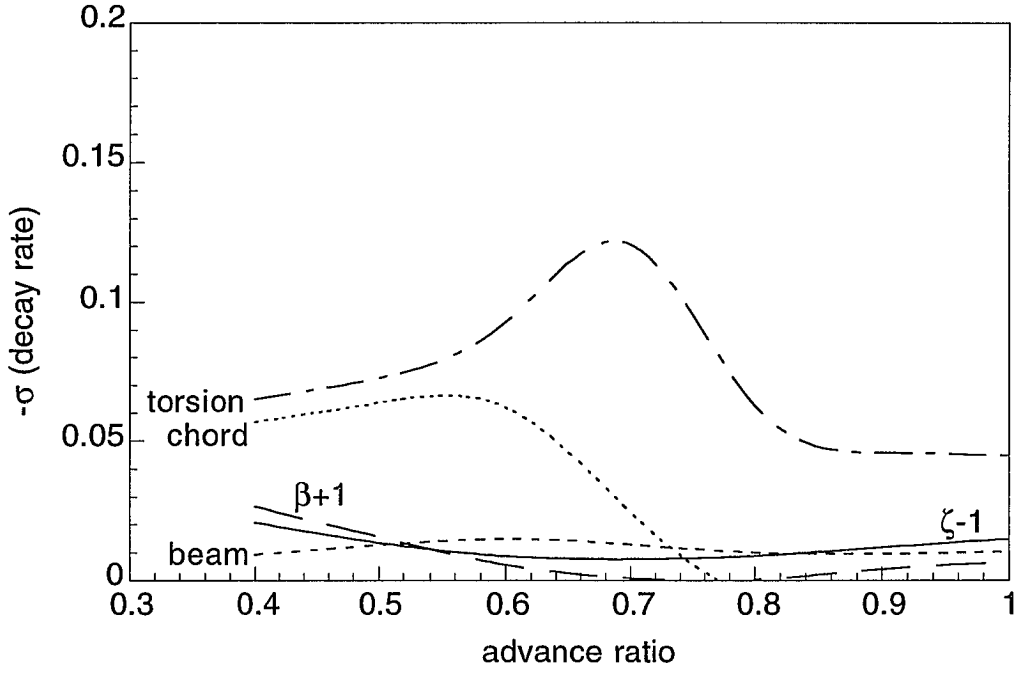

Figure 6.31: Effect of velocity on stability for 3:1 planform taper for blade tip (outboard 15% span, $C_T/\sigma = 0.01$, constant thrust-weighted solidity)

Reproduced with permission of the copyright owner. Further reproduction prohibited without permission.

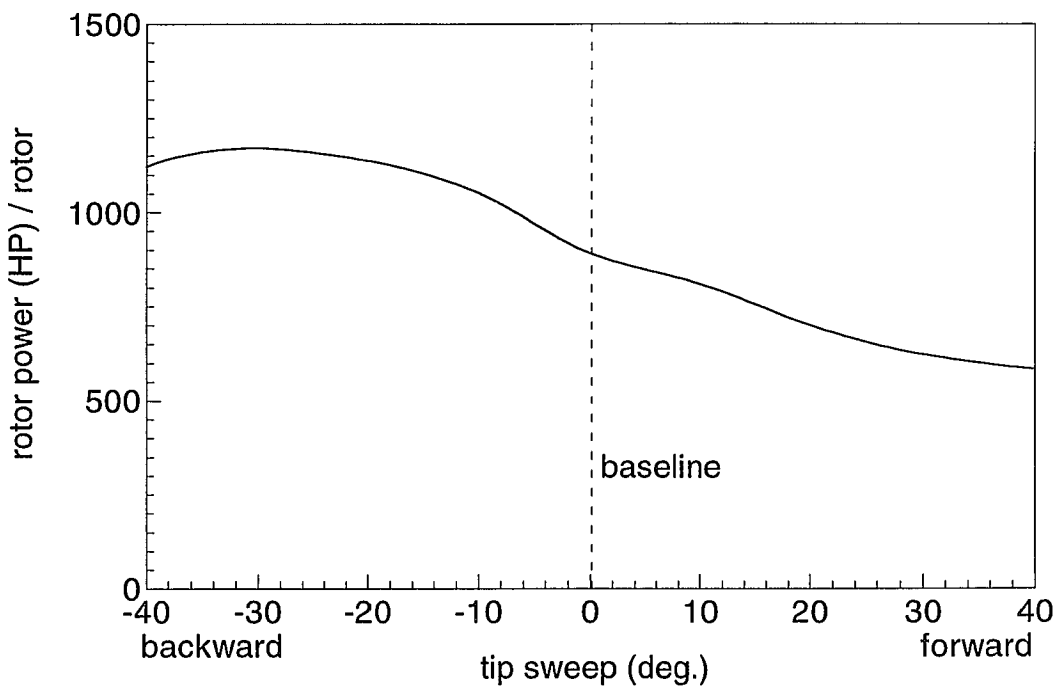

Figure 6.32: Rotor power requirements for outboard 15% tip sweep ($C_T/\sigma = 0.01$, $V = 240$ knots)

Reproduced with permission of the copyright owner. Further reproduction prohibited without permission.

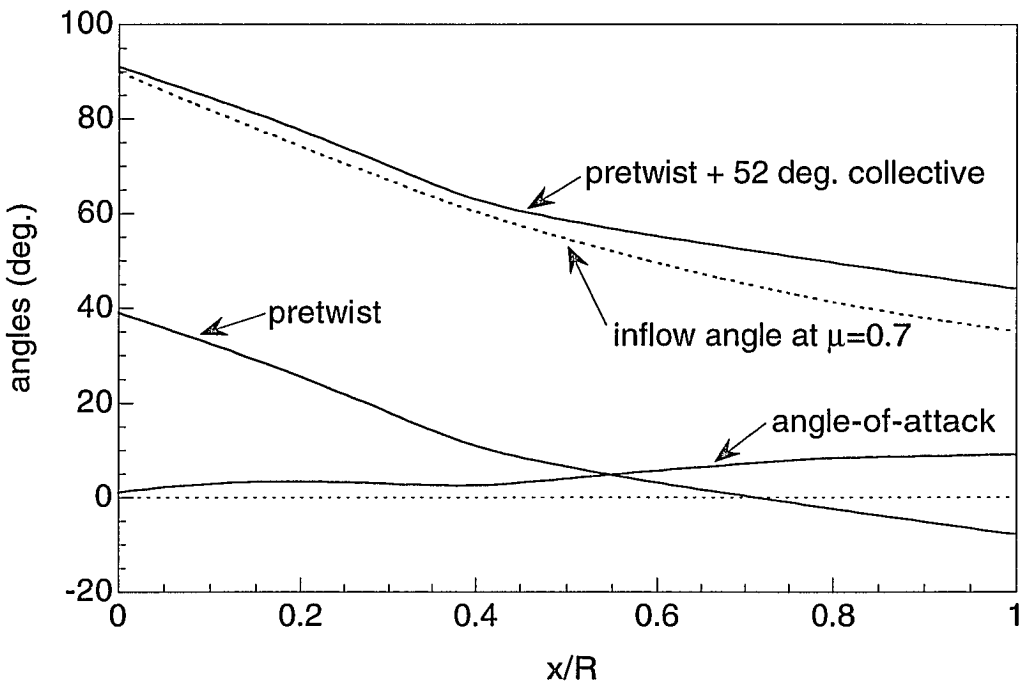

Figure 6.33: Variation of angle-of-attack along blade span for a straight blade configuration ($C_T/\sigma = 0.01$, $V = 240$ knots)

Reproduced with permission of the copyright owner. Further reproduction prohibited without permission.

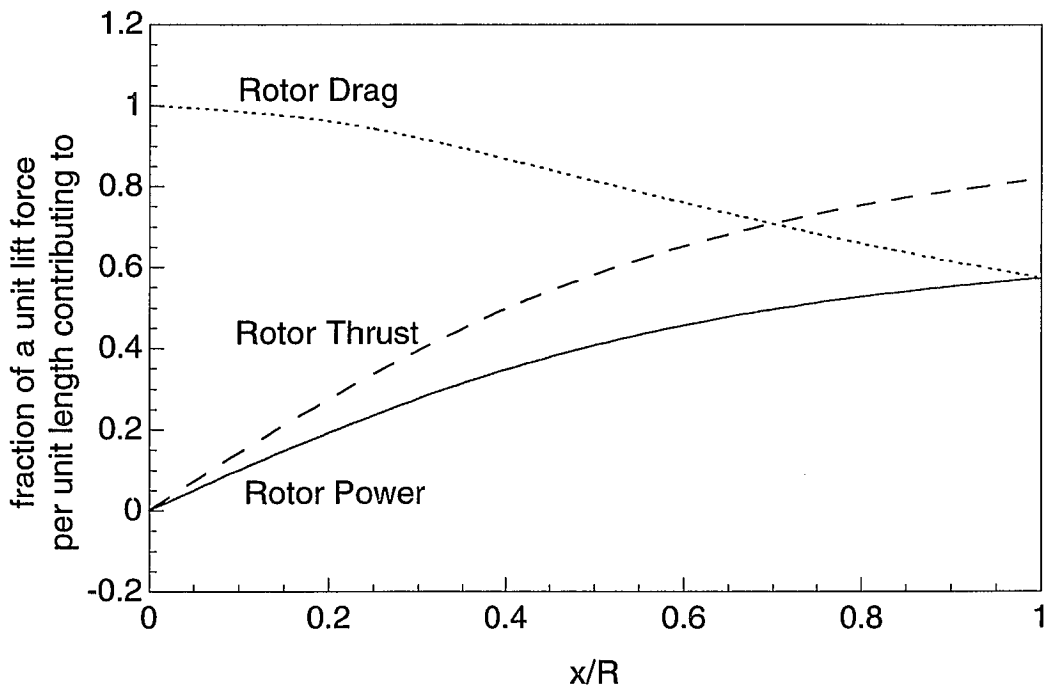

Figure 6.34: Contribution of a unit lift force to thrust, drag and power for a straight blade configuration ($C_T/\sigma = 0.01$, $V = 240$ knots)

Reproduced with permission of the copyright owner. Further reproduction prohibited without permission.

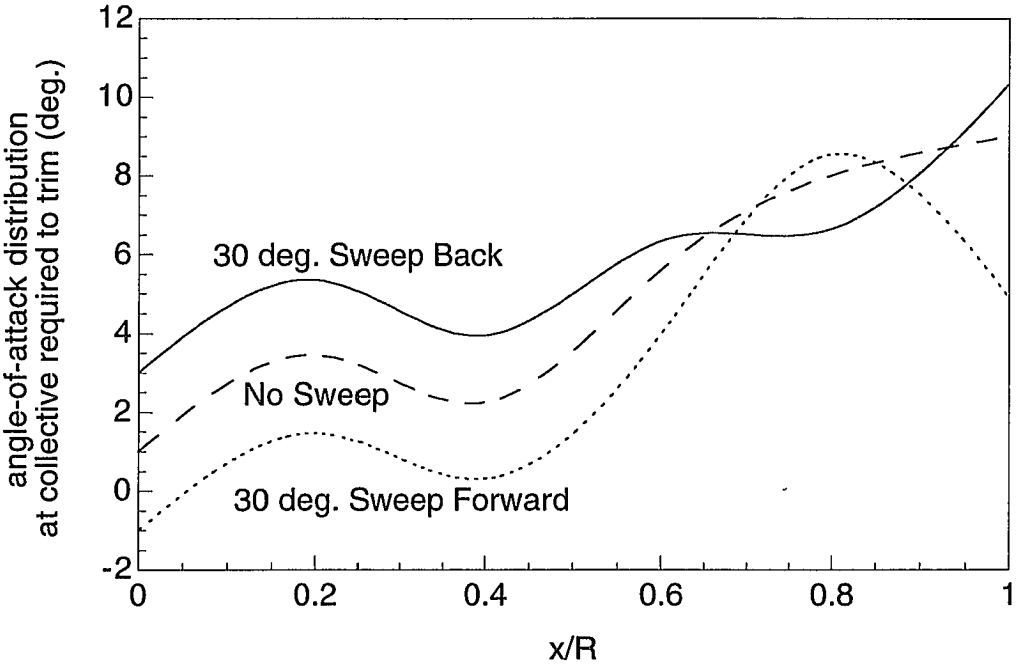

Figure 6.35: Variation of angle-of-attack along blade span for unswept blade, 30 deg. sweep forward for blade tip and 30 deg. sweep backward for blade tip ($C_T/\sigma = 0.01$, $V = 240$ knots)

Reproduced with permission of the copyright owner. Further reproduction prohibited without permission.

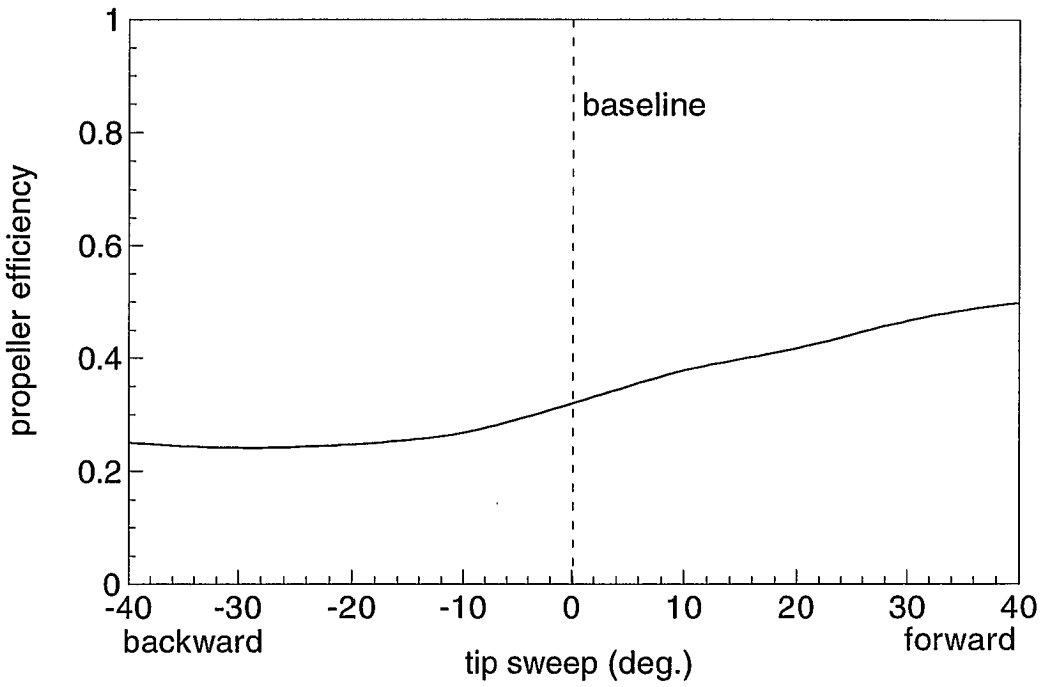

Figure 6.36: Propeller efficiency plot for outboard 15% tip sweep ($C_T/\sigma = 0.01$, $V = 240$ knots)

Reproduced with permission of the copyright owner. Further reproduction prohibited without permission.

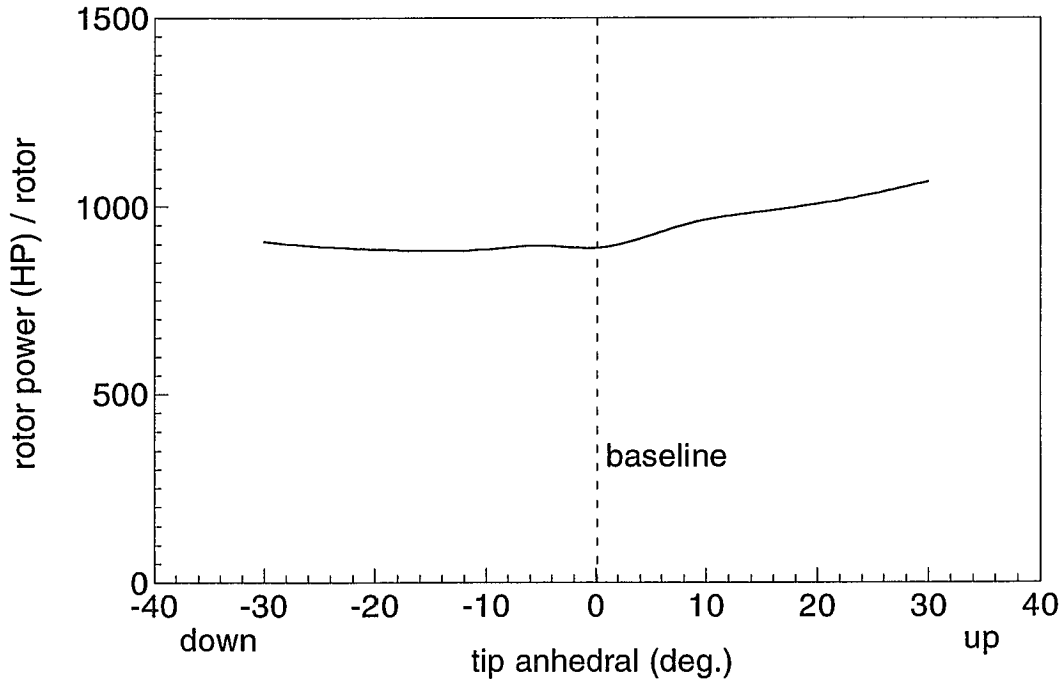

Figure 6.37: Rotor power requirements for outboard 15% tip anhedral ($C_T/\sigma = 0.01$, $V = 240$ knots)

Reproduced with permission of the copyright owner. Further reproduction prohibited without permission.

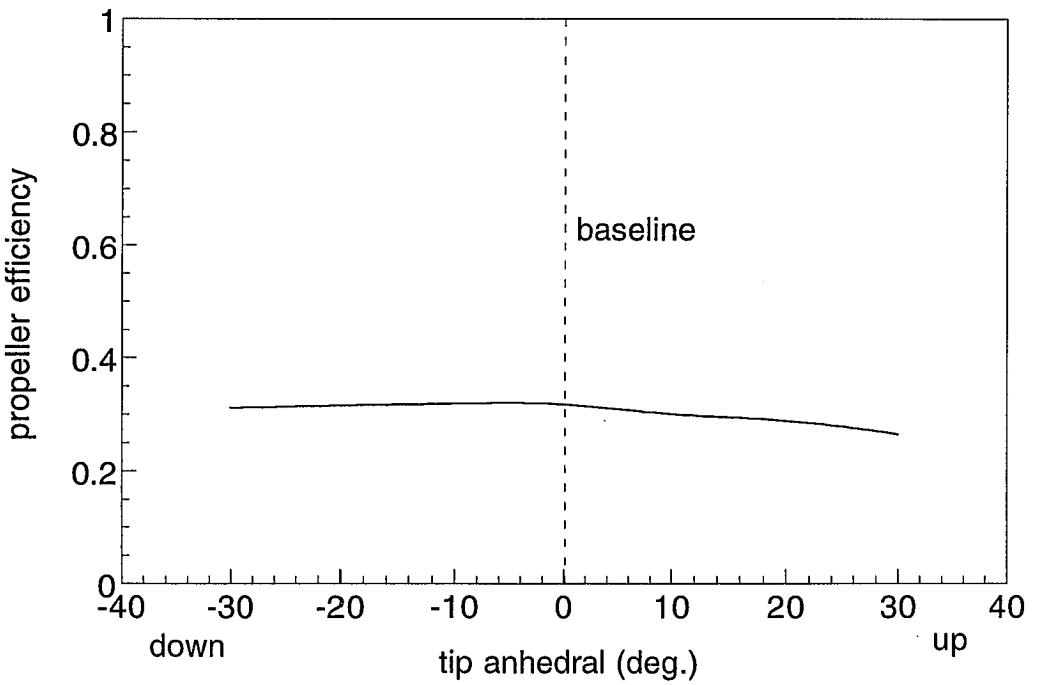

Figure 6.38: Propeller efficiency plot for outboard 15% tip anhedral ($C_T/\sigma = 0.01$, $V = 240$ knots)

Reproduced with permission of the copyright owner. Further reproduction prohibited without permission.

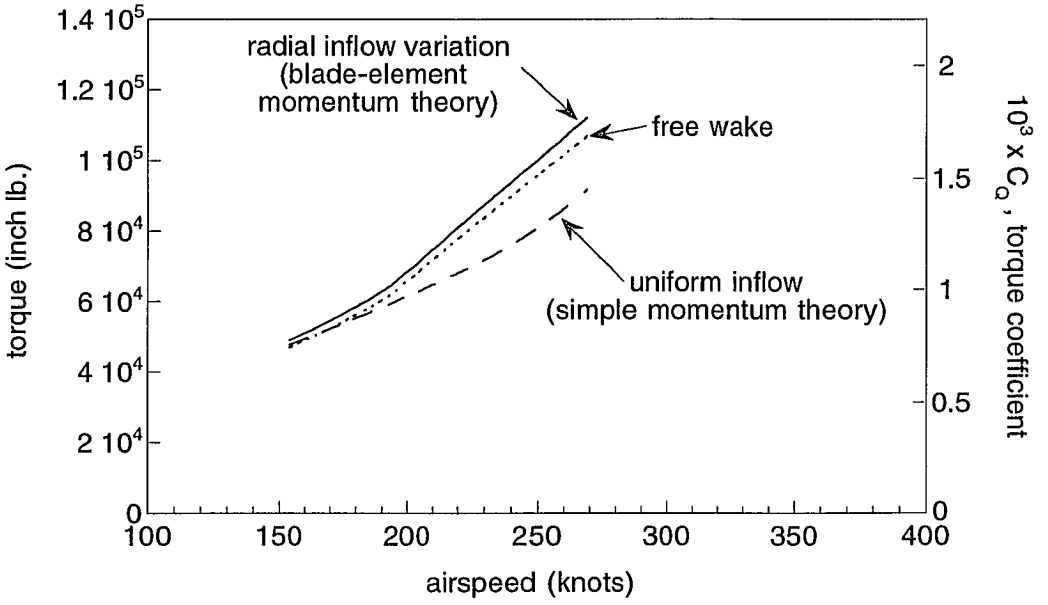

Figure 6.39: Comparison of predicted rotor torque using different inflow models ($C_T/\sigma = 0.01$)

Reproduced with permission of the copyright owner. Further reproduction prohibited without permission.

Chapter 7

Fuselage Modeling

The analysis presented in the previous chapters models only the right half of the tiltrotor configuration without any fuselage motion. The wing is assumed to be semi-span and is cantilevered at its root. The rotor system is mounted on a pylon on the wing (usually at the tip of the wing semi-span). This model can be used to study most of the commonly occuring instabilities, i.e., with the wing symmetric modes. The effects of fuselage motion and wing antisymmetric modes, however, cannot be studied using the model described previously. The present chapter deals with modeling the tiltrotor fuselage along with the full span of the wing as well as the two contra-rotating rotors at the wing tips. The fuselage and the wing are modeled using beam finite elements, similar to the procedure done for the rotor blades. For computational efficiency, the size of the problem is reduced by using the free vibration normal modes of the fuselage and the wing.

7.1 Wing Normal Mode Reduction

The inclusion of fuselage motion in the model is implemented as an option. For the case when the fuselage motion is neglected and only the semi-span wing is

Reproduced with permission of the copyright owner. Further reproduction prohibited without permission.

considered, the wing equations of motion, describing discrete wing displacements, are reduced to normal mode form.

7.1.1 Wing Free Vibration

As described in a previous chapter, the wing is modeled with 5 to 10 beam finite elements. The wing element stiffness and mass matrices are assembled into global wing matrices; the damping matrix is neglected for the calculation of free vibration. The appropriate boundary conditions for the cantilevered wing are applied; all six degrees of freedom associated with the wing root are constrained. The homogeneous system of equations is then solved to obtain the natural frequencies and eigenmodes of the wing. The wing equations are written as

$$\left[M_{ww}^{G}\right]^{S} \overset{**}{\hat{q}}{}_{w}^{G} + \left[K_{ww}^{G}\right]^{S} \hat{q}_{w}^{G} = 0 \tag{7.1}$$

where the superscript G refers to the global matrices and degrees-of-freedom. The superscript S indicates that only contributions from the structural formulation are included for the calculation of the system natural vibration characteristics. The system is then solved to obtain eigenvalues that are positive and real and eigenvectors that are real and orthogonal.

7.1.2 Implementation of Stability Analysis

The rotor and wing equations are written in discrete displacement form as

$$\begin{bmatrix} M_{rr} & M_{ri} & M_{rw} \\ M_{ir} & M_{ii} & M_{iw} \\ M_{wr} & M_{wi} & M_{ww} \end{bmatrix} \begin{Bmatrix} \overset{**}{\hat{q}}_r \\ \overset{**}{\hat{q}}_i \\ \overset{**}{\hat{q}}_w \end{Bmatrix} + \begin{bmatrix} C_{rr} & C_{ri} & C_{rw} \\ C_{ir} & C_{ii} & C_{iw} \\ C_{wr} & C_{wi} & C_{ww} \end{bmatrix} \begin{Bmatrix} \overset{*}{\hat{q}}_r \\ \overset{*}{\hat{q}}_i \\ \overset{*}{\hat{q}}_w \end{Bmatrix} + \begin{bmatrix} K_{rr} & K_{ri} & K_{rw} \\ K_{ir} & K_{ii} & K_{iw} \\ K_{wr} & K_{wi} & K_{ww} \end{bmatrix} \begin{Bmatrix} \hat{q}_r \\ \hat{q}_i \\ \hat{q}_w \end{Bmatrix} = 0 \tag{7.2}$$

Reproduced with permission of the copyright owner. Further reproduction prohibited without permission.

where $\hat{q}_r$, $\hat{q}_i$, and $\hat{q}_w$ are the discrete rotor, intermediate and wing displacements respectively. The intermediate set of displacements are defined as

$$\hat{q}_i = \begin{cases} \begin{Bmatrix} \beta_{GC} \\ \beta_{GS} \\ \phi_h \end{Bmatrix} \text{for windmilling condition} \\ \begin{Bmatrix} \beta_{GC} \\ \beta_{GS} \end{Bmatrix} \text{for powered condition} \end{cases} \tag{7.3}$$

The normal mode reduction is done at this stage of the analysis using the free vibration modes of the rotor blade and wing separately. The rotor displacements can be expressed as

$$\hat{q}_{r_{n\times 1}} = [\Phi]_{r_{n\times m}} \hat{p}_{r_{m\times 1}} \tag{7.4}$$

where $\hat{p}_r$ is the rotor modal displacement vector and Φ_r is the rotor normal mode matrix. Similarly, the wing displacements can be written as

$$\hat{q}_{w_{j\times 1}} = [\Phi]_{w_{j\times k}} \hat{p}_{w_{k\times 1}} \tag{7.5}$$

where $\hat{p}_w$ is the wing modal displacement vector and Φ_w is the wing normal mode matrix. Rewriting the rotor and wing discrete displacements in terms of their modal displacements and multiplying the first and third row partitions of the system matrices by the transpose of the rotor and wing normal mode matrices respectively, the system equations become

$$\begin{bmatrix} \bar{M}_{rr} & \bar{M}_{ri} & \bar{M}_{rw} \\ \bar{M}_{ir} & M_{ii} & \bar{M}_{iw} \\ \bar{M}_{wr} & \bar{M}_{wi} & \bar{M}_{ww} \end{bmatrix} \begin{Bmatrix} \overset{\star\star}{\hat{p}}_r \\ \overset{\star\star}{\hat{q}}_i \\ \overset{\star\star}{\hat{p}}_w \end{Bmatrix} + \begin{bmatrix} \bar{C}_{rr} & \bar{C}_{ri} & \bar{C}_{rw} \\ \bar{C}_{ir} & C_{ii} & \bar{C}_{iw} \\ \bar{C}_{wr} & \bar{C}_{wi} & \bar{C}_{ww} \end{bmatrix} \begin{Bmatrix} \overset{\star}{\hat{p}}_r \\ \overset{\star}{\hat{q}}_i \\ \overset{\star}{\hat{p}}_w \end{Bmatrix}$$
$$+ \begin{bmatrix} \bar{K}_{rr} & \bar{K}_{ri} & \bar{K}_{rw} \\ \bar{K}_{ir} & K_{ii} & \bar{K}_{iw} \\ \bar{K}_{wr} & \bar{K}_{wi} & \bar{K}_{ww} \end{bmatrix} \begin{Bmatrix} \hat{p}_r \\ \hat{q}_i \\ \hat{p}_w \end{Bmatrix} = 0 \tag{7.6}$$

Reproduced with permission of the copyright owner. Further reproduction prohibited without permission.

where

$$
\begin{aligned}
\bar{M}_{rr} &= [\Phi]_r^T M_{rr} [\Phi]_r \\
\bar{M}_{ri} &= [\Phi]_r^T M_{ri} \\
\bar{M}_{rw} &= [\Phi]_r^T M_{rw} [\Phi]_w \\
\bar{M}_{ir} &= M_{ir} [\Phi]_r \\
\bar{M}_{iw} &= M_{iw} [\Phi]_w \\
\bar{M}_{wr} &= [\Phi]_w^T M_{wr} [\Phi]_r \\
\bar{M}_{wi} &= [\Phi]_w^T M_{wi} \\
\bar{M}_{ww} &= [\Phi]_w^T M_{ww} [\Phi]_w
\end{aligned}
\tag{7.7}
$$

The system of equations obtained from the normal mode reduction is much smaller than the original system. This system is solved using standard eigenanalysis techniques to obtain the stability eigenvalues and eigenvectors. The identification of the stability eigenmodes is also easier after the normal mode reduction since the amplitude of each wing mode is easily determined from the eigenvector.

The discrete displacements for the wing typically number about 30 to 50. After the normal mode reduction is performed, the number of wing modes needed to obtain comparable accuracy as the full finite element solution is about 5 to 10 modes. This obviously represents a major saving in computational expense.

7.2 Implementation of Fuselage Model

The fuselage is modeled as a beam in the longitudinal direction. Although the fuselage is, in reality, a shell-like structure with variations in structural and inertial

Reproduced with permission of the copyright owner. Further reproduction prohibited without permission.

properties in all three dimensions, it can be modeled as a beam-like structure for the purpose of aeroelastic analysis. The intent in including fuselage motion in this analysis is to simulate wing symmetric and antisymmetric motion for stability calculations; this motion is adequately provided by the present model. Beam finite elements similar to those used for the rotor blade and wing are used to model the fuselage properties. Since a finite element model is used, detailed modeling of the empennage can be included at a later stage if necessary.

A user-specified number of finite elements is used in the model. The only constraint is that the wing elastic axis attachment point on the fuselage coincides with the junction of two fuselage elements. A specified number of finite elements is used on the fuselage, fore and aft of the wing elastic axis attachment point. A schematic of the fuselage and wing modeled by using beam finite elements is shown in Figure 7.1. Effects of wing sweep, anhedral and pretwist are included in the model. Aerodynamic effects of the fuselage are neglected in the present implementation, although those effects could be included easily.

The fuselage-and-wing model is used first to obtain the natural vibration characteristics of the fuselage and wing combination. These natural vibration modes are then used in the stability analysis by performing a normal mode reduction of the problem. A twin-rotor model with one rotor located on each wing (usually at each wing tip), is assembled onto the fuselage model. The equations are then solved to obtain the stability of the complete system.

Reproduced with permission of the copyright owner. Further reproduction prohibited without permission.

7.2.1 Free Vibration Analysis

For the free vibration analysis, the fuselage is considered as a free-free beam spanning from the aft section to the fore section. The wing is considered in two parts; the right wing semi-span is modeled as done previously and its root is attached to the junction of two specified fuselage elements. The left wing semi-span is modeled as a mirror-image about the fuselage longitudinal axis, of the right semi-span in terms of structural, inertial and aerodynamic properties and is attached to the fuselage at the same junction. The individual wing and fuselage element matrices are calculated and assembled into a fuselage-and-wing global matrix. The global displacement vector for a simple example is shown in Figure 7.2. The example has two elements modeling the semi-span of the wing and two elements modeling the fuselage, one forward and the second aft of the wing attachment point; the 15 degree-of-freedom element described in a previous chapter is used in the model. For the wing, the axial displacement u is defined as positive to the right in the lateral direction. Similarly for the fuselage, the axial displacement is defined as positive forward in the longitudinal direction. The other displacements for the fuselage elements are defined likewise. At the attachment point of the wing (with no sweep or droop) to the fuselage, the following constraints are imposed:

Fuselage dof		Wing dof
u	$=$	v
v	$=$	$-u$
w	$=$	w

Reproduced with permission of the copyright owner. Further reproduction prohibited without permission.

$$
\begin{aligned}
v' &= v' \\
w' &= \hat{\phi} \\
\hat{\phi} &= -w'
\end{aligned} \tag{7.8}
$$

The assembled equations are solved for their natural vibration characteristics similar to that done for the cantilevered wing. The homogeneous system of equations is written as

$$
\left[M_{ff}^{G}\right]^{S} \ddot{\hat{q}}_{f/w}^{G} + \left[K_{ff}^{G}\right]^{S} \hat{q}_{f/w}^{G} = 0 \tag{7.9}
$$

and the eigenvalues and eigenmodes are obtained. The normal mode matrix for the fuselage/wing is denoted as Φ_f. Since the free vibration analysis is performed on a free body (wing attached to a free-free fuselage), the normal mode matrix contains rigid body modes as well as elastic deflection modes. Since each element is allowed to deform in three translational directions as well as three rotations, there are six, usually coupled, rigid body modes present in the normal mode matrix.

7.2.2 Stability Analysis

The stability analysis and implementation for the complete tiltrotor model is more complex than for the single rotor and cantilevered wing combination. The assembly of the equations for the complete system includes the equations for the wing (full-span) and the fuselage as well as the coupled rotor/body equations for the two contrarotating rotors.

Reproduced with permission of the copyright owner. Further reproduction prohibited without permission.

The system equations are written in discrete displacement form as shown below.

$$\begin{bmatrix} M_{r_1r_1} & M_{r_1i_1} & M_{r_1w_1} & 0 & 0 & 0 & 0 \\ M_{i_1r_1} & M_{i_1i_1} & M_{i_1w_1} & 0 & 0 & 0 & 0 \\ M_{w_1r_1} & M_{w_1i_1} & M_{w_1w_1} & M_{w_1f} & 0 & 0 & 0 \\ 0 & 0 & M_{fw_1} & M_{ff} & M_{fw_2} & 0 & 0 \\ 0 & 0 & 0 & M_{w_2f} & M_{w_2w_2} & M_{w_2i_2} & M_{w_2r_2} \\ 0 & 0 & 0 & 0 & M_{i_2w_2} & M_{i_2i_2} & M_{i_2r_2} \\ 0 & 0 & 0 & 0 & M_{r_2w_2} & M_{r_2i_2} & M_{r_2r_2} \end{bmatrix} \begin{Bmatrix} \overset{\star\star}{\hat{q}}_{r_1} \\ \overset{\star\star}{\hat{q}}_{i_1} \\ \overset{\star\star}{\hat{q}}_{w_1} \\ \overset{\star\star}{\hat{q}}_{f} \\ \overset{\star\star}{\hat{q}}_{w_2} \\ \overset{\star\star}{\hat{q}}_{i_2} \\ \overset{\star\star}{\hat{q}}_{r_2} \end{Bmatrix}$$

$$+C\,\overset{\star}{\hat{Q}} + K\hat{Q} \;=\; 0 \tag{7.10}$$

where the subscripts 1 and 2 refer to the right and left rotor/wing respectively. M, C and K refer to the mass, damping and stiffness matrices respectively. The C and K matrices are partitioned in the same manner as the M matrix is. The vector $\hat{q}_f$ contains the degrees-of-freedom associated with the wing root attachment to the fuselage.

$$\hat{q}_{i_1} = \begin{Bmatrix} \beta_{GC_1} \\ \beta_{GS_1} \\ \phi_{h_1} \end{Bmatrix} \text{for windmilling condition}$$

$$\begin{Bmatrix} \beta_{GC_1} \\ \beta_{GS_1} \end{Bmatrix} \text{for powered condition} \tag{7.11}$$

and

$$\hat{q}_{i_2} = \begin{Bmatrix} \phi_{h_2} \\ \beta_{GS_2} \\ \beta_{GC_2} \end{Bmatrix} \text{for windmilling condition}$$

$$\begin{Bmatrix} \beta_{GS_2} \\ \beta_{GC_2} \end{Bmatrix} \text{for powered condition} \tag{7.12}$$

Similarly, $\hat{q}_{r_2}$ consists of the rotor displacements arranged in the reverse order as compared to those in $\hat{q}_{r_1}$.

Reproduced with permission of the copyright owner. Further reproduction prohibited without permission.

A normal mode reduction is performed on this large system using the normal modes for the rotor and the fuselage/wing. The rotor displacements can be expressed as

$$\hat{q}_{r_1 n\times 1} = [\Phi]_{r_{n\times m}} \hat{p}_{r_1 m\times 1} \tag{7.13}$$

$$\hat{q}_{r_2 n\times 1} = [\Phi]_{r_{n\times m}} \hat{p}_{r_2 m\times 1} \tag{7.14}$$

where Φ_r is the normal mode matrix for the rotor. Similarly, the fuselage/wing displacements can be written as

$$\left\{ \begin{array}{c} \hat{q}_{w_1} \\ \hat{q}_f \\ \hat{q}_{w_2} \end{array} \right\}_{j\times 1} = [\Phi]_{f_{j\times k}} \hat{p}_{f_{k\times 1}} \tag{7.15}$$

where $\hat{p}_f$ is the fuselage/wing modal displacement vector and Φ_f is the fuselage/wing normal mode matrix. Rewriting the system of equations in terms of these modal displacement vectors, the equations become

$$\left[\begin{array}{ccccc} \bar{M}_{r_1r_1} & \bar{M}_{r_1i_1} & \bar{M}_{r_1f} & 0 & 0 \\ \bar{M}_{i_1r_1} & M_{i_1i_1} & \bar{M}_{i_1f} & 0 & 0 \\ \bar{M}_{fr_1} & \bar{M}_{fi_1} & \bar{M}_{ff} & \bar{M}_{fi_2} & \bar{M}_{fr_2} \\ 0 & 0 & \bar{M}_{i_2f} & M_{i_2i_2} & \bar{M}_{i_2r_2} \\ 0 & 0 & \bar{M}_{r_2f} & \bar{M}_{r_2i_2} & \bar{M}_{r_2r_2} \end{array} \right] \left\{ \begin{array}{c} \overset{\star\star}{\hat{p}}_{r_1} \\ \overset{\star\star}{\hat{q}}_{i_1} \\ \overset{\star\star}{\hat{p}}_f \\ \overset{\star\star}{\hat{q}}_{i_2} \\ \overset{\star\star}{\hat{p}}_{r_2} \end{array} \right\} + C' \overset{\star}{\hat{Q}}' + K'\hat{Q}' = 0 \tag{7.16}$$

where

$$\bar{M}_{r_1r_1} = [\Phi]_r^T M_{r_1r_1} [\Phi]_r$$

$$\bar{M}_{r_1i_1} = [\Phi]_r^T M_{r_1i_1}$$

$$\bar{M}_{r_1f} = [\Phi]_r^T \left[\begin{array}{ccc} M_{r_1w_1} & M_{r_1f} & M_{r_1w_2} \end{array} \right] [\Phi]_f$$

$$\bar{M}_{i_1r_1} = M_{i_1r_1} [\Phi]_r$$

Reproduced with permission of the copyright owner. Further reproduction prohibited without permission.

$$
\begin{aligned}
\bar{M}_{i_1 f} &= \left[\begin{array}{ccc} M_{i_1 w_1} & M_{i_1 f} & M_{i_1 w_2} \end{array} \right] [\Phi]_f \\
\bar{M}_{f r_1} &= [\Phi]_f^T \left\{ \begin{array}{c} M_{w_1 r_1} \\ M_{f r_1} \\ M_{w_2 r_1} \end{array} \right\} [\Phi]_r \\
\bar{M}_{f i_1} &= [\Phi]_f^T \left\{ \begin{array}{c} M_{w_1 i_1} \\ M_{f i_1} \\ M_{w_2 i_1} \end{array} \right\} \\
\bar{M}_{ff} &= [\Phi]_f^T \left[\begin{array}{ccc} M_{w_1 w_1} & M_{w_1 f} & M_{w_1 w_2} \\ M_{f w_1} & M_{ff} & M_{f w_2} \\ M_{w_2 w_1} & M_{w_2 f} & M_{w_2 w_2} \end{array} \right] [\Phi]_f
\end{aligned}
\tag{7.17}
$$

and

$$
\hat{Q}' = \left\{ \begin{array}{c} \hat{p}_{r_1} \\ \hat{q}_{i_1} \\ \hat{p}_f \\ \hat{q}_{i_2} \\ \hat{p}_{r_2} \end{array} \right\} \tag{7.18}
$$

The full mass matrix given in Eqn.7.16 is referred to as M'. The matrices C' and K' are expressed, similarly, in terms of the partitioned C and K matrices respectively.

7.2.3 Twin-Rotor Modeling

The twin-rotor model for the contrarotating rotors is implemented using the rotor analysis performed on the right rotor alone. The tiltrotor is assumed to be in straight, level flight where the two rotors face exactly the same operating conditions; the trim conditions for the two rotors are hence identical. The stability of the two rotors, however, depends on the rotor forcing as well as the wing/fuselage forcing on the rotors. The inclusion of wing antisymmetric modes in the model creates differing forcing functions on the right and left rotors; these modes could, hence, be important in the prediction of instabilities.

Figure 7.3 shows the coordinate system used for the derivation of the equations

Reproduced with permission of the copyright owner. Further reproduction prohibited without permission.

of motion for the right rotor system. The equations are rotor/body coupled equations derived by using a right-handed coordinate system. The left rotor operates with a rotational speed in the opposite direction as that of the right rotor. Using a left-handed coordinate system for the left rotor by reversing the direction of the y axis, but maintaining the x and z axes of the right-handed system, the rotor system could be described by using the same equations as those used for the right rotor system (in the right-handed coordinate system). This powerful, yet simple, method was suggested by Johnson [38]. As a result of this simplification, the left rotor equations are valid in the left-handed coordinate system seen in Figure 7.3. The rotor and hub equations for the left rotor can be implemented, as such, in the analysis. The reversal of the y axis for the left rotor, however, changes one hub force direction and two hub moment directions (since ζ_h and ϕ_h are also reversed). The assembly of these equations into the global matrices, therefore, needs to account for changes in these variables. The motion of the left wing-tip is coupled to the left rotor hub by the six wing-tip nodal displacements which correspond to six of the hub degrees. For a straight wing, the constraint equations are

Wing dof		Left rotor hub dof
u	$=$	$-y_h$
v	$=$	$-x_h$
v'	$=$	$-\zeta_h$
w	$=$	z_h
w'	$=$	ϕ_h

Reproduced with permission of the copyright owner. Further reproduction prohibited without permission.

$$\hat{\phi} = -\alpha_h \tag{7.19}$$

The left rotor system can, in this way, be modeled by using the rotor equations of the right rotor. This procedure is far more difficult to implement than is apparent from this description.

The stability analysis procedure used in this stage is similar to that described in Chapter 4. The system equations are transformed into first-order form for eigenanalysis. The system state vector, in this case, is expressed as

$$\hat{Y} = \left\{ \begin{array}{c} \overset{\star}{\hat{p}}_{r_1} \\ \overset{\star}{\hat{q}}_{i_1} \\ \overset{\star}{\hat{p}}_{f} \\ \overset{\star}{\hat{q}}_{i_2} \\ \overset{\star}{\hat{p}}_{r_2} \\ \hat{p}_{r_1} \\ \hat{q}_{i_1} \\ \hat{p}_{f} \\ \hat{q}_{i_2} \\ \hat{p}_{r_2} \end{array} \right\} \tag{7.20}$$

The system equations are then written in first-order form as

$$\left[\begin{array}{cc} M' & 0 \\ 0 & I' \end{array} \right] \overset{\star}{\hat{Y}} + \left[\begin{array}{cc} C' & K' \\ I' & 0 \end{array} \right] \hat{Y} = 0 \tag{7.21}$$

where I' is a partitioned matrix with unit matrices along its main diagonal. This equation can be rearranged notationally as

$$\overset{\star}{\hat{Y}} = [A(\psi, \hat{Y}_0)]\hat{Y} \tag{7.22}$$

The stability matrix $\hat{A}$ is a function of the trim solution vector $\hat{Y}_0$. Floquet theory or constant coefficient method is used to obtain the eigenvalues of this system. $\hat{p}_r$ and $\hat{p}_f$ are the modal displacements of the rotor and fuselage/wing respectively.

Reproduced with permission of the copyright owner. Further reproduction prohibited without permission.

7.3 Results

Sample results, obtained by using the model for the complete tiltrotor configuration, are discussed in this section. The results are for an XV-15 configuration described earlier in this report. The rotor and wing properties for this configuration are given in previous chapters. The fuselage properties, for the detailed fuselage model, were inferred from gross properties such as the exterior dimensions, weight, c.g. location, moments of inertia, etc., since all the necessary information for the fuselage is not available in the open literature. Some of the important fuselage properties, for the XV-15, as utilized to obtain the results presented in this section, are given in Table 7.1.

7.3.1 Rigid Body Modes

The fuselage is modeled as a free-free beam with the wing/pylon/rotors attached to it. Six rigid body degrees-of-freedom exist for the fuselage; three are translational motions and three more are rotational motions about the three axes. For the XV-15 fuselage, modeled using the properties given in Table 7.1, six fully-coupled rigid body modes are present in the eigensolution. The modes are fully-coupled due to the inertial properties, in particular the radii of gyration. The rigid body eigenvectors are all distinct and have a zero frequency of vibration. When the fuselage undergoes rigid body motion, the wing that is attached to it also undergoes the same motion. As can be seen from the results, the wing sometimes undergoes some elastic motion too along with rigid body motion.

The six rigid body modes for the configuration analyzed are shown in Figures

Reproduced with permission of the copyright owner. Further reproduction prohibited without permission.

7.4 through 7.9; the ordering of the rigid body modes is done arbitrarily in the analysis since they all have zero frequencies. The translational displacements are all nondimensionalized by the rotor radius. The spanwise coordinate is nondimensionalized by the wing semi-span for the wing, and by the fuselage half-length for the fuselage. Thus, a coordinate of -1.0 refers to the fuselage nose and the left wing tip and a coordinate of 1.0 refers to the fuselage tail-end and the right wing tip, as the case may be. Fuselage longitudinal, lateral, plunge and roll motions are shown in the figures. Pitching and yawing motions are not shown since they are just the slopes of the plunging and lateral motions respectively. Similar results are shown for the wing axial, lag, flap and torsional motions as well. The fuselage motions are plotted using solid lines and the wing motions are shown using dotted lines. If any of the above mentioned motions is not shown as part of a specific mode, it can be assumed that the respective component is either absent or negligible in that mode. Fuselage longitudinal motion is in the same direction as wing lag motion. Fuselage plunge is in the same direction as wing flap motion (positive up). Fuselage lateral motion is in the opposite direction as wing axial motion; lateral motion is positive to the left. Rolling motion is positive for the fuselage going to the right.

The first rigid body mode is shown in Figure 7.4. Fuselage longitudinal and plunge motions couple with wing flap, lag and torsional motions in this mode. The longitudinal motion is in the forward direction and the plunge motion is nose-down (due to pitching motion). As a result, wing torsion motion is negative, which is also nose-down. Wing lag motion includes fuselage longitudinal motion as well as a relatively small elastic antisymmetric chordwise displacement. Wing flap

Reproduced with permission of the copyright owner. Further reproduction prohibited without permission.

motion is purely elastic in the absence of fuselage roll and plunge motions (at the wing attachment point which is zero spanwise coordinate); antisymmetric beam bending motion is exhibited in this mode. Also, wing flap motion and fuselage plunge motion are equal at zero spanwise coordinate which the attachment point of the wing to the fuselage. The same is true for the fuselage longitudinal and wing lag motions.

Fuselage lateral motion and wing axial motions, however, are defined to be positive in opposite directions. The two motions should have the same magnitude but opposite sign at the zero spanwise coordinate; this can be seen from the fuselage lateral and wing axial motions in the second rigid body mode shown in Figure 7.5. The figure also shows that fuselage plunge as well as roll motions contribute to the wing flapwise translational motion. Similarly, fuselage longitudinal as well as lateral motions contribute to wing lag motion.

Figure 7.7 shows the component displacements of the fourth rigid body mode. Wing lag motion is exactly the same as the fuselage longitudinal motion in this mode; this means that elastic wing lag motion is absent in this mode. Also, wing axial motion has exactly the same magnitude but the opposite sign compared to fuselage lateral motion. Figure 7.9 shows the sixth rigid body mode; both wing lag and flap motions have elastic components apart from the rigid body motion induced by the fuselage.

Reproduced with permission of the copyright owner. Further reproduction prohibited without permission.

7.3.2 Validation of Stability Predictions

The stability predictions for the antisymmetric wing mode frequencies and damping are validated with flight test data in airplane mode and with predictions from other analyses. Flight test data and predictions from other comprehensive aeroelastic analyses of XV-15 aeroelastic stability in high speed axial flight is given in Ref. [73]. The flight test data were taken at an altitude of 10,000 feet and at a rotor speed of 517 rpm. The rotor hub had a precone angle of 2.5^o and data were taken in windmilling flight (see Table 5.2). Fuselage data used in this analysis were obtained from aircraft configuration characteristics [73]. Three other tiltrotor comprehensive aeroelastic analyses - DYN4, DYN5 and PASTA - were used to predict stability characteristics in Ref. [73]. Fifteen coupled fuselage/wing modes were used in the stability prediction in the current analysis, including the six coupled rigid-body modes of the fuselage/wing; these modes included the fundamental symmetric and antisymmetric wing modes in the beam, chord and torsion directions.

Figures 7.10 through 7.15 show the comparison of predicted stability frequencies and damping from this analysis with predictions from the other analyses and with flight test data. Frequency and damping comparison for the wing antisymmetric beam mode varying with forward flight speed are shown in Figures 7.10 and 7.11. The current analysis predicts the frequencies satisfactorily; this is true for the other analyses as well. The damping values for this mode are underpredicted by DYN5, PASTA and the current analysis; DYN4 overpredicts the damping. The reason for the DYN4 predictions differing from the other analyses predictions could not

Reproduced with permission of the copyright owner. Further reproduction prohibited without permission.

be ascertained from available literature on these analyses. The flight test data, however, show considerable scatter.

Figures 7.12 and 7.13 show a similar comparison for the wing antisymmetric chord mode. The frequency predictions are satisfactory from DYN5, PASTA and the current analysis while DYN4 underpredicts the frequencies. The damping plot shows that all the analyses underpredict the damping variation with airspeed. This plot also shows considerable scatter in the flight test data. The corresponding plots for the wing antisymmetric torsion mode are shown in Figures 7.14 and 7.15 respectively. All analyses overpredict the frequencies. DYN4, DYN5 and PASTA underpredict the damping in this mode while the current analysis slightly overpredicts the damping. DYN5 and PASTA predict a decrease in antisymmetric torsion mode damping with increasing airspeed while the test data show no such trend.

7.3.3 Parametric Studies

Parametric studies of blade tip geometry modifications (sweep, anhedral and planform taper) and their effect on tiltrotor flutter speed predictions were discussed in Chapter 6; these results, however, were based on the right-half tiltrotor configuration only and, fuselage motion and wing antisymmetric modes were not included. The present section discusses the effect of the same blade tip geometry modifications on the predicted stability of the wing antisymmetric modes in airplane mode of flight. Figure 7.16 shows the variation of damping of the antisymmetric wing modes with advance ratio for a straight blade configuration (baseline case).

Reproduced with permission of the copyright owner. Further reproduction prohibited without permission.

A velocity sweep from an advance ratio of 0.4 (about 140 knots) to an advance ratio of 1.0 (about 340 knots) was performed; the figure shows the negative of the real part of the stability eigenvalue (so as to compare easily with the results in Chapter 6). Any mode becomes unstable if the damping of the mode goes below the x-axis in the plot. The fuselage modes (both rigid body and elastic modes) are not significantly affected by changes in blade tip geometry; they are always stable and are, hence, not shown in the figure. The figure shows the antisymmetric wing beam, chord and torsion modes. The beam mode damping remains roughly constant throughout the entire speed range. The chord mode comes close to instability (around 280 knots, $\mu = 0.82$) but remains stable throughout the speed range. The torsion mode is quite heavily damped for all advance ratios. The figure also summarizes the results for the blade and symmetric wing modes for this case (from Figure 6.26); for the straight blade configuration, the symmetric chord mode becomes unstable around 275 knots ($\mu = 0.81$). Since no antisymmetric wing mode instability is predicted in this case, the fuselage model is not important in predicting the flutter speeds for this configuration.

The next case examined was a rotor with the outboard 15% of the blade given a 30° sweep back. The damping plot, shown in Figure 7.17, shows a drastic increase in the damping values compared to Figure 7.16; antisymmetric wing beam, chord and torsion modes are all more damped at high advance ratios than the corresponding modes for the baseline case. For this configuration, the symmetric wing beam mode is predicted to become unstable around 370 knots (Figure 6.27); no instability of the antisymmetric wing modes was observed for this configuration.

Reproduced with permission of the copyright owner. Further reproduction prohibited without permission.

The effect of a 30° tip sweep forward is studied next and is shown in Figure 7.18. The corresponding study with the symmetric wing modes and blade modes is shown in Figure 6.28. No appreciable change in damping is observed in this case as compared to the baseline case shown in Figure 7.16. This configuration is predicted to be unstable for all advance ratios due to the high frequency flap mode becoming unstable.

Figure 7.19 shows the effect of forward flight velocity on antisymmetric wing mode stability for a 5° droop given to the outboard 15% span of the blade. The wing beam, chord and torsion modes show an increase in damping compared to the baseline case. For this configuration, the symmetric chord mode is predicted to become unstable around a speed of 350 knots ($\mu = 1.03$) as shown in Figure 6.29. No antisymmetric wing mode instabilities are predicted to occur before the symmetric chord mode instability.

The effect of velocity on antisymmetric wing mode stability for a 5° anhedral (up) given to the outboard 15% span of the blade is shown in Figure 7.20. This case does not exhibit any significant change in wing mode damping compared to the baseline case (Figure 7.16). For this configuration, the cyclic flap mode becomes unstable at a speed of 140 knots (corresponding to $\mu = 0.4$) as shown in Figure 6.30.

The next case studied is a blade with planform taper ratio of 3:1 given to the outboard 15% span, shown in Figure 7.21. Damping for the wing beam, chord and torsion modes is similar to that shown in Figure 7.16. The symmetric chord mode is predicted to become unstable around a speed of 260 knots ($\mu = 0.76$) for

Reproduced with permission of the copyright owner. Further reproduction prohibited without permission.

this configuration as shown in Figure 6.31. In this case too, antisymmetric wing mode instability does not occur before or even beyond the symmetric mode flutter speed.

For all the cases studied in this section, the antisymmetric wing modes are stable throughout the speed range, whereas the instabilities occur for the symmetric wing modes. The blade mode instabilities are due to destabilizing coupling introduced in the rotor as discussed in Chapter 6. The symmetric wing mode instabilities are key to the mechanism of whirl flutter. Symmetric wing modes are more susceptible to whirl flutter instabilities than are the antisymmetric wing modes (for the configuration studied).

The interaction level between the wing frequencies and its effect on whirl flutter would depend directly on the placement of rotor and wing frequencies (as seen in Chapter 2). For the configuration studied, the wing antisymmetric modes do not interact with the symmetric wing modes to accelerate or delay the predicted occurrence of whirl flutter. The symmetric wing torsion mode frequency is very close to the antisymmetric wing torsion mode frequency; but the symmetric torsion mode has relatively high damping and is, hence, not affected by the inclusion of the antisymmetric wing torsion mode. The symmetric wing beam mode frequency, on the other hand, is much lower than the antisymmetric torsion mode frequency; the torsion mode, hence, does not affect the symmetric wing beam mode significantly. This, however, may not be the case for another set of parameters (or any other configuration).

Reproduced with permission of the copyright owner. Further reproduction prohibited without permission.

Influence of Rigid Body Modes

The fuselage/wing rigid body modes allow fully-coupled motion of the tiltrotor configuration in three translational and three rotational degrees-of-freedom. The elastic fuselage/wing modes allow elastic motion; these modes include the symmetric and antisymmetric wing beam, chord and torsion modes. To study the effect of rigid body motion on the predicted stability of the configuration, the six rigid body modes were neglected from the stability analysis. Nine elastic fuselage/wing modes were included in the analysis. Figure 7.22 shows the effect of velocity on antisymmetric wing mode stability, neglecting the effect of the rigid body modes, for a straight blade tiltrotor configuration. The rotor modes and symmetric wing modes were not affected when rigid body modes were neglected from the analysis; they are, therefore, not shown in the figure. Figure 7.16 shows the effect of velocity on antisymmetric wing mode stability including the six rigid body modes; 15 modes, including the same nine elastic modes used in this study, were used for the results presented in Figure 7.16. A comparison of the two figures shows that the antisymmetric wing modes are affected by the exclusion of the rigid body modes from the analysis. Trends in the variation of damping with advance ratio are the similar (for all three modes shown) for the two cases. Slight differences in the behavior of the antisymmetric wing torsion mode, at high advance ratios, can be seen from the figures. This shows that the inclusion of rigid body modes affects the behavior of the antisymmetric wing modes, but the effects are minimal.

Reproduced with permission of the copyright owner. Further reproduction prohibited without permission.

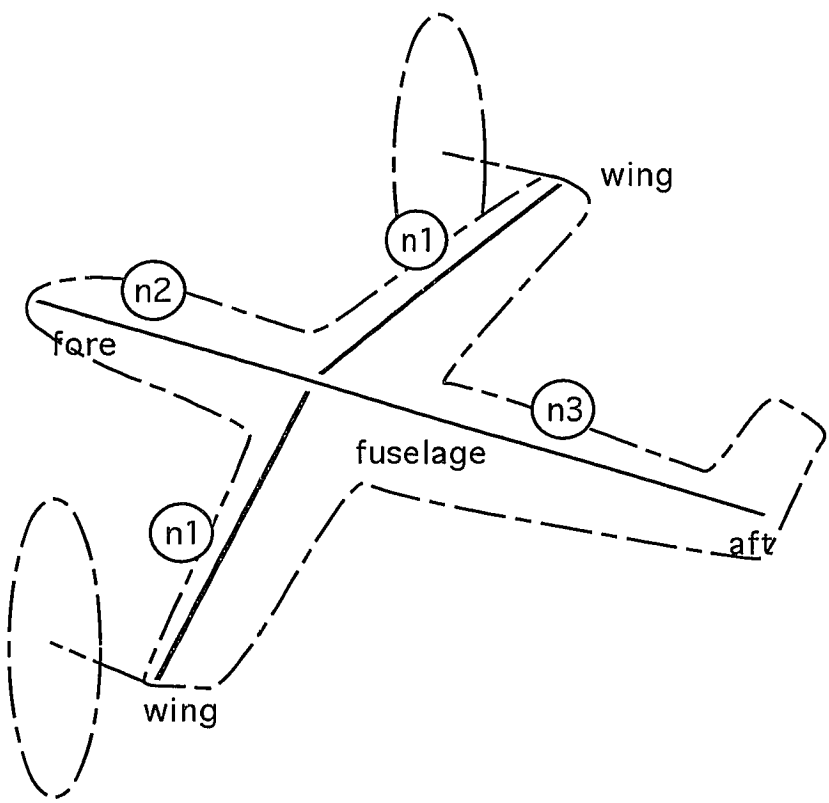

Figure 7.1: Schematic of finite element model of fuselage and wing showing number of elements used for each component

Reproduced with permission of the copyright owner. Further reproduction prohibited without permission.

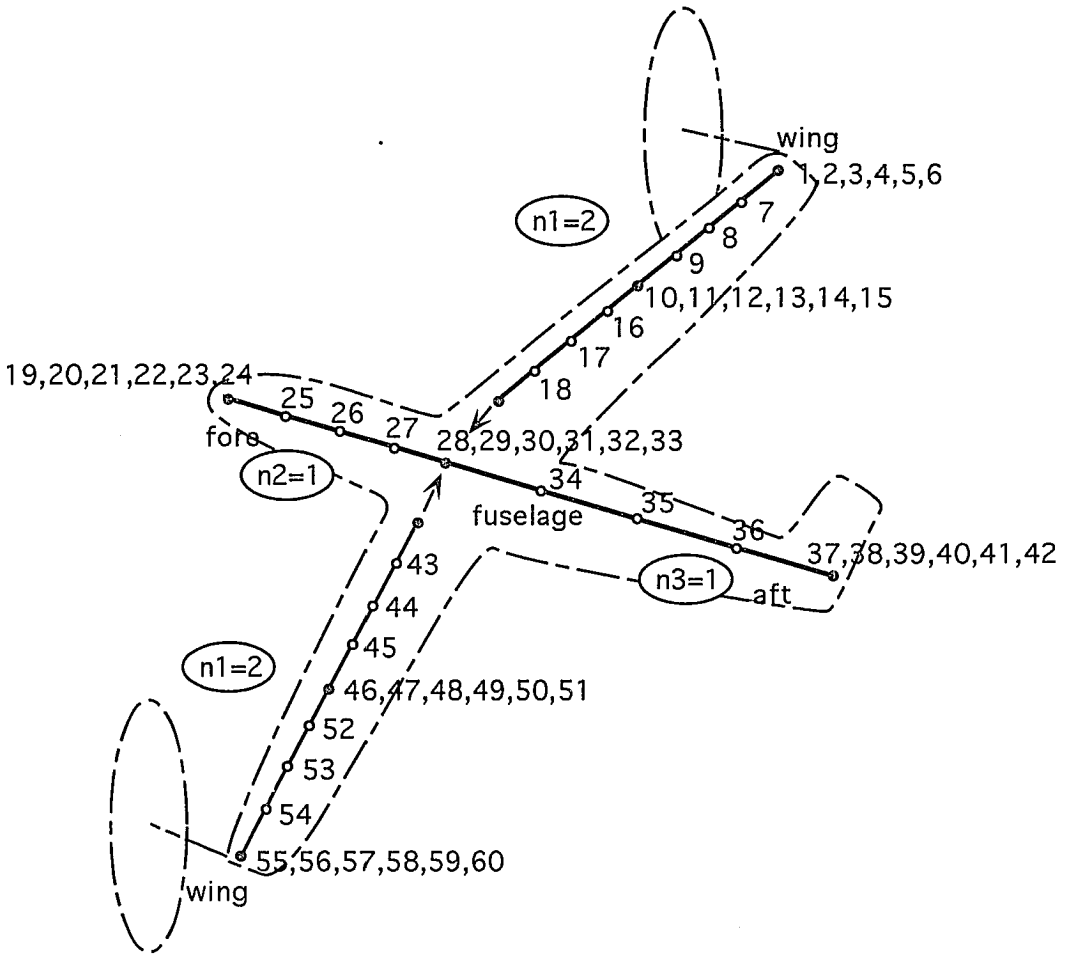

Figure 7.2: Assembly of wing and fuselage 15 dof elements showing global displacement numbering (example with 2 elements for wing semi-span and 2 elements for fuselage, 1 fore and 1 aft) - schematic, not drawn to scale

Reproduced with permission of the copyright owner. Further reproduction prohibited without permission.

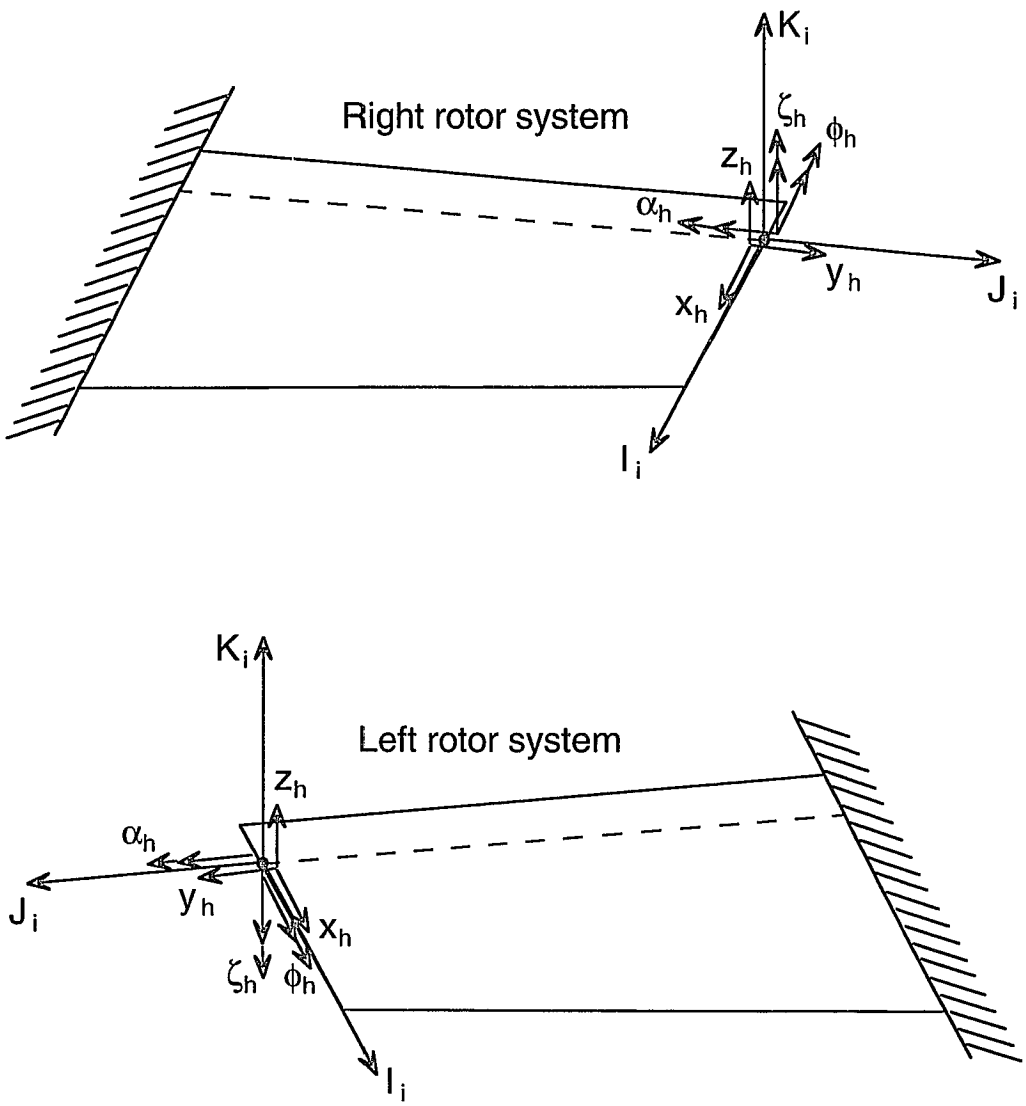

Figure 7.3: Right-handed and left-handed reference frames used for the right and left rotor systems respectively

Reproduced with permission of the copyright owner. Further reproduction prohibited without permission.

Element Property (non-dim.)	Fore element	Aft element
Length, l/R	1.0	1.0
Chord, c/R	0.4	0.4
Mass	105	60
Beamwise Stiffness	10	10
Chordwise Stiffness	10	10
Axial Stiffness	1000	1000
Torsional Stiffness	4	4
Offset - c.g. from e.a.	0	0
Offset - t.a. from e.a.	0	0
Offset - a.c. from e.a.	0	0
Radius of Gyration, $K_{m_1}^2$	0.06	0.04
Radius of Gyration, $K_{m_2}^2$	0.06	0.04

Table 7.1: XV-15 fuselage properties - 2 finite elements used

Reproduced with permission of the copyright owner. Further reproduction prohibited without permission.

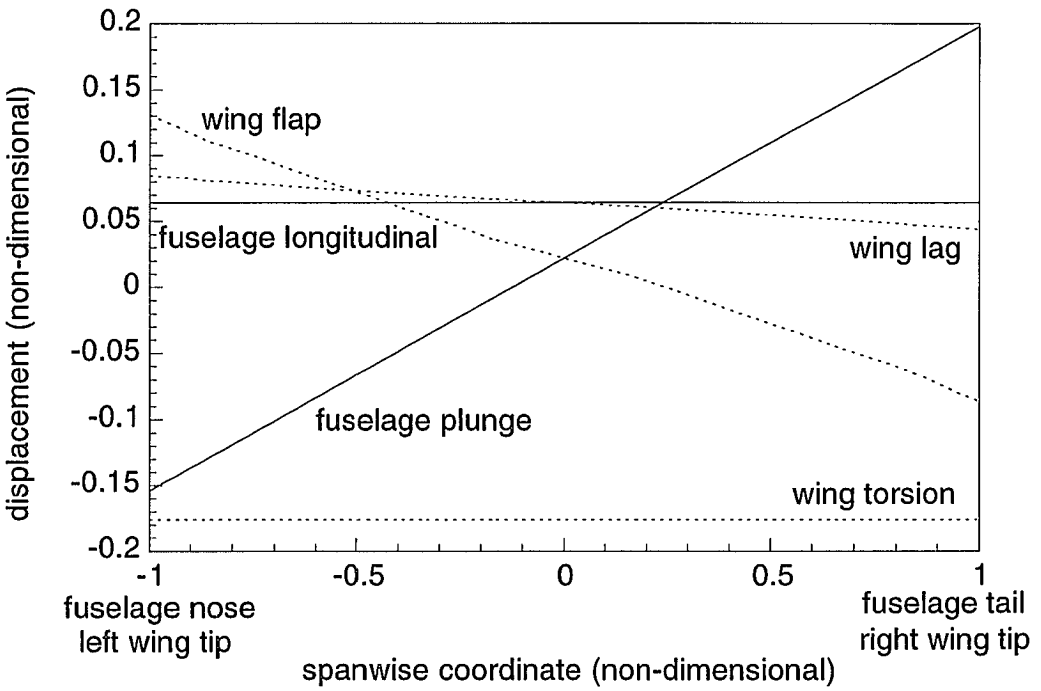

Figure 7.4: First fuselage/wing rigid body mode

Reproduced with permission of the copyright owner. Further reproduction prohibited without permission.

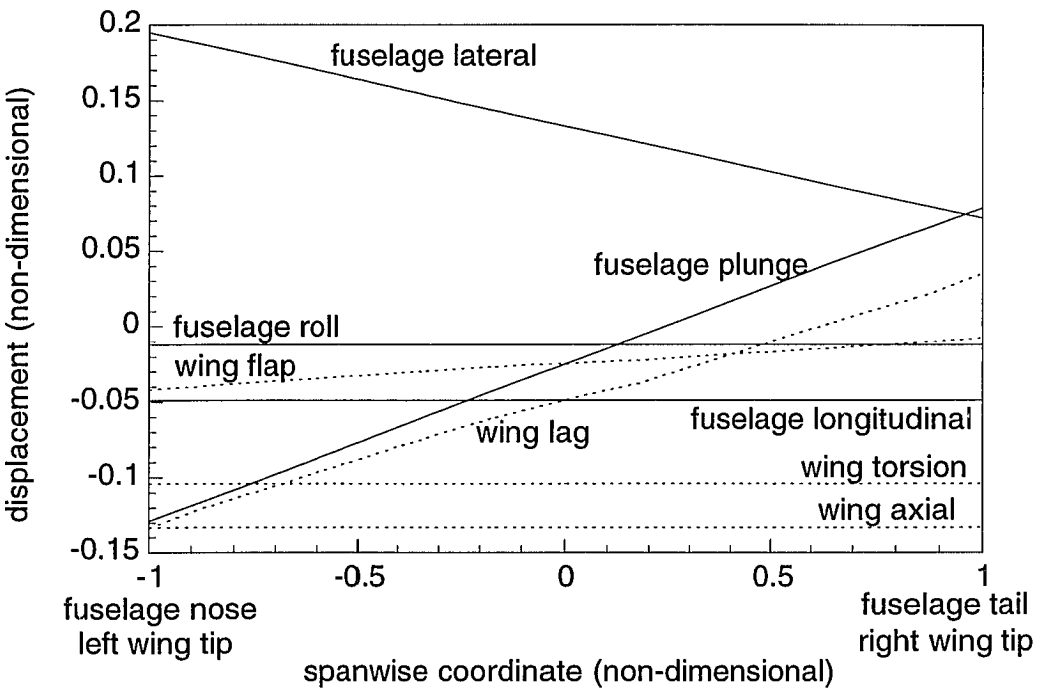

Figure 7.5: Second fuselage/wing rigid body mode

Reproduced with permission of the copyright owner. Further reproduction prohibited without permission.

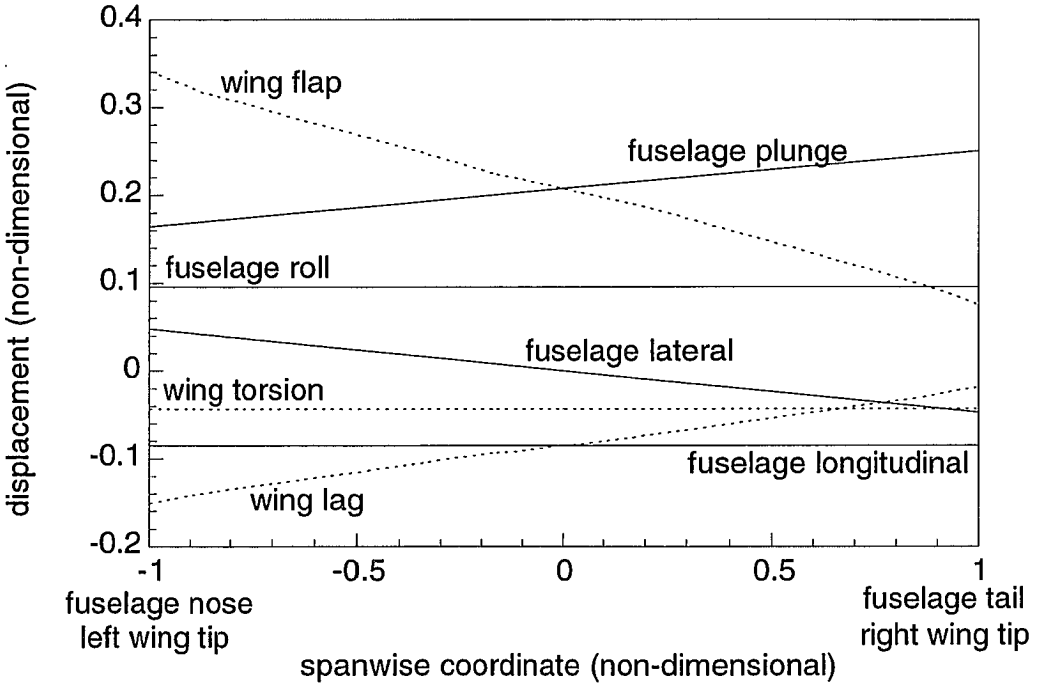

Figure 7.6: Third fuselage/wing rigid body mode

Reproduced with permission of the copyright owner. Further reproduction prohibited without permission.

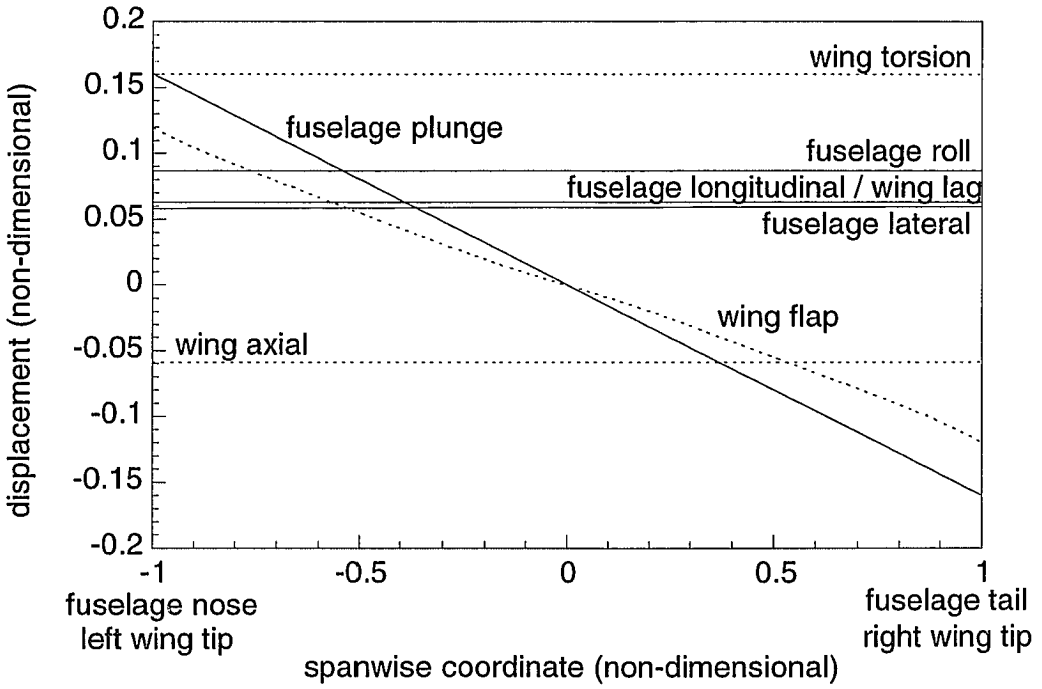

Figure 7.7: Fourth fuselage/wing rigid body mode

Reproduced with permission of the copyright owner. Further reproduction prohibited without permission.

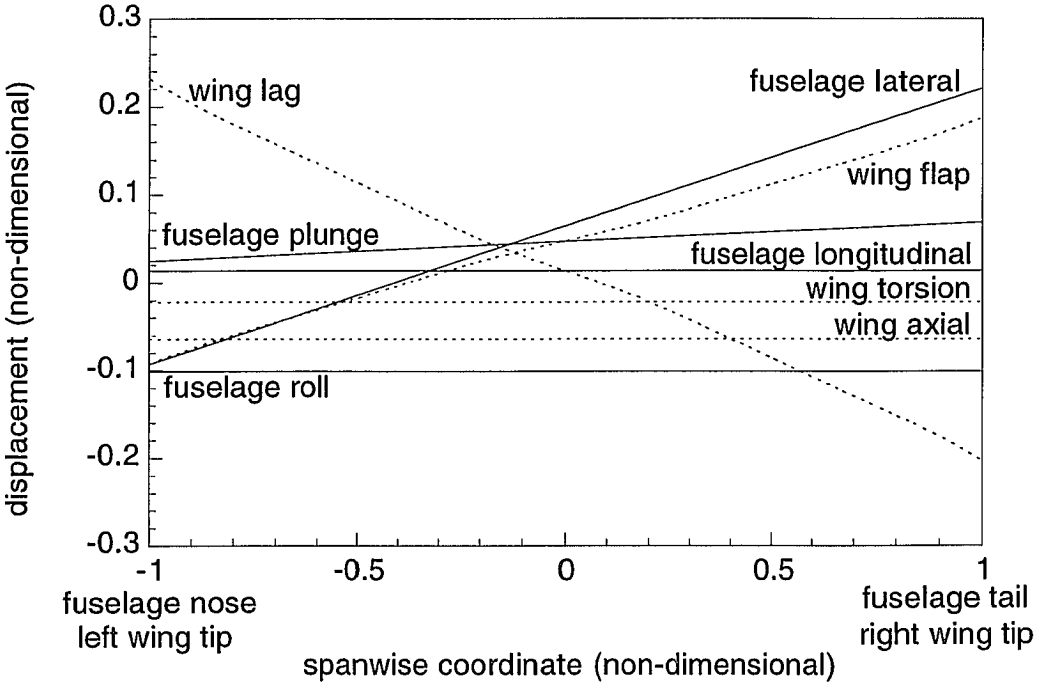

Figure 7.8: Fifth fuselage/wing rigid body mode

Reproduced with permission of the copyright owner. Further reproduction prohibited without permission.

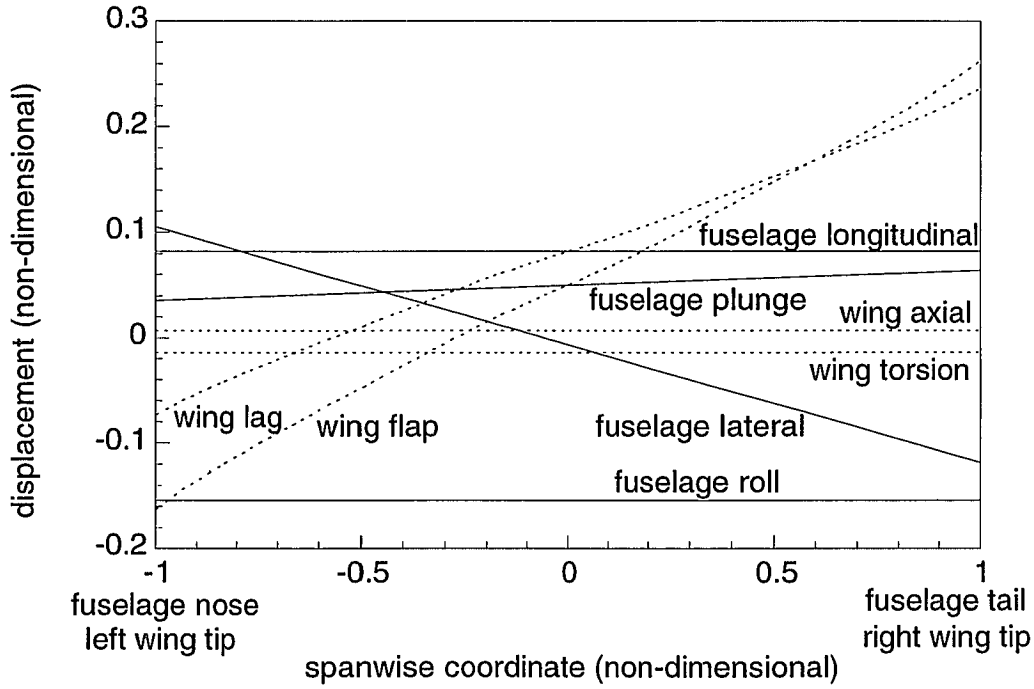

Figure 7.9: Sixth fuselage/wing rigid body mode

Reproduced with permission of the copyright owner. Further reproduction prohibited without permission.

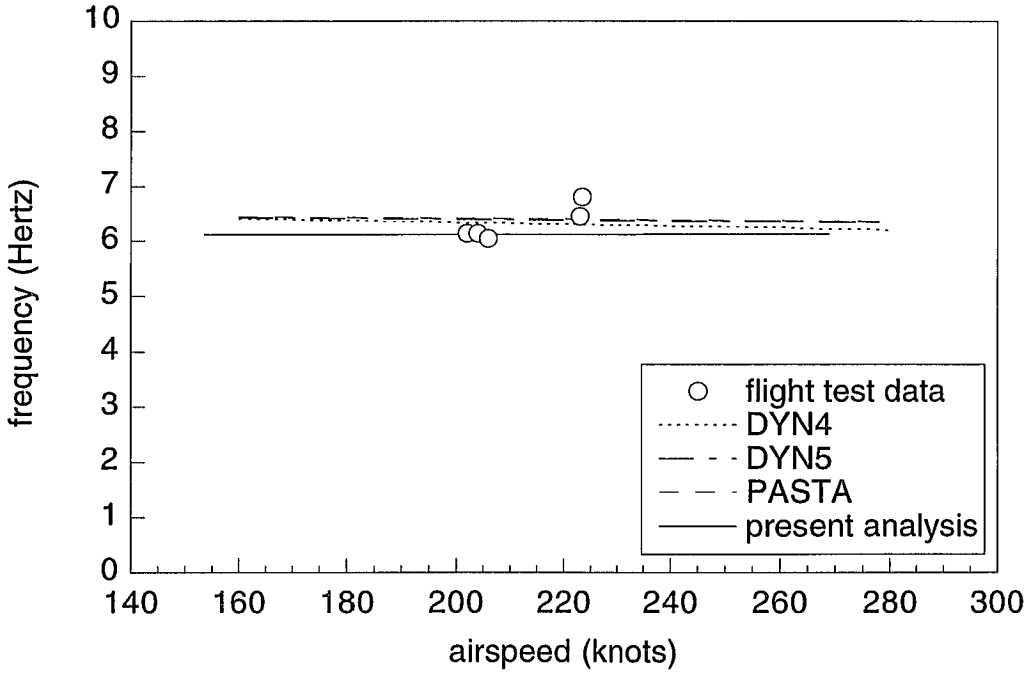

Figure 7.10: Validation of wing antisymmetric beam mode frequencies for the XV-15

Reproduced with permission of the copyright owner. Further reproduction prohibited without permission.

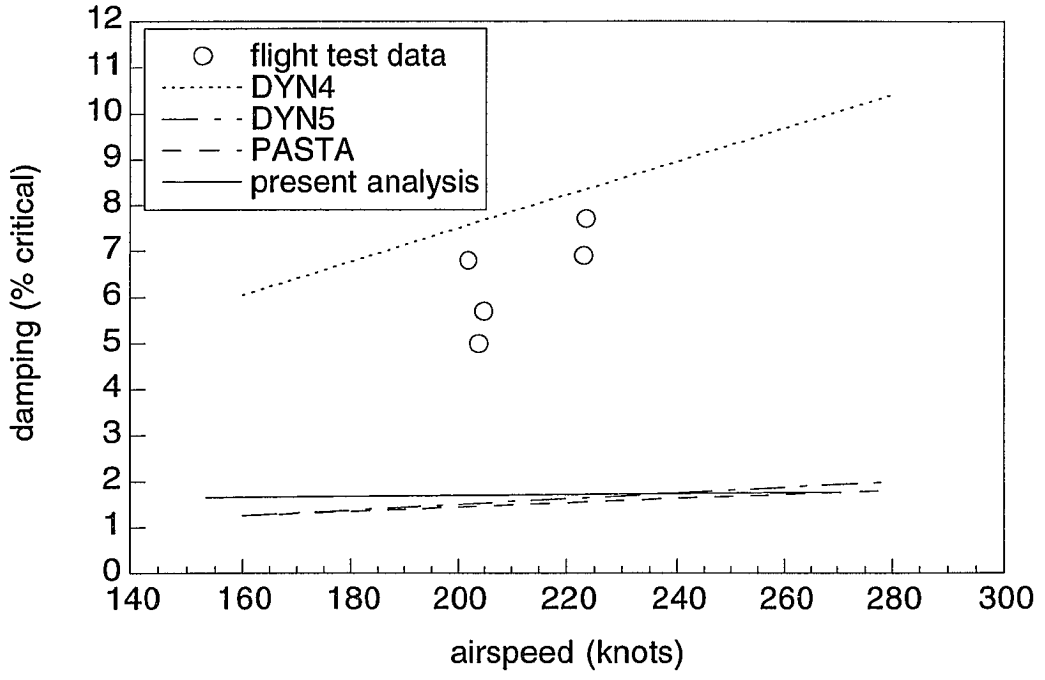

Figure 7.11: Validation of wing antisymmetric beam mode damping for the XV-15

Reproduced with permission of the copyright owner. Further reproduction prohibited without permission.

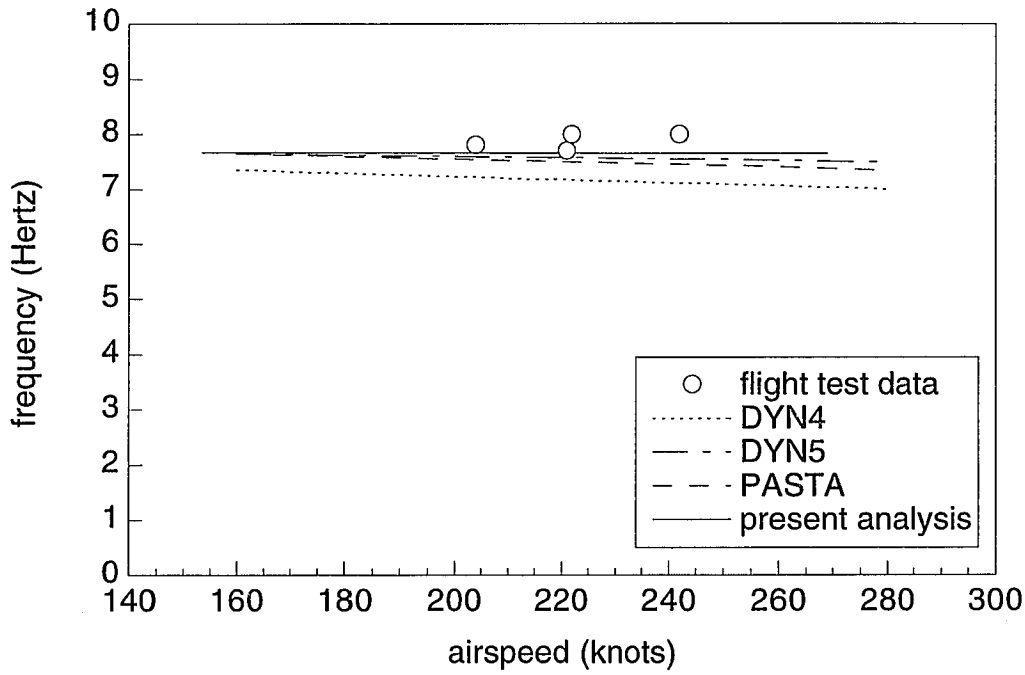

Figure 7.12: Validation of wing antisymmetric chord mode frequencies for the XV-15

Reproduced with permission of the copyright owner. Further reproduction prohibited without permission.

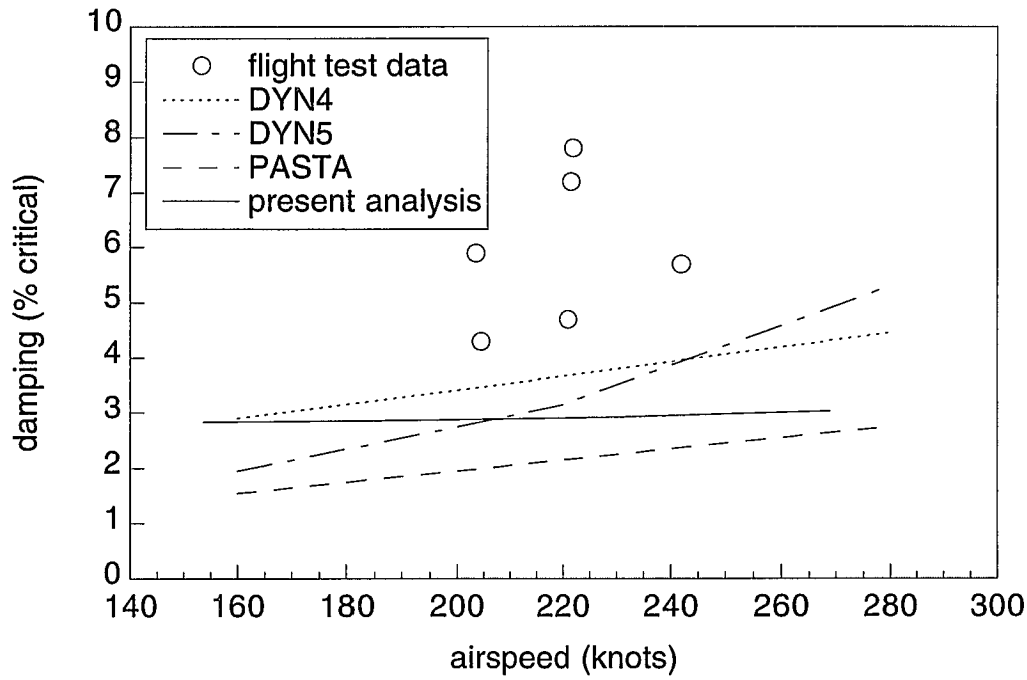

Figure 7.13: Validation of wing antisymmetric chord mode damping for the XV-15

Reproduced with permission of the copyright owner. Further reproduction prohibited without permission.

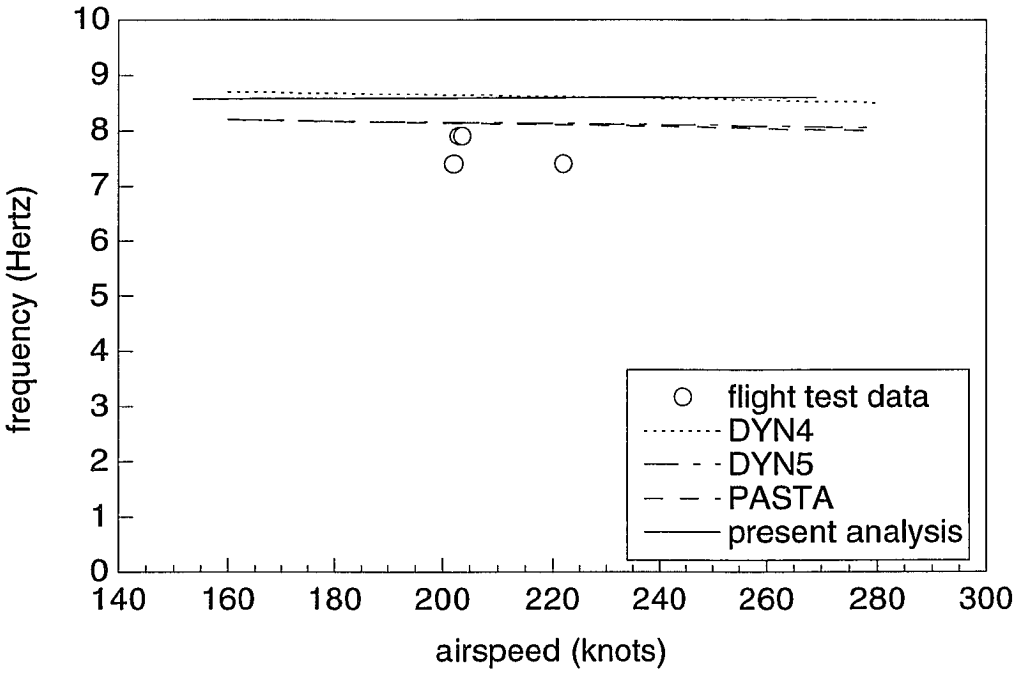

Figure 7.14: Validation of wing antisymmetric torsion mode frequencies for the XV-15

Reproduced with permission of the copyright owner. Further reproduction prohibited without permission.

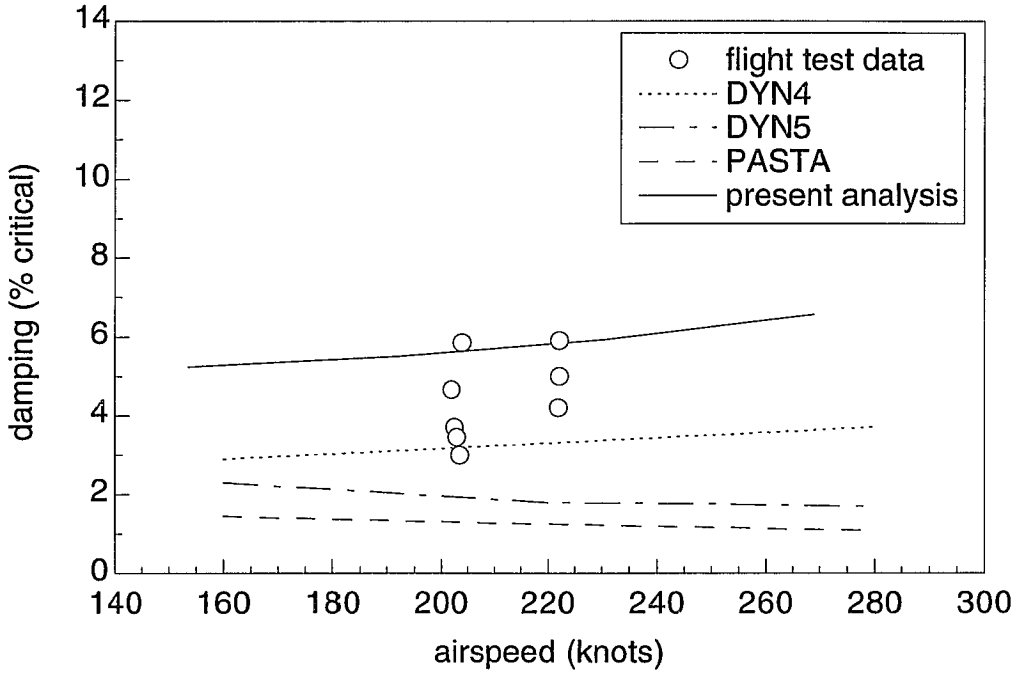

Figure 7.15: Validation of wing antisymmetric torsion mode damping for the XV-15

Reproduced with permission of the copyright owner. Further reproduction prohibited without permission.

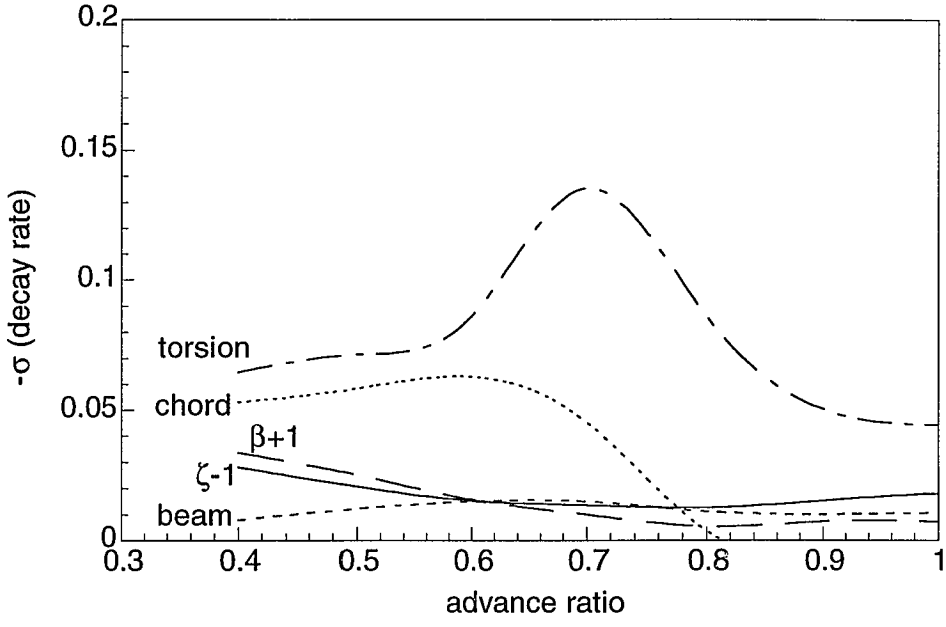

(a) symmetric wing modes and rotor modes

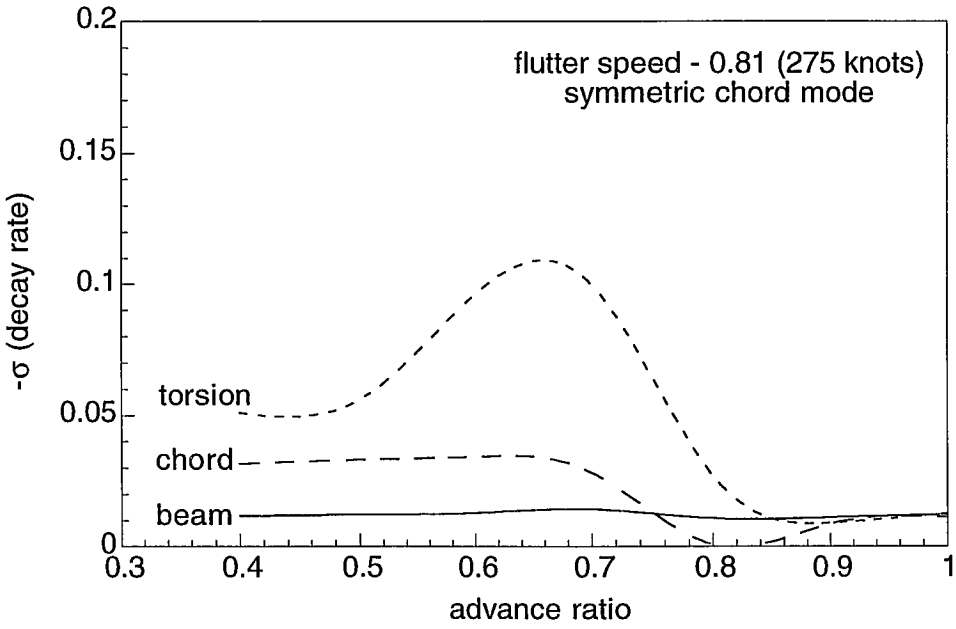

(b) antisymmetric wing modes

Figure 7.16: Effect of velocity on antisymmetric wing mode stability for straight blade (C_T/σ=0.01)

Reproduced with permission of the copyright owner. Further reproduction prohibited without permission.

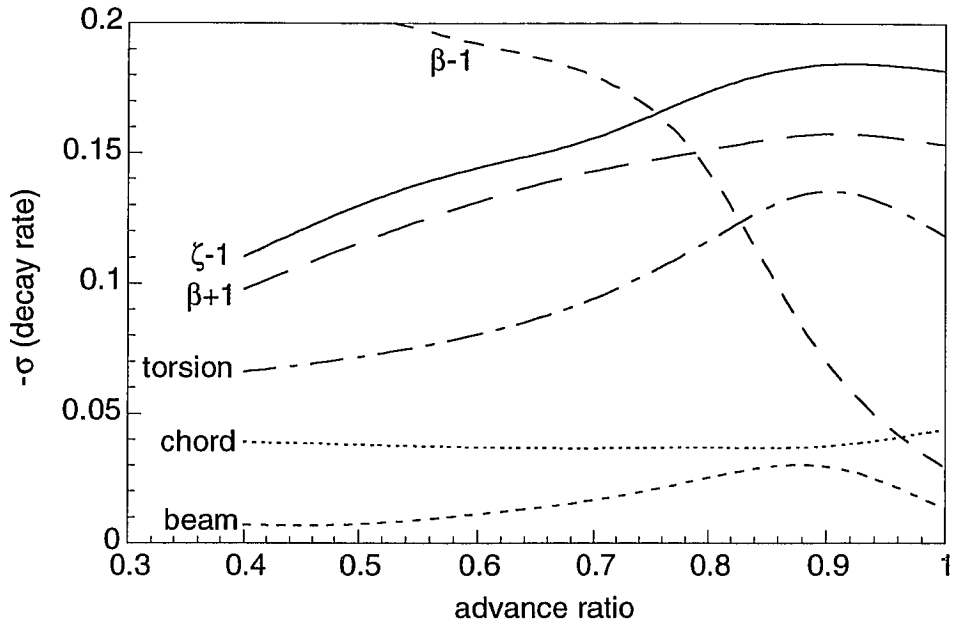

(a) symmetric wing modes and rotor modes

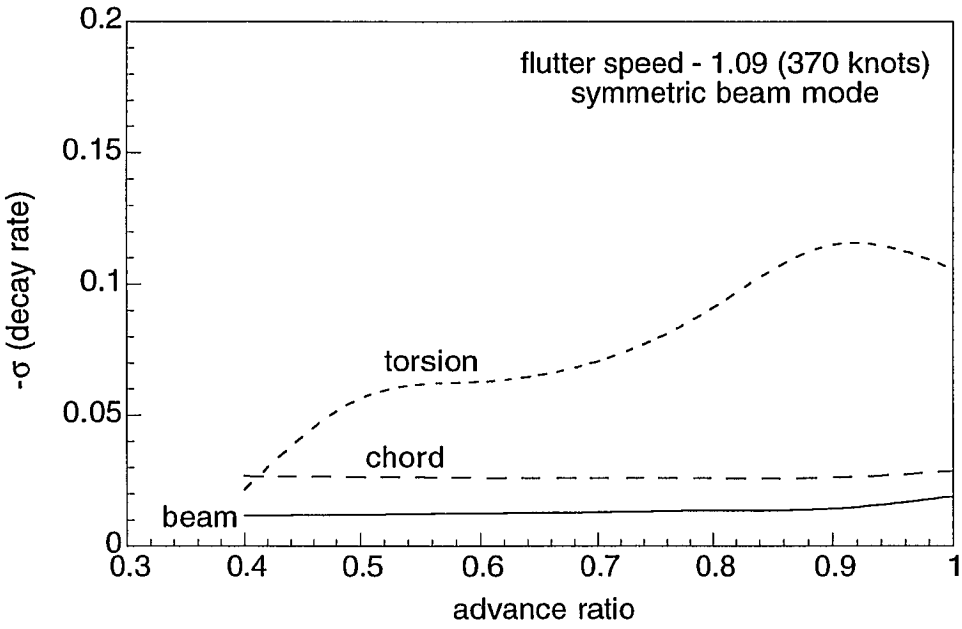

(b) antisymmetric wing modes

Figure 7.17: Effect of velocity on antisymmetric wing mode stability for 30° backward sweep for blade tip (outboard 15% span, C_T/σ=0.01)

Reproduced with permission of the copyright owner. Further reproduction prohibited without permission.

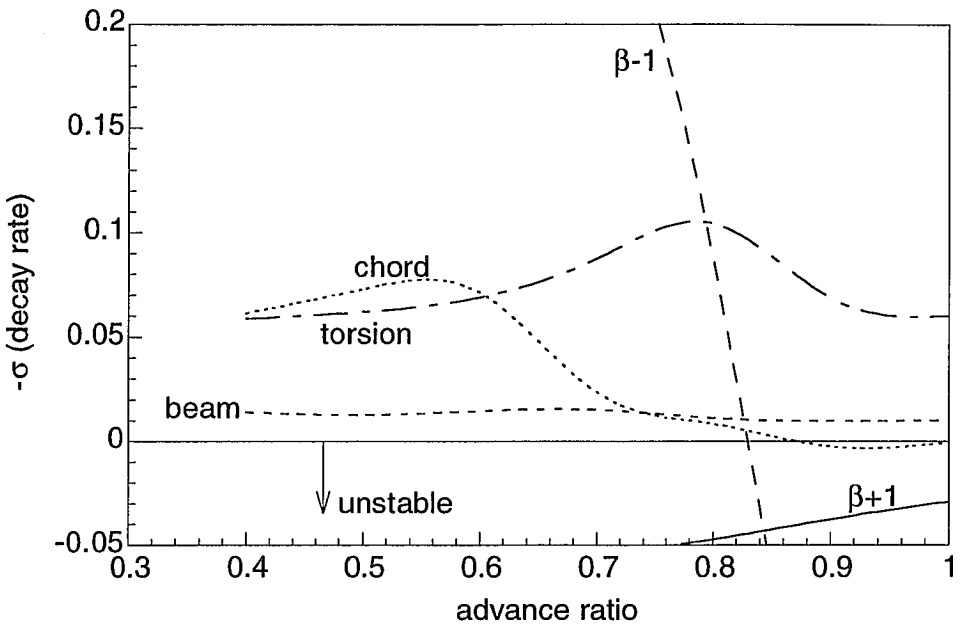

(a) symmetric wing modes and rotor modes

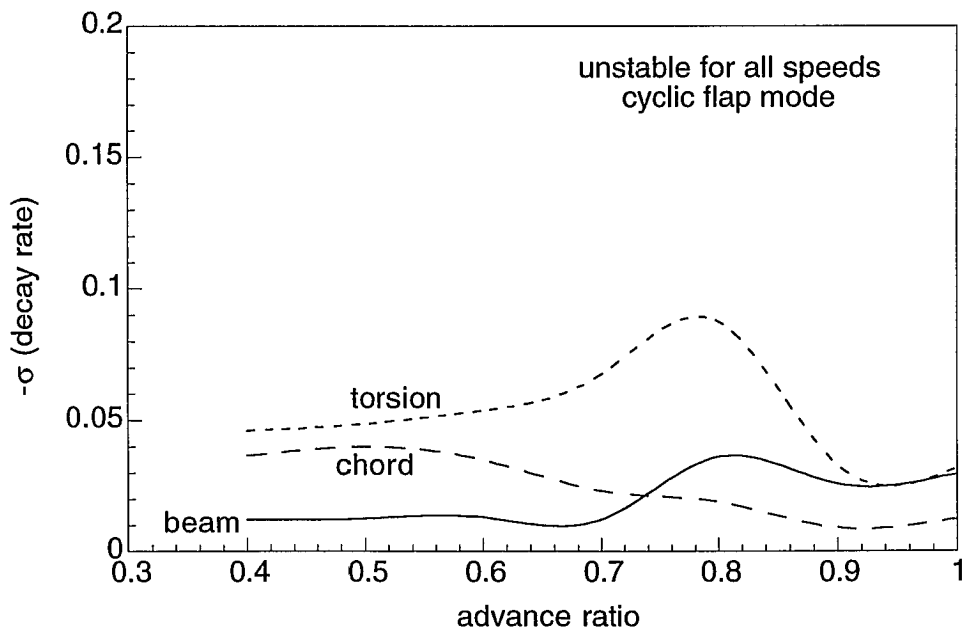

(b) antisymmetric wing modes

Figure 7.18: Effect of velocity on antisymmetric wing mode stability for 30° forward sweep for blade tip (outboard 15% span, C_T/σ=0.01)

Reproduced with permission of the copyright owner. Further reproduction prohibited without permission.

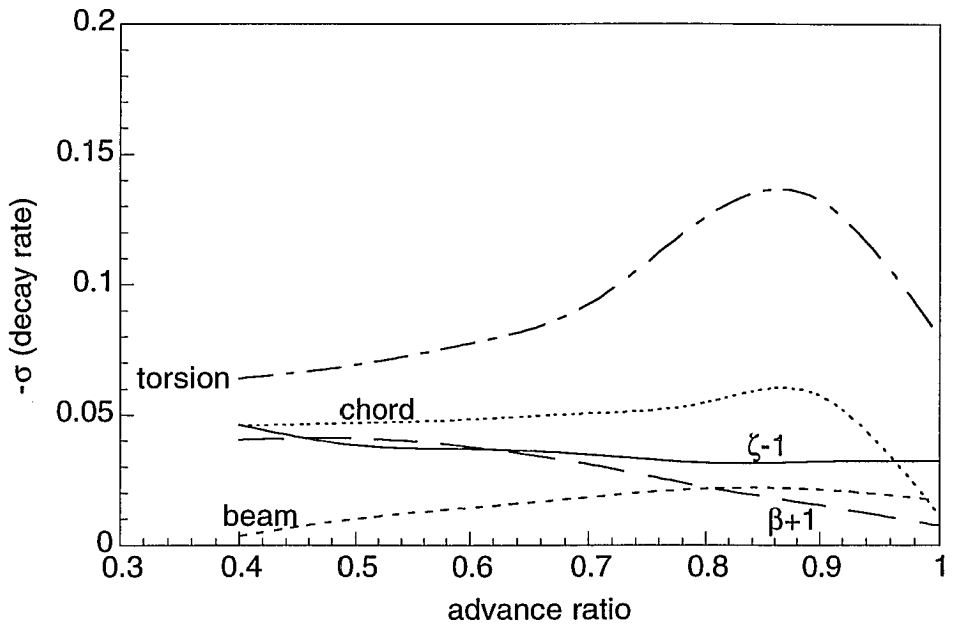

(a) symmetric wing modes and rotor modes

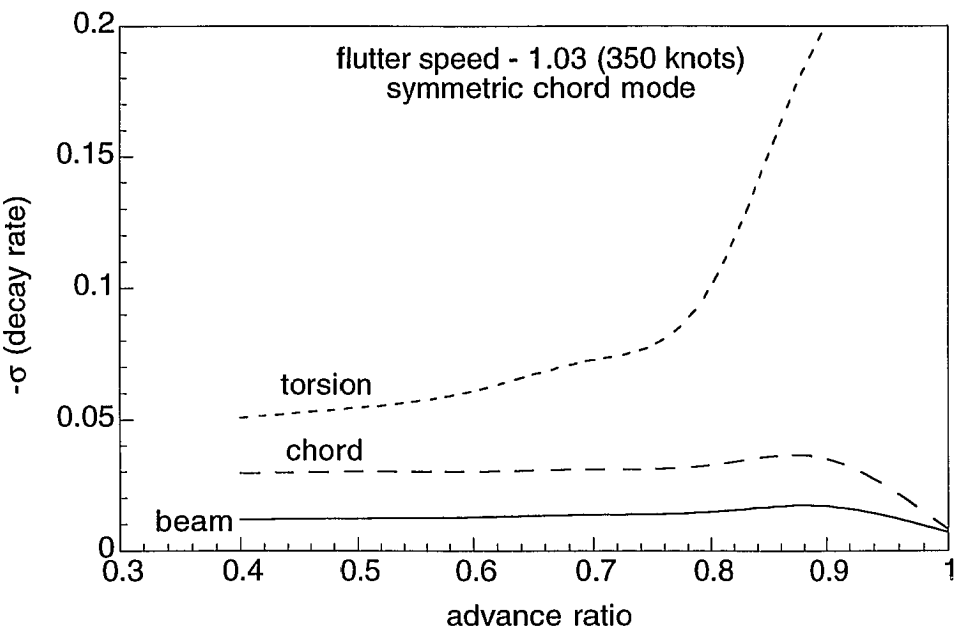

(b) antisymmetric wing modes

Figure 7.19: Effect of velocity on antisymmetric wing mode stability for 5° droop for blade tip (outboard 15% span, C_T/σ=0.01)

Reproduced with permission of the copyright owner. Further reproduction prohibited without permission.

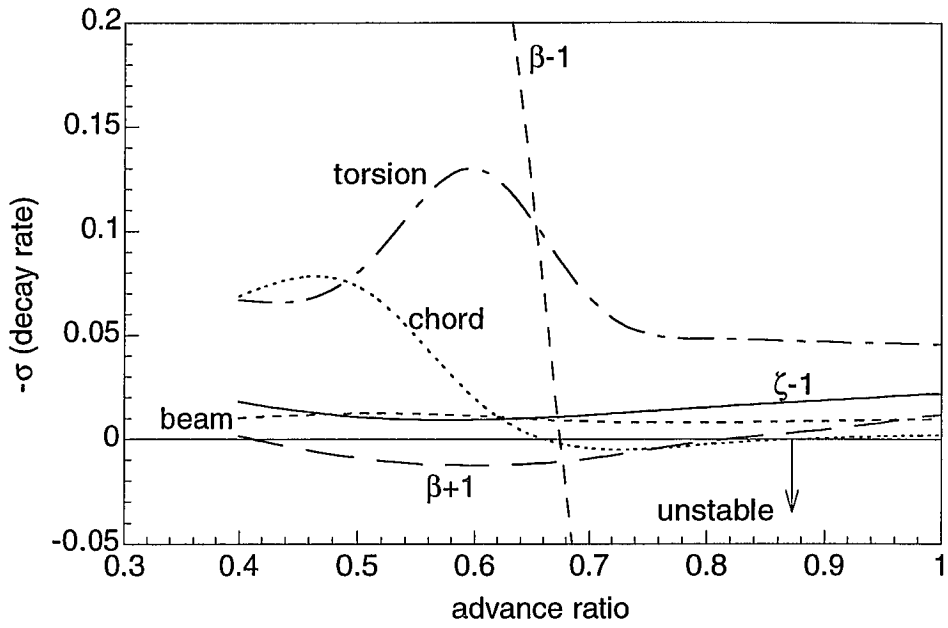

(a) symmetric wing modes and rotor modes

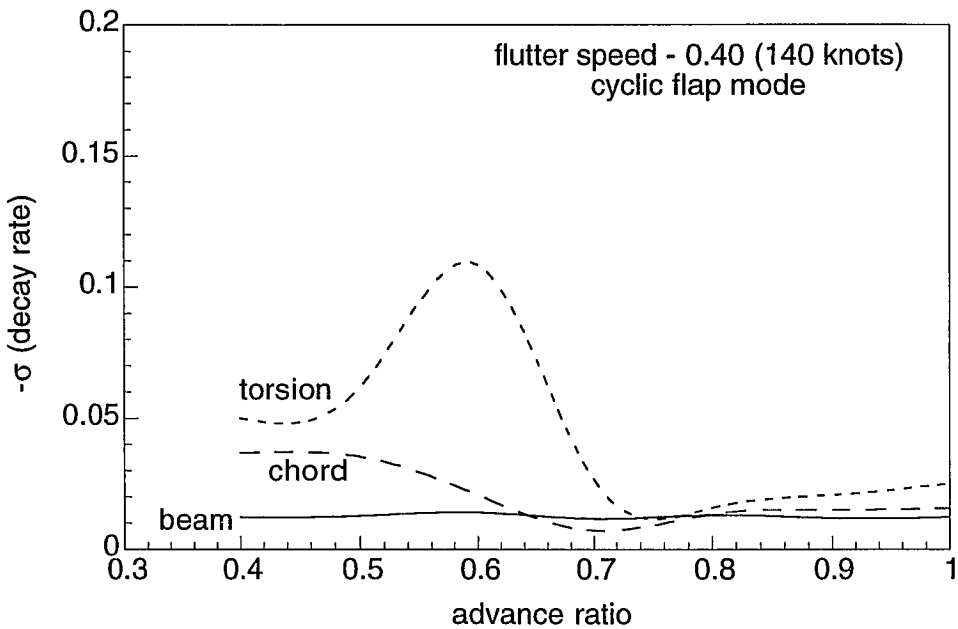

(b) antisymmetric wing modes

Figure 7.20: Effect of velocity on antisymmetric wing mode stability for 5° anhedral for blade tip (outboard 15% span, C_T/σ=0.01)

Reproduced with permission of the copyright owner. Further reproduction prohibited without permission.

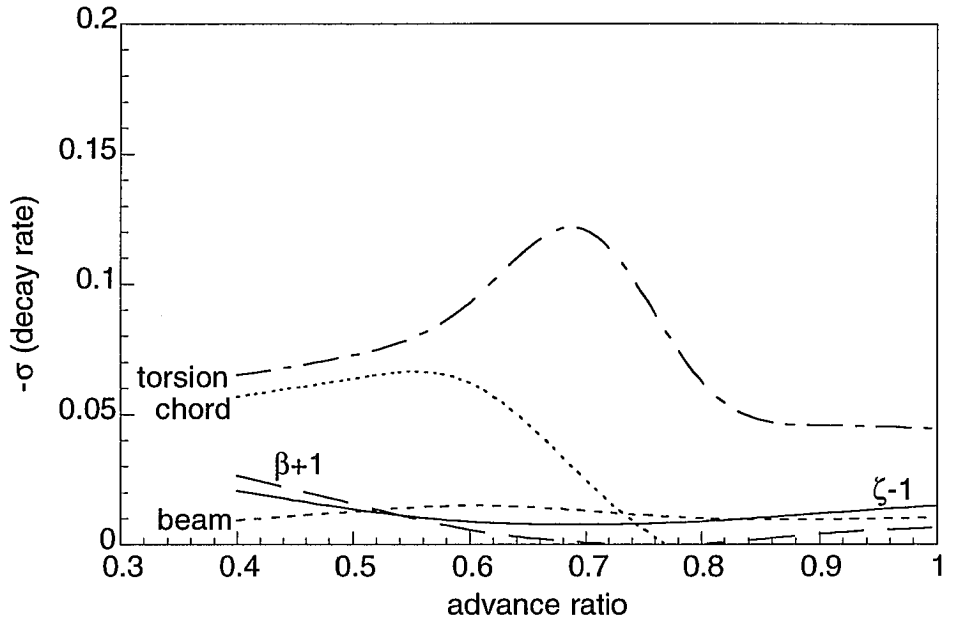

(a) symmetric wing modes and rotor modes

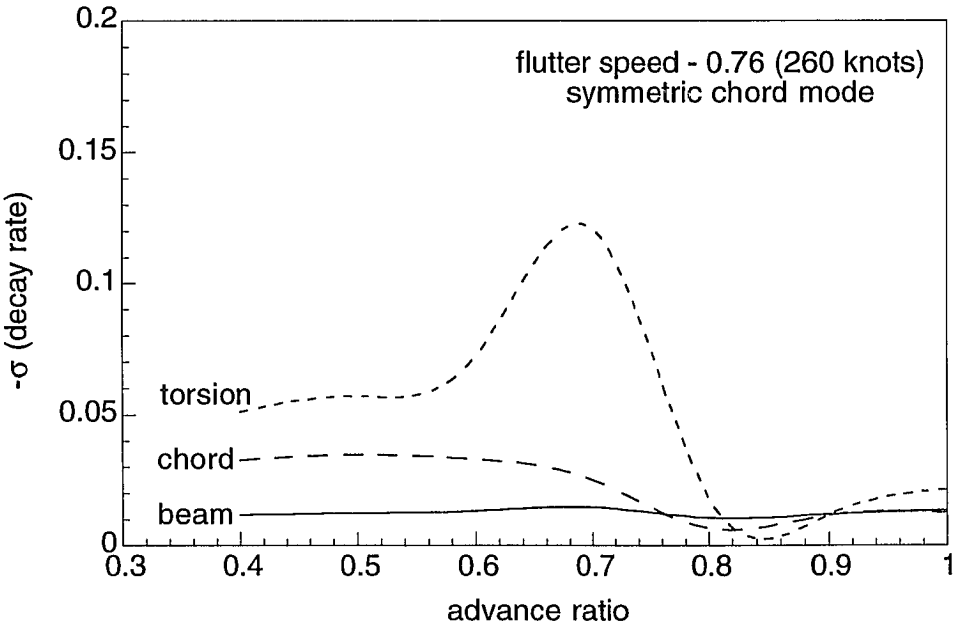

(b) antisymmetric wing modes

Figure 7.21: Effect of velocity on antisymmetric wing mode stability for 3:1 planform taper for blade tip (outboard 15% span, C_T/σ=0.01)

Reproduced with permission of the copyright owner. Further reproduction prohibited without permission.

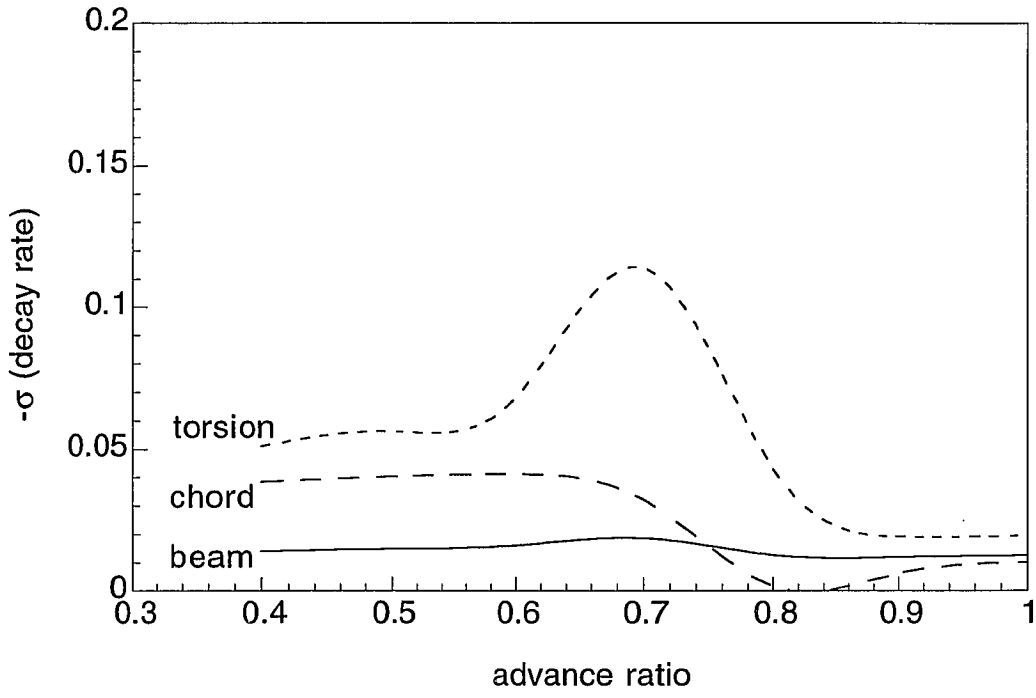

Figure 7.22: Effect of velocity on antisymmetric wing mode stability for straight blade neglecting all six fuselage/wing rigid body modes (C_T/σ=0.01)

Reproduced with permission of the copyright owner. Further reproduction prohibited without permission.

Chapter 8

Summary and Conclusions

The research work presented in this dissertation has been broadly divided into five main parts. First, a simple rigid-blade, elastic wing tiltrotor analysis for high speed axial flight was developed, and used to investigate the effects of important design parameters on the occurrence of tiltrotor whirl flutter instabilities. Second, the system equations for the analytical model, with advanced geometry, composite-coupled rotor blades and wing for a tiltrotor, were derived. Third, the predictions from this analysis of rotor response, trim controls, blade loads and aeroelastic stability, were correlated with flight test data. Fourth, parametric studies were conducted on rotor blades with advanced tip shapes to study their effects on tiltrotor system stability and performance. Finally, the analytical model was made more comprehensive by modeling the complete tiltrotor configuration, including the fuselage, full-span wing and the twin rotors. The aeroelastic stability of the complete configuration was then studied, and the results validated with test data. The major conclusions reached from each of the five parts of this research, as well as some recommendations for future research on this topic, are presented in this final chapter.

Reproduced with permission of the copyright owner. Further reproduction prohibited without permission.

8.1 Rigid Blade Tiltrotor Analysis

The tiltrotor configuration was modeled with a simple linear rigid-blade rotor model and an elastic wing model operating in high speed axial flight. Parametric studies were conducted on the effects of key system design parameters on the whirl flutter stability of the tiltrotor. The influence of rotor frequencies, wing sweep, Lock number, pitch-flap coupling δ_3, and pitch-lag coupling δ_4, on tiltrotor stability were investigated. Fundamental whirl flutter studies conducted with this model are reported in Chapter 2. The study substantiates the following conclusions of Johnson [38] and Nixon [39]:

1. Increased separation between the wing beam and torsion frequencies has a stabilizing effect on beam mode flutter velocity.

2. Optimum flap and lag frequencies exist, that can significantly increase the system flutter velocity. Significant increases in flutter velocity can be achieved by carefully choosing these frequencies. The optimal placement of the low frequency flap and lag modes on the frequency plot has a significant impact on stability.

3. Increase in Lock number is destabilizing.

4. The mechanism of flutter is usually that the rotor forces destabilizing the wing beam/chord modes.

5. For a stiff in-plane rotor, introducing positive pitch-flap coupling is less detrimental to stability than negative pitch-flap coupling is.

Also, the important mechanisms responsible for the phenomenon of whirl flutter have been identified in this study, and the results are consistent with observations

Reproduced with permission of the copyright owner. Further reproduction prohibited without permission.

made in Refs. [38] and [39].

The effect of varying the blade pitch-lag coupling was not examined in Refs. [38] and [39]. From the present study, it is concluded that the introduction of pitch-lag coupling (δ_4, positive or negative) is detrimental to the system stability of a stiff-inplane tiltrotor.

8.2 Formulation of an Elastic Blade Tiltrotor Analysis

The model developed in this study represents the most general formulation to date for highly twisted composite-coupled advanced geometry blades for tiltrotors in helicopter mode (including hover), airplane mode and conversion mode. A design tool capable of modeling the dynamics of such tiltrotors and predicting the system response, loads and aeroelastic stability has been formulated. The rotor blade kinematic pitch-flap and pitch-lag couplings were modeled. The advanced geometry rotor was modeled for blades with arbitrary variation of sweep, anhedral, pretwist, and planform taper with span. The only constraint imposed on the formulation is that the elastic axes of successive beam segments used in the model be connected as piecewise continuous straight lines. Aerodynamics of advanced geometry blade tips were modeled using blade element theory. The formulation handles offsets of blade section center of mass, aerodynamic center, and tension center from the elastic axis. The blade segments are each modeled by using one or more finite elements and inter-segment compatibility relations are satisfied through nonlinear transformations. The tiltrotor wing can also have sweep, anhedral, pretwist and

Reproduced with permission of the copyright owner. Further reproduction prohibited without permission.

planform taper and is modeled using finite elements. The rotor hub is capable of six degrees-of-freedom and has the capability to model gimballed tiltrotors. Large pylon-tilt angles are also modeled. The wing is cantilevered at its root and has the rotor/pylon system mounted at its tip.

A fully-coupled aeroelastic trim and response prediction capability in axial flight, in a wind tunnel, or in free flight is included in the analysis. The blade response equations are solved using a robust finite element in time procedure for obtaining the steady-state periodic solution. Loads are calculated using a force summation approach. Rotor inflow models ranging from the simplest momentum-theory based uniform inflow and radially varying inflow models to the vortex-transport based prescribed wake and free wake models are implemented in the tiltrotor analysis. Aeroelastic stability of the system is calculated using a linearized eigenanalysis and through either Floquet Theory or Constant Coefficient method. A detailed description of the formulation and the analysis procedure is given in Chapters 3 and 4.

8.3 Validation Studies

The validation studies reported in Chapter 5 consisted of two parts. The first was a comparison of the stability results from the rigid blade tiltrotor study with results from the elastic blade study and with test data to understand the strengths and limitations of the rigid blade study. The second is a validation of the results from the elastic blade analysis, for trim controls, rotor response, loads and aeroelastic stability, with other comprehensive analyses and with test data.

Reproduced with permission of the copyright owner. Further reproduction prohibited without permission.

The following conclusions were drawn from comparing the rigid blade predictions with other predictions and test data:

(1) The rigid blade analysis captures the occurrence of whirl flutter instability in the wing modes, as well as the elastic blade analysis, only for straight rectangular planform blades. This shows that a rigid rotor analysis can accurately capture the destabilizing rotor forces that cause whirl flutter.

(2) The rigid rotor analysis does not, however, predict the behavior of different blade modes accurately. Uncoupled flap and lag modes are modeled in the analysis, and this assumption proves to be restrictive in accurately modeling the behavior of the blade modes in high speed axial flight when the rotor collective is very high, and the blade flap and lag modes are highly coupled.

(3) Although rotor precone is not modeled directly in the rigid blade analysis, its effect on stability can be captured through an equivalent model by using appropriate values of negative pitch-lag coupling. The predictions of flutter velocity using this approach compare well with those from the elastic blade analysis.

(4) The analysis predicts the correct trends in flutter velocity variation with rotor precone. As rotor precone angle is increased, the effective pitch-lag coupling increases in high speed flight, and the flutter velocity decreases from this destabilizing effect.

(5) Predictions of flutter velocity variation with blade pitch-flap coupling correlate very well with wind tunnel test data.

(6) Predicted wing beam mode damping variation with airspeed correlates well with other analyses and with test data; the same is true for the predicted beam

Reproduced with permission of the copyright owner. Further reproduction prohibited without permission.

mode flutter speed as well.

The elastic blade analysis results were compared with results from other comprehensive analyses and with test data. The following observations were made from that study:

(1) The present analysis predictions for fuselage pitch attitude in high speed trimmed flight compare satisfactorily with test data. The prediction of rotor collective correlates well with C81 analysis predictions and with test data. Variation of rotor longitudinal and lateral cyclic controls with flight speed are predicted well by the present analysis.

(2) Variation of rotor gimbal response with flight speed is predicted well by the present analysis; the predictions compared favorably with C81 predictions and with test data.

(3) Predictions of rotor torque variation with airspeed from the present analysis compare well with test data; it is expected that better correlation might be obtained if rotor/wing aerodynamic interactional effects are modeled in the analysis.

(4) The analysis predicts the magnitudes of the oscillatory beamwise and chordwise bending moments well; their variation with airspeed is captured satisfactorily.

(5) Predicted stability frequencies for the wing symmetric beam, chord and torsion modes compare very well with those from other comprehensive analyses and with flight test data.

(6) The present analysis predicts the wing symmetric beam and chord mode damping values well; the predictions for the wing symmetric torsion mode damping were lower than the actual damping values recorded during the flight test. The

Reproduced with permission of the copyright owner. Further reproduction prohibited without permission.

damping predictions from the present analysis compare well with those from other analyses.

(7) Predictions of wing beam mode damping (for the symmetric mode) compare well with full-scale wind tunnel test data and with CAMRAD predictions.

These conclusions show that the present analysis predicts the magnitude of trim controls, rotor response, loads and aeroelastic stability, along with their variation with forward flight velocity, satisfactorily.

8.4 Parametric Studies

Advanced geometry blades with tip sweep, anhedral and planform taper were investigated for tiltrotor configurations. The effects of such blades on system natural frequencies, rotor response and aeroelastic stability were discussed in Chapter 6. The following conclusions were made from the study:

(1) Tip sweep and anhedral have a significant effect on the first torsion and coupled flap-lag-torsion rotating blade natural frequencies. Planform taper, on the other hand, has a negligible influence on natural frequencies.

(2) Tip sweep, anhedral and planform taper alter the blade response significantly. The blade torsional response along the span is modified considerably. Backward tip sweep given to the blade causes a nose-down torsional response over most part of the blade while forward tip sweep causes a nose-up torsional response. Blade tip droop and tip planform taper result in a nose-up torsional response along the blade span compared to the baseline. The blade loading is, therefore, redistributed by the inclusion of sweep, anhedral or taper.

Reproduced with permission of the copyright owner. Further reproduction prohibited without permission.

(3) Tip sweep and anhedral affect the collective pitch angle, required to trim the configuration to a specified thrust at a given forward velocity. For example, a backward tip sweep of 30° increases the collective required by about 2° while a forward tip sweep of 30° decreases the collective by about 2°. The inclusion of tip droop causes an increase in the collective required. Inclusion of planform taper, however, does not change the collective angle significantly. The predicted changes in collective pitch with blade tip sweep or anhedral are due to changes in the torsional response of the blade along its span (dynamic effects).

(4) Blade tip sweep back increases the stability margin of the high frequency elastic flap mode at the cruise speed; tip sweep-forward makes this mode unstable. A similar effect of sweep is observed on the wing modes as well. This is due to the pitch-flap coupling effect resulting from blade tip sweep.

(5) Small values of blade tip droop stabilizes the rotor modes at the cruise speed; anhedral, on the other hand, strongly destabilizes the rotor. Tip droop of about 5° stabilizes the wing modes by offsetting the destabilizing pitch-lag coupling effect of rotor precone in the baseline configuration. Tip anhedral destabilizes the wing modes by increasing the magnitude of destabilizing negative pitch-lag coupling in the rotor.

(6) Planform taper marginally destabilizes both the rotor and wing modes, at cruise. This can be attributed to an outboard shift (for this configuration) in the aerodynamic loading, with increasing planform taper.

(7) The predicted flutter speed increases from 275 knots for the baseline configuration to about 370 knots for a 30° blade tip sweep-back; this represents a phe-

Reproduced with permission of the copyright owner. Further reproduction prohibited without permission.

nomenal increase in the maximum speed capability. A forward sweep of about 30°, given to the blade tip, makes the system unstable over the speed ranges studied. Blade tip sweep results in flap-torsion coupling in the rotor blade. This coupling effect is stabilizing for backward sweep and destabilizing for forward sweep.

(8) Blade tip anhedral has a powerful effect on system stability. Tip droop of 5° increases the flutter speed of the configuration to around 350 knots (an increase of 75 knots over the baseline). Anhedral of 5°, however, makes the flutter speed drop to around 140 knots (a decrease of 135 knots from baseline). Tip anhedral results in negative pitch-lag coupling which is destabilizing. Blade tip droop, on the other hand, results in positive pitch-lag coupling which offsets the negative pitch-lag coupling due to rotor precone (in this configuration); tip droop is, therefore, stabilizing.

(9) Planform taper, maintaining thrust-weighted rotor solidity constant, decreases the flutter speed. Tip taper (root chord/tip chord ratio 3:1) given to the outboard 15% of the blade, decreases the flutter speed to 260 knots (a decrease of 15 knots from baseline). This destabilizing effect arises from the outboard shift in aerodynamic loading (for this configuration), with increasing planform taper.

(10) Rotor power required increases with blade backward tip sweep and decreases with forward tip sweep. This effect is primarily due to the tip sweep affecting the torsional response along the blade span resulting in large changes in power required. Propeller efficiency (a measure of the rotor performance) decreases with backward tip sweep and increases with forward tip sweep.

(11) Rotor power required increases with blade tip anhedral (up) but remains

Reproduced with permission of the copyright owner. Further reproduction prohibited without permission.

the same for tip droop. This effect is also due to the torsional response along the blade span with blade tip anhedral. Propeller efficiency decreases for blade tip anhedral (up) but remains the same for tip droop.

(12) Predicted values for rotor torque are dependent on the type of induced-inflow model used in the analysis. The radially varying inflow model performs as well as the more complex free-wake model in predicting the rotor torque. The uniform inflow model does not compare well with the other predictions. The choice of inflow model, however, plays a very insignificant role in the prediction of aeroelastic stability in high speed flight. Aeroelastic stability in airplane mode is dependent on high inflow aerodynamics. The inflow velocity, due to high forward speed, is orders of magnitude higher than the rotor induced-inflow. The choice of induced-inflow model, therefore, does not have a significant effect on predicted aeroelastic stability in airplane mode.

8.5 Fuselage Modeling

The tiltrotor aeroelastic analysis described in Chapters 3 and 4 was made more comprehensive by aeroelastically modeling the complete tiltrotor configuration. This included modeling the fuselage as a free-free beam; attached to the fuselage is a full-span wing with twin rotors, one at each wing tip. The formulation included different states for each of the two rotors which could be excited by rotor blade motion and through hub motion arising from wing symmetric and antisymmetric motion. Coupled fuselage rigid-body modes are also included in the analysis.

For robust modeling, the fuselage, wing and rotor blades are modeled using

Reproduced with permission of the copyright owner. Further reproduction prohibited without permission.

beam finite elements. For computational efficiency, the problem size is reduced by utilizing normal modes (obtained from the free vibration analysis) in the stability analysis. Normal modes for the fuselage/wing are calculated within the analysis; but normal modes for the fuselage and wing, calculated from very detailed dynamic analyses (which model the fuselage and wing structure in detail), can be included in the analysis with relative ease.

An XV-15 fuselage, wing and rotor system was modeled using this analysis. The six rigid body modes obtained from the free vibration analysis involved coupled motion between many of the six rigid-body degrees-of-freedom and wing elastic modes.

The predicted stability of the wing antisymmetric modes, obtained by using the present analysis was compared with results from other analyses and with flight test data. The following conclusions were drawn from the validation study:

(1) Predictions of stability frequencies from the present analysis for the wing antisymmetric beam, chord and torsion modes compare well with test data and those from other analyses.

(2) Damping predictions for the wing antisymmetric beam, chord and torsion modes are lower than the damping recorded during the flight test; the predictions from the present analysis compare favorably with those from other aeroelastic analyses. Underprediction of the wing damping, as is the case with the present analysis, is, however, better than overprediction of the damping values (since underprediction leads to conservative damping estimates).

Overall, satisfactory correlation was obtained from the validation of wing anti-

Reproduced with permission of the copyright owner. Further reproduction prohibited without permission.

symmetric mode stability.

Parametric studies were performed to investigate the effects of modeling the fuselage, full wing-span and twin-rotors on the predicted stability of advanced blade tip configurations. The following conclusions were drawn:

(1) The antisymmetric wing modes showed increased stability over the straight blade baseline case for the cases where 30° backward sweep was given to the blade tip (outboard 15% span) and 5° droop was given to the blade tip. Blade tip forward sweep, blade tip anhedral (up) and blade tip planform taper did not affect the damping of the antisymmetric wing modes significantly (for the configuration studied).

(2) The symmetric wing modes are more susceptible to whirl flutter instabilities than are the antisymmetric wing modes.

(3) The inclusion of antisymmetric wing modes in the analysis did not affect the predicted whirl flutter speeds of the symmetric wing modes or the blade modes (for this configuration).

(4) Inclusion of fuselage/wing rigid body modes in the stability analysis affects the predicted behavior of the antisymmetric wing modes, but the effects are very small.

8.6 Recommendations for Future Work

The research presented in this study has shown that there is a good potential for improving tiltrotor aeroelastic performance by tailoring the blade tip shapes. There are, however, some areas in which the present investigation was limited by

Reproduced with permission of the copyright owner. Further reproduction prohibited without permission.

modeling constraints. This section suggests some areas for improvement in the present analysis as well as some other issues of relevance that could be studied.

(1) The present analysis has used a simple drive-train dynamics model. The two cases considered are constant rotor speed (powered configuration) and a zero frequency rotor speed perturbation (windmilling configuration). A detailed drive-train dynamics model including the torsional inertia, damping and stiffness characteristics of the drive system should be included in a future analysis.

(2) In high speed axial flight, when the pylon is tilted forward into the relative wind, it usually rests on a downstop that has its own stiffness properties. The downstop acts as a restraint for the pylon, and could play an important role in the predictions of aeroelastic stability. A simple model of the downstop should be included in a future analysis to consider its effect on tiltrotor stability.

(3) The fuselage is modeled in the present formulation using beam finite elements. Although this model is adequate for studying wing symmetric and anti-symmetric motion, a more detailed fuselage model (including the three-dimensional characteristics of the fuselage) is necessary to accurately investigate fuselage vibratory loads and stability.

(4) The accurate calculation of rotor loads is a challenging task for all rotorcraft researchers. It is more of a challenge in tiltrotor research due to the complex aerodynamic flow-field resulting from interactions between the rotors and the wing, fuselage and empennage. In hover, and in conversion mode, a significant download due to the thrusting rotor acts on the wing and affects the aircraft performance. A fountain effect resulting from the rotor inflow impinging on the wing results in

Reproduced with permission of the copyright owner. Further reproduction prohibited without permission.

massive recirculation in the flow-field. Also, as the blade rotates over the wing, it is subjected to a 1/rev excitation from the presence of the wing; this would modify the rotor loads and affect performance. Also, vortex-transport type rotor inflow models such as the prescribed-wake and free-wake models need to account for the rotor/wing interactional effects. A detailed wing download and rotor/wing interference model should be included in this analysis to improve the rotor load predictions.

(5) A blade-element model is used in this analysis to calculate the aerodynamic loads. More sophisticated aerodynamic analyses (such as CFD analyses) are necessary to accurately predict the aerodynamics of blade tips with sweep or anhedral. Aerodynamic tip loss effects would also need to be included in a future analysis. These loss effects could be dependent on blade sweep and anhedral and on rotor operating conditions.

(6) The present analysis allows for the modeling and implementation of bearingless and elastomeric hubs since the analysis is based on a robust finite-element approach. The effect of blade shape tailoring on tiltrotors with such advanced hubs needs to be studied so that novel designs could be examined to gain significant performance pay-offs.

(7) Experimental research in tiltrotors is a very expensive proposition; more experimental investigations, however, need to be undertaken to gather valuable data on blade loads, performance and aeroelastic stability of elastically-coupled advanced blade tips for tiltrotors.

(8) The present research has dealt with tailoring the blade tip shape and other

Reproduced with permission of the copyright owner. Further reproduction prohibited without permission.

important design parameters to alleviate aeroelastic instabilities. Similar results might be achieved by employing the use of feed-back control systems for stability augmentation.

(9) Recent developments in the application of smart structures to rotorcraft are promising in the areas of vibration control and (both external and internal) noise reduction. The viability of such concepts for tiltrotor applications needs to be examined.

(10) Gust response of tiltrotors is very important to passenger ride quality and fatigue-life of structural components of the airframe. The large disk area of tiltrotors, compared to conventional turbo-prop aircraft makes the tiltrotor more sensitive to gusts from all directions. A transient response analysis for evaluating the gust response characteristics of tiltrotors could be included in the present analysis.

(11) There is tremendous research activity currently taking place in the field of tiltrotor aeroacoustics. A coordinated effort involving aeroacousticians, dynamicists and aerodynamicists needs to be put together if the dream of a civilian/low-noise efficient tiltrotor is to become a reality.

Reproduced with permission of the copyright owner. Further reproduction prohibited without permission.

Appendix A

Rigid Blade Tiltrotor Model

A.1 Analytical Model

The tiltrotor configuration is modeled as a simple linear rigid-blade rotor model in the airplane mode. Such a model provides good insight into the aeroelastic phenomena causing the occurrence of tiltrotor instabilities. The equations of motion are derived, in this chapter, from first principles for a tiltrotor cantilevered wing model in the axial flight mode. The formulation of the rotor system equations of motion follows closely the formulation presented by Johnson [38] and Nixon [39]. The improvement in the present formulation over that of Johnson is the coupling of the rotor equations with a wing finite element model rather than with a limited wing modal representation (using only three wing modes). The present formulation is more comprehensive than that described in Ref. [39] since it includes both pitch-flap and pitch-lag kinematic couplings for the rotor blade. Wing sweep is also modeled in the formulation.

Reproduced with permission of the copyright owner. Further reproduction prohibited without permission.

A.1.1 Rotor and Hub Structural Model

Figure A.1 shows a rigid bladed rotor system on a rigid pylon. The rotor blade has two fundamental degrees-of-freedom, uncoupled flap and lag, and the pylon motion at the pivot point has six associated degrees of freedom. The pivot point is located a distance h behind the blade hub and the rotor is shown to be oriented symmetrically with respect to the oncoming flow (tiltrotor axial flight mode). The translational degrees of freedom at the pylon pivot are x_p, y_p, and z_p that represent the vertical, lateral and longitudinal motions respectively, and the rotational degrees of freedom at the pylon pivot are α_x, α_y and α_z that represent the pylon yaw, pitch and roll motions respectively. There are six rotor forces defined at the rotor hub (in the fixed reference frame) which can be translated back to the pylon pivot. These forces have both inertial and aerodynamic contributions from the rotor system.

The rotor system is assumed to be three-bladed with a gimballed hub (which is representative of current tiltrotor configurations). There are two degrees of freedom per blade which are associated with the fundamental flap and lag blade modes defined relative to the hub plane. These modes are assumed to be uncoupled. This is not a good approximation of the elastic motion of a tiltrotor blade because of the high twist and high collective pitch typically associated with these blades. Also advanced geometry blades with sweep, anhedral and planform taper variation with span as well as composite-coupled blades and bearingless rotors cannot be modeled adequately with this formulation. However, for the case in consideration, the predominant blade flap motion is a rigid body rotation about the center of

Reproduced with permission of the copyright owner. Further reproduction prohibited without permission.

rotation because of the presence of the gimbal. Thus, an assumption of uncoupled flap and lag motions should not have a major influence in this case. Kvaternik [35] showed that accurate representation of basic tiltrotor dynamics can be achieved without inclusion of lag motion.

Rigid pitch motion of the blade about its feathering axis is considered in this formulation. The steady pitch is a sum of the root collective and built-in blade twist. A perturbation of the pitch motion is associated with a small change in the control inputs with kinematic pitch/flap coupling (δ_3 due to flap hinge skew angle) and kinematic pitch/lag coupling (δ_4 due to lag hinge skew angle). The rotor is assumed to rotate freely on the shaft (windmilling state) such that no torque is transmitted to the pylon pivot and pylon roll motion does not influence the rotor rotation rate. This state is modeled after the equations of motion are transformed into the fixed frame by assuming a zero frequency for the collective lag mode. The initial equations of motion for the rotor system, with hub motions included, are derived in the rotating reference frame for a constant rotational speed Ω.

The equations of motion for the blade in the rotating reference frame including hub motion are given in Refs.[38] and [39] in nondimensional form as:

$$I_{\beta}^{\star}\left[\overset{\star\star}{\beta}+\nu_{\beta}^{2}\beta\right]+I_{\beta\alpha}^{\star}\left[-\left(\overset{\star\star}{\alpha}_{y}-2\,\overset{\star}{\alpha}_{x}\right)\cos\psi_{m}+\left(\overset{\star\star}{\alpha}_{x}+2\,\overset{\star}{\alpha}_{y}\right)\sin\psi_{m}\right]$$
$$+S_{\beta}^{\star}\,\overset{\star\star}{z}_{P} = \frac{\gamma M_{F}}{ac} \qquad \text{(A.1)}$$

$$I_{\zeta}^{\star}\left[\overset{\star\star}{\zeta}+\nu_{\zeta}^{2}\zeta\right]+S_{\zeta}^{\star}\left[\left(\overset{\star\star}{x}_{P}+h\,\overset{\star\star}{\alpha}_{y}\right)\sin\psi_{m}-\left(\overset{\star\star}{y}_{P}-h\,\overset{\star\star}{\alpha}_{x}\right)\cos\psi_{m}\right]$$
$$-I_{\zeta\alpha}^{\star}\,\overset{\star\star}{\alpha}_{z} = \frac{\gamma M_{L}}{ac} \qquad \text{(A.2)}$$

where M_F and M_L represent the flap and lag components of the distributed aero-

Reproduced with permission of the copyright owner. Further reproduction prohibited without permission.

dynamic forces.

The inertia constants are nondimensionalized by the rigid-blade flap inertia about the blade root, I_b (such as $I^{\star}_{\beta} = I_\beta / I_b$). These are defined in terms of the blade section mass and the blade mode shapes.

$$I_b = \int_0^R r^2 m \, dr \tag{A.3}$$

$$I_\beta = \int_0^R \eta_\beta^2 m \, dr \tag{A.4}$$

$$I_{\beta\alpha} = \int_0^R \eta_\beta m r \, dr \tag{A.5}$$

$$S_\beta = \int_0^R \eta_\beta m \, dr \tag{A.6}$$

$$I_\zeta = \int_0^R \eta_\zeta^2 m \, dr \tag{A.7}$$

$$I_{\zeta\alpha} = \int_0^R \eta_\zeta m r \, dr \tag{A.8}$$

$$S_\zeta = \int_0^R \eta_\zeta m \, dr \tag{A.9}$$

The blade flap bending mode is represented by η_β and the lag bending mode is represented by η_ζ, and the mode shapes are $\eta_\beta = r$ for rigid flap motion and $\eta_\zeta = r$ for rigid lag motion. Coriolis inertial coupling is neglected in these equations because these forces are small compared to the aerodynamic forces associated with high inflow aerodynamics where the forces in the lag direction are of the same magnitude as the flap direction.

The equations of motion are transformed into the fixed frame using the Fourier coordinate transformation for a three bladed rotor.

$$I^{\star}_{\beta_0} \left(\overset{\star\star}{\beta}_0 + \nu^2_{\beta_0} \beta_0 \right) + S^{\star}_{\beta_0} \overset{\star\star}{z}_P = \frac{\gamma M_{F_0}}{ac} \tag{A.10}$$

$$I^{\star}_{\beta} \left[\overset{\star\star}{\beta}_{1C} + 2 \overset{\star}{\beta}_{1S} + \left(\nu^2_\beta - 1 \right) \beta_{1C} \right] + I^{\star}_{\beta\alpha} \left(- \overset{\star\star}{\alpha}_y + 2 \overset{\star}{\alpha}_x \right) = \frac{\gamma M_{F_{1C}}}{ac} \tag{A.11}$$

Reproduced with permission of the copyright owner. Further reproduction prohibited without permission.

$$I_{\beta}^{\star}\left[\overset{\star\star}{\beta}_{1S} - 2\overset{\star}{\beta}_{1C} + \left(\nu_{\beta}^{2} - 1\right)\beta_{1S}\right] + I_{\beta\alpha}^{\star}\left(\overset{\star\star}{\alpha}_{x} + 2\overset{\star}{\alpha}_{y}\right) = \frac{\gamma M_{F_{1S}}}{ac} \quad \text{(A.12)}$$

$$I_{\zeta_0}^{\star}\left(\overset{\star\star}{\zeta}_{0} + \nu_{\zeta_0}^{2}\zeta_{0}\right) - I_{\zeta_0\alpha}^{\star}\overset{\star\star}{\alpha}_{z} = \frac{\gamma M_{L_0}}{ac} \quad \text{(A.13)}$$

$$I_{\zeta}^{\star}\left[\overset{\star\star}{\zeta}_{1C} + 2\overset{\star}{\zeta}_{1S} + \left(\nu_{\zeta}^{2} - 1\right)\zeta_{1C}\right] + S_{\zeta}^{\star}\left(-\overset{\star\star}{y}_{P} + h\overset{\star\star}{\alpha}_{x}\right) = \frac{\gamma M_{L_{1C}}}{ac} \quad \text{(A.14)}$$

$$I_{\zeta}^{\star}\left[\overset{\star\star}{\zeta}_{1S} - 2\overset{\star}{\zeta}_{1C} + \left(\nu_{\zeta}^{2} - 1\right)\zeta_{1S}\right] + S_{\zeta}^{\star}\left(\overset{\star\star}{x}_{P} + h\overset{\star\star}{\alpha}_{y}\right) = \frac{\gamma M_{L_{1S}}}{ac} \quad \text{(A.15)}$$

The frequencies and inertial parameters in the fixed frame vary between the collective mode and cyclic mode equations of motion. This is because of the root constraint conditions varying for a gimballed rotor system depending on the rotor mode in consideration. For a gimballed rotor, the collective flap and cyclic lag modes of the blade behave as if in a cantilevered condition, while the cyclic flap modes act as though the blade is hinged at the center of rotation. In collective lag, the blade acts as if it is cantilevered if the rotor is assumed to turn at constant speed. Since a windmilling rotor assumption is made in this formulation, the blade is hence free to rotate about the shaft such that

$$\nu_{\zeta_0} = 0 \quad \text{(A.16)}$$

$$I_{\zeta_0}^{\star} = 1 \quad \text{(A.17)}$$

$$I_{\zeta_0\alpha}^{\star} = 1 \quad \text{(A.18)}$$

The flap aerodynamic moments in the fixed frame are given by:

$$M_{F_0} = \frac{1}{N_b}\sum_{m} M_{F_m} \quad \text{(A.19)}$$

$$M_{F_{1C}} = \frac{2}{N_b}\sum_{m} M_{F_m}\cos\psi_m \quad \text{(A.20)}$$

$$M_{F_{1S}} = \frac{2}{N_b}\sum_{m} M_{F_m}\sin\psi_m \quad \text{(A.21)}$$

Reproduced with permission of the copyright owner. Further reproduction prohibited without permission.

A.1.2 Rotor Aerodynamics

The rotor aerodynamics are based on linear strip theory with section lift and drag defined as

$$L = \frac{1}{2}\rho c\left(u_T^2 + u_P^2\right) c_l \tag{A.22}$$

$$D = \frac{1}{2}\rho c\left(u_T^2 + u_P^2\right) c_d \tag{A.23}$$

where c_l and c_d are the local blade section lift and drag coefficients respectively. The velocity components are defined with respect to the hub plane as shown in Figure A.2 which also illustrates definition of the angle of attack, inflow angle and pitch angle of the blade section. Resolving the section aerodynamic forces into the hub plane, and nondimensionalizing by ac, the blade loads are written as follows:

$$\frac{F_z}{ac} = U\left(u_T\frac{c_l}{2a} - u_P\frac{c_d}{2a}\right) \tag{A.24}$$

$$\frac{F_x}{ac} = U\left(u_P\frac{c_l}{2a} + u_T\frac{c_d}{2a}\right) \tag{A.25}$$

$$\frac{F_r}{ac} = Uu_R\frac{c_d}{2a} - \beta\frac{F_z}{2a} \tag{A.26}$$

where all forces are nondimensionalized by the air density ρ. The hub forces in the fixed frame are required since these forces act on the wing. In coefficient form, the required hub forces are defined in terms of the blade section forces as

$$\frac{C_T}{\sigma a} = \frac{1}{N_b}\sum_m \int_0^1 \frac{F_z}{ac}\,dr \tag{A.27}$$

$$\frac{2C_H}{\sigma a} = \frac{2}{N_b}\sum_m \left(\cos\psi_m \int_0^1 \frac{F_r}{ac}\,dr + \sin\psi_m \int_0^1 \frac{F_x}{ac}\,dr\right) \tag{A.28}$$

$$\frac{2C_Y}{\sigma a} = \frac{2}{N_b}\sum_m \left(\sin\psi_m \int_0^1 \frac{F_r}{ac}\,dr - \cos\psi_m \int_0^1 \frac{F_x}{ac}\,dr\right) \tag{A.29}$$

$$\frac{C_Q}{\sigma a} = \frac{1}{N_b}\sum_m \int_0^1 \frac{F_x}{ac} r\,dr \tag{A.30}$$

Reproduced with permission of the copyright owner. Further reproduction prohibited without permission.

$$\frac{2C_{M_x}}{\sigma a} = \frac{2}{N_b}\sum_m \sin\psi_m \int_0^1 \frac{F_r}{ac} r\,dr \tag{A.31}$$

$$\frac{2C_{M_y}}{\sigma a} = -\frac{2}{N_b}\sum_m \cos\psi_m \int_0^1 \frac{F_r}{ac} r\,dr \tag{A.32}$$

Evaluation of these force integrals requires substitution of the aerodynamic parameters in terms of perturbation quantities resulting from blade and hub motion. The damping and stiffness associated with these perturbations determine the stability of the system. Each velocity component can be written as a sum of steady and perturbation (which are small) parts where the steady parts are given by:

$$u_T = \Omega r \tag{A.33}$$

$$u_P = V + \nu \tag{A.34}$$

$$u_R = 0 \tag{A.35}$$

For high inflow, this results in

$$\nu = \frac{C_T}{2V} \tag{A.36}$$

The perturbation parts of the velocities arise from blade and hub motions.

$$\begin{aligned}\delta u_T = {} & r\left(\overset{\star}{\alpha}_z - \overset{\star}{\zeta}\right) - h\left(\overset{\star}{\alpha}_y \sin\psi_m + \overset{\star}{\alpha}_x \cos\psi_m\right) + \\ & V\left(\alpha_y \sin\psi_m + \alpha_x \cos\psi_m\right) + \overset{\star}{y}_P \cos\psi_m - \overset{\star}{x}_P \sin\psi_m\end{aligned} \tag{A.37}$$

$$\delta u_P = r\left(\overset{\star}{\beta} - \overset{\star}{\alpha}_y \cos\psi_m + \overset{\star}{\alpha}_x \sin\psi_m\right) + \overset{\star}{z}_P \tag{A.38}$$

$$\begin{aligned}\delta u_R = {} & h\left(-\overset{\star}{\alpha}_y \cos\psi_m + \overset{\star}{\alpha}_x \sin\psi_m\right) + V\left(\alpha_y \cos\psi_m - \alpha_x \sin\psi_m\right) \\ & - \overset{\star}{y}_P \sin\psi_m - \overset{\star}{x}_P \cos\psi_m\end{aligned} \tag{A.39}$$

Rewriting the tangential and normal velocity perturbation components facilitates the integration of terms involving these perturbation quantities.

$$\delta u_T = r\delta u_{T_A} + \delta u_{T_B} \tag{A.40}$$

Reproduced with permission of the copyright owner. Further reproduction prohibited without permission.

$$\delta u_P = r\delta u_{P_B} + \delta u_{P_A} \tag{A.41}$$

The perturbations of the remaining aerodynamic parameters are given by

$$\delta c_l = \frac{\partial c_l}{\partial \alpha}\delta\alpha + \frac{\partial c_l}{\partial M}\delta M \tag{A.42}$$

$$\delta c_d = \frac{\partial c_d}{\partial \alpha}\delta\alpha + \frac{\partial c_d}{\partial M}\delta M \tag{A.43}$$

$$\delta\alpha = \delta\theta - \frac{u_T\delta u_p - u_p\delta u_t}{U^2} \tag{A.44}$$

$$\delta U = \frac{u_T\delta u_T + u_p\delta u_P}{U} \tag{A.45}$$

$$\delta M = M_{tip}\delta U \tag{A.46}$$

$$\delta\theta = \theta - K_{P_\beta}\beta - K_{P_\zeta}\zeta \tag{A.47}$$

Substitution of the perturbation quantities into the integral force equations results in complicated expressions that can be simplified by expanding the force equations in terms of aerodynamic coefficients.

$$\int_0^1 \frac{F_z}{ac} r\,dr = M_0 + \check{M}_\mu\delta u_{T_B} + M_{\overset{\star}{\zeta}}\delta u_{T_A} + M_\lambda\delta u_{P_A} + M_{\overset{\star}{\beta}}\delta u_{P_B} + M_\theta\delta\theta \tag{A.48}$$

$$\int_0^1 \frac{F_x}{ac} dr = H_0 + H_\mu\delta u_{T_B} + H_{\overset{\star}{\zeta}}\delta u_{T_A} + H_\lambda\delta u_{P_A} + H_{\overset{\star}{\beta}}\delta u_{P_B} + H_\theta\delta\theta \tag{A.49}$$

$$\int_0^1 \frac{F_z}{ac} dr = T_0 + T_\mu\delta u_{T_B} + T_{\overset{\star}{\zeta}}\delta u_{T_A} + T_\lambda\delta u_{P_A} + T_{\overset{\star}{\beta}}\delta u_{P_B} + T_\theta\delta\theta \tag{A.50}$$

$$\int_0^1 \frac{F_x}{ac} r\,dr = Q_0 + Q_\mu\delta u_{Q_B} + Q_{\overset{\star}{\zeta}}\delta u_{Q_A} + Q_\lambda\delta u_{P_A} + Q_{\overset{\star}{\beta}}\delta u_{P_B} + Q_\theta\delta\theta \tag{A.51}$$

$$\int_0^1 \frac{F_r}{ac} dr = R_\mu\delta u_R - \beta\frac{C_T}{\sigma a} \tag{A.52}$$

The aerodynamic forces M, H, T, Q and R denote the flap moment, inplane drag force, thrust, torque, and blade radial force respectively. The subscripts of these terms denote the source of the force or moment - 0 is the trim value, μ is hub inplane velocity, $\overset{\star}{\zeta}$ is blade lag velocity, $\overset{\star}{\beta}$ is flap velocity, λ is hub longitudinal or inflow velocity, and θ is pitch control.

Reproduced with permission of the copyright owner. Further reproduction prohibited without permission.

The blade forces are then transformed into the fixed frame to obtain the final aerodynamic force relations in terms of the forward flight velocity and the blade and hub motions.

$$
\begin{aligned}
M_{F_0} &= M_0 + M_{\overset{\star}{\zeta}}\left(\overset{\star}{\alpha}_z - \overset{\star}{\zeta}_0\right) + M_{\overset{\star}{\beta}}\,\overset{\star}{\beta}_0 + M_\lambda\,\overset{\star}{z}_P + \\
&\quad M_\theta\left(\theta_0 - K_{P_\beta}\beta_0 - K_{P_\zeta}\zeta_0\right) && \text{(A.53)} \\
M_{F_{1C}} &= M_\mu\left(-h\,\overset{\star}{\alpha}_x + V\alpha_x + \overset{\star}{y}_P\right) + M_{\overset{\star}{\beta}}\left(\overset{\star}{\beta}_{1C} + \beta_{1S} - \overset{\star}{\alpha}_y\right) + \\
&\quad M_{\overset{\star}{\zeta}}\left(-\overset{\star}{\zeta}_{1C} - \zeta_{1S}\right) + M_\theta\left(\theta_{1C} - K_{P_\beta}\beta_{1C} - K_{P_\zeta}\zeta_{1C}\right) && \text{(A.54)} \\
M_{F_{1S}} &= M_\mu\left(-h\,\overset{\star}{\alpha}_y + V\alpha_y - \overset{\star}{x}_P\right) + M_{\overset{\star}{\beta}}\left(\overset{\star}{\beta}_{1S} - \beta_{1C} + \overset{\star}{\alpha}_x\right) + \\
&\quad M_{\overset{\star}{\zeta}}\left(-\overset{\star}{\zeta}_{1S} + \zeta_{1C}\right) + M_\theta\left(\theta_{1S} - K_{P_\beta}\beta_{1S} - K_{P_\zeta}\zeta_{1S}\right) && \text{(A.55)} \\
-M_{L_0} &= Q_0 + Q_{\overset{\star}{\zeta}}\left(\overset{\star}{\alpha}_z - \overset{\star}{\zeta}_0\right) + Q_{\overset{\star}{\beta}}\,\overset{\star}{\beta}_0 + Q_\lambda\,\overset{\star}{z}_P + \\
&\quad Q_\theta\left(\theta_0 - K_{P_\beta}\beta_0 - K_{P_\zeta}\zeta_0\right) && \text{(A.56)} \\
-M_{L_{1C}} &= Q_\mu\left(-h\,\overset{\star}{\alpha}_x + V\alpha_x + \overset{\star}{y}_P\right) + Q_{\overset{\star}{\beta}}\left(\overset{\star}{\beta}_{1C} + \beta_{1S} - \overset{\star}{\alpha}_y\right) + \\
&\quad Q_{\overset{\star}{\zeta}}\left(-\overset{\star}{\zeta}_{1C} - \zeta_{1S}\right) + Q_\theta\left(\theta_{1C} - K_{P_\beta}\beta_{1C} - K_{P_\zeta}\zeta_{1C}\right) && \text{(A.57)} \\
-M_{L_{1S}} &= Q_\mu\left(-h\,\overset{\star}{\alpha}_y + V\alpha_y - \overset{\star}{x}_P\right) + Q_{\overset{\star}{\beta}}\left(\overset{\star}{\beta}_{1S} - \beta_{1C} + \overset{\star}{\alpha}_x\right) + \\
&\quad Q_{\overset{\star}{\zeta}}\left(-\overset{\star}{\zeta}_{1S} + \zeta_{1C}\right) + Q_\theta\left(\theta_{1S} - K_{P_\beta}\beta_{1S} - K_{P_\zeta}\zeta_{1S}\right) && \text{(A.58)}
\end{aligned}
$$

Substitution of these expressions into Eqns. A.10-A.15 and grouping terms as coefficients of the blade and hub degrees of freedom completes the equations of motion for the rotor system.

After substitution of the perturbation quantities into the integral force expressions given by Eqns. A.27-A.32, and carrying out the integration, the blade forces are transformed into the fixed frame to obtain the hub forces in terms of the

Reproduced with permission of the copyright owner. Further reproduction prohibited without permission.

forward flight velocity and the blade and hub motions.

$$\frac{C_T}{\sigma a} = T_0 + T_{\overset{\star}{\zeta}}\left(\overset{\star}{\alpha}_z - \overset{\star}{\zeta}_0\right) + T_{\overset{\star}{\beta}}\overset{\star}{\beta}_0 + T_\lambda \overset{\star}{z}_P + T_\theta\left(\theta_0 - K_{P_\beta}\beta_0 - K_{P_\zeta}\zeta_0\right) \tag{A.59}$$

$$\frac{2C_H}{\sigma a} = (H_\mu + R_\mu)\left[-h\overset{\star}{\alpha}_y + V\alpha_y - \overset{\star}{x}_P\right] + H_{\overset{\star}{\zeta}}\left(-\overset{\star}{\zeta}_{1S} + \zeta_{1C}\right) + H_{\overset{\star}{\beta}}\left(\overset{\star}{\beta}_{1S} + \overset{\star}{\alpha}_x\right) + H_\theta\left(\theta_{1S} - K_{P_\beta}\beta_{1S} - K_{P_\zeta}\zeta_{1S}\right) - H_{\overset{\star}{\beta}}\beta_{1C} \tag{A.60}$$

$$\frac{2C_Y}{\sigma a} = -(H_\mu + R_\mu)\left[-h\overset{\star}{\alpha}_x + V\alpha_x + \overset{\star}{y}_P\right] - H_{\overset{\star}{\zeta}}\left(-\overset{\star}{\zeta}_{1C} - \zeta_{1S}\right) - H_{\overset{\star}{\beta}}\left(\overset{\star}{\beta}_{1C} + \overset{\star}{\alpha}_y\right) - H_\theta\left(\theta_{1C} - K_{P_\beta}\beta_{1C} - K_{P_\zeta}\zeta_{1C}\right) - H_{\overset{\star}{\beta}}\beta_{1S} \tag{A.61}$$

$$\frac{C_Q}{\sigma a} = Q_0 + Q_{\overset{\star}{\zeta}}\left(\overset{\star}{\alpha}_z - \overset{\star}{\zeta}_0\right) + Q_{\overset{\star}{\beta}}\overset{\star}{\beta}_0 + Q_\lambda \overset{\star}{z}_P + Q_\theta\left(\theta_0 - K_{P_\beta}\beta_0 - K_{P_\zeta}\zeta_0\right) \tag{A.62}$$

An inertial force contribution to the hub forces should be added to the above aerodynamic contributions as follows:

$$\left(\frac{C_T}{\sigma a}\right)_i = -\frac{S_{\overset{\star}{\beta}_0}}{\gamma}\overset{\star\star}{\beta}_0 - \frac{M_{\overset{\star}{b}}}{\gamma}\overset{\star\star}{z}_P \tag{A.63}$$

$$\left(\frac{2C_H}{\sigma a}\right)_i = -\frac{S_{\overset{\star}{\zeta}}}{\gamma}\overset{\star\star}{\zeta}_{1S} - \frac{2}{\gamma}M_{\overset{\star}{b}}\left(\overset{\star\star}{x}_P + h\overset{\star\star}{\alpha}_y\right) \tag{A.64}$$

$$\left(\frac{2C_Y}{\sigma a}\right)_i = \frac{S_{\overset{\star}{\zeta}}}{\gamma}\overset{\star\star}{\zeta}_{1C} - \frac{2}{\gamma}M_{\overset{\star}{b}}\left(\overset{\star\star}{y}_P - h\overset{\star\star}{\alpha}_x\right) \tag{A.65}$$

$$\left(\frac{C_Q}{\sigma a}\right)_i = -\frac{I_{\overset{\star}{\zeta_0\alpha}}}{\gamma}\overset{\star\star}{\zeta}_0 - \frac{I_{\overset{\star}{0}}}{\gamma}\overset{\star\star}{\alpha}_z \tag{A.66}$$

Instead of carrying out the aerodynamic integral expressions for the hub moment terms C_{M_x} and C_{M_y} and then adding in the inertial contributions, these moments can be written as a resultant spring moment which includes both the aerodynamic and inertial contributions:

$$\left(\frac{2C_{M_x}}{\sigma a}\right)_{total} = \frac{I_{\overset{\star}{\beta}}}{\gamma}\left(\nu_\beta^2 - 1\right)\beta_{1S} \tag{A.67}$$

Reproduced with permission of the copyright owner. Further reproduction prohibited without permission.

$$\left(\frac{2C_{M_y}}{\sigma a}\right)_{total} = -\frac{I^{\star}_{\beta}}{\gamma}\left(\nu_{\beta}^2 - 1\right)\beta_{1C} \tag{A.68}$$

It is seen from these expressions that the hub moments are zero when the in-vacuo flap frequency ν_β is equal to unity such as the case of an articulated rotor hinged at the center of rotation and the hub moments increase as the flap frequency increases for given values of the flap angles.

The formulation of the aerodynamic contributions would be complete if the integral expressions for the aerodynamic coefficients are defined and evaluated. These expressions are listed below and are evaluated numerically in the present analysis.

$$T_0 = \frac{1}{2a}\int_0^1 U\left(u_T c_l - u_P c_d\right) dr \tag{A.69}$$

$$T_\theta = \frac{1}{2a}\int_0^1 U(u_T c_{l_\alpha} - u_P c_{d_\alpha}) dr \tag{A.70}$$

$$T_\mu = \frac{1}{2a}\int_0^1 \left[\frac{u_T u_P}{U}c_{l_\alpha} + \frac{u_T^2}{U}Mc_{l_M} + Uc_l - \frac{u_P^2}{U}c_{d_\alpha} - \frac{u_T u_P}{U}Mc_{d_M} + \frac{u_T^2}{U}c_l - \frac{u_T u_P}{U}c_d\right] dr \tag{A.71}$$

$$T^{\star}_{\zeta} = \frac{1}{2a}\int_0^1 \left[\frac{u_T u_P}{U}c_{l_\alpha} + \frac{u_T^2}{U}Mc_{l_M} + Uc_l - \frac{u_P^2}{U}c_{d_\alpha} - \frac{u_T u_P}{U}Mc_{d_M} + \frac{u_T^2}{U}c_l - \frac{u_T u_P}{U}c_d\right] r dr \tag{A.72}$$

$$T_\lambda = \frac{1}{2a}\int_0^1 \left[-\frac{u_T^2}{U}c_{l_\alpha} + \frac{u_T u_P}{U}Mc_{l_M} - Uc_d + \frac{u_T u_P}{U}c_{d_\alpha} - \frac{u_P^2}{U}Mc_{d_M} + \frac{u_T u_P}{U}c_l - \frac{u_P^2}{U}c_d\right] dr \tag{A.73}$$

$$T^{\star}_{\beta} = \frac{1}{2a}\int_0^1 \left[-\frac{u_T^2}{U}c_{l_\alpha} + \frac{u_T u_P}{U}Mc_{l_M} - Uc_d + \frac{u_T u_P}{U}c_{d_\alpha} - \frac{u_P^2}{U}Mc_{d_M} + \frac{u_T u_P}{U}c_l - \frac{u_P^2}{U}c_d\right] r dr \tag{A.74}$$

Reproduced with permission of the copyright owner. Further reproduction prohibited without permission.

$$M_0 = \frac{1}{2a}\int_0^1 U(u_T c_l - u_P c_d) r dr \tag{A.75}$$

$$M_\theta = \frac{1}{2a}\int_0^1 U(u_T c_{l_\alpha} - u_P c_{d_\alpha}) r dr \tag{A.76}$$

$$M_\mu = \frac{1}{2a}\int_0^1 \left[\frac{u_T u_P}{U} c_{l_\alpha} + \frac{u_T^2}{U} M c_{l_M} + U c_l - \frac{u_P^2}{U} c_{d_\alpha} - \frac{u_T u_P}{U} M c_{d_M} + \frac{u_T^2}{U} c_l - \frac{u_T u_P}{U} c_d\right] r dr \tag{A.77}$$

$$M_\zeta^\star = \frac{1}{2a}\int_0^1 \left[\frac{u_T u_P}{U} c_{l_\alpha} + \frac{u_T^2}{U} M c_{l_M} + U c_l - \frac{u_P^2}{U} c_{d_\alpha} - \frac{u_T u_P}{U} M c_{d_M} + \frac{u_T^2}{U} c_l - \frac{u_T u_P}{U} c_d\right] r^2 dr \tag{A.78}$$

$$M_\lambda = \frac{1}{2a}\int_0^1 \left[-\frac{u_T^2}{U} c_{l_\alpha} + \frac{u_T u_P}{U} M c_{l_M} - U c_d + \frac{u_T u_P}{U} c_{d_\alpha} - \frac{u_P^2}{U} M c_{d_M} + \frac{u_T u_P}{U} c_l - \frac{u_P^2}{U} c_d\right] r dr \tag{A.79}$$

$$M_\beta^\star = \frac{1}{2a}\int_0^1 \left[-\frac{u_T^2}{U} c_{l_\alpha} + \frac{u_T u_P}{U} M c_{l_M} - U c_d + \frac{u_T u_P}{U} c_{d_\alpha} - \frac{u_P^2}{U} M c_{d_M} + \frac{u_T u_P}{U} c_l - \frac{u_P^2}{U} c_d\right] r^2 dr \tag{A.80}$$

$$H_0 = \frac{1}{2a}\int_0^1 U(u_P c_l + u_T c_d) dr \tag{A.81}$$

$$H_\theta = \frac{1}{2a}\int_0^1 U(u_P c_{l_\alpha} + u_T c_{d_\alpha}) dr \tag{A.82}$$

$$H_\mu = \frac{1}{2a}\int_0^1 \left[\frac{u_P^2}{U} c_{l_\alpha} + \frac{u_T u_P}{U} M c_{l_M} + U c_d + \frac{u_T u_P}{U} c_{d_\alpha} + \frac{u_T^2}{U} M c_{d_M} + \frac{u_T u_P}{U} c_l + \frac{u_T^2}{U} c_d\right] dr \tag{A.83}$$

$$H_\zeta^\star = \frac{1}{2a}\int_0^1 \left[\frac{u_P^2}{U} c_{l_\alpha} + \frac{u_T u_P}{U} M c_{l_M} + U c_d + \frac{u_T u_P}{U} c_{d_\alpha} + \frac{u_T^2}{U} M c_{d_M} + \frac{u_T u_P}{U} c_l + \frac{u_T^2}{U} c_d\right] r dr \tag{A.84}$$

$$H_\lambda = \frac{1}{2a}\int_0^1 \left[-\frac{u_T u_P}{U} c_{l_\alpha} + \frac{u_P^2}{U} M c_{l_M} + U c_l - \frac{u_T^2}{U} c_{d_\alpha} + \frac{u_T u_P}{U} M c_{d_M} + \frac{u_P^2}{U} c_l + \frac{u_T u_P}{U} c_d\right] dr \tag{A.85}$$

Reproduced with permission of the copyright owner. Further reproduction prohibited without permission.

$$H^{\star}_{\beta} = \frac{1}{2a}\int_0^1 \left[-\frac{u_T u_P}{U}c_{l_\alpha} + \frac{u_P^2}{U}Mc_{l_M} + Uc_l - \frac{u_T^2}{U}c_{d_\alpha} + \frac{u_T u_P}{U}Mc_{d_M} + \frac{u_P^2}{U}c_l + \frac{u_T u_P}{U}c_d\right] rdr \quad \text{(A.86)}$$

$$Q_0 = \frac{1}{2a}\int_0^1 U(u_P c_l + u_T c_d) rdr \quad \text{(A.87)}$$

$$Q_\theta = \frac{1}{2a}\int_0^1 U(u_P c_{l_\alpha} + u_T c_{d_\alpha}) rdr \quad \text{(A.88)}$$

$$Q_\mu = \frac{1}{2a}\int_0^1 \left[\frac{u_P^2}{U}c_{l_\alpha} + \frac{u_T u_P}{U}Mc_{l_M} + Uc_d + \frac{u_T u_P}{U}c_{d_\alpha} + \frac{u_T^2}{U}Mc_{d_M} + \frac{u_T u_P}{U}c_l + \frac{u_T^2}{U}c_d\right] rdr \quad \text{(A.89)}$$

$$Q^{\star}_{\zeta} = \frac{1}{2a}\int_0^1 \left[\frac{u_P^2}{U}c_{l_\alpha} + \frac{u_T u_P}{U}Mc_{l_M} + Uc_d + \frac{u_T u_P}{U}c_{d_\alpha} + \frac{u_T^2}{U}Mc_{d_M} + \frac{u_T u_P}{U}c_l + \frac{u_T^2}{U}c_d\right] r^2 dr \quad \text{(A.90)}$$

$$Q_\lambda = \frac{1}{2a}\int_0^1 \left[-\frac{u_T u_P}{U}c_{l_\alpha} + \frac{u_P^2}{U}Mc_{l_M} + Uc_l - \frac{u_T^2}{U}c_{d_\alpha} + \frac{u_T u_P}{U}Mc_{d_M} + \frac{u_P^2}{U}c_l + \frac{u_T u_P}{U}c_d\right] rdr \quad \text{(A.91)}$$

$$Q^{\star}_{\beta} = \frac{1}{2a}\int_0^1 \left[-\frac{u_T u_P}{U}c_{l_\alpha} + \frac{u_P^2}{U}Mc_{l_M} + Uc_l - \frac{u_T^2}{U}c_{d_\alpha} + \frac{u_T u_P}{U}Mc_{d_M} + \frac{u_P^2}{U}c_l + \frac{u_T u_P}{U}c_d\right] r^2 dr \quad \text{(A.92)}$$

The numerical integration is performed by discretizing the blade into several segments and summing up the aerodynamic contribution of each segment. A trim procedure is implemented based on changes only in collective pitch until a desired rotor thrust level is obtained (usually zero for a windmilling rotor). The numerical approach allows flexibility in the blade section aerodynamics. The influence of stall and compressibility is included in the analysis. Numerical integration of the aerodynamic coefficients requires definition of c_{l_α}, c_l, c_{d_α}, c_d, Mc_{l_M}, and Mc_{d_M} at

Reproduced with permission of the copyright owner. Further reproduction prohibited without permission.

each blade segment which are based on the local pitch, inflow, and attack angles and local Mach number. The definitions in Ref.[38] are used for the unstalled lift parameters and include Mach number corrections. The stall angle is defined at 12°.

A.1.3 Wing Structural Model

The wing structural model is based on a finite-element formulation of a standard Euler beam undergoing beam (flap) bending, chordwise bending (lag) and torsion (see Figure A.3). The wing continuous degrees of freedom are given by

$$\hat{u} = \{w \; v \; \phi\} \tag{A.93}$$

which are related to the discrete degrees-of-freedom for an element by

$$\hat{q} = \{w_1 \; v_1 \; \phi_1 \; v_1' \; w_1' \; w_2 \; v_2 \; \phi_2 \; v_2' \; w_2'\} \tag{A.94}$$

as

$$\hat{u} = [H]\,\hat{q} \tag{A.95}$$

where $[H]$ is a matrix of shape functions.

The strain energy for linear beam theory is defined in terms of the beam continuous degrees of freedom of the present formulation as:

$$V = \frac{1}{2}\int_0^l \left[EI_c\,(v'')^2 + EI_b\,(w'')^2 + GJ\,(\phi')^2\right] dx \tag{A.96}$$

where EI_c, EI_b and GJ are the chordwise, beamwise and torsional wing stiffnesses respectively. The kinetic energy is formulated on the assumption that the wing

Reproduced with permission of the copyright owner. Further reproduction prohibited without permission.

c.g. may be offset from the wing elastic axis by a distance y. The translational velocity of an arbitrary point on the beam cross section is written as:

$$\dot{u}_x = 0 \tag{A.97}$$

$$\dot{u}_y = \dot{v} \tag{A.98}$$

$$\dot{u}_z = \dot{w} + y\dot{\phi} \tag{A.99}$$

In matrix form, the accelerations of an arbitrary point may be written as:

$$\ddot{\hat{u}} = \begin{bmatrix} \ddot{u}_y \\ \ddot{u}_z \end{bmatrix} = \begin{bmatrix} 0 & 1 & 0 \\ 1 & 0 & y \end{bmatrix} \begin{bmatrix} \ddot{w} \\ \ddot{v} \\ \ddot{\phi} \end{bmatrix} \tag{A.100}$$

The variation of the kinetic energy is then given by:

$$T = \int_V \rho\, \delta\hat{u}^T\, \ddot{\hat{u}}\, dV = \int_0^l \delta\hat{u}^T \left[\iint_A \rho \begin{bmatrix} 1 & 0 & y \\ 0 & 1 & 0 \\ y & 0 & y^2 \end{bmatrix} dA \right] \ddot{\hat{u}}\, dx \tag{A.101}$$

For derivation of the structural model, Hamilton's principle is applied.

$$\int_{t_1}^{t_2} \delta\left(T - V\right)\, dt = 0 \tag{A.102}$$

Substituting, the appropriate expressions for strain and kinetic energies and the discrete relations, the structural mass and stiffness matrices can be obtained:

$$\left[M^S\right] = \int_0^l [H]^T [M_s][H]\, dx \tag{A.103}$$

$$\left[K^S\right] = \int_0^l [H]^T [K_s][H]\, dx \tag{A.104}$$

where

$$[M_s] = \begin{bmatrix} m & 0 & S_\alpha \\ 0 & m & 0 \\ S_\alpha & 0 & I_0 \end{bmatrix} \tag{A.105}$$

$$[K_s] = \begin{bmatrix} EI_b & 0 & 0 \\ 0 & EI_c & 0 \\ 0 & 0 & GJ \end{bmatrix} \tag{A.106}$$

These integrations are performed symbolically and result in 10 x 10 beam element structural mass and stiffness matrices.

Reproduced with permission of the copyright owner. Further reproduction prohibited without permission.

A.1.4 Wing Aerodynamics

The wing aerodynamic model is based on a quasi-steady lift approximation:

$$\alpha_{eff} = \alpha_0 + \phi - \frac{\dot{w}}{U} \tag{A.107}$$

where U is the free stream velocity. The components of aerodynamic forces are given by

$$L_w = qcc_{l_\alpha}\left(\alpha_0 + \phi - \frac{\dot{w}}{U}\right) \tag{A.108}$$

$$L_v = 0 \tag{A.109}$$

$$M_\phi = L_w\, e \tag{A.110}$$

where e is the chordwise distance of the elastic axis behind the aerodynamic center. These forces may be expressed with aerodynamic coefficient matrices as:

$$\begin{Bmatrix} L_w \\ L_v \\ M_\phi \end{Bmatrix} = [A_0]\begin{Bmatrix} \alpha_0 \\ 0 \\ \alpha_0 \end{Bmatrix} + [A_0]\begin{Bmatrix} w \\ v \\ \phi \end{Bmatrix} + [A_1]\begin{Bmatrix} \dot{w} \\ \dot{v} \\ \dot{\phi} \end{Bmatrix} \tag{A.111}$$

where

$$[A_0] = \begin{bmatrix} 0 & 0 & qcc_{l_\alpha} \\ 0 & 0 & 0 \\ 0 & 0 & qcec_{l_\alpha} \end{bmatrix} \tag{A.112}$$

$$[A_1] = \begin{bmatrix} -qcc_{l_\alpha}/U & 0 & 0 \\ 0 & 0 & 0 \\ -qcec_{l_\alpha}/U & 0 & 0 \end{bmatrix} \tag{A.113}$$

The variation of work done by the aerodynamic forces is written as

$$\delta W = \int_0^l \{\delta w\ \delta v\ \delta\phi\}\begin{Bmatrix} L_w \\ L_v \\ M_\phi \end{Bmatrix} dx \tag{A.114}$$

which, after substitution of the aerodynamic coefficient expressions and the relations between the discrete and continuous degrees of freedom, leads to the aerody-

Reproduced with permission of the copyright owner. Further reproduction prohibited without permission.

namic damping and stiffness matrices.

$$\left[K^A\right] = \int_0^l [H]^T [A_1][H]\, dx \tag{A.115}$$

$$\left[C^A\right] = \int_0^l [H]^T [A_2][H]\, dx \tag{A.116}$$

These integrations are performed symbolically and result in 10 x 10 beam element aerodynamic damping and stiffness matrices. Application of Hamilton's principle in the nonconservative form shows that the aerodynamic matrices can be subtracted from the structural matrices to give the total mass, damping, and stiffness matrices for the wing.

$$[M_w] = \left[M^S\right] \tag{A.117}$$

$$[C_w] = \left[C^S\right] - \left[C^A\right] \tag{A.118}$$

$$[K_w] = \left[K^S\right] - \left[K^A\right] \tag{A.119}$$

Swept Wing Aerodynamics

For a swept wing, the aerodynamic contributions to the system matrices have to be modified. A wing swept back at an angle Λ is shown in Figure A.4. The quasi-steady lift approximation is written as

$$\alpha_{eff} = \alpha_0 + \phi \cos\Lambda - \frac{\dot{w}}{U} - w' \sin\Lambda \tag{A.120}$$

where a continuous degree-of-freedom w' is required for the formulation. The new relationship between the continuous and discrete degrees of freedom is written as

$$\hat{u}^A = \{w\ v\ \phi\ v'\ w'\} \tag{A.121}$$

which is related to the discrete degrees of freedom for an element by

Reproduced with permission of the copyright owner. Further reproduction prohibited without permission.

$$\hat{q} = \{w_1\ v_1\ \phi_1\ v_1'\ w_1'\ w_2\ v_2\ \phi_2\ v_2'\ w_2'\} \tag{A.122}$$

as

$$\hat{u}^A = \left[H^A\right]\ \hat{q} \tag{A.123}$$

where $[H^A]$ is the new matrix of shape functions for the swept wing.

To be compatible with the new vector of continuous displacements, the work is expressed as:

$$\delta W = \int_0^l \{\delta w\ \delta v\ \delta\phi\ \delta v'\ \delta w'\} \begin{Bmatrix} L_w \\ L_v \\ M_\phi \\ M_z \\ M_y \end{Bmatrix} dx \tag{A.124}$$

The components of aerodynamic forces are written in aerodynamic coefficient form as

$$\begin{Bmatrix} L_w \\ L_v \\ M_\phi \\ M_z \\ M_y \end{Bmatrix} = [A_2] \begin{Bmatrix} \alpha_0 \\ 0 \\ \alpha_0 \\ 0 \\ 0 \end{Bmatrix} + [A_2] \begin{Bmatrix} w \\ v \\ \phi \\ v' \\ w' \end{Bmatrix} + [A_3] \begin{Bmatrix} \dot{w} \\ \dot{v} \\ \dot{\phi} \\ \dot{v}' \\ \dot{w}' \end{Bmatrix} \tag{A.125}$$

where the new matrices are 5 x 5 rather than 3 x 3, and are listed as follows:

$$[A_2] = \begin{bmatrix} 0 & 0 & qcc_{l_\alpha}\cos\Lambda & 0 & qcc_{l_\alpha}\sin\Lambda \\ 0 & 0 & 0 & 0 & 0 \\ 0 & 0 & qcec_{l_\alpha}\cos\Lambda & 0 & qcec_{l_\alpha}\sin\Lambda \\ 0 & 0 & 0 & 0 & 0 \\ 0 & 0 & 0 & 0 & 0 \end{bmatrix} \tag{A.126}$$

$$[A_3] = \begin{bmatrix} -qcc_{l_\alpha}/U & 0 & 0 & 0 & 0 \\ 0 & 0 & 0 & 0 & 0 \\ -qecc_{l_\alpha}/U & 0 & 0 & 0 & 0 \\ 0 & 0 & 0 & 0 & 0 \\ 0 & 0 & 0 & 0 & 0 \end{bmatrix} \tag{A.127}$$

The variation of work performed by the aerodynamic forces then leads to the aerodynamic damping and stiffness matrices

$$\left[K^A\right] = \int_0^l \left[H^A\right]^T [A_4] \left[H^A\right] dx \tag{A.128}$$

Reproduced with permission of the copyright owner. Further reproduction prohibited without permission.

$$\left[C^A\right] = \int_0^l \left[H^A\right]^T [A_5] \left[H^A\right] dx \tag{A.129}$$

A.1.5 Coupling of the Wing and Rotor Systems

The wing is coupled to the rotor through the discrete degrees of freedom at the wing tip. There are two ways in which the coupling occurs: (1) the rotor system degrees of freedom at the pylon pivot point are related to the discrete degrees of freedom at the wing tip and (2) the rotor hub forces, which are written in terms of the rotor perturbation parameters, act on the wing.

The discrete displacements at the wing tip can be written as:

$$\hat{q}_t = \{\delta w_2 \ \delta v_2 \ \delta\phi_2 \ \delta v_2' \ \delta w_2'\} \tag{A.130}$$

where the subscript 2 indicates association with the second node of the wing tip beam element. With sweep introduced into the wing, these are related to the pylon pivot degrees of freedom (x_p, y_p, z_p , α_x, α_y and α_z) as:

$$x_p = w_2 \tag{A.131}$$

$$y_p = v_2 \sin\Lambda \tag{A.132}$$

$$z_p = v_2 \cos\Lambda \tag{A.133}$$

$$\alpha_x = v_2' \tag{A.134}$$

$$\alpha_y = \phi_2 \cos\Lambda - w_2' \sin\Lambda \tag{A.135}$$

$$\alpha_z = -\phi_2 \sin\Lambda - w_2' \cos\Lambda \tag{A.136}$$

and these relationships are substituted into the rotor system equations (Eqns. A.10-A.15 and Eqns. A.53-A.58) and the net hub force equations (Eqns. A.64-A.66).

Reproduced with permission of the copyright owner. Further reproduction prohibited without permission.

Work is performed on the wing by the rotor hub forces but only on the wing tip. After a transformation for the wing sweep, the work may be written as:

$$\delta W = \{\delta w_2 \ \delta v_2 \ \delta \phi_2 \ \delta v_2' \ \delta w_2'\} \begin{Bmatrix} H \\ T\cos\Lambda + Y\sin\Lambda \\ (M_y + hH)\cos\Lambda + Q\sin\Lambda \\ M_z - hY \\ -Q\cos\Lambda + (M_y + hH)\sin\Lambda \end{Bmatrix} \tag{A.137}$$

No integration is necessary at this point since the degrees of freedom are discrete. The work is nondimensionalized by dividing throughout by $(\frac{N_b}{2} I_b \Omega^2)$ which gives the coefficient form of the rotor hub forces:

$$\frac{\delta W}{\frac{N_b}{2} I_b \Omega^2} = \delta \hat{q}_t \left(\frac{2\gamma}{\sigma a}\right) \begin{Bmatrix} C_H \\ C_T\cos\Lambda + C_Y\sin\Lambda \\ \left(C_{M_y} + \bar{h}C_H\right)\cos\Lambda + C_Q\sin\Lambda \\ C_{M_z} - \bar{h}C_Y \\ -C_Q\cos\Lambda + \left(C_{M_y} + \bar{h}C_H\right)\sin\Lambda \end{Bmatrix} \tag{A.138}$$

Substitution of the expressions for the hub forces into the above equation yields the expression for the work performed on the wing tip beam element in terms of the wing tip and blade perturbation motions. Writing this system as coefficients of the wing and blade motion yields damping and stiffness matrices which may be added to those associated with the rotor system (Eqns. A.10-A.15 and Eqns. A.53-A.58).

The wing and rotor system equations are then assembled using standard finite element techniques where the parts of each matrix associated with common global degrees of freedom are added together. The rotor matrices are already in global form because they are written in terms of the discrete wing tip degrees of freedom. The wing matrices are assembled based on conversion of the element degrees of freedom into global degrees of freedom but, as only one element is associated with the wing tip node, the five degrees of freedom at that location are already global. The common global degrees of freedom for the rotor and wing systems are those

Reproduced with permission of the copyright owner. Further reproduction prohibited without permission.

five degrees of freedom associated with the wing tip node. The listing of rotor and wing matrices used in the analysis is given in Appendix A.

A.2 Listing of Matrices

A.2.1 Listing of the Rotor/Wing Matrices

The inertial and aerodynamic rotor/wing matrices are listed in the form used in the rigid-blade analysis (similar to that found in Ref. [39]). The notation appearing in the listing is as follows: *mroti(i,j)* is the mass matrix which has only inertial contributions, *crotf(i,j)* is the aerodynamic damping matrix, *croti(i,j)* is the inertial damping matrix, *krotf(i,j)* is the aerodynamic stiffness matrix, and *kroti(i,j)* is the inertial stiffness matrix. The element matrices are separated by aerodynamic and inertial contributions so that one of these effects may be easily excluded from the analysis if so desired. The numbering *i or j* associated with each degrees of freedom is

$1 = w_2$

$2 = v_2$

$3 = \phi_2$

$4 = v_2'$

$5 = w_2'$

$6 = \beta_{1c}$

$7 = \beta_{1s}$

$8 = \zeta_{1c}$

Reproduced with permission of the copyright owner. Further reproduction prohibited without permission.

$9 = \zeta_{1s}$

$10 = \beta_0$

$11 = \zeta_0$

where the first 5 are the discrete degrees of freedom associated with the wing tip and the last 6 are the rotor system fixed frame degrees of freedom. Parameters appearing in the listing are defined as follows:

csl = $\cos\Lambda$

snl = $\sin\Lambda$

Mbstar = $M^{\star}_{b}$

Szstar = $S^{\star}_{\zeta}$

Sb0star = $S^{\star}_{\beta_0}$

Ibastar = $I^{\star}_{\beta\alpha}$

Ibetstar = $I^{\star}_{\beta}$

Iz0star = $I^{\star}_{\zeta_0}$

Izetstar = $I^{\star}_{\zeta}$

Iz0astar = $I^{\star}_{\zeta_0\alpha}$

nubeta = ν_β

kp = kinematic pitch-flap coupling

kz = kinematic pitch-lag coupling

hmu = Aerodynamic coefficient H_μ

tth = Aerodynamic coefficient T_θ

Reproduced with permission of the copyright owner. Further reproduction prohibited without permission.

and the remaining terms can be understood from these examples. The term *autorot* has a value of 1 if constant rotor speed assumption is desired (no rotor speed perturbation degree of freedom) and has a value of 0 otherwise. The nonzero contributions to the rotor wing matrices are now listed as:

```
mroti(1,1) = 2*Mbstar;

mroti(1,3) = 2*Mbstar*csl*h;

mroti(1,5) = 2*Mbstar*h*snl;

mroti(1,9) = Szstar;

mroti(2,2) = 2*Mbstar*csl^2 + 2*Mbstar*snl^2;

mroti(2,4) = -2*Mbstar*h*snl;

mroti(2,8) = -(Szstar*snl);

mroti(2,10) = 2*SbOstar*csl;

mroti(3,1) = 2*Mbstar*csl*h;

mroti(3,3) = 2*Mbstar*csl^2*h^2 + 2*IOstar*autorot*snl^2;

mroti(3,5) = -2*IOstar*autorot*csl*snl + 2*Mbstar*csl*h^2*snl;

mroti(3,9) = Szstar*csl*h;

mroti(3,11) = 2*IzOastar*autorot*snl;

mroti(4,2) = -2*Mbstar*h*snl;

mroti(4,4) = 2*Mbstar*h^2;

mroti(4,8) = Szstar*h;

mroti(5,1) = 2*Mbstar*h*snl;

mroti(5,3) = -2*IOstar*autorot*csl*snl + 2*Mbstar*csl*h^2*snl;

mroti(5,5) = 2*IOstar*autorot*csl^2 + 2*Mbstar*h^2*snl^2;
```


Reproduced with permission of the copyright owner. Further reproduction prohibited without permission.

```
mroti(5,9) = Szstar*h*snl;

mroti(5,11) = -2*Iz0astar*autorot*csl;

mroti(6,3) = -(Ibastar*csl);

mroti(6,5) = -(Ibastar*snl);

mroti(6,6) = Ibetstar;

mroti(7,4) = Ibastar;

mroti(7,7) = Ibetstar;

mroti(8,2) = -(Szstar*snl);

mroti(8,4) = Szstar*h;

mroti(8,8) = Izetstar;

mroti(9,1) = Szstar;

mroti(9,3) = Szstar*csl*h;

mroti(9,5) = Szstar*h*snl;

mroti(9,9) = Izetstar;

mroti(10,2) = Sb0star*csl;

mroti(10,10) = Ib0star;

mroti(11,3) = Iz0astar*autorot*snl;

mroti(11,5) = -(Iz0astar*autorot*csl);

mroti(11,11) = Iz0star;


crotf(1,1) = gamma*hmu;

crotf(1,3) = csl*gamma*h*hmu;

crotf(1,4) = -(gamma*hbd);
```


Reproduced with permission of the copyright owner. Further reproduction prohibited without permission.

```
crotf(1,5) = gamma*h*hmu*snl;

crotf(1,7) = -(gamma*hbd);

crotf(1,9) = gamma*hzd;

crotf(2,2) = gamma*hmu*snl^2 - 2*csl^2*gamma*tlam;

crotf(2,3) = -(csl*gamma*hbd*snl) + 2*csl*gamma*snl*tzd;

crotf(2,4) = -(gamma*h*hmu*snl);

crotf(2,5) =( -(gamma*hbd*snl^2) - 2*csl^2*gamma*tzd)*autorot;

crotf(2,6) = gamma*hbd*snl;

crotf(2,8) = -(gamma*hzd*snl);

crotf(2,10) = -2*csl*gamma*tbd;

crotf(2,11) = 2*csl*gamma*tzd;

crotf(3,1) = csl*gamma*h*hmu;

crotf(3,2) = -2*autorot*csl*gamma*qlam*snl;

crotf(3,3) = csl^2*gamma*h^2*hmu + 2*autorot*gamma*qzd*snl^2;

crotf(3,4) = -(csl*gamma*h*hbd);

crotf(3,5) = csl*gamma*h^2*hmu*snl - 2*autorot*csl*gamma*qzd*snl;

crotf(3,7) = -(csl*gamma*h*hbd);

crotf(3,9) = csl*gamma*h*hzd;

crotf(3,10) = -2*autorot*gamma*qbd*snl;

crotf(3,11) = 2*autorot*gamma*qzd*snl;

crotf(4,2) = -(gamma*h*hmu*snl);

crotf(4,3) = csl*gamma*h*hbd;

crotf(4,4) = gamma*h^2*hmu;
```


Reproduced with permission of the copyright owner. Further reproduction prohibited without permission.

```
crotf(4,5) = gamma*h*hbd*snl;

crotf(4,6) = -(gamma*h*hbd);

crotf(4,8) = gamma*h*hzd;

crotf(5,1) = gamma*h*hmu*snl;

crotf(5,2) = 2*autorot*csl^2*gamma*qlam;

crotf(5,3) = csl*gamma*h^2*hmu*snl - 2*autorot*csl*gamma*qzd*snl;

crotf(5,4) = -(gamma*h*hbd*snl);

crotf(5,5) = 2*autorot*csl^2*gamma*qzd + gamma*h^2*hmu*snl^2;

crotf(5,7) = -(gamma*h*hbd*snl);

crotf(5,9) = gamma*h*hzd*snl;

crotf(5,10) = 2*autorot*csl*gamma*qbd;

crotf(5,11) = -2*autorot*csl*gamma*qzd;

crotf(6,2) = -(gamma*mmu*snl);

crotf(6,3) = csl*gamma*mbd;

crotf(6,4) = gamma*h*mmu;

crotf(6,5) = gamma*mbd*snl;

crotf(6,6) = -(gamma*mbd);

crotf(6,8) = gamma*mzd;

crotf(7,1) = gamma*mmu;

crotf(7,3) = csl*gamma*h*mmu;

crotf(7,4) = -(gamma*mbd);

crotf(7,5) = gamma*h*mmu*snl;

crotf(7,7) = -(gamma*mbd);
```


Reproduced with permission of the copyright owner. Further reproduction prohibited without permission.

```
crotf(7,9) = gamma*mzd;

crotf(8,2) = -(gamma*qmu*snl);

crotf(8,3) = csl*gamma*qbd;

crotf(8,4) = gamma*h*qmu;

crotf(8,5) = gamma*qbd*snl;

crotf(8,6) = -(gamma*qbd);

crotf(8,8) = gamma*qzd;

crotf(9,1) = gamma*qmu;

crotf(9,3) = csl*gamma*h*qmu;

crotf(9,4) = -(gamma*qbd);

crotf(9,5) = gamma*h*qmu*snl;

crotf(9,7) = -(gamma*qbd);

crotf(9,9) = gamma*qzd;

crotf(10,2) = -(csl*gamma*mlam);

crotf(10,3) = autorot*gamma*mzd*snl;

crotf(10,5) = -(autorot*csl*gamma*mzd);

crotf(10,10) = -(gamma*mbd);

crotf(10,11) = gamma*mzd;

crotf(11,2) = -(csl*gamma*qlam);

crotf(11,3) = autorot*gamma*qzd*snl;

crotf(11,5) = -(autorot*csl*gamma*qzd);

crotf(11,10) = -(gamma*qbd);

crotf(11,11) = gamma*qzd;
```


Reproduced with permission of the copyright owner. Further reproduction prohibited without permission.

```
croti(6,4) = 2*Ibastar;

croti(6,7) = 2*Ibetstar;

croti(7,3) = 2*Ibastar*csl;

croti(7,5) = 2*Ibastar*snl;

croti(7,6) = -2*Ibetstar;

croti(8,9) = 2*Izetstar;

croti(9,8) = -2*Izetstar;


krotf(1,3) = -(V*gamma*hmu);

krotf(1,6) = gamma*hbd;

krotf(1,7) = gamma*hth*kp;

krotf(1,8) = -(gamma*hzd);

krotf(1,9) = gamma*hth*kz;

krotf(2,4) = V*gamma*hmu*snl;

krotf(2,6) = -(gamma*hth*kp*snl);

krotf(2,7) = gamma*hbd*snl;

krotf(2,8) = -gamma*hth*kz*snl;

krotf(2,9) = -(gamma*hzd*snl);

krotf(2,10) = 2*csl*gamma*kp*tth;

krotf(2,11) = 2*csl*gamma*kz*tth;

krotf(3,3) = -(V*csl*gamma*h*hmu);

krotf(3,6) = csl*gamma*h*hbd;
```


Reproduced with permission of the copyright owner. Further reproduction prohibited without permission.

```
krotf(3,7) = csl*gamma*h*hth*kp;

krotf(3,8) = -(csl*gamma*h*hzd);

krotf(3,9) = csl*gamma*h*hth*kz;

krotf(3,10) = 2*autorot*gamma*kp*qth*snl;

krotf(3,11) = 2*autorot*gamma*kz*qth*snl;

krotf(4,4) = -(V*gamma*h*hmu);

krotf(4,6) = gamma*h*hth*kp;

krotf(4,7) = -(gamma*h*hbd);

krotf(4,8) = gamma*h*hth*kz;

krotf(4,9) = gamma*h*hzd;

krotf(5,3) = -(V*gamma*h*hmu*snl);

krotf(5,6) = gamma*h*hbd*snl;

krotf(5,7) = gamma*h*hth*kp*snl;

krotf(5,8) = -(gamma*h*hzd*snl);

krotf(5,9) = gamma*h*hth*kz*snl;

krotf(5,10) = -2*autorot*csl*gamma*kp*qth;

krotf(5,11) = -2*autorot*csl*gamma*kz*qth;

krotf(6,4) = -(V*gamma*mmu);

krotf(6,6) = gamma*kp*mth;

krotf(6,7) = -(gamma*mbd);

krotf(6,8) = gamma*kz*mth;

krotf(6,9) = gamma*mzd;

krotf(7,3) = -(V*gamma*mmu);
```


Reproduced with permission of the copyright owner. Further reproduction prohibited without permission.

```
krotf(7,6) = gamma*mbd;

krotf(7,7) = gamma*kp*mth;

krotf(7,8) = -(gamma*mzd);

krotf(7,9) = gamma*kz*mth;

krotf(8,4) = -(V*gamma*qmu);

krotf(8,6) = gamma*kp*qth;

krotf(8,7) = -(gamma*qbd);

krotf(8,8) = gamma*kz*qth;

krotf(8,9) = gamma*qzd;

krotf(9,3) = -(V*gamma*qmu);

krotf(9,6) = gamma*qbd;

krotf(9,7) = gamma*kp*qth;

krotf(9,8) = -(gamma*qzd);

krotf(9,9) = gamma*kz*qth;

krotf(10,10) = gamma*kp*mth;

krotf(10,11) = gamma*kz*mth;

krotf(11,10) = gamma*kp*qth;

krotf(11,11) = gamma*kz*qth;


kroti(3,6) = -(Ibastar*csl) + Ibastar*csl*nubeta^2;

kroti(4,7) = Ibastar - Ibastar*nubeta^2;

kroti(5,6) = -(Ibastar*snl) + Ibastar*nubeta^2*snl;

kroti(6,6) = -Ibetstar + Ibetstar*nubeta^2;
```


Reproduced with permission of the copyright owner. Further reproduction prohibited without permission.

```
kroti(7,7) = -Ibetstar + Ibetstar*nubeta^2;

kroti(8,8) = -Izetstar + Izetstar*nuzeta^2;

kroti(9,9) = -Izetstar + Izetstar*nuzeta^2;

kroti(10,10) = Ib0star*nub0^2;

kroti(11,11) = Iz0star*nuz0^2;
```

A.2.2 Listing of the Wing Element Matrices

The wing element matrices with both aerodynamic and structural contributions are listed in the form used in the rigid-blade analysis. The notation appearing in the listing is as follows: *m(i,j)* is the mass matrix which has only inertial contributions, *c(i,j)* is the damping matrix which has both structural and aerodynamic contributions, and *k(i,j)* is the stiffness matrix which also has both structural and aerodynamic contributions. The numbering *i or j* associated with each degree of freedom is:

$1 = w_1$

$2 = v_1$

$3 = \phi_1$

$4 = v_1'$

$5 = w_1'$

$6 = w_2$

$7 = v_2$

$8 = \phi_2$

Reproduced with permission of the copyright owner. Further reproduction prohibited without permission.

$9 = v_2'$

$10 = w_2'$

where the first 5 are the discrete degrees of freedom associated with node 1 (node closer to wing root) and the last 5 are the discrete degrees of freedom associated with node 2. Some of the parameters appearing in the listing are defined as follows:

mcg = mass per unit length

Salf = 1st mass moment of inertia about elastic axis per unit length

Icg = 2nd mass moment of inertia about elastic axis per unit length

R = blade radius

l = element length

Cla = wing lift curve slope

cord = blade chord, c/R

qou = dynamic pressure over free stream velocity, q/U

sdamp = structural damping

eic = EI_c

eif = EI_b

gj = GJ

The nonzero contributions to the wing matrices are now listed as follows:

```
Wing element mass matrix:
```


Reproduced with permission of the copyright owner. Further reproduction prohibited without permission.

```
m(1,1) = 13*R^2*l*mcg/35;

m(1,3) = 7*R*Salf*l/20;

m(1,5) = -11*R*l^2*mcg/210;

m(1,6) = 9*R^2*l*mcg/70;

m(1,8) = 3*R*Salf*l/20;

m(1,10) = 13*R*l^2*mcg/420;

m(2,2) = 13*R^2*l*mcg/35;

m(2,4) = 11*R*l^2*mcg/210;

m(2,7) = 9*R^2*l*mcg/70;

m(2,9) = -13*R*l^2*mcg/420;

m(3,1) = 7*R*Salf*l/20;

m(3,3) = Icg*l/3;

m(3,5) = -(Salf*l^2)/20;

m(3,6) = 3*R*Salf*l/20;

m(3,8) = Icg*l/6;

m(3,10) = Salf*l^2/30;

m(4,2) = 11*R*l^2*mcg/210;

m(4,4) = l^3*mcg/105;

m(4,7) = 13*R*l^2*mcg/420;

m(4,9) = -(l^3*mcg)/140;

m(5,1) = -11*R*l^2*mcg/210;

m(5,3) = -(Salf*l^2)/20;

m(5,5) = l^3*mcg/105;
```


Reproduced with permission of the copyright owner. Further reproduction prohibited without permission.

```
m(5,6) = -13*R*l^2*mcg/420;

m(5,8) = -(Salf*l^2)/30;

m(5,10) = -(l^3*mcg)/140;

m(6,1) = 9*R^2*l*mcg/70;

m(6,3) = 3*R*Salf*l/20;

m(6,5) = -13*R*l^2*mcg/420;

m(6,6) = 13*R^2*l*mcg/35;

m(6,8) = 7*R*Salf*l/20;

m(6,10) = 11*R*l^2*mcg/210;

m(7,2) = 9*R^2*l*mcg/70;

m(7,4) = 13*R*l^2*mcg/420;

m(7,7) = 13*R^2*l*mcg/35;

m(7,9) = -11*R*l^2*mcg/210;

m(8,1) = 3*R*Salf*l/20;

m(8,3) = Icg*l/6;

m(8,5) = -(Salf*l^2)/30;

m(8,6) = 7*R*Salf*l/20;

m(8,8) = Icg*l/3;

m(8,10) = Salf*l^2/20;

m(9,2) = -13*R*l^2*mcg/420;

m(9,4) = -(l^3*mcg)/140;

m(9,7) = -11*R*l^2*mcg/210;

m(9,9) = l^3*mcg/105;
```


Reproduced with permission of the copyright owner. Further reproduction prohibited without permission.

```
m(10,1) = 13*R*l^2*mcg/420;

m(10,3) = Salf*l^2/30;

m(10,5) = -(l^3*mcg)/140;

m(10,6) = 11*R*l^2*mcg/210;

m(10,8) = Salf*l^2/20;

m(10,10) = l^3*mcg/105;


Wing damping matrix:


c(1,1) = 13*Cla*R^2*cord*l*qou/35 + sdamp_w;

c(1,5) = -11*Cla*R*cord*l^2*qou/210;

c(1,6) = 9*Cla*R^2*cord*l*qou/70;

c(1,10) = 13*Cla*R*cord*l^2*qou/420;

c(2,2)= sdamp_v;

c(3,1) = 7*Cla*R*cord*e*l*qou/20;

c(3,3) = sdamp_phi;

c(3,5) = -(Cla*cord*e*l^2*qou)/20;

c(3,6) = 3*Cla*R*cord*e*l*qou/20;

c(3,10) = Cla*cord*e*l^2*qou/30;

c(5,1) = -11*Cla*R*cord*l^2*qou/210;

c(5,5) = Cla*cord*l^3*qou/105;

c(5,6) = -13*Cla*R*cord*l^2*qou/420;

c(5,10) = -(Cla*cord*l^3*qou)/140;
```


Reproduced with permission of the copyright owner. Further reproduction prohibited without permission.

```
c(6,1) = 9*Cla*R^2*cord*l*qou/70;

c(6,5) = -13*Cla*R*cord*l^2*qou/420;

c(6,6) = 13*Cla*R^2*cord*l*qou/35 + sdamp_w;

c(6,10) = 11*Cla*R*cord*l^2*qou/210;

c(7,7) = sdamp_v;

c(8,1) = 3*Cla*R*cord*e*l*qou/20;

c(8,5) = -(Cla*cord*e*l^2*qou)/30;

c(8,6) = 7*Cla*R*cord*e*l*qou/20;

c(8,8) = sdamp_phi;

c(8,10) = Cla*cord*e*l^2*qou/20;

c(10,1) = 13*Cla*R*cord*l^2*qou/420;

c(10,5) = -(Cla*cord*l^3*qou)/140;

c(10,6) = 11*Cla*R*cord*l^2*qou/210;

c(10,10) = Cla*cord*l^3*qou/105;


Wing stiffness matrix:


k(1,1) = 12*R^2*eif/l^3 - Cla*R^2*cord*q*snl/2;

k(1,3) = -7*Cla*R*cord*l*q*csl/20;

k(1,5) = -6*R*eif/l^2 + Cla*R*cord*l*q*snl/10;

k(1,6) = -12*R^2*eif/l^3 + Cla*R^2*cord*q*snl/2;

k(1,8) = -3*Cla*R*cord*l*q*csl/20;

k(1,10) = -6*R*eif/l^2 - Cla*R*cord*l*q*snl/10;
```


Reproduced with permission of the copyright owner. Further reproduction prohibited without permission.

```
k(2,2) = 12*R^2*eic/l^3;

k(2,4) = 6*R*eic/l^2;

k(2,7) = -12*R^2*eic/l^3;

k(2,9) = 6*R*eic/l^2;

k(3,1) = -(Cla*R*cord*e*q*snl)/2;

k(3,3) = gj/l - Cla*cord*e*l*q*csl/3;

k(3,5) = Cla*cord*e*l*q*snl/12;

k(3,6) = Cla*R*cord*e*q*snl/2;

k(3,8) = -(gj/l) - Cla*cord*e*l*q*csl/6;

k(3,10) = -(Cla*cord*e*l*q*snl)/12;

k(4,2) = 6*R*eic/l^2;

k(4,4) = 4*eic/l;

k(4,7) = -6*R*eic/l^2;

k(4,9) = 2*eic/l;

k(5,1) = -6*R*eif/l^2 + Cla*R*cord*l*q*snl/10;

k(5,3) = Cla*cord*l^2*q*csl/20;

k(5,5) = 4*eif/l;

k(5,6) = 6*R*eif/l^2 - Cla*R*cord*l*q*snl/10;

k(5,8) = Cla*cord*l^2*q*csl/30;

k(5,10) = 2*eif/l + Cla*cord*l^2*q*snl/60;

k(6,1) = -12*R^2*eif/l^3 - Cla*R^2*cord*q*snl/2;

k(6,3) = -3*Cla*R*cord*l*q*csl/20;

k(6,5) = 6*R*eif/l^2 - Cla*R*cord*l*q*snl/10;
```


Reproduced with permission of the copyright owner. Further reproduction prohibited without permission.

```
k(6,6) = 12*R^2*eif/l^3 + Cla*R^2*cord*q*snl/2;

k(6,8) = -7*Cla*R*cord*l*q*csl/20;

k(6,10) = 6*R*eif/l^2 + Cla*R*cord*l*q*snl/10;

k(7,2) = -12*R^2*eic/l^3;

k(7,4) = -6*R*eic/l^2;

k(7,7) = 12*R^2*eic/l^3;

k(7,9) = -6*R*eic/l^2;

k(8,1) = -(Cla*R*cord*e*q*snl)/2;

k(8,3) = -(gj/l) - Cla*cord*e*l*q*csl/6;

k(8,5) = -(Cla*cord*e*l*q*snl)/12;

k(8,6) = Cla*R*cord*e*q*snl/2;

k(8,8) = gj/l - Cla*cord*e*l*q*csl/3;

k(8,10) = Cla*cord*e*l*q*snl/12;

k(9,2) = 6*R*eic/l^2;

k(9,4) = 2*eic/l;

k(9,7) = -6*R*eic/l^2;

k(9,9) = 4*eic/l;

k(10,1) = -6*R*eif/l^2 - Cla*R*cord*l*q*snl/10;

k(10,3) = -(Cla*cord*l^2*q*csl)/30;

k(10,5) = 2*eif/l - Cla*cord*l^2*q*snl/60;

k(10,6) = 6*R*eif/l^2 + Cla*R*cord*l*q*snl/10;

k(10,8) = -(Cla*cord*l^2*q*csl)/20;
```


Reproduced with permission of the copyright owner. Further reproduction prohibited without permission.

```
k(10,10) = 4*eif/l;
```


Reproduced with permission of the copyright owner. Further reproduction prohibited without permission.

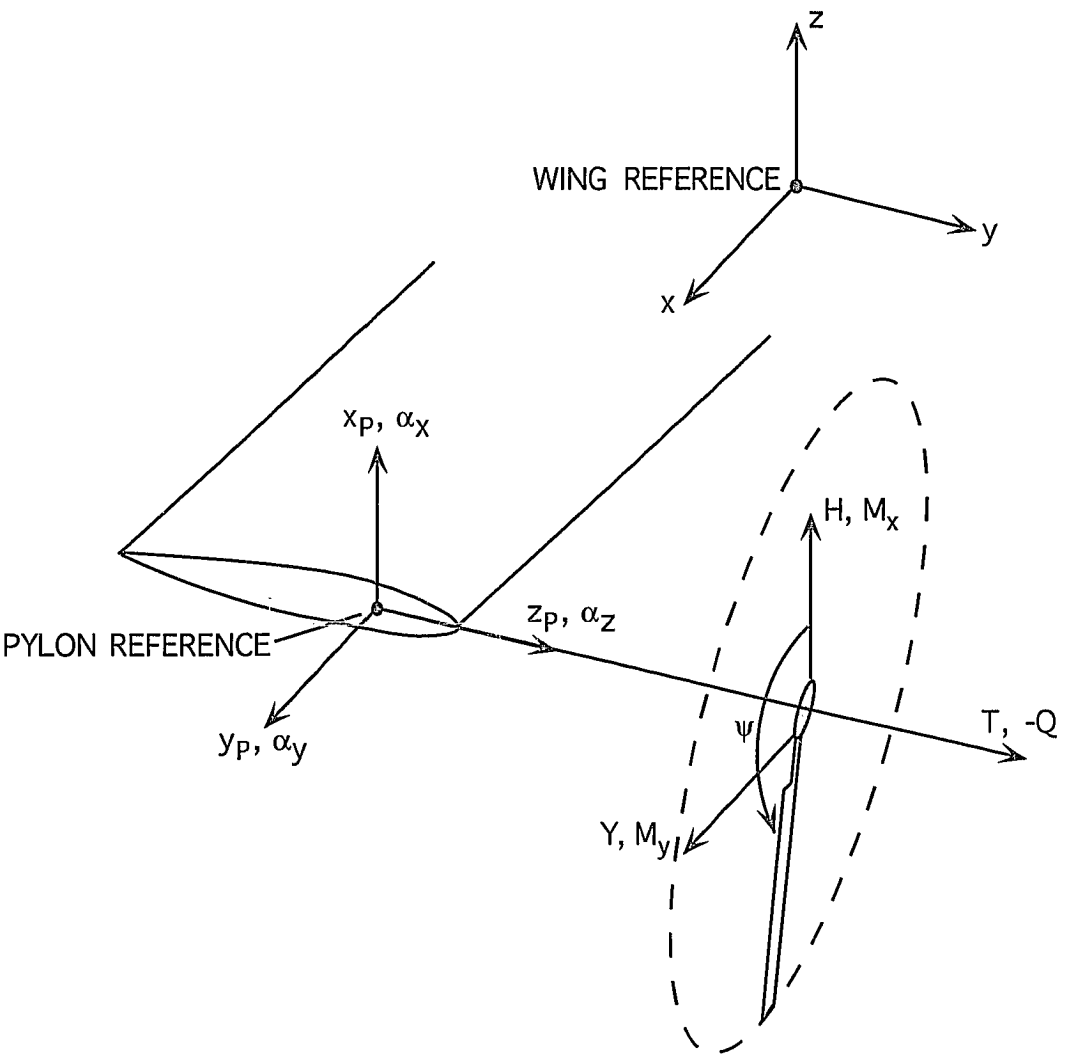

Figure A.1: Coordinate systems for rotor and wing

Reproduced with permission of the copyright owner. Further reproduction prohibited without permission.

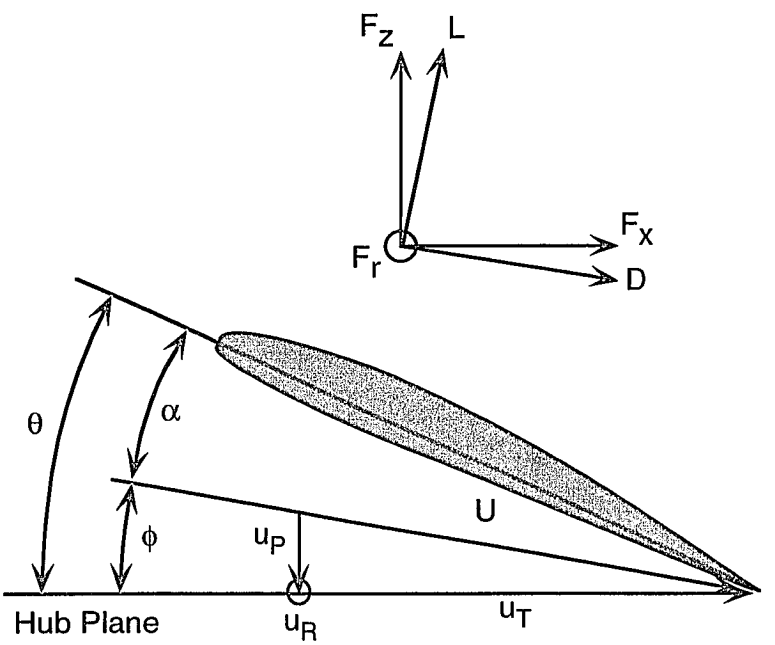

Figure A.2: Velocity and force components on a typical blade section

Reproduced with permission of the copyright owner. Further reproduction prohibited without permission.

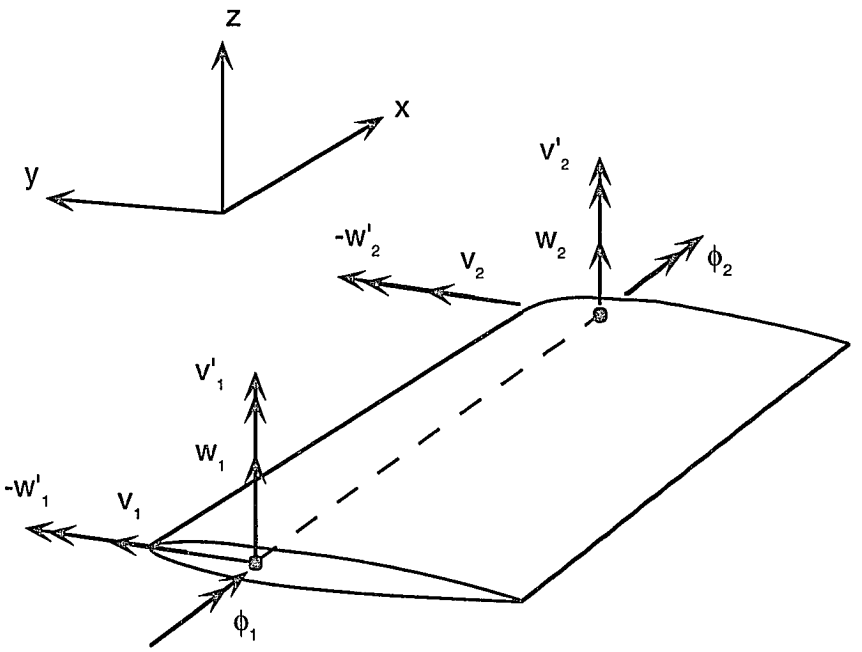

Figure A.3: Wing element degrees-of-freedom (v, w and ϕ are lagwise, flapwise and torsional displacements respectively)

Reproduced with permission of the copyright owner. Further reproduction prohibited without permission.

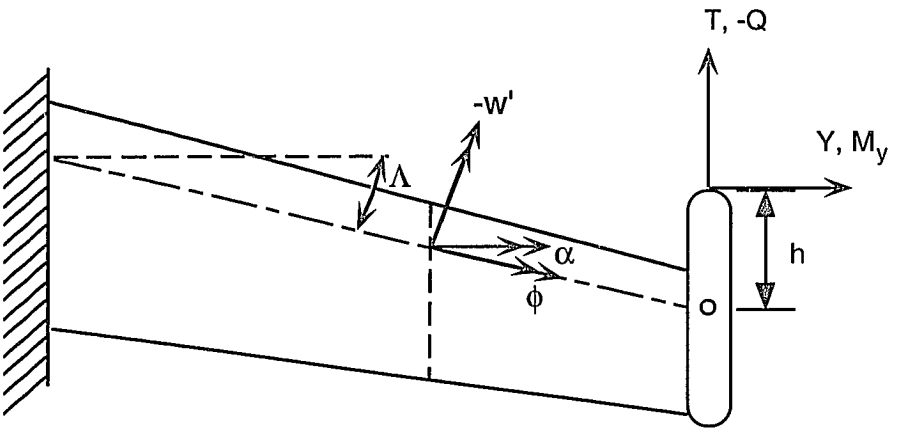

Figure A.4: Schematic of the swept wing configuration

Reproduced with permission of the copyright owner. Further reproduction prohibited without permission.

Appendix B

Listing of the T_{FL} Matrix

The T_{FL} matrix transforms the blade section aerodynamic loads into the hub reference frame.

$$\begin{Bmatrix} F^A_{x_h} \\ F^A_{y_h} \\ F^A_{z_h} \\ M^A_{\alpha_h} \\ M^A_{\phi_h} \\ M^A_{\zeta_h} \\ M^A_{\beta_{GC}} \\ M^A_{\beta_{GS}} \end{Bmatrix} = T_{FL} \begin{Bmatrix} L^A_u \\ L^A_v \\ L^A_w \\ M^A_{\hat{\phi}} \end{Bmatrix} \tag{B.1}$$

The matrix can be expressed as a combination of its constant, linear and nonlinear parts.

$$T_{FL} = T_{FL_0} + T_{FL_q} + T_{FL_x} + T_{FL_{q^2}} + T_{FL_{qx}} + T_{FL_{x^2}} \tag{B.2}$$

where T_{FL_0} is the linear part of the matrix, T_{FL_q} and T_{FL_x} constitute the linear part and the remaining terms make up the nonlinear part of the transformation matrix.

Reproduced with permission of the copyright owner. Further reproduction prohibited without permission.

Constant Terms of the T_{FL} matrix

$$
\begin{aligned}
T_{FL_0}(1,1) &= \cos\alpha_p \cos\psi - \beta_p \sin\alpha_p \\
T_{FL_0}(1,2) &= -(\cos\alpha_p \sin\psi) \\
T_{FL_0}(1,3) &= -(\beta_p \cos\alpha_p \cos\psi) - \sin\alpha_p \\
T_{FL_0}(1,4) &= 0 \\
T_{FL_0}(2,1) &= \sin\psi \\
T_{FL_0}(2,2) &= \cos\psi \\
T_{FL_0}(2,3) &= -(\beta_p \sin\psi) \\
T_{FL_0}(2,4) &= 0 \\
T_{FL_0}(3,1) &= \beta_p \cos\alpha_p + \cos\psi \sin\alpha_p \\
T_{FL_0}(3,2) &= -(\sin\alpha_p \sin\psi) \\
T_{FL_0}(3,3) &= \cos\alpha_p - \beta_p \cos\psi \sin\alpha_p \\
T_{FL_0}(3,4) &= 0 \\
T_{FL_0}(4,1) &= \cos\psi h + \cos\psi \sin\theta_0 T_{12}(s+L_1) + \beta_p \cos\theta_0 \sin\psi T_{12}(s+L_1) + \\
&\quad \cos\theta_0 \cos\psi T_{13}(s+L_1) - \beta_p \sin\theta_0 \sin\psi T_{13}(s+L_1) + \cos\psi \sin\theta_0 T_{22} L_2 + \\
&\quad \beta_p \cos\theta_0 \sin\psi T_{22} L_2 + \cos\theta_0 \cos\psi T_{23} L_2 - \\
&\quad \beta_p \sin\theta_0 \sin\psi T_{23} L_2 + \cos\psi \sin\theta_0 T_{32} L_3 + \\
&\quad \beta_p \cos\theta_0 \sin\psi T_{32} L_3 + \cos\theta_0 \cos\psi T_{33} L_3 - \beta_p \sin\theta_0 \sin\psi T_{33} L_3 \\
T_{FL_0}(4,2) &= -(h \sin\psi) - \beta_p \sin\psi T_{11}(s+L_1) - \sin\theta_0 \sin\psi T_{12}(s+L_1) - \\
&\quad \cos\theta_0 \sin\psi T_{13}(s+L_1) - \beta_p \sin\psi T_{21} L_2 - \sin\theta_0 \sin\psi T_{22} L_2 - \\
&\quad \cos\theta_0 \sin\psi T_{23} L_2 - \beta_p \sin\psi T_{31} L_3 - \sin\theta_0 \sin\psi T_{32} L_3 - \\
&\quad \cos\theta_0 \sin\psi T_{33} L_3 \\
T_{FL_0}(4,3) &= -(\beta_p \cos\psi h) - \cos\psi T_{11}(s+L_1) + \cos\theta_0 \sin\psi T_{12}(s+L_1) - \\
&\quad \sin\theta_0 \sin\psi T_{13}(s+L_1) - \cos\psi T_{21} L_2 + \cos\theta_0 \sin\psi T_{22} L_2 - \\
&\quad \sin\theta_0 \sin\psi T_{23} L_2 - \cos\psi T_{31} L_3 + \cos\theta_0 \sin\psi T_{32} L_3 - \\
&\quad \sin\theta_0 \sin\psi T_{33} L_3 \\
T_{FL_0}(4,4) &= \sin\psi T_{11} + \cos\theta_0 \cos\psi T_{12} - \beta_p \sin\theta_0 \sin\psi T_{12} - \\
&\quad \cos\psi \sin\theta_0 T_{13} - \beta_p \cos\theta_0 \sin\psi T_{13} \\
T_{FL_0}(5,1) &= -(\cos\alpha_p h \sin\psi) + \beta_p \cos\alpha_p \cos\theta_0 \cos\psi T_{12}(s+L_1) + \\
&\quad \cos\theta_0 \sin\alpha_p T_{12}(s+L_1) - \cos\alpha_p \sin\theta_0 \sin\psi T_{12}(s+L_1) - \\
&\quad \beta_p \cos\alpha_p \cos\psi \sin\theta_0 T_{13}(s+L_1) - \sin\alpha_p \sin\theta_0 T_{13}(s+L_1) - \\
&\quad \cos\alpha_p \cos\theta_0 \sin\psi T_{13}(s+L_1) + \beta_p \cos\alpha_p \cos\theta_0 \cos\psi T_{22} L_2 + \\
&\quad \cos\theta_0 \sin\alpha_p T_{22} L_2 - \cos\alpha_p \sin\theta_0 \sin\psi T_{22} L_2 -
\end{aligned}
$$

Reproduced with permission of the copyright owner. Further reproduction prohibited without permission.

$$
\begin{aligned}
& \beta_p \cos\alpha_p \cos\psi \sin\theta_0 T_{23} L_2 - \sin\alpha_p \sin\theta_0 T_{23} L_2 - \\
& \cos\alpha_p \cos\theta_0 \sin\psi T_{23} L_2 + \beta_p \cos\alpha_p \cos\theta_0 \cos\psi T_{32} L_3 + \\
& \cos\theta_0 \sin\alpha_p T_{32} L_3 - \cos\alpha_p \sin\theta_0 \sin\psi T_{32} L_3 - \\
& \beta_p \cos\alpha_p \cos\psi \sin\theta_0 T_{33} L_3 - \sin\alpha_p \sin\theta_0 T_{33} L_3 - \\
& \cos\alpha_p \cos\theta_0 \sin\psi T_{33} L_3
\end{aligned}
$$

$$
\begin{aligned}
T_{FL_0}(5,2) = & -(\cos\alpha_p \cos\psi h) - \beta_p \cos\alpha_p \cos\psi T_{11}(s+L_1) - \sin\alpha_p T_{11}(s+L_1) - \\
& \cos\alpha_p \cos\psi \sin\theta_0 T_{12}(s+L_1) + \beta_p \sin\alpha_p \sin\theta_0 T_{12}(s+L_1) - \\
& \cos\alpha_p \cos\theta_0 \cos\psi T_{13}(s+L_1) + \\
& \beta_p \cos\theta_0 \sin\alpha_p T_{13}(s+L_1) - \beta_p \cos\alpha_p \cos\psi T_{21} L_2 - \sin\alpha_p T_{21} L_2 - \\
& \cos\alpha_p \cos\psi \sin\theta_0 T_{22} L_2 + \beta_p \sin\alpha_p \sin\theta_0 T_{22} L_2 - \\
& \cos\alpha_p \cos\theta_0 \cos\psi T_{23} L_2 + \beta_p \cos\theta_0 \sin\alpha_p T_{23} L_2 - \\
& \beta_p \cos\alpha_p \cos\psi T_{31} L_3 - \sin\alpha_p T_{31} L_3 - \cos\alpha_p \cos\psi \sin\theta_0 T_{32} L_3 + \\
& \beta_p \sin\alpha_p \sin\theta_0 T_{32} L_3 - \cos\alpha_p \cos\theta_0 \cos\psi T_{33} L_3 + \\
& \beta_p \cos\theta_0 \sin\alpha_p T_{33} L_3
\end{aligned}
$$

$$
\begin{aligned}
T_{FL_0}(5,3) = & \beta_p \cos\alpha_p h \sin\psi + \cos\alpha_p \sin\psi T_{11}(s+L_1) + \cos\alpha_p \cos\theta_0 \cos\psi T_{12}(s+L_1) - \\
& \beta_p \cos\theta_0 \sin\alpha_p T_{12}(s+L_1) - \cos\alpha_p \cos\psi \sin\theta_0 T_{13}(s+L_1) + \\
& \beta_p \sin\alpha_p \sin\theta_0 T_{13}(s+L_1) + \\
& \cos\alpha_p \sin\psi T_{21} L_2 + \cos\alpha_p \cos\theta_0 \cos\psi T_{22} L_2 - \beta_p \cos\theta_0 \sin\alpha_p T_{22} L_2 - \\
& \cos\alpha_p \cos\psi \sin\theta_0 T_{23} L_2 + \beta_p \sin\alpha_p \sin\theta_0 T_{23} L_2 + \cos\alpha_p \sin\psi T_{31} L_3 + \\
& \cos\alpha_p \cos\theta_0 \cos\psi T_{32} L_3 - \beta_p \cos\theta_0 \sin\alpha_p T_{32} L_3 - \\
& \cos\alpha_p \cos\psi \sin\theta_0 T_{33} L_3 + \beta_p \sin\alpha_p \sin\theta_0 T_{33} L_3
\end{aligned}
$$

$$
\begin{aligned}
T_{FL_0}(5,4) = & \cos\alpha_p \cos\psi T_{11} - \beta_p \sin\alpha_p T_{11} - \beta_p \cos\alpha_p \cos\psi \sin\theta_0 T_{12} - \\
& \sin\alpha_p \sin\theta_0 T_{12} - \cos\alpha_p \cos\theta_0 \sin\psi T_{12} - \beta_p \cos\alpha_p \cos\theta_0 \cos\psi T_{13} - \\
& \cos\theta_0 \sin\alpha_p T_{13} + \cos\alpha_p \sin\theta_0 \sin\psi T_{13}
\end{aligned}
$$

$$
\begin{aligned}
T_{FL_0}(6,1) = & -(h \sin\alpha_p \sin\psi) - \cos\alpha_p \cos\theta_0 T_{12}(s+L_1) + \\
& \beta_p \cos\theta_0 \cos\psi \sin\alpha_p T_{12}(s+L_1) - \sin\alpha_p \sin\theta_0 \sin\psi T_{12}(s+L_1) + \\
& \cos\alpha_p \sin\theta_0 T_{13}(s+L_1) - \beta_p \cos\psi \sin\alpha_p \sin\theta_0 T_{13}(s+L_1) - \\
& \cos\theta_0 \sin\alpha_p \sin\psi T_{13}(s+L_1) - \cos\alpha_p \cos\theta_0 T_{22} L_2 + \\
& \beta_p \cos\theta_0 \cos\psi \sin\alpha_p T_{22} L_2 - \sin\alpha_p \sin\theta_0 \sin\psi T_{22} L_2 + \\
& \cos\alpha_p \sin\theta_0 T_{23} L_2 - \beta_p \cos\psi \sin\alpha_p \sin\theta_0 T_{23} L_2 - \\
& \cos\theta_0 \sin\alpha_p \sin\psi T_{23} L_2 - \cos\alpha_p \cos\theta_0 T_{32} L_3 + \\
& \beta_p \cos\theta_0 \cos\psi \sin\alpha_p T_{32} L_3 - \sin\alpha_p \sin\theta_0 \sin\psi T_{32} L_3 + \\
& \cos\alpha_p \sin\theta_0 T_{33} L_3 - \beta_p \cos\psi \sin\alpha_p \sin\theta_0 T_{33} L_3 -
\end{aligned}
$$

Reproduced with permission of the copyright owner. Further reproduction prohibited without permission.

$$
\begin{aligned}
& \cos\theta_0 \sin\alpha_p \sin\psi T_{33} L_3 \\
T_{FL_0}(6,2) &= -(\cos\psi h \sin\alpha_p) + \cos\alpha_p T_{11}(s+L_1) - \beta_p \cos\psi \sin\alpha_p T_{11}(s+L_1) - \\
& \beta_p \cos\alpha_p \sin\theta_0 T_{12}(s+L_1) - \cos\psi \sin\alpha_p \sin\theta_0 T_{12}(s+L_1) - \\
& \beta_p \cos\alpha_p \cos\theta_0 T_{13}(s+L_1) - \\
& \cos\theta_0 \cos\psi \sin\alpha_p T_{13}(s+L_1) + \cos\alpha_p T_{21} L_2 - \beta_p \cos\psi \sin\alpha_p T_{21} L_2 - \\
& \beta_p \cos\alpha_p \sin\theta_0 T_{22} L_2 - \cos\psi \sin\alpha_p \sin\theta_0 T_{22} L_2 - \\
& \beta_p \cos\alpha_p \cos\theta_0 T_{23} L_2 - \cos\theta_0 \cos\psi \sin\alpha_p T_{23} L_2 + \cos\alpha_p T_{31} L_3 - \\
& \beta_p \cos\psi \sin\alpha_p T_{31} L_3 - \beta_p \cos\alpha_p \sin\theta_0 T_{32} L_3 - \\
& \cos\psi \sin\alpha_p \sin\theta_0 T_{32} L_3 - \beta_p \cos\alpha_p \cos\theta_0 T_{33} L_3 - \\
& \cos\theta_0 \cos\psi \sin\alpha_p T_{33} L_3 \\
T_{FL_0}(6,3) &= \beta_p h \sin\alpha_p \sin\psi + \sin\alpha_p \sin\psi T_{11}(s+L_1) + \beta_p \cos\alpha_p \cos\theta_0 T_{12}(s+L_1) + \\
& \cos\theta_0 \cos\psi \sin\alpha_p T_{12}(s+L_1) - \beta_p \cos\alpha_p \sin\theta_0 T_{13}(s+L_1) - \\
& \cos\psi \sin\alpha_p \sin\theta_0 T_{13}(s+L_1) + \\
& \sin\alpha_p \sin\psi T_{21} L_2 + \beta_p \cos\alpha_p \cos\theta_0 T_{22} L_2 + \cos\theta_0 \cos\psi \sin\alpha_p T_{22} L_2 - \\
& \beta_p \cos\alpha_p \sin\theta_0 T_{23} L_2 - \cos\psi \sin\alpha_p \sin\theta_0 T_{23} L_2 + \sin\alpha_p \sin\psi T_{31} L_3 + \\
& \beta_p \cos\alpha_p \cos\theta_0 T_{32} L_3 + \cos\theta_0 \cos\psi \sin\alpha_p T_{32} L_3 - \\
& \beta_p \cos\alpha_p \sin\theta_0 T_{33} L_3 - \cos\psi \sin\alpha_p \sin\theta_0 T_{33} L_3 \\
T_{FL_0}(6,4) &= \beta_p \cos\alpha_p T_{11} + \cos\psi \sin\alpha_p T_{11} + \cos\alpha_p \sin\theta_0 T_{12} - \\
& \beta_p \cos\psi \sin\alpha_p \sin\theta_0 T_{12} - \cos\theta_0 \sin\alpha_p \sin\psi T_{12} + \cos\alpha_p \cos\theta_0 T_{13} - \\
& \beta_p \cos\theta_0 \cos\psi \sin\alpha_p T_{13} + \sin\alpha_p \sin\theta_0 \sin\psi T_{13} \\
T_{FL_0}(7,1) &= \cos\psi \sin\theta_0 T_{12}(s+L_1) + \beta_p \cos\theta_0 \sin\psi T_{12}(s+L_1) + \\
& \cos\theta_0 \cos\psi T_{13}(s+L_1) - \beta_p \sin\theta_0 \sin\psi T_{13}(s+L_1) + \cos\psi \sin\theta_0 T_{22} L_2 + \\
& \beta_p \cos\theta_0 \sin\psi T_{22} L_2 + \cos\theta_0 \cos\psi T_{23} L_2 - \\
& \beta_p \sin\theta_0 \sin\psi T_{23} L_2 + \cos\psi \sin\theta_0 T_{32} L_3 + \\
& \beta_p \cos\theta_0 \sin\psi T_{32} L_3 + \cos\theta_0 \cos\psi T_{33} L_3 - \beta_p \sin\theta_0 \sin\psi T_{33} L_3 \\
T_{FL_0}(7,2) &= -(\beta_p \sin\psi T_{11}(s+L_1)) - \sin\theta_0 \sin\psi T_{12}(s+L_1) - \cos\theta_0 \sin\psi T_{13}(s+L_1) - \\
& \beta_p \sin\psi T_{21} L_2 - \sin\theta_0 \sin\psi T_{22} L_2 - \cos\theta_0 \sin\psi T_{23} L_2 - \\
& \beta_p \sin\psi T_{31} L_3 - \sin\theta_0 \sin\psi T_{32} L_3 - \cos\theta_0 \sin\psi T_{33} L_3 \\
T_{FL_0}(7,3) &= -(\cos\psi T_{11}(s+L_1)) + \cos\theta_0 \sin\psi T_{12}(s+L_1) - \sin\theta_0 \sin\psi T_{13}(s+L_1) - \\
& \cos\psi T_{21} L_2 + \cos\theta_0 \sin\psi T_{22} L_2 - \sin\theta_0 \sin\psi T_{23} L_2 - \\
& \cos\psi T_{31} L_3 + \cos\theta_0 \sin\psi T_{32} L_3 - \sin\theta_0 \sin\psi T_{33} L_3 \\
T_{FL_0}(7,4) &= \sin\psi T_{11} + \cos\theta_0 \cos\psi T_{12} - \beta_p \sin\theta_0 \sin\psi T_{12} - \\
& \cos\psi \sin\theta_0 T_{13} - \beta_p \cos\theta_0 \sin\psi T_{13}
\end{aligned}
$$

Reproduced with permission of the copyright owner. Further reproduction prohibited without permission.

$$
\begin{aligned}
T_{FL_0}(8,1) &= \beta_p \cos\theta_0 \cos\psi T_{12}(s+L_1) - \sin\theta_0 \sin\psi T_{12}(s+L_1) - \\
&\quad \beta_p \cos\psi \sin\theta_0 T_{13}(s+L_1) - \cos\theta_0 \sin\psi T_{13}(s+L_1) + \beta_p \cos\theta_0 \cos\psi T_{22} L_2 - \\
&\quad \sin\theta_0 \sin\psi T_{22} L_2 - \beta_p \cos\psi \sin\theta_0 T_{23} L_2 - \cos\theta_0 \sin\psi T_{23} L_2 + \\
&\quad \beta_p \cos\theta_0 \cos\psi T_{32} L_3 - \sin\theta_0 \sin\psi T_{32} L_3 - \\
&\quad \beta_p \cos\psi \sin\theta_0 T_{33} L_3 - \cos\theta_0 \sin\psi T_{33} L_3 \\
T_{FL_0}(8,2) &= -(\beta_p \cos\psi T_{11}(s+L_1)) - \cos\psi \sin\theta_0 T_{12}(s+L_1) - \cos\theta_0 \cos\psi T_{13}(s+L_1) - \\
&\quad \beta_p \cos\psi T_{21} L_2 - \cos\psi \sin\theta_0 T_{22} L_2 - \cos\theta_0 \cos\psi T_{23} L_2 - \\
&\quad \beta_p \cos\psi T_{31} L_3 - \cos\psi \sin\theta_0 T_{32} L_3 - \cos\theta_0 \cos\psi T_{33} L_3 \\
T_{FL_0}(8,3) &= \sin\psi T_{11}(s+L_1) + \cos\theta_0 \cos\psi T_{12}(s+L_1) - \cos\psi \sin\theta_0 T_{13}(s+L_1) + \\
&\quad \sin\psi T_{21} L_2 + \cos\theta_0 \cos\psi T_{22} L_2 - \cos\psi \sin\theta_0 T_{23} L_2 + \\
&\quad \sin\psi T_{31} L_3 + \cos\theta_0 \cos\psi T_{32} L_3 - \cos\psi \sin\theta_0 T_{33} L_3 \\
T_{FL_0}(8,4) &= \cos\psi T_{11} - \beta_p \cos\psi \sin\theta_0 T_{12} - \cos\theta_0 \sin\psi T_{12} - \\
&\quad \beta_p \cos\theta_0 \cos\psi T_{13} + \sin\theta_0 \sin\psi T_{13}
\end{aligned}
$$

Linear Terms of the T_{FL} matrix dependent on Blade dofs

$$
\begin{aligned}
T_{FL_q}(1,1) &= 0 \\
T_{FL_q}(1,2) &= 0 \\
T_{FL_q}(1,3) &= 0 \\
T_{FL_q}(1,4) &= 0 \\
T_{FL_q}(2,1) &= 0 \\
T_{FL_q}(2,2) &= 0 \\
T_{FL_q}(2,3) &= 0 \\
T_{FL_q}(2,4) &= 0 \\
T_{FL_q}(3,1) &= 0 \\
T_{FL_q}(3,2) &= 0 \\
T_{FL_q}(3,3) &= 0 \\
T_{FL_q}(3,4) &= 0 \\
T_{FL_q}(4,1) &= \cos\psi \sin\theta_0 T_{12} u + \cos\theta_0 \cos\psi T_{13} u + \cos\psi \sin\theta_0 T_{22} v + \\
&\quad \cos\theta_0 \cos\psi T_{23} v + \cos\psi \sin\theta_0 T_{32} w + \cos\theta_0 \cos\psi T_{33} w \\
T_{FL_q}(4,2) &= -(\sin\theta_0 \sin\psi T_{12} u) - \cos\theta_0 \sin\psi T_{13} u - \sin\theta_0 \sin\psi T_{22} v - \\
&\quad \cos\theta_0 \sin\psi T_{23} v - \sin\theta_0 \sin\psi T_{32} w - \cos\theta_0 \sin\psi T_{33} w \\
T_{FL_q}(4,3) &= -(\cos\psi T_{11} u) + \cos\theta_0 \sin\psi T_{12} u - \sin\theta_0 \sin\psi T_{13} u - \\
&\quad \cos\psi T_{21} v + \cos\theta_0 \sin\psi T_{22} v - \sin\theta_0 \sin\psi T_{23} v - \cos\psi T_{31} w + \\
&\quad \cos\theta_0 \sin\psi T_{32} w - \sin\theta_0 \sin\psi T_{33} w
\end{aligned}
$$

Reproduced with permission of the copyright owner. Further reproduction prohibited without permission.

$$
\begin{aligned}
T_{FL_q}(4,4) &= \sin\psi T_{21}v' + \cos\theta_0\cos\psi T_{22}v' - \cos\psi\sin\theta_0 T_{23}v' + \\
&\quad \sin\psi T_{31}w' + \cos\theta_0\cos\psi T_{32}w' - \cos\psi\sin\theta_0 T_{33}w' \\
T_{FL_q}(5,1) &= \cos\theta_0\sin\alpha_p T_{12}u - \cos\alpha_p\sin\theta_0\sin\psi T_{12}u - \sin\alpha_p\sin\theta_0 T_{13}u - \\
&\quad \cos\alpha_p\cos\theta_0\sin\psi T_{13}u + \cos\theta_0\sin\alpha_p T_{22}v - \cos\alpha_p\sin\theta_0\sin\psi T_{22}v - \\
&\quad \sin\alpha_p\sin\theta_0 T_{23}v - \cos\alpha_p\cos\theta_0\sin\psi T_{23}v + \cos\theta_0\sin\alpha_p T_{32}w - \\
&\quad \cos\alpha_p\sin\theta_0\sin\psi T_{32}w - \sin\alpha_p\sin\theta_0 T_{33}w - \cos\alpha_p\cos\theta_0\sin\psi T_{33}w \\
T_{FL_q}(5,2) &= -(\sin\alpha_p T_{11}u) - \cos\alpha_p\cos\psi\sin\theta_0 T_{12}u - \\
&\quad \cos\alpha_p\cos\theta_0\cos\psi T_{13}u - \sin\alpha_p T_{21}v - \cos\alpha_p\cos\psi\sin\theta_0 T_{22}v - \\
&\quad \cos\alpha_p\cos\theta_0\cos\psi T_{23}v - \sin\alpha_p T_{31}w - \cos\alpha_p\cos\psi\sin\theta_0 T_{32}w - \\
&\quad \cos\alpha_p\cos\theta_0\cos\psi T_{33}w \\
T_{FL_q}(5,3) &= \cos\alpha_p\sin\psi T_{11}u + \cos\alpha_p\cos\theta_0\cos\psi T_{12}u - \\
&\quad \cos\alpha_p\cos\psi\sin\theta_0 T_{13}u + \cos\alpha_p\sin\psi T_{21}v + \cos\alpha_p\cos\theta_0\cos\psi T_{22}v - \\
&\quad \cos\alpha_p\cos\psi\sin\theta_0 T_{23}v + \cos\alpha_p\sin\psi T_{31}w + \cos\alpha_p\cos\theta_0\cos\psi T_{32}w - \\
&\quad \cos\alpha_p\cos\psi\sin\theta_0 T_{33}w \\
T_{FL_q}(5,4) &= \cos\alpha_p\cos\psi T_{21}v' - \sin\alpha_p\sin\theta_0 T_{22}v' - \\
&\quad \cos\alpha_p\cos\theta_0\sin\psi T_{22}v' - \cos\theta_0\sin\alpha_p T_{23}v' + \cos\alpha_p\sin\theta_0\sin\psi T_{23}v' + \\
&\quad \cos\alpha_p\cos\psi T_{31}w' - \sin\alpha_p\sin\theta_0 T_{32}w' - \cos\alpha_p\cos\theta_0\sin\psi T_{32}w' - \\
&\quad \cos\theta_0\sin\alpha_p T_{33}w' + \cos\alpha_p\sin\theta_0\sin\psi T_{33}w' \\
T_{FL_q}(6,1) &= -(\cos\alpha_p\cos\theta_0 T_{12}u) - \sin\alpha_p\sin\theta_0\sin\psi T_{12}u + \\
&\quad \cos\alpha_p\sin\theta_0 T_{13}u - \cos\theta_0\sin\alpha_p\sin\psi T_{13}u - \cos\alpha_p\cos\theta_0 T_{22}v - \\
&\quad \sin\alpha_p\sin\theta_0\sin\psi T_{22}v + \cos\alpha_p\sin\theta_0 T_{23}v - \cos\theta_0\sin\alpha_p\sin\psi T_{23}v - \\
&\quad \cos\alpha_p\cos\theta_0 T_{32}w - \sin\alpha_p\sin\theta_0\sin\psi T_{32}w + \cos\alpha_p\sin\theta_0 T_{33}w - \\
&\quad \cos\theta_0\sin\alpha_p\sin\psi T_{33}w \\
T_{FL_q}(6,2) &= \cos\alpha_p T_{11}u - \cos\psi\sin\alpha_p\sin\theta_0 T_{12}u - \cos\theta_0\cos\psi\sin\alpha_p T_{13}u + \\
&\quad \cos\alpha_p T_{21}v - \cos\psi\sin\alpha_p\sin\theta_0 T_{22}v - \cos\theta_0\cos\psi\sin\alpha_p T_{23}v + \\
&\quad \cos\alpha_p T_{31}w - \cos\psi\sin\alpha_p\sin\theta_0 T_{32}w - \cos\theta_0\cos\psi\sin\alpha_p T_{33}w \\
T_{FL_q}(6,3) &= \sin\alpha_p\sin\psi T_{11}u + \cos\theta_0\cos\psi\sin\alpha_p T_{12}u - \\
&\quad \cos\psi\sin\alpha_p\sin\theta_0 T_{13}u + \sin\alpha_p\sin\psi T_{21}v + \cos\theta_0\cos\psi\sin\alpha_p T_{22}v - \\
&\quad \cos\psi\sin\alpha_p\sin\theta_0 T_{23}v + \sin\alpha_p\sin\psi T_{31}w + \cos\theta_0\cos\psi\sin\alpha_p T_{32}w - \\
&\quad \cos\psi\sin\alpha_p\sin\theta_0 T_{33}w \\
T_{FL_q}(6,4) &= \cos\psi\sin\alpha_p T_{21}v' + \cos\alpha_p\sin\theta_0 T_{22}v' - \\
&\quad \cos\theta_0\sin\alpha_p\sin\psi T_{22}v' + \cos\alpha_p\cos\theta_0 T_{23}v' + \sin\alpha_p\sin\theta_0\sin\psi T_{23}v' + \\
&\quad \cos\psi\sin\alpha_p T_{31}w' + \cos\alpha_p\sin\theta_0 T_{32}w' - \cos\theta_0\sin\alpha_p\sin\psi T_{32}w' +
\end{aligned}
$$

Reproduced with permission of the copyright owner. Further reproduction prohibited without permission.

$$\cos\alpha_p \cos\theta_0 T_{33} w' + \sin\alpha_p \sin\theta_0 \sin\psi T_{33} w'$$

$$T_{FL_q}(7,1) = \cos\psi \sin\theta_0 T_{12} u + \cos\theta_0 \cos\psi T_{13} u + \cos\psi \sin\theta_0 T_{22} v + \cos\theta_0 \cos\psi T_{23} v + \cos\psi \sin\theta_0 T_{32} w + \cos\theta_0 \cos\psi T_{33} w$$

$$T_{FL_q}(7,2) = -(\sin\theta_0 \sin\psi T_{12} u) - \cos\theta_0 \sin\psi T_{13} u - \sin\theta_0 \sin\psi T_{22} v - \cos\theta_0 \sin\psi T_{23} v - \sin\theta_0 \sin\psi T_{32} w - \cos\theta_0 \sin\psi T_{33} w$$

$$T_{FL_q}(7,3) = -(\cos\psi T_{11} u) + \cos\theta_0 \sin\psi T_{12} u - \sin\theta_0 \sin\psi T_{13} u - \cos\psi T_{21} v + \cos\theta_0 \sin\psi T_{22} v - \sin\theta_0 \sin\psi T_{23} v - \cos\psi T_{31} w + \cos\theta_0 \sin\psi T_{32} w - \sin\theta_0 \sin\psi T_{33} w$$

$$T_{FL_q}(7,4) = \sin\psi T_{21} v' + \cos\theta_0 \cos\psi T_{22} v' - \cos\psi \sin\theta_0 T_{23} v' + \sin\psi T_{31} w' + \cos\theta_0 \cos\psi T_{32} w' - \cos\psi \sin\theta_0 T_{33} w'$$

$$T_{FL_q}(8,1) = -(\sin\theta_0 \sin\psi T_{12} u) - \cos\theta_0 \sin\psi T_{13} u - \sin\theta_0 \sin\psi T_{22} v - \cos\theta_0 \sin\psi T_{23} v - \sin\theta_0 \sin\psi T_{32} w - \cos\theta_0 \sin\psi T_{33} w$$

$$T_{FL_q}(8,2) = -(\cos\psi \sin\theta_0 T_{12} u) - \cos\theta_0 \cos\psi T_{13} u - \cos\psi \sin\theta_0 T_{22} v - \cos\theta_0 \cos\psi T_{23} v - \cos\psi \sin\theta_0 T_{32} w - \cos\theta_0 \cos\psi T_{33} w$$

$$T_{FL_q}(8,3) = \sin\psi T_{11} u + \cos\theta_0 \cos\psi T_{12} u - \cos\psi \sin\theta_0 T_{13} u + \sin\psi T_{21} v + \cos\theta_0 \cos\psi T_{22} v - \cos\psi \sin\theta_0 T_{23} v + \sin\psi T_{31} w + \cos\theta_0 \cos\psi T_{32} w - \cos\psi \sin\theta_0 T_{33} w$$

$$T_{FL_q}(8,4) = \cos\psi T_{21} v' - \cos\theta_0 \sin\psi T_{22} v' + \sin\theta_0 \sin\psi T_{23} v' + \cos\psi T_{31} w' - \cos\theta_0 \sin\psi T_{32} w' + \sin\theta_0 \sin\psi T_{33} w'$$

Linear Terms of the T_{FL} matrix dependent on Hub dofs

$$T_{FL_x}(1,1) = 0$$

$$T_{FL_x}(1,2) = 0$$

$$T_{FL_x}(1,3) = 0$$

$$T_{FL_x}(1,4) = 0$$

$$T_{FL_x}(2,1) = 0$$

$$T_{FL_x}(2,2) = 0$$

$$T_{FL_x}(2,3) = 0$$

$$T_{FL_x}(2,4) = 0$$

$$T_{FL_x}(3,1) = 0$$

$$T_{FL_x}(3,2) = 0$$

$$T_{FL_x}(3,3) = 0$$

$$T_{FL_x}(3,4) = 0$$

$$T_{FL_x}(4,1) = -(h\phi_h \sin\alpha_p \sin\psi) - \cos\alpha_p \cos\theta_0 \phi_h T_{12}(s + L_1) +$$

Reproduced with permission of the copyright owner. Further reproduction prohibited without permission.

$$
\begin{aligned}
& \beta_{GC}\cos\theta_0\cos\psi\sin\psi T_{12}(s+L_1) - \phi_h\sin\alpha_p\sin\theta_0\sin\psi T_{12}(s+L_1) + \\
& \beta_{GS}\cos\theta_0\sin^2\psi T_{12}(s+L_1) + \cos\alpha_p\phi_h\sin\theta_0 T_{13}(s+L_1) - \\
& \cos\theta_0\phi_h\sin\alpha_p\sin\psi T_{13}(s+L_1) - \beta_{GC}\cos\psi\sin\theta_0\sin\psi T_{13}(s+L_1) - \\
& \beta_{GS}\sin\theta_0\sin^2\psi T_{13}(s+L_1) - \cos\psi\sin\alpha_p x_h - \cos\alpha_p\cos\theta_0\phi_h T_{22}L_2 + \\
& \beta_{GC}\cos\theta_0\cos\psi\sin\psi T_{22}L_2 - \phi_h\sin\alpha_p\sin\theta_0\sin\psi T_{22}L_2 + \\
& \beta_{GS}\cos\theta_0\sin^2\psi T_{22}L_2 + \cos\alpha_p\phi_h\sin\theta_0 T_{23}L_2 - \\
& \cos\theta_0\phi_h\sin\alpha_p\sin\psi T_{23}L_2 - \beta_{GC}\cos\psi\sin\theta_0\sin\psi T_{23}L_2 - \\
& \beta_{GS}\sin\theta_0\sin^2\psi T_{23}L_2 - \cos\alpha_p\cos\theta_0\phi_h T_{32}L_3 + \\
& \beta_{GC}\cos\theta_0\cos\psi\sin\psi T_{32}L_3 - \phi_h\sin\alpha_p\sin\theta_0\sin\psi T_{32}L_3 + \\
& \beta_{GS}\cos\theta_0\sin^2\psi T_{32}L_3 + \cos\alpha_p\phi_h\sin\theta_0 T_{33}L_3 - \\
& \cos\theta_0\phi_h\sin\alpha_p\sin\psi T_{33}L_3 - \beta_{GC}\cos\psi\sin\theta_0\sin\psi T_{33}L_3 - \\
& \beta_{GS}\sin\theta_0\sin^2\psi T_{33}L_3 - \cos\alpha_p h\sin\psi\zeta_h + \\
& \cos\theta_0\sin\alpha_p T_{12}(s+L_1)\zeta_h - \cos\alpha_p\sin\theta_0\sin\psi T_{12}(s+L_1)\zeta_h - \\
& \sin\alpha_p\sin\theta_0 T_{13}(s+L_1)\zeta_h - \cos\alpha_p\cos\theta_0\sin\psi T_{13}(s+L_1)\zeta_h + \\
& \cos\theta_0\sin\alpha_p T_{22}L_2\zeta_h - \cos\alpha_p\sin\theta_0\sin\psi T_{22}L_2\zeta_h - \\
& \sin\alpha_p\sin\theta_0 T_{23}L_2\zeta_h - \cos\alpha_p\cos\theta_0\sin\psi T_{23}L_2\zeta_h + \\
& \cos\theta_0\sin\alpha_p T_{32}L_3\zeta_h - \cos\alpha_p\sin\theta_0\sin\psi T_{32}L_3\zeta_h - \\
& \sin\alpha_p\sin\theta_0 T_{33}L_3\zeta_h - \cos\alpha_p\cos\theta_0\sin\psi T_{33}L_3\zeta_h + \cos\alpha_p\cos\psi z_h
\end{aligned}
$$

$$
\begin{aligned}
T_{FL_x}(4,2) = & -(\cos\psi h\phi_h\sin\alpha_p) + \cos\alpha_p\phi_h T_{11}(s+L_1) + \sin\alpha_p\sin\psi x_h - \\
& \beta_{GC}\cos\psi\sin\psi T_{11}(s+L_1) - \beta_{GS}\sin^2\psi T_{11}(s+L_1) - \\
& \cos\psi\phi_h\sin\alpha_p\sin\theta_0 T_{12}(s+L_1) - \cos\theta_0\cos\psi\phi_h\sin\alpha_p T_{13}(s+L_1) + \\
& \cos\alpha_p\phi_h T_{21}L_2 - \beta_{GC}\cos\psi\sin\psi T_{21}L_2 - \\
& \beta_{GS}\sin^2\psi T_{21}L_2 - \cos\psi\phi_h\sin\alpha_p\sin\theta_0 T_{22}L_2 - \\
& \cos\theta_0\cos\psi\phi_h\sin\alpha_p T_{23}L_2 + \cos\alpha_p\phi_h T_{31}L_3 - \\
& \beta_{GC}\cos\psi\sin\psi T_{31}L_3 - \beta_{GS}\sin^2\psi T_{31}L_3 - \\
& \cos\psi\phi_h\sin\alpha_p\sin\theta_0 T_{32}L_3 - \cos\theta_0\cos\psi\phi_h\sin\alpha_p T_{33}L_3 - \\
& \cos\alpha_p\cos\psi h\zeta_h - \sin\alpha_p T_{11}(s+L_1)\zeta_h - \cos\alpha_p\cos\psi\sin\theta_0 T_{12}(s+L_1)\zeta_h - \\
& \cos\alpha_p\cos\theta_0\cos\psi T_{13}(s+L_1)\zeta_h - \sin\alpha_p T_{21}L_2\zeta_h - \\
& \cos\alpha_p\cos\psi\sin\theta_0 T_{22}L_2\zeta_h - \cos\alpha_p\cos\theta_0\cos\psi T_{23}L_2\zeta_h - \\
& \sin\alpha_p T_{31}L_3\zeta_h - \cos\alpha_p\cos\psi\sin\theta_0 T_{32}L_3\zeta_h - \\
& \cos\alpha_p\cos\theta_0\cos\psi T_{33}L_3\zeta_h - \cos\alpha_p\sin\psi z_h
\end{aligned}
$$

$$
\begin{aligned}
T_{FL_x}(4,3) = & -(\beta_{GC}\cos^2\psi h) - \beta_{GS}\cos\psi h\sin\psi + \\
& \phi_h\sin\alpha_p\sin\psi T_{11}(s+L_1) + \cos\theta_0\cos\psi\phi_h\sin\alpha_p T_{12}(s+L_1) -
\end{aligned}
$$

Reproduced with permission of the copyright owner. Further reproduction prohibited without permission.

$$
\begin{aligned}
& \cos\psi\phi_h \sin\alpha_p \sin\theta_0 T_{13}(s+L_1) - \cos\alpha_p x_h + \phi_h \sin\alpha_p \sin\psi T_{21} L_2 + \\
& \cos\theta_0 \cos\psi\phi_h \sin\alpha_p T_{22} L_2 - \cos\psi\phi_h \sin\alpha_p \sin\theta_0 T_{23} L_2 + \\
& \phi_h \sin\alpha_p \sin\psi T_{31} L_3 + \cos\theta_0 \cos\psi\phi_h \sin\alpha_p T_{32} L_3 - \\
& \cos\psi\phi_h \sin\alpha_p \sin\theta_0 T_{33} L_3 + \cos\alpha_p \sin\psi T_{11}(s+L_1)\zeta_h + \\
& \cos\alpha_p \cos\theta_0 \cos\psi T_{12}(s+L_1)\zeta_h - \cos\alpha_p \cos\psi \sin\theta_0 T_{13}(s+L_1)\zeta_h + \\
& \cos\alpha_p \sin\psi T_{21} L_2 \zeta_h + \cos\alpha_p \cos\theta_0 \cos\psi T_{22} L_2 \zeta_h - \\
& \cos\alpha_p \cos\psi \sin\theta_0 T_{23} L_2 \zeta_h + \cos\alpha_p \sin\psi T_{31} L_3 \zeta_h + \\
& \cos\alpha_p \cos\theta_0 \cos\psi T_{32} L_3 \zeta_h - \cos\alpha_p \cos\psi \sin\theta_0 T_{33} L_3 \zeta_h - \sin\alpha_p z_h
\end{aligned}
$$

$$
\begin{aligned}
T_{FL_x}(4,4) = \; & \cos\psi\phi_h \sin\alpha_p T_{11} + \cos\alpha_p \phi_h \sin\theta_0 T_{12} - \\
& \cos\theta_0 \phi_h \sin\alpha_p \sin\psi T_{12} - \beta_{GC} \cos\psi \sin\theta_0 \sin\psi T_{12} - \\
& \beta_{GS} \sin\theta_0 \sin^2\psi T_{12} + \cos\alpha_p \cos\theta_0 \phi_h T_{13} - \\
& \beta_{GC} \cos\theta_0 \cos\psi \sin\psi T_{13} + \phi_h \sin\alpha_p \sin\theta_0 \sin\psi T_{13} - \\
& \beta_{GS} \cos\theta_0 \sin^2\psi T_{13} + \cos\alpha_p \cos\psi T_{11} \zeta_h - \\
& \sin\alpha_p \sin\theta_0 T_{12} \zeta_h - \cos\alpha_p \cos\theta_0 \sin\psi T_{12} \zeta_h - \\
& \cos\theta_0 \sin\alpha_p T_{13} \zeta_h + \cos\alpha_p \sin\theta_0 \sin\psi T_{13} \zeta_h
\end{aligned}
$$

$$
\begin{aligned}
T_{FL_x}(5,1) = \; & \alpha_h h \sin\alpha_p \sin\psi + \alpha_h \cos\alpha_p \cos\theta_0 T_{12}(s+L_1) + \\
& \beta_{GC} \cos\alpha_p \cos\theta_0 \cos^2\psi T_{12}(s+L_1) + \\
& \beta_{GS} \cos\alpha_p \cos\theta_0 \cos\psi \sin\psi T_{12}(s+L_1) + \\
& \alpha_h \sin\alpha_p \sin\theta_0 \sin\psi T_{12}(s+L_1) - \alpha_h \cos\alpha_p \sin\theta_0 T_{13}(s+L_1) - \\
& \beta_{GC} \cos\alpha_p \cos^2\psi \sin\theta_0 T_{13}(s+L_1) + \alpha_h \cos\theta_0 \sin\alpha_p \sin\psi T_{13}(s+L_1) - \\
& \beta_{GS} \cos\alpha_p \cos\psi \sin\theta_0 \sin\psi T_{13}(s+L_1) + \alpha_h \cos\alpha_p \cos\theta_0 T_{22} L_2 + \\
& \beta_{GC} \cos\alpha_p \cos\theta_0 \cos^2\psi T_{22} L_2 + \beta_{GS} \cos\alpha_p \cos\theta_0 \cos\psi \sin\psi T_{22} L_2 + \\
& \alpha_h \sin\alpha_p \sin\theta_0 \sin\psi T_{22} L_2 - \alpha_h \cos\alpha_p \sin\theta_0 T_{23} L_2 - \\
& \beta_{GC} \cos\alpha_p \cos^2\psi \sin\theta_0 T_{23} L_2 + \alpha_h \cos\theta_0 \sin\alpha_p \sin\psi T_{23} L_2 - \\
& \beta_{GS} \cos\alpha_p \cos\psi \sin\theta_0 \sin\psi T_{23} L_2 + \alpha_h \cos\alpha_p \cos\theta_0 T_{32} L_3 + \\
& \beta_{GC} \cos\alpha_p \cos\theta_0 \cos^2\psi T_{32} L_3 + \beta_{GS} \cos\alpha_p \cos\theta_0 \cos\psi \sin\psi T_{32} L_3 + \\
& \alpha_h \sin\alpha_p \sin\theta_0 \sin\psi T_{32} L_3 - \alpha_h \cos\alpha_p \sin\theta_0 T_{33} L_3 - \\
& \beta_{GC} \cos\alpha_p \cos^2\psi \sin\theta_0 T_{33} L_3 + \alpha_h \cos\theta_0 \sin\alpha_p \sin\psi T_{33} L_3 - \\
& \beta_{GS} \cos\alpha_p \cos\psi \sin\theta_0 \sin\psi T_{33} L_3 + \cos\psi \sin\alpha_p y_h - \cos\psi h \zeta_h - \\
& \cos\psi \sin\theta_0 T_{12}(s+L_1)\zeta_h - \cos\theta_0 \cos\psi T_{13}(s+L_1)\zeta_h - \\
& \cos\psi \sin\theta_0 T_{22} L_2 \zeta_h - \cos\theta_0 \cos\psi T_{23} L_2 \zeta_h - \\
& \cos\psi \sin\theta_0 T_{32} L_3 \zeta_h - \cos\theta_0 \cos\psi T_{33} L_3 \zeta_h - \sin\psi z_h
\end{aligned}
$$

$$
T_{FL_x}(5,2) = \alpha_h \cos\psi h \sin\alpha_p - \alpha_h \cos\alpha_p T_{11}(s+L_1) -
$$

Reproduced with permission of the copyright owner. Further reproduction prohibited without permission.

$$
\begin{aligned}
& \beta_{GC}\cos\alpha_p\cos^2\psi T_{11}(s+L_1) - \beta_{GS}\cos\alpha_p\cos\psi\sin\psi T_{11}(s+L_1) + \\
& \alpha_h\cos\psi\sin\alpha_p\sin\theta_0 T_{12}(s+L_1) + \beta_{GC}\cos^3\psi\sin\alpha_p\sin\theta_0 T_{12}(s+L_1) + \\
& \beta_{GS}\cos^2\psi\sin\alpha_p\sin\theta_0\sin\psi T_{12}(s+L_1) + \\
& \beta_{GC}\cos\psi\sin\alpha_p\sin\theta_0\sin^2\psi T_{12}(s+L_1) + \\
& \beta_{GS}\sin\alpha_p\sin\theta_0\sin^3\psi T_{12}(s+L_1) + \alpha_h\cos\theta_0\cos\psi\sin\alpha_p T_{13}(s+L_1) + \\
& \beta_{GC}\cos\theta_0\cos^3\psi\sin\alpha_p T_{13}(s+L_1) + \\
& \beta_{GS}\cos\theta_0\cos^2\psi\sin\alpha_p\sin\psi T_{13}(s+L_1) + \\
& \beta_{GC}\cos\theta_0\cos\psi\sin\alpha_p\sin^2\psi T_{13}(s+L_1) + \\
& \beta_{GS}\cos\theta_0\sin\alpha_p\sin^3\psi T_{13}(s+L_1) - \\
& \alpha_h\cos\alpha_p T_{21}L_2 - \beta_{GC}\cos\alpha_p\cos^2\psi T_{21}L_2 - \\
& \beta_{GS}\cos\alpha_p\cos\psi\sin\psi T_{21}L_2 + \alpha_h\cos\psi\sin\alpha_p\sin\theta_0 T_{22}L_2 + \\
& \beta_{GC}\cos^3\psi\sin\alpha_p\sin\theta_0 T_{22}L_2 + \beta_{GS}\cos^2\psi\sin\alpha_p\sin\theta_0\sin\psi T_{22}L_2 + \\
& \beta_{GC}\cos\psi\sin\alpha_p\sin\theta_0\sin^2\psi T_{22}L_2 + \beta_{GS}\sin\alpha_p\sin\theta_0\sin^3\psi T_{22}L_2 + \\
& \alpha_h\cos\theta_0\cos\psi\sin\alpha_p T_{23}L_2 + \beta_{GC}\cos\theta_0\cos^3\psi\sin\alpha_p T_{23}L_2 + \\
& \beta_{GS}\cos\theta_0\cos^2\psi\sin\alpha_p\sin\psi T_{23}L_2 + \\
& \beta_{GC}\cos\theta_0\cos\psi\sin\alpha_p\sin^2\psi T_{23}L_2 + \beta_{GS}\cos\theta_0\sin\alpha_p\sin^3\psi T_{23}L_2 - \\
& \alpha_h\cos\alpha_p T_{31}L_3 - \beta_{GC}\cos\alpha_p\cos^2\psi T_{31}L_3 - \\
& \beta_{GS}\cos\alpha_p\cos\psi\sin\psi T_{31}L_3 + \alpha_h\cos\psi\sin\alpha_p\sin\theta_0 T_{32}L_3 + \\
& \beta_{GC}\cos^3\psi\sin\alpha_p\sin\theta_0 T_{32}L_3 + \beta_{GS}\cos^2\psi\sin\alpha_p\sin\theta_0\sin\psi T_{32}L_3 + \\
& \beta_{GC}\cos\psi\sin\alpha_p\sin\theta_0\sin^2\psi T_{32}L_3 + \beta_{GS}\sin\alpha_p\sin\theta_0\sin^3\psi T_{32}L_3 + \\
& \alpha_h\cos\theta_0\cos\psi\sin\alpha_p T_{33}L_3 + \beta_{GC}\cos\theta_0\cos^3\psi\sin\alpha_p T_{33}L_3 + \\
& \beta_{GS}\cos\theta_0\cos^2\psi\sin\alpha_p\sin\psi T_{33}L_3 + \\
& \beta_{GC}\cos\theta_0\cos\psi\sin\alpha_p\sin^2\psi T_{33}L_3 + \beta_{GS}\cos\theta_0\sin\alpha_p\sin^3\psi T_{33}L_3 - \\
& \sin\alpha_p\sin\psi y_h + h\sin\psi\zeta_h + \sin\theta_0\sin\psi T_{12}(s+L_1)\zeta_h + \\
& \cos\theta_0\sin\psi T_{13}(s+L_1)\zeta_h + \sin\theta_0\sin\psi T_{22}L_2\zeta_h + \\
& \cos\theta_0\sin\psi T_{23}L_2\zeta_h + \sin\theta_0\sin\psi T_{32}L_3\zeta_h + \\
& \cos\theta_0\sin\psi T_{33}L_3\zeta_h - \cos\psi z_h
\end{aligned}
$$

$$
\begin{aligned}
T_{FL_x}(5,3) \;=\; & \beta_{GC}\cos\alpha_p\cos\psi h\sin\psi + \beta_{GS}\cos\alpha_p h\sin^2\psi - \\
& \alpha_h\sin\alpha_p\sin\psi T_{11}(s+L_1) - \alpha_h\cos\theta_0\cos\psi\sin\alpha_p T_{12}(s+L_1) - \\
& \beta_{GC}\cos\theta_0\cos^3\psi\sin\alpha_p T_{12}(s+L_1) - \\
& \beta_{GS}\cos\theta_0\cos^2\psi\sin\alpha_p\sin\psi T_{12}(s+L_1) - \\
& \beta_{GC}\cos\theta_0\cos\psi\sin\alpha_p\sin^2\psi T_{12}(s+L_1) - \\
& \beta_{GS}\cos\theta_0\sin\alpha_p\sin^3\psi T_{12}(s+L_1) +
\end{aligned}
$$

Reproduced with permission of the copyright owner. Further reproduction prohibited without permission.

$$
\begin{aligned}
&\alpha_h \cos\psi \sin\alpha_p \sin\theta_0 T_{13}(s+L_1) + \beta_{GC} \cos^3\psi \sin\alpha_p \sin\theta_0 T_{13}(s+L_1) + \\
&\beta_{GS} \cos^2\psi \sin\alpha_p \sin\theta_0 \sin\psi T_{13}(s+L_1) + \\
&\beta_{GC} \cos\psi \sin\alpha_p \sin\theta_0 \sin^2\psi T_{13}(s+L_1) + \\
&\beta_{GS} \sin\alpha_p \sin\theta_0 \sin^3\psi T_{13}(s+L_1) - \alpha_h \sin\alpha_p \sin\psi T_{21} L_2 - \\
&\alpha_h \cos\theta_0 \cos\psi \sin\alpha_p T_{22} L_2 - \beta_{GC} \cos\theta_0 \cos^3\psi \sin\alpha_p T_{22} L_2 - \\
&\beta_{GS} \cos\theta_0 \cos^2\psi \sin\alpha_p \sin\psi T_{22} L_2 - \\
&\beta_{GC} \cos\theta_0 \cos\psi \sin\alpha_p \sin^2\psi T_{22} L_2 - \beta_{GS} \cos\theta_0 \sin\alpha_p \sin^3\psi T_{22} L_2 + \\
&\alpha_h \cos\psi \sin\alpha_p \sin\theta_0 T_{23} L_2 + \beta_{GC} \cos^3\psi \sin\alpha_p \sin\theta_0 T_{23} L_2 + \\
&\beta_{GS} \cos^2\psi \sin\alpha_p \sin\theta_0 \sin\psi T_{23} L_2 + \\
&\beta_{GC} \cos\psi \sin\alpha_p \sin\theta_0 \sin^2\psi T_{23} L_2 + \beta_{GS} \sin\alpha_p \sin\theta_0 \sin^3\psi T_{23} L_2 - \\
&\alpha_h \sin\alpha_p \sin\psi T_{31} L_3 - \alpha_h \cos\theta_0 \cos\psi \sin\alpha_p T_{32} L_3 - \\
&\beta_{GC} \cos\theta_0 \cos^3\psi \sin\alpha_p T_{32} L_3 - \beta_{GS} \cos\theta_0 \cos^2\psi \sin\alpha_p \sin\psi T_{32} L_3 - \\
&\beta_{GC} \cos\theta_0 \cos\psi \sin\alpha_p \sin^2\psi T_{32} L_3 - \beta_{GS} \cos\theta_0 \sin\alpha_p \sin^3\psi T_{32} L_3 + \\
&\alpha_h \cos\psi \sin\alpha_p \sin\theta_0 T_{33} L_3 + \beta_{GC} \cos^3\psi \sin\alpha_p \sin\theta_0 T_{33} L_3 + \\
&\beta_{GS} \cos^2\psi \sin\alpha_p \sin\theta_0 \sin\psi T_{33} L_3 + \\
&\beta_{GC} \cos\psi \sin\alpha_p \sin\theta_0 \sin^2\psi T_{33} L_3 + \beta_{GS} \sin\alpha_p \sin\theta_0 \sin^3\psi T_{33} L_3 + \\
&\cos\alpha_p y_h + \cos\psi T_{11}(s+L_1)\zeta_h - \cos\theta_0 \sin\psi T_{12}(s+L_1)\zeta_h + \\
&\sin\theta_0 \sin\psi T_{13}(s+L_1)\zeta_h + \cos\psi T_{21} L_2 \zeta_h - \\
&\cos\theta_0 \sin\psi T_{22} L_2 \zeta_h + \sin\theta_0 \sin\psi T_{23} L_2 \zeta_h + \\
&\cos\psi T_{31} L_3 \zeta_h - \cos\theta_0 \sin\psi T_{32} L_3 \zeta_h + \\
&\sin\theta_0 \sin\psi T_{33} L_3 \zeta_h
\end{aligned}
$$

$$
\begin{aligned}
T_{FL_x}(5,4) \;=\; &-(\alpha_h \cos\psi \sin\alpha_p T_{11}) - \beta_{GC} \cos\psi \sin\alpha_p T_{11} - \\
&\beta_{GS} \sin\alpha_p \sin\psi T_{11} - \alpha_h \cos\alpha_p \sin\theta_0 T_{12} - \\
&\beta_{GC} \cos\alpha_p \cos^2\psi \sin\theta_0 T_{12} + \alpha_h \cos\theta_0 \sin\alpha_p \sin\psi T_{12} - \\
&\beta_{GS} \cos\alpha_p \cos\psi \sin\theta_0 \sin\psi T_{12} - \alpha_h \cos\alpha_p \cos\theta_0 T_{13} - \\
&\beta_{GC} \cos\alpha_p \cos\theta_0 \cos^2\psi T_{13} - \beta_{GS} \cos\alpha_p \cos\theta_0 \cos\psi \sin\psi T_{13} - \\
&\alpha_h \sin\alpha_p \sin\theta_0 \sin\psi T_{13} - \sin\psi T_{11}\zeta_h - \cos\theta_0 \cos\psi T_{12}\zeta_h + \\
&\cos\psi \sin\theta_0 T_{13}\zeta_h
\end{aligned}
$$

$$
\begin{aligned}
T_{FL_x}(6,1) \;=\; &-(\cos\psi h \phi_h) - \alpha_h \cos\alpha_p h \sin\psi + \sin\psi x_h + \\
&\alpha_h \cos\theta_0 \sin\alpha_p T_{12}(s+L_1) + \beta_{GC} \cos\theta_0 \cos^2\psi \sin\alpha_p T_{12}(s+L_1) - \\
&\cos\psi \phi_h \sin\theta_0 T_{12}(s+L_1) + \beta_{GS} \cos\theta_0 \cos\psi \sin\alpha_p \sin\psi T_{12}(s+L_1) - \\
&\alpha_h \cos\alpha_p \sin\theta_0 \sin\psi T_{12}(s+L_1) - \cos\theta_0 \cos\psi \phi_h T_{13}(s+L_1) - \\
&\alpha_h \sin\alpha_p \sin\theta_0 T_{13}(s+L_1) - \beta_{GC} \cos^2\psi \sin\alpha_p \sin\theta_0 T_{13}(s+L_1) -
\end{aligned}
$$

Reproduced with permission of the copyright owner. Further reproduction prohibited without permission.

$$
\begin{aligned}
& \alpha_h \cos\alpha_p \cos\theta_0 \sin\psi T_{13}(s+L_1) - \beta_{GS} \cos\psi \sin\alpha_p \sin\theta_0 \sin\psi T_{13}(s+L_1) + \\
& \alpha_h \cos\theta_0 \sin\alpha_p T_{22} L_2 + \beta_{GC} \cos\theta_0 \cos^2\psi \sin\alpha_p T_{22} L_2 - \\
& \cos\psi\phi_h \sin\theta_0 T_{22} L_2 + \beta_{GS} \cos\theta_0 \cos\psi \sin\alpha_p \sin\psi T_{22} L_2 - \\
& \alpha_h \cos\alpha_p \sin\theta_0 \sin\psi T_{22} L_2 - \cos\theta_0 \cos\psi\phi_h T_{23} L_2 - \\
& \alpha_h \sin\alpha_p \sin\theta_0 T_{23} L_2 - \beta_{GC} \cos^2\psi \sin\alpha_p \sin\theta_0 T_{23} L_2 - \\
& \alpha_h \cos\alpha_p \cos\theta_0 \sin\psi T_{23} L_2 - \beta_{GS} \cos\psi \sin\alpha_p \sin\theta_0 \sin\psi T_{23} L_2 + \\
& \alpha_h \cos\theta_0 \sin\alpha_p T_{32} L_3 + \beta_{GC} \cos\theta_0 \cos^2\psi \sin\alpha_p T_{32} L_3 - \\
& \cos\psi\phi_h \sin\theta_0 T_{32} L_3 + \beta_{GS} \cos\theta_0 \cos\psi \sin\alpha_p \sin\psi T_{32} L_3 - \\
& \alpha_h \cos\alpha_p \sin\theta_0 \sin\psi T_{32} L_3 - \cos\theta_0 \cos\psi\phi_h T_{33} L_3 - \\
& \alpha_h \sin\alpha_p \sin\theta_0 T_{33} L_3 - \beta_{GC} \cos^2\psi \sin\alpha_p \sin\theta_0 T_{33} L_3 - \\
& \alpha_h \cos\alpha_p \cos\theta_0 \sin\psi T_{33} L_3 - \beta_{GS} \cos\psi \sin\alpha_p \sin\theta_0 \sin\psi T_{33} L_3 - \\
& \cos\alpha_p \cos\psi y_h
\end{aligned}
$$

$$
\begin{aligned}
T_{FL_x}(6,2) = \; & -(\alpha_h \cos\alpha_p \cos\psi h) + h\phi_h \sin\psi - \alpha_h \sin\alpha_p T_{11}(s+L_1) - \\
& \beta_{GC} \cos^2\psi \sin\alpha_p T_{11}(s+L_1) - \beta_{GS} \cos\psi \sin\alpha_p \sin\psi T_{11}(s+L_1) - \\
& \alpha_h \cos\alpha_p \cos\psi \sin\theta_0 T_{12}(s+L_1) - \beta_{GC} \cos\alpha_p \cos^3\psi \sin\theta_0 T_{12}(s+L_1) - \\
& \beta_{GS} \cos\alpha_p \cos^2\psi \sin\theta_0 \sin\psi T_{12}(s+L_1) + \phi_h \sin\theta_0 \sin\psi T_{12}(s+L_1) - \\
& \beta_{GC} \cos\alpha_p \cos\psi \sin\theta_0 \sin^2\psi T_{12}(s+L_1) - \\
& \beta_{GS} \cos\alpha_p \sin\theta_0 \sin^3\psi T_{12}(s+L_1) - \\
& \alpha_h \cos\alpha_p \cos\theta_0 \cos\psi T_{13}(s+L_1) - \beta_{GC} \cos\alpha_p \cos\theta_0 \cos^3\psi T_{13}(s+L_1) - \\
& \beta_{GS} \cos\alpha_p \cos\theta_0 \cos^2\psi \sin\psi T_{13}(s+L_1) + \cos\theta_0\phi_h \sin\psi T_{13}(s+L_1) - \\
& \beta_{GC} \cos\alpha_p \cos\theta_0 \cos\psi \sin^2\psi T_{13}(s+L_1) - \\
& \beta_{GS} \cos\alpha_p \cos\theta_0 \sin^3\psi T_{13}(s+L_1) + \\
& \cos\psi x_h - \alpha_h \sin\alpha_p T_{21} L_2 - \beta_{GC} \cos^2\psi \sin\alpha_p T_{21} L_2 - \\
& \beta_{GS} \cos\psi \sin\alpha_p \sin\psi T_{21} L_2 - \alpha_h \cos\alpha_p \cos\psi \sin\theta_0 T_{22} L_2 - \\
& \beta_{GC} \cos\alpha_p \cos^3\psi \sin\theta_0 T_{22} L_2 - \beta_{GS} \cos\alpha_p \cos^2\psi \sin\theta_0 \sin\psi T_{22} L_2 + \\
& \phi_h \sin\theta_0 \sin\psi T_{22} L_2 - \beta_{GC} \cos\alpha_p \cos\psi \sin\theta_0 \sin^2\psi T_{22} L_2 - \\
& \beta_{GS} \cos\alpha_p \sin\theta_0 \sin^3\psi T_{22} L_2 - \alpha_h \cos\alpha_p \cos\theta_0 \cos\psi T_{23} L_2 - \\
& \beta_{GC} \cos\alpha_p \cos\theta_0 \cos^3\psi T_{23} L_2 - \beta_{GS} \cos\alpha_p \cos\theta_0 \cos^2\psi \sin\psi T_{23} L_2 + \\
& \cos\theta_0\phi_h \sin\psi T_{23} L_2 - \beta_{GC} \cos\alpha_p \cos\theta_0 \cos\psi \sin^2\psi T_{23} L_2 - \\
& \beta_{GS} \cos\alpha_p \cos\theta_0 \sin^3\psi T_{23} L_2 - \alpha_h \sin\alpha_p T_{31} L_3 - \\
& \beta_{GC} \cos^2\psi \sin\alpha_p T_{31} L_3 - \beta_{GS} \cos\psi \sin\alpha_p \sin\psi T_{31} L_3 - \\
& \alpha_h \cos\alpha_p \cos\psi \sin\theta_0 T_{32} L_3 - \beta_{GC} \cos\alpha_p \cos^3\psi \sin\theta_0 T_{32} L_3 - \\
& \beta_{GS} \cos\alpha_p \cos^2\psi \sin\theta_0 \sin\psi T_{32} L_3 + \phi_h \sin\theta_0 \sin\psi T_{32} L_3 -
\end{aligned}
$$

Reproduced with permission of the copyright owner. Further reproduction prohibited without permission.

$$\beta_{GC}\cos\alpha_p\cos\psi\sin\theta_0\sin^2\psi T_{32}L_3 - \beta_{GS}\cos\alpha_p\sin\theta_0\sin^3\psi T_{32}L_3 -$$
$$\alpha_h\cos\alpha_p\cos\theta_0\cos\psi T_{33}L_3 - \beta_{GC}\cos\alpha_p\cos\theta_0\cos^3\psi T_{33}L_3 -$$
$$\beta_{GS}\cos\alpha_p\cos\theta_0\cos^2\psi\sin\psi T_{33}L_3 + \cos\theta_0\phi_h\sin\psi T_{33}L_3 -$$
$$\beta_{GC}\cos\alpha_p\cos\theta_0\cos\psi\sin^2\psi T_{33}L_3 - \beta_{GS}\cos\alpha_p\cos\theta_0\sin^3\psi T_{33}L_3 +$$
$$\cos\alpha_p\sin\psi y_h$$

$$T_{FL_x}(6,3) = \beta_{GC}\cos\psi h\sin\alpha_p\sin\psi + \beta_{GS}h\sin\alpha_p\sin^2\psi +$$
$$\cos\psi\phi_h T_{11}(s+L_1) + \alpha_h\cos\alpha_p\sin\psi T_{11}(s+L_1) +$$
$$\alpha_h\cos\alpha_p\cos\theta_0\cos\psi T_{12}(s+L_1) + \beta_{GC}\cos\alpha_p\cos\theta_0\cos^3\psi T_{12}(s+L_1) +$$
$$\beta_{GS}\cos\alpha_p\cos\theta_0\cos^2\psi\sin\psi T_{12}(s+L_1) - \cos\theta_0\phi_h\sin\psi T_{12}(s+L_1) +$$
$$\beta_{GC}\cos\alpha_p\cos\theta_0\cos\psi\sin^2\psi T_{12}(s+L_1) +$$
$$\beta_{GS}\cos\alpha_p\cos\theta_0\sin^3\psi T_{12}(s+L_1) -$$
$$\alpha_h\cos\alpha_p\cos\psi\sin\theta_0 T_{13}(s+L_1) - \beta_{GC}\cos\alpha_p\cos^3\psi\sin\theta_0 T_{13}(s+L_1) -$$
$$\beta_{GS}\cos\alpha_p\cos^2\psi\sin\theta_0\sin\psi T_{13}(s+L_1) + \phi_h\sin\theta_0\sin\psi T_{13}(s+L_1) -$$
$$\beta_{GC}\cos\alpha_p\cos\psi\sin\theta_0\sin^2\psi T_{13}(s+L_1) -$$
$$\beta_{GS}\cos\alpha_p\sin\theta_0\sin^3\psi T_{13}(s+L_1) +$$
$$\cos\psi\phi_h T_{21}L_2 + \alpha_h\cos\alpha_p\sin\psi T_{21}L_2 +$$
$$\alpha_h\cos\alpha_p\cos\theta_0\cos\psi T_{22}L_2 + \beta_{GC}\cos\alpha_p\cos\theta_0\cos^3\psi T_{22}L_2 +$$
$$\beta_{GS}\cos\alpha_p\cos\theta_0\cos^2\psi\sin\psi T_{22}L_2 - \cos\theta_0\phi_h\sin\psi T_{22}L_2 +$$
$$\beta_{GC}\cos\alpha_p\cos\theta_0\cos\psi\sin^2\psi T_{22}L_2 + \beta_{GS}\cos\alpha_p\cos\theta_0\sin^3\psi T_{22}L_2 -$$
$$\alpha_h\cos\alpha_p\cos\psi\sin\theta_0 T_{23}L_2 - \beta_{GC}\cos\alpha_p\cos^3\psi\sin\theta_0 T_{23}L_2 -$$
$$\beta_{GS}\cos\alpha_p\cos^2\psi\sin\theta_0\sin\psi T_{23}L_2 + \phi_h\sin\theta_0\sin\psi T_{23}L_2 -$$
$$\beta_{GC}\cos\alpha_p\cos\psi\sin\theta_0\sin^2\psi T_{23}L_2 - \beta_{GS}\cos\alpha_p\sin\theta_0\sin^3\psi T_{23}L_2 +$$
$$\cos\psi\phi_h T_{31}L_3 + \alpha_h\cos\alpha_p\sin\psi T_{31}L_3 +$$
$$\alpha_h\cos\alpha_p\cos\theta_0\cos\psi T_{32}L_3 + \beta_{GC}\cos\alpha_p\cos\theta_0\cos^3\psi T_{32}L_3 +$$
$$\beta_{GS}\cos\alpha_p\cos\theta_0\cos^2\psi\sin\psi T_{32}L_3 - \cos\theta_0\phi_h\sin\psi T_{32}L_3 +$$
$$\beta_{GC}\cos\alpha_p\cos\theta_0\cos\psi\sin^2\psi T_{32}L_3 + \beta_{GS}\cos\alpha_p\cos\theta_0\sin^3\psi T_{32}L_3 -$$
$$\alpha_h\cos\alpha_p\cos\psi\sin\theta_0 T_{33}L_3 - \beta_{GC}\cos\alpha_p\cos^3\psi\sin\theta_0 T_{33}L_3 -$$
$$\beta_{GS}\cos\alpha_p\cos^2\psi\sin\theta_0\sin\psi T_{33}L_3 + \phi_h\sin\theta_0\sin\psi T_{33}L_3 -$$
$$\beta_{GC}\cos\alpha_p\cos\psi\sin\theta_0\sin^2\psi T_{33}L_3 - \beta_{GS}\cos\alpha_p\sin\theta_0\sin^3\psi T_{33}L_3 +$$
$$\sin\alpha_p y_h$$

$$T_{FL_x}(6,4) = \alpha_h\cos\alpha_p\cos\psi T_{11} + \beta_{GC}\cos\alpha_p\cos\psi T_{11} +$$
$$\beta_{GS}\cos\alpha_p\sin\psi T_{11} - \phi_h\sin\psi T_{11} - \cos\theta_0\cos\psi\phi_h T_{12} -$$
$$\alpha_h\sin\alpha_p\sin\theta_0 T_{12} - \beta_{GC}\cos^2\psi\sin\alpha_p\sin\theta_0 T_{12} -$$

Reproduced with permission of the copyright owner. Further reproduction prohibited without permission.

$$
\begin{aligned}
& \alpha_h \cos\alpha_p \cos\theta_0 \sin\psi T_{12} - \beta_{GS} \cos\psi \sin\alpha_p \sin\theta_0 \sin\psi T_{12} - \\
& \alpha_h \cos\theta_0 \sin\alpha_p T_{13} - \beta_{GC} \cos\theta_0 \cos^2\psi \sin\alpha_p T_{13} + \\
& \cos\psi\phi_h \sin\theta_0 T_{13} - \beta_{GS} \cos\theta_0 \cos\psi \sin\alpha_p \sin\psi T_{13} + \\
& \alpha_h \cos\alpha_p \sin\theta_0 \sin\psi T_{13}
\end{aligned}
$$

$$
\begin{aligned}
T_{FL_x}(7,1) &= \beta_{GC} \cos\theta_0 \cos\psi \sin\psi T_{12}(s+L_1) + \beta_{GS} \cos\theta_0 \sin^2\psi T_{12}(s+L_1) - \\
& \beta_{GC} \cos\psi \sin\theta_0 \sin\psi T_{13}(s+L_1) - \beta_{GS} \sin\theta_0 \sin^2\psi T_{13}(s+L_1) + \\
& \beta_{GC} \cos\theta_0 \cos\psi \sin\psi T_{22} L_2 + \beta_{GS} \cos\theta_0 \sin^2\psi T_{22} L_2 - \\
& \beta_{GC} \cos\psi \sin\theta_0 \sin\psi T_{23} L_2 - \beta_{GS} \sin\theta_0 \sin^2\psi T_{23} L_2 + \\
& \beta_{GC} \cos\theta_0 \cos\psi \sin\psi T_{32} L_3 + \beta_{GS} \cos\theta_0 \sin^2\psi T_{32} L_3 - \\
& \beta_{GC} \cos\psi \sin\theta_0 \sin\psi T_{33} L_3 - \beta_{GS} \sin\theta_0 \sin^2\psi T_{33} L_3 \\
T_{FL_x}(7,2) &= -(\beta_{GC} \cos\psi \sin\psi T_{11}(s+L_1)) - \beta_{GS} \sin^2\psi T_{11}(s+L_1) - \\
& \beta_{GC} \cos\psi \sin\psi T_{21} L_2 - \beta_{GS} \sin^2\psi T_{21} L_2 - \\
& \beta_{GC} \cos\psi \sin\psi T_{31} L_3 - \beta_{GS} \sin^2\psi T_{31} L_3 \\
T_{FL_x}(7,3) &= 0 \\
T_{FL_x}(7,4) &= -(\beta_{GC} \cos\psi \sin\theta_0 \sin\psi T_{12}) - \beta_{GS} \sin\theta_0 \sin^2\psi T_{12} - \\
& \beta_{GC} \cos\theta_0 \cos\psi \sin\psi T_{13} - \beta_{GS} \cos\theta_0 \sin^2\psi T_{13} \\
T_{FL_x}(8,1) &= \beta_{GC} \cos\theta_0 \cos^2\psi T_{12}(s+L_1) + \beta_{GS} \cos\theta_0 \cos\psi \sin\psi T_{12}(s+L_1) - \\
& \beta_{GC} \cos^2\psi \sin\theta_0 T_{13}(s+L_1) - \beta_{GS} \cos\psi \sin\theta_0 \sin\psi T_{13}(s+L_1) + \\
& \beta_{GC} \cos\theta_0 \cos^2\psi T_{22} L_2 + \beta_{GS} \cos\theta_0 \cos\psi \sin\psi T_{22} L_2 - \\
& \beta_{GC} \cos^2\psi \sin\theta_0 T_{23} L_2 - \beta_{GS} \cos\psi \sin\theta_0 \sin\psi T_{23} L_2 + \\
& \beta_{GC} \cos\theta_0 \cos^2\psi T_{32} L_3 + \beta_{GS} \cos\theta_0 \cos\psi \sin\psi T_{32} L_3 - \\
& \beta_{GC} \cos^2\psi \sin\theta_0 T_{33} L_3 - \beta_{GS} \cos\psi \sin\theta_0 \sin\psi T_{33} L_3 \\
T_{FL_x}(8,2) &= -(\beta_{GC} \cos^2\psi T_{11}(s+L_1)) - \beta_{GS} \cos\psi \sin\psi T_{11}(s+L_1) - \\
& \beta_{GC} \cos^2\psi T_{21} L_2 - \beta_{GS} \cos\psi \sin\psi T_{21} L_2 - \\
& \beta_{GC} \cos^2\psi T_{31} L_3 - \beta_{GS} \cos\psi \sin\psi T_{31} L_3 \\
T_{FL_x}(8,3) &= 0 \\
T_{FL_x}(8,4) &= -(\beta_{GC} \cos^2\psi \sin\theta_0 T_{12}) - \beta_{GS} \cos\psi \sin\theta_0 \sin\psi T_{12} - \\
& \beta_{GC} \cos\theta_0 \cos^2\psi T_{13} - \beta_{GS} \cos\theta_0 \cos\psi \sin\psi T_{13}
\end{aligned}
$$

Reproduced with permission of the copyright owner. Further reproduction prohibited without permission.

Appendix C

Rigid Blade Tiltrotor Trim

The objective of the rigid-blade flap analysis is to provide initial estimates (to be used for the elastic blade coupled trim procedure) for the blade collective and cyclic controls θ_{75}, θ_{1c}, and θ_{1s}, and the fuselage angle of attack, α_f. If the coupled-trim is for a cantilevered wing model attached to a fixed fuselage, then α_f is not required and the procedure is simplified. If the trim is being performed for the rotor thrust only, then the rotor cyclic controls θ_{1c} and θ_{1s} are not used and the trim procedure is further simplified.

A rigid-bladed tiltrotor trim formulation was developed by Nixon [39] from first principles and is utilized in this analysis to provide initial estimates for the tiltrotor controls. This formulation handles axial flight, hover, and conversion modes of operation providing initial control estimates for axial flight trim, wind tunnel trim and free flight trim options. The rigid-blade analysis consists of three parts: 1) estimation of the fuselage angle of attack and the rotor thrust based on the gross airframe forces, but excluding rotor hub forces other than thrust and excluding blade flap motion, 2) estimation of the rotor collective required to obtain the estimated rotor thrust from (1), and 3) simultaneous solution of the coupled

Reproduced with permission of the copyright owner. Further reproduction prohibited without permission.

rotor/fuselage system with rotor flap motion included, with the initial guesses for fuselage angle of attack and rotor collective, resulting in an estimation of the four desired controls θ_{75}, θ_{1c}, and θ_{1s}, and α_f as well as the rotor flapping unknowns β_0, β_{1c}, and β_{1s}.

C.1 Estimation of Fuselage Angle of Attack and Rotor Thrust

If free-flight trim is not required, then the rotor thrust estimate is provided directly as input, the fuselage angle is set to zero, and the analysis of the present section is skipped. If free flight trim is required, an initial approximation for α_f is obtained from a balance of forces on the fuselage. The hub forces from the rotor are not known, but the rotor thrust can be estimated since it balances the aircraft drag and weight. The lift on the wing and horizontal tail depend on α_f, hence the estimate of α_f is an iterative process. The lift and drag contributions from the wing and horizontal tail are calculated as:

$$D_f = \frac{\mu^2}{2}\frac{\gamma N_b}{3\sigma a}\frac{f}{A} \tag{C.1}$$

$$D_w = \frac{\mu^2}{2}\frac{\gamma N_b}{3\sigma a}S_w C_{d_w} \tag{C.2}$$

$$D_t = \frac{\mu^2}{2}\frac{\gamma N_b}{3\sigma a}S_t C_{d_t} \tag{C.3}$$

$$L_w = \frac{\mu^2}{2}\frac{\gamma N_b}{3\sigma a}S_w c_{l_{\alpha_w}}(\alpha_f + \alpha_{0_w}) \tag{C.4}$$

$$M_w = \frac{\mu^2}{2}\frac{\gamma N_b}{3\sigma a}S_w C_{m_w} c_w \tag{C.5}$$

$$M_t = \frac{\mu^2}{2}\frac{\gamma N_b}{3\sigma a}S_t C_{m_t} c_t \tag{C.6}$$

$$T_{fh} = D_f + D_w + D_t \tag{C.7}$$

Reproduced with permission of the copyright owner. Further reproduction prohibited without permission.

$$T_r = \frac{T_{fh}}{\sin\alpha_p}, \text{ if } \sin\alpha_p \neq 0 \text{ (conversion, airplane modes)} \quad \text{(C.8)}$$

$$= W, \text{ if } \sin\alpha_p = 0 \text{ (helicopter mode)} \quad \text{(C.9)}$$

$$T_{fv} = T\cos\alpha_p, \text{ if } \sin\alpha_p \neq 0 \text{ (conversion, airplane modes)} \quad \text{(C.10)}$$

$$= W, \text{ if } \sin\alpha_p = 0 \text{ (helicopter mode)} \quad \text{(C.11)}$$

where the lift and drag expressions for the wing, tail, and fuselage are the same as those used in the elastic blade trim equations, T_r is the estimate of rotor thrust, T_{fh} is the horizontal component of rotor thrust which should balance the drag forces, and T_{fv} is the vertical component of rotor thrust which should balance the airframe lift forces. The horizontal force balance is achieved by setting the horizontal component of rotor thrust equal to the sum of the drag forces. Based on the pylon angle, this then defines the thrust and the vertical component of the thrust which is used to define a force residual in the vertical direction:

$$F_1 = W - L_w - L_t - T_{fv} \quad \text{(C.12)}$$

The lift contribution of the horizontal tail is calculated from the pitching moment balance:

$$L_t = \frac{(M_w + M_t - D_t(z_w - z_t) - Wx_w - W\alpha_f z_w - D_f z_w)}{(x_t - x_w)} \quad \text{(C.13)}$$

since it is assumed that the elevator angle of the tail can be set to produce this balance. A Jacobian is calculated from the force residual equation:

$$J = \frac{T_{fh}}{\sin^2\alpha_p} + \frac{L_w}{\alpha_f} + \frac{L_t}{\alpha_f} \quad \text{(C.14)}$$

and is used to calculate the new estimate for α_f as:

$$(\alpha_f)_{new} = (\alpha_f)_{old} + F_1/J \quad \text{(C.15)}$$

Reproduced with permission of the copyright owner. Further reproduction prohibited without permission.

C.2 Derivation of Blade and Hub Forces

Following convergence of the α_f estimate, the next step is to determine the collective setting required to produce the rotor thrust T_r. This calculation is also an iterative process, and the aerodynamic model of the rotor forces should first be formulated.

The rotor fixed-frame (hub) forces are calculated based on a rigid-blade flapping model with flap frequency ν_β and a high-inflow aerodynamic model. The local velocities on a blade section at any spanwise station along the blade are defined as:

$$U_t = t_c + t_w w + t_{w'} w' + t_{\dot{w}} \dot{w} \tag{C.16}$$

$$U_p = p_c + p_w w + p_{w'} w' + p_{\dot{w}} \dot{w} \tag{C.17}$$

where U_t is the tangential velocity component, U_p is the perpendicular (upward) velocity component; subscript c denotes constant values, w and w' indicate dependence of the local velocity on displacement w, and $\dot{w}$ indicates dependence of the local velocity on blade flap velocity. The velocity components are defined as:

$$t_c = \mu \cos\alpha_p \cos\theta_1 \sin\psi + \mu\beta_p \cos\alpha_p \cos\psi \sin\theta_1 + \lambda \sin\theta_1 + \mu \sin\alpha_p \sin\theta_1 + x \cos\theta_1 \tag{C.18}$$

$$t_w = -\beta_p \cos\theta_1 \tag{C.19}$$

$$t_{w'} = -\mu \sin\theta_1 \left(\cos\alpha_p \cos\theta_1 \sin\psi + \sin\alpha_p \sin\theta_1\right) \tag{C.20}$$

$$t_{\dot{w}} = \sin\theta_1 \tag{C.21}$$

$$p_c = \mu\beta_p \cos\alpha_p \cos\psi \cos\theta_1 + \lambda \cos\theta_1 + \mu \cos\theta_1 \sin\alpha_p -$$

Reproduced with permission of the copyright owner. Further reproduction prohibited without permission.

$$\mu \cos \alpha_p \sin \psi \sin \theta_1 - x \sin \theta_1 \tag{C.22}$$

$$p_w = -\beta_p \sin \theta_1 \tag{C.23}$$

$$p_{w'} = -\mu \cos \theta_1 \left(\cos \alpha_p \cos \theta_1 \sin \psi + \sin \alpha_p \sin \theta_1 \right) \tag{C.24}$$

$$p_{\dot{w}} = \cos \theta_1 \tag{C.25}$$

and the blade displacement w is defined in terms of the flap angle β such that:

$$w = x\beta \tag{C.26}$$

$$w' = \beta \tag{C.27}$$

$$\dot{w} = x\dot{\beta} \tag{C.28}$$

The control angle θ is substituted for in terms of its harmonic components as:

$$\theta = \theta_{75} + \theta_{1c} \cos \psi + \theta_{1s} \sin \psi \tag{C.29}$$

At this stage, assuming that the blade produces lift proportional to the nominal lift curve slope a, the forces on the blade along the chord line and perpendicular to it are given by:

$$v_{b0} = \frac{\gamma}{6} u_p^2 \tag{C.30}$$

$$w_{b0} = -\frac{\gamma}{6} u_t u_p \tag{C.31}$$

which are transformed into the hub plane as:

$$F_x = -v_{b0} \cos \theta_1 + w_{b0} \sin \theta_1 \tag{C.32}$$

$$F_z = v_{b0} \sin \theta_1 + w_{b0} \cos \theta_1 \tag{C.33}$$

$$F_r = -\beta F_z \tag{C.34}$$

Reproduced with permission of the copyright owner. Further reproduction prohibited without permission.

The rotor forces are calculated by transforming the following integrals into the fixed system:

$$T = \int_0^1 F_z \, dx \tag{C.35}$$

$$H = \int_0^1 (F_x \sin\psi + F_r \cos\psi) \, dx \tag{C.36}$$

$$M_x = \int_0^1 x F_z \sin\psi \, dx \tag{C.37}$$

$$M_y = \int_0^1 x F_z \cos\psi \, dx \tag{C.38}$$

The flap moment equilibrium on the blade is given by:

$$M_\beta(\psi) = \int_0^1 x F_z \, dx \tag{C.39}$$

which can be written as

$$M_\beta(\psi) = M_0 + M_{1c} \cos\psi + M_{1s} \sin\psi \tag{C.40}$$

where M_0 represents the constant terms, and M_{1c} and M_{1s} represent the coefficients of the periodic terms $\cos\psi$ and $\sin\psi$, respectively. The final terms in these force equations (4 hub forces and 3 flapping moments) are listed in the following section.

C.3 Hub Force and Blade Moment Expressions

The integration of Eqns. C.35-C.40 results in lengthy expressions for the four hub forces and three blade moments, all in the rotating frame and containing the seven unknowns.

The equation of motion for a flapping rotor blade is given by:

$$\ddot{\beta} + \nu_\beta^2 \beta = \gamma M_\beta + \frac{\omega_{\beta_0}^2}{\Omega^2} \beta_p \tag{C.41}$$

Reproduced with permission of the copyright owner. Further reproduction prohibited without permission.

which in nondimensional form and after substitution of the flap angle in terms of harmonics:

$$\beta(\psi) = \beta_0 + \beta_{1c}\cos\psi + \beta_{1s}\sin\psi \tag{C.42}$$

can be written as three equations which are coefficients of the periodic terms:

$$\beta_0 = \frac{1}{\nu_\beta^2}(\gamma M_0 + \omega_{\beta_0}^2 \beta_p) \tag{C.43}$$

which is uncoupled from the cyclic equations:

$$\frac{\nu_{\beta^2} - 1}{\gamma}\beta_{1c} = M_{1c} \tag{C.44}$$

$$\frac{\nu_{\beta^2} - 1}{\gamma}\beta_{1s} = M_{1s} \tag{C.45}$$

The cyclic equations are coupled because M_{1c} and M_{1s} each contain terms with both β_{1c} and β_{1s}. The actual terms of the aerodynamic moments are listed as follows: the steady moment is written as

$$M_0 = \sum_{i=1}^{14} b_i \tag{C.46}$$

with the coefficients given as follows:

$$b_1 = -(\lambda_i \cos^3\theta_{75})/6 \tag{C.47}$$

$$b_2 = -(\mu \cos^3\theta_{75} \sin\alpha_p)/6 \tag{C.48}$$

$$b_3 = \cos^2\theta_{75} \sin\theta_{75}/8 \tag{C.49}$$

$$b_4 = \mu^2 \cos^2\alpha_p \cos^2\theta_{75} \sin\theta_{75}/8 \tag{C.50}$$

$$b_5 = -(\lambda_i \cos\theta_{75} \sin^2\theta_{75})/6 \tag{C.51}$$

$$b_6 = -(\mu \cos\theta_{75} \sin\alpha_p \sin^2\theta_{75})/6 \tag{C.52}$$

$$b_7 = \sin^3\theta_{75}/8 \tag{C.53}$$

Reproduced with permission of the copyright owner. Further reproduction prohibited without permission.

$$b_8 = \mu^2 \cos^2 \alpha_p \sin^3\theta_{75}/8 \quad \text{(C.54)}$$

$$b_9 = \mu \cos \alpha_p \cos^3\theta_{75}\theta_{1s}/6 \quad \text{(C.55)}$$

$$b_{10} = \lambda_i \mu \cos \alpha_p \cos^2\theta_{75} \sin\theta_{75}\theta_{1s}/8 \quad \text{(C.56)}$$

$$b_{11} = \mu^2 \cos \alpha_p \cos^2\theta_{75} \sin \alpha_p \sin\theta_{75}\theta_{1s}/8 \quad \text{(C.57)}$$

$$b_{12} = \mu \cos \alpha_p \cos\theta_{75} \sin^2\theta_{75}\theta_{1s}/6 \quad \text{(C.58)}$$

$$b_{13} = \lambda_i \mu \cos \alpha_p \sin^3\theta_{75}\theta_{1s}/8 \quad \text{(C.59)}$$

$$b_{14} = \mu^2 \cos \alpha_p \sin \alpha_p \sin^3\theta_{75}\theta_{1s}/8 \quad \text{(C.60)}$$

The cosine moment is written as

$$M_{1c} = \sum_{i=15}^{32} b_i \quad \text{(C.61)}$$

with

$$b_{15} = -(\beta_{1s} \cos^3\theta_{75})/8 \quad \text{(C.62)}$$

$$b_{16} = -(\mu\beta_0 \cos \alpha_p \cos^3\theta_{75})/6 \quad \text{(C.63)}$$

$$b_{17} = -(\mu\beta_p \cos \alpha_p \cos^3\theta_{75})/6 \quad \text{(C.64)}$$

$$b_{18} = \mu\beta_0\beta_p^2 \cos \alpha_p \cos^3\theta_{75}/6 \quad \text{(C.65)}$$

$$b_{19} = -(\mu^2\beta_{1s} \cos^2 \alpha_p \cos^3\theta_{75})/8 \quad \text{(C.66)}$$

$$b_{20} = -(\beta_{1s} \cos\theta_{75} \sin^2\theta_{75})/8 \quad \text{(C.67)}$$

$$b_{21} = -(\mu\beta_0 \cos \alpha_p \cos\theta_{75} \sin^2\theta_{75})/6 \quad \text{(C.68)}$$

$$b_{22} = -(\mu\beta_p \cos \alpha_p \cos\theta_{75} \sin^2\theta_{75})/6 \quad \text{(C.69)}$$

$$b_{23} = \mu\beta_0\beta_p^2 \cos \alpha_p \cos\theta_{75} \sin^2\theta_{75}/6 \quad \text{(C.70)}$$

$$b_{24} = -(\mu^2\beta_{1s} \cos^2 \alpha_p \cos\theta_{75} \sin^2\theta_{75})/8 \quad \text{(C.71)}$$

Reproduced with permission of the copyright owner. Further reproduction prohibited without permission.

$$b_{25} = \cos^3\theta_{75}\theta_{1c}/8 \tag{C.72}$$

$$b_{26} = \mu^2 \cos^2\alpha_p \cos^3\theta_{75}\theta_{1c}/8 \tag{C.73}$$

$$b_{27} = \lambda_i \cos^2\theta_{75} \sin\theta_{75}\theta_{1c}/6 \tag{C.74}$$

$$b_{28} = \mu \cos^2\theta_{75} \sin\alpha_p \sin\theta_{75}\theta_{1c}/6 \tag{C.75}$$

$$b_{29} = \cos\theta_{75} \sin^2\theta_{75}\theta_{1c}/8 \tag{C.76}$$

$$b_{30} = \mu^2 \cos^2\alpha_p \cos\theta_{75} \sin^2\theta_{75}\theta_{1c}/8 \tag{C.77}$$

$$b_{31} = \lambda_i \sin^3\theta_{75}\theta_{1c}/6 \tag{C.78}$$

$$b_{32} = \mu \sin\alpha_p \sin^3\theta_{75}\theta_{1c}/6 \tag{C.79}$$

and the sine moment is written as

$$M_{1s} = \sum_{i=33}^{50} b_i \tag{C.80}$$

with

$$b_{33} = \beta_{1c} \cos^3\theta_{75}/8 \tag{C.81}$$

$$b_{34} = -(\lambda_i \mu \cos\alpha_p \cos^3\theta_{75})/4 \tag{C.82}$$

$$b_{35} = -(\mu^2 \beta_{1c} \cos^2\alpha_p \cos^3\theta_{75})/8 \tag{C.83}$$

$$b_{36} = -(\mu^2 \cos\alpha_p \cos^3\theta_{75} \sin\alpha_p)/4 \tag{C.84}$$

$$b_{37} = \mu \cos\alpha_p \cos^2\theta_{75} \sin\theta_{75}/3 \tag{C.85}$$

$$b_{38} = \beta_{1c} \cos\theta_{75} \sin^2\theta_{75}/8 \tag{C.86}$$

$$b_{39} = -(\lambda_i \mu \cos\alpha_p \cos\theta_{75} \sin^2\theta_{75})/4 \tag{C.87}$$

$$b_{40} = -(\mu^2 \beta_{1c} \cos^2\alpha_p \cos\theta_{75} \sin^2\theta_{75})/8 \tag{C.88}$$

$$b_{41} = -(\mu^2 \cos\alpha_p \cos\theta_{75} \sin\alpha_p \sin^2\theta_{75})/4 \tag{C.89}$$

Reproduced with permission of the copyright owner. Further reproduction prohibited without permission.

$$b_{42} = \mu \cos\alpha_p \sin^3\theta_{75}/3 \tag{C.90}$$

$$b_{43} = \cos^3\theta_{75}\theta_{1s}/8 \tag{C.91}$$

$$b_{44} = 3\mu^2 \cos^2\alpha_p \cos^3\theta_{75}\theta_{1s}/16 \tag{C.92}$$

$$b_{45} = \lambda_i \cos^2\theta_{75} \sin\theta_{75}\theta_{1s}/6 \tag{C.93}$$

$$b_{46} = \mu \cos^2\theta_{75} \sin\alpha_p \sin\theta_{75}\theta_{1s}/6 \tag{C.94}$$

$$b_{47} = \cos\theta_{75} \sin^2\theta_{75}\theta_{1s}/8 \tag{C.95}$$

$$b_{48} = 3\mu^2 \cos^2\alpha_p \cos\theta_{75} \sin^2\theta_{75}\theta_{1s}/16 \tag{C.96}$$

$$b_{49} = \lambda_i \sin^3\theta_{75}\theta_{1s}/6 \tag{C.97}$$

$$b_{50} = \mu \sin\alpha_p \sin^3\theta_{75}\theta_{1s}/6 \tag{C.98}$$

The four hub force expressions, presently written in the rotating hub plane, are converted to a fixed frame. The Fourier coordinate transformation into the fixed frame depends on the number of blades, but, as this rigid-blade analysis only provides an estimate of control parameters and the aerodynamic model is based only on a representative lift curve slope, it is adequate to assume an arbitrary number of blades to represent the tip-path-plane tilt for any typical N_b bladed system. This assumption greatly simplifies the hub force equations. The transformation to fixed frame is based on a three-bladed system, and the resulting hub forces are written as follows:

The rotor thrust is given by

$$T = \frac{\gamma N_b}{6} \sum_{i=1}^{14} a_i \tag{C.99}$$

Reproduced with permission of the copyright owner. Further reproduction prohibited without permission.

where

$$a_1 = -(\lambda_i \cos^3\theta_{75})/2 \tag{C.100}$$

$$a_2 = -(\mu \cos^3\theta_{75} \sin\alpha_p)/2 \tag{C.101}$$

$$a_3 = \cos^2\theta_{75} \sin\theta_{75}/3 \tag{C.102}$$

$$a_4 = \mu^2 \cos^2\alpha_p \cos^2\theta_{75} \sin\theta_{75}/2 \tag{C.103}$$

$$a_5 = -(\lambda_i \cos\theta_{75} \sin^2\theta_{75})/2 \tag{C.104}$$

$$a_6 = -(\mu \cos\theta_{75} \sin\alpha_p \sin^2\theta_{75})/2 \tag{C.105}$$

$$a_7 = \sin^3\theta_{75}/3 \tag{C.106}$$

$$a_8 = \mu^2 \cos^2\alpha_p \sin^3\theta_{75}/2 \tag{C.107}$$

$$a_9 = \mu \cos\alpha_p \cos^3\theta_{75}\theta_{1s}/2 \tag{C.108}$$

$$a_{10} = \lambda_i\mu \cos\alpha_p \cos^2\theta_{75} \sin\theta_{75}\theta_{1s}/2 \tag{C.109}$$

$$a_{11} = \mu^2 \cos\alpha_p \cos^2\theta_{75} \sin\alpha_p \sin\theta_{75}\theta_{1s}/2 \tag{C.110}$$

$$a_{12} = \mu \cos\alpha_p \cos\theta_{75} \sin^2\theta_{75}\theta_{1s}/2 \tag{C.111}$$

$$a_{13} = \lambda_i\mu \cos\alpha_p \sin^3\theta_{75}\theta_{1s}/2 \tag{C.112}$$

$$a_{14} = \mu^2 \cos\alpha_p \sin\alpha_p \sin^3\theta_{75}\theta_{1s}/2 \tag{C.113}$$

and the rotor drag force is given by

$$H = \frac{\gamma N_b}{6} \sum_{i=15}^{34} a_i \tag{C.114}$$

where

$$a_{15} = 3\lambda_i\beta_{1c} \cos^3\theta_{75}/4 \tag{C.115}$$

$$a_{16} = 3\mu\beta_{1c} \cos^3\theta_{75} \sin\alpha_p/4 \tag{C.116}$$

Reproduced with permission of the copyright owner. Further reproduction prohibited without permission.

$$a_{17} = -(\beta_{1c}\cos^2\theta_{75}\sin\theta_{75})/3 \quad \text{(C.117)}$$

$$a_{18} = \lambda_i\mu\cos\alpha_p\cos^2\theta_{75}\sin\theta_{75}/2 \quad \text{(C.118)}$$

$$a_{19} = \mu^2\cos\alpha_p\cos^2\theta_{75}\sin\alpha_p\sin\theta_{75}/2 \quad \text{(C.119)}$$

$$a_{20} = 3\lambda_i\beta_{1c}\cos\theta_{75}\sin^2\theta_{75}/4 \quad \text{(C.120)}$$

$$a_{21} = 3\mu\beta_{1c}\cos\theta_{75}\sin\alpha_p\sin^2\theta_{75}/4 \quad \text{(C.121)}$$

$$a_{22} = -(\beta_{1c}\sin^3\theta_{75})/3 \quad \text{(C.122)}$$

$$a_{23} = \lambda_i\mu\cos\alpha_p\sin^3\theta_{75}/2 \quad \text{(C.123)}$$

$$a_{24} = \mu^2\cos\alpha_p\sin\alpha_p\sin^3\theta_{75}/2 \quad \text{(C.124)}$$

$$a_{25} = \lambda_i\cos^3\theta_{75}\theta_{1s}/4 \quad \text{(C.125)}$$

$$a_{26} = \mu\cos^3\theta_{75}\sin\alpha_p\theta_{1s}/4 \quad \text{(C.126)}$$

$$a_{27} = \lambda_i^2\cos^2\theta_{75}\sin\theta_{75}\theta_{1s}/2 \quad \text{(C.127)}$$

$$a_{28} = \lambda_i\mu\cos^2\theta_{75}\sin\alpha_p\sin\theta_{75}\theta_{1s} \quad \text{(C.128)}$$

$$a_{29} = \mu^2\cos^2\theta_{75}\sin^2\alpha_p\sin\theta_{75}\theta_{1s}/2 \quad \text{(C.129)}$$

$$a_{30} = \lambda_i\cos\theta_{75}\sin^2\theta_{75}\theta_{1s}/4 \quad \text{(C.130)}$$

$$a_{31} = \mu\cos\theta_{75}\sin\alpha_p\sin^2\theta_{75}\theta_{1s}/4 \quad \text{(C.131)}$$

$$a_{32} = \lambda_i^2\sin^3\theta_{75}\theta_{1s}/2 \quad \text{(C.132)}$$

$$a_{33} = \lambda_i\mu\sin\alpha_p\sin^3\theta_{75}\theta_{1s} \quad \text{(C.133)}$$

$$a_{34} = \mu^2\sin^2\alpha_p\sin^3\theta_{75}\theta_{1s}/2 \quad \text{(C.134)}$$

The roll and pitch moments in the fixed frame are written in terms of the flapping restraint as was done in the rigid-bladed rotor analysis of Chapter 2:

$$M_x = \frac{\gamma N_b}{6}(\nu_\beta^2 - 1)\beta_{1s} \quad \text{(C.135)}$$

Reproduced with permission of the copyright owner. Further reproduction prohibited without permission.

$$M_y = -\frac{\gamma N_b}{6}(\nu_\beta^2 - 1)\beta_{1c} \tag{C.136}$$

C.4 Estimation of Rotor Collective Pitch

An iterative process is used to establish an initial value for the collective pitch based on achieving the desired level of thrust on the rigid-blade. The force residual equation is simply

$$F_1 = T - T_r \tag{C.137}$$

where T is the calculated thrust based on the current value of θ_{75} and T_r is the desired thrust level calculated from the first section of this analysis. The new value of the collective is calculated from the analytical Jacobian:

$$J = \frac{\partial T}{\partial \theta_{75}} = \frac{\gamma N_b}{6} \sum_{i=1}^{14} \frac{\partial a_i}{\partial \theta_{75}} \tag{C.138}$$

$$(\theta_{75})_{new} = (\theta_{75})_{old} + F_1/J \tag{C.139}$$

Convergence, in this case, results in the estimate for the collective setting, and ends the analysis for the axisymmetric hover and axial flight cases. For these cases, only the fuselage angle of attack and collective setting are required. Otherwise, the analysis continues to determine the appropriate cyclic control values.

C.5 Coupled Rotor/Airframe and Flapping Blade Analysis

For conversion and airplane mode, an appropriate starting value for the collective and fuselage angle of attack are now known. Using these initial values, a new process is begun that considers the equilibrium of the entire airframe with the four

Reproduced with permission of the copyright owner. Further reproduction prohibited without permission.

hub forces and blade flapping included. There are seven unknowns in this sequence: the three pitch controls, θ_{75}, θ_{1c}, and θ_{1s}, the fuselage angle of attack α_f, and the three flap angles, β_0, β_{1c}, and β_{1s}. Initial guesses for the unknowns θ_{1c}, θ_{1s}, β_{1c}, and β_{1s} are initially set to small values (.01 rad). The value of β_0 is obtained throughout the iterative process by Eqn. C.43 using the present values of θ_{75} and θ_{1s}. The new values of the remaining unknowns are obtained through formulation of a numerical 6 x 6 Jacobian matrix and 6 force residual equations. Airframe forces and rotor forces are combined to write the equilibrium of the aircraft as:

$$F_1 = 2T_{fh} - (D_w + D_f + D_t) \tag{C.140}$$

$$F_2 = W - (L_w + L_t + 2T_{fv}) \tag{C.141}$$

$$F_3 = 2M_y + 2hH + M_w + M_t - L_t(x_t - x_w) - D_t(z_w - z_t) - Wx_w - Wz_w\alpha_f - D_f z_w \tag{C.142}$$

$$F_4 = M_x \tag{C.143}$$

$$F_5 = \frac{(\nu_\beta^2 - 1)}{\gamma}\beta_{1s} - M_{1c} \tag{C.144}$$

$$F_6 = \frac{(\nu_\beta^2 - 1)}{\gamma}\beta_{1c} - M_{1s} \tag{C.145}$$

where F_1 represents the horizontal force equilibrium, F_2 represents the vertical force equilibrium, F_3 represents the pitch moment equilibrium, F_4 represents the roll equilibrium of the rotor in the fixed system, and F_5 and F_6 represent the cyclic moment balances of the blade in the rotating frame which primarily influence the unknowns β_{1c} and β_{1s}. A Jacobian matrix is numerically generated by calculating the change in the six force residuals due to individual perturbations of the six independent unknowns (β_0 is a dependent quantity). The new controls are written

Reproduced with permission of the copyright owner. Further reproduction prohibited without permission.

in terms of the previous iteration as:

$$(\hat{\theta})_{new} = (\hat{\theta})_{old} + (1 - R)[J]^{-1}\hat{F} \tag{C.146}$$

where $\hat{\theta}$ is a vector of the six independent unknowns and $\hat{F}$ is a vector of the six force residuals, and R is a parameter used to control numerical damping of the control updates. The iteration process continues until convergence is reached, which is determined by the magnitude of the force residual vector:

$$\text{magnitude}(F) = \sqrt{\sum_{i=1}^{6} F_i^2} < \text{e-6 for convergence} \tag{C.147}$$

The convergence of the problem is controlled by the application of appropriate damping factors on the update step size taken, and by recalculation of the Jacobian matrix, if necessary, after a selected number of iterations.

Reproduced with permission of the copyright owner. Further reproduction prohibited without permission.

Appendix D

Swept Tip Blade

Figure 6.3 shows two different ways of modeling blade sweep. The blade shown in the top part of the figure is the manner in which blade tip sweep is modeled in this formulation (swept tip). The blade shown in the bottom part of Figure 6.3 represents the construction of some swept tips (shear tip). This chapter examines some of the errors arising from modeling shear tips as swept tips. The rotor, investigated in Chapter 6, had a root cut-out of 10% and a rotor thrust-weighted solidity (baseline) of 0.089. Solidity of the planform-tapered blade was maintained constant for different taper ratios. For the swept blade, however, the chord (assumed perpendicular to the swept elastic axis of the blade) was maintained constant, irrespective of the sweep angle. This results in a change in the planform area of the rotor blade as well as in the thrust-weighted solidity.

Change in Planform Area

For the baseline configuration (straight rectangular blades), the rotor blade planform area (for one blade) is 0.0837 square feet. For a 30° backward tip sweep (modeled as a shear tip) given to the outboard 15% span of the rotor blade, the

Reproduced with permission of the copyright owner. Further reproduction prohibited without permission.

planform area remains exactly the same as for the baseline configuration. But for a 30° backward tip sweep (modeled as a swept tip), the planform area (of one rotor blade) is 0.0825 square feet, which represents a decrease of 1.49% in planform area. While for a fixed-wing, this may be a small effect, for a rotating-wing, it is the radially-weighted area that is important.

Change in Rotor Thrust-Weighted Solidity

Hover:

The thrust-weighted solidity is calculated by giving appropriate weightage to the thrusting capability of each blade section, from root to tip.

$$\sigma_{th} = 3 \int_{root}^{tip} \sigma_x r^2 dr \tag{D.1}$$

where σ_{th} is the thrust-weighted rotor solidity and σ_x is the local solidity (based on local chord, defined in Chapter 4). For the baseline configuration as well as for the 30° tip sweep (shear tip), the thrust-weighted solidity (for the case examined) is:

$$\sigma_{th} = 3 \int_{0.1}^{1} 0.089 r^2 dr = 0.089 r^3 \,|_{0.1}^{1} = 0.0889 \tag{D.2}$$

For a 30° tip sweep (modeled as a swept tip) given to the outboard 15% span of the blade, the thrust weighted solidity is:

$$\begin{aligned} \sigma_{th} &= 3 \int_{0.1}^{0.85} 0.089 r^2 dr + 3 \int_{0.85}^{1} r^2 \cos^2 30^o dr \\ &= 0.089 \left[0.6131 + 0.2894\right] = 0.0803 \end{aligned} \tag{D.3}$$

The error in thrust-weighed solidity is 9.66%, which is a significant decrease with respect to the baseline case. Consequently, when two such configurations which dif-

Reproduced with permission of the copyright owner. Further reproduction prohibited without permission.

fer significantly in their thrust-weighted solidities are compared with one another, the results from such comparisons have to be interpreted with caution.

Airplane Cruise:

Tiltrotor aircraft, however, are designed to operate in airplane mode cruise flight as well as in hover. Aeroelastic instabilities, such as whirl flutter, examined in this study are related to high-speed airplane flight condition. Airplane cruise corresponds to an advance ratio of 0.7. The thrust-weighted solidity, in airplane mode cruise, can be defined as:

$$\sigma_{ff} = 3 \int_{root}^{tip} \sigma_x \left[r^2 + (0.7)^2 \right] dr \tag{D.4}$$

where σ_{ff}, the thrust-weighted rotor solidity in airplane cruise, is defined to account for the axial velocity (in airplane mode) as well as for the inplane velocity (due to rotation). The baseline thrust-weighted solidity in airplane cruise (as well as for the 30° tip sweep, modeled as a shear tip), for the given rotor parameters, is 0.2067. For a 30° tip sweep (modeled as a swept tip), the thrust-weighted solidity in airplane cruise is:

$$\begin{aligned} \sigma_{ff} &= 3 \int_{0.1}^{0.85} 0.089 \left[r^2 + (0.7)^2 \right] dr + 3 \int_{0.85}^{1} 0.089 \left[r^2 \cos^2 30^o + (0.7)^2 \right] dr \\ &= 0.1981 \end{aligned} \tag{D.5}$$

Error in thrust-weighted solidity (in modeling the blade tip as a swept tip) is 4.16%, which is relatively low. Therefore, the comparisons made in airplane mode (in Chapter 6), between the baseline configuration and the swept tip configuration (as modeled in this formulation) can be justified since the difference in thrust-weighted solidity in airplane cruise is relatively small. However, if larger sweep

Reproduced with permission of the copyright owner. Further reproduction prohibited without permission.

angles are considered or if a larger portion of the blade span is swept, the error in thrust-weighted solidity could be considerably higher. Comparisons of results between different configurations could be misleading if the errors are significant. The blade chord, in that case, has to be recalculated to maintain thrust-weighted solidity constant.

Reproduced with permission of the copyright owner. Further reproduction prohibited without permission.

Bibliography

[1] Chopra, I., "Perspectives in Aeromechanical Stability of Helicopter Rotors," *Vertica*, Vol. 14, No. 4, pp. 457-508, 1990.

[2] Johnson, W., "Recent Developments in the Dynamics of Advanced Rotor Systems," NASA TM 86-669, March 1985; also, Part I, *Vertica*, Vol. 10, 1986, pp. 73-107 and Part II, *Vertica*, Vol. 10, 1986, pp. 109-150.

[3] Friedmann, P.P., "Helicopter Rotor Dynamics and Aeroelasticity: Some Key Ideas and Insights," *Vertica*, Vol. 14, No. 1, 1990, pp. 101-121.

[4] Quigley, H.C., and Koenig, D.G., "A Flight Study of the Dynamic Stability of a Tilting-Rotor Convertiplane," NASA TN D-778, April 1961.

[5] Gaffey, T.M., Yen, J.G., and Kvaternik, R.G., "Analysis and Model Tests of the Proprotor Dynamics of a Tilt-Proprotor VTOL Aircraft," U.S. Air Force V/STOL Technology and Planning Conference, Las Vegas, Nevada, Sept. 1969.

[6] Richardson, J.R., and Naylon, H.F.W., "Whirl Flutter of Propellers with Hinged Blades," Report No. 24, Engineering Research Associates, Toronto, Canada, 1962.

[7] Richardson, J.R., McKillop, J.A., Naylor, H.F.W., and Bandler, P.A., "Whirl

Reproduced with permission of the copyright owner. Further reproduction prohibited without permission.

Flutter of Propellers with Flexible Twisted Blades," Report No. 43, Engineering Research Associates, Toronto, Canada, 1962.

[8] Richardson, D.A., "The Application of Hingeless Rotors to Tilting Proprotor Aircraft," *Journal of the American Helicopter Society*, Vol. 16, No. 3, July 1971, pp. 34-38.

[9] Reed, W.H., III, "Propeller-Rotor Whirl Flutter: A State-of-the-Art Review," *Journal of Sound and Vibration*, Vol. 4, No. 3, Nov. 1966, pp. 526-544.

[10] Reed, W.H., III, "Review of Propeller-Rotor Whirl Flutter," NASA TR R-264, 1967.

[11] Hall, W.E., Jr., "Prop-Rotor Stability at High Advance Ratios," *Journal of the American Helicopter Society*, Vol. 11, No. 2, April 1966, pp. 11-26.

[12] Tiller, F.E., Jr., and Nicholson, R., "Stability and Control Considerations for a Tilt-Fold-Proprotor Aircraft," *Journal of the American Helicopter Society*, Vol. 16, No. 3, July 1971, pp. 23-33.

[13] Young, M.I., and Lytwyn, R.T., "The Influence of Blade Flapping Restraint on the Dynamic Stability of Low Disk Loading Propeller-Rotors," Proceedings of the American Helicopter Society 23rd Annual Forum, Washington, D.C., May 1967, pp. 38-54.

[14] Wernicke, K.G., "Tilt Proprotor Composite Aircraft, Design State of the Art," *Journal of the American Helicopter Society*, Vol. 14, No. 2, April 1969, pp. 10-25.

Reproduced with permission of the copyright owner. Further reproduction prohibited without permission.

[15] Wernicke, K.G., and Gaffey, T.M., "Review and Discussion of The Influence of Blade Flapping Restraint on the Dynamic Stability of Low Disk Loading Propeller-Rotors," Proceedings of the American Helicopter Society 23rd Annual Forum, Washington, D.C., May 1967, pp. 55-60.

[16] Wernicke, K.G., and Edenborough, H.K., "Full-Scale Proprotor Development," *Journal of the American Helicopter Society*, Vol. 17, No. 1, Jan 1970, pp. 31-40.

[17] Edenborough, H.K., "Investigation of Tilt-Rotor VTOL Aircraft Rotor-Pylon Stability," *Journal of Aircraft*, Vol. 5, No. 6, March-April 1968.

[18] Edenborough, H.K., Gaffey, T.M., and Weiberg, J.A., "Analysis and Tests Confirm Design of Proprotor Aircraft," AIAA Paper 72-803, 1972.

[19] Marr, R.L., and Neal, G.T., "Assessment of Model Testing of a Tilt-Proprotor VTOL Aircraft," Mideast Region Symposium, American Helicopter Society, Philadelphia, Pennsylvania, Oct. 26-27, 1972.

[20] Sambell, K.W., "Proprotor Short-Haul Aircraft - STOL and VTOL," *Journal of Aircraft*, Vol. 9, No. 10, Oct. 1972, pp. 744-750.

[21] DeTore, J.A., and Gaffey, T.M., "The Stopped-Rotor Variant of the Proprotor VTOL Aircraft," *Journal of the American Helicopter Society*, Vol. 15, No. 3, July 1970, pp. 45-56.

[22] Koenig, D.G., Grief, R.H., and Kelly, M.W., "Full Scale Wind Tunnel Investigation of the Longitudinal Characteristics of a Tilting-Rotor Convertiplane,"

Reproduced with permission of the copyright owner. Further reproduction prohibited without permission.

NASA TN D-35, 1959.

[23] Deckert, W.H., and Ferry, R.C., "Limited Flight Evaluation of the XV-3 Aircraft," Air Force Flight Test Center, TR-60-4, May 1960.

[24] Houbolt, J.C., and Reed, W.H, III, "Propeller-Nacelle Whirl Flutter," *Journal of Aerospace Science*, Vol. 29, No. 3, March 1962, pp. 333-346.

[25] DeLarm, L., "Whirl Flutter and Divergence Aspects of Tilt-Wing and Tilt-Rotor Aircraft," U.S. Air Force V/STOL Technology Planning Conference, Las Vegas, Nevada, September 1969.

[26] Magee, J.P., Maisel, M.D., and Davenport, F.H., "The Design and Performance Prediction of Propeller/Rotors for VTOL Applications," Paper No. 325, Presented at the 25th Annual Forum of the American Helicopter Society, Washington, D.C., May 14-16, 1969.

[27] Magee, J.P., and Pruyn, R.R., "Prediction of the Stability Derivatives of Large Flexible Prop/Rotors by a Simplified Analysis," Presented at the 26th Annual Forum of the American Helicopter Society, Washington, D.C., June 1970.

[28] Baird, E.F., Bauer, E.M., and Kohn, J.S., "Model Tests and Analyses of Prop-Rotor Dynamics for Tilt-Rotor Aircraft," Mideast Region Symposium of the American Helicopter Society, Philadelphia, Pennsylvania, Oct. 1972.

[29] Magee, J.P., and Alexander, H.R., "Wind Tunnel Tests of a Full Scale Hingeless Prop/Rotor Designed for the Boeing Model 222 Tilt Rotor Aircraft,"

Reproduced with permission of the copyright owner. Further reproduction prohibited without permission.

NASA CR 114664, Boeing Vertol Co., Oct. 1973.

[30] "Advancement of Proprotor Technology Task II - Wind Tunnel Test Results," NASA CR-114363, Bell Helicopter Co., Sept. 1971.

[31] "V/STOL Tilt-Rotor Aircraft Study Volume II - Preliminary Design of Research Aircraft," NASA CR-114438, Boeing Vertol Co., March 1972.

[32] Kaza, K.R., "Effect of Steady State Coning Angle and Damping on Whirl Flutter Stability," *Journal of Aircraft*, Vol. 10, No. 11, Nov. 1973, pp. 664-669.

[33] Yen, J.C., Weber, G.E., and Gaffey, T.M., "A Study of Folding Proprotor VTOL Aircraft Dynamics," AFFDL-TR-71-7, Vol. 1, Bell Helicopter Co., Sept. 1971.

[34] Alexander, H.R., Amos, A.K., Tarzanin, F.J., and Taylor, R.B., "V/STOL Dynamics and Aeroelastic Rotor-Airframe Technology," AFFDL-TR-72-40, Vol. 2, Sept. 1972, Boeing Vertol Co.

[35] Kvaternik, R.G., "Studies in Tilt-Rotor VTOL Aircraft Aeroelasticity," Ph.D. Dissertation, Case Western Reserve University, 1973.

[36] Kvaternik, R.G., "Experimental and Analytical Studies in Tilt-Rotor Aeroelasticity," Presented at the AHS/NASA Ames Specialists' Meeting on Rotorcraft Dynamics, Moffett Field, California, February 1974.

[37] Kvaternik, R.G., "A Review of Some Tilt-Rotor Aeroelastic Research at NASA Langley," *Journal of Aircraft*, Vol. 13, No. 5, May 1976, pp. 357-363.

Reproduced with permission of the copyright owner. Further reproduction prohibited without permission.

[38] Johnson, W., "Dynamics of Tilting Proprotor Aircraft in Cruise Flight," NASA TN D-7677, May 1974.

[39] Nixon, M.W., "Aeroelastic Response and Stability of Tiltrotors with Elastically Coupled Composite Rotor Blades," Ph.D. Dissertation, University of Maryland, College Park, 1993.

[40] Houbolt, J.C., and Brooks, G.W., "Differential Equations of Motion for Combined Flapwise Bending, Chordwise Bending, and Torsion of Twisted Nonuniform Rotor Blades," NACA Report 1346, 1958.

[41] Hodges, D.H., and Ormiston, R.A., "Nonlinear Equations for Bending of Rotating Beams with Application to Linear Flap-Lag Stability," NASA TM X-2770, May 1973.

[42] Hodges, D.H., and Dowell, E.H., "Nonlinear Equations of Motion for the Elastic Bending and Torsion of Twisted Nonuniform Rotor Blades," NASA TN D-7818, 1974.

[43] Rosen, A., and Friedmann, P.P., "Nonlinear Equations of Equilibrium for Elastic Helicopter or Wind Turbine Blades Undergoing Moderate Deformation," Report UCLA-ENG 7718, University of California at Los Angeles, June, 1977 (also, NASA CR-159478, 1978).

[44] Johnson, W., "Aeroelastic Analysis for Rotorcraft in Flight or in a Wind Tunnel," NASA TN D-8515, 1977.

Reproduced with permission of the copyright owner. Further reproduction prohibited without permission.

[45] Coleman, R.P., and Feingold, A.M., "Theory of Self-Excited Mechanical Oscillations of Helicopter Rotors With Hinged Blades," NACA Rep. 1351, 1958.

[46] Kaza, K.R., and Kvaternik, R.G., "Nonlinear Aeroelastic Equations for Combined Flapwise Bending, Chordwise Bending, Torsion and Extension of Twisted, Nonuniform Rotor Blades in Forward Flight," NASA TM 74059, 1977.

[47] Wernicke, K.G., "The Tiltrotor: Better for VTOL Than the Tilt-Wing," Bell Helicopter Textron Report, Fort Worth, Texas, January 1990.

[48] Johnson, W., " A Comprehensive Analytical Model of Rotorcraft Aerodynamics and Dynamics," Johnson Aeronautics, Palo Alto, California, 1988.

[49] Johnson, W., "An Assessment of the Capability to Calculate Tilting Proprotor Aircraft Performance, Loads, and Stability," NASA TP-2291, 1984.

[50] Popelka, D., Sheffler, M., and Bilger, J., "Correlation of stability test results and analysis for the 1/5 Scale V-22 Aeroelastic Model," Proceedings of the 41st Annual Forum of the American Helicopter Society, Fort Worth, Texas, May 1985.

[51] Settle, T.B., and Kidd, D.L., "Evolution and Test History of the V-22 0.2-Scale Aeroelastic Model," Presented at the American Helicopter Society National Specialists' Meeting on Rotorcraft Dynamics, Arlington, Texas, Nov. 1989.

Reproduced with permission of the copyright owner. Further reproduction prohibited without permission.

[52] Johnson, W., "Recent Developments in the Dynamics of Advanced Rotor Systems," NASA TM 86669, March 1985.

[53] Bilger, J.M., Marr, R.L., and Zahedi, A., "Results of Structural Dynamic Testing of the XV-15 Tilt Rotor Research Aircraft, *Journal of the American Helicopter Society*, Vol. 27, No. 2, April 1982.

[54] McVeigh, M.A., Rosenstein, H.J., and McHugh, F.J., " Aerodynamic Design of the XV-15 Advanced Composite Tiltrotor Blade," Presented at the 39th Annual Forum of the American Helicopter Society, St. Louis, Missouri, May 1983.

[55] Farrell, M.K., "Aerodynamic Design of the V-22 Osprey Proprotor," Presented at the 45th Annual Forum of the American Helicopter Society, Boston, Massachusetts, May 1989.

[56] Felker, F.F., "A Review of Tilt Rotor Download Research," Proceedings of the 14th European Rotorcraft Forum, Milano, Italy, September 1988.

[57] "V/STOL Tilt-Rotor Study Task II - Research Aircraft Design," NASA CR-114442, Bell Helicopter Co., March 1972.

[58] Johnson, W., "Optimum Control Alleviation of Tilting Proprotor Gust Response," *Journal of Aircraft*, Vol. 14, No. 3, March 1977, pp. 301-308.

[59] Huston, R.J., Golub, R.A., and Yu, J.C., "Noise Considerations for Tiltrotors," Presented at the AIAA/ASME/SAE/ASEE 25th Joint Propulsion Conference, Monterey, California, July 1989.

Reproduced with permission of the copyright owner. Further reproduction prohibited without permission.

[60] Edwards, B.D., "External Noise of the XV-15 Tiltrotor Aircraft," NASA Contractor Report 187463, May 1991.

[61] Abbott, F.T., Jr., Kelly, H.N., and Hampton, K.D., "Investigation of a 1/8-size Dynamic Aeroelastic Model of the Lockheed Electra Airplane in the Langley Transonic Dynamics Tunnel," NASA TM SX-456, November 1960.

[62] Taylor, E.S., and Browne, K.A., "Vibration Isolation of Aircraft Power Plants," *Journal of the Aeronautical Sciences*, Vol. 6, Dec. 1938, pp. 43-49.

[63] Johnson, W., "Analytical modeling requirements for Tilting Proprotor Aircraft Dynamics," NASA TN D-8013, 1975.

[64] Johnson, W., "Analytical Model for Tilting Proprotor Aircraft Dynamics, Including Blade Torsion and Coupled Bending Modes, and Conversion Mode Operation," NASA TM X-62,369, August 1974.

[65] Johnson, W., "The Influence of Engine/ Transmission/ Governor on Tilting Proprotor Aircraft Dynamics, NASA TM X-62455, June 1975.

[66] Johnson, W., Lau, B.H., and Bowles, J.V., "Calculated performance, Stability, and Maneuverability of High Speed Tilting Proprotor Aircraft," *Vertica*, Vol. 11, No. 1/2, pp. 317-339, 1987.

[67] Kottapalli, S., and Meza, V., "Analytical Aeroelastic Stability Considerations and Conversion Loads for an XV-15 Tilt-Rotor in a Wind Tunnel Simulation," AIAA Paper No. 92-2258, Presented at the 33rd Structures, Structural Dynamics and Materials Conference, Dallas, Texas, April 1992.

Reproduced with permission of the copyright owner. Further reproduction prohibited without permission.

[68] Nixon, M.W., "Extension-Twist Coupling of Composite Circular Tubes with Application to Tiltrotor Blade Design," Proceedings of the AIAA/ASME/ASCE/AHS 28th Structures, Structural Dynamics and Materials Conference, AIAA Paper No. 87-0772, Monterrey, California, April 1987.

[69] Bauchau, O.A., Loewy, R.G., and Bryan, P.S., "An Approach to Ideal Twist Distribution in Tilt-Rotor VTOL Blade Designs," RTC Report No. D-86-2, Rensselaer Polytechnic Institute, Troy, New York, July 1986.

[70] "University of Maryland Advanced Rotorcraft Code (UMARC)," Theory Manual, Center for Rotorcraft Education and Research, University of Maryland, College Park, MD, July 1994.

[71] Nasu, K., "Tilt-Rotor Flutter Control in Cruise Flight," NASA TM 88315, December 1986.

[72] Vorwald, J.G., and Chopra, I., "Stabilizing Pylon Whirl Flutter on a Tilt-Rotor Aircraft," Presented at the 32nd AIAA/ASME/ASCE/AHS/ASC Structures, Structural Dynamics, and Materials Conference, Baltimore, Maryland, April 8-10, 1991.

[73] "XV-15 Full Scale Test Data Correlation Report," *Bell-Boeing* Report No. 901-909-003, Joint Project Office, Fort Worth, Texas, Nov. 1985.

[74] Desopper, A., "Study of Unsteady Transonic Flow on Rotor Blades with Different Tip Shapes," *Vertica*, Vol. 9, No. 3, July 1985.

Reproduced with permission of the copyright owner. Further reproduction prohibited without permission.

[75] Philippe, J.J., and Vuillet, A., "Aerodynamic Designs of Advanced Rotors with New Tip Shapes," Presented at the 39th Annual Forum of the American Helicopter Society, St. Louis, Missouri, May 1983.

[76] Tarzanin, F.J., and Vlaminck, R.R., "Investigation of the Effects of Blade Sweep on Rotor Vibratory Loads," NASA CR-166526, Oct. 1983.

[77] Celi, R., and Friedmann, P.P., "Aeroelastic Modeling of Swept Tip Rotor Blades Using Finite Elements," *Journal of the American Helicopter Society*, Vol. 33, No. 2, April 1988, pp. 43-52.

[78] Benquet, P., and Chopra, I., "Calculated Dynamic Response and Loads for an Advanced Tip Rotor in Forward Flight," Proceedings of the 15th European Rotorcraft Forum, Amsterdam, Netherlands, Sept. 1989.

[79] Panda, B., "Assembly of Moderate-Rotation Finite Elements Used in Helicopter Rotor Dynamics," Technical Note, *Journal of the American Helicopter Society*, Vol. 32, No. 4, Oct. 1987, pp. 63-69.

[80] Kim, K.C., and Chopra, I., "Aeroelastic Analysis of Swept, Anhedral, and Tapered Tip Rotor Blades," *Journal of the American Helicopter Society*, Vol. 37, No. 1, Jan. 1992, pp. 15-30.

[81] Yuan, K.A., Friedmann, P.P., and Venkatesan, C., "A New Aeroelastic Model for Composite Rotor Blades with Straight and Swept Tips," Proceedings of the 33rd AIAA/ ASME/ ASCE/ AHS/ ASC Structures, Structural Dynamics and Materials Conference, Dallas, Texas, April 1992.

Reproduced with permission of the copyright owner. Further reproduction prohibited without permission.

[82] Yuan, K.A., Friedmann, P.P., and Venkatesan, C., "Aeroelastic Behavior of Composite Rotor Blades with Swept Tips," Proceedings of the 48th Annual Forum of the American Helicopter Society, Vol. 2, Washington, D.C., June 3-5, 1992.

[83] Kosmatka, J.B., and Friedmann, P.P., "Vibration Analysis of Composite Turbopropellers Using a Nonlinear Beam-Type Finite Element Approach," *AIAA Journal*, Vol. 27, No. 11, Nov. 1989.

[84] Bir, G.S., and Chopra, I., "Aeromechanical Stability of Rotorcraft with Advanced Geometry Blades," Proceedings of the 34th AIAA/ ASME/ ASCE/ AHS/ ASC Structures, Structural Dynamics, and Materials Conference, La-Jolla, CA, April 1993.

[85] Bauchau, O.A., and Kang, N.K., "A Multibody Formulation for Helicopter Structural Dynamic Analysis," *Journal of the American Helicopter Society*, Vol. 38, No. 2, April 1993, pp. 3-14.

[86] Kondoh, K., Tanaka, K., and Atluri, S.N., "An Explicit Expression for the Tangent Stiffness of a Finitely Deformed 3-D Beam and Its Use in the Analysis of Space Frames," *Computers and Structures*, Vol. 24, 1986.

[87] Celi, R., and Friedmann, P.P., "Structural Optimization with Aeroelastic Constraints of Rotor Blades with Straight and Swept Tips," *AIAA Journal*, Vol. 28, No. 5, May 1990, pp. 928-945.

[88] Friedmann, P.P., Venkatesan, C., and Yuan, K.A., "Development of a Struc-

Reproduced with permission of the copyright owner. Further reproduction prohibited without permission.

tural Optimization Capability for the Aeroelastic Tailoring of Composite Rotor Blades with Straight and Swept Tips," Presented at the 4th AIAA Symposium on Multidisciplinary Analysis and Optimization, Cleveland, Ohio, Sept. 1992.

[89] Ganguli, R., "Aeroelastic Optimization of Advanced Geometry and Composite Helicopter Rotors," Ph.D. Dissertation, University of Maryland, College Park, 1994.

[90] Ganguli, R., and Chopra, I., "Aeroelastic Optimization of an Advanced Geometry Helicopter Rotor," Proceedings of the 33rd AIAA/ ASME/ ASCE/ AHS/ ASC Structures, Structural Dynamics and Materials Conference, Dallas, Texas, April 1992.

[91] Hodges, R.V., Nixon, M.W., and Rehfield, L.W., "Comparison of Composite Rotor Blade Models - A Coupled-Beam Analysis and an MSC/NASTRAN Finite-Element Model," NASA TM 89024, 1987.

[92] Gessow, A., and Myers, G.C., Jr., "Aerodynamics of the Helicopter," College Park Press, College Park, MD, 1985.

[93] Bagai, A., and Leishman, J.G., "Rotor Free-Wake Modeling using a Pseudo-Implicit Relaxation Algorithm," AIAA Paper No. 94-1918, AIAA 12th Applied Aerodynamics Conference, Colorado Springs, Colorado, June 1994.

[94] Srinivas, V., "The UM Free-Wake Analysis in UMARC," UM-AERO Report No. 95-26, Department of Aerospace Engineering, University of Maryland,

Reproduced with permission of the copyright owner. Further reproduction prohibited without permission.

College Park, Maryland, July 1995.

[95] Panda, B., and Chopra, I., "Dynamics of Composite Rotor Blades in Forward Flight," *Vertica*, Vol. 11, No. 1/2, Jan. 1987, pp. 187-209.

[96] McLarty, T.T., *et al.*, "Rotorcraft Flight Simulation Program C81 with Coupled Rotor Aeroelastic Stability Analysis," USAAMRDL TR76-41A, Engineers Manual, May 1977.

[97] Van Gaasbeek, J.R., "Rotorcraft Flight Simulation Computer Program C81 with Datamap Interface," USAAVRADCOM TR-80-D-38A, Users Manual, October 1981.

Reproduced with permission of the copyright owner. Further reproduction prohibited without permission.